



I. R. IRAN

ISSN: 1728-144X

e-ISSN: 1735-9244



International Journal of Engineering

Journal Homepage: www.ije.ir



TRANSACTIONS B: APPLICATIONS

Volume 37, Number 05, May 2024

Materials and Energy Research Center

INTERNATIONAL JOURNAL OF ENGINEERING

Transactions B: Applications

DIRECTOR-IN-CHARGE

H. Omidvar

EDITOR IN CHIEF

G. D. Najafpour

ASSOCIATE EDITOR

A. Haerian

EDITORIAL BOARD

- | | | | |
|------|--|-------|--|
| S.B. | Adeloju, Charles Sturt University, Wagga, Australia | A. | Mahmoudi, Bu-Ali Sina University, Hamedan, Iran |
| K. | Badie, Iran Telecomm. Research Center, Tehran, Iran | O.P. | Malik, University of Calgary, Alberta, Canada |
| M. | Balaban, Massachusetts Ins. of Technology (MIT), USA | G.D. | Najafpour, Babol Noshirvani Univ. of Tech., Babol, Iran |
| M. | Bodaghi, Nottingham Trent University, Nottingham, UK | F. | Nateghi-A, Int. Ins. Earthquake Eng. Seis., Tehran, Iran |
| E. | Clausen, Univ. of Arkansas, North Carolina, USA | S. E. | Oh, Kangwon National University, Korea |
| W.R. | Daud, University Kebangsaan Malaysia, Selangor, Malaysia | M. | Osanloo, Amirkabir Univ. of Tech., Tehran, Iran |
| M. | Ehsan, Sharif University of Technology, Tehran, Iran | M. | Pazouki, MERC, Karaj, Iran |
| J. | Faiz, Univ. of Tehran, Tehran, Iran | J. | Rashed-Mohassel, Univ. of Tehran, Tehran, Iran |
| H. | Farrahi, Sharif University of Technology, Tehran, Iran | S. K. | Sadrnezhaad, Sharif Univ. of Tech, Tehran, Iran |
| K. | Firoozbakhsh, Sharif Univ. of Technology, Tehran, Iran | R. | Sahraeian, Shahed University, Tehran, Iran |
| A. | Haerian, Sajad Univ., Mashhad, Iran | A. | Shokuhfar, K. N. Toosi Univ. of Tech., Tehran, Iran |
| H. | Hassanpour, Shahrood Univ. of Tech., Shahrood, Iran | R. | Tavakkoli-Moghaddam, Univ. of Tehran, Tehran, Iran |
| W. | Hogland, Linnaeus Univ, Kalmar Sweden | T. | Teng, Univ. Sains Malaysia, Gelugor, Malaysia |
| A.F. | Ismail, Univ. Tech. Malaysia, Skudai, Malaysia | P. | Tiong, Nanyang Technological University, Singapore |
| M. | Jain, University of Nebraska Medical Center, Omaha, USA | X. | Wang, Deakin University, Geelong VIC 3217, Australia |
| M. | Keyanpour rad, Materials and Energy Research Center, Karaj, Iran | H. | Omidvar, Amirkabir Univ. of Tech., Tehran, Iran |

EDITORIAL ADVISORY BOARD

- | | | | |
|-------|--|-------|---|
| S. T. | Akhavan-Niaki, Sharif Univ. of Tech., Tehran, Iran | A. | Kheyroddin, Semnan Univ., Semnan, Iran |
| M. | Amidpour, K. N. Toosi Univ of Tech., Tehran, Iran | N. | Latifi, Mississippi State Univ., Mississippi State, USA |
| M. | Azadi, Semnan university, Semnan, Iran | H. | Oraee, Sharif Univ. of Tech., Tehran, Iran |
| M. | Azadi, Semnan University, Semnan, Iran | S. M. | Seyed-Hosseini, Iran Univ. of Sc. & Tech., Tehran, Iran |
| F. | Behnamfar, Isfahan University of Technology, Isfahan | M. T. | Shervani-Tabar, Tabriz Univ., Tabriz, Iran |
| R. | Dutta, Sharda University, India | E. | Shirani, Isfahan Univ. of Tech., Isfahan, Iran |
| M. | Eslami, Amirkabir Univ. of Technology, Tehran, Iran | A. | Siadat, Arts et Métiers, France |
| H. | Hamidi, K.N.Toosi Univ. of Technology, Tehran, Iran | C. | Triki, Hamad Bin Khalifa Univ., Doha, Qatar |
| S. | Jafarmadar, Urmia Univ., Urmia, Iran | | |

TECHNICAL STAFF

M. Khavarpour; M. Mohammadi; V. H. Bazzaz, R. Esfandiar; T. Ebadi

DISCLAIMER

The publication of papers in International Journal of Engineering does not imply that the editorial board, reviewers or publisher accept, approve or endorse the data and conclusions of authors.

International Journal of Engineering *Transactions A: Basics* (ISSN 1728-1431) (EISSN 1735-9244)

International Journal of Engineering *Transactions B: Applications* (ISSN 1728-144X) (EISSN 1735-9244)

International Journal of Engineering *Transactions C: Aspects* (ISSN 2423-7167) (EISSN 1735-9244)

Web Sites: www.ije.ir & www.ijeir.info E-mails: ije.editor8@gmail.com, Tel: (+9821) 88771578, Fax: (+9821) 88773352

Materials and Energy Research Center (MERC)

CONTENTS

Transactions B: Applications

I. Mirzadeh, R. Shirinabadi, G. Mohammadi, S. H. Lajevardi	Direct and Indirect Tensile Behavior of Cement-Zeolite-amended Sand Reinforced with Kenaf Fiber	818-832
A. Al-bosham, A. Ebrahimzadeh, A. Bagheri	Optimal Node Selection for Cooperative Spectrum Sensing in Cognitive Radio Sensor Networks with Energy Harvesting	833-841
S. Niknezhad, A. Moazemi Goudarzi, M. Hasan Ghasemi	Design and Evaluation a New Type of Semi-active Lower Limb with Knee Joint Booster	842-851
A. Palaev G., Z. Fuming, T. Yifan	Method for Assessing Damage to Gas Distribution Network Pipelines based on Nonlinear Guided Wave	852-859
F. Nasiri Khamesloo, D. Domiri Ganji	Optimizing Heat Transfer in Microchannel Heat Sinks: A Numerical Investigation with Nanofluids and Modified Geometries	860-875
Z. Esmailzadeh, H. Falaghi, M. Ramezani	Risk-Based AC/DC Hybrid Distribution System Planning	876-886
S. Howldar, B. Balaji, K. Srinivasa Rao	Investigation and Analysis of Dual Metal Gate Overlap on Drain Side Tunneling Field Effect Transistor with Spacer in 10nm Node	887-895
G. F. Baimukhametov, A. V. Dengaev, E. U. Safiullina, A. A. Kayumov, I. M. Drozdov, V. V. Shishulin, A. Boushra, A. V. Vakhin, B. V. Sargin, M. S. Sidibe	Relaxation Process in Crude Oil after Ultrasonic Treatment	896-903
Y. Rozhkova, A. Lekomtsev, V. Lisin, V. Poilov, E. Safiullina, D. Efremenko, A. Dengaev, W. Kang, Z. Li, H. Yang	Comprehensive Review of Demulsifiers based on Magnetic Nanoparticles for Oil-water and Water-oil Separation	904-919
A. M. Rathod, N. P. Gulhane, U. M. Siddique	Heat Transfer Augmentation for Impingement of Steady Air Jet under Exponential Heat Flux Boundary Condition	920-930

U. Jureje, M. W. Tjaronge, M. A. Caronge	Basic Engineering Properties of Concrete with Refractory Brick as Coarse Aggregate: Compressive Stress-Time Relationship Assessment	931-940
A. Fallahi, A. Pourghazi, H. Mokhtari	A Multi-product Humanitarian Supply Chain Network Design Problem: A Fuzzy Multi-objective and Robust Optimization Approach	941-958
M. Mohammadzadeh, M. Navabakhsh, A. Hafezalkotob	Performance Evaluating Energy, Economic and Environmental Performance with an Integrated Approach of Data Envelopment Analysis and Game Theory	959-973
H. Raad Shaker, W. AlSaraj, L. A. AL-Jaberi	Behavior of Reinforced Geopolymer Concrete Beams under Repeated Load	974-983
A. Muis, S. Sunardi, A. Yudhana	CNN-based Approach for Enhancing Brain Tumor Image Classification Accuracy	984-996
A. Ranjith, M. K. Yashwanth, B. M. Kiran, V. R. Ananda	Machine Learning Models for Mechanical and Micro Structural Properties of Recycled Fine Aggregate Concrete Using Different Mixing Approaches	997-1011
F. Firouzi, S. K. Sadrnezhaad	Thermodynamic Simulation of an Efficient Flash Ironmaking Technology for Chadormalu Mining and Industrial Company	1012-1021
E. Sahragard, H. Farsi, S. Mohamadzadeh	Semantic Segmentation of Aerial Imagery: A Novel Approach Leveraging Hierarchical Multi-scale Features and Channel-based Attention for Drone Applications	1022-1035
M. Abdollahi, J. Bolouri Bazaz, A. Akhtarpour	Cyclic and Monotonic Behavior of Non-plastic Silts with the Presence of Initial Static Shear Stress Using Strain Energy Approach: A Case Study for a Tailings Dam	1036-1049



Direct and Indirect Tensile Behavior of Cement-Zeolite-amended Sand Reinforced with Kenaf Fiber

I. Mirzadeh^a, R. Shirinabadi^{*b,c}, G. Mohammadi^b, S. H. Lajevardi^d

^a Department of Civil Engineering, South Tehran Branch, Islamic Azad University, Tehran, Iran

^b Department of Petroleum and Mining Engineering, South Tehran Branch, Islamic Azad University, Tehran, Iran

^c Research Center for Modeling and Optimization in Science and Engineering, South Tehran Branch, Islamic Azad University, Tehran, Iran

^d Department of Civil Engineering, Arak Branch, Islamic Azad University, Arak, Iran

PAPER INFO

Paper history:

Received 22 June 2023

Received in revised form 15 December 2023

Accepted 26 December 2023

Keywords:

Sand

Cement

Zeolite

Kenaf Fiber

Compaction

Direct Tensile Strength

Indirect Tensile Strength

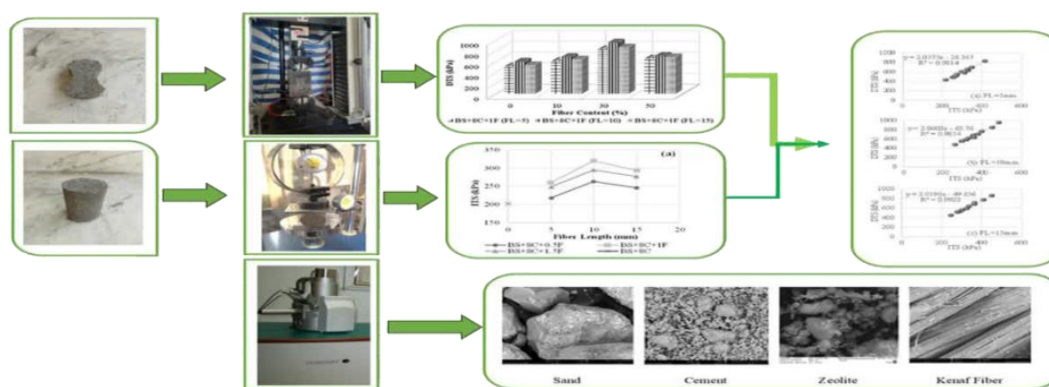
Micro-structural Analysis

ABSTRACT

Dealing with problematic soils is one of the most challenging parts of geotechnical engineers' careers. Loose sand is one of them due to its low cohesion and can be found worldwide, specifically in coastal regions. Chemical stabilizers like cement are of the prevalent ones among engineers to deal with the weaknesses of loose sand. However, the substitution of these traditional stabilizers with pozzolanic materials like natural zeolite become approved since it helps reduce cement consumption and hence, lower CO₂ emission. Despite all advantages, brittle behavior is an unwelcome consequence of these stabilizers. Therefore, the aim of this study is to reduce the brittleness of the cement-zeolite-stabilized sand employing natural kenaf fibers. To this end, two cement contents, four amounts of zeolite replacement of cement, and three fiber contents in three lengths were adapted in two relative compactions (RC) to investigate the compaction, 8-shape direct tensile strength (DTS), and indirect tensile strength (ITS) behaviors. Experimental efforts revealed that compaction behavior is sensitive to stabilizer contents and fiber content and length. The addition of the 8% cement, increase of the zeolite up to 50%, and fiber increment up to 1.5% led to the reduction of the compaction properties; however, optimum moisture content increased with the rise in kenaf fiber. A notable influence on the DTS and ITS behavior was observed while 30% zeolite replacement in 8%-cemented samples and reinforced with 1% kenaf fiber with 10mm length. Furthermore, a linear relationship was presented between DTS and ITS. In the end, the reinforced sample was analyzed using Scanning Electron Microscope (SEM) images.

doi: 10.5829/ije.2024.37.05b.01

Graphical Abstract



*Corresponding Author Email: R.Shirinabadi@azad.ac.ir (R. Shirinabadi)

1. INTRODUCTION

Due to population growth of many countries, suitable ground for construction is surprisingly decreasing. Therefore, every remaining local weak land may require to be prepared for constructional practices including building foundations, dams, pavements, excavations, and embankments. Loose sand is one of the problematic soils that, due to its poor cohesion, intensively challenges engineers in many regions, especially coastal areas (1, 2). Construction of various types of structures on these soils usually eventuates in different issues such as lack of shear strength, uneven settlements, foundation failures, internal and surface tunneling erosion, and liquefaction (2, 3).

The stabilization of weak soils through the employment of various additives has been implemented for decades (4). The effect of materials such as cement, lime, fly ash, polymers, resins, acids, and ions has been investigated by researchers for years (2). As one of the conventional and most prevalent soil stabilizers, numerous geotechnical researchers have justified cement to hand over many advantages, including higher strength and stiffness, liquefaction resistance, lifespan increment, and curbing deformations (2, 5, 6).

Sariosseiri and Muhunthan (7) investigated the effect of cement on the engineering characteristics of several types of soils (sand, silt, and clay). They declared that addition of cement to the soil incremented the plasticity index (PI) at low cement content (about 2.5%); however, higher percentages of cement reduced that index leading to better workability than the base soil. The optimum water content increased by introducing cement to the soils while the maximum dry unit weight was reduced. Stabilization of these soil with cement highly enhanced the unconfined compression strength (UCS); however, leading to a more brittle failure than the base soils. Nguyen and Phan (8) reported that addition of the 8 to 10% cement notably improved the compressive strength, splitting tensile strength, and elastic modulus of stabilized fine-grade soil. Ghanbari et al. (9) stated that introducing cement to the peat soil developed UCS values, diminished strain related to the peak stress, and induced brittle behavior in the amended samples with the increase in curing time. Eme et al. (10) demonstrated that adding 5.5% cement along with 12% water content to the sand enhanced the California Bearing Ratio (CBR) and UCS of the stabilized samples up to 200% and 2500kPa, respectively.

Nevertheless, the cement production process is responsible for a massive amount of greenhouse gases released into the earth's atmosphere, including mainly carbon dioxide (CO₂), methane (CH₄), and nitrous oxide (N₂O) (11). Such an indication impelled the researchers to look for substitutions like supplementary cementitious materials (SCMs) that remained from industrial

processes, agricultural practices or existed naturally (12-16) with pozzolanic inherent. Natural resources preservation, reduction of the adverse environmental effects of cement production, energy conservation, and also helping waste management are instances of the advantages that the employment of SCMs for cement replacement renders (6). Among those, zeolite as a natural pozzolan notably improves the strength of the cemented soil, reduces undesirable expansion, and decreases the porosity (17). MolaAbasi et al. (18) evaluated the feasibility of employing zeolite as an influential replacement for cement in stabilizing sand. They stated that the replacement of cement with zeolite reduced the UCS of the treated samples in early curing time (7 days). But surprisingly, up to 30% zeolite replacement remarkably enhanced the UCS of the samples in 28 and 90 days of curing time. In another study, MolaAbasi et al. (19) expressed that while 30% zeolite replacement in cemented sand, chemical components of SiO₂ and Al₂O₃ came into a balance with CaO, which resulted in the most desirable pozzolanic reaction, and consequently, the highest UCS and also the tensile strength at 28 days of curing. Kordnaeij et al. (20) evaluated the effect of water on cementitious materials (W/CM) and zeolite replacement on the UCS of the grouted loose sand. They perceived that in all W/CM, up to 30% zeolite replacement was the optimum amount. In an investigation of the cement-zeolite stabilized expansive clay, Ahmadi et al. (11) affirmed that an increase in zeolite replacement of cemented samples led to the decrement and increment of the maximum dry density (MDD) and optimum moisture content (OMC), respectively. They also revealed that raising zeolite replacement up to 30% induced the highest mechanical parameters such as UCS, stiffness (E₅₀), and absorbed energy (AE) in treated samples. Khajeh et al. (21) stated that the incorporation of 30% zeolite replacement satisfyingly compensates the strength reduction caused by employing EPS beads in the cement treatment of loose sand. Another investigation of Khajeh et al. (22) disclosed that the substitution of lime by 25% zeolite resulted in attaining the highest UCS and unconsolidated undrained (UU) triaxial strength, and also the least PI of an amended clayey soil.

Considering the remarkable effectiveness of these cementitious materials on soils' geotechnical properties, they prompt abrupt strength reduction and hence, brittle failure under different types of loadings (23). To ameliorate the deficiencies of those additives, randomly distributed fibers have been investigated by researchers widely in the last several decades. It has been observed that syntactic or natural fiber-reinforced soils demonstrate more desirable engineering behavior like compressive, shear, tensile, strength, California Bearing Ratio (CBR), resistance against wet-dry and freeze-thaw

cycles, decreasing the swelling potential, and more importantly, failure strain and flexural performance than unreinforced soils (3, 24-26). Since the production of synthetic fibers induces unfavorable effects on the environment, a promising prospect for pollution decrement is achievable through the adoption of natural fibers (27). These fibers represent acceptable reinforcing influence in addition to their biodegradability and economic availability (26).

Kenaf fiber, as one of the non-wood plant fibers, can be a possible choice for engineers as a reinforcement element of cemented mixtures giving out remarkable tensile strength, Young's modulus, and economical cost. Several investigations have been implemented on the influence of kenaf fiber addition on the engineering properties of different types of soils. Shirvani et al. (28) investigated the influence of the kenaf fiber and clay addition on the mechanical characteristics of sandy soil. Direct shear tests were implemented on the sand samples reinforced with different fiber content and clay. The results showed that 0.75% fiber inclusion with no clay content in the reinforced sample increased the fraction angle by about 13%. In addition, the sample containing 0.75% fiber and 15% clay additive showed a 15% cohesion improvement. Ghadakpour et al. (3) investigated the effect of kenaf fiber content and length on the geotechnical properties of cemented sand samples. The results evaluation indicated that the kenaf fiber reinforcement of cemented sand incremented the UCS, STS, absorbed energy, and reduced the brittle index, elasticity modulus, and ultrasonic pulse velocity.

In the current investigation, the influence of randomly distributed kenaf fiber on the mechanical behavior of cement-zeolite-stabilized sand was evaluated. To that end, standard proctor compaction tests were implemented on designated mixtures of 0%, and 8% cement, replacing cement with 0, 10, 30, and 50% zeolite, the addition of the kenaf fiber in 0, 0.5, 1, and 1.5% with the length of 0.5, 1 and 1.5mm. After that, to analyze the effect of kenaf content and length in the reinforcement effort, 8-shape DTS and ITS experiments were conducted on the samples prepared due to the designed mixtures mentioned earlier and the two relative compaction of 100% and 95%, cured for 28 days.

2. MATERIALS METHOD

2.1. Materials

The base soil (BS) used in this investigation program was a poorly-graded sand (SP) according to the United Soil Classification System (29) collected from the southern coastal regain of the Caspian Sea, Iran. The soil's physical characteristics were measured as presented in Table 1. The particle size distribution of the base sand can be seen in Figure 1.

The base stabilizer of this research opted to be the

TABLE 1. Specification of materials utilized in this study

Soil			
Maximum Unit Weight	1.58 kN/m ³	Minimum unit weight	1.27 kN/m ³
Uniformity Coefficient (C _u)	4.99	Mean Effective Diameter (D ₆₀)	2.18 mm
G _s	2.67	Coefficient of Curvature (C _c)	0.99
Cement			
G _s	3.11	Blaine	≥ 2800 (cm ² /g)
Autoclave Expansion	≤ 0.6 (%)	Initial Setting Time	≥ 120 min
Final Setting Time	3:30 (hr)		
Zeolite			
G _s	2.2		
Kenaf Fiber			
G _s	1.32	Diameter	0.1<d<0.14 mm
Water Absorption	≤ 2.2% by weight	Tensile Strength	365 MPa
Modulus of Elasticity	17.6 GPa		

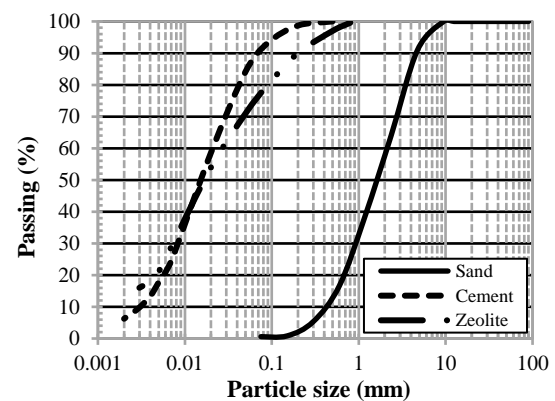


Figure 1. Particle size analysis of the base sand

Portland cement type II. The cement's physical properties were presented by its production factory as demonstrated in Table 1.

The alternative stabilizer of this study was natural zeolite. The employed zeolite is a clinoptilolite type acquired from Semnan Province, Iran. It is a non-plastic material that in accordance with the Unified Soil Classification System (29), is classified as silt (ML) and its specific gravity (G_s) is presented in Table 1. Figure 1 illustrates the particle size analysis results of all three materials utilized in this research. The graphs were obtained in accordance with ASTM D422 (30).

The reinforcement element of the soil-stabilizer mixtures was determined to be the kenaf fiber. The utilized kenaf fibers had physical properties as presented in Table 1. The fibers were cut in three lengths of 5, 10, and 15 mm to be used for sample preparation.

2. 2. Sample Preparation

To conduct experiments, 179 stabilized and reinforced cylindrical samples and 179 8-shaped ones were prepared for the DTS and ITS tests, respectively. The presented values are the average of two measurements. Two percentages of cement ($C= 0$ and 8%) were adopted as the base stabilizer, and four percentages of cement replacement with zeolite ($Z= 0, 10, 30,$ and 50%) were employed as the pozzolanic alternative to substitute the cement. Kenaf fiber was randomly distributed to the samples in four percentages ($F= 0, 0.5, 1,$ and 1.5%) with three lengths ($L= 0.5, 1,$ and 1.5 mm).

All samples were prepared using the maximum dry density (MDD) and the optimum moisture content (OMC) achieved from the standard proctor compaction test of each designated additive content. The soil and stabilizers were mixed homogeneously, and then the water was added to the soil-stabilizer matrix. After blending the fiber with the mixture, 8-shape DTS samples were cast in an 8-shape metal mold with a thickness of 2.8cm, widest width of 4cm at both sides, middle width of 3cm, and length of 9cm. The ITS samples were also prepared in cylindrical PVC mold with a height of 10 cm a diameter of 5 cm, compacted in three equal layers using a steel rod for the target relative compaction of 95 and 100%. The top of each layer was sacrificed in order to prepare sufficient interlock between the layers. Afterward, samples were cured in sealed plastic bags for 28 at room temperature (21-24°C) to evaluate the effect of a long curing period on the pozzolanic reaction.

2. 3. Experimental Procedure

A series of various tests were implemented to evaluate the effect of different dosages of stabilizers and reinforcement elements on the geotechnical properties of the sandy soil. Standard proctor compaction tests were conducted according to ASTM D698 (31) to obtain the MDD and OMC of the soil-additive mixtures. Afterward, DTS tests were implemented on 8-shape samples in accordance with the reported data by Yao et al. (25). Figure 2a illustrates the direct tensile loading device used in this study. The ITS tests were carried out following ASTM D3967 (32). To do so, the cylindrical samples were positioned horizontally between two hard metal plates, and the load was applied until failure. Both types of loads were applied to the samples at the rate of 0.1mm/min. According to the mentioned standard, the ITS can be calculated as presented below:

$$q_t = \frac{2P}{\pi LD} \quad (1)$$

where $q_t = ITS$ (kPa), $P =$ applied load at failure (kN), $L =$ height of the cylindrical sample (m), and $D =$ diameter of the sample (m). Figure 2(b) demonstrates the loading instrument employed for ITS tests.

Table 2 presented in the following demonstrates the nomenclature used in the figures of this article.

3. RESULTS AND DISCUSSION

3. 1. Compaction Tests

To achieve the compaction characteristics of the soil-stabilizer-fiber mixtures, 54 standard proctor compaction tests were implemented on each designed combination. Figures 3, 4, and 5 demonstrate the alteration of MDD and OMC of the samples due to changes in several parameters such as fiber length, fiber content, cement content, and zeolite replacement. It can be deduced from all figures that fiber reinforcement of the base soil and the soil-stabilizer mixtures remarkably reduced the MDD and increased the OMC of the samples.

Figure 3 shows the change in MDD and OMC with respect to the variation of the fiber length and content for base soil, 8% cement-treated sand, and 30% zeolite-replaced-cemented sand as representatives. As shown, it can be perceived that the addition of fiber to the base soil notably decreased the MDD of the sample. Additionally, an increase in fiber content resulted in a severe reduction in MDD. Such an observation is consistent with the investigations of Santoni et al. (33), Tran et al. (34), and Mohamed (35). This behavior is due to the lower unit weight of the fiber than the soil when increment of fiber content reduces the number of soil particles. Nevertheless, such a fiber introduction and content

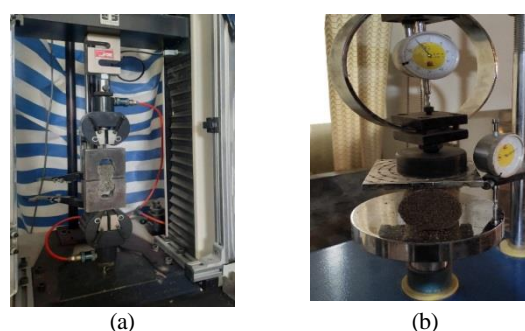


Figure 2. Devices used for (a) DTS, and (b) ITS tests

TABLE 2. The nomenclature used for additives of this study

Parameter	Percentage of Cement Content (%)	Percentage of Zeolite Replacement (%)	Percentage of Fiber Content (%)	length of Fiber (mm)
Abbreviation	C (number)	Z (number)	F (number)	F (number)
Example	C8	Z30	F1.5	F15

increment induced an opposite trend in the OMC of the samples, where it rose as the fiber content incremented. A similar trend is reported by Maity et al. (36) and Tran et al. (34) when reinforcing sand with natural fiber. It can be attributed to the water absorption of fibers. Figure 3 also revealed that the more the fibers' length increased, the more the MDD and OMC of the samples diminished. Prabakar and Sridhar (37) reported the same behavior of using sisal fiber as soil reinforcement. Analogous fashion was observed while adding different fiber percentages to the solely-cemented and also 30%-zeolite replaced samples.

Figure 4 illustrates the variation of MDD and OMC of the samples containing 1% fiber due to the change in fiber length and cement content. Analyzing this figure indicated that introducing 8% cement to the base and enhanced the MDD of the sample while decreasing trend of the OMC was observed. Lopez-querol et al. (38) also declared the same trend. Noteworthy, diminishing trends of MDD and OMC were detected when incrementing fiber lengths in samples with 1% fiber content. Such behaviors also were noticed in samples containing 0.5 and 1.5% fiber.

Figure 5 displays the alteration of the MDD and OMC of the 8%-cemented samples containing 1% fiber respecting the variation of zeolite replacement and fiber length. It can be perceived that in a specific fiber length,

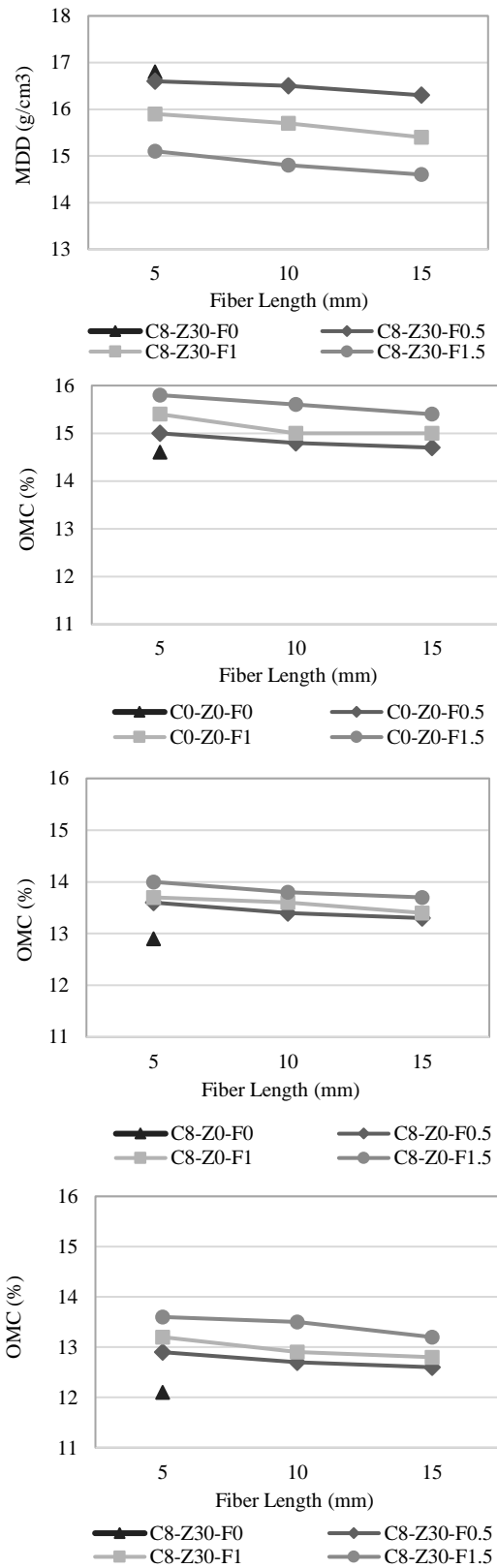
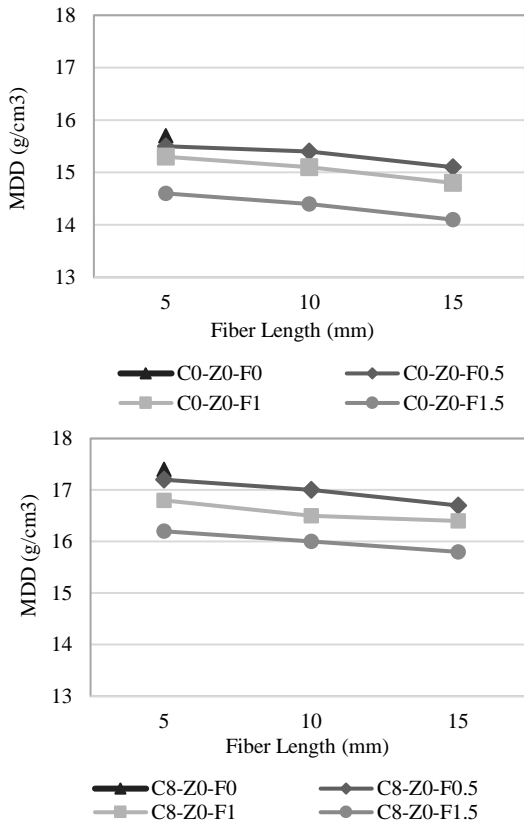


Figure 3. The alteration of MDD and OMC of the base soil, 8% cement-treated sand, and 30% zeolite-replaced-cemented sand due to the change in fiber length and content

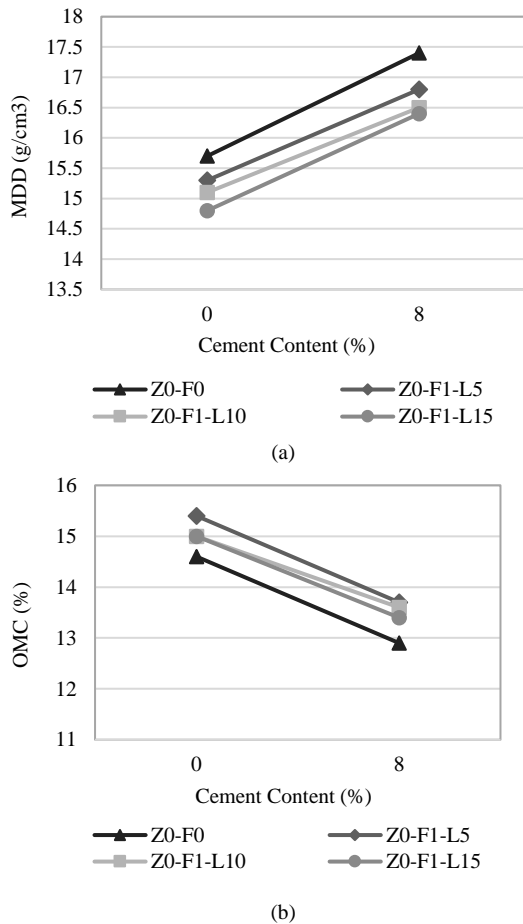


Figure 4. The alteration of MDD and OMC of the samples containing 1% fiber due to the change in cement content and fiber length

an increase in zeolite replacement led to the decrement of both MDD and OMC of the samples. Ahmadi et al. (11) observed analogous behavior in their research. The lower specific gravity of the zeolite than the cement prompted MDD reduction. In addition, larger particle size of the zeolite than cement decreased the OMC. Similar to what occurred earlier, in a specific zeolite replacement (in a single binder content), the increment of fiber length had a reducing effect on both the MDD and OMC of the samples.

3. 2. Direct Tensile Strength (DTS)

Tables 3 and 4 present the conducted DTS test results of 8-shape samples with $R_c=100\%$ and $R_c=95\%$, respectively, for 28 days of curing. The strength of each sample specified with the designated cement and fiber contents, zeolite replacement, and fiber length can be found in these tables. To demonstrate the alteration of DTS concerning the aforementioned parameters, several figures have been presented as representatives of the whole.

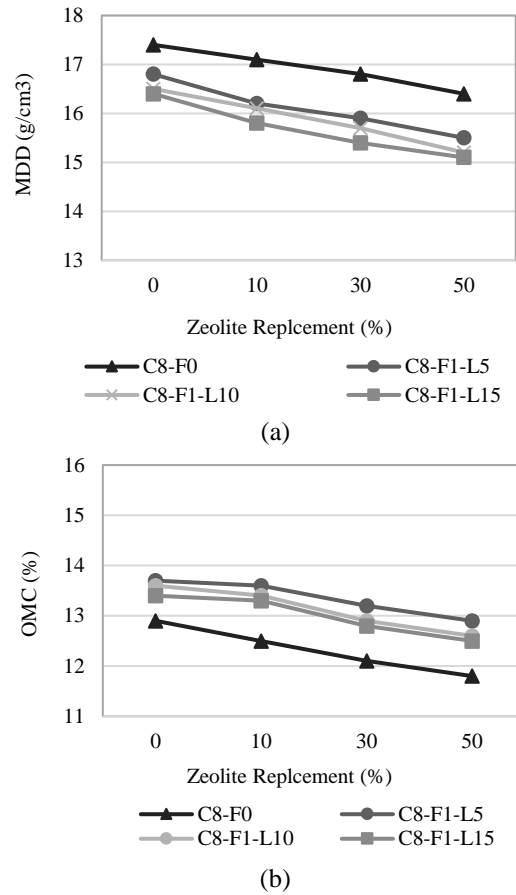


Figure 5. The alteration of MDD and OMC of the samples containing 1% fiber due to the change in zeolite replacement and fiber length

Figure 6 shows the change of DTS in the samples containing 8% cement, different zeolite replacements, and 10mm fiber length due to the variation of fiber length. It is perceivable that the introduction of kenaf fiber to the cement-treated sand in any amount effectively enhanced the DTS of the samples. The increment of fiber content from 0.5% to 1% led to a striking rise in the DTS of reinforced samples. The addition of fiber further to 1.5%, however, induced a deteriorating effect on the strength. Such trends were observed for added fibers with lengths of 5mm and 15mm. The behavior noticed at 1% fiber content could be ascribed to the optimum interaction of fibers, sand, and cementitious materials, which could not be achieved in the other fiber content statements. Yao et al. (25) reported 1% polyvinyl alcohol fiber content as the percentage resulting in the maximum DTS of silty soil.

Figure 7(a) and (b) illustrate the DTS variation of the samples treated with 8% cement, 0%, and 30% zeolite replacements for different fiber contents due to the change in fiber length. As can be seen, an increase in fiber

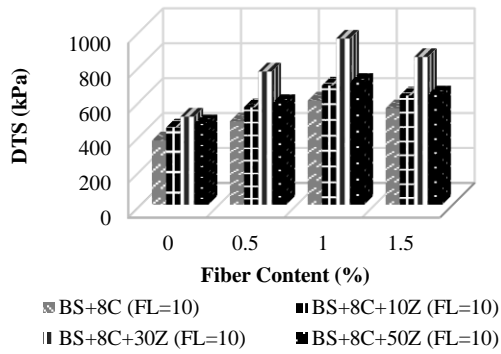


Figure 6. The alteration DTS of the samples containing 8% cement and different zeolite replacement due to the change in fiber content

TABLE 3. The UCS tests results of the samples with Rc=100% cured for 28 days

28 curing days		DTS (kPa)					
F.C (%)	F.L (mm)	%C	8				
		%Z	0	0	10	30	50
0	0		23.4	368.2	441.8	504.3	466.2
	5		27.6	430.2	486.5	630.7	513
0.5	10		35.8	477.5	557.8	763	582.5
	15		34.2	449.2	519.1	711.8	563.9
1	5		36.7	508	605.6	828	654.2
	10		44.1	596.5	682.9	951.4	703.5
1.5	15		40.4	530.3	636.3	860.4	680.1
	5		31.5	485.7	548.1	695.2	582.1
1.5	10		39.9	551.7	625.3	845.9	631.5
	15		35	513.9	550.8	770.1	590.4

TABLE 4. The UCS tests results of the samples with Rc=95% cured for 28 days

28 curing days		DTS (kPa)					
F.C (%)	F.L (mm)	%C	8				
		%Z	0	0	10	30	50
0	0		20.4	311.2	385.6	446.3	415.4
	5		24	353.9	431	532.8	446.1
0.5	10		32.8	404.2	515.8	662.7	522.8
	15		28.5	382	451.2	602	450.4
1	5		33.6	467.1	525.6	671.4	522.6
	10		38.9	536.1	602.4	777.3	641
1.5	15		35.2	480.2	540.3	730.9	567.2
	5		28.7	406.4	495.1	621.4	484.3
1.5	10		35.1	503	561.4	736	570.9
	15		31.9	450.1	512.6	645.2	521.5

length from 5mm to 10mm remarkably improved the DTS of the cement-treated samples and with 30% zeolite replacement ones. But a further increase from 10mm to 15mm reduced the DTS of the samples. Nevertheless, samples containing 15mm fibers showed a higher DTS than the 5mm ones. Similar behavior was observed for zeolite replacements. Such an enhancement at reinforced samples with 10mm fibers can be attributed to the better distribution condition and hence, better interaction of the sand and cementitious materia along the body of the fiber. The fiber length of 10mm was also reported as optimum by Li et al. (39) while the addition of syntactic fiber for soil reinforcement.

Figure 8 indicates the variation of DTS in the samples containing 8% cement and 1% fiber content at three specified fiber lengths concerning the change in zeolite replacement. As can be deduced, in each specific fiber length, zeolite replacement induced an enhancing effect on the DTS of the reinforced samples. The rise of zeolite replacement from 10% up to 30% prompted an increment in DTS to the highest level and any further increase of zeolite replacement up to 50% resulted in a detrimental effect on DTS compared with 30%. Cement triggers a chemical reaction called hydration, as the water is added to the mixture, which has two main products. The cementitious material that emerges when the hydration reaction is calcium-silicate-hydrate (C-S-H) gel and the

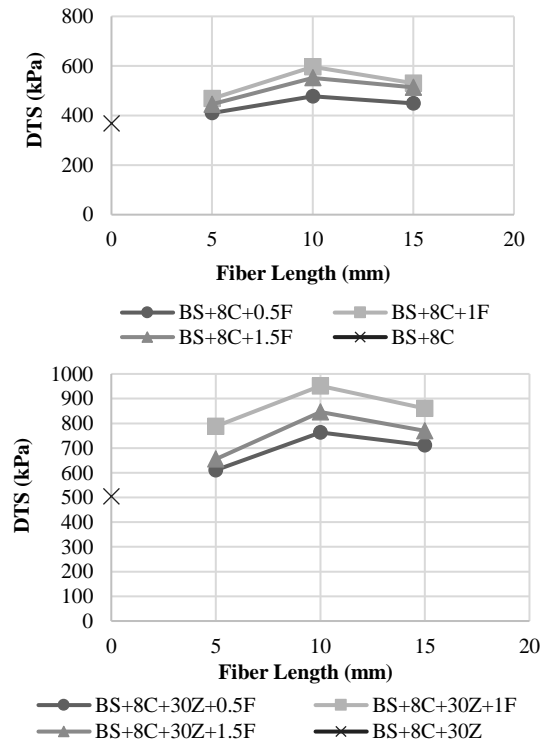


Figure 7. The alteration DTS of the samples containing 8% cement due to the change in fiber length for (a) 0%, and (b) 30% zeolite replacement

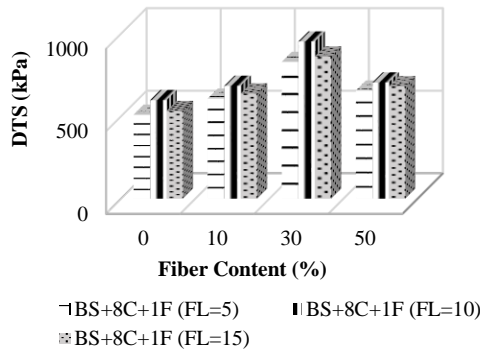


Figure 8. The alteration DTS of the samples containing 8% cement and 1% fiber content at different fiber lengths due to the change in zeolite replacement

other by-product is calcium hydroxide (Ca(OH)₂). When cement gets replaced by zeolite, SiO₂ and Al₂O₃ offered by zeolite react with Ca(OH)₂ (pozzolanic reaction) and produce more C-S-H gel (11). The reason that 30% zeolite replacement handed the best strength performance is that the amount of Ca(OH)₂, SiO₂, and Al₂O₃ came into a balanced situation, leading to the optimum pozzolanic reaction.

3. 3. Indirect Tensile Strength (ITS) Tables 5 and 6 represent the ITS of the cement-zeolite-stabilized and also reinforced samples cured for 28 days and cast in two RC of 100% and 95%, respectively. Using these Tables, the exact value of each test according to the stabilizers' dosages, kenaf fiber content, and fiber length can be determined. In the following, several graphs have been presented to elucidate the changing trend of the ITS values due to the existing variable.

Figure 9 shows the ITS alteration of the samples containing 8% cement with different proportion of zeolite as cement replacement along with changes of fiber content.

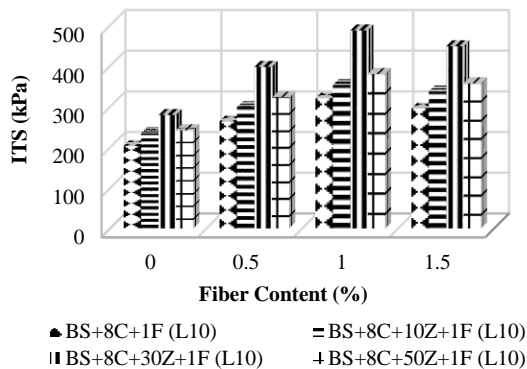


Figure 9. The alteration ITS of the samples containing 8% cement and different zeolite replacement due to the change in fiber content

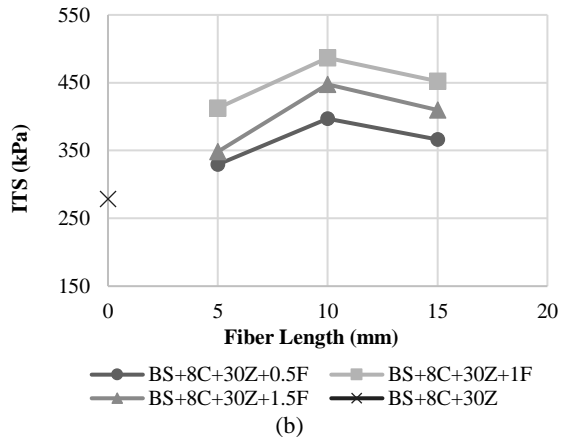
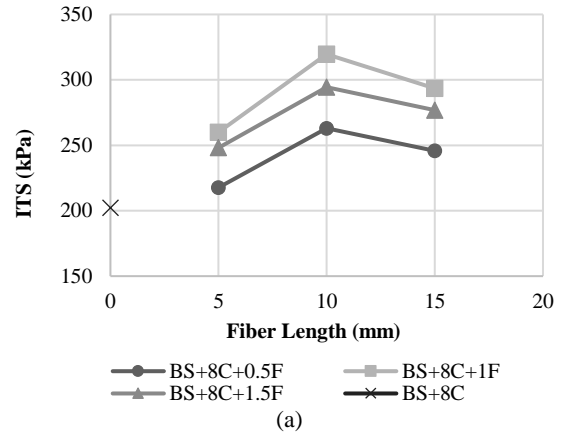


Figure 10. The alteration ITS of the samples containing 8% cement due to the change in fiber length for a) 0%, and b) 30% zeolite replacement

Figure 10 shows the ITS alteration of the samples containing 8% cement with different fiber length for 0% and 30% zeolite as cement.

Figure 11 depicts the ITS alteration of the samples containing 8% cement and 1% fiber at different fiber lengths for the variation of zeolite as cement replacement.

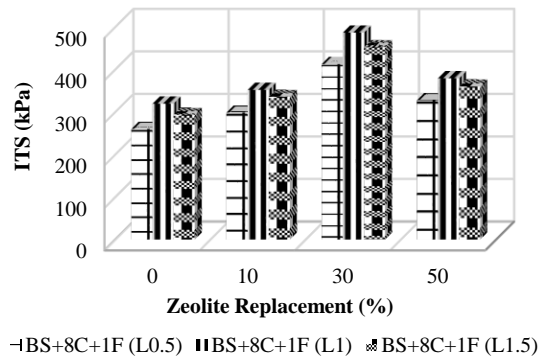


Figure 11. The alteration ITS of the samples containing 8% cement and 1% fiber content at different fiber lengths due to the change in zeolite replacement

TABLE 5. ITS tests results of the samples with Rc=100% cured for 28 days

		ITS (kPa)					
F (%)	L (mm)	%C	0		8		
		%Z	0	0	10	30	50
0	0		13.2	202.2	233.7	278.6	241.2
	5		15.6	217.7	258.7	329.4	267.4
0.5	10		20.1	263	297.8	396.9	321.3
	15		18.9	245.8	279.3	366.1	303.2
1	5		21.1	260	298.4	412.6	327.5
	10		25.3	319.6	352.1	486.6	379.3
1.5	15		22.8	293.4	335.6	452	359.9
	5		17.7	248.1	272.9	348.3	310.8
1.5	10		23.1	294.4	336.3	447.6	356.3
	15		21.7	276.8	300.6	409.6	326.2

TABLE 6. ITS tests results of the samples with Rc=100% cured for 28 days

		ITS (kPa)					
F (%)	L (mm)	%C	0		8		
		%Z	0	0	10	30	50
0	0		12.1	178.2	219.3	262.1	235.8
	5		14.3	192.7	242.3	305.7	247.4
0.5	10		18.5	239.9	293.2	373	301.5
	15		17.2	219.3	262.6	348.1	283
1	5		20.1	241.3	287.4	360.8	300.5
	10		24	310.2	347.2	460	364.3
1.5	15		21	276.7	314.9	426.4	330.2
	5		16.8	214.7	266.4	338.3	282.5
1.5	10		21.1	288	321	415.9	334.1
	15		19.7	261.7	296.4	380.5	313.9

Analyzing Figure 12 reveals that in a single fiber length, for example, 10mm, ITS enhanced remarkably with direct addition of fiber and incrementing it up to 1%. The reason is attributed to the better performance of fibers at this content, presenting the best distribution in the mixture, hence, the optimum interaction between cemented particles and fibers. Further increase in fiber content negatively affected the ITS of the reinforcement samples, which is a direct consequence of inappropriate distribution and flocculation of the fibers while mixing. Such behavior was observable in samples reinforced with other fiber contents. However, the effect of fibers on ITS was more pronounced in 1% fiber content. Analogous

fashion has been reported by Rabab’ah et al. (40), reinforcing clay with glass fibers.

Figure 13(a) and (b) demonstrate the change in ITS of the samples stabilized with 8% cement and also having 30% of cement replaced with zeolite, respectively, for all fiber contents due to the variation of fiber length. These figures have been chosen as representatives of all samples since similar trends were observed for other series. It can be deduced from Figure 13(a) that in 8% of cemented samples, increasing the fiber length up to 10mm induced an increasing behavior of the ITS resulting in the peak tensile strength in reinforced samples. For the addition of fibers longer than 10mm up to 15mm, a reduction of the ITS was noticed; however, the ITS values were still larger than the ones for samples reinforced with 5mm fibers. Such a trend was noticed by Yang et al. (41) when using polypropylene fiber to reinforce loess.

Figure 14 demonstrates the alteration of ITS against the change in zeolite replacement considering samples reinforced with 1% fiber. It is transparent that conducting zeolite replacement and increases up to 30% improved

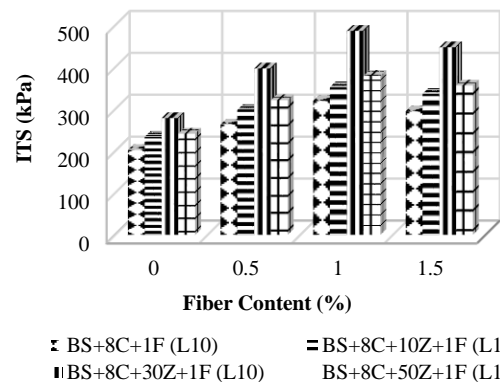
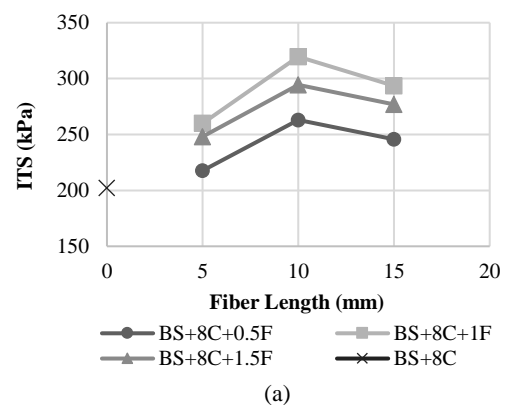
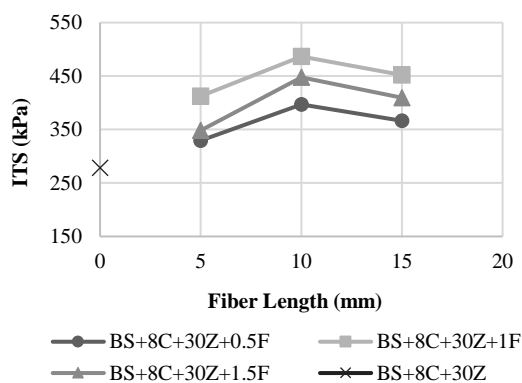


Figure 12. The alteration ITS of the samples containing 8% cement and different zeolite replacement due to the change in fiber content



(a)



(b)

Figure 13. The alteration ITS of the samples containing 8% cement due to the change in fiber length for a) 0%, and b) 30% zeolite replacement

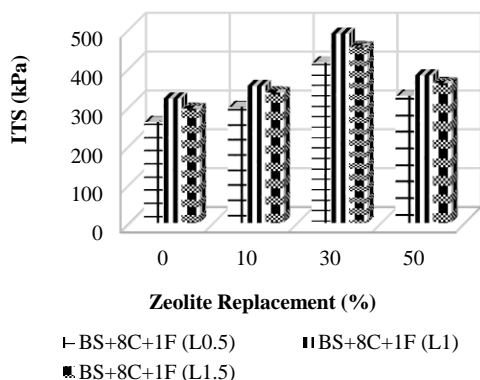


Figure 14. The alteration ITS of the samples containing 8% cement and 1% fiber content at different fiber lengths due to the change in zeolite replacement

the ITS substantially. For further zeolite replacement up to 50%, an STS-reducing fashion was distinguished. The improvement of ITS is attributed to the pozzolanic reaction intensified at 28 days of curing, resulting in more C-S-H gel rather than only-cemented samples (42).

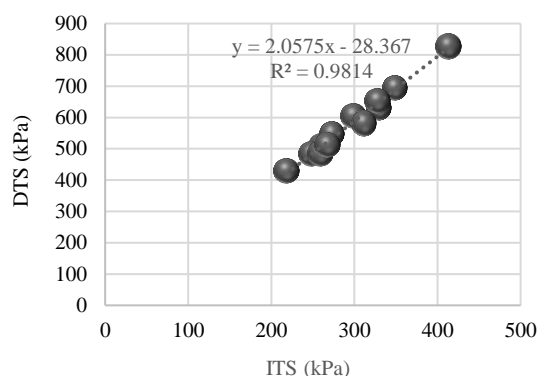
3. RELATIONSHIP BETWEEN DTS AND ITS

3.1. Linear Regression

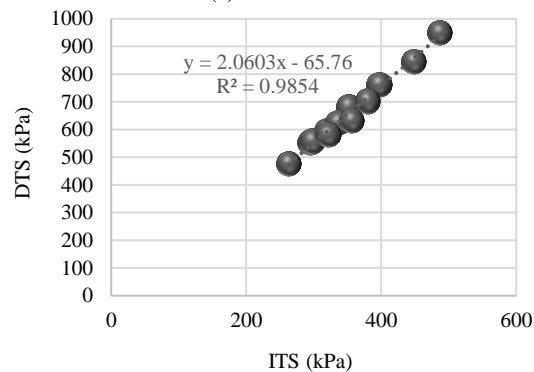
A few relationships have yet to be presented by researchers correlating DTS to the ITS of the fiber-reinforced soils (43). In this section, the results of 80 DTS and 80 ITS tests conducted on samples stabilized with 8% cement, 0, 10, 30, and 50% zeolite replacement, and also the ones reinforced with 0.5, 1, and 1.5% kenaf fiber in three lengths of 5, 10, and 15mm were considered. Half of the samples were cast with RC=100% and the other half with RC=95%, and all samples were cured for 28 days. Conducting linear regression, the results of these tests demonstrated that

linear relationships with acceptable correlation coefficients equal to $R^2=0.9814$, 0.9923 , and 0.9923 for FL=5mm, FL=10mm, and FL=15mm, respectively, are definable for samples with RC=100% and to $R^2=0.9598$, 0.9895 , and 0.985 for FL=5mm, FL=10mm, and FL=15mm, respectively, can be presented for RC=95%. The functions and the coefficient of correlations are presented in Figure 15. Evaluating these figures can reveal that the ITS alters with the same trend in which DTS changes irrelevant to the stabilizers and reinforcing elements.

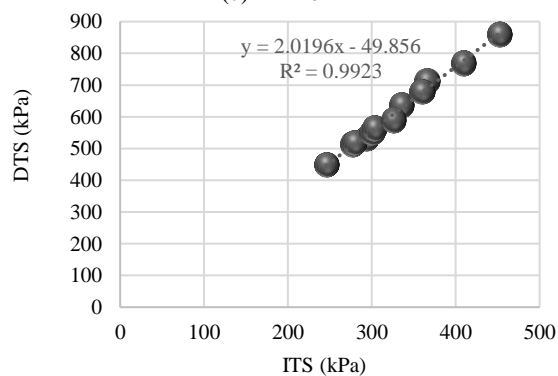
The significance of the ITS on changes in DTS values was investigated employing an ANOVA analysis of variance in Microsoft Excel area; the results are shown in



(a) FL=5mm



(b) FL=10mm



(c) FL=15mm

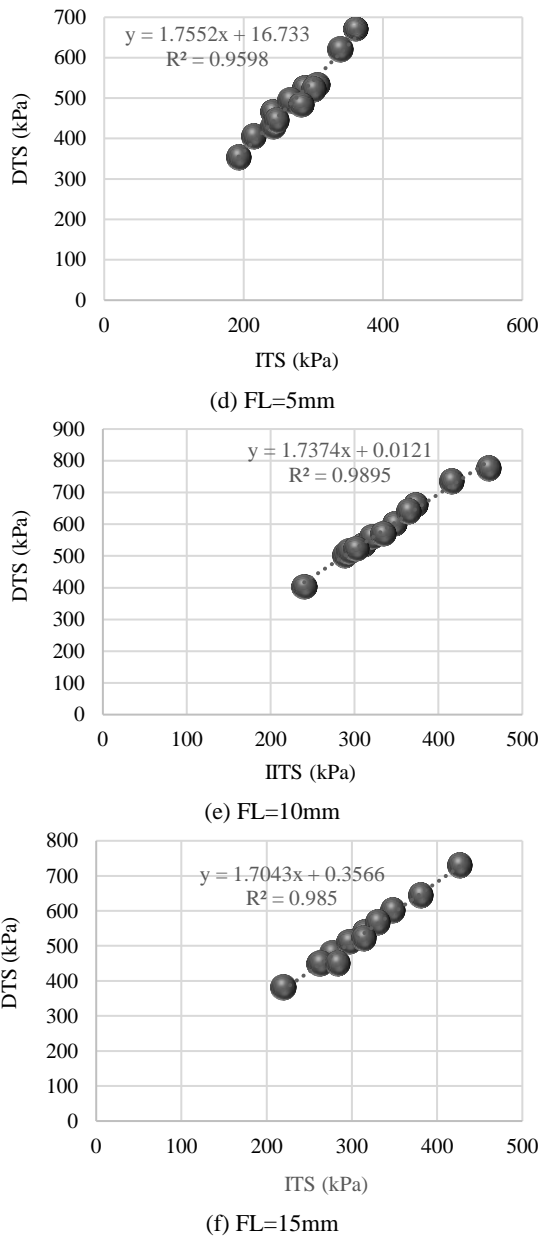


Figure 15. Correlation between DTS and ITS of the cement-zeolite-stabilized samples reinforced with kenaf fiber at (a),(b), and (c) for Rc=100%, and (d), (e), and (f) for Rc=95%

Table 7. When the corresponding p-value is lower than 5%, it can be stated with 95% confidence that the observed alteration is due to the different levels of the investigated factor and not just a random error that happens through the test's implementations. This is when a factor's influence is typically accounted for significantly. According to the findings of this study as presented in Table 7, the alteration of investigated DTS values was significantly in relation to ITS values (with p-values very much lower than 5%). Therefore, the

TABLE 7. P-values of the equations presented in Figure 14-b

Equation	a	b	c	d	e	f
p-value	5.58E ⁻¹⁰	1.64E ⁻¹⁰	6.67E ⁻¹²	2.61E ⁻⁰⁸	3.10E ⁻¹¹	1.91E ⁻¹⁰

presented relationships are statistically significant and it can be stated that the DTS alters in a definable relationship with ITS.

4. MICROSTRUCTURAL ANALYSIS

In this study, Scanning Electron Microscope (SEM) images were utilized to investigate the soil microstructure of stabilized samples, as well as stabilized fiber-reinforced samples at the optimal amount of binder and fiber content. Investigating the microstructural behavior of soil dominates in understanding the behavior of soil since the shear strength of soil mass is transferred from the contact surface of its solid elements. In fact, the weakest area in the limiting factors of soil resistance is the transition area (empty spaces between solid elements).

According to the type of binders and reinforcing elements employed in soil stabilization, the resistance of the transition areas may be higher than the base soil mass. During the hydration reaction, at the beginning of the processing time, the size of the voids is large and the transfer areas have a larger volume, which causes the sample to show a lower resistance. However, with time, the hydration reaction products diminish the volume of these areas. Also, hydration reaction products are generally more resistant than the soil mass. Production of new binding materials in transition areas is from the reaction of the cement and zeolite, which leads to the formation of the calcium-silicate-hydrate gel.

To demonstrate the alteration happening after soil stabilization and also reinforcement, a failed sample's picture is illustrated in Figure 16, and the pure image of the solid constituents of the samples is depicted in Figure 17. In addition, the microstructural view of the optimally-stabilized samples without and with kenaf fiber is illustrated in Figure 18 considering the sand sample images in Figures 17 and 18. It is perceivable that adding cement and zeolite resulted in the formation of binding gel and the reduction of the transition areas.

In the images of Figure 19, it is clearly displayed that the fiber is imbedded between sand and cementitious material and has a proper interaction with them on the failure surface. Due to having a relatively significant tensile strength, the fibers have been stretched but not torn, and this has a great contribution to the cohesion of the particles at the moment of rupture, keeping the particles interlocked and increasing the tensile and shear strength. As can be seen in Figure 20 (a), after the indirect



Figure 16. A fractured 8-shaped sample tested in this investigation

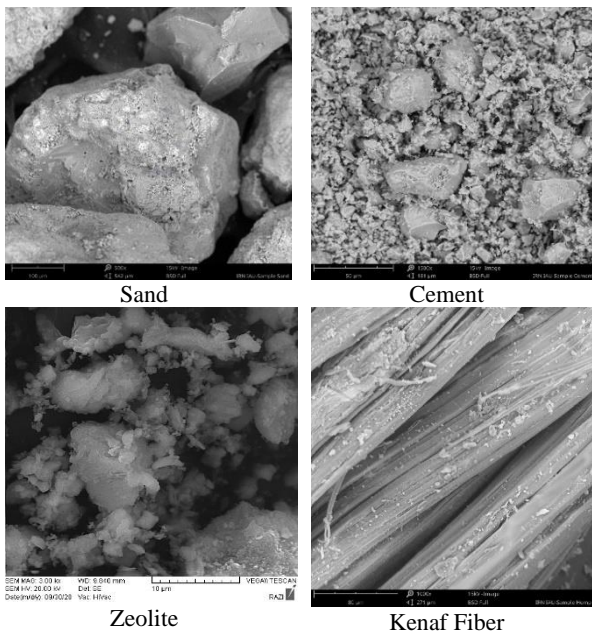


Figure 17. The SEM view of the materials used in this study

tensile test, it was observed that the unreinforced samples have wider cracks from the fractured cross-section, which are caused by the force applied in the direction of sample failure and the joining of microcracks with each other. However, Figure 20 (b) demonstrates that the fibers help uniformity of the samples and fewer cracks appeared.

Microcracks form at the transition zone of the aggregate-paste. Brittle materials, such as friable soil, fail through crack propagation, which ultimately joins together to create arrays of continuous fracture surfaces, and the deformation commences to intensify along with that. Loose particles may exist on the surface, and a fracture surface represents a weak plane through the cementitious paste rather than material failure. Additionally, the mobilized shear strength can be lower than the fully softened shear strength along the failure surface.

Meanwhile, the bonding strength between cemented matrix and fiber constrains the occurrence and development of microcracks all over the matrix, curbing the creation of macrocracks, and the peak tensile strength happens at higher strain deformation. The occurrence of microcracks induces an abrupt breakage of unreinforced specimens, while the fiber addition in the specimen, on the other hand, has a significant influence on the post-cracking behavior.

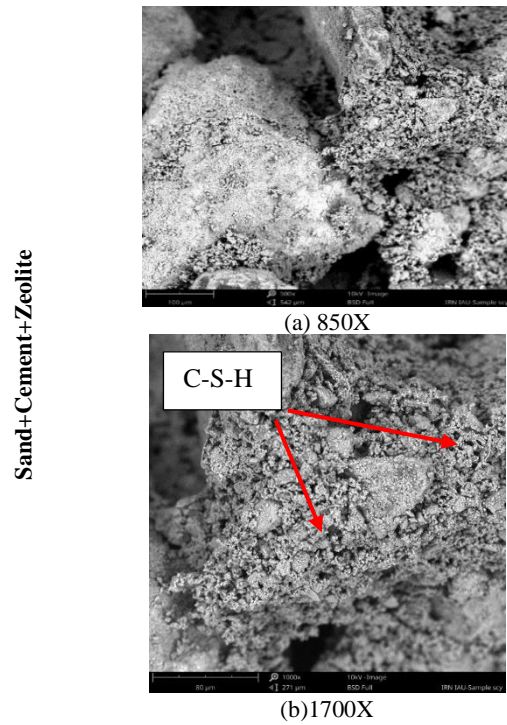
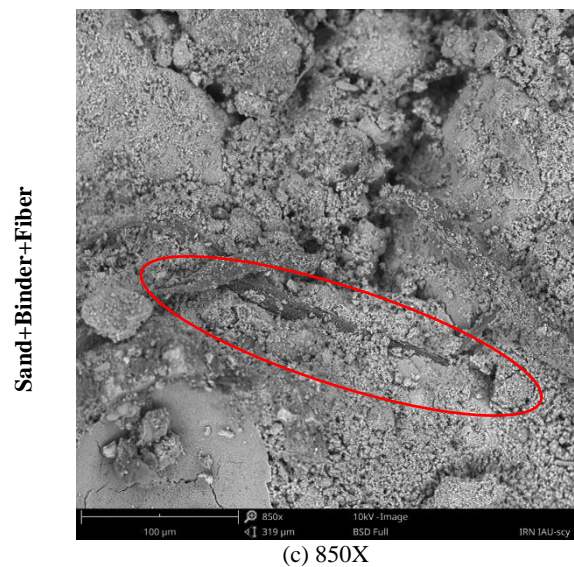
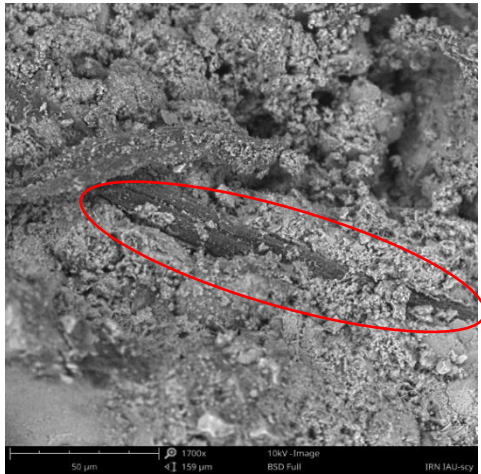


Figure 18. Microstructural view of the stabilized samples without and with kenaf fiber



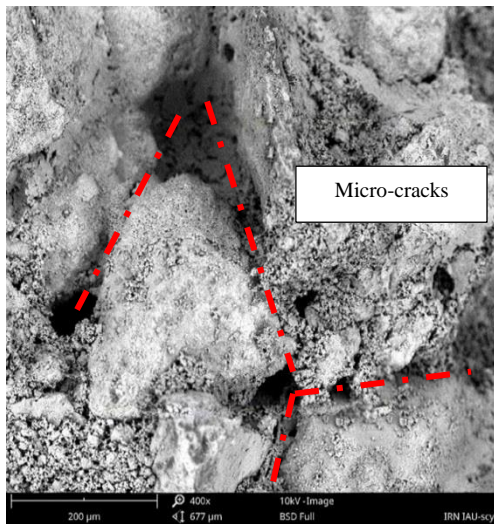
Sand+Binder+Fiber

(c) 850X

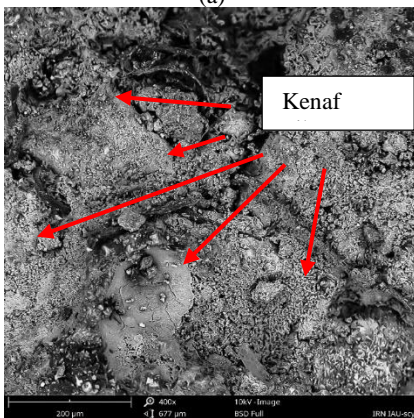


(d) 1700X

Figure 19. Microstructural view of the stabilized samples with kenaf fiber



(a)



(b)

Figure 20. Micro-cracks created during failure, and (b) Kenaf fiber interaction with cementitious materials in the reinforced sample

5. CONCLUSIONS

The aim of this study is to investigate the effect of kenaf fiber on the mechanical behavior of sand, such as compaction, direct tensile strength (DTS), and indirect tensile strength (ITS). To this end, laboratory experiments were conducted on various mixtures of cement, zeolite, kenaf fiber, and sand, and their results are presented in the following:

- Increasing the fiber content diminished the MDD; on the other hand, it raised the OMC of the mixture.
- The increment in fiber length resulted in the reduction of the MDD and OMC of the mixtures.
- Cement addition increased the MDD and decreased OMC of the mixtures.
- Conducting zeolite replacement reduced the MDD and OMC of the reinforced mixtures.
- Adding kenaf fiber up to 1% resulted in the highest DTS and ITS of the fiber-reinforced samples. Further fiber addition negatively influenced the mentioned parameters compared to the samples with 1% kenaf fiber content.
- Fibers with a length of 10mm resulted in the highest DTS and ITS of the reinforced samples.
- Zeolite replacement of up to 30% resulted in the best DTS and ITS performance of the reinforced samples in comparison with the only-cement-stabilized fiber-reinforced samples. However, further zeolite replacement induced a weakening effect on the mentioned parameters.
- A linear relationship was presented correlating DTS to ITS with acceptable accuracy.
- Through SEM images, it was shown that kenaf fibers properly helped keeping the uniformity of the samples and diminished the transition areas.

6. REFERENCES

1. MolaAbasi H, Saberian M, Kordnaeij A, Omer J, Li J, Kharazmi P. Predicting the stress-strain behaviour of zeolite-cemented sand based on the unconfined compression test using GMDH type neural network. *Journal of Adhesion Science and Technology*. 2019;33(9):945-62. 10.1080/01694243.2019.1571659
2. Liu J, Bai Y, Song Z, Kanungo DP, Wang Y, Bu F, et al. Stabilization of sand using different types of short fibers and organic polymer. *Construction and Building Materials*. 2020;253:119164. 10.1016/j.conbuildmat.2020.119164
3. Ghadakpour M, Choobbasti AJ, Kutanaei SS. Investigation of the Kenaf fiber hybrid length on the properties of the cement-treated sandy soil. *Transportation Geotechnics*. 2020;22:100301. 10.1016/j.trgeo.2019.100301
4. ShahriarKian M, Kabiri S, Bayat M. Utilization of zeolite to improve the behavior of cement-stabilized soil. *International Journal of Geosynthetics and Ground Engineering*. 2021;7(2):35. 10.1007/s40891-021-00284-9
5. Meddah A, Merzoug K. Feasibility of using rubber waste fibers as reinforcements for sandy soils. *Innovative Infrastructure Solutions*. 2017;2(1):5. 10.1007/s41062-017-0053-z

6. Mola-Abasi H, Saberian M, Semsani SN, Li J, Khajeh A. Triaxial behaviour of zeolite-cemented sand. *Proceedings of the Institution of Civil Engineers-Ground Improvement*. 2020;173(2):82-92. 10.1680/jgrim.18.00009
7. Sariosseiri F, Muhunthan B. Effect of cement treatment on geotechnical properties of some Washington State soils. *Engineering geology*. 2009;104(1-2):119-25. 10.1016/j.enggeo.2008.09.003
8. Nguyen D, Phan V. Engineering properties of soil stabilized with cement and fly ash for sustainable road construction. *International Journal of Engineering, Transactions C: Aspects*. 2021;34(12):2665-71. 10.5829/IJE.2021.34.12C.12
9. Ghasem Ghanbari P, Momeni M, Mousivand M, Bayat M. Unconfined compressive strength characteristics of treated peat soil with cement and basalt fibre. *International Journal of Engineering, Transactions B: Applications*. 2022;35(5):1089-95. 10.5829/ije.2022.35.05b.24
10. Eme D, Nwofor T, Sule S. Correlation between the California bearing ratio (CBR) and unconfined compressive strength (UCS) of stabilized sand-cement of the niger delta. *International Journal of Civil Engineering*. 2016;3(3):7-13. 10.14445/23488352/ijce-v3i3p103
11. Chenarboni HA, Lajevardi SH, MolaAbasi H, Zeighami E. The effect of zeolite and cement stabilization on the mechanical behavior of expansive soils. *Construction and Building Materials*. 2021;272:121630. 10.1016/j.conbuildmat.2020.121630
12. Aprianti E, Shafiqh P, Bahri S, Farahani JN. Supplementary cementitious materials origin from agricultural wastes—A review. *Construction and Building Materials*. 2015;74:176-87. 10.1016/j.conbuildmat.2014.10.010
13. Rabbani P, Tolooiyan A, Lajevardi SH, Daghigh Y, Falah M. The effect of the depth of cutter soil mixing on the compressive behavior of soft clay treated by alkali-activated slag. *KSCE Journal of Civil Engineering*. 2019;23(10):4237-49. 10.1007/s12205-019-0335-4
14. Harichane K, Ghrici M, Kenai S. Effect of the combination of lime and natural pozzolana on the compaction and strength of soft clayey soils: a preliminary study. *Environmental Earth Sciences*. 2012;66:2197-205. 10.1007/s12665-011-1441-x
15. Rabbani P, Lajevardi SH, Tolooiyan A, Daghigh Y, Falah M. Effect of Cutter Soil Mixing (CSM) method and curing pressures on the tensile strength of a treated soft clay. *Heliyon*. 2019;5(8). 10.1016/j.heliyon.2019.e02186
16. Heidarzadeh Y, Lajevardi SH, Sharifipour M, Kamalian M. Experimental characterization of the small strain shear modulus of soft clay stabilized with cement and nano-SiO₂ using bender element tests. *Bulletin of Engineering Geology and the Environment*. 2021;80:2523-34. 10.1007/s10064-020-02096-z
17. Mola-Abasi H, Khajeh A, Semsani SNS. Porosity/(SiO₂ and Al₂O₃ particles) ratio controlling compressive strength of zeolite-cemented sands. *Geotechnical and Geological Engineering*. 2018;36:949-58. 10.1007/s10706-017-0367-9
18. Mola-Abasi H, Kordtabar B, Kordnaej A. Effect of natural zeolite and cement additive on the strength of sand. *Geotechnical and Geological Engineering*. 2016;34:1539-51. 10.1007/s10706-016-0060-4
19. MolaAbasi H, Saberian M, Li J. Prediction of compressive and tensile strengths of zeolite-cemented sand using porosity and composition. *Construction and Building Materials*. 2019;202:784-95. 10.1016/j.conbuildmat.2019.01.065
20. Kordnaej A, Moayed RZ, Soleimani M. Unconfined compressive strength of loose sandy soils grouted with zeolite and cement. *Soils and Foundations*. 2019;59(4):905-19. 10.1016/j.sandf.2019.03.012
21. Khajeh A, Ebrahimi SA, MolaAbasi H, Jamshidi Chenari R, Payan M. Effect of EPS beads in lightening a typical zeolite and cement-treated sand. *Bulletin of Engineering Geology and the Environment*. 2021;80(11):8615-32. 10.1007/s10064-021-02458-1
22. Khajeh A, Jamshidi Chenari R, MolaAbasi H, Payan M. An experimental investigation on geotechnical properties of a clayey soil stabilised with lime and zeolite in base and subbase courses. *Road Materials and Pavement Design*. 2022;23(12):2924-41. 10.1080/14680629.2021.1997789
23. Bai Y, Liu J, Cui Y, Shi X, Song Z, Qi C. Mechanical behavior of polymer stabilized sand under different temperatures. *Construction and Building Materials*. 2021;290:123237. 1016/j.conbuildmat.2021.123237
24. Kumar KR, Gobinath R, Shyamala G, Viloría E, Varela N. Free thaw resistance of stabilized and fiber-reinforced soil vulnerable to landslides. *Materials Today: Proceedings*. 2020;27:664-70. 10.1016/j.matpr.2020.02.041
25. Yao X, Huang G, Wang M, Dong X. Mechanical properties and microstructure of PVA fiber reinforced cemented soil. *KSCE Journal of Civil Engineering*. 2021;25:482-91. 10.1007/s12205-020-0998-x
26. Wang Y-X, Guo P-P, Ren W-X, Yuan B-X, Yuan H-P, Zhao Y-L, et al. Laboratory investigation on strength characteristics of expansive soil treated with jute fiber reinforcement. *International Journal of Geomechanics*. 2017;17(11):04017101. 10.1061/(asce)gm.1943-5622.0000998
27. Zhou C, Cai L, Chen Z, Li J. Effect of kenaf fiber on mechanical properties of high-strength cement composites. *Construction and Building Materials*. 2020;263:121007. 10.1016/j.conbuildmat.2020.121007
28. EsmailpourShirvani N, TaghaviGhalesari A, Tabari MK, Choobbasti AJ. Improvement of the engineering behavior of sand-clay mixtures using kenaf fiber reinforcement. *Transportation Geotechnics*. 2019;19:1-8. 10.1016/j.trgeo.2019.01.004
29. ASTM D-. Standard practice for classification of soils for engineering purposes (unified soil classification system). West Conshohocken, PA; 2011.
30. ASTM. ASTM D422-63: Standard Test Method for Particle-Size Analysis of Soils. ASTM International West Conshohocken^ ePA PA; 2007.
31. Soil ACD-o, Rock. Standard Test Methods for Laboratory Compaction Characteristics of Soil Using Modified Effort (56,000 Ft-Lbf/Ft³ (2,700 KN-M/M³)) 1: ASTM international; 2009.
32. Standard A. Standard test method for splitting tensile strength of intact rock core specimens. ASTM D3967-08 ASTM International, West Conshohocken, USA. 2008.
33. Santoni RL, Tingle JS, Webster SL. Engineering properties of sand-fiber mixtures for road construction. *Journal of Geotechnical and Geoenvironmental Engineering*. 2001;127(3):258-68. 10.1061/(ASCE)1090-0241
34. Tran KQ, Satomi T, Takahashi H. Improvement of mechanical behavior of cemented soil reinforced with waste cornsilk fibers. *Construction and Building Materials*. 2018;178:204-10. 10.1016/j.conbuildmat.2018.05.104
35. Mohamed AEMK. Improvement of swelling clay properties using hay fibers. *Construction and Building Materials*. 2013;38:242-7. 10.1016/j.conbuildmat.2012.08.031
36. Maity J, Chattopadhyay B, Mukherjee S, editors. Variation of compaction characteristics of sand randomly mixing with various natural fibers. *Proceedings of Indian geotechnical conference*, December; 2011.

37. Prabakar J, Sridhar R. Effect of random inclusion of sisal fibre on strength behaviour of soil. *Construction and Building materials*. 2002;16(2):123-31. 10.1016/S0950-0618(02)00008-9
38. Lopez-Querol S, Arias-Trujillo J, Maria G-E, Matias-Sanchez A, Cantero B. Improvement of the bearing capacity of confined and unconfined cement-stabilized aeolian sand. *Construction and Building Materials*. 2017;153:374-84. 10.1016/j.conbuildmat.2017.07.124
39. Li Q, Chen J, Hu H. The tensile and swelling behavior of cement-stabilized marine clay reinforced with short waste fibers. *Marine Georesources & Geotechnology*. 2019;37(10):1236-46. 10.1080/1064119X.2018.1547936
40. Rabab'ah S, Al Hattamleh O, Aldeeky H, Alfoul BA. Effect of glass fiber on the properties of expansive soil and its utilization as subgrade reinforcement in pavement applications. *Case Studies in Construction Materials*. 2021;14:e00485. 10.1016/j.cscm.2020.e00485
41. Yang B-h, Weng X-z, Liu J-z, Kou Y-n, Jiang L, Li H-l, et al. Strength characteristics of modified polypropylene fiber and cement-reinforced loess. *Journal of Central South University*. 2017;24(3):560-8. 10.1007/s11771-017-3458-0
42. Mola-Abasi H, Khajeh A, Naderi Semsani S. Variables controlling tensile strength of stabilized sand with cement and zeolite. *Journal of Adhesion Science and Technology*. 2018;32(9):947-62. 10.1080/01694243.2017.1388052
43. Tran KQ, Satomi T, Takahashi H. Tensile behaviors of natural fiber and cement reinforced soil subjected to direct tensile test. *Journal of Building Engineering*. 2019;24:100748. 10.1016/j.jobe.2019.100748

COPYRIGHTS

©2024 The author(s). This is an open access article distributed under the terms of the Creative Commons Attribution (CC BY 4.0), which permits unrestricted use, distribution, and reproduction in any medium, as long as the original authors and source are cited. No permission is required from the authors or the publishers.



Persian Abstract

چکیده

مقابله با خاک های مشکل دار یکی از چالش برانگیزترین بخش های شغلی مهندسان ژئوتکنیک است. یکی از آنها ماسه سست با چسبندگی کم است و در سرتاسر جهان به ویژه در مناطق ساحلی یافت می شود. تثبیت کننده های شیمیایی مانند سیمان از جمله موارد رایج در میان مهندسان برای مقابله با نقاط ضعف ماسه سست هستند. با این حال، جایگزینی این تثبیت کننده های سنتی با مواد پوزولانی مانند زئولیت طبیعی تایید شده است زیرا به کاهش مصرف سیمان و در نتیجه کاهش انتشار CO₂ کمک می کند. با وجود تمام مزایا، رفتار شکننده پیامد ناخوشایند این تثبیت کننده ها است. بنابراین، هدف از این مطالعه کاهش شکنندگی ماسه تثبیت شده با سیمان-زئولیت با استفاده از الیاف کناف طبیعی است. برای این منظور، دو مقدار سیمان، چهار مقدار سیمان جایگزین شده با زئولیت، و سه مقدار الیاف در سه طول در دو تراکم نسبی خاک (Rc) برای بررسی تراکم، مقاومت کششی مستقیم 8-شکل (DTS) و کشش غیرمستقیم تطبیق داده شد. رفتارهای قدرتی (ITS) تلاش های تجربی نشان داد که رفتار تراکم به محتویات پایدارکننده و محتوای فیبر و طول حساس است. افزودن ۸ درصد سیمان، افزایش زئولیت تا ۵۰ درصد و افزایش الیاف تا ۱.۵ درصد منجر به کاهش خواص تراکم شد. با این حال، رطوبت بهینه با افزایش فیبر کناف افزایش یافت. تأثیر قابل توجهی بر رفتار DTS و ITS در حالی که ۳۰ درصد جایگزینی زئولیت در نمونه های سیمانی ۸ درصد و تقویت شده با ۱ درصد الیاف کناف با طول ۱۰ میلی متر مشاهده شد. علاوه بر این، یک رابطه خطی بین DTS و ITS ارائه شد. در پایان، نمونه تقویت شده با استفاده از تصاویر میکروسکوپ الکترونی روبشی (SEM) مورد تجزیه و تحلیل قرار گرفت.



Optimal Node Selection for Cooperative Spectrum Sensing in Cognitive Radio Sensor Networks with Energy Harvesting

A. Al-bosham^a, A. Ebrahimzadeh^{b*}, A. Bagheri^c

^a Department of Electronic and Communication, Engineering Collage, Al-Qadisiya University, Al-Diwaniya, Iraq

^b Faculty of Electrical and Computer Engineering, Babol Noshirvani University of Technology, Babol, Mazandaran, Iran

^c Department of Electrical Engineering, Esfarayen University of Technology, Esfarayen, North Khorasan, Iran

PAPER INFO

Paper history:

Received 22 August 2023

Received in revised form 30 October 2023

Accepted 04 November 2023

Keywords:

Cognitive Radio

Energy Harvesting

Fifth Generation Communication

Mathematical Optimization

Spectrum Sensing

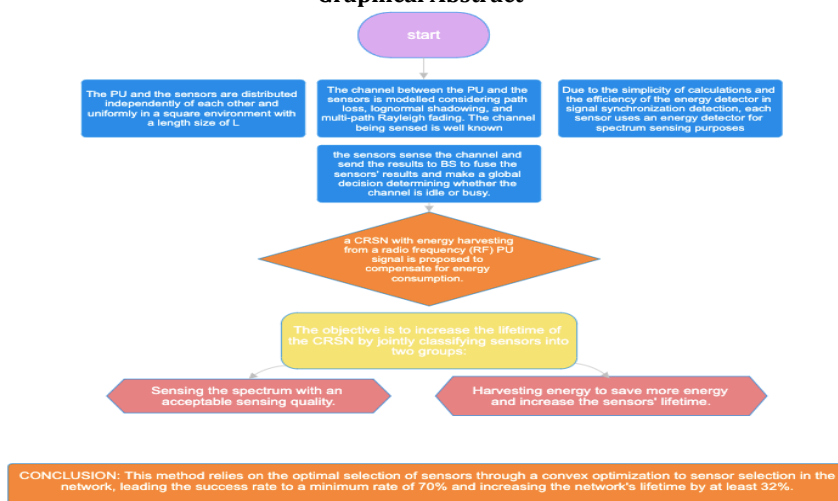
Wireless Sensor Network

ABSTRACT

5G communication technology supports the Internet of Things, remote health care centers, and cloud computing by tuning their communication services over a very wide range of frequency bands with low-cost, low-battery consumption, and low latency. However, the development of such wireless technology is highly dependent on radio frequency spectra. The Cognitive Radio Sensor Network (CRSN) is an excellent candidate to improve radio spectrum utilization and manage the heavy communication data traffic in 5G wireless networks. CRSN can sense the frequency channels, making it possible for secondary users (who are denied service) to use the free channels. Despite the outstanding features of CRSNs, some limitations overshadow their performance. The most critical limitation is energy and its optimal consumption to increase the network's lifetime. Recent research has shown that energy harvesting can be an effective way to increase the lifetime of CRSNs. However, the sensors should sense the frequency spectrum with a high success rate. In this paper, several optimal sensor nodes using energy harvesting with the approach of increasing the network's lifetime are proposed to solve the mentioned challenge. This way, the sensor nodes are divided into two independent groups for simultaneous spectrum sensing and energy harvesting in each time frame. We will solve this problem based on mathematical optimization and the use of proposed solutions for convex problems. Finally, simulations are developed to evaluate the ability of the proposed solution, assuming the systems use IEEE802.15.4/Zigbee and IEEE802.11af.

doi: 10.5829/ije.2024.37.05b.02

Graphical Abstract



*Corresponding Author Email: e_zadeh@nit.ac.ir (A. Ebrahimzadeh)

Please cite this article as: Al-bosham A, Ebrahimzadeh A, Bagheri A. Optimal Node Selection for Cooperative Spectrum Sensing in Cognitive Radio Sensor Networks with Energy Harvesting. International Journal of Engineering, Transactions B: Applications. 2024;37(05):833-41.

1. INTRODUCTION

Advances in wireless communication systems have led to challenges such as very high data rates and dense congestion of users, with higher requirements on end-to-end performance and user experience. Challenges arising from new application areas are ultra-low latency, energy, and cost (1). 5G uses mmWave access technology where a spectrum above 6 GHz and networks should address emerging needs such as wide bandwidth, lower latency, and higher capacity (2). More capacity requires more spectrum, which leads to the integration of Cognitive Radio (CR) into 5G networks. CR focuses on enabling much more efficient use of the spectrum. CR can improve the utilization of dense spectrum in a wireless network because some parts of the spectrum allocated to a licensed user often need to be utilized, ultimately enabling more dynamic and flexible spectrum access (3).

A Cognitive Radio Sensor Network (CRSN) consists of a large number of sensor nodes with various facilities to sense the frequency spectrum and detect the free channels. These scattered frequency sensors can process their sensing results and send them to a final node or data fusion center to cooperatively decide about the busy state of under-sensed frequency channels. The Secondary Users (SUs) can use the free detected channels (4, 5). Spectrum sensing, as the first and most crucial activity in CRSNs, requires the highest possible degree of accuracy and speed, and the limited energy of sensors must be used optimally in spectrum sensing. Therefore, it improves radio spectrum utilization and helps manage the heavy communication data traffic in 5G wireless networks (6). However, each node in a CRSN has limitations due to its small size and lightweight. The sensors' first and most important limitation is their limited power and battery. If the battery runs out, the sensor will not survive in the network, limiting the lifetime of the CRSN (7). Due to environmental and economic issues, reducing energy consumption and increasing energy efficiency in these systems have become particularly important.

On the other hand, CRSNs often use batteries as a source of energy; hence, the amount of energy consumed and the battery life is significant in these networks. In addition, in some applications of CRSNs, such as spectrum sensing in military or remote areas, it is difficult or sometimes impossible to recharge the sensors (8). Therefore, network lifetime is a significant challenge in the design of CRSNs, and energy efficiency is one of the main goals of academic and industrial research centers. One of the methods to overcome this challenge in CRSNs is to recharge the battery of sensor nodes using energy harvesting (EH) techniques. The purpose of energy harvesting is to supply energy for the sensor networks. There are different types of EH, such as solar, wind, thermal, and mechanical (9).

In this paper, to increase the lifetime of CRSNs, we present an electromagnetic energy harvesting method that divides the sensors into two categories: energy harvesters and spectrum sensors in a time frame. By this method, the sensors that do not sense the spectrum in

each time frame harvest energy from the spectrum to extend its lifetime by increasing the total energy of the sensor network. The proposed method uses convex optimization to select the network nodes according to the measurement of the accurate spectrum sensing and the amount of remaining energy. Choosing the duty of each node according to these two parameters will increase the network's lifetime along with the network's efficiency and accurate spectrum sensing to an acceptable level. Because in the existing methods in other similar works, the optimization of the network is not done correctly according to the energy and brightness. On the other hand, relying on convex optimization, the proposed method can be used for other cognitive radio networks and significantly reduce the volume of calculations compared to other algorithms.

The rest of the paper is as follows: Section 2 contains an overview of recent related works. In section 3, we have first introduced the proposed network model and then energy harvesting in it, and finally, we have formulated the proposed method for this model. The simulation results are included in section 4, and according to this section, we conclude in section 5.

2. RELATED WORKS

In the literature, the ability to harvest energy in the sensors of the CRSNs has been used to optimize various network parameters. For example, based on the Markov chain model introduced by Ercan et al. (10) for energy-efficient and spectrum-efficient slot-synchronized IoT cellular networks, these networks perform RF energy harvest, transfers, and share their spectrum opportunistically among other cellular networks. However, this research uses energy harvesting for cellular network efficiency. Nevertheless, the selection of energy harvester nodes, which PU randomly selects, is modeled in the Markov chain. With this random selection, the maximum lifetime of the network cannot be achieved because the network's energy is not considered a critical parameter in the algorithm. In other words, to share the spectrum with other networks, energy harvesting will happen in a limited and random manner to balance the amount of energy in the network.

Halima and Boujemâa (11) derived a new expression for Packet Error Probability (PEP) of several relay techniques when unlicensed users harvest licensed user RF signals and also presented the use of adaptive power to avoid interference. In this method, the proposed model adds several intermediary decision-making relays to the network; in each time frame of information transmission, one part of a slot is dedicated to harvesting energy and the other to sensing the network. With the increase in the number of nodes in the network, the number of intermediate relays also increases, and the problem of relay energy is also expressed as a challenging factor. The division of each time slot to harvest energy and sense the spectrum makes the energy harvesting and sensing of the network be done in a limited and constant manner in

each time frame. As a result, the probability of correct detection of the cooperative spectrum sensing, as well as the lifetime of the network, is optimized in a limited way.

Alsharoa et al. (12) addressed the RF multi-band energy harvesting using a Support Vector Machine (SVM); using this method, the secondary user senses the spectrum to decide on harvest and communication geographical regions of primary users. In this approach, complexity increases with the training data set. Relying on a multi-class SVM in this method requires a large amount of training data to implement the method for each network. Also, in this method, the energy harvesting in each SU is limited to a specific region of the network, and the need to check the area by the SU causes additional energy consumption in the network, which can reduce the network's lifetime by transmitting additional packets to sense the region.

Due to dynamic channel availability, limited node transmission range, and position-dependent energy arrival, an EH-based multi-hop clustering routing protocol (RFMCRP) was proposed by Wang and Ge (13). In this method, the main focus was on the routing and clustering of nodes so that the energy harvesting is limited to each cluster, and in the cases where the clustering becomes uneven, the energy consumption is out of the optimal state, and the network lifetime is reduced.

Due to the uncertainty of the energy harvesting process and the behavior of the primary user (PU), allocating and managing limited network resources is a crucial problem. Deng et al. (14) proposed a Q-learning-based channel selection method for energy harvesting and the randomness of the PU's behavior in the sensor network. By continuously interacting and learning with the environment, the method guides the secondary user (SU) to select the better-quality channel. In this method, energy harvesting is implemented by optimizing channel selection to sense the radio network, and due to the uncertainty of energy harvesting in this method, the network's lifetime will not reach the maximum achievable level.

Zheng et al. (15) proposed a hybrid active-passive communication scheme in which the SU adaptively makes channel selection and specific action decisions based on its knowledge of the channel availability and the amount of available energy. The decision to harvest energy or sense each node in this method has not been made for each time frame slot, and non-RF energy sources have been used to compensate for the amount of energy required in the problem of energy harvesting and in environments where energy sources are limited to RF sources, will lose its efficiency.

Salehi et al. (16) introduced a new multilevel inverter configuration that can harvest the unused energies and return them to another output which leads to the harvest of the maximum input energy. The multilevel inverter

with a focus on harvesting maximum energy (HME) comprises two terminals: one connected to an AC load and the other linked to a DC load or rechargeable batteries. Additionally, this inverter boasts a relatively low number of switches when compared to alternative configurations that do not harness unused energy.

A wideband planar monopole antenna design was put forth (17). This design incorporates fractal geometry and integrates a slender slot on the radiation patch, intended for energy harvesting purposes. The optimization of the antenna occurs at multiple stages throughout its development.

3. PROPOSED WORK

In this section, we first introduce the desired system model and formulate the energy harvesting for this model, and at the end, we describe the proposed optimization method.

3.1. System Model The single channel 5G CRSN consists of a Base Station (BS), N sensor nodes distributed randomly, and a primary user (PU) with a random position. Other assumptions considered are:

- The PU and the sensors are distributed independently of each other and uniformly in a square environment with a length size of L .
- The channel between the PU and the sensors is modelled considering path loss, lognormal shadowing, and multi-path Rayleigh fading. The channel being sensed is well known.
- Due to the simplicity of calculations and the efficiency of the energy detector in signal synchronization detection, each sensor uses an energy detector for spectrum sensing purposes.
- We assume a centralized cooperative spectrum sensing scheme, i.e., the sensors sense the channel and send the results to the centrally-located BS to fuse the sensors' results and make a global decision determining whether the channel is idle or busy.

Figure 1 shows the overview of the introduced network model. The objective is to specify the cooperating nodes to sense the channel and the nodes that harvest energy in such a way that:

$$\forall n_s, n_h \subset \{1, 2, \dots, N\} \quad \begin{cases} n_h \cap n_s = \emptyset \\ n_h \cup n_s = n \end{cases} \quad (1)$$

where n_h is the set of energy harvester sensors, and n_s is the set of channel sensing sensors. In other words, each sensor can be selected to perform one task at any time as shown in Figure 2, so the similarity of two sets of n_h and n_s must be empty, and their sum must be the total set of sensors n .

3. 2. Energy Harvesting CRSN may consume high energy due to sensing the spectrum. Hence, a CRSN with energy harvesting from a radio frequency (RF) PU signal is proposed to compensate for energy consumption. Here we assume each sensor node of the CRSN has both spectrum sensing and energy harvesting abilities, which can sense the PU channel or harvest the RF energy of the PU signal. The energy harvester model is specified in Figure 3.

Here spectrum sensing by a sensor n is modeled as a test of a binary hypothesis in which $H_{0,n}$ and $H_{1,n}$ are the absence and presence of the PU signal in the under-sensed channel, respectively. As a result, the channel can be used by SUs who are denied services when it appears. Therefore, we will have:

$$\begin{cases} H_{1,n}; X(k) = H_n \cdot S(k) + V_n(k) \\ H_{0,n}; X(k) = V_n(k) \end{cases} \quad (2)$$

where $V_n(k)$ is the k_{th} sample of additive white Gaussian noise with zero mean and variance σ_v^2 . $S(k)$ is the k_{th} sample of the PU signal, a random process with zero mean and variance σ_s^2 . It is assumed that $S(k)$ and $V_n(k)$ are independent. The random variable H_n denotes the channel gain between the PU and the sensor n . However, the channel is modeled considering path-loss attenuation, lognormal shadowing, and multi-path Rayleigh fading, which is assumed to be well-known

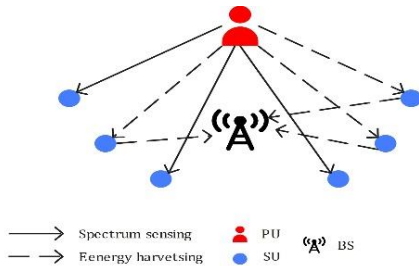


Figure 1. The desired model of CRSN

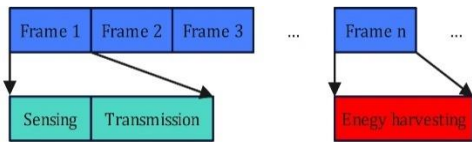


Figure 2. The frame structure of the proposed CRSN

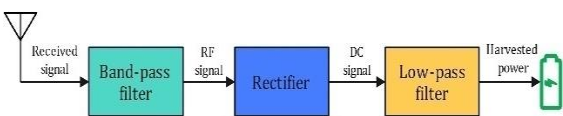


Figure 3. Energy harvesting model

(18). Accordingly, $X_n(k)$ denotes the k_{th} sample of the received signal from the under-sense channel observed by the sensor n .

The Energy Detector (ED) is used in the receiver of sensors due to its low complexity (19). Hence, the received signal energy is measured by the sensor n as:

$$RS_n = \frac{1}{K} \sum_{k=1}^K |X_n(k)|^2 \quad (3)$$

in which K is the number of samples calculated by:

$$K = \delta f_s \quad (4)$$

where δ and f_s are sensing time and sampling frequency, respectively. Then, the signal energy is compared with a threshold γ to generate a decision bit D_n . This bit shows the detected status of the channel by the sensor n , as follows:

$$\begin{cases} \text{if } RS_n \geq \gamma; D_n = 1 \\ \text{if } RS_n < \gamma; D_n = 0 \end{cases} \quad (5)$$

Therefore, the probabilities of correct detection in spectrum sensing for each sensor n can be calculated as follows:

$$\begin{aligned} P_{d_n} &= P(H_{1,n} | H_{1,n}) = P(RS_n \geq \gamma | H_{1,n}) \\ &= Q\left(\left(\frac{\gamma}{\sigma_v^2} - SNR_n - 1\right) \sqrt{\frac{\delta f_s}{2SNR_n + 1}}\right) \end{aligned} \quad (6)$$

in which SNR_n is the received signal-to-noise-ratio from the under-sensed channel in the sensor n due to reported data by Bagheri et al. (20). According to a similar process, false alarm probability is defined by:

$$\begin{aligned} P_{f_n} &= P(H_{1,n} | H_{0,n}) = P(RS_n \geq \gamma | H_{0,n}) \\ &= Q\left(\left(\frac{\gamma}{\sigma_v^2} - 1\right) \sqrt{\delta f_s}\right) \end{aligned} \quad (7)$$

Due to fading or shadowing effects and a limited sensing range of sensors, sensing the channel by only a single sensor may fail to detect the PU signal correctly. Any lost detection leads to a secondary transmission that interferes with unidentified active PU, and more false alarm leads to less frequency reuse opportunities for the SUs. Then if spectrum sensing is performed only by one sensor node, a more complicated and reliable detector (than an energy detector) is needed which may consume more energy. Therefore, this paper proposes centralized cooperative spectrum sensing to increase the sensing quality. On the other hand, the participation of all sensors in spectrum sensing could be more optimal. Because if all sensors participate in sensing, it leads to high energy consumption and false alarm without increasing significant correct detection. Thus, energy consumption

can be saved by determining the appropriate nodes for spectrum sensing. At the same time, the remaining sensors can be involved in energy harvesting, which is an excellent way to increase the network's lifetime.

In the sensing section, a group of sensor nodes cooperatively detect the presence of PU by sensing the channel. In contrast, the other nodes use simultaneous energy harvesting to collect the RF energy of the PU signal, and the frame structure of a CRSN for energy harvesting through spectrum sensing is shown in Figure 2. The harvested energy is then stored in the rechargeable batteries of the harvested nodes. Sensor and harvester nodes can change their modes in each frame to achieve energy balance. The figure shows the structure of energy harvesting that the RF energy of wireless signals is converted to DC energy with a rectifier circuit. The harvested energy for each sensor is denoted by EH_n and calculated as follows:

$$EH_n = \mu(1 + SNR_n)\sigma_n^2 \quad (8)$$

where μ is the efficiency of energy harvesting. The energy consumption of the sensor nodes can be divided into two parts. The first part of the consumption energy is used in ED to make a decision bit about the idle or busy state of the channel, which is denoted by ES_n . The second part of the energy is used to safely send the decision bit to BS, which is denoted by E_m . Therefore, the total energy consumption of each sensor E_{cn} involved in cooperative spectrum sensing is calculated as follows:

$$E_{cn} = E_{sn} + E_m \quad (9)$$

We assume that all sensors have the same structure and, therefore, all sensors are the same but can differ for different sensors that are calculated for each sensor as follows:

$$E_m = E_{t-elec} + e_{amp} \cdot d_n^2 \quad (10)$$

where E_{t-elec} is the energy consumption of the electronic circuits of the transmitter sensor, e_{amp} is the amplifier coefficient, the gain required to satisfy the database receiver's sensitivity, and d_n is the distance between the sensor n and the BS.

3.3. Optimization Algorithm The objective is to increase the lifetime of the CRSN by jointly classifying sensors into two groups:

- Sensing the spectrum with an acceptable sensing quality.
- Harvesting energy to save more energy and increase the sensors' lifetime.

For the first group, we select suitable sensors for cooperative spectrum sensing, considering the conditions on the maximum probability of false alarm denoted by α and the minimum probability of correct detection

denoted by β . To model the object as an optimization problem, we use an allocation index φ_n which determines whether a sensor is selected for the cooperative spectrum sensing or performs EH. According to the mentioned model for energy and also assuming the initial energy $E_{0,n}$ for the sensor n , the residual energy of the sensor after each period of sensing or harvesting is calculated by the following equation:

$$E_n = E_{0,n} + (1 - \varphi_n)EH_n - \varphi_n EC_n \quad (11)$$

If sensor n is selected for the cooperative channel sensing, $\varphi_n = 1$, and if it performs EH, $\varphi_n = 0$. Also, according to the proposed allocation index, we will have the global probability of false alarm and the global probability of correct detection, based on the OR fusion rule in the BS, as follows:

$$P_d = 1 - \prod_{n \in \mathcal{N}_s} (1 - \varphi_n P_{d_n}) \quad (12)$$

$$P_f = 1 - \prod_{n \in \mathcal{N}_s} (1 - \varphi_n P_{f_n}) \quad (13)$$

Now, we can mathematically define the problem as an optimization problem as follows:

$$\max_{\varphi_n} \{lifetime\} \quad (14)$$

Subject to:

$$P_f \leq \alpha \quad (14-1)$$

$$P_d \geq \beta \quad (14-2)$$

$$\varphi_n \in \{0,1\} \quad (14-3)$$

Equations 14-1 and 14-2 show the cooperative spectrum sensing efficiency constraints in this definition. Precisely, the smaller value of α provides probably more opportunities for the 5G SUs to use the free channel, and the larger β leads to less probability of interfering with the PU signal in the channel. However, there is no precise formula for a sensor network lifetime, and different related research has proposed different formulas based on their subject. In this paper, we propose the network lifetime as the time until the number of active sensors drops below LN where $0 < L \leq 1$ (21).

Also, we propose energy harvesting to extend the network lifetime. We define an active sensor as a node that its remaining energy is upper than lower bound, denoted as E_{min} . This proposed solution causes balanced energy use in the CRSN and extends the network lifetime. Upon the formulization, we can use the "max-min" method for optimizing the network lifetime. By this method, the minimum remaining energy of sensors will be maximized. Thus, the sensors that have the lower remaining energy are not selected for sensing, and they perform EH. It leads to the remaining energy level of

sensors keep balanced, consequently extending the network lifetime. The remaining energy and the minimum remaining energy of sensors are denoted by E_n and E_{th} , respectively. Now, the problem can be written as follows (22):

$$\max_{\varphi_n} \{ \min\{E_n\} = E_{th} \} \tag{15}$$

Subject to:

$$E_n \geq \varphi_n \cdot E_{th} \tag{15-1}$$

$$E_{th} \geq E_{min} \tag{15-1}$$

$$P_f \leq \alpha \tag{15-1}$$

$$P_d \geq \beta \tag{15-2}$$

$$\varphi_n \in \{0,1\} \tag{15-3}$$

We added the first constraint to emphasize that all sensors must have a residual energy level above to be selected for spectrum sensing. This constraint balances the energy consumption in the network and keeps the remaining energy of sensors at an almost balanced level. The second constraint is added to satisfy that a sensor harvests energy if it has less remaining energy and it is not selected to cooperate in spectrum sensing. Also, Equation 15-3 can be replaced with an equivalent condition. A short note on Equations 7 and 13 reveals that the false alarm probability for a sensor is independent of the SNR received by that sensor. Therefore, the global probability of a false alarm can be converted to another form, as follows:

$$P_f = 1 - \prod_{n \in J} \left(1 - \varphi_n \cdot Q \left(\left(\frac{\gamma}{\sigma_v^2} - 1 \right) \sqrt{\delta f_s} \right) \right) \leq \alpha \tag{16}$$

Then:

$$\sum_{n \in J} \ln \left(1 - Q \left(\left(\frac{\gamma}{\sigma_v^2} - 1 \right) \sqrt{\delta f_s} \right) \right) \leq \ln(1 - \alpha) \tag{17}$$

Finally, with the following definition, Equation 17 can be replaced with an equivalent condition that is easy to attend to:

$$|J| \leq J_{max} \triangleq \left\lceil \frac{\ln(1 - \alpha)}{\ln \left(1 - Q \left(\left(\frac{\gamma}{\sigma_v^2} - 1 \right) \sqrt{\delta f_s} \right) \right)} \right\rceil \tag{18}$$

where $|J|$ denotes the number of sensors participating in the sensing, and J_{max} shows the maximum number of sensors that can participate. If more sensors are selected for cooperative spectrum sensing, the condition for the probability of a false alarm will not be met. However, the global probability of correct detection for cooperative

spectrum sensing is met with fewer sensors. In that case, it is unnecessary to choose more sensors because it causes more energy consumption, while it has no advantage. Now, the problem can be rewritten as follows:

$$\max_{\varphi_n} \{E_{th}\} \tag{19}$$

Subject to:

$$E_{th} - \varphi_n \cdot E_n \leq 0 \tag{19-1}$$

$$E_{th} \geq E_{min} \tag{19-2}$$

$$\sum_{n=1}^N (\varphi_n - J_{max}) \leq 0 \tag{19-3}$$

$$\beta - \left(1 - \prod_{j \in J} (1 - \varphi_j \cdot P_{d_j}) \right) \leq 0 \tag{19-4}$$

$$\varphi_n \in \{0,1\} \tag{19-5}$$

Equation 19 cannot be considered a convex optimization problem because condition in Equation 19-4 is not convex. Therefore, using the Lagrange method (23), the priority of each sensor is obtained through the following:

$$PR_n \triangleq \frac{\rho_n (E_{0,n} - E_{th}) + \lambda \cdot P_{d_n}}{2 \rho_n \cdot E_{c,n}} \tag{20}$$

where ρ_n and λ are Lagranges multipliers. Finally, the pseudocode of algorithm is shown in Table 1.

TABLE 1. Pseudocode of optimization algorithm

```

Compute  $J_{max}$ 
While  $off\_sensors < (1-L)N$ 
     $\lambda = \frac{\lambda_{min} + \lambda_{max}}{2}$ ,  $\rho_n = \frac{\rho_{n,min} + \rho_{n,max}}{2}$ 
    While  $error > \epsilon$ 
        For  $j = 1:J_{max}$ 
            for  $n = 1:N$ 
                if  $E_n \geq E_n^c$ : Compute the  $PR_n$  and add
                sensor to selected sensors, counter =
                counter + 1
            Else:  $PR_n = 0$ 
        end
        Sort selected sensors
         $P_{d_m} = 1$ 
        if  $counter < J_{max}$  &  $P_{d_m} < \beta_m$ 
             $sl =$  selected from selected sensors
    
```

$$P_{d_n} = 1 - (P_{d_n} \times (1 - P_{d_{n,d}}))$$

end

end

end

Update E_n

$$\lambda = \max(\min(\lambda_{max}, \lambda), \lambda_{min}), \rho_n = \max(\min(\rho_{n,max}, \rho_n), \rho_{n,min})$$

end

4. SIMULATION AND RESULTS

In this section, the proposed algorithms are numerically evaluated using MATLAB computer simulations. We use the Monte Carlo method with 1000 iterations. It is assumed that a region with $400 * 400$ (m²), a sink node located in the center, N sensors, and one PU are distributed identically in this region. Here, the cognitive sensors use the IEEE 802.15.4/Zigbee (24). The simulation parameters are presented in Table 1. The sampling frequency of the sensor's energy in the detector equals the Nyquist frequency.

We compare our proposed method with two benchmark methods, detection based and random. In the detection base method, sensors are selected based on the probability of correct detection in the network sense, and this method increases its efficiency in meeting the optimization conditions. In the random method, the selected sensors for sensing the network are randomly selected, and the reason for the presence of this method in this comparison is its low complexity.

One of the critical parameters in the algorithm's efficiency is its success rate, which refers to the ratio of successful iterations of the algorithm to the total number of iterations. This parameter is shown in Figure 4 for a network with a different number of sensors. The success rate from the point of view of changing the network area is also compared in Figure 5.

TABLE 2. Simulation parameters

$f_s = 2.45GHz$	$E_{0,n} = 0.2mJ$
$e_{amp} = 40.4 \frac{pJ}{m^2}$	$E_s = 190nJ$
$E_{t-elec} = 80nJ$	$\sigma_s^2 = 10^{-11}W$
$\alpha = 0.1$	$\sigma_z^2 = 3dB$
$\beta = 0.9$	$\mu = 0.8$
$p_t = 20mW$	$L = 0.25$

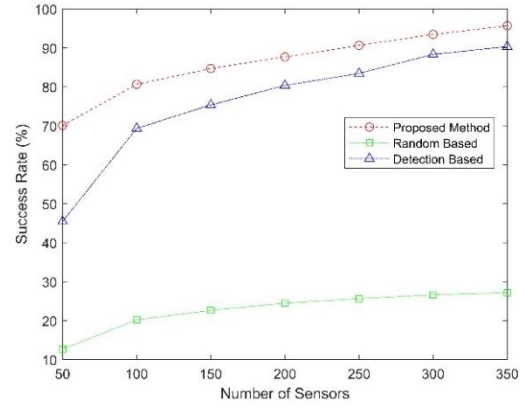


Figure 4. Success rate for different sensor numbers in a square area with 200 m length

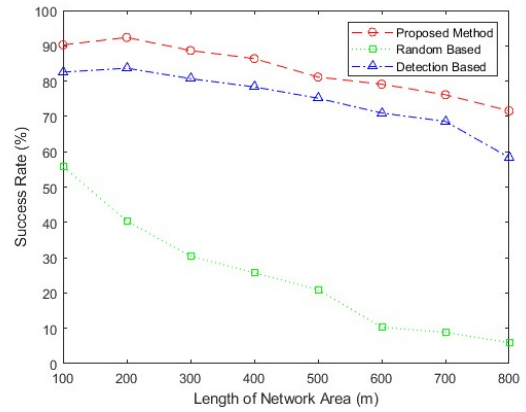


Figure 5. Success rate for different area with 200 sensors

The number of successful iterations as the network's lifetime, as shown in Figure 6. This figure shows that the proposed algorithm can perform better by increasing the number of sensors due to more optimal energy harvesting, which is superior to the detection-based method. Because by optimally choosing sensors based on the remaining energy and the probability of correct detection, it meets the optimization constraints in more iterations.

Figure 7 shows the simulation results for the minimum remaining energy in each iteration. This figure shows that according to the selection of sensors based on energy consumption and correct detection, the proposed algorithm performs more efficiently. Because in the other two methods, the amount of remaining energy is not checked.

The results in Figure 8 show that the number of alive sensors is more in the proposed algorithm. This is because energy harvesting is done according to the amount of remaining energy and correct detection by that sensor. In the other two methods, the energy harvester sensor is selected regardless of its priority regarding remaining energy.

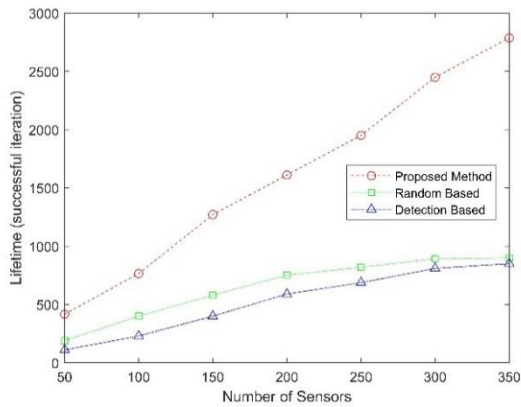


Figure 6. Lifetime for a CSRN in square area with 200m length

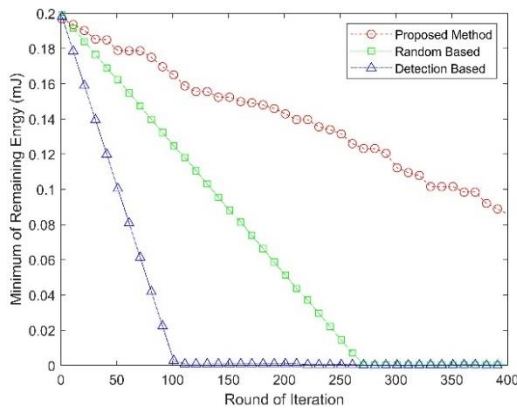


Figure 7. Minimum remaining energy in a CSRN with 200 sensors and 200m length

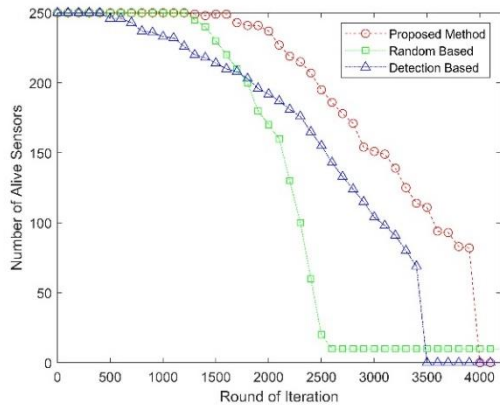


Figure 8. Number of alive sensors in a CSRN with 250 sensors and 200m length

5. CONCLUSION

Energy efficiency and lifetime are considered the main challenges of CRSN. In this paper, we improved the

performance of these networks by relying on convex optimization and providing an optimal method to harvest energy in the above networks. The results show that the proposed algorithm has a significant advantage over other methods in increasing the network lifetime and success rate.

This method relies on the optimal selection of sensors through a convex optimization to sensor selection in the network, leading the success rate to a minimum rate of 70% and increasing the network's lifetime by at least 32%. On the other hand, this method can be used in networks with more nodes because increasing the number of sensors does not limit the network's lifetime. Additionally, the amount of remaining energy in the network is reduced at a lower rate, which can improve the reliability of the network, and, due to the survival of a larger number of nodes, accurate sensing along with the optimal lifetime of the network can be achieved.

However, the convergence of this algorithm may decrease with the increase in the network size and the number of sensors. Also, in multi-channel networks, the selection of the channel used by each sensor to harvest energy can be added as an additional optimization factor to the proposed method. These issues considered one of the research focuses in the future to optimize the convergence rate of this optimization compared to the network size.

6. REFERENCES

1. Salina JL, Salina P. Next Generation Networks: perspectives and potentials: John Wiley & Sons; 2008.
2. Uwaechia AN, Mahyuddin NM. A comprehensive survey on millimeter wave communications for fifth-generation wireless networks: Feasibility and challenges. *IEEE Access*. 2020;8:62367-414. <https://doi.org/10.1109/ACCESS.2020.2984204>
3. Adigun O, Pirmoradian M, Politis C. Cognitive radio for 5G wireless networks. *Fundamentals of 5G Mobile Networks*. 2015:149-63. <https://doi.org/10.1002/9781118867464.CH6>
4. Setoodeh P, Haykin S. *Fundamentals of cognitive radio*: John Wiley & Sons; 2017.
5. Mergu K, Khan H. Mitigation of spectrum sensing data falsification attack in cognitive radio networks using trust based cooperative sensing. *International Journal of Engineering, Transactions C: Aspects*. 2021;34(6):1468-74. <https://doi.org/10.5829/IJE.2021.34.06C.10>
6. Tseng F-H, Chao H-c, Wang J. Ultra-dense small cell planning using cognitive radio network toward 5G. *IEEE Wireless Communications*. 2015;22(6):76-83. <https://doi.org/10.1109/MWC.2015.7368827>
7. Suraweera HA, Smith PJ, Shafi M. Capacity limits and performance analysis of cognitive radio with imperfect channel knowledge. *IEEE Transactions on Vehicular Technology*. 2010;59(4):1811-22. <https://doi.org/10.1109/TVT.2010.2043454>
8. Zheng K, Liu X, Zhu Y, Chi K, Li Y. Impact of battery charging on spectrum sensing of CRN with energy harvesting. *IEEE Transactions on Vehicular Technology*. 2020;69(7):7545-57. <https://doi.org/10.1109/TVT.2020.2994005>

9. Guo J, Hu H, Da X, Liu J, Li W. Optimization of energy efficiency for cognitive radio with partial RF energy harvesting. *AEU-International Journal of Electronics and Communications*. 2018;85:74-7. <https://doi.org/10.1016/J.AEUE.2017.12.030>
10. Ercan AÖ, Sunay MO, Akyildiz IF. RF energy harvesting and transfer for spectrum sharing cellular IoT communications in 5G systems. *IEEE Transactions on Mobile Computing*. 2017;17(7):1680-94. <https://doi.org/10.1109/TMC.2017.2740378>
11. Halima NB, Boujemâa H. Energy harvesting with adaptive transmit power for cognitive radio networks. *Telecommunication Systems*. 2019;72(1):41-52. <https://doi.org/10.1007/S11235-019-00548-W/METRICS>
12. Alsharouf A, Neihart NM, Kim SW, Kamal AE, editors. Multi-band RF energy and spectrum harvesting in cognitive radio networks. 2018 IEEE International Conference on Communications (ICC); 2018: IEEE.
13. Wang J, Ge Y. A radio frequency energy harvesting-based multihop clustering routing protocol for cognitive radio sensor networks. *IEEE Sensors Journal*. 2022;22(7):7142-56. <https://doi.org/10.1109/JSEN.2022.3156088>
14. Deng X, Guan P, Hei C, Li F, Liu J, Xiong N. An intelligent resource allocation scheme in energy harvesting cognitive wireless sensor networks. *IEEE Transactions on Network Science and Engineering*. 2021;8(2):1900-12. <https://doi.org/10.1109/TNSE.2021.3076485>
15. Zheng K, Wang J, Liu X, Yao X-W, Xu Y, Liu J. A Hybrid Communication Scheme for Throughput Maximization in Backscatter-aided Energy Harvesting Cognitive Radio Networks. *IEEE Internet of Things Journal*. 2023. <https://doi.org/10.1109/JIOT.2023.3267453>
16. Salehi SJ, Shmasi-Nejad M, Najafi HR. A new multilevel inverter based on harvest of unused energies for photovoltaic applications. *International Journal of Engineering, Transactions C: Aspects*. 2022;35(12):2377-85. <https://doi.org/10.5829/ije.2022.35.12c.14>
17. Fakharian M. A wideband fractal planar monopole antenna with a thin slot on radiating stub for radio frequency energy harvesting applications. *International Journal of Engineering, Transactions B: Applications*. 2020;33(11):2181-7. <https://doi.org/10.5829/ije.2020.33.11b.08>
18. Bagheri A, Ebrahimzadeh A, Najimi M. Game-theory-based lifetime maximization of multi-channel cooperative spectrum sensing in wireless sensor networks. *Wireless networks*. 2020;26(6):4705-21. <https://doi.org/10.1007/S11276-020-02369-1/METRICS>
19. Maleki S, Chepuri SP, Leus G. Optimization of hard fusion based spectrum sensing for energy-constrained cognitive radio networks. *Physical Communication*. 2013;9:193-8. <https://doi.org/10.1016/J.PHYCOM.2012.07.003>
20. Bagheri A, Ebrahimzadeh A, Najimi M. Energy-efficient sensor selection for multi-channel cooperative spectrum sensing based on game theory. *Journal of Ambient Intelligence and Humanized Computing*. 2021;12:9363-74. <https://doi.org/10.1007/S12652-020-02651-2/METRICS>
21. Noori M, Ardakani M. Lifetime analysis of random event-driven clustered wireless sensor networks. *IEEE Transactions on mobile computing*. 2010;10(10):1448-58. <https://doi.org/10.1109/TMC.2010.254>
22. Najimi M, Ebrahimzadeh A, Andargoli SMH, Fallahi A. Lifetime maximization in cognitive sensor networks based on the node selection. *IEEE sensors Journal*. 2014;14(7):2376-83. <https://doi.org/10.1109/JSEN.2014.2311154>
23. Boyd SP, Vandenberghe L. *Convex optimization*: Cambridge university press; 2004.
24. Han D-M, Lim J-H. Smart home energy management system using IEEE 802.15. 4 and zigbee. *IEEE Transactions on Consumer Electronics*. 2010;56(3):1403-10. <https://doi.org/10.1109/TCE.2010.5606276>

COPYRIGHTS

©2024 The author(s). This is an open access article distributed under the terms of the Creative Commons Attribution (CC BY 4.0), which permits unrestricted use, distribution, and reproduction in any medium, as long as the original authors and source are cited. No permission is required from the authors or the publishers.

**Persian Abstract****چکیده**

فناوری ارتباطی 5G از اینترنت اشیا، مراکز مراقبت بهداشتی از راه دور و محاسبات ابری با تنظیم خدمات ارتباطی آنها در طیف بسیار وسیعی از باندهای فرکانسی با هزینه، مصرف باتری و تأخیر کم پشتیبانی می‌کند. با این حال، توسعه چنین فناوری بی سیم به شدت به طیف فرکانس رادیویی وابسته است. شبکه حسگر رادیویی شناختی (CRSN) یک پیشنهاد عالی برای بهبود استفاده از طیف رادیویی و مدیریت ترافیک داده‌های ارتباطی سنگین در شبکه‌های بی سیم 5G است. CRSN می‌تواند با شنجش کانال‌های فرکانسی استفاده از کانال‌های رایگان را برای کاربران ثانویه (که از خدمات محروم هستند) ممکن سازد. با وجود ویژگی‌های برجسته CRSN، برخی محدودیت‌ها بر عملکرد آنها سایه می‌اندازد. مهم‌ترین محدودیت، مسئله انرژی و مصرف بهینه آن برای افزایش طول عمر شبکه است. تحقیقات اخیر نشان داده است که برداشت انرژی می‌تواند راه حل موثری برای افزایش طول عمر CRSN باشد. از طرفی، حسگرها باید طیف فرکانس را با نرخ موفقیت بالا شنجش کنند. در این مقاله انتخاب چندین گره حسگر بهینه برای برداشت انرژی با رویکرد افزایش طول عمر شبکه برای حل چالش مذکور پیشنهاد شده است. به این ترتیب که گره‌های حسگر به دو گروه مستقل برای شنجش همزمان طیف و برداشت انرژی در هر بازه زمانی تقسیم می‌شوند. این مسئله را بر اساس بهینه‌سازی ریاضی و استفاده از راه‌حل‌های پیشنهادی برای مسائل محدب حل خواهیم کرد. در نهایت، شبیه‌سازی‌ها برای ارزیابی توانایی راه‌حل پیشنهادی، بر پایه IEEE802.15.4/Zigbee و IEEE802.11af توسعه داده می‌شوند.



Design and Evaluation a New Type of Semi-active Lower Limb with Knee Joint Booster

S. Niknezhad, A. Moazemi Goudarzi*, M. Hasan Ghasemi

Department of Mechanical Engineering, Noshirvani University of Technology, Babol, Iran

PAPER INFO

Paper history:

Received 09 October 2023
 Received in revised form 30 October 2023
 Accepted 04 November 2023

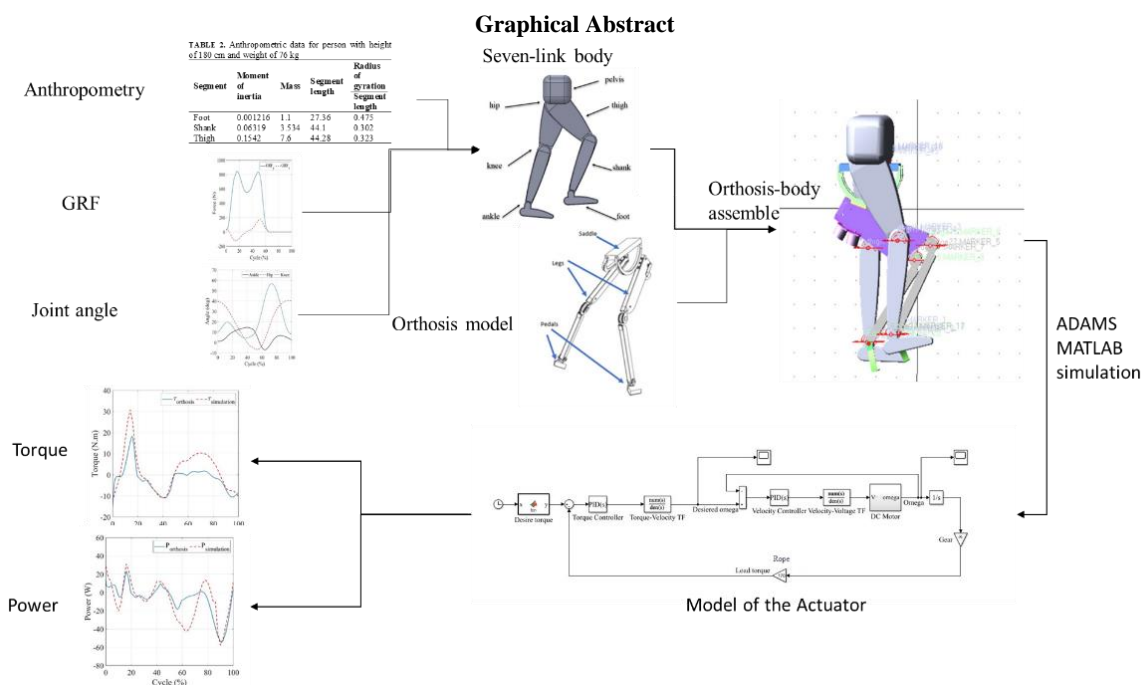
Keywords:

Lower Limb Orthosis
 Series Elastic Actuator
 Adjustable Stiffness
 Gait Assistance
 Knee Rehabilitation

A B S T R A C T

This article presents a new lower limb orthosis for helping weak knees during human locomotion. The orthosis structure has 10 degrees of freedom. It utilizes a series elastic actuator, equipped with an elastic rope that transfers torque generated by the motor to the orthosis link. The performance of the proposed lower limb orthosis is virtually simulated by using ADAMS-MATLAB Co-simulation software. The orthosis is designed based on the anthropometric data of a normal human body with a mass of 76 kg and a height of 180 cm. The simulation scenario involves walking with an average speed of 1 m/s on a straight path, and the knee orthosis can bear 40% of the torque exerted by the knee joint during the gait cycle. The simulation aims to evaluate the effectiveness and efficiency of the orthosis in assisting the weak knee joint. The simulation results indicate that The orthosis reduced the knee joint torque by more than 13 Nm in a healthy person, which indicates lower forces on the weak knee. Moreover, the orthosis decreases the maximum energy needed per gait cycle, which implies a higher efficiency and reduces the metabolic cost of the body in the gait cycle.

doi: 10.5829/ije.2024.37.05b.03



*Corresponding Author Email: goudarzi@nit.ac.ir (A. Moazemi Goudarzi)

1. INTRODUCTION

The knee joint performs a vital role in human mobility, as it carries the weight of the body, enables lower limb swing, and absorbs impact from the ground. It is the largest joint in the body and experiences varying forces and torques while walking. The maximum amount of these torques are applied to the knee joint in the stance phase (1). The human movement relies on the knee joint's function and will be impaired if it is not working properly. Prior studies of wearable robots have noted the importance of rehabilitating people who have weak knee joints (2, 3).

Movement disorders affecting various parts of the body are prevalent worldwide, and they can stem from a variety of factors. The aging of the global population is one of the most important medical and social problems worldwide (4). Based on reports from the World Health Organization, it is anticipated that by 2030, approximately one in six individuals globally will be 60 years or above. This demographic shift is expected to lead to an increased demand for rehabilitation services, due to factors such as accidents, a growing number of stroke patients, weight gain, and weakness of some muscles like gluteal muscles, quadriceps, adductors, hamstrings, gastrocnemius, and soleus (5, 6).

Additionally, the lack of physiotherapists is one of the reasons for the shift to robot-assisted rehabilitation (7). The development of rehabilitation devices is of utmost importance in enabling patients to acquire the necessary ability to lead normal lives. These devices serve as a training tool, assisting patients in their physical and cognitive therapy, which in turn, enables them to regain their independence. The provision of such devices, therefore, plays a crucial role in the restoration of patients' physical and mental health.

In this manner, wearable robots are designed to reduce the torque on the joints and body parts (8), alleviate the exhaustion resulting from prolonged walking (9), and even enhance the speed of walking (10). Orthoses are a common types of wearable robot that provide external support for the neuromuscular and skeletal systems. They are worn parallel to the body's limbs and are used to assist patients in correcting or restoring movement functions. Orthoses can be classified into three types: active (11, 12), semi-active (13), and passive (14). Active and semi-active orthoses rely on an external power source for transmission and are mainly used by patients with limbs and joints diseases (15).

Although there have been notable improvements in the design of them, these devices continue to encounter some obstacles. Despite the notable technological advancements that have revolutionized the orthosis industry, the cost of these medical devices remains a pressing concern for a considerable number of individuals. Unfortunately, a significant portion of the

population is still unable to afford the high prices of orthotic devices. It is an ongoing challenge to ensure safe interaction between orthosis devices and the human body. Comfort, ergonomic suitability, and potential skin irritation are important factors that must be fully addressed to ensure user satisfaction and long-term usability since these devices are intended to be worn or attached to the body.

In this manner, this article aims to improve the design of orthoses by addressing some of its weaknesses. By positioning the orthosis between the legs, the hands can move freely and the center of mass is brought closer to the body's own center of mass. This reduces the moments of inertia of the body. Moreover, the orthosis design eliminates interaction with the lower limbs, making it even safer to use with series elastic actuators (16). It also considered ergonomics when designing the knee structures to minimize misalignment, an aspect that has been overlooked in previous studies.

On the other hand in contrast of reported data (17, 18) by replacing the traditional spring and ball screw with elastic rope, the cost of the orthosis can be significantly reduced. The elastic rope connects the motor to the knee joint of the orthosis and takes up minimal space by being positioned between the orthosis link. Notably, unlike in previous studies, the user will not experience any additional weight from the orthosis (19, 20).

To summarize the content of this article, a newly designed lower limb orthosis was explored by modeling it in a walking position using Adams software. The orthosis includes two links for each leg, two pedals, and a saddle positioned between the legs. For this study, a series elastic actuator was chosen as it offers an electric motor and an elastic rope to regulate the pivot's stiffness. This stiffness is managed by a feedback loop that measures the torque and the pivot's angular displacement. A closed-loop torque control system with a reaction torque sensor is utilized that can precisely achieve assistive or resistive torques for different physical therapies. As a result, this controllable stiffness pivot mechanism offers a flexible and adaptable approach to support a weakened knee joint.

The remainder of this paper is structured as follows: In the second section, the physical model of the orthosis is described, along with a detailed explanation of the actuator model and its components. The third section covers the participant's properties, as well as the collection of his kinematic and anthropometric data. In section four, the knee torque of a healthy individual is simulated using Adams software, which is later evaluated using experimental data. Finally, the orthosis is implemented on it. The results of this implementation are presented and discussed in section five. The paper concludes with the presentation of the conclusions in the final section.

2. MODEL DESCRIPTION

2. 1. ORTHOSIS The orthotic device comprises two interconnected links, namely the shank and thigh, and incorporates a saddle positioned between the user's legs. The design of the orthosis is intended to offer stable support to the lower extremities, enhancing the user's mobility and overall functionality Figure 1(a). The device is equipped with two degrees of freedom, allowing the user to move in both the sagittal and frontal planes. Additionally, it features a pedal that connects to the soles of an individual's shoes through a two-degree-of-freedom joint, allowing movement in both sagittal and transverse planes as shown in Figure 1(b). When simulating movement in the sagittal plane, there are six degrees of freedom, with one in each joint. The ankle and hip joints are aligned with those of a typical human model, but the knee joints are parallel to the wearer's knee, not in alignment with it as shown in Figure 2(a). The orthosis that has been suggested, when combined with the thigh and leg of the user's lower limbs, creates a four-bar mechanism as shown in Figure 2(b). Only the knee joints of orthosis are active and can perform mechanical work. To avoid disturbing the user and minimize the weight burden on the knee joint, it is recommended to place the motor at the back of the thigh link, near the center of mass instead of directly on the knee joint.

In order to enhance stability and mitigate torque during walking, the knee joint of the orthosis is connected to a motor via an elastic rope. The elastic rope is responsible for applying a 15 Nm preload in the direction of knee extension, thereby preventing the leg from bending while the person is in the stance position. During the swing phase, which accounts for 55-80 percent of the walking cycle, the motor produces a torque in the direction of flexion to assist the patient in maintaining their foot position. In order to maintain the safety of the patient, we gradually reduce the amount of applied torque.

It is important to be mindful that the use of orthosis aims to decrease the forces exerted on the knee joint. Therefore, it is crucial to ensure that the weight of the orthosis does not impede walking and that the auxiliary device's size does not hinder mobility. In general, reducing the weight of the orthosis and increasing its strength will increase the cost of the orthosis, and it may not be economically utilizable for all people in society. The design must strike a balance between the cost of the design and the structural characteristics of the orthosis. The orthosis links are typically made of aluminum alloy, which is not only lightweight but also has high-strengt (21).

The present orthosis offers a noteworthy economic advantage over the existing series elastic actuator-based orthoses, particularly in terms of its power transfer system. This is accomplished through the elimination of

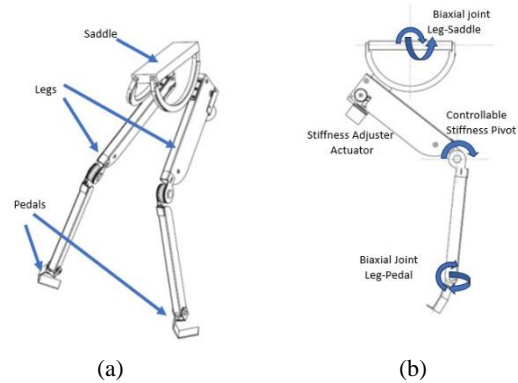


Figure 1. Characteristics of designed lower limb orthosis (a) main mechanical component (b) device degrees of freedom

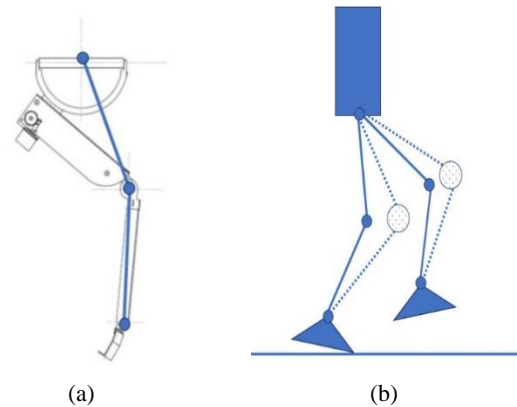


Figure 2. Schematic of how orthosis act on knee joint (a) the simplicity of orthosis components and assumption of joints place (b) Forming a four-bar mechanism by orthosis links and individual's legs

components such as ball screws and replacement of springs with elastic ropes. The resulting cost reduction and improved efficiency make it a promising choice for business and academic settings alike. Moreover, the orthosis's design situated between the legs allows for unhindered movement of the hands. The orthosis can also support a portion of the user's body weight while they are sitting on a saddle that is in direct contact with the ground. This layout improves communication between individuals and robots.

2. 2. ACTUATOR The actuator which is selected to assist human gait is the series elastic actuator. Actuator components include four main groups motor, elastic agent, control system, and sensors.

1) Motor

The motor is one of the significant components of the series elastic actuator, which provides the necessary power and torque to assist in walking. power capacity and maximum torque are the two primary performance

factors in properly selecting a motor for a specific application or use. A motor's capacity is determined by the maximum permissible power, which can be measured by multiplying the torque it generates by the angular velocity. The speed and torque of the motor are inversely related. The speed must be decreased proportionally if we want to increase the output torque. In order to increase output torque and transmit power, gearboxes are commonly utilized in robotic applications. For this particular research, the Maxon RE35 24V DC graphite brush motor was employed, which has a power rating of 90 watts and weights 340 grams. To further enhance performance, the study also utilized the GP42C planetary gearhead, which weights 465 grams and has a transmission ratio of 156:1. This combination of motor and gearbox is capable of consistently handling a maximum torque input of 15 Nm. The characteristics of proposed motor are listed in Table 1.

2) elastic element

This particular design employs an elastic rope as the elastic component. This component is installed within the orthosis thigh link to serve as a connection between the motor and the knee joint. The elasticity rope is connected to two flexible ropes that are carefully wrapped around pulleys, as illustrated in Figure 3.

Another advantage of this type of elastic design is that it is placed between the motor and the load and softens the power or torque transmitted from the motor to the orthosis link. It also acts as an energy buffer, storing energy when the constraint joint does negative work and helping it when it does positive work. By increasing the stiffness of the rope, the controllability of the system improves at higher frequencies. But it should be noted a hard elastic element is less sensitive to small torques, and this causes the accuracy of torque control to decrease. In addition, the stiffer the rope, its nonlinear terms increase and it no longer obeys Hooke's law. Spring constant values for walking aids are usually in the range of 100 to 300 Nm/rad (22), and the maximum torque they can apply is from 10 to 100 Nm (23). According to the mentioned points, the constant value of the spring was determined to be 170 Nm/rad.

3) Control system

Due to the interaction between the orthosis and the body, this device must be mechanically compatible with the anatomy of the wearer's body so as not to interfere with his walking (24). In the arms of industrial robots, a high impedance actuator is used in a large frequency bandwidth to effectively reject disturbances. But because both legs are in contact with the ground separately as a rigid body during gait, a low impedance actuator is used to increase safety and comfort and prevent resistance to human movement (25). In general, low impedance excitation means that the actuators control the force or torque applied to the load rather than the commanding position or angle. The series elastic actuator has

TABLE 1. Parameters of motor used to drive series elastic element

Nominal Voltage	24 V
Terminal Resistance	0.582 Ω
Terminal Inductance	0.191 mH
Torque Constant	0.0292 Nm/A
Back EMF Constant	0.0292 V s/rad
Rotor and Gearhead Inertia	88.1 g cm ²
Damping Constant	0.0013 Nms



Figure 3. Form of the elastic element inside hip link of orthosis

inherently low impedance due to the use of a spring between the gearbox and the load. In this design, the speed control loop provided by Robinson (26) is used for the motor. Using the speed controller in the motor overcomes some undesirable effects of the motor and gearbox such as non-linearity and stickiness, and it is much simpler than the flow controller from the point of view of implementation. By creating a torque controller on the speed controller in a cascade manner, the desired result can be achieved in the output of the actuator. This result applies as torque to the orthosis link. One of the most common control algorithms used in the industry is the Proportional Integrative Derivative (PID) control. This algorithm is widely applied in the industry because of its simplicity and easy implementation in control system (27).

4) Sensors

By getting feedback from key components, this structure can achieve extremely high control accuracy (28). The sensors that used in this study are: an encoder is placed at the end of the motor and before the gearbox to measure the motor's output speed, so it is possible to determine the type of gearbox and speed reduction ratio based on that information. A potentiometer measures the

angle of the orthosis joint. By subtracting it from the gearbox output angle, it is multiplied by the spring stiffness and determines the final torque that enters the orthosis link. A potentiometer is also needed in the person's knee joint to detect the beginning of the gait cycle. It is also needed to turn on the motor to help the gait cycle. In addition, by using two switches in the toe and heel parts of a person's sole, it is possible to recognize the beginning and end of the stance phase.

3. BIOMECHANICAL CONSIDERATION

3. 1. Gait Analysis

Walking can reveal consequential information about people's health status. By having the information obtained from how to walk and their detailed analysis, it is possible to treat many diseases and disabilities related to the lower limbs. This information can even prevent many problems.

The analysis of human walking is one of the most challenging issues in biomechanics due to the many nonlinearities in the walking equations, GRF, and the force exerted by the muscles.

Among the approaches to obtain the necessary information for gait analysis, the method of using clinical gait analysis, known as motion capture, is straightforward, more accurate, and more widely used than other methods. Motion capture laboratories are usually equipped with cameras and force plates. These devices are used to determine kinematic information and external forces acting on the body. In this regard, Kirtley (29) conducted various experiments on the way the organs are placed in the walking cycle and the forces transferred when the foot contacts the ground, the result of which is the basis of the current research (Figure 4). Using inverse kinematics has some advantages such as avoiding position error, that may occur in the use of the forward kinematic approach (30).

It is essential to understand how these angles are defined to examine the graph of joint angles during the gait cycle. In this article, joint motion in this plane is simply referred to as flexion and dorsiflexion (positive direction), extension and plantarflexion (negative direction) (31). It should be noted that this data is for a person who moves at 1 m/s on a straight path. Increasing walking speed decreases the percentage of the stance phase, which includes double support and single support, and increases the swing phase. Also, as the person's speed increases, the maximum angle of the joints in the walking cycle increases.

In a general review of the position of the limbs in a walking cycle, it can be found that if movement is on a straight path and the body's speed remains constant, the position of the limbs relative to each other is repeated periodically. In other words, the information obtained from one walking cycle can be generalized to the entire

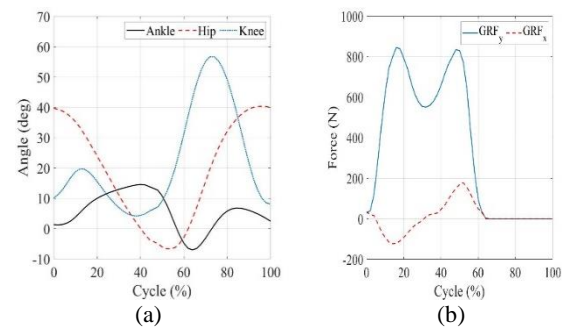


Figure 4. The properties of a person with 76 kg weight with the speed of 1 m/s. (a) the measure of joints angle during the gait cycle (b) the ground reaction force (GRF) applied to the foot

TABLE 2. Anthropometric data for person with height of 180 cm and weight of 76 kg

Segment	Moment of inertia	Mass	Segment length	Radius of gyration Segment length
Foot	0.001216	1.1	27.36	0.475
Shank	0.06319	3.534	44.1	0.302
Thigh	0.1542	7.6	44.28	0.323

walking process in other cycles with an acceptable approximation. The vertical force of Earth's reaction is more than in other directions. At some stages of the walking cycle, this force reaches even higher and lower than body weight. One of the reasons for this is the decreasing and increasing acceleration of the lower limbs during the walking cycle. For example, when the foot hits the ground, the speed is negative, and its amount decreases, as a result, the acceleration will be positive, and according to Newton's second law, the sum of this positive value along with the force caused by the body's weight will enter the foot.

3. 2. Inverse Dynamics

In this article inverse dynamics' method is used to obtain forces and moments in the joints whereby kinematic information and external forces are used. The inertia, size, and mass of each body part must be known to correctly estimate joint torques. Considering that it is difficult for each person to measure anthropometric characteristics, the size of these parameters is usually estimated from the determined values of corpses collected by Winter (32). This information for a subject with a weight of 76 kg and a height of 180 cm can be seen in the Table 2. Since many muscles cause movement in the joint, it is impossible to accurately measure which muscles contribute to applying force. But on the other hand, the inverse dynamics method is used of obtaining kinematic information, as well as forces and moments in joints and limbs.

where the moment of inertia is around the center of mass of the organs and is obtained according to the following formula:

$$I_i = m(L_i\rho_i)^2 \quad (1)$$

where L_i is the length of each member, ρ_i is the radius of gyration to the length of each member at the center of gravity.

4. SIMULATION

4.1. GAIT In order to showcase the mechanics of walking, certain simplifications are commonly employed. Specifically, it is assumed that the upper body and hands remain stationary during human locomotion. Additionally, the lower limbs are presumed to be symmetrical, meaning that information gleaned from one leg can be applied to the other foot as well.

After simplifying the model, Adams software is used to design the seven-link model with rigid components. Due to the assumption that walking movements mostly occur in the sagittal plane, movements in other planes can be disregarded. As a consequence, the joints are modeled as a hinge joints. Use a simply hinged 1 degree of freedom system is designed to facilitate system control through the simplification of dynamic models; it also serves the purpose of improved durability. In reality, however, human joints do not simply rotate around one axis. The mass and center of mass of these links are determined according to Table 2. As a movement agent, a motion is placed on each of the joints, which is only able to move in the sagittal plane. The input function of each of these motions is the angular information obtained from the fitting of Kirtley's experiments are shown in Figure 4.

Interpolation involves identifying data points come before and after a given set of information. In Adams, the joint angle curve is imported as spline data, and a third-order spline curve is utilized to interpolate these points. Due to the limitations of the contact model in Adams and to correctly apply the GRF to the individual's foot, this force was introduced to the center of pressure (COP) the foot in each part of the cycle. center of pressure (COP) is the term given to the point of application of the ground reaction force vector. The ground reaction force vector represents the sum of all forces acting between a physical object and its supporting surface. The way to enter this force in the software is to consider during the stance phase, the center of pressure varies from the heel to the toe. Therefore, each percent of the cycle is attributed to a specific point of the foot.

With the help of the reference coordinate device, it is possible to calculate the position, speed, and acceleration of each component using kinematic equations based on the reference coordinates device. If it is assumed that the

person moves at a constant speed, considering that the trunk is fixed during walking, then the horizontal acceleration for the trunk part is equal to zero. For example, for thigh link:

$$\begin{aligned} a_t &= a_{tr} + a_{t/tr} \\ a_{t/tr} &= \alpha_t \times r_t + \omega_t \times (\omega_t \times r_t) \\ a_{t/tr} &= \alpha_t \vec{k} \times (r \sin \theta_h \vec{i} + r \cos \theta_h \vec{j}) + \\ &\omega_t \vec{k} \times [\omega_t \vec{k} \times (r \sin \theta_h \vec{i} + r \cos \theta_h \vec{j})] \end{aligned} \quad (2)$$

where a_t is the acceleration of the thigh link, a_{tr} is the acceleration of the trunk and $a_{t/tr}$ is the acceleration of the thigh relative to the trunk.

To use the inverse dynamic method, we consider all the forces that come from the ground and the linear and angular acceleration of the links. This helps us calculate the forces, moments, and power for each joint.

The force of the foot determines from the kinematic equations according to the newton's second law. The torque of the ankle joint can obtain as follow:

$$\begin{aligned} \sum M_a &= I\alpha_a \\ M_a + f_x r \sin(\beta) + G_x r \sin(\beta) + f_y r \cos(\beta) - \\ G_y r \sin(\beta) &= I\alpha_a \end{aligned} \quad (3)$$

where $\beta = \theta_h - \theta_k - \theta_a$ which respectively are the angle of hip, knee and ankle joints.

In the same way, the shank and thigh forces and torques are also calculated. In general, stance and swing dynamic equations are different. Because GRF component is disappeared in swing phase.

The results of gait simulation are shown in Figure 5. The comparison of torque in experimental data and simulation has an average error percentage of 9.51%. Comparison of power in laboratory mode and simulation has an average error percentage of 5.74%.

4.2. ORTHOSIS Orthosis components, the links, and the physical model are transferred from the Solidworks to Adams. However, the actuator model is simulated in Simulink.

First, the motor model is created according to the specifications given in Table 1. This model includes two mechanical and electrical parts that follow the following two general equations:

$$V = L \frac{di}{dt} + Ri + e \quad (4)$$

$$T = J \frac{d\omega}{dt} + B\omega + T_L \quad (5)$$

According to the explanations, the actuator model is simulated in the MATLAB/Simulink environment. This model includes an internal velocity PID controller, and a torque PID controller cascaded on the velocity controller. A gear system is installed between the motor output and the spring input. The gear ratio causes the motor output

speed to be reduced while the torque transmitted to the orthosis links is increased.

Gear head modeling consists of several gears, which are alternated by a gain block in Simulink. The elastic element is also placed between the gearbox and the orthosis link, modeled using the block. The schematic model of the actuator can be seen in Figure 6.

The model of actuator applied on leg with orthosis is shown in Figure 7.

5. RESULTS AND DISCUSSION

The orthosis and body model were exported and The physical model of the orthosis was implemented on the body in Adams software (Figure 8). The placement of the orthosis was thoughtfully considered, as the wearer's center of gravity is closer to the inner part of the body, this ensures that it exerts minimal force on their lower limbs and does not impede their ability to walk. In addition, the hand movements are executed with ease and do not hinder movement while walking. In order to assess how orthoses affect an individual's legs, it is crucial to establish a linkage between the actuator model in

Simulink and the physical models in Adams. This work is done with ADAMS-MATLAB Co-simulation. To define the orthosis model in Adams software, it is necessary to define an inputs and outputs. As previously stated, the input to the system is the torque that the actuator must apply to the orthosis. The system outputs

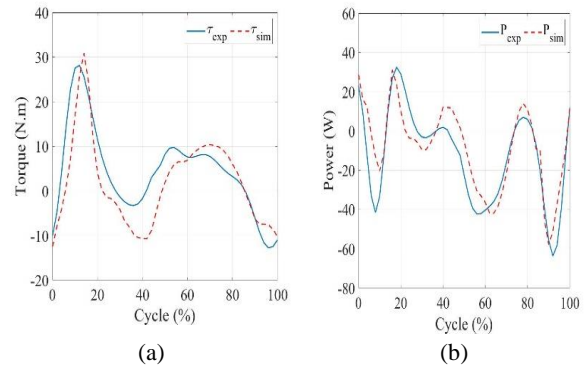


Figure 5. Validation of the knee (a) torque and (b) power obtained in Adams simulation with Kirtly's experiment for healthy individual

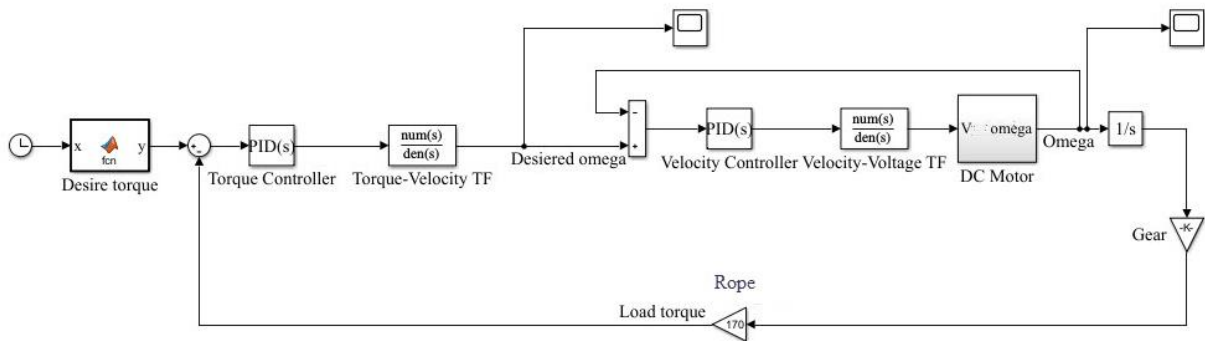


Figure 6. The schematic model of the actuator that simulated in MATLAB/Simulink environment. Both torque and velocity controllers are PID types. Transfer functions convert the output of controllers to the velocity input of the motor.

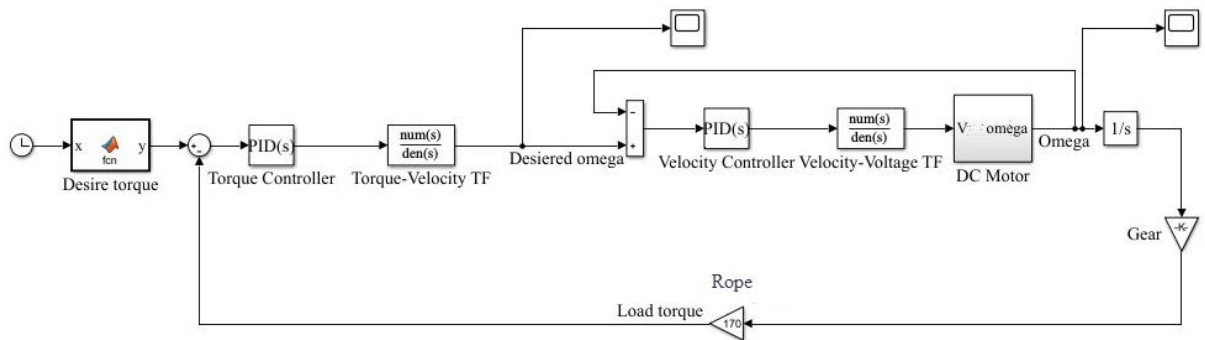


Figure 7. The model of actuator applied on leg with orthosis. The sensor measure angle of orthosis joint and reduced from the engine output angle. This angle multiplies by spring stiffness and applies torque to the orthosis link.

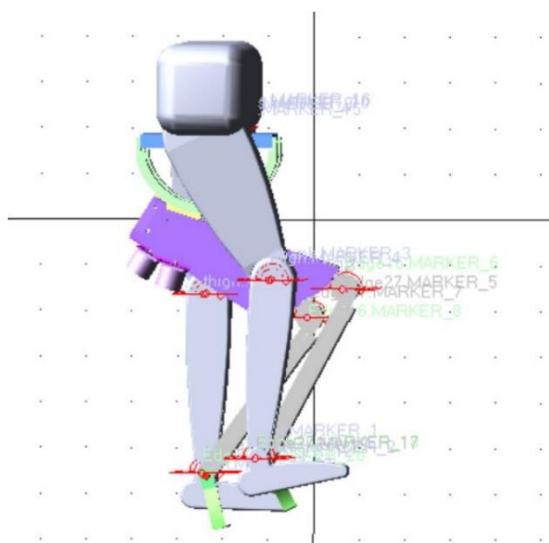


Figure 8. Physical model of orthosis applied on the body in MSC Adams

include a sensor located at the knee joint of the orthosis that provides angle information to the system, as well as the torque and angular velocity in the knee joint of the lower body model. These outputs are the ultimate objectives of this study. Finally, The model is exported to Simulink, the actuator's output is connected to the torque input defined in the orthosis joint, and an angle sensor measures information about the orthosis knee angle (Figure 7).

After running the simulation, the results are obtained as shown in Figures 9 and 10.

The data reveals that when the orthosis is present, the knee joint is subjected to a maximum torque of approximately 18 Nm. This value exhibits a significant reduction of over 40 percent when compared to the torque experienced in the normal state. It is worth noting that the reduction in torque can be attributed to the maximum output power of the motor. If a motor with a higher power is used, it would enable the knee joint to experience greater torques at the same velocity.

This device is particularly useful in the swing phase of a person's gait. The elastic rope present in the orthosis has pre-tension, which causes the orthosis link to extend at the beginning of the swing phase. However, the motor applies a torque to the orthosis link, preventing the extension and causing the foot to flex with the lowest possible torque step to zero. This action enables the person to pass through the swing phase with ease and efficiency, improving their overall gait pattern.

When it comes to evaluating the efficacy of an exoskeleton, a crucial metric to consider is the metabolic cost required to walk or run. This metric measures the amount of energy expended during locomotion. In technical terms, energy is the integral of power over time,

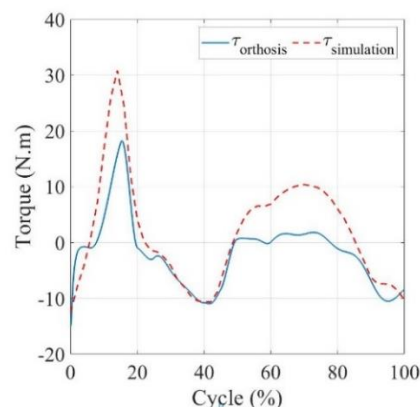


Figure 9. Reduce of knee torque with orthosis against without orthosis

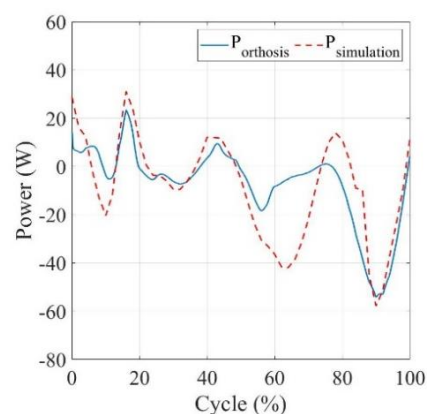


Figure 10. Comparison between knee power with orthosis and without orthosis

which means that if an exoskeleton is designed to reduce the power required in the joints, it can also decrease the amount of energy consumed. In fact, studies have shown that exoskeletons can reduce energy expenditure by up to 21% per gait cycle. This energy reduction can have significant benefits for individuals who use exoskeletons, as it can reduce fatigue and increase endurance, making it easier for them to perform daily activities and engage in physical exercise.

6. CONCLUSIONS

The study presents a new lower limb orthosis that has potential benefits for people with knee disorders and those who want to reduce the torque on their knees while walking. The research emphasizes the importance of design factors such as weight, strength, cost, and anatomical compatibility to create orthoses that enhance mobility while prioritizing user comfort and safety. To accomplish this, the orthosis was virtually simulated

using MATLAB and Adams and assembled with a seven-link human lower limb model to evaluate its efficacy during individual walking. The results of the study indicate that the application of the orthosis to a healthy leg reduces the maximum torque exerted on the knee joint during walking by approximately 13 Nm. This device can also be beneficial to individuals with a 40% weakness in their knee joint. Furthermore, the study reveals that users of this orthosis consume around 21% less energy when compared to normal walking. These findings suggest that the use of this orthosis can have a significant impact on the joint health and energy expenditure of individuals with knee joint weaknesses.

For future work, A preliminary version of this orthotic device can be fabricated to assess its effectiveness in reducing body torque and energy expenditure by placing it on individuals' lower limbs. Additionally, other joints in the orthosis can be equipped with either passive or active actuators to address other movement disorders or muscle weaknesses. This provides a more comprehensive approach to treating musculoskeletal conditions, as the orthosis can be customized to meet individual needs. By incorporating these specialized actuators, patients can experience increased mobility and functionality, leading to improved quality of life.

7. REFERENCES

- de Andrade RM, Martins JSR, Pinotti M, Filho AB, Vimieiro CBS. Novel active magnetorheological knee prosthesis presents low energy consumption during ground walking. *Journal of Intelligent Material Systems and Structures*. 2021;32(14):1591-603. 10.1177/1045389X20983923
- Lee D, Kwak EC, McLain BJ, Kang I, Young AJ. Effects of assistance during early stance phase using a robotic knee orthosis on energetics, muscle activity, and joint mechanics during incline and decline walking. *IEEE Transactions on Neural Systems and Rehabilitation Engineering*. 2020;28(4):914-23. 10.1109/TNSRE.2020.2972323
- Long Y, Peng Y. Design and control of a quasi-direct drive actuated knee exoskeleton. *Journal of Bionic Engineering*. 2022;19(3):678-87. <https://doi.org/10.1007/s42235-022-00168-2>
- Rudnicka E, Napierała P, Podfigurna A, Męczekalski B, Smolarczyk R, Grymowicz M. The World Health Organization (WHO) approach to healthy ageing. *Maturitas*. 2020;139:6-11. 10.1016/j.maturitas.2020.05.018
- Paranjape S, Singhanian N. Effect of body positions on quadriceps angle measurement. *SciMedicine Journal*. 2019;1(1):20-4. 10.28991/SciMedJ-2019-0101-3
- Mirrahshid N, Alibeiki Ü, Rakhtala S. Development and control of an upper limb rehabilitation robot via ant colony optimization-PID and fuzzy-PID controllers. *International Journal of Engineering, Transactions B: Applications*. 2022;35(8):1488-93. 10.5829/ije.2022.35.08b.04
- Lee T, Lee D, Song B, Baek YS. Design and control of a polycentric knee exoskeleton using an electro-hydraulic actuator. *Sensors*. 2019;20(1):211. 10.3390/s20010211
- Sado F, Yap HJ, Ghazilla RAR, Ahmad N. Design and control of a wearable lower-body exoskeleton for squatting and walking assistance in manual handling works. *Mechatronics*. 2019;63:102272. <https://doi.org/10.1016/j.mechatronics.2019.102272>
- Ikeuchi Y, Ashihara J, Hiki Y, Kudoh H, Noda T, editors. Walking assist device with bodyweight support system. 2009 IEEE/RSJ International Conference on Intelligent Robots and Systems; 2009: IEEE. 10.1109/IROS.2009.5354543
- Sloot LH, Baker LM, Bae J, Porciuncula F, Clément BF, Siviý C, et al. Effects of a soft robotic exosuit on the quality and speed of overground walking depends on walking ability after stroke. *Journal of neuroengineering and rehabilitation*. 2023;20(1):113. 10.1186/s12984-023-01231-7
- Freire J, Marafa N, Sampaio R, Sumihara Y, de Barros J, Vidal Filho W, et al., editors. Mechanical Design of an Active Hip and Knee Orthosis for Rehabilitation Applications. Brazilian Congress on Biomedical Engineering; 2020: Springer.
- Hung K, Cheung HY, Wan N, Lee E, Lai CN, Pan K, et al. Design, development, and evaluation of upper and lower limb orthoses with intelligent control for rehabilitation. *IET Science, Measurement & Technology*. 2021;15(9):738-48. <https://doi.org/10.1049/smt2.12074>
- Gil J, Sánchez-Villamañán MC, Gómez J, Ortiz A, Pons JL, Moreno JC, et al., editors. Design and implementation of a novel semi-active hybrid unilateral stance control knee ankle foot orthosis. 2018 IEEE/RSJ International Conference on Intelligent Robots and Systems (IROS); 2018: IEEE. 10.1109/IROS.2018.8594219
- de Sousa AC, Sousa FS, Baptista RdS, Bó AP. Passive knee orthoses assistance in functional electrical stimulation cycling in an individual with spinal cord injury. *IEEE Transactions on Neural Systems and Rehabilitation Engineering*. 2021;29:690-8. 10.1109/TNSRE.2021.3070468
- Lozano A, Ballesteros M, Cruz-Ortiz D, Chairez I. Active neck orthosis for musculoskeletal cervical disorders rehabilitation using a parallel mini-robotic device. *Control Engineering Practice*. 2022;128:105312. <https://doi.org/10.1016/j.conengprac.2022.105312>
- Zhong B, Guo K, Yu H, Zhang M. Toward gait symmetry enhancement via a cable-driven exoskeleton powered by series elastic actuators. *IEEE robotics and automation letters*. 2021;7(2):786-93. 10.1109/LRA.2021.3130639
- Silawatchananai C, Howimanporn S, Ruangurai P. Development of Force Compliant in Series Elastic Actuator Systems. *Int J Mech Eng Robot Res*. 2022;11:422-8. 10.18178/ijmerr.11.6.422-428
- Truong KD, Luu AKL, Tong NP, Nguyen HH, Nguyen TT, editors. A study on series elastic actuator applied for human-interactive robot. 2020 International Conference on Advanced Mechatronic Systems (ICAMechS); 2020: IEEE. 10.1109/ICAMechS49982.2020.9310091
- Cai VAD, Bidaud P, Hayward V, Gosselin F, Desailly E, editors. Self-adjusting, isostatic exoskeleton for the human knee joint. 2011 Annual International Conference of the IEEE Engineering in Medicine and Biology Society; 2011: IEEE. 10.1109/IEMBS.2011.6090136
- Zhou L, Chen W, Chen W, Bai S, Wang J, Zhang J, editors. Design of a compact rotary series elastic actuator with nonlinear stiffness for lower limb exoskeletons. 2019 IEEE/ASME International Conference on Advanced Intelligent Mechatronics (AIM); 2019: IEEE. 10.1109/AIM.2019.8868598
- Young AJ, Ferris DP. State of the art and future directions for lower limb robotic exoskeletons. *IEEE Transactions on Neural Systems and Rehabilitation Engineering*. 2016;25(2):171-82. 10.1109/TNSRE.2016.2521160
- Carpino G, Accoto D, Sergi F, Luigi Tagliamonte N, Guglielmelli E. A novel compact torsional spring for series elastic actuators for

- assistive wearable robots. *Journal of Mechanical Design*. 2012;134(12):121002. 10.1115/1.4007695
23. Kong K, Bae J, Tomizuka M. A compact rotary series elastic actuator for human assistive systems. *IEEE/ASME transactions on mechatronics*. 2011;17(2):288-97. 10.1109/TMECH.2010.2100046
 24. Cenciari M, Dollar AM, editors. *Biomechanical considerations in the design of lower limb exoskeletons*. 2011 IEEE International conference on rehabilitation robotics; 2011: IEEE. 10.1109/ICORR.2011.5975366
 25. Dos Santos WM, Caurin GA, Siqueira AA. Design and control of an active knee orthosis driven by a rotary series elastic actuator. *Control Engineering Practice*. 2017;58:307-18. <https://doi.org/10.1016/j.conengprac.2015.09.008>
 26. Robinson DW. *Design and analysis of series elasticity in closed-loop actuator force control*: Massachusetts Institute of Technology; 2000.
 27. Morales LA, Fabara P, Pozo DF. An Intelligent Controller Based on LAMDA for Speed Control of a Three-Phase Inductor Motor. *Emerging Science Journal*. 2023;7(3):676-90. 10.28991/ESJ-2023-07-03-01
 28. Kumar G, Mandal NP. Experimental Analysis of Square Position on Variable Displacement Electrohydraulic Actuation System by Open Loop Control. *International Journal of Engineering, Transactions C: Aspects*. 2023;36(6):1185-92. 10.5829/ije.2023.36.06c.17
 29. Kirtley C. *Clinical gait analysis: theory and practice*: Elsevier Health Sciences; 2006.
 30. Sridhar Reddy A, Satish Chembuly V, Kesava Rao V. Collision-free inverse kinematics of redundant manipulator for agricultural applications through optimization techniques. *International Journal of Engineering, Transactions A: Basics*. 2022;35(7):1343-54. 10.5829/ije.2022.35.07a.13
 31. Dollar AM, Herr H. Lower extremity exoskeletons and active orthoses: Challenges and state-of-the-art. *IEEE Transactions on robotics*. 2008;24(1):144-58. 10.1109/TRO.2008.915453
 32. Winter DA. *Biomechanics and motor control of human movement*: John Wiley & sons; 2009.

COPYRIGHTS

©2024 The author(s). This is an open access article distributed under the terms of the Creative Commons Attribution (CC BY 4.0), which permits unrestricted use, distribution, and reproduction in any medium, as long as the original authors and source are cited. No permission is required from the authors or the publishers.

**Persian Abstract****چکیده**

در این مقاله یک ارتز جدید اندام تحتانی معرفی می شود که برای کمک به زانوهای ضعیف در حین راه رفتن طراحی شده است. ساختار ارتز دارای ۱۰ درجه آزادی است. این دستگاه از یک محرک الاستیک سری، مجهز به یک طناب الاستیک استفاده می کند که گشتاور تولید شده توسط موتور را به لینک ارتز منتقل می کند. عملکرد ارتز اندام تحتانی پیشنهادی به صورت مجازی با استفاده از لینک نرم افزارهای شبیه سازی آدامز و متلب شبیه سازی شده است. ارتز بر اساس داده های آنروپومتری یک انسان عادی با وزن بدن ۷۶ کیلوگرم و قد ۱۸۰ سانتی متر طراحی شده است. سناریوی شبیه سازی شامل راه رفتن با سرعت متوسط ۱ متر بر ثانیه در یک مسیر مستقیم، با کمک ۴۰ درصدی ارتز زانو است. هدف از شبیه سازی ارزیابی اثربخشی و کارایی ارتز در کمک به مفصل ضعیف زانو است. نتایج شبیه سازی نشان می دهد که ارتز باعث کاهش بیش از ۱۳ نیوتن متر گشتاور مفصل زانو در یک فرد سالم می شود که نشان دهنده نیروی کمتر بر روی زانوی ضعیف است. علاوه بر این، ارتز حداکثر انرژی مورد نیاز در هر چرخه راه رفتن را کاهش می دهد که به معنی کارایی و استقامت بالاتر در چرخه راه رفتن است.



Method for Assessing Damage to Gas Distribution Network Pipelines based on Nonlinear Guided Wave

A. Palaev G., Z. Fuming*, T. Yifan

Department of Petroleum Engineering, Saint Petersburg Mining University, 2, 21st line, Saint Petersburg, Russian Federation

PAPER INFO

Paper history:

Received 16 October 2023

Received in revised form 08 November 2023

Accepted 09 November 2023

Keywords:

Prediction

Service Life

Random Forest

Elimination of Recursive Features

Polyethylene Pipe

Rapid Crack Expansion

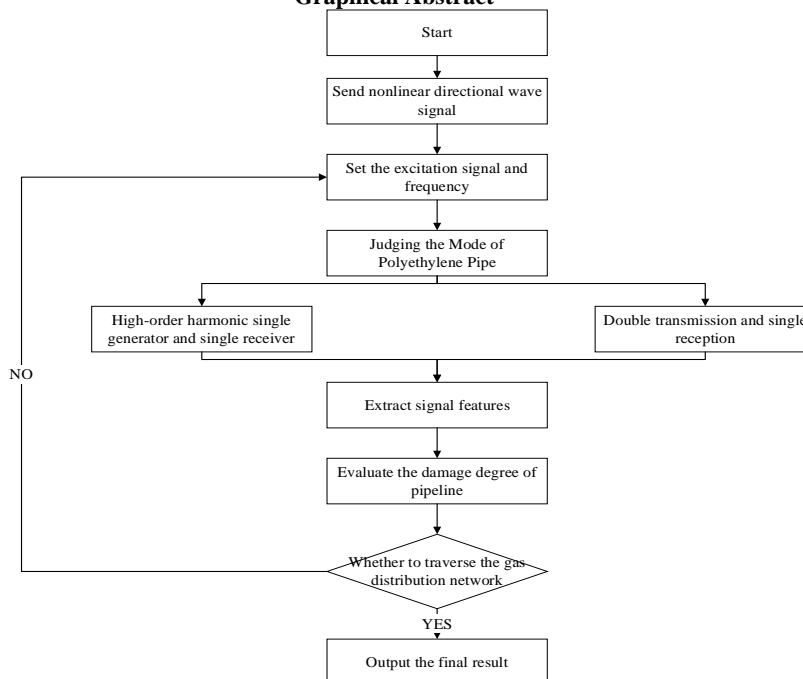
Critical Pressure Value

ABSTRACT

Polyethylene pipeline is an essential infrastructure of gas distribution network, and there are some problems such as complex damage assessment and tedious assessment process. How to choose an effective damage assessment method for polyethylene pipelines is the focus of the implementation of the gas distribution network at present. In this paper, a nonlinear directional wave method is proposed to detect the damage of polyethylene pipeline by an acoustic wave, and the damage results of polyethylene pipeline are searched. The rationality of this method is verified by calculating the aerodynamic equation. The results show that the nonlinear fixed wave method can accurately determine the damage and crack propagation degree of the pipeline and simplify the damage assessment process, and the results are superior to the linear directional wave method. Therefore, the nonlinear directional wave can be used to assess the damage to ethylene pipelines in gas distribution networks, which has strong rationality and practicality and provides support for the actual pipeline damage assessment.

doi: 10.5829/ije.2024.37.05b.04

Graphical Abstract



*Corresponding Author Email: fumin96@mail.ru (Z. Fuming)

1. INTRODUCTION

Polyethylene as an important foundation of the natural gas network (1, 2), the gas distribution network plays a very important role in guaranteeing the supply of natural gas, and its material selection is directly proportional to network security (3, 4). Polyethylene pipeline belongs to a special composite process (5, 6), which has excellent transmission performance and corrosion resistance, and it is not easy to leave natural gas impurities on the inner wall of the pipeline (7-9). Compared with ordinary steel structure pipes, polyethylene pipes also have strong toughness and mechanical strength, which is suitable for long-distance foundation laying (10, 11). In addition, polyethylene pipes are suitable for harsh external environments and complex internal fluid pressure and have an extensive range of applications (12, 13). The survey results show that 34% of accidents in the natural gas field are caused by pipeline leakage, pipeline rupture, and cracks (14-16). Among them, the steel structure pipeline accident probability accounts for 70% (8), polyethylene pipeline accounts for 5.6%, and other types of pipeline account for 24.4% (17). Some scholars believe that the safety of polyethylene pipelines is high, but if it is laid for a long distance (18-21) or used for a long time, the polyethylene pipeline will have cracks, leaks, and other problems (22, 23). Moreover, the toughness and adhesion of the polyethylene pipeline itself will lead to cracks and other damages that are not easily detected (24, 25) and cannot even be identified by x-rays. Some scholars believe that the essence of polyethylene pipeline cracks is the aging of materials or the complete result of external culture, humidity, and internal stress. The previous methods, such as ray and light diffraction, cannot be effectively detected (26, 27). Some scholars believe that the previous testing methods for cracks in polyethylene pipes (28) have the problems of long testing time and complex testing process, which can not be continuously tested and affect the use of polyethylene pipes (29-32). Therefore, finding an effective detection method for polyethylene pipeline cracks is a problem that needs to be solved at present, and it is also to avoid major economic losses and casualties caused by polyethylene pipelines (33, 34). Based on this, this paper presents a nonlinear orientation-based assessment method of polyethylene pipeline damage in the gas distribution network, aiming at improving the identification effect of polyethylene pipeline damage.

2. DETECTION METHOD OF POLYETHYLENE PIPELINE DAMAGE IN THE GAS DISTRIBUTION NETWORK

2. 1. Damage Process of Polyethylene Pipeline

The damage to the polyethylene pipeline will change the

density and shape of polyethylene. The damage process of polyethylene pipeline can be simplified as density calculation, which can be calculated by universal theory function and modified density function (35-37). Suppose A: The mass of polyethylene per unit area is M_{to} , the mass obtained by the universal theory function is M_a (38), and the mass obtained by the modified density function is , then the calculation process of polyethylene pipeline damage is shown in Equation 1:

$$f(\rho) = \sum \alpha \cdot \frac{M_a + M_b}{B(M_{to}) \cdot V} + A(\zeta) \quad (1)$$

Among them, α is the density coefficient of polyethylene pipeline changes according to cracks, fatigue, creep, bonding degree, and so on; ρ is the pipe density; $f(\rho)$ is the pipeline damage function; $A(\zeta)$ is the density revision function; $B(M_{to})$ is a universal density function; V is the volume of the pipeline; ζ is the revised coefficient of the pipeline.

2. 2. Nonlinear Directional Wave Detection

Nonlinear directional waves can measure the lattice arrangement of polyethylene material, test irregular, and discontinuous damage, reduce the incidence of the linear excitation signal, and realize microscopic identification of the damage location. Compared with linear directional waves, nonlinear directional waves have fewer stress-strain hysteresis and nonlinear dissipation problems (18), and have a higher recognition rate for crack, fatigue, creep, and other characteristics, which can realize early recognition of polyethylene materials. Suppose B: The nonlinear ultrasonic test result function is $R(x)$, the position vector of ultrasonic propagation in the pipeline is x (19), the amplitude is u , the wave number is k , the angular frequency is ω , the product thickness is $f(h)$, the capacitance vector function is $\phi(x)$, the expansion vector function is $\varphi(x)$, and the test dimension is l , then the nonlinear directional wave detection process is shown in Equation 2.

$$R(x) = \sum_l \sum_u \sum_t A \cos(kx - \omega t) \cdot \mu \cdot \phi(x) \cdot fh + \frac{(\lambda + \mu) \cdot \varphi(x)}{\rho} \quad (2)$$

Among them λ is the Euler coefficient of the pipeline; t is the propagation time; μ is the Lagrange coefficient of damage, l test dimensions, including longitudinal, torsional, bending, etc.

There are two kinds of velocities for nonlinear directional wave propagation in polyethylene pipe, group velocity, and relative velocity. With the extension of propagation distance, directional waves with different frequencies will be separated (39), which will cause large-area dissipation of directional waves in a certain time domain and cause interference with the extraction of characteristic signals (40, 41). Therefore, when choosing non-directional waves, try to choose directional waves

with slow speed changes (42). In addition, non-directional waves have multimodality. Under the same frequency, directional waves have many propagation modes, and each propagation mode presents different propagation velocities (43, 44). Therefore, the analysis of the directional wave's group velocity and relative velocity in different modes is the basis of polyethylene pipe damage detection (45).

2. 3. Propagation Modes of Nonlinear Directional Waves in Polyethylene Pipes

In order to realize the damage detection of polyethylene pipeline, the characteristic dispersion equation of non-directional wave in the pipeline should be calculated, and the displacement equation and stress expression equation of simultaneous directional wave in the pipeline should be established. Among them, the construction methods of the characteristic dispersion equation are divided into transfer matrix and global matrix methods (43). By calculating the boundary characteristics of non-directional waves, the transfer matrix method gradually eliminates the unknowns in the equation and obtains the dispersion characteristic solution. The global matrix method is to establish a large matrix, brings all the nonlinear directional wave values into the matrix, and combines the characteristics of each frequency directional wave to obtain the final calculation result. Because the global matrix method has a wider range of applications, can calculate the dispersion eigenvalues under different modes, and has higher robustness, this paper chooses the global matrix method to solve it. Assuming that the inner diameter of the polyethylene pipe is α , the propagation of nonlinear directional waves in the pipe should satisfy the Navier displacement equilibrium equation, and the results are shown in Equation 3.

$$\mu \cdot d^2 + (\lambda + \mu)d = \rho \frac{\partial^2 d}{\partial t^2} \quad (3)$$

Among them is the propagation displacement of nonlinear directional waves in the pipeline (note: it is not directional). In the actual test process, the nonlinear directional wave will be disturbed by external factors, so Helmholtz's law is introduced to decompose the nonlinear directional wave, and the calculation results are shown in Equation 4:

$$\begin{cases} F_m(x) = [A_m \cdot \mu \cdot d^2 + \frac{B_m \cdot (\lambda + \mu) \cdot d}{r}] \cdot \cos n\theta \cdot \cos(\omega t + kz) \\ F_{\theta m}(x) = [\frac{C_m \cdot \mu \cdot d^2}{r} + D_m \cdot (\lambda + \mu) \cdot d] \cdot \sin n\theta \cdot \cos(\omega t + kz) \\ F_{zm}(x) = [\frac{E_m \cdot \mu \cdot d^2}{r} + F_m \cdot (\lambda + \mu) \cdot d] \cdot \cos n\theta \cdot \cos(\omega t + kz) \end{cases} \quad (4)$$

Among them m is the number of layers of polyethylene pipes; when $F_{rm}(x)$, $F_{\theta m}(x)$ and $F_{zm}(x)$ are the radial, axial and circumferential components of the

displacement of particles in the pipeline under directional waves, respectively. When $F_{rm}(x) \neq 0$, and $F_{\theta m}(x)$ and $F_{zm}(x)$ are equal to 0, it means that the guided wave is a longitudinal mode; When $F_{\theta m}(x) \neq 0$ and $F_{rm}(x)$, $F_{zm}(x)$ are equal to 0, the guided wave is a torsional mode; When $F_{zm}(x) \neq 0$ and $F_{rm}(x)$, $F_{\theta m}(x)$ are equal to 0, the guided wave is bending mode. According to Equation 4, the directional wave dispersion equation of a polyethylene pipeline can be constructed, and the result is shown in Equation 5.

$$[c_{ij}]_{6 \times 6} [A, B, A_1, B_1, A_2, B_2]^T = [0, 0, 0, 0, 0, 0]^T \quad (5)$$

Among them, the results in the matrix are related to wave number k and angular frequency ω , and the specific element coefficients are complex. Moreover, the coefficient is related to size, density, Young's modulus, and Poisson's ratio. In addition, the solution of the coefficient in Equation 5 depends on the wavelength, the thickness of the tube wall h , and the shear frequency of the tube wall, so only the approximate solution can be obtained when $[C_{1j}] = 0$ it shows that the longitudinal directional wave mode is in the pipeline when it shows that the transverse directional wave mode is in the pipeline when $[C_{1i}] = 0$ it shows that the bending directional wave mode is in the pipeline.

2. 5. Steps for Evaluating the Damage of Polyethylene Pipeline Caused by Nonlinear Directional Waves

Because nonlinear ultrasound has a high sensitivity to polyethylene pipeline damage, Different excitation signals and frequencies should be selected according to the nonlinear ultrasonic modulation phenomenon inside the pipeline, and receiving sensors should be arranged on the surface of the pipeline, and signals should be received by using the single-generator and single-receiver method of higher harmonics and the double-generator and single-receiver method of sidelobe components. The specific evaluation steps are shown in Figure 1.

Step 1: Determine the network structure of the polyethylene pipeline, obtain the mode of the pipeline, record the characteristics of nonlinear waves, and determine the distribution of dispersion, excitation signal, and frequency.

Step 2: Set the threshold and weight of frequency, dispersion, angular frequency, and other indexes, and extract the relevant eigenvalues by Fourier series. At the same time, the iteration times of polyethylene pipeline damage are set.

Step 3: Determine the nonlinear directional wave signals under different modes, and calculate the damage situation of the polyethylene pipeline.

Step 4: Statistic evaluation results of polyethylene pipeline damage, compare and output the final evaluation results.

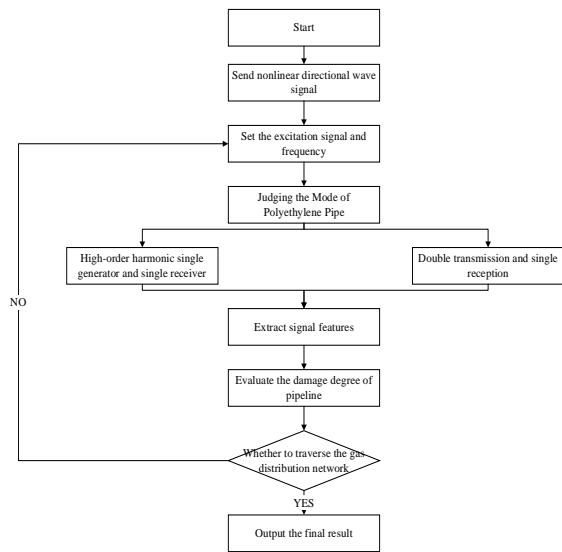


Figure 1. Damage assessment process of polyethylene pipeline caused by nonlinear directional wave

Step 5: Carry out iterative updating according to Equations 1-5, calculate the final damage of the polyethylene pipeline and output the final evaluation results under different modes.

Step 6: Whether the polyethylene pipeline in the gas distribution network is traversed, if not all traversed, repeat steps 1 to 5; otherwise, stop damage assessment.

3. CASE ANALYSIS OF DAMAGE ASSESSMENT OF POLYETHYLENE PIPELINE IN THE GAS DISTRIBUTION NETWORK

3.1. Basic Condition of Polyethylene Pipeline in Gas Distribution Network Taking the urban gas pipeline reconstruction project as a research case, the

pipeline line is 10.32 kilometers long, with 15 straight-through pipes, 65 elbows, 72 reducers, 14 pipe caps, and 11 saddle-shaped bypass pipes. The basic information of specific pipelines is shown in Table 1.

It can be seen from Table 1 that the basic information of the polyethylene pipeline, the test frequency of the nonlinear directional wave, the calculated depth, and the error can be obtained. After obtaining the specific information about the polyethylene pipeline, the parameters of the nonlinear directional wave transmitter should be determined, and the specific results are shown in Table 2.

According to the parameters in Tables 1 and 2, the amplitude and dispersion components are analyzed by using a nonlinear directional wave acquisition card and supporting software. At the same time, the judgment standard of polyethylene pipeline damage is set, and the results are shown in Table 3.

At the same time, the frequency standard of the receiver is three levels, which are 1~2Hz, 2~3Hz, and 3~4Hz, respectively. Under different frequency standards, there are three modes: longitudinal mode, bending mode, and torsion mode.

TABLE 1. Parameters of polyethylene pipe

Pipe shape	Inner diameter (mm)	Outer Diameter (mm)	Thickness (mm)	Test frequency (Hz)	Depth of focus (mm)
Lining	74.29±1.23	89.59±4.32	3.86±0.56	6.5~7.6	7~9
Through	78.78±2.42	86.73±4.32	3.67±0.23	5.6~7.3	17~21
Elbows	83.27±2.37	82.86±3.62	4.69±0.71	6.1~7.4	22~25
Reducer	89.82±3.56	80.82±4.35	5.86±0.35	6.3~7.2	10~12
Tube cap	85.33±4.23	82.41±5.36	6.90±0.23	6.6~7.8	30~33
Saddle bypass	90.62±6.23	82.55±6.32	7.24±0.37	6.8~7.9	24~28

TABLE 2. Parameters of nonlinear directional waves

Device type	Emission frequency (Hz)	Magnification (times)	Accepted frequency (Hz)	Test accuracy (%)	Scanning angle (°)	Wave velocity (m/s)
Agilent	6~14	5.32	5~16	1	20~70	(-2341,+2457)
HFVA-41 power amplifier	8~19	6.25	10~28	1	30~80	(-3121,+3417)
REKHF piezoelectric amplifier	11~19	5.62	12~19	10	20~75	(-2611,+2737)

Note: + stands for shear wave, and stands for longitudinal wave

TABLE 3. Parameters corresponding to the damage state

Damage parameters	Injury status					
	1	2	3	4	5	6
Degree of damage (grade)	I	III	IV	VI	IV	VV
Depth of damage (mm)	0~0.5	0.5~1	1~1.5	1.5~2	2~2.5	2.5~3

3.2. Harmonic Assessment of Polyethylene Pipeline Damage in the Gas Distribution Network

The damage assessment of polyethylene pipelines is mainly based on the amplitude and dispersion of directional waves, so it is necessary to analyze the damage location above and get the response results. According to the criteria in Table 3, the amplitude change of polyethylene pipeline damage is obtained, and the

results are shown in Figure 2 of the tough-brittle transformation of the internal structure of the pipe.

By amplifying the spectrum, it is found that the nonlinear directional wave has a concentrated peak value, and the amplitude of the third harmonic is higher than that of the second harmonic. There are many reasons for the above phenomenon. One possibility is that the attenuation speed of the third harmonic in the gas distribution network is slower than that of the second harmonic. Another possibility is that the reception effect of the third harmonic is better, and the amplitude changes more. The third possibility is that the third harmonic is more sensitive to polyethylene pipeline structure. After the signal in Figure 2 is transformed by Equation 4, the amplitude changes under different damage states are obtained, and the results are shown in Figure 3.

According to the results shown in Figure 3, it can be seen that the harmonic amplitude changes with the increase of the width under different damage states. The transmitted signal fluctuates irregularly in the amplitude of the second harmonic wave, and there is no obvious law. The reason why the second harmonic amplitude does not appear obvious regularity with the increase of damage state may be that the second harmonic is less

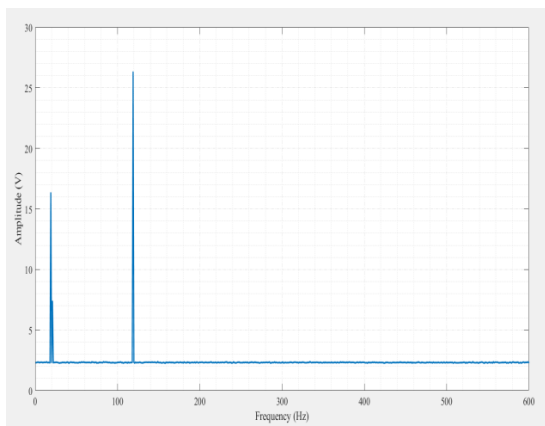


Figure 2. Receiving spectrum of damage signal

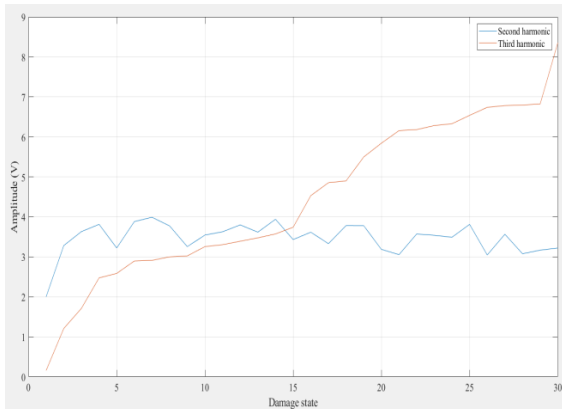


Figure 3. Amplitude variation of second and third harmonics

sensitive to the damage of the polyethylene pipeline. The third harmonic amplitude increases with the increase of the damage state due to the increase in dispersion rate caused by damage to the polyethylene pipeline. Moreover, the scattering rate of the nonlinear directional wave at the damage location is higher, which leads to more received harmonics, which verifies the effectiveness of nonlinear directional waves in the damage assessment of polyethylene pipelines. However, the rising trend of the third harmonic amplitude lacks regularity and presents fluctuating changes, mainly because the gas flow in the gas distribution network will affect the wave conductivity of the medium under different damages. In addition, the angular frequency, wave number of the nonlinear directional wave, and pipeline mode will affect the conductivity of the directional wave, and then affect the excitation signal received every time, and cause a different degree of amplitude change.

3. 3. Energy Assessment of Polyethylene Pipeline Damage in the Gas Distribution Network

According to the spectrum information in Figure 2, the difference frequency component, sum frequency component, energy value, and energy coefficient of nonlinear directional wave are extracted. Among them, the reference standards are shown in Table 4.

The frequency reference values in Table 4 allow better signal response, and sum frequency and difference frequency components can be obtained, as shown in Figure 4.

From the signal results shown in Figure 4, it can be seen that the signals of *Groups 2 and 3* have little change in difference frequency amplitude and sum frequency amplitude under the same damage, and the whole show a

TABLE 4. Parameters corresponding to the damage state

Stimulus signal group	1	2	3
High-frequency excitation signals	120	220	320
Low-frequency excitation signal	100	200	300
Sum frequency signal	80	180	280
Difference frequency signal	140	240	340

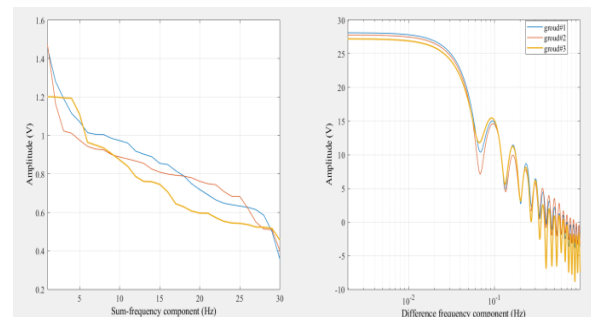


Figure 4. Amplitude variation of sum frequency component and difference frequency component

downward trend of ups and downs. It can be seen from the difference frequency component that the frequencies of high frequency and low frequency are close, and the difference frequencies produced in polyethylene pipeline are similar, so different frequencies have different evaluation results on polyethylene pipeline damage, and high and low frequencies can be selected according to pipeline damage. At the same time, in different groups of excitation signals, the difference frequency component and sum frequency component fluctuations tend to be consistent, and later fluctuations are gentler, mainly because the nonlinear directional wave energy values of each group show consistent attenuation in the later period. Therefore, the damage to the polyethylene pipeline can be well evaluated using different excitation signals, sum frequency, and difference frequency components.

4. DISCUSSION

According to the parameters in Table 1, the damage to the polyethylene pipeline in the gas distribution network is evaluated, and the following evaluation results are obtained, as shown in Table 5.

As can be seen from Table 5, there is no significant difference between nonlinear directional wave and linear directional wave in calculation time, but the nonlinear directional wave is higher in accuracy. The reason is that when the directional wave passes through the damage position, the amplitude of dispersion and angular frequency is small, which leads to no significant amplitude difference of the received signals, especially crack, fatigue, creep, and bonding degree. In addition, because the attenuation speed of the directional wave is slow, the energy and energy coefficient of the conduction wave change little after passing through the damaged position, so it is impossible to identify at the receiving point. The energy attenuation of nonlinear directional waves is faster, and the difference between different and sum frequencies is more prominent.

TABLE 5. Evaluation results of polyethylene pipeline damage by different methods

Scope	Component	Nonlinear directional waves		Linear directional waves	
		Accuracy (%)	Time (min)	Accuracy (%)	Time (min)
Pipeline	Lining	93.34	4.41	88.33	4.32
	Through	94.37	5.23	88.39	5.36
	Elbows	92.33	6.24	85.34	6.42
Annex	Reducer	92.14	11.34	88.33	10.23
	Tube cap	91.27	8.25	88.32	9.25
	Saddle bypass	90.23	4.32	84.32	4.63
	Different modalities	99.31	5.23	85.34	5.12

5. CONCLUSION

In this paper, a nonlinear directional wave method is proposed to evaluate the damage to a polyethylene pipeline in a gas distribution network, and the rationality of the evaluation method is verified. The damage to the polyethylene pipeline was analyzed by taking the amplitude, sum frequency component, and difference frequency component of the nonlinear directional wave as the main observation indices. The results show that the amplitude of the third harmonic wave of the nonlinear directional wave changes regularly and is proportional to the damage to the pipeline. At the same time, the sum frequency and difference frequency components are inversely proportional to the damage to the pipeline. All three indexes can reflect the damage of the polyethylene pipeline, which verifies the rationality of the damage evaluation of the nonlinear directional wave. Compared with the linear directional wave, the nonlinear directional wave is more accurate in evaluating the damage to polyethylene pipeline. There is no difference in the evaluation time, so the nonlinear directional wave can better evaluate the damage of polyethylene pipeline and has better rationality. However, in the study of nonlinear directional waves, there are few studies on the influence of propagation medium and the error in artificial measurement, so we will focus on optimizing the above contents in the future.

6. REFERENCES

- Guo Z, Xu R, Xue P. Study on preparation of ultra-high-molecular-weight polyethylene pipe of good thermal-mechanical properties modified with organo-montmorillonite by screw extrusion. *Materials*. 2020;13(15):3342. <https://doi.org/10.3390/ma13153342>
- Nikolaev A, Samigullin G, Samigullina L, Fetisov V, editors. Non-stationary operation of gas pipeline based on selections of travel. IOP conference series: Materials Science and Engineering; 2018: IOP Publishing.
- Istrate I-R, Juan R, Martin-Gamboa M, Domínguez C, García-Muñoz RA, Dufour J. Environmental life cycle assessment of the incorporation of recycled high-density polyethylene to polyethylene pipe grade resins. *Journal of Cleaner Production*. 2021;319:128580. <https://doi.org/10.1016/j.jclepro.2021.128580>
- Wee J-W, Park S-Y, Choi B-H. Modeling and application of discontinuous slow crack growth behaviors of high-density polyethylene pipe with various geometries and loading conditions. *Engineering Fracture Mechanics*. 2020;236:107205. <https://doi.org/10.1016/j.engfracmech.2020.107205>
- Patadia H, Lively K, Lamborn M, Maeger P, Sukhadia A. Rapid crack propagation (RCP) performance of unimodal medium density polyethylene (MDPE) pipe. *Plastics Engineering*. 2013;69(5):12-7. <https://doi.org/10.1016/j.engfracmech.2020.107205>
- Deblieck RA, van Beek D, McCarthy M, Mindermann P, Remerie K, Langer B, et al. A simple intrinsic measure for rapid crack propagation in bimodal polyethylene pipe grades validated by elastic-plastic fracture mechanics analysis of data from instrumented Charpy impact test. *Polymer Engineering & Science*. 2017;57(1):13-21. <https://doi.org/10.1002/j.1941-9635.2013.tb01002.x>

7. Fetisov V, Ilyushin YV, Vasiliev GG, Leonovich IA, Müller J, Riazi M, et al. Development of the automated temperature control system of the main gas pipeline. *Scientific Reports*. 2023;13(1):3092. <https://doi.org/10.1038/s41598-023-29570-4>
8. Fedorov YY, Popov S, Savvina A, Vasilyev S, Rodionov A, editors. A simplified method to determine resistance to rapid crack propagation in polyethylene pipes. *AIP Conference Proceedings*; 2017: AIP Publishing.
9. Gafur S, Andrey S, Liliya S, Vadim F. Assessment of damage of metallic elements in oil and gas facilities using small punch test. *International Journal of Applied Engineering Research*. 2017;12(21):11583-7. https://www.ripublication.com/ijaer17/ijaerv12n21_148.pdf
10. Yayla P, Leever P. Rapid crack propagation in pressurised plastic pipe—II. Critical pressures for polyethylene pipe. *Engineering Fracture Mechanics*. 1992;42(4):675-82. [https://doi.org/10.1016/0013-7944\(92\)90049-K](https://doi.org/10.1016/0013-7944(92)90049-K)
11. Sajid T, Tanveer S, Sabir Z, Guirao J. Impact of activation energy and temperature-dependent heat source/sink on Maxwell–Sutterby fluid. *Mathematical Problems in Engineering*. 2020;2020:1-15. <https://doi.org/10.1155/2020/5251804>
12. Bo Y, Yijiang L, Maodong L, Wei Z, Wenbo L, Zhigang W. Research progress in cyclic crack round bar test for polyethylene pipes. *China Plastics*. 2019;33(10):128. [10.5829/ije.2023.36.12c.14](https://doi.org/10.5829/ije.2023.36.12c.14)
13. Guirao JL, Sabir Z, Saeed T. Design and numerical solutions of a novel third-order nonlinear Emden–Fowler delay differential model. *Mathematical Problems in Engineering*. 2020;2020:1-9. <https://doi.org/10.1155/2020/7359242>
14. Baratian A, Kashani H. Probabilistic framework to quantify the seismic resilience of natural gas distribution networks. *International Journal of Disaster Risk Reduction*. 2022;81:103282. <https://doi.org/10.1016/j.ijdrr.2022.103282>
15. Fetisov V, Shalygin AV, Modestova SA, Tyan VK, Shao C. Development of a numerical method for calculating a gas supply system during a period of change in thermal loads. *Energies*. 2022;16(1):60. <https://doi.org/10.3390/en16010060>
16. Bukka SR, Law YZ, Santo H, Chan ES. Reduced order model for nonlinear multi-directional ocean wave propagation. *Physics of Fluids*. 2021;33(11). <https://doi.org/10.1063/5.0070246>
17. Cavana M, Leone P. Smart Gas Network with Linepack Managing to Increase Biomethane Injection at the Distribution Level. *Energies*. 2022;15(21):8198. <https://doi.org/10.3390/en15218198>
18. Chen Y, Zhang L, Wei X, Xu J, Fu S, Liao C. Debris-flow-induced damage assessment for a submarine pipeline network in regional-scale natural terrain. *Engineering Geology*. 2022;311:106917. <https://doi.org/10.1016/j.enggeo.2022.106917>
19. Cui Y, Fang J, Qu Z, Song M, Zhao J. Research on Damage Assessment of Buried Standard and Carbon-Fibre-Reinforced Polymer Petroleum Pipeline Subjected to Shallow Buried Blast Loading in Soil. *Shock and Vibration*. 2021;2021:1-19. <https://doi.org/10.1155/2021/1459260>
20. Nikolaev A, Dokoukin V, Lykov Y, Fetisov V, editors. Research of processes of heat exchange in horizontal pipeline. *IOP Conference Series: Materials Science and Engineering*; 2018: IOP Publishing.
21. Guzzo G, Cheli L, Carcasci C. Hydrogen blending in the Italian scenario: Effects on a real distribution network considering natural gas origin. *Journal of Cleaner Production*. 2022;379:134682. <https://doi.org/10.1016/j.jclepro.2022.134682>
22. Hosseini-Toudeshky H, Jannesari M. An investigation on creep life assessment of welded steam pipeline intersection using classical and progressive damage analyses. *Welding in the World*. 2022;66(8):1653-64. <https://doi.org/10.1007/s40194-022-01324-2>
23. Hu Y, Liu J, Xu X. Dynamic Interactions between Local Energy Systems Coupled by Power and Gas Distribution Networks. *Energies*. 2022;15(22):8420. <https://doi.org/10.3390/en15228420>
24. Fetisov V, Davardoost H, Mogylevets V. Technological aspects of methane–hydrogen mixture transportation through operating gas pipelines considering industrial and fire safety. *Fire*. 2023;6(10):409. <https://doi.org/10.3390/fire6100409>
25. Kim I-J, Kim C-M, Baek J-H, Kim Y-P, Lee Y, Jang Y-C. Structural Integrity Assessment of Defected Gas Pipelines Using a Simplified Ductile Damage Model. *Journal of Pressure Vessel Technology*. 2022;144(1):011302. <https://doi.org/10.1115/1.4050775>
26. Zadkov D, Gabov V, Babyr N, Stebnev A, Teremetskaya V. Adaptable and energy-efficient powered roof support unit. *Min Informational Anal Bull*. 2022;6:46-61. https://doi.org/10.25018/0236_1493_2022_6_0_46
27. Kimmoun O, Hsu H-C, Hoffmann N, Chabchoub A. Experiments on uni-directional and nonlinear wave group shoaling. *Ocean Dynamics*. 2021;71:1105-12. <https://doi.org/10.1007/s10236-021-01485-6>
28. Klahn M, Madsen PA, Fuhrman DR. Mean and variance of the Eulerian and Lagrangian horizontal velocities induced by nonlinear multi-directional irregular water waves. *Proceedings of the Royal Society A*. 2021;477(2256):20210516. <https://doi.org/10.1098/rspa.2021.0516>
29. Schipachev A, Fetisov V, Nazyrov A, Khamrakulov A. Study of the pipeline in emergency operation and assessing the magnitude of the gas leak. *Energies*. 2022;15(14):5294. <https://doi.org/10.3390/en15145294>
30. Cui Y, Quddus N, Mashuga CV. Bayesian network and game theory risk assessment model for third-party damage to oil and gas pipelines. *Process Safety and Environmental Protection*. 2020;134:178-88. <https://doi.org/10.1016/j.psep.2019.11.038>
31. Fetisov V, Tsvetkov P, Müller J. Tariff approach to regulation of the European gas transportation system: Case of Nord Stream. *Energy Reports*. 2021;7:413-25. <https://doi.org/10.1016/j.egy.2021.08.023>
32. Bouziou D, Van Ballegooy S, Storie L, O'Rourke T. Development of pipeline damage assessment tools using liquefaction-induced ground movements and CPT-based liquefaction metrics. *Earthquake Geotechnical Engineering for Protection and Development of Environment and Constructions: CRC Press*; 2019. p. 1527-36.
33. Litvinenko V, Bowbrick I, Naumov I, Zaitseva Z. Global guidelines and requirements for professional competencies of natural resource extraction engineers: Implications for ESG principles and sustainable development goals. *Journal of Cleaner Production*. 2022;338:130530. [10.1016/j.jclepro.2022.130530](https://doi.org/10.1016/j.jclepro.2022.130530)
34. Stroykov G, Babyr N, Ilin I, Marchenko R. System of Comprehensive Assessment of Project Risks in the Energy Industry. *International Journal of Engineering, Transactions A: Basics*. 2021;34(7):1778-84. [10.5829/ije.2021.34.07A.22](https://doi.org/10.5829/ije.2021.34.07A.22)
35. Aazami R, Dabestani S, Shirkhani M. Optimal Capacity and Location for Renewable-based Microgrids Considering Economic Planning in Distribution Networks. *International Journal of Engineering, Transactions C: Aspects*. 2023;36(12):2175-83. [10.5829/ije.2023.36.12c.06](https://doi.org/10.5829/ije.2023.36.12c.06)
36. Aleksander G P, Yifan T, Fuming Z. Predicting Service Life of Polyethylene Pipes under Crack Expansion using. *International Journal of Engineering, Transactions C: Aspects*. 2023;36(12):2243-52. [10.5829/ije.2023.36.12c.14](https://doi.org/10.5829/ije.2023.36.12c.14)
37. Shammazov I, Karyakina E. The LNG Flow Simulation in Stationary Conditions through a Pipeline with Various Types of Insulating Coating. *Fluids*. 2023;8(2):68. <https://doi.org/10.3390/fluids8020068>

38. Zemenkova MY, Chizhevskaya EL, Zemenkov YD. Intelligent monitoring of the condition of hydrocarbon pipeline transport facilities using neural network technologies. *Записки Горного института*. 2022;258:933-44. <https://doi.org/10.31897/PMI.2022.105>
39. Baktizin RN, Zaripov RM, Korobkov GE, Masalimov RB. Assessment of internal pressure effect, causing additional bending of the pipeline. *Записки Горного института*. 2020;242:160-8. <https://doi.org/10.31897/pmi.2020.2.160>
40. Vasiliev GG, Dzhajabov AA, Leonovich IA. Analysis of the causes of engineering structures deformations at gas industry facilities in the permafrost zone. *Записки Горного института*. 2021;249:377-85. <https://doi.org/10.31897/PMI.2021.3.6>
41. Ustinov D, Nazarychev A, Pelenev D, Babyr K, Pugachev A. Investigation of the Effect of Current Protections in Conditions of Single-Phase Ground Fault through Transient Resistance in the Electrical Networks of Mining Enterprises. *Energies*. 2023;16(9):3690. <https://doi.org/10.3390/en16093690>
42. Nguyen VT, Pham TV, Rogachev MK, Korobov GY, Parfenov DV, Zhurkevich AO, et al. A comprehensive method for determining the dewaxing interval period in gas lift wells. *Journal of Petroleum Exploration and Production Technology*. 2023;13(4):1163-79. <https://doi.org/10.1007/s13202-022-01598-8>
43. Afanaseva O, Bezyukov O, Pervukhin D, Tukeev D. Experimental Study Results Processing Method for the Marine Diesel Engines Vibration Activity Caused by the Cylinder-Piston Group Operations. *Inventions*. 2023;8(3):71. <https://doi.org/10.3390/inventions8030071>
44. Islamov S, Bondarenko A, Gabibov A, Mardashov D. Polymer compositions for well killing operation in fractured reservoirs. *Advances in raw material industries for sustainable development goals*. 2021:343-51. [10.1201/9781003164395-43](https://doi.org/10.1201/9781003164395-43)
45. Islamov S, Bondarenko A, Mardashov D. A selection of emulsifiers for preparation of invert emulsion drilling. *Topical Issues of Rational Use of Natural Resources, Volume 2*. 2019:487. [10.1201/9781003014638-2](https://doi.org/10.1201/9781003014638-2)

COPYRIGHTS

©2024 The author(s). This is an open access article distributed under the terms of the Creative Commons Attribution (CC BY 4.0), which permits unrestricted use, distribution, and reproduction in any medium, as long as the original authors and source are cited. No permission is required from the authors or the publishers.

**Persian Abstract****چکیده**

خط لوله پلی اتیلن زیرساخت ضروری شبکه توزیع گاز است و مشکلاتی از جمله ارزیابی پیچیده خسارت و فرآیند خسته کننده ارزیابی وجود دارد. نحوه انتخاب روش موثر ارزیابی خسارت برای خطوط لوله پلی اتیلن در حال حاضر محور اجرای شبکه توزیع گاز است. در این مقاله، یک روش موج جهت دار غیر خطی برای تشخیص آسیب خط لوله پلی اتیلن توسط موج صوتی پیشنهاد شده است و نتایج آسیب خط لوله پلی اتیلن جستجو می شود. منطقی بودن این روش با محاسبه معادله آیرودینامیکی تأیید می شود. نتایج نشان می دهد که روش موج ثابت غیرخطی می تواند به طور دقیق میزان آسیب و انتشار ترک خط لوله را تعیین کند و فرآیند ارزیابی آسیب را ساده کند و نتایج نسبت به جهت خطی برتری دارد. روش موج بنا بر این، موج غیر خطی جهت دار را می توان برای ارزیابی آسیب به خطوط لوله اتیلن در شبکه های توزیع گاز استفاده کرد که از عقلانیت و عملی قوی برخوردار است و از ارزیابی واقعی آسیب خط لوله پشتیبانی می کند.



Optimizing Heat Transfer in Microchannel Heat Sinks: A Numerical Investigation with Nanofluids and Modified Geometries

F. Nasiri Khamesloo, D. Domiri Ganji*

Department of Mechanical Engineering, Babol Noshirvani University of Technology, Babol, Iran

PAPER INFO

Paper history:

Received 26 September 2023

Received in revised form 26 November 2023

Accepted 27 November 2023

Keywords:

Numerical Study

Microchannel Heat Sink

Fractal

Nanofluid

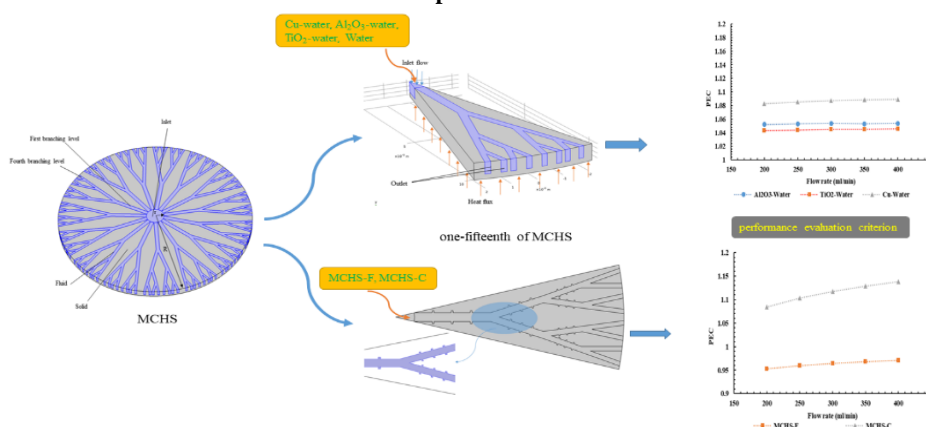
Geometry Change

ABSTRACT

The utilization of microchannel heat sinks stands as one of the most reliable solutions for dissipating heat generated in electronic chips. In this numerical study, a fractal microchannel heat sink employing three nanofluids Cu-water, Al_2O_3 -water, and TiO_2 -water with variable volume fractions of 2 and 4 percent as the cooling fluid within the microchannels was investigated. The fluid flow inside the microchannels was analyzed from both hydrodynamic and thermal perspectives. The parameters such as pump power, Nusselt number, and performance evaluation criterion (PEC) were studied. Results demonstrate that heat transfer increases with an increase in the flow rate and volume fraction of nanoparticles. The maximum temperature reduction for the Cu-water nanofluid at an inlet flow rate of 200 ml/min and a volume fraction of 4% is 2.41%, the highest among the investigated nanofluids. However, this nanofluid also exhibits the highest pressure drop, reaching 25% at a 4% volume fraction. The PEC number analysis reveals an overall performance increase for all three microchannels. The Cu-water nanofluid exhibits the best comprehensive performance, providing an 8% overall enhancement, followed by Al_2O_3 -water and TiO_2 -water nanofluids, which increase the system performance by 5% and 4%, respectively. Furthermore, the study introduced fins and cavities to the microchannel branches to enhance heat transfer and overall performance. Results indicate an increase in heat transfer for both modified geometries. The microchannel with fins exhibits a 3.5% lower maximum temperature compared to the original geometry at an inlet flow rate of 200 ml/min, while the microchannel with cavities showed a 1% reduction. However, the microchannel with fins experiences a 400% higher pressure drop than the initial geometry, while the microchannel with cavities has a 4% increase. PEC number analysis demonstrated that the microchannel with cavities improves system performance by 8%, whereas the microchannel with fins reduced system performance by 4%.

doi: 10.5829/ije.2024.37.05b.05

Graphical Abstract



*Corresponding Author Email: mirgang@nit.ac.ir (D. Domiri Ganji)

Please cite this article as: Nasiri Khamesloo F, Domiri Ganji D. Optimizing Heat Transfer in Microchannel Heat Sinks: A Numerical Investigation with Nanofluids and Modified Geometries. International Journal of Engineering, Transactions B: Applications. 2024;37(05):860-75.

Highlights

- Design of a Fractal Microchannel Heat Sink for Numerical Investigation
- Utilization of Three Different Nanofluids for Cooling the Heat Sink and Their Hydraulic and Thermal Comparison
- Cu-Water Nanofluid Demonstrates the Best Overall Performance
- Creation of Fins and Cavities in the Microchannel
- Improved Performance of the Microchannel with Cavities in Terms of Overall Performance

NOMENCLATURE

R	radius of the heat sink (mm)	f	fluid
r	inlet radius (mm)	nf	nanofluid
i	branching level	W_{pump}	pumping power (mW)
u_m	average velocity (m/s)	q_v	flow rate ($m^3 \cdot s^{-1}$)
D_h	hydraulic diameter (mm)	q	Heat flux ($W \cdot m^{-2}$)
c_p	specific heat capacity ($J/(kg \cdot K)$)	$Nu_{m,i}$	Nusselt number
T_f	temperature of fluid (K)	Greek Symbols	
T_s	temperature of the solid (K)	ρ_f	density of fluid (kg/m^3)
k_f	thermal conductivity of fluid ($W/(m \cdot K)$)	μ_f	dynamic viscosity of fluid ($N \cdot s/m^2$)
k_s	thermal conductivity of solid ($W/(m \cdot K)$)	ϕ	volume fraction

1. INTRODUCTION

Since the advent of the first digital electronic devices in the 1940s, efficient heat dissipation has been pivotal in ensuring the performance of subsequent generations of these devices. According to a survey conducted by a multinational corporation, the annual cost of cooling residential computer and telecommunications equipment stands for \$4.1 billion. Projections suggest that this expenditure is expected to escalate to \$4.8 billion in the foreseeable future. This study underscores the imperative to transcend conventional cooling systems and adopt innovative approaches (1). Heat sinks serve as heat exchangers in electronic devices, managing and dissipating the heat generated by electronic or mechanical chips. Functioning as a thermal management solution, a heat sink absorbs and disperses heat into the surrounding fluid, thereby preventing the temperature of the electronic component from reaching damaging levels. The significance of a heat sink becomes more pronounced when temperature-sensitive components are integrated into the circuit or device. With the ongoing trend of electronic component miniaturization and the associated increase in device temperatures, various methods have been developed to address heat dissipation, including fluid jet impingement, sprays, heat pipes, piezoelectric droplets, and more. Among these techniques, microchannel heat sinks emerge as the most pragmatic choice, boasting advantageous features such as lightweight design, compactness, and a high heat transfer rate to volume ratio (2). Microchannel heat sinks find applications in industries with high heat flux, including oil and gas, steel and metallurgical, energy production and the power electronics industries. They are used for cooling various components such as heat exchangers, piping systems, refinery equipment, steel components, metal smelting furnaces, distillation devices, turbines,

generators, power converters, and transistors. These heat sinks are also employed in thermal power plants, photovoltaic concentrator systems, and other high heat flux power plants to cool heat-generating components and systems.

In 1981, Tuckerman and Pease (3) designed the first microchannel heat sink and laid the groundwork for research and development in this field. Weisberg et al. (4) further investigated microchannel heatsinks for cooling electronic chips. They analyzed microchannel heat exchangers using numerical methods and considered dual heat transfer, which involves determining simultaneous temperature fields in solid and fluid media. Additionally, they presented a design algorithm for selecting heat exchangers. Jeevan et al. (5) used a genetic algorithm to optimize the thermal resistance of microchannels along with one-dimensional and two-dimensional finite element methods. They showed that using a genetic algorithm for practical microchannel design can be useful. Bionic fractal microchannels were first introduced by Bejan and Errera (6). They presented a strategy for constructing channels using structural theory, where the flow resistance along the path is minimized. Inspired by the fractal pattern of circulatory and respiratory systems in mammals, Chen and Cheng (7) proposed a new design of an H-shaped fractal branching channel network for cooling electronic chips. The novel design has a stronger capacity for heat transfer and needs less pumping power, according to results comparing it to conventional parallel networks. Pence (8) compared two microchannel heat sinks, tree-shaped and H-shaped, under the same conditions. The results showed that the tree-shaped microchannel has 60% less pressure drop and a 30°C lower wall temperature than the other design. In another study, Xu et al. (9) designed four different models of microchannels (parallel, rectangular, spiral, and tree-shaped) and investigated the effect of different

MCHS structures on chilling electronic components. Zaretabar et al. (10) present a simulation of heat transfer in a heatsink on a computer's mainboard transistorized square chip. Xu et al. (11) investigated the heat transfer performance of a fractal microchannel network made of silicon and cooled by water under pulsation flow conditions, both experimentally and numerically. Oyewola et al. (12) present an air-cooled temperature management module using a unique pin-fin heat sink for Li-ion cells. Among different pin-fin geometries, the uniform height heat sink (case 2) stands out, showing superior performance. Alrwashdeh et al. (13) focus on the impact of heat exchanger length on parallel and counterflow HEs. Computer simulations reveal that increasing the HE length improves heat transfer, enhances temperature distribution, and boosts energy transfer efficiency within the HEs. Yan et al. (14) designed an optimal dual-objective thermal-hydraulic model and compared it with optimal hydraulic and optimal thermal models. The results showed that the optimal dual-objective model with 15 main branches has the best overall performance.

In recent years, the use of nanofluids and mixing nanoparticles with base fluids to increase heat transfer has been the subject of much research. Nanofluids are new fluids made from the dispersion of nano-scale materials such as nanoparticles, nanotubes, and nanowires in a base fluid. In other words, nanofluids are suspensions in which solid nanomaterials are added to the base fluid and suspended within the fluid to increase the base fluid's heat transfer properties. Adding nanoscale particles with higher thermal conductivity coefficients to the base fluid is one of the most common techniques to increase heat transfer. The idea of using nanoparticles was first proposed by Maxwell in 1881, which sparked a major change in the study of heat transfer in fluids. Later on, Choi and Eastman (15) used nanofluids to increase heat transfer. Keblinski et al. (16), based on studies of nanofluids, found that thermal conductivity increases with decreasing particle size. They showed that the key factors in comprehending the thermal properties of nanofluids are the nature of the motion path rather than diffusion, heat transfer in nanoparticles, and the direct or mediated effects of fluid clustering that provide pathways for rapid heat transfer. Abu-Nada et al. (17) studied natural heat transfer in circular loops by using nanofluids. They showed that adding different types and different volume fractions of nanoparticles has different effects on heat transfer properties. Pasha and Domiri-Ganji (18) analyzed heat transfer and angular velocity of micropolar ethylene-glycol nanofluid over various fins on a stretching sheet, revealing maximum temperature at the last fin and higher angular velocity for triangular and chamfer fins. Ho and Chen (19) investigated experimentally forced convection heat transfer utilizing an Al_2O_3 -water nanofluid in a copper minichannel heat

sink. In their study, Hatami and Ganji (20) investigated the heat transfer characteristics of a MCHS with multiple fins. The cooling fluid flow employed in their experiment was a water-copper nanofluid and optimized the heat sink geometry considering the minimum friction coefficient. Jalili et al. (21) evaluate the heat transfer of Al_2O_3 -water nanofluid in a heatsink with a magnetic field using the KKL model. Abdollahi et al. (22) investigate the flow and thermal characteristics of a MCHS using a hybrid nanofluid with copper nanoparticles. The results showed the impact of nanoparticle volume fraction and Darcy number on heat transfer and temperature distribution. Jalili et al. (23) looked at how different things affected the temperature, speed, and concentration distribution of a micro-polar nanofluid in a rotating system with parallel plates. Jalili et al. (24) compared the accuracy of three methods using Finite Element, and Runge-Kutta for simulating thermal diffusivity profiles in oblique stenosis arteries by hybrid nanofluids with Al_2O_3 and Cu nanoparticles. The Finite Element method came in second place (with less than 9% error), with Akbari-Ganji method having the highest accuracy (less than 7% error). In another study, Jalili et al. (25) investigate the impact of thermo-diffusion, electrical field, and nonlinear thermal radiation on the flow of a non-Darcy Casson fluid on stretched surfaces using the Hybrid Analytical and Numerical (HAN) Method, considering various parameters and their effects on velocity, temperature, and concentration. In recent study, Jalili et al. (26) examined the flow of a viscous fluid between porous disks under a magnetic field, comparing Akbari-Ganji Method (AGM) and the Finite Element Method (FEM). Valuable research has been conducted in the fields of microchannels, nanofluids, and heat transfer, which are reported in literature (27-32) and can be beneficial for future studies.

In the present study, fluid flow and heat transfer in a fractal microchannel heat sink have been simulated using the COMSOL Multiphysics software. The use of a fractal structure is motivated by its higher heat transfer capability and lower pumping power compared to a parallel microchannel structure. The fractal microchannel investigated in this research has been proposed by scientists in recent years and features 15 branches, representing the most thermo-hydraulically optimized configuration. Since nanofluids have not been used in this particular geometry before, and considering the need for enhanced heat transfer in heat sinks to prevent chip overheating, three different nanofluids (water-copper, water- Al_2O_3 , and water- TiO_2) have been employed as coolant fluids at various volume fractions compared to the base fluid (water). The three nanofluids have been evaluated hydrodynamically and thermally, considering parameters such as pumping power and Nusselt number, and the best nanofluid for overall performance enhancement of the fractal microchannel has been determined. Furthermore, to increase the efficiency of the

microchannel and investigate the effect of geometric modifications inside the fractal microchannel, cavities and fins have been introduced. Both new geometries have been evaluated thermo-hydraulically and compared to the base geometry. Ultimately, a new and optimized geometry has been proposed for future work to further enhance performance.

2. PROBLEM STATEMENT

2.1. Physical Model In this study, fluid flow and heat transfer in a fractal microchannel heat sink in the presence of three nanofluids will be investigated using numerical simulation. The use of numerical methods allows for the flexibility to modify problem conditions, including boundary conditions and various parameters, based on the physics and geometry of the problem. The microchannel heat sink geometry studied in this research is presented by Yan et al. (14). The fractal microchannels are inspired by the fractal patterns found in mammalian circulatory and respiratory systems, and they exhibit enhanced heat transfer and reduced pumping power compared to other microchannels. The fractal microchannel studied in this research represents an optimized thermo-hydraulic configuration which is shown in Figure 1. It consists of 15 main branches, as depicted in Figure 1, but for computational convergence and improved computational efficiency, a one-fifteenth section of the overall structure, as shown in Figure 2, is considered for numerical simulation. The COMSOL Multiphysics software, known for its capabilities in fluid mechanics, is used for the numerical simulation. Since COMSOL can import geometry from CAD software, the simulation geometry is designed in Solidworks and imported into COMSOL. The studied geometry consists of an inlet in the center and eight outlet branches formed along the radius, as shown in Figure 2. The overall radius of the geometry is 11 millimeters, the inlet branch radius is 1 millimeter, the height of the channel bed is 0.2 millimeters, and the channel height is 0.5 millimeters. Heat flux is applied from the bottom to the heat sink, and the fluid flow inside the microchannel induces heat transfer.

Given the enhanced heat transfer characteristics of nanoparticles, the utilization of nanofluids can improve the performance of microchannel fractal heat sinks. However, this aspect has not been addressed in previous studies. In this research, the aim is to enhance heat transfer using copper (Cu), alumina (Al_2O_3), and titanium dioxide (TiO_2) nanoparticles in water as the base fluid, with nanoparticle volume fractions ranging from 0 to 4%. Various parameters, including temperature distribution, pressure drop, pumping power, and heat sink performance coefficient, have been investigated within an inlet flow rate range of 200 to 400 ml/min and a

constant heat flux of 100 W/cm^2 . Finally, a comparison has been made among the three nanofluids.

To enhance the geometric properties, square-shaped fins and cavities have been introduced within the initial three branches of the microchannel fractal. The cross-sectional shape of both the cavities and fins is square, with their respective heights being equal to the height of the microchannel. Six fins or cavities have been produced in each microchannel branch, as depicted in Figure 3.

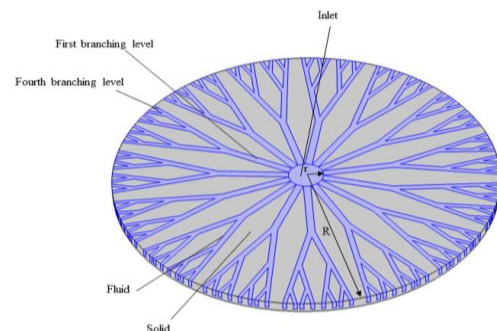


Figure 1. Schematic geometry of MCHS

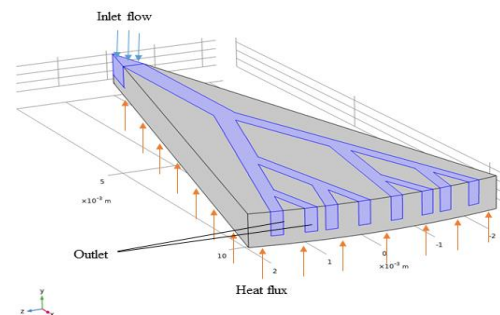


Figure 2. Schematic geometry and boundary conditions

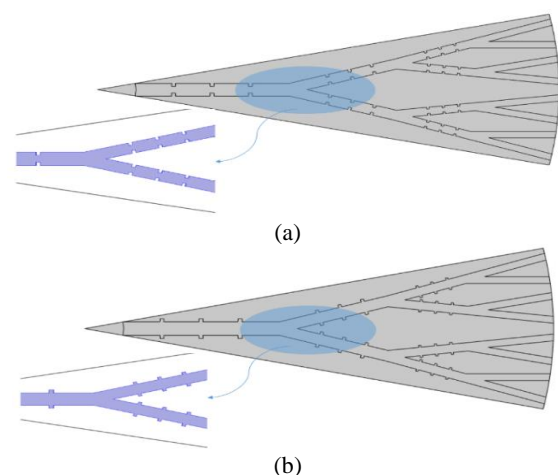


Figure 3. Geometry of microchannel a: with fin b: with cavity

2. 2. Numerical Model

The properties of nanofluids have been calculated using the following equations:

The viscosity of nanofluids for spherical nanoparticles can be estimated using the following equation (33):

$$\mu_{nf} = \frac{\mu_f}{(1-\varphi)^{2.5}} \quad (1)$$

The density and specific heat capacity of a nanofluid with any shape of nanoparticle can be obtained from the following equations:

$$\rho_{nf} = \left(\frac{m}{V}\right)_{nf} = (1-\varphi)\rho_f + \varphi\rho_s \quad (2)$$

$$(\rho \cdot c_p)_{nf} = (1-\varphi)(\rho \cdot c_p)_f + \varphi(\rho \cdot c_p)_s \quad (3)$$

The effective thermal conductivity coefficient of a nanofluid can be approximately obtained from the following equation by Hamilton-Crosser model (34):

$$\frac{k_{nf}}{k_f} = \frac{k_s + (n-1)k_f - (n-1)(k_f - k_s)\varphi}{k_s + (n-1)k_f + (k_f - k_s)\varphi} \quad (4)$$

where n is the shape factor of nanoparticles, which for spherical nanoparticles is equal to 3. As a result, only spherical nanoparticles can be used with this equation; other shapes of nanoparticles are not taken into account. The use of this model is suitable for studying the enhancement of heat transfer using appropriate nanoparticles. In the above equations, φ represents the volume fraction of nanoparticles. The thermodynamic properties of the base fluid and nanoparticles are introduced in Table 1.

Fluid behavior in a control volume is described using the Navier-Stokes equations (35), which are expressed as:

Continuity equation: To investigate the conservation of mass, the continuity equation is used in the following form:

$$\nabla \cdot (\rho_f \vec{u}) = 0 \quad (5)$$

Momentum equation:

$$\vec{u} \cdot \nabla (\rho_f \vec{u}) = -\nabla p + \nabla \cdot (\mu_f \nabla \vec{u}) \quad (6)$$

Energy equation for fluid:

$$\vec{u} \cdot \nabla (\rho_f c_{p,f} T_f) = \nabla \cdot (k_f \nabla T_f) \quad (7)$$

TABLE 1. Thermodynamic Properties (17)

Thermodynamic properties		ρ (Kg/m ³)	c_p (J/KgK)	k (W/mK)
Base fluid	Water	997.1	4179	0.613
	Cu	8933	385	401
Nanoparticles	Al ₂ O ₃	3970	765	40
	TiO ₂	4250	686.2	8.9538

Energy equation for solid:

$$\nabla \cdot (k_s \nabla T_s) = 0 \quad (8)$$

where \vec{u} is the velocity, ρ_f is the coolant fluid density, \vec{p} is the hydrodynamic pressure, μ_f is the viscosity of the fluid, $c_{p,f}$ is the specific heat capacity of the fluid, T_f represents the temperature of the fluid, k_f is the fluid's thermal conductivity coefficient, k_s and T_s respectively represent the thermal conductivity coefficient of the solid and the temperature of the solid section.

The following parameters are used to evaluate the efficacy of a MCHS:

Pumping power:

$$W_{pump} = \Delta P_{tot} \times q_v \quad (9)$$

where ΔP_{tot} represents the total pressure drop and q_v denotes the volumetric flow rate.

Average Re in each branch:

$$Re_{m,i} = \frac{\rho \times u_{m,i} \times D_h}{\mu} \quad (10)$$

Average Nusselt number in each branch:

$$Nu_{m,i} = \frac{q \times D_{h,i}}{k_f \times (T_{m,wi} - T_{m,fi})} \quad (11)$$

where D_h is the hydraulic diameter, q is the heat flux. Additionally, $T_{m,wi}$ and $T_{m,fi}$ represent the average wall temperature and the bulk fluid temperature, respectively. Friction factor:

$$f = 2\Delta P \frac{D_h}{L} \frac{1}{\rho u_{in}^2} \quad (12)$$

performance evaluation criterion:

$$PEC = \frac{\left(\frac{Nu_{ave}}{Nu_{ave,\varphi=0}}\right)}{\left(\frac{f}{f_{\varphi=0}}\right)^{\frac{1}{3}}} \quad (13)$$

2. 3. Boundary Conditions

Based on Figure 2, the boundary conditions are determined. In the operating temperature range, the fluid flow is steady, incompressible, and has constant thermophysical properties. The volume fraction of the nanoparticles under investigation in this study is 2% and 4%. The inlet temperature is 293 K, the inlet flow rate is 200 ml/min, and the outlet pressure is equal to atmospheric pressure. The heat sink is made of copper and is isolated from the surrounding environment. The heat flux entering the heatsink's bottom wall is 100 W/cm². A no-slip condition is applied to the walls, and the effects of radiation and gravity are neglected.

2. 4. Grid Independence

In the numerical solution process in software, one of the most important issues is creating an appropriate grid or mesh. The importance of grid generation in numerical simulation is that if the grid is not fine enough, calculations will not have high

accuracy, and if the grid is too fine, the cost and time of performing the simulation will be significantly high. Therefore, the grid should be fine enough that the results do not differ significantly from each other and are essentially independent of the mesh. In grid generation, it should be noted that the meshes near the walls and edges, where the gradient of flow variables is more intense, should be finer to have a higher accuracy in the calculations. Also, the grid in the solid part can be larger than the liquid part. To evaluate the accuracy of the results, the maximum temperature and pressure drop were investigated in five different grid generations. The numbers of grids 384073, 698638, 903316, 1314415, and 1693388 were studied. Considering the obtained results, the changes in the maximum temperature and pressure drop in the third grid and later are very negligible. Therefore, a mesh number of 903316 has been chosen to continue the process.

2. 5. Validation For validation, the obtained pumping power from the simulation has been compared with the pumping power versus flow rate graph introduced by Yan et al. (14). In this validation, the coolant fluid is water, and the heat flux is 50 W/cm^2 . As can be seen in Figure 4, the obtained results have a good agreement with the data in the article.

3. RESULTS AND DISCUSSION

This study seeks to assess the thermal performance of a microchannel heat sink operating under laminar flow conditions. Moreover, endeavors are undertaken to enhance the heat sink's efficiency by introducing nanofluid flow and incorporating fins and cavities within the microchannel. Through a thorough investigation, the optimal nanoparticles and geometry have been identified to improve the thermal-hydraulic performance. The primary objective of employing a heat sink is to mitigate the temperature rise of the electronic chip, with achieving a low maximum heat sink temperature being crucial for

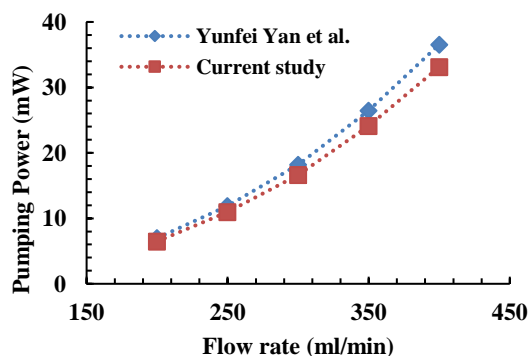


Figure 4. Model validation

this purpose. Maintaining a low maximum temperature ensures improved heat sink performance and prevents chip failure resulting from elevated temperatures. Therefore, the enhancement of system geometry and the utilization of nanoparticles in thermal systems not only guarantee efficiency and improved performance but also contribute to cost reduction and energy consumption.

3. 1. Applications of Nanofluids

Figure 5 illustrates the variations in the maximum temperature of the heatsink in relation to the flow rate for nanofluids: Cu-water, Al_2O_3 -water, and TiO_2 -water. As observed, as the inlet flow rate and fractional volume of nanoparticles increase from zero to four percent, the maximal temperature of the MCHS decreases. An increase in the inlet flow rate causes an increase in the inlet velocity, which raises the Reynolds number. The temperature differential between the inlet and outlet of the flow is decreased by raising the inlet flow rate while keeping the heat flux constant. As a result, the flow's output temperature drops when the incoming flow temperature is constant. In general, it can be said that when the inlet flow rate rises, the efficiency of heat transfer between the fluid and the wall also increases, which lowers the temperature of the microchannel heat sink. The heat sink's maximum temperature for water flow is 349.28 K at a flow rate of 200 ml/min and 334.1 K at a flow rate of 400 ml/min.

Figure 5 shows the impact of introducing solid nanoparticles at flow rates between 200 and 400 ml/min at volume fractions of 2% and 4% on the heat sink's maximum temperature. The addition of solid nanoparticles improves thermophysical characteristics, such as the thermal conductivity of the coolant fluid and heat transfer, as shown in Figure 5. It is worth mentioning that increasing the inlet flow rate (increasing fluid velocity) and the fractional volume of solid nanoparticles result in a reduction in the temperature gradient along the fluid path. Consequently, the heat sink's maximum temperature is decreased, and its temperature distribution is more uniform.

In Figure 6, contour plots depicting the influence of two parameters, namely volume fraction and inlet flow rate, on temperature are observed. As evident from the plot, an increase in volume fraction and inlet flow rate results in a decrease in the temperature of the heat sink. These plots, which display the variations in temperature profiles, provide valuable insights into the three parameters under discussion. Furthermore, the three-dimensional plot enhances our understanding of the intricate behavior of fluid flow.

In Figure 7, the maximal temperature of the MCHS in the presence of Al_2O_3 -water, TiO_2 -water, and Cu-water nanofluids at a 4% volume fraction has been compared. As observed, the Cu-water nanofluid has the lowest temperature, followed by Al_2O_3 -water and TiO_2 -water.

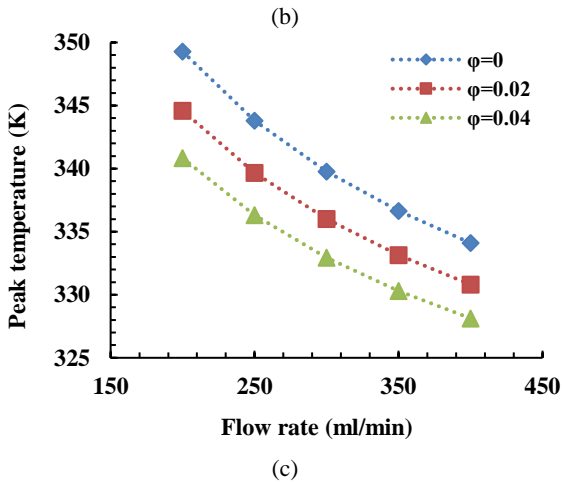
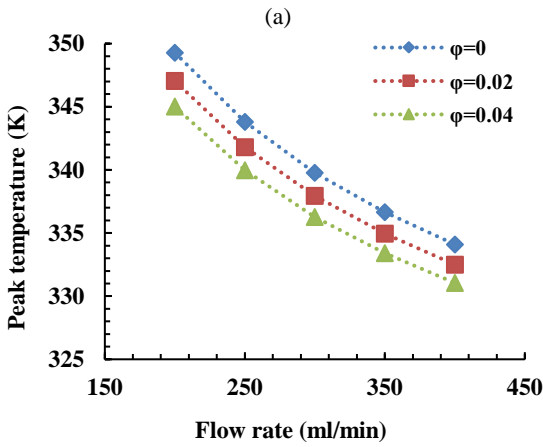
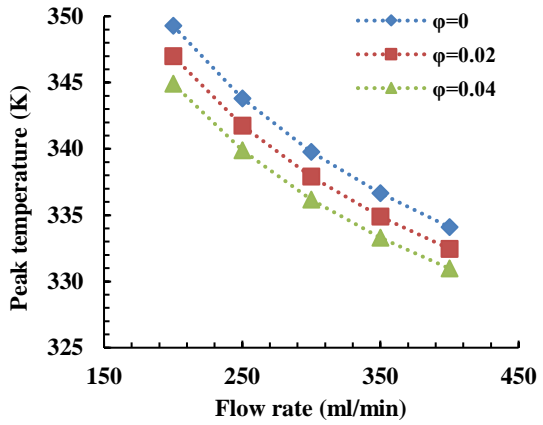


Figure 5. Maximum temperature in the heat sink for (a) Al₂O₃-water, (b) TiO₂-water, and (c) Cu-water

The maximum temperature at a flow rate of 200 ml/min for Cu-water, Al₂O₃-water, and TiO₂-water nanofluids is 340.83, 344.91, and 345.01 K, respectively. The reason for this is the thermal conductivity coefficient, which is higher for water-copper than the other two nanofluids.

Figure 8 depicts the temperature distribution observed when water and three different nanofluids, each with a fractional volume of 4%, are subjected to a flow

rate of 200 ml/min. The use of nanoparticles effectively mitigates the temperature gradient, leading to a homogeneous distribution of temperature within the fractal microchannel heat sink. Hot spots can be noticed in certain regions where fluid flow pathways are absent, and these hot spots can be mitigated by employing tree-like structures. The utilization of fractal-based compensatory structures has been employed to mitigate heat transfer degradation and establish regions of enhanced heat transfer. By increasing the number of branches in the fractal tree structure, the temperature

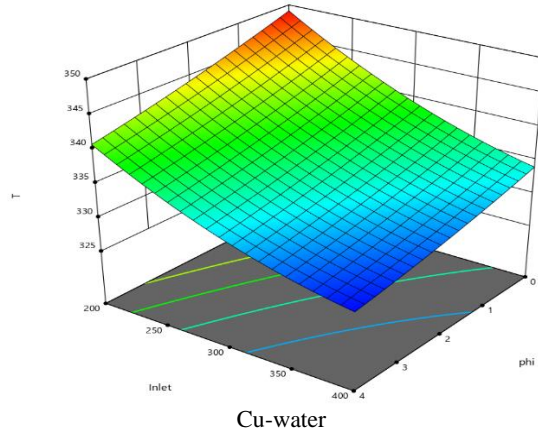
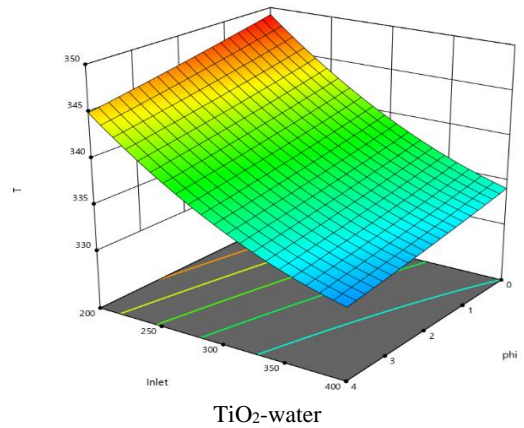
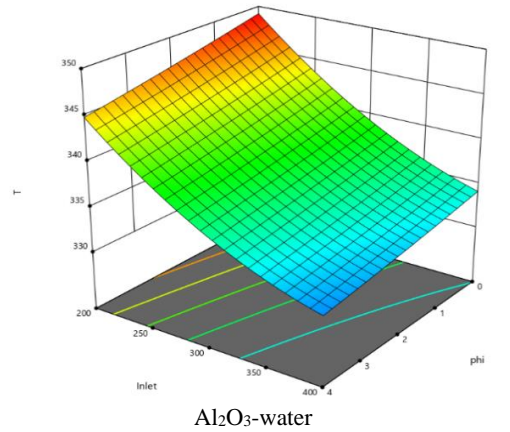


Figure 6. Effects of various operating parameters

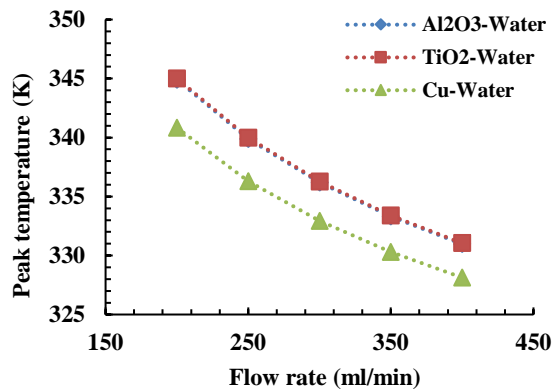


Figure 7. maximum temperature in the heat sink at 4% volume fraction

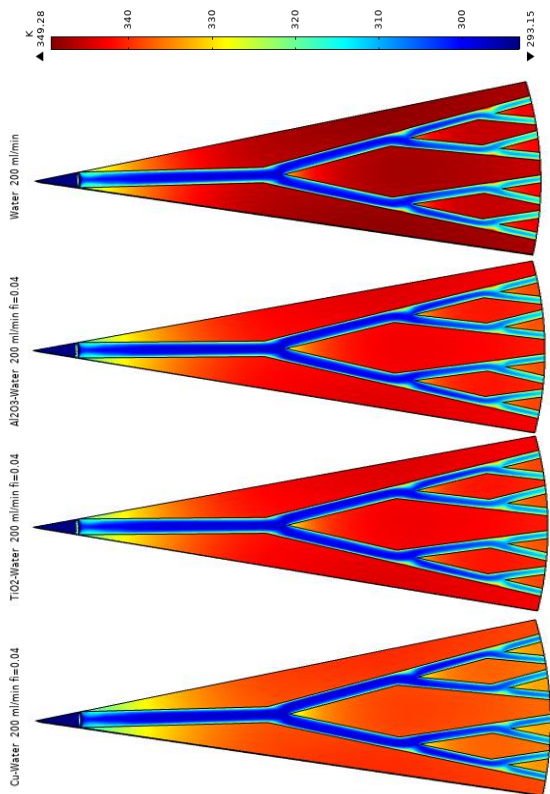


Figure 8. Temperature distribution in heat sink

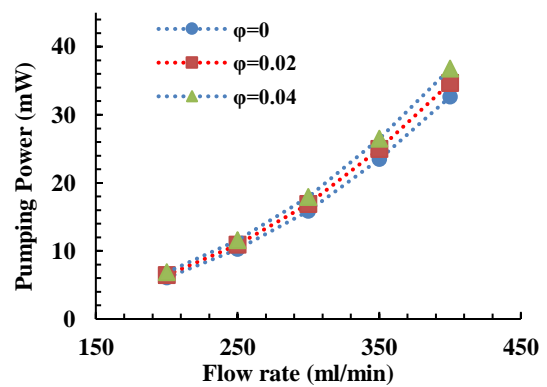
distribution in these regions becomes more uniform, preventing the formation of abrupt temperature gradients. Furthermore, it can be observed that in the branching regions of the new microchannel configurations, the boundary layer becomes turbulent and redevelops inside the microchannel. This phenomenon leads to enhanced heat transfer in these regions compared to the core of the microchannel. Additionally, it is noticeable that near the walls, lower temperatures are present compared to the regions away from the walls. This is attributed to the

increased heat transfer between the wall and the fluid. An increase in the solid volume fractions in nanofluids has been found to significantly enhance several thermophysical parameters, with particular emphasis on the thermal conductivity of the coolant fluid. This phenomenon accelerates the process of thermal energy transmission and guarantees a consistent distribution of temperature throughout the surfaces.

Figure 9 depicts the variations in pumping power as a function of flow rate, considering the fractional volume of the three discussed nanofluids. It should be noted that the pumping power is obtained based on Equation 9. The pumping power is influenced by both geometric parameters and thermophysical variables, including density, dynamic viscosity, and inlet velocity. As observed, the pumping power increases with an increase in the inlet flow.

With the inclusion of nanoparticles, the coolant fluid becomes denser and more viscous, increasing the fractional volume and pumping power of all three nanofluids. As a result of the incorporation of nanoparticles into the base fluid, which increases the density and viscosity of the coolant fluid, more pumping force is required to transport nanofluid through microchannels. A notable observation in Figure 9 is that there is a positive correlation between the fractional volume of nanoparticles, the inlet flow rate, and the rate of increase in pumping power. As seen, the pumping power for various volume fractions differs minimally at low inlet flow rates, but this disparity increases at higher flow rates. At a flow rate of 200 ml/min, the pumping power is 6.04 mW, and at a flow rate of 400 ml/min, it is 32.63 mW.

Figure 10 illustrates three-dimensional plots of the pump power profile, volume fraction profile, and inlet flow rate profile for three different nanofluids. As observed, an increase in the volume fraction and inlet flow rate leads to an increase in pump power. By increasing the volume fraction of nanoparticles in the nanofluid, the density and viscosity of the nanofluid



(a)

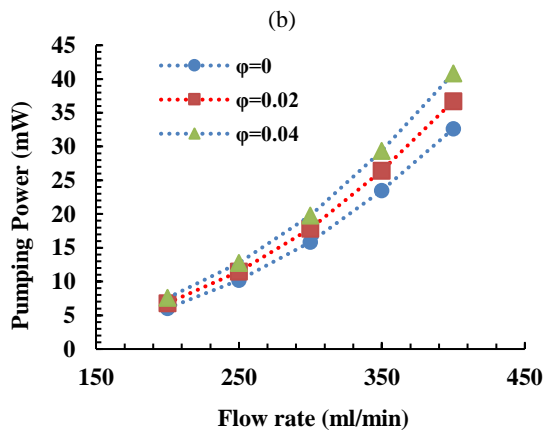
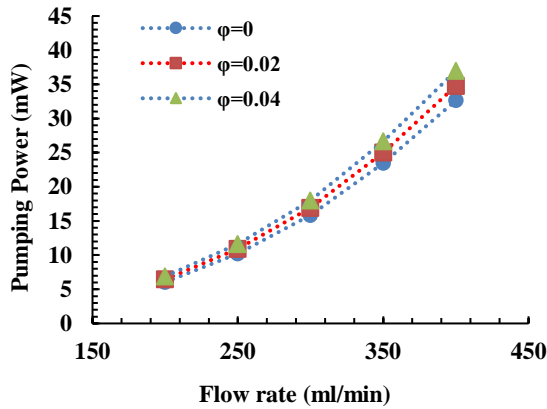


Figure 9. Pumping power for (a) Al₂O₃-water, (b) TiO₂-water, and (c) Cu-water

increase. Moreover, with an increase in the inlet velocity, the collision between the wall and the nanofluid intensifies, further contributing to an increase in density and viscosity. These factors collectively result in an increase in the pumping power required for fluid circulation.

The pressure drop is increased when nanofluids are used in place of water. This is because the nanofluid has a higher viscosity coefficient than water does. In other

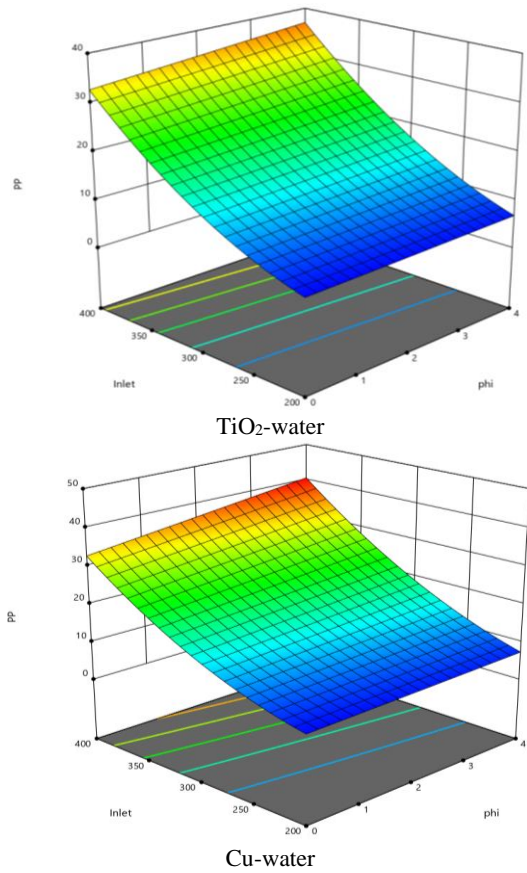
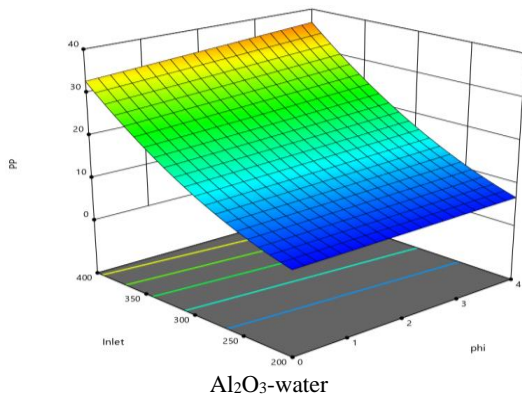


Figure 10. Effects of diverse operating parameters

words, as the base fluid's nanoparticle concentration rises, viscosity rises as well, which in turn raises the pressure drop. The interaction between the additional nanoparticles and the microchannel walls is what caused the increase in viscosity coefficient. Increasing the Reynolds number or flow rate results in a greater velocity gradient, intensifying the collision between nanoparticles and walls, particularly at higher volume fractions. When the inlet flow rate increases, the collision between nanoparticles and microchannel walls becomes more intense, and the force imparted by the walls on the nanoparticles increases, resulting in a higher pressure drop.

Figure 11 compares the pumping power of the fractal microchannel in the presence of nanofluids containing 4% volume fractions of Al₂O₃-water, TiO₂-water, and Cu-water. It is evident that the Al₂O₃-water nanofluid exhibits the lowest pumping power, with TiO₂-water and Cu-water nanofluids following in succession. For water-aluminum oxide, water-titanium oxide, and water-copper nanofluids, respectively, the pumping power at a flow rate of 200 ml/min is 6.86, 6.89, and 7.56 mW. The pumping powers of the TiO₂-water and Al₂O₃-water nanofluids are extremely close, with the Al₂O₃-water pumping power being somewhat lower.

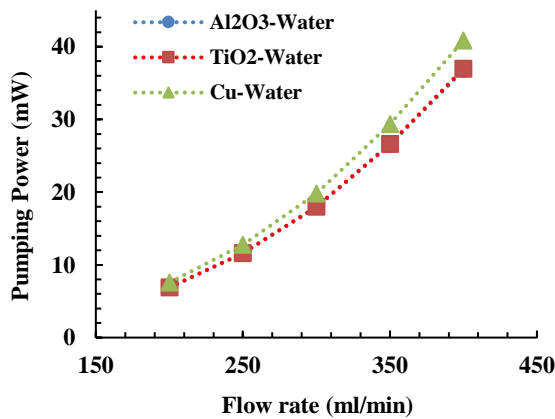


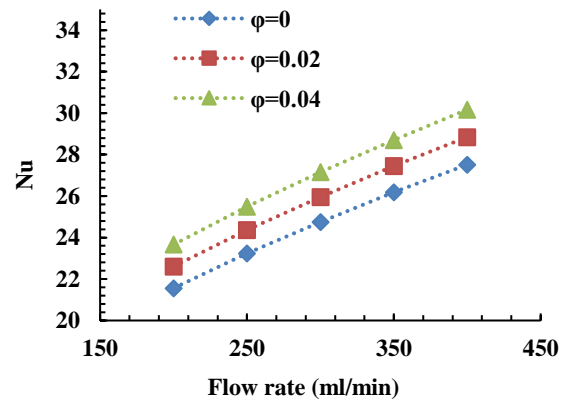
Figure 11. Pumping Power for Nanofluids at a Volume Fraction of 4%

Figure 12 demonstrates that the average Nusselt number varies with the nanoparticle volume fraction at various flow rates. It is significant to remember that the Nusselt numbers differ depending on the volume percentage of the nanoparticles, although the geometric structure of the microchannel and heat flux are the same for all of the scenarios shown in Figure 12. Increasing the inlet flow rate results in a rise in velocity, which improves heat transfer. Due to the reduction in the temperature difference between the wall and the fluid flow, Equation 11 predicts that the Nusselt number will rise. According to Figure 12, the Nusselt number for water is 21.55 for a flow rate of 200 ml/min and 27.51 for a flow rate of 400 ml/min.

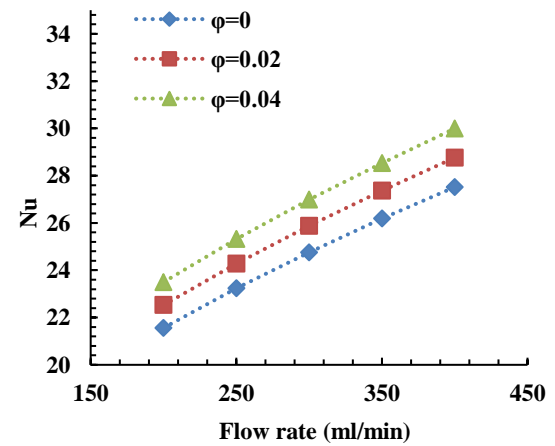
The thermal conductivity of the nanofluid increases in comparison to the base fluid by the addition of nanoparticles. As a result, the temperature difference between the nanofluid and the wall is reduced, and the nanofluid and wall exchange more heat. The Nusselt number exhibits rises due to a reduction in the differential temperature across the wall and the nanofluid flow. Copper nanoparticles have led to a greater increase in the Nusselt number than the other two nanoparticles.

In Figure 13, the Nusselt number in a microchannel is compared with a 4% volumetric fraction of water-copper, water-aluminum oxide, and water-titanium oxide. The TiO₂-water nanofluid has the lowest Nusselt number, followed by Al₂O₃-water and water-copper, respectively. The Nusselt numbers at a flow rate of 200 ml/min for TiO₂-water, Al₂O₃-water, and Cu-water nanofluids are 23.49, 23.66, and 25.15, respectively. Al₂O₃-water and TiO₂-water nanofluids have similar Nusselt numbers, with Al₂O₃-water being slightly higher. To consider an idea practical in the study of a subject, it is necessary to examine all aspects of that idea. In the case of thermal performance analysis in microchannels, hydrodynamic parameters must also be considered in addition to thermal parameters. For example, an idea may

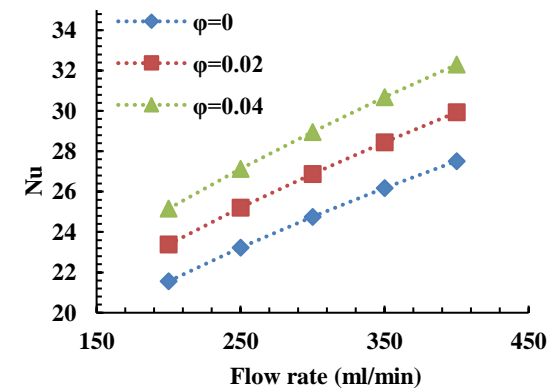
improve thermal performance but impair the hydrodynamic performance of the flow. Therefore, a parameter must be defined that simultaneously examines both thermal and hydrodynamic performance. In this situation, the Performance Evaluation Criterion (PEC), which considers both the Nusselt number and the friction coefficient, is determined using Equation 13. Figure 14



(a)



(b)



(c)

Figure 12. Nusselt Number for (a) Al₂O₃-water, (b) TiO₂-water, and (c) Cu-water

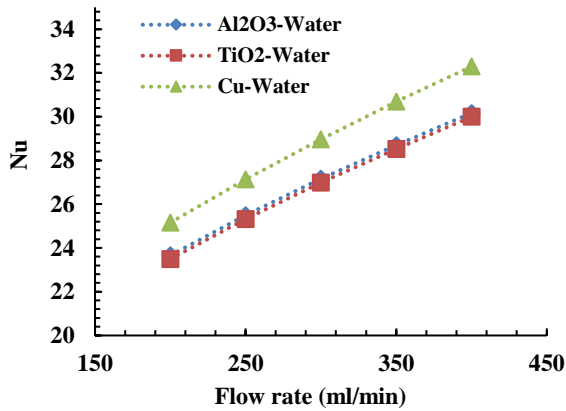


Figure 13. Nusselt Number for Nanofluids at a Volume Fraction of 4 percent

depicts the performance evaluation criteria for the three nanofluids with a 4% volumetric fraction: Al₂O₃-water, TiO₂-water, and Cu-water. The PEC is the ratio of the rise in the Nusselt number to the rise in friction coefficient for each solid volumetric fraction in comparison to the base fluid. Heat transfer and flow fields are influenced by variables such as introducing nanoparticles at various volumetric fractions, fluid velocity, and fluid type. Different things can happen with PEC, depending on how the heat transfer is improved and how much the friction rate goes up. According to Figure 14, each of the three nanofluids has a PEC value above one, demonstrating that the system performs better as a whole when nanoscale particles are added to the base fluid in this configuration. The water-copper nanofluid exhibits the highest PEC. The PEC value is independent of flow rate due to the microchannel shape and laminar flow regime, and only minor changes in the PEC value occur with increasing flow rate.

Based on the above content, it can be concluded that the best overall performance is related to the Cu-water nanofluid, and by adding copper nanoparticles to the

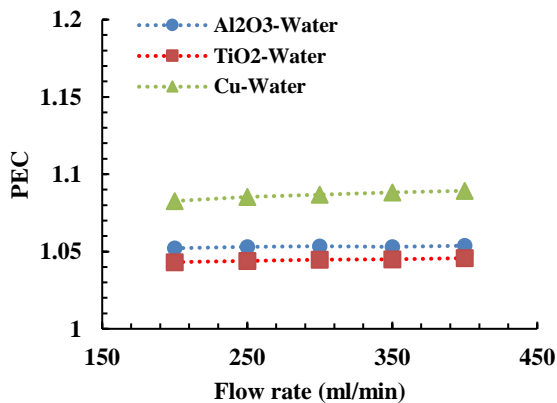


Figure 14. PEC for Nanofluids

water-based fluid, the overall performance of the system can be improved. After Cu-water, the best performance is related to the Al₂O₃-water nanofluid. In the following, to improve the thermal performance of the heat sink, the geometry of the problem will be changed, and the above parameters will be calculated for the new geometries to evaluate the effect of the geometry change as well.

3. 2. Geometry Improvement

Figure 15 shows the highest temperature of a heat sink for different inlet mass flow rates for a simple microchannel, a microchannel with cavities, and a microchannel with fins. As observed, as the inlet mass flow rate increases, the maximal temperature of the heat sink decreases. The addition of fins and cavities to the microchannel increases the fluid-solid contact area. This also disturbs the boundary layer, which dissipates and then redevelops. Because of these factors, heat transfer in the new microchannels is better than in the first case, which makes the highest temperature of the heatsink lower. Additionally, the presence of fins in the microchannel boosts flow velocity and causes fluid rotation following the fin, which improves heat transmission and lowers the temperature of the heat sink. The microchannel with fins performs thermally better than the other two microchannels. The presence of cavities and fins in the microchannel leads to the generation of turbulence in the boundary layer and its reformation. This phenomenon, when repeated in the microchannel, enhances heat transfer. Furthermore, increasing the flow rate results in higher heat transfer coefficients and overall heat transfer, leading to a decrease in the overall temperature of the heat sink. The maximum temperature of the heat sink for a flow rate of 200 ml/min is 349.28 for the base microchannel, 345.75 for the microchannel with cavities, and 337.02 K for the microchannel with fins.

Figure 16 depicts the contours of temperature for the three different geometries. Figure 16 shows that the temperature distribution is better and more uniform in the

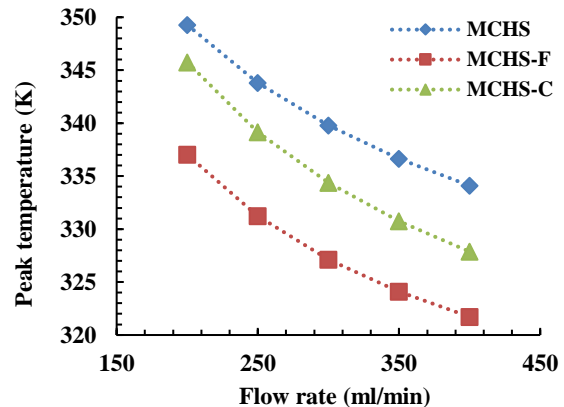


Figure 15. Maximum temperature of the heat sink for three geometries

microchannel with fins (MCHS-F). Additionally, it is evident from Figure 16 that the simple microchannel's maximum temperature is located in the geometry's center, specifically near the second and third branches. However, for the two new geometries, the highest temperature is around the radius of the geometry and the fourth branch. The minimum temperature is located at the center of the microchannel and increases along the microchannel walls. Additionally, the effects of branching and the addition of cavities and fins are noticeable, leading to turbulence in the boundary layer. In cavities, the boundary layer becomes turbulent and then redevelops. Furthermore, the presence of cavities creates stagnant regions and increases the fluid-wall contact area, which results in enhanced heat transfer. In microchannels with fins, in addition to these factors, the fluid velocity experiences a sudden increase at the locations where fins are present, leading to further enhancement of heat transfer.

Figure 17 shows how the pumping power changes when the flow rate changes for a basic microchannel, a microchannel with a cavity (MCHS-C), and a microchannel with a fin (MCHS-F). Notably, Equation 9 is used to determine the pumping power. As can be seen, the pumping power rises as the flow rate rises. Following the formation of cavities or fins, the branches produce a reverse pressure gradient, increasing the overall pressure drop. The cavity and fin cause turbulence in the fluid flow, which causes low-pressure and high-pressure areas

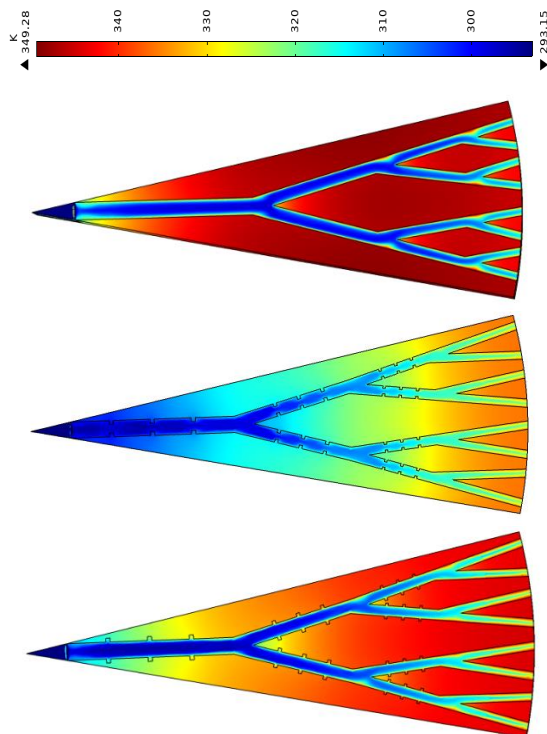


Figure 16. Temperature distribution in heat sink

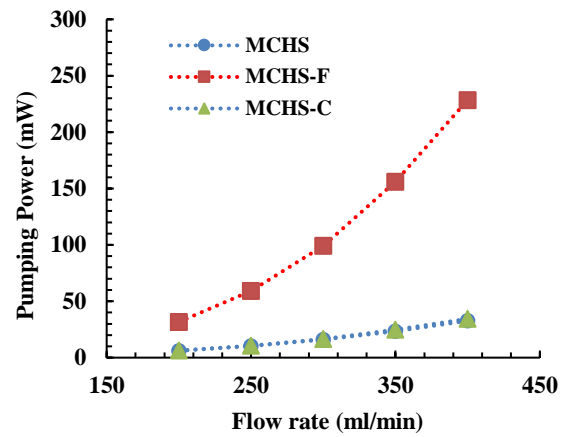


Figure 17. Pumping power for three geometries

to occur all around them. Consequently, the non-uniform distribution of pressure leads to an overall increase in the magnitude of the pressure drop. By adding cavities and fins, the boundary layer becomes turbulent, and the presence of cavity and fin walls creates local flow patterns in different paths, leading to increased pressure drop and pump power consumption. Based on Figure 17, it is clear that adding fins significantly reduces the pressure drop as compared to the cavity, and this difference is larger as the inlet flow rate rises.

Figure 18 shows a comparison of the Nusselt number in three different geometries. The microchannel with the fin has the highest Nusselt number, indicating greater heat transfer and a smaller temperature difference between the microchannel wall and bulk fluid. The reason for this increase is the higher fluid velocity in the microchannel with fins, which leads to enhanced heat transfer between the channel walls and the fluid. As a result, the temperature difference between the microchannel walls and the bulk fluid temperature decreases. The Nusselt number for a simple

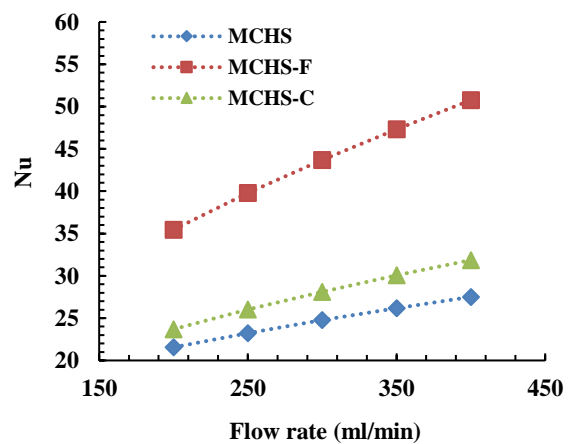


Figure 18. Nusselt number for three geometries

microchannel at an inlet flow rate of 200 ml/min is 21.55, while for a microchannel with cavities and a microchannel with fins, it is 23.69 and 35.45, respectively.

The microchannel with fins (MCHS-F) has greater heat transfer performance, but it also has a higher pressure drop and pumping power compared to the other two geometries, according to the information presented. The Performance Evaluation Criteria (PEC) was investigated in order to thoroughly study the pressure drop and heat transfer characteristics, as illustrated in Figure 19. As can be observed, the mass flow rate increases with all PEC values, suggesting that greater mass flow rates (higher velocities) are advantageous for enhancing heat sinks' general performance. With an increase in mass flow rate and flow velocity, heat transfer is enhanced, and the impact of viscous forces is diminished. Figure 19 reveals that the PEC value for the MCHS-F microchannel is lower than that of the microchannel without fins, indicating that fins reduce the overall system performance. The microchannel with cavities exhibits a PEC value greater than one, suggesting an enhancement in the overall performance of the system.

Based on the parameters discussed above, it can be concluded that the microchannel with cavities exhibits better overall performance compared to the other two microchannels. The geometry of the microchannel with cavity can be a suitable option for heat dissipation in electronic chips and significantly reduces the temperature of the heat sink.

In Figure 20, the results of geometry modification and cavity creation are compared with the results presented in Yan et al.'s paper (36). They utilized a double-layered microchannel heat sink in their study and investigated various parameters. The baseline geometry of both heat sinks is the same, and a new geometry is proposed in both studies. The performance evaluation coefficient is the parameter discussed in both papers. As evident from the figure, at flow rates ranging from 200 to 400 ml/min,

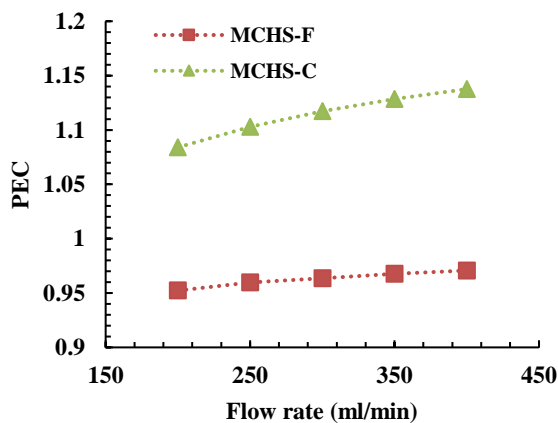


Figure 19. PEC for two new geometries

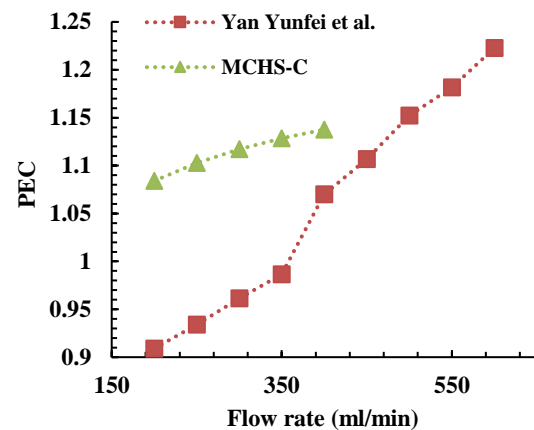


Figure 20. Comparison of Results with Yunfei's Paper

the proposed geometry in the current paper (microchannel with cavity) exhibited better overall performance and could be beneficial for future applications. However, with an increase in flow rate, the geometry proposed by Yan et al. [36] showed a significant improvement in performance, and at high flow rates, using that geometry could be advantageous.

4. CONCLUSIONS

This study utilized the COMSOL Multiphysics software, incorporating heat transfer in solids and fluids along with laminar flow physics in three dimensions. The investigation specifically delved into the characteristics of fluid flow when employing nanofluids, including water-copper, water-aluminum oxide, and water-titanium oxide, at various volume fractions and flow rates ranging from 200 to 400 ml/min. Following these analyses, modifications were made to the geometry of the problem to enhance the heat sink's performance, involving the introduction of fins and cavities within the microchannel. To comprehensively assess the thermal and hydraulic performance of the microchannel, the performance evaluation criterion was calculated to identify the optimal case from both thermal and hydraulic perspectives. A detailed summary of the results will be presented in the subsequent analysis.

4. 1. Examination of the Results of Nanofluid Utilization:

- Initially, the results showed that using nanofluids increases heat transfer and improves thermal conditions, which is due to the increased heat transfer coefficient. The maximum heatsink temperature for the Al_2O_3 -water nanofluid at a flow rate of 200 ml/min and a 4% volume fraction decreased by 1.25% compared to water. This value

was 1.22% for TiO₂-water and 2.41% for Cu-water. According to the results, the Cu-water nanofluid has the highest increase in heat transfer and the lowest maximum temperature.

- Although using nanofluids can increase heat transfer, it also increases pressure drop and, consequently, increases pumping power. However, the increase in the heat transfer coefficient has a significant impact on reducing the maximum temperature, and it is better to bear the cost if needed to compensate for the pressure drop. The pressure drops for the Al₂O₃-water nanofluid at a flow rate of 200 ml/min and a 4% volume fraction increased by 13% compared to water. This value was 14% for TiO₂-water and 25% for Cu-water. Therefore, the pressure drop for the Cu-water nanofluid is higher than the other two nanofluids.
- The examination of the Nusselt number reveals an increase in heat transfer enhancement when using nanofluids. The Nusselt number shows an ascending trend with an increase in volume fraction and flow rate. The average Nusselt number for the Al₂O₃-water nanofluid at a flow rate of 200 ml/min and a volume fraction of 4% increased by 9% compared to water. For the TiO₂-water nanofluid, the increase was 8%, and for the Cu-water nanofluid, it was 16%. Therefore, the average Nusselt number for the Cu-water nanofluid is higher than the other two nanofluids.
- The analysis of the PEC number indicates that all three nanofluids increase the performance coefficient of the heatsink, and at a volume fraction of 4%, this increase is 5, 4, and 8 percent for Al₂O₃-water, TiO₂-water, and Cu-water, respectively. Considering the results, the Cu-water nanofluid has the best overall performance and can be the best option for improving the thermal-hydraulic performance in heat sinks.

4. 2. Examination of the Results of Geometric Changes:

- The microchannel with fins and cavities increases the fluid-solid contact area. This also affects the boundary layer, which breaks up and then forms again. Additionally, the use of fins within the microchannel enhances the velocity of flow. Due to these considerations, heat transfer in the new microchannels is superior to that of the original case, resulting in a lower maximum temperature of the heatsink. The maximum temperature reduction at the heat sink in the microchannel with fins, at a flow rate of 200 ml/min, is 3.5% compared to the initial configuration. For the microchannel with a cavity, this reduction is 1%.
- Although the microchannel with fin provides a more uniform temperature distribution, its pressure drop is

much higher than the other two geometries. The pumping power of the flow in the microchannel with fins at a flow rate of 200 ml/min increases by 400% compared to the initial state, while this value is 4% for the microchannel with cavities. Also, with an increasing flow rate, the rate of increase in pressure drop and pumping power of the microchannel with fins is higher.

- Considering the two parameters of heat transfer and pressure drop, the microchannel with cavities performs better, and the performance of the microchannel with fins is lower than the base microchannel. The overall system performance drops by 4% when using a microchannel with fins, and if a microchannel with cavities is used, the performance improves by 8%.

5. REFERENCES

1. Agostini B, Fabbri M, Park JE, Wojtan L, Thome JR, Michel B. State of the art of high heat flux cooling technologies. *Heat transfer engineering*. 2007;28(4):258-81. <https://doi.org/10.1080/01457630601117799>
2. Wang G, Qian N, Ding G. Heat transfer enhancement in microchannel heat sink with bidirectional rib. *International Journal of Heat and Mass Transfer*. 2019;136:597-609. <https://doi.org/10.1016/j.ijheatmasstransfer.2019.02.018>
3. Tuckerman DB, Pease RFW. High-performance heat sinking for VLSI. *IEEE Electron device letters*. 1981;2(5):126-9. <https://doi.org/10.1109/EDL.1981.25367>
4. Weisberg A, Bau HH, Zemel J. Analysis of microchannels for integrated cooling. *International Journal of Heat and Mass Transfer*. 1992;35(10):2465-74. [https://doi.org/10.1016/0017-9310\(92\)90089-B](https://doi.org/10.1016/0017-9310(92)90089-B)
5. Jeevan K, Quadir G, Seetharamu K, Azid I, Zainal Z. Optimization of thermal resistance of stacked micro-channel using genetic algorithms. *International Journal of Numerical Methods for Heat & Fluid Flow*. 2005;15(1):27-42. <https://doi.org/10.1108/09615530510571930>
6. Bejan A, Errera MR. Deterministic tree networks for fluid flow: geometry for minimal flow resistance between a volume and one point. *Fractals*. 1997;5(04):685-95. <https://doi.org/10.1142/S0218348X97000553>
7. Chen Y, Cheng P. Heat transfer and pressure drop in fractal tree-like microchannel nets. *International Journal of Heat and Mass Transfer*. 2002;45(13):2643-8. [https://doi.org/10.1016/S0017-9310\(02\)00013-3](https://doi.org/10.1016/S0017-9310(02)00013-3)
8. Pence D. Reduced pumping power and wall temperature in microchannel heat sinks with fractal-like branching channel networks. *Microscale Thermophysical Engineering*. 2003;6(4):319-30. <https://doi.org/10.1080/10893950290098359>
9. Xu S, Hu G, Qin J, Yang Y. A numerical study of fluid flow and heat transfer in different microchannel heat sinks for electronic chip cooling. *Journal of mechanical science and technology*. 2012;26:1257-63. <https://doi.org/10.1007/s12206-012-0209-x>
10. Zaretabar M, Asadian H, Ganji D. Numerical simulation of heat sink cooling in the mainboard chip of a computer with temperature dependent thermal conductivity. *Applied Thermal Engineering*. 2018;130:1450-9. <https://doi.org/10.1016/j.applthermaleng.2017.10.127>

11. Xu S, Wang W, Fang K, Wong C-N. Heat transfer performance of a fractal silicon microchannel heat sink subjected to pulsation flow. *International Journal of Heat and Mass Transfer*. 2015;81:33-40. <https://doi.org/10.1016/j.ijheatmasstransfer.2014.10.002>
12. Oyewola OM, Awonusi AA, Ismail OS. Performance improvement of air-cooled battery thermal management system using sink of different pin-fin shapes. *Emerging Science Journal*. 2022;6(4):851-65. <https://doi.org/10.28991/ESJ-2022-06-04-013>
13. Alrwashdeh SS, Ammari H, Madanat MA, Al-Falahat AaM. The effect of heat exchanger design on heat transfer rate and temperature distribution. *Emerging Science Journal*. 2022;6(1):128-37. <https://doi.org/10.28991/ESJ-2022-06-01-010>
14. Yan Y, Yan H, Yin S, Zhang L, Li L. Single/multi-objective optimizations on hydraulic and thermal management in micro-channel heat sink with bionic Y-shaped fractal network by genetic algorithm coupled with numerical simulation. *International Journal of Heat and Mass Transfer*. 2019;129:468-79. <https://doi.org/10.1016/j.ijheatmasstransfer.2018.09.120>
15. Choi SU, Eastman JA. Enhancing thermal conductivity of fluids with nanoparticles. Argonne National Lab.(ANL), Argonne, IL (United States); 1995. <https://www.osti.gov/biblio/19652>
16. Keblinski P, Phillpot S, Choi S, Eastman J. Mechanisms of heat flow in suspensions of nano-sized particles (nanofluids). *International journal of heat and mass transfer*. 2002;45(4):855-63. [https://doi.org/10.1016/S0017-9310\(01\)00175-2](https://doi.org/10.1016/S0017-9310(01)00175-2)
17. Abu-Nada E, Masoud Z, Hijazi A. Natural convection heat transfer enhancement in horizontal concentric annuli using nanofluids. *International Communications in Heat and Mass Transfer*. 2008;35(5):657-65. <https://doi.org/10.1016/j.icheatmasstransfer.2007.11.004>
18. Pasha P, Domiri-Ganji D. Hybrid analysis of micropolar ethylene-glycol nanofluid on stretching surface mounted triangular, rectangular and chamfer fins by FEM strategy and optimization with RSM method. *International Journal of Engineering*. 2022;35(5):845-54. <https://doi.org/10.5829/ije.2022.35.05b.01>
19. Ho C-J, Chen W. An experimental study on thermal performance of Al₂O₃/water nanofluid in a minichannel heat sink. *Applied Thermal Engineering*. 2013;50(1):516-22. <https://doi.org/10.1016/j.applthermaleng.2012.07.037>
20. Hatami M, Ganji D. Thermal and flow analysis of microchannel heat sink (MCHS) cooled by Cu–water nanofluid using porous media approach and least square method. *Energy Conversion and management*. 2014;78:347-58. <https://doi.org/10.1016/j.enconman.2013.10.063>
21. Jalili B, Rezaeian A, Jalili P, Omni F, Ganji DD. Numerical modeling of magnetic field impact on the thermal behavior of a microchannel heat sink. *Case Studies in Thermal Engineering*. 2023;45:102944. <https://doi.org/10.1016/j.csite.2023.102944>
22. Abdollahi S, Jalili P, Jalili B, Nourozpour H, Safari Y, Pasha P, et al. Computer simulation of Cu: AlOOH/water in a microchannel heat sink using a porous media technique and solved by numerical analysis AGM and FEM. *Theoretical and Applied Mechanics Letters*. 2023;13(3):100432. <https://doi.org/10.1016/j.taml.2023.100432>
23. Jalili P, Narimisa H, Jalili B, Ganji D. Micro-polar nanofluid in the presence of thermophoresis, hall currents, and Brownian motion in a rotating system. *Modern Physics Letters B*. 2023;37(01):2250197. <https://doi.org/10.1142/S0217984922501974>
24. Jalili P, Sadeghi Ghahare A, Jalili B, Domiri Ganji D. Analytical and numerical investigation of thermal distribution for hybrid nanofluid through an oblique artery with mild stenosis. *SN Applied Sciences*. 2023;5(4):95. <https://doi.org/10.1007/s42452-023-05312-z>
25. Jalili P, Azar AA, Jalili B, Ganji DD. Study of nonlinear radiative heat transfer with magnetic field for non-Newtonian Casson fluid flow in a porous medium. *Results in Physics*. 2023;48:106371. <https://doi.org/10.1016/j.rinp.2023.106371>
26. Jalili B, Roshani H, Jalili P, Jalili M, Pasha P, Ganji DD. The magnetohydrodynamic flow of viscous fluid and heat transfer examination between permeable disks by AGM and FEM. *Case Studies in Thermal Engineering*. 2023;45:102961. <https://doi.org/10.1016/j.csite.2023.102961>
27. Jalili P, D Afifi M, Jalili B, Mirzaei A, D Ganji D. Numerical Study and Comparison of Two-dimensional Ferrofluid Flow in Semi-porous Channel under Magnetic Field. *International Journal of Engineering, Transactions B: Applications*. 2023;36(11):2087-101. <https://doi.org/10.5829/ije.2023.36.11b.13>
28. Alibeigi M, Farahani S. Effect of porous medium positioning on heat transfer of micro-channel with jet. *International Journal of Engineering*. 2020;33(10):2057-64. <https://doi.org/10.5829/ije.2020.33.10a.24>
29. Vatani M, Domiri-Ganji D. Experimental examination of gas-liquid two-phase flow patterns in an inclined rectangular channel with 90 bend for various vertical lengths. *International Journal of Engineering*. 2022;35(4):685-91.
30. Ranjbar A, Ramiar A. The effect of viscous dissipation and variable properties on nanofluids flow in two dimensional microchannels. *International Journal of Engineering, Transactions A: Basics*. 2011;24(2):131-42. <https://doi.org/10.5829/ije.2022.35.04A.07>
31. Tayari E, Torkzadeh L, Domiri Ganji D, Nouri K. Analytical solution of electromagnetic force on nanofluid flow with brownian motion effects between parallel disks. *International Journal of Engineering, Transactions B: Applications*. 2022;35(8):1651-61. <https://doi.org/10.5829/ije.2022.35.08b.21>
32. Tarrad AH. 3d numerical modeling to evaluate the thermal performance of single and double u-tube ground-coupled heat pump. *HighTech and Innovation Journal*. 2022;3(2):115-29. <https://doi.org/10.28991/HIJ-2022-03-02-01>
33. Brinkman HC. The viscosity of concentrated suspensions and solutions. *The Journal of chemical physics*. 1952;20(4):571. <https://doi.org/10.1063/1.1700493>
34. Hamilton RL, Crosser O. Thermal conductivity of heterogeneous two-component systems. *Industrial & Engineering chemistry fundamentals*. 1962;1(3):187-91. <https://doi.org/10.1021/i160003a005>
35. Zamani M, Shafaghat R, Alizadeh Kharkeshi B. Numerical Study of the Hydrodynamic Behavior of an Archimedes Screw Turbine by Experimental Data in order to Optimize Turbine Performance: The Genetic Algorithm. *Journal of Applied and Computational Mechanics*. 2023. <https://doi.org/10.22055/jacm.2023.43137.4031>
36. Yan Y, Yan H, Feng S, Li L. Thermal-hydraulic performances and synergy effect between heat and flow distribution in a truncated doubled-layered heat sink with Y-shaped fractal network. *International Journal of Heat and Mass Transfer*. 2019;142:118337. <https://doi.org/10.1016/j.ijheatmasstransfer.2019.06.093>

COPYRIGHTS

©2024 The author(s). This is an open access article distributed under the terms of the Creative Commons Attribution (CC BY 4.0), which permits unrestricted use, distribution, and reproduction in any medium, as long as the original authors and source are cited. No permission is required from the authors or the publishers.

**Persian Abstract****چکیده**

استفاده از سینک حرارتی میکروکانال یکی از مطمئن‌ترین راه‌حل‌ها برای دفع گرمای تولید شده در تراشه‌های الکترونیکی است. در این مطالعه عددی یک سیک حرارتی میکروکانال فرکتالی مورد بررسی قرار گرفته و از سه نانوسیال آب-مس، آب-اکسید آلومینیوم و آب-اکسید تیتانیوم در کسر حجمی متغیر ۲ و ۴ درصد به عنوان سیال خنک کننده درون میکروکانال استفاده شده است. جریان سیال درون میکروکانال از جهت هیدرودینامیکی و حرارتی مورد بررسی قرار گرفت و پارامترهایی مانند توان پمپاژ، عدد ناسلت و ضریب ارزیابی عملکرد بدست آمد. با توجه به نتایج با افزایش دبی جریان و کسر حجمی نانوذرات انتقال حرارت افزایش پیدا می‌کند. نتایج نشان دادند که حداکثر دمای سینک حرارتی برای نانوسیال آب-مس در دبی ۲۰۰ میلی‌لیتر بر دقیقه و کسر حجمی ۴ درصد، نسبت به آب خالص ۲/۴۱ درصد کاهش داشته‌است که بیشترین مقدار بین نانوسیال‌های دیگر است. ولی از طرف دیگر بیشترین مقدار افت فشار نیز متعلق به نانوسیال آب-مس با مقدار ۲۵ درصد در کسر حجمی ۴ درصد است. با بررسی عدد ضریب ارزیابی عملکرد، مشخص شد که عملکرد هر سه میکروکانال افزایش پیدا می‌کند و نانوسیال آب-مس بهترین عملکرد جامع را دارد که عملکرد کلی را ۸ درصد افزایش می‌دهد و بعد از نانوسیال‌های آب-اکسید آلومینیوم و آب-اکسید تیتانیوم قرار دارند که به ترتیب ۵ و ۴ درصد عملکرد سیستم را افزایش می‌دهند. در ادامه برای بهبود عملکرد میکروکانال با هدف افزایش انتقال حرارت و عملکرد کلی سینک حرارتی، فین و حفره‌هایی در سه شاخه اولیه میکروکانال ایجاد شده است. نتایج نشان از افزایش انتقال حرارت برای هر دو هندسه جدید را دارد. حداکثر دمای سینک حرارتی برای میکروکانال با دنده در دبی ۲۰۰ میلی‌لیتر بر دقیقه، نسبت به هندسه اولیه ۳/۵ درصد کاهش داشته‌است که این مقدار برای میکروکانال با حفره ۱ درصد است. با این حال، افت فشار برای میکروکانال با دنده ۴۰۰ درصد بیشتر از هندسه اولیه است که این مقدار برای میکروکانال با حفره ۴ درصد می‌باشد. بررسی عدد ضریب ارزیابی عملکرد نشان داد که استفاده از میکروکانال با حفره عملکرد سیستم را ۸ درصد بهبود می‌بخشد و میکروکانال با دنده عملکرد سیستم را ۴ درصد کاهش می‌دهد.



Risk-Based AC/DC Hybrid Distribution System Planning

Z. Esmaeilzadeh, H. Falaghi*, M. Ramezani

Faculty of Electrical and Computer Engineering, University of Birjand, Birjand, Iran

PAPER INFO

Paper history:

Received 02 September 2023

Received in revised form 14 November 2023

Accepted 12 December 2023

Keywords:

AC/DC Hybrid Distribution System

Distribution Generations

Load Demands

MATLAB/GAMS Hybrid

K-means

Planning

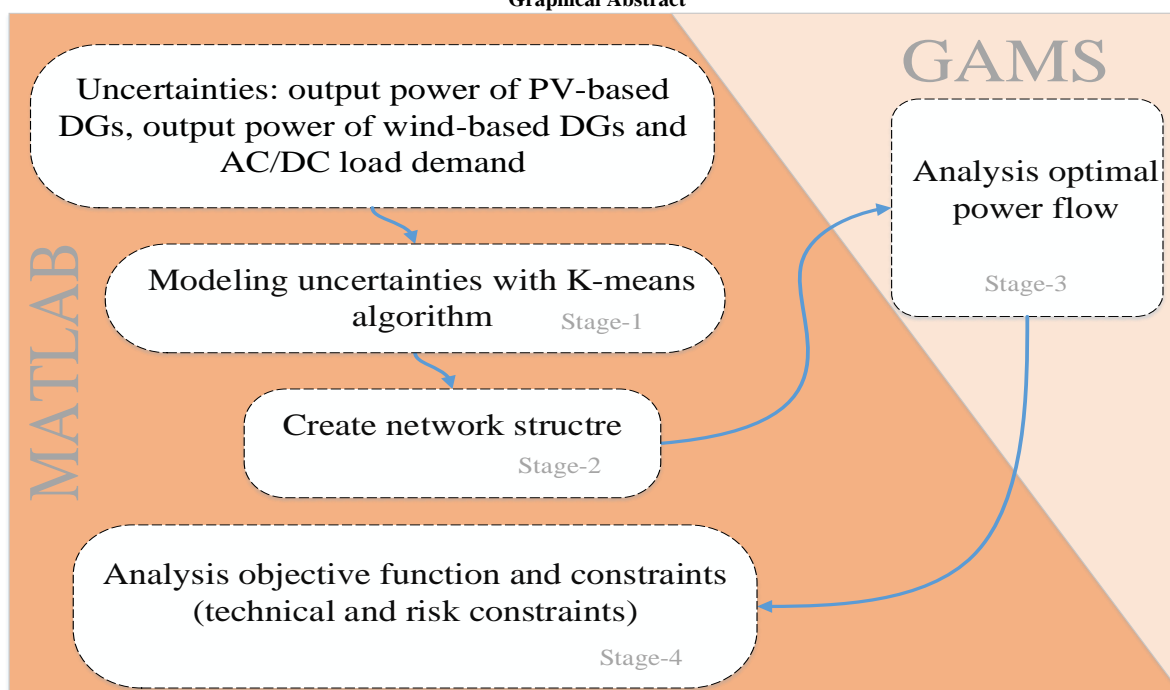
Risk-based

ABSTRACT

With the growing movement of using direct current (DC) load demands, as well as DC distribution generations (DGs), the distribution system has undergone significant changes on the production and demand side. Due to alternating current (AC) and DC generators and load demands, it is not cost-effective to continue in the AC distribution system. Therefore, AC/DC hybrid distribution system planning is economical despite various demands and generations. On the other hand, uncertainty in load demand and output power of DGs cause the possible behavior of the distribution system. This behavior leads to risk in the distribution system. In this paper, the AC/DC distribution system planning is discussed by considering the risk. The planning problem in the matrix laboratory and general algebraic modeling system (MATLAB/GAMS) hybrid space has been formulated and solved. Using the K-means algorithm, the uncertainty related to renewable DG output power and load demand has been modeled. To verify the proposed method, it was implemented in a sample distribution system.

doi: 10.5829/ije.2024.37.05b.06

Graphical Abstract



* Corresponding Author Email: falaghi@birjand.ac.ir (H. Falaghi)

NOMENCLATURE

Acronyms		Parameters	
AC	Alternating current	r_d	Discount rate, %
DC	Direct current	X_{mn}, X_{mx}	Minimum and maximum limit of the variable X
DG	Distributed generation	N_{con}	Number of lines that can be connected to each bus
DSS	Distribution substation	C_{G_g}	Energy cost of generator g, \$/MWh
DNLP	Nonlinear programming problem with discontinuous derivatives	K	Total number of clusters
EV	Electric vehicle	N	Number of network buses
GAMS	General algebraic modeling system	Pr	Probability of scenario, %
LV	Low voltage	Variables	
MATLAB	Matrix laboratory	$V_{i,\omega}, \theta_{i,\omega}$	Voltage magnitude and phase angle at bus i for scenario ω
MCS	Monte Carlo simulation	$Pinj_{i,\omega}, Qinj_{i,\omega}$	Active and reactive power injections at bus i for scenario ω
MV	Medium voltage	$Pcal_{i,\omega}, Qcal_{i,\omega}$	Active and reactive power calculated at bus i for scenario ω
OPF	Optimal power flow	$Ptr_{i,j,\omega}, Qtr_{i,j,\omega}, Str_{i,j,\omega}$	Active, reactive and apparent power transmitted from bus i to bus j for scenario ω
PV	Photovoltaic	$P_{nv,\omega}, Q_{nv,\omega}, S_{nv,\omega}$	the active, reactive and apparent power of the VSC
PEM	Point estimate method	$MO_{i,j,\omega}$	Modulation index of the VSC connected between bus i and bus j for scenario ω
SSE	The sum of the squared error	$P_{G_g,\omega}, Q_{G_g,\omega}$	Active and reactive power of generator g for scenario ω
VSC	Voltage source converter	OC_t	Cost of network operation at year t
IGDT	Information gap decision theory	LC	Cost of network lines
Sets		$VSCC$	Cost of converters
Ω_B	Set of all buses	$INVC$	Investment cost
$\Omega_B^{DC}, \Omega_B^{AC}$	Set of the total of DC and AC buses respectively	MOC	Cost of maintenance and operation of the system
Ω_{vsc}	Set of AC/DC converters in the system	MC	Cost of maintenance
Ω_G	Set of all generators in the system	TC	Total cost of the system
$\Omega_G^{AC}, \Omega_G^{DC}$	Set of AC and DC generators	OPC	Cost of system operation
Ω_s	Set of all scenarios	M	Matrix of connection between buses
T	Planning horizon	Q	Line-type matrix connected between buses
Indices		A	Bus type vector
i, j	Index of buses	n_s^{fs}	The numbers of feasible solutions from the evaluation of system OPF
ω	Index of scenarios	n_s	The total number of solutions
g	Index of generators	N_{G_k}	Number of samples in the cluster k
nv	Index of converters	μ_k	Center of cluster k
t	Index of years		

1. INTRODUCTION

In the distribution system, due to the ever-increasing progress in the field of exploiting renewable energy sources and the multiplicity of DC-type loads, this system has undergone significant transformations and changes. On the other hand, the traditional distribution system is the AC system. Therefore, the distribution system includes additional DC DGs and load demands along with AC loads and generators. With all types of loads and DGs, the implementation of an AC/DC distribution system is an attractive solution for planners. In AC/DC system, load forecasting and power generation

of renewable sources such as solar and wind is always associated with uncertainty. Thus, the distribution system has faced risk (1-6).

An overview of the studies carried out in hybrid distribution system planning is given below. A new model for AC/DC distribution network planning is presented in literature (7-10). In this model, the type of lines, buses, and network structure are determined. In the AC/DC system planning, it is focused on determining the location and capacity of DGs (11-15) and electric vehicles (EVs) (12, 14). A novel two-stage stochastic planning model is proposed by Sabzian Molaei et al. (13). In this paper, the lifetime of the voltage source

converter (VSC) is modeled, and it is included in the hybrid planning problem. The AC/DC microgrid planning is discussed in literature (16-21). The decision variables of the problem are the capacity of DGs (19, 21), and the type of feeders (AC or DC) (16-18, 20). A bi-level planning model for the AC/DC distribution system considering N-1 events is presented by Wu et al. (22). The high-level model optimizes the total investment and operating costs in the AC and DC system over the entire planning horizon. In the low-level model, the goal is to improve the reliability of the DC system under the worst case of N-1. Yu et al. (23) introduced and discussed advantages of the DC system. At the end, they added the DC system to the usual AC system and explained the advantages of the hybrid system. Number of investigators (24-26) dealt with the planning and expansion of the AC/DC distribution system. In general, there are several methods for modeling uncertainties in problems, including interval optimization, robust optimization, stochastic optimization, possibility method, hybrid optimization method, and information gap decision theory (IGDT) (27). However, in the studies conducted in the field of AC/DC planning, the Monte Carlo simulation (MCS) technique (7-9, 12, 13), robust optimization (18), and scenario approach (24, 25) have been used to model the random behavior of load demand and power generation of DGs in the problem.

Among the advantages of the conducted studies, we can mention the implementation of AC/DC distribution system planning. Traditionally, the distribution system is planned as AC. However, due to the large number of DC load demands and DC DGs, the need for a converter to convert power in the traditional system will increase. Therefore, the AC/DC distribution system is one of the solutions in the presence of multiple DC loads and DGs. On the other hand, in several studies conducted in the field of AC/DC planning, the uncertainties in the problem have been modeled. However, one of the disadvantages of studies in this field is not considering the risk. Because the distribution system inherently has probabilistic behavior. This possible behavior leads to risk in the problem. Therefore, it is necessary to model the risk governing the AC/DC distribution system planning problem.

So far, the AC/DC hybrid distribution system has been studied from different perspectives. However, none of the studies conducted were considered risk in the AC/DC hybrid distribution system planning. Risk-based AC/DC distribution system planning is discussed in this paper. Considering the uncertainties in load demand and output power of DGs, the possible evaluation of the system has been done. The K-means algorithm has been used to model the uncertainties of the problem. The planning goal is to minimize the investment and operation costs under the risk of uncertainties. The proposed mathematical model has been solved in the

MATLAB/GAMS hybrid space. The effectiveness of the proposed model is demonstrated by applying it to a distribution test system under different risk levels.

2. AC/DC HYBRID DISTRIBUTION SYSTEM PLANNING MODEL

In the AC/DC distribution system planning problem, full knowledge of consumption information leads to reliable planning. On the other hand, due to the different conditions governing the amount of consumption, registration, and collection of cargo information, this information is always associated with uncertainty. Another problem is the existence of renewable sources, such as wind and solar energy, in AC/DC distribution system planning. These resources depend highly on natural factors such as wind speed and solar radiation. For this reason, the output power of these sources is associated with uncertainty. Therefore, the AC/DC distribution system planning problem includes some parameters with possible behavior. The uncertainty related to renewable DG output power and the load variability is the leading cause of this behavior. It is necessary to explain that the possible behavior of these parameters causes risk. Obviously, the greater the uncertainty in the system information, the greater the deviation from the actual values (28, 29).

In this paper, AC/DC distribution system planning is discussed by considering the risk caused by the uncertainty in AC and DC load demands and the output power of renewable sources such as wind and photovoltaic (PV). Figure 1 shows the schematic view of the risk-based planning problem.

2. 1. Modeling of Uncertainties

Among the uncertainty modeling methods, MCS and point estimate method (PEM) have been used in many problems. In the MCS method, the results are highly accurate, but the calculations are time-consuming. In the PEM method, for

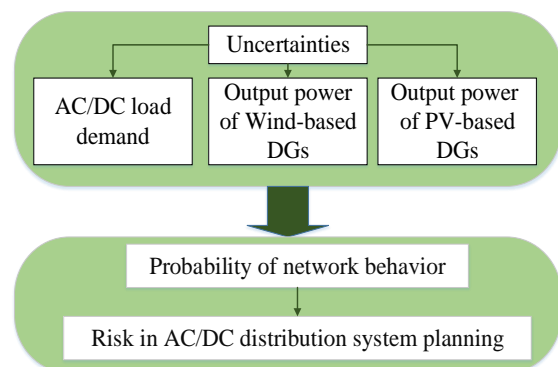


Figure 1. Schematic view of risk-based hybrid distribution system planning

large-scale problems, the volume of calculations is heavy, which is not practical. Recently, clustering methods have been given attention in non-deterministic problems. Among these methods, the K-means algorithm is popular. The reasons for this popularity include very high execution speed, the simplicity of the algorithm, and the ability to use this algorithm for large amounts of data. This algorithm is an iterative algorithm that divides the data set into K distinct non-overlapping clusters according to their characteristics (27, 30). The implementation process of this algorithm is described in the following.

In AC/DC hybrid distribution system planning, the stochastic nature of renewable sources, load demand, and EV demand are considered. The algorithm of K-means is utilized to cluster the uncertainties in the problem. The purpose of this algorithm is to find the center of clusters so that the data distance of each cluster to the center of that cluster is minimized. The process of implementing the K-means algorithm is as follows (31):

- Step 1, determine the number of clusters (K)
- Step 2, select K samples as the cluster center coordinates
- Step 3, assign all samples to the nearest cluster center
- Step 4, calculate the center of the clusters as follows (d_s represents the data s):

$$\mu_k = \frac{1}{N_{G_k}} \sum_{s \in G_k} d_s \quad (1)$$

Step 5, calculate the sum of the squared error (SSE) function in the form of Equation 2:

$$SSE = \sum_{k \in K} \sum_{s \in G_k} \|d_s - \mu_k\|^2 \quad (2)$$

Step 6, repeat steps 3 to 5 until the stopping criteria of the algorithm are not met. The criteria for stopping in this algorithm are no change in the members of each cluster, no change in the center of each cluster, or minimum SSE.

Therefore, in the output of the K-means algorithm, the center of the clusters of all uncertain parameters is obtained.

2. 2. Network Structure Formation

The structure of the AC/DC network consists of a combination of AC and DC distribution systems along with converters. The equipment of these systems is AC and DC loads, AC and DC energy sources, and a voltage source converter (VSC). VSC is used to convert AC to DC power or vice versa. Figure 2 shows the types of buses in the AC/DC distribution system (2, 32, 33).

Therefore, in the problem of AC/DC distribution system planning, the system structure consists of 3 parts. In the first part, the connection between the buses (M) is obtained by the N×N binary matrix. So, if there is a connection between the buses, it is equal to one;

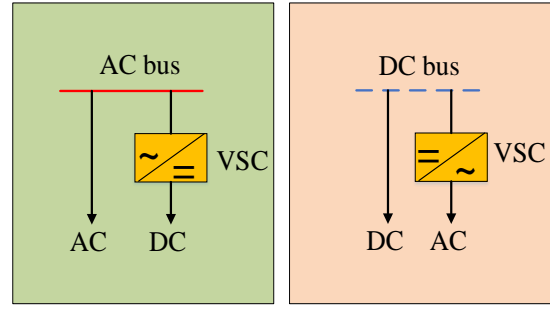


Figure 2. Types of buses in AC/DC hybrid network

otherwise, it is zero. In the second part, the type of connection between the buses (Q) is also determined by the N×N binary matrix. If the communication line between bus i and bus j is of DC type, then Q(i,j) is one; otherwise, it is zero. The third part also consists of the binary vector of system bus type (A). If bus i is DC, then A(i) is one; otherwise, zero.

3. PROBLEM FORMULATION

The planning problem is formulated as a stochastic optimization problem with the following objective function and constraints.

3. 1. Objective Function

The objective is to minimize the investment and operation costs as follows:

$$\min(TC) = INVC + MOC \quad (3)$$

$$INVC = LC + VSCC \quad (4)$$

$$MOC = \sum_{t \in T} \frac{MC + OC_t}{(1+r_d)^t} \quad (5)$$

$$OC_t = 8760 \sum_{\omega \in \Omega_s} OPC_{t,\omega} \times pr_{\omega} \quad (6)$$

In AC/DC hybrid planning, optimal power flow (OPF) is employed to determine the operating cost of the system structure. The problem of OPF is modeled in GAMS as a nonlinear programming problem with discontinuous derivatives (DNLP). CONOPT is one of the nonlinear solvers which has been used to solve the OPF problem. The goal of OPF is to minimize the cost of energy generation as follows:

$$\min(OPC) = \sum_{g \in \Omega_G} C_{G_g} \times P_{G_g} \quad (7)$$

3. 2. Constraints

The constraints are categorized into two groups: 1) technical constraints and 2) risk constraint.

3. 2. 1. Technical Constraints The technical constraints include the equations of active and reactive power balance, voltage constraints, thermal constraints of the equipment capacity, energy generation constraints, and network structure constraints. Constraints 8-16 are considered the constraints of the OPF problem. Constraints 17-19 indicate the binary variables of the structure matrices. In order to avoid congestion and isolation of each bus, communication is limited to Constraints 20 and 21 (7).

$$P_{inj_{i,\omega}} = P_{cal_{i,\omega}}, \forall i \in \Omega_B, \omega \in \Omega_S \quad (8)$$

$$Q_{inj_{i,\omega}} = Q_{cal_{i,\omega}}, \forall i \in \Omega_B, \omega \in \Omega_S \quad (9)$$

$$V_{mn} \leq V_{i,\omega} \leq V_{mx}, \forall i \in \Omega_B, \omega \in \Omega_S \quad (10)$$

$$\theta_{mn} \leq \theta_{i,\omega} \leq \theta_{mx}, \forall i \in \Omega_B, \omega \in \Omega_S \quad (11)$$

$$\sqrt{Ptr_{i,j,\omega}^2 + Qtr_{i,j,\omega}^2} \leq Str_{mx}, \forall i, j \in \Omega_B, \omega \in \Omega_S \quad (12)$$

$$Mo_{mn} \leq Mo_{i,j,\omega} \leq Mo_{mx}, \forall i, j \in \Omega_B, \omega \in \Omega_S \quad (13)$$

$$\sqrt{P_{nv,\omega}^2 + Q_{nv,\omega}^2} \leq S_{mx}, \forall nv \in \Omega_{vsc}, \omega \in \Omega_S \quad (14)$$

$$P_{G_{g,mn}} \leq P_{G_{g,\omega}} \leq P_{G_{g,mx}}, \forall g \in \Omega_G, \omega \in \Omega_S \quad (15)$$

$$Q_{G_{g,mn}} \leq Q_{G_{g,\omega}} \leq Q_{G_{g,mx}}, \forall g \in \Omega_G, \omega \in \Omega_S \quad (16)$$

$$A(i) \in \{0,1\} \quad \forall i \in \Omega_B \quad (17)$$

$$M(i, j) \in \{0,1\} \quad \forall i, j \in \Omega_B \quad (18)$$

$$Q(i, j) \in \{0,1\} \quad \forall i, j \in \Omega_B \quad (19)$$

$$\sum_{j \in \Omega_B} M(i, j) \geq Ncon_{mn}, 1 \leq Ncon_{mn} \leq Ncon_{mx}, \quad (20)$$

$$, \forall i \in \Omega_B$$

$$\sum_{j \in \Omega_B} M(i, j) \leq Ncon_{mx}, Ncon_{mn} \leq Ncon_{mx} \leq N-1 \quad (21)$$

$$, \forall i \in \Omega_B$$

3. 2. 2. Risk Constraint In general, the behavior of the distribution system is inherently probabilistic. This possible behavior is related to the uncertainties in the load demand and the output power of renewable energy sources. On the other hand, this behavior is the main source of risk in the distribution network. In this paper, risk is considered as one of the

constraints of the problem, and it is calculated based on the following steps:

Step 1, modeling random parameters in the planning problem using the K-means algorithm.

Step 2, generation of scenarios (combines the center of clusters of random parameters of the set of scenarios).

Step 3, run OPF for each scenario.

Step 4, repeat step 3 for all scenarios.

Step 5, calculates the percentage of system risk (based on the ratio of the total number of feasible solutions of OPF to the total number of solutions). The mathematical model of risk is defined by (an infeasible OPF solution due to the violation of one or more of the constraints):

$$Risk = 1 - \frac{n_s^{fs}}{n_s} \quad (22)$$

In this paper, a genetic algorithm (GA) is used to solve the optimization problem. In the AC/DC hybrid distribution system planning, the connection of lines between buses, the type of connection, and the type of buses (the type means AC or DC) are the decision variables of the problem. Each chromosome, which is a member of a population, shows a network structure. The structure of the proposed chromosome contains several substrings, as shown in Figure 3. The first part of the chromosome, which consists of two substrings, has the Nc gene. The first substring (M) represents the connection between buses. The value of zero and one in the genes of this substring M(i,j) indicates the lack of connection and connection between the buses i and j, respectively. The second substring (Q) indicates the type of communication between the buses, So the value of zero and one in the gene Q(i,j) represents the type of AC and DC line between buses i and j, respectively. The second part of a chromosome (A) has the number of N genes that indicate the type of network buses. The values of zero and one in these genes represent AC and DC buses, respectively.

4. TEST SYSTEM AND SIMULATION RESULTS

The proposed model and method for the planning problem of the AC/DC distribution system have been tested on a sample distribution system of 13 buses, as shown in Figure 4. In this system, there is a variety of AC

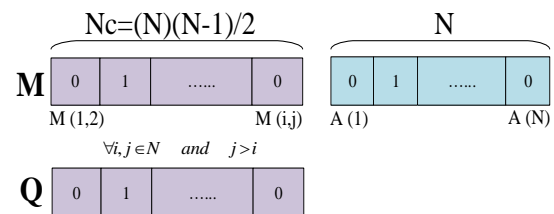


Figure 3. Proposed chromosome structure

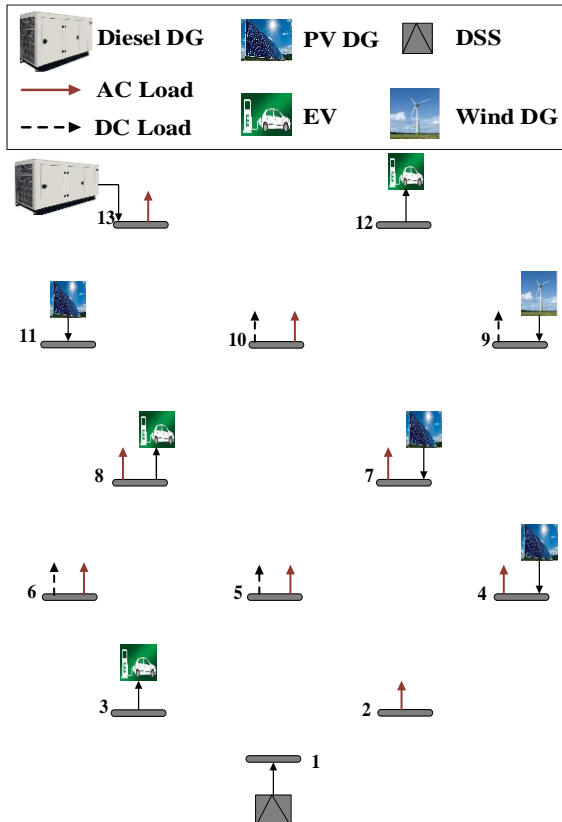


Figure 4. The studied system

and DC-type loads and sources. The distribution substation (DSS) is connected to bus 1. All input information required in this system is extracted from literature (7). The proposed planning method was implemented in the MATLAB/GAMS hybrid environment. By performing numerous experiments in this numerical study, the population, number of generations, probability of crossover, and mutation operator were set to 300, 150, 0.9, and 0.125, respectively. It should be noted that in this paper, the number of clusters for all random parameters in the system is 3 clusters. In the following, the AC and AC/DC distribution system planning under 4 cases have been discussed.

4. 1. Case 1: Distribution System Planning and Comparison

In this case, the AC and AC/DC system planning problem has been addressed without considering the risk constraint. The purpose of implementing this case is to show the validity of the proposed method. By implementing this case, the optimal structure of AC and AC/DC distribution system planning has been achieved, similar to the optimal structure of the AC and AC/DC distribution system (7). Also, the results were compared with the reported data in literature and also presented in Table 1. Therefore, the sameness of the

optimal structure of the AC and AC/DC distribution system, as well as the comparison of the cost results of this case with the mentioned reference, shows the correctness of the optimization method.

In Tables 1 and 2, a and b show AC and AC/DC distribution system planning, respectively.

4. 2. Case 2: Distribution System Planning under Risk Less than 20%

In this case, the distribution system planning has been done considering the risk of less than 20%. From the implementation of this case, the optimal planning structure of the AC and AC/DC distribution system has been obtained according to Figures 5 and 6, respectively. The results of planning costs under a risk of less than 20% are given in Table 2. In AC system planning, all buses and lines are of AC type. Therefore, in this planning, only the system structure is the decision variable of the optimization algorithm. However, in AC/DC system planning, the type of lines and buses, as well as the system structure is determined by the optimization algorithm. In AC planning, because all lines and buses are of AC type, more converters are needed in this planning. This increase in the number of converters leads to increase in investment costs and total planning costs. The results in Table 2 under the risk of less than 20% show that the lowest planning costs are related to AC/DC network planning. According to the studied network, buses 11 and 12 are composed of PV and EV, respectively. In the optimal AC network planning (Figure 5), a converter is

TABLE 1. The results of costs in the distribution system from the implementation of case 1

Type	Case	LC M\$	VSCC M\$	INVC M\$	TC M\$
a	Case 1	1.7136	2.0485	3.7621	47.3564
	[7]	1.7136	2.0485	3.7621	47.3567
b	Case 1	1.2264	1.7595	2.9859	45.6586
	[7]	1.2264	1.7595	2.9859	45.6596

TABLE 2. Cost of different distribution systems under different conditions

Case	Type	LC M\$	VSCC M\$	INVC M\$	TC M\$
Case 2	a	1.5120	2.0485	3.5605	44.7625
	b	1.2152	1.5725	2.7877	39.4667
Case 3	a	1.6128	2.0485	3.6613	45.1517
	b	1.2152	1.5725	2.7933	42.4984
Case 4	a	1.6464	2.0485	3.6949	46.6823
	b	1.2208	1.6575	2.8783	45.1494

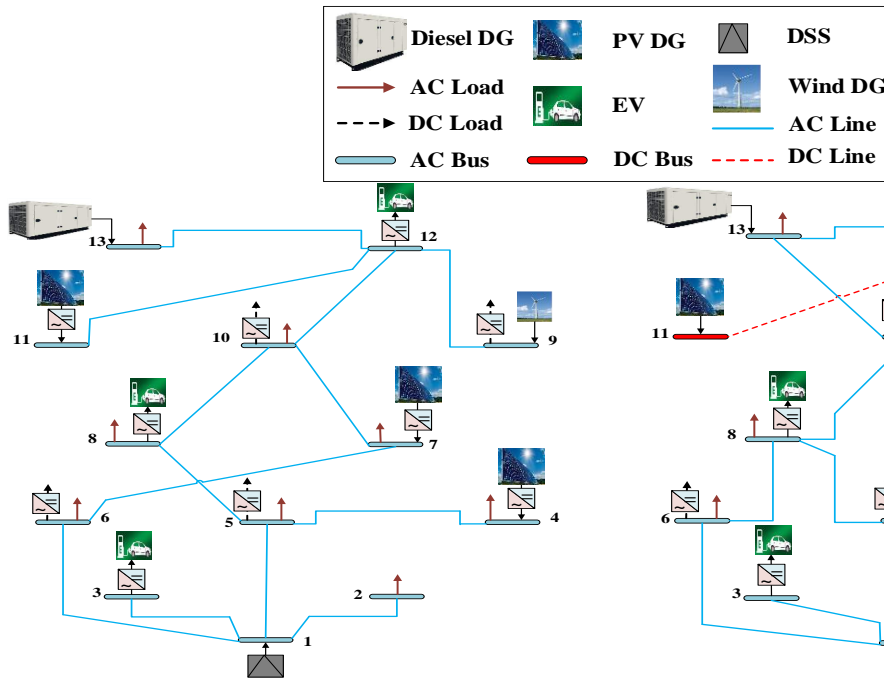


Figure 5. The optimal structure of AC distribution system under case 2

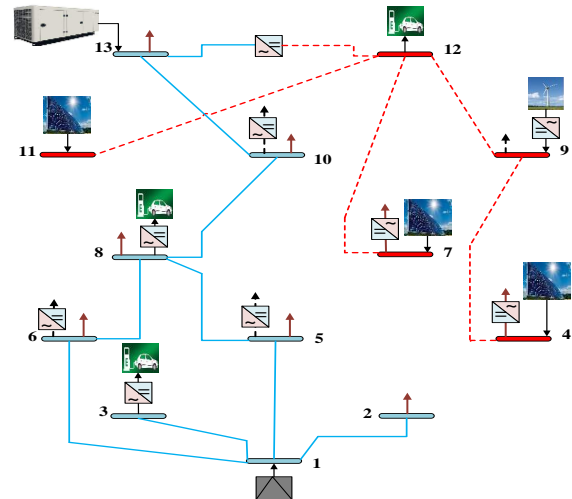


Figure 6. The optimal structure of AC/DC distribution system under case 2

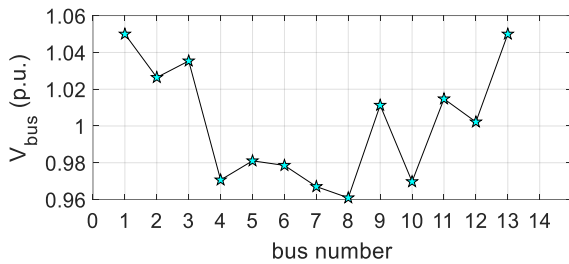


Figure 7. Bus voltage profile for AC distribution system under case 2

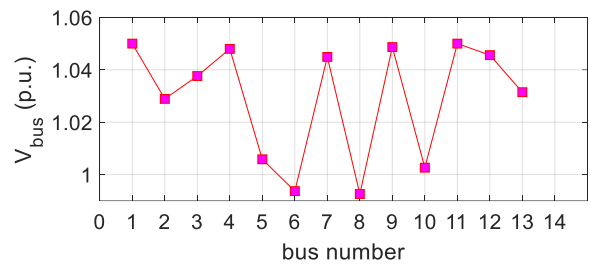


Figure 8. Bus voltage profile for AC/DC distribution system under case 2

4. 3. Case 3: Distribution System Planning under Risk Less than 10%

In this case, the goal is to find the AC and AC/DC distribution system planning where the risk is less than 10%. The results of planning costs from the implementation of this case are given in Table 2. The optimal planning structure of AC and AC/DC distribution system is also shown in Figures 9 and 10, respectively. Also, the bus voltage profile for AC and AC/DC system planning is shown in Figures 11 and 12, respectively. According to the results of this case, AC/DC distribution system planning has lower costs than AC system planning. Therefore, by planning the AC/DC distribution system, it is possible to achieve an optimal structure with minimum planning costs. Also, according to the results of this case, with the reduction of risk, all planning costs have increased compared to the results of the previous case.

4. 4. Case 4: Distribution System Planning under Zero Risk

In this case, the problem of distribution system planning has been discussed, considering the condition of zero risk. Therefore, in AC system planning, the goal is to find an optimal structure in which risk does not occur. Also, in AC/DC planning, the goal is to find the type of buses and lines as well as the system structure so that the risk of the problem is zero. The results of this case are presented in Table 2. The optimal structure and bus voltage profile for AC and AC/DC system planning under zero risk are shown in Figures 13 to 16. According to the results of Table 2, when the planning problem is implemented under zero risk, the costs of AC and AC/DC system planning have increased compared to the previous two cases. Therefore, reducing the risk of the problem leads to an increase in planning costs. The results of this case are similar to the results of cases 2 and 3, indicating

that AC/DC system planning has lower planning costs than AC system planning. In AC/DC planning, the type of buses and lines and the system structure are determined by the optimization algorithm with the aim of

the lowest planning costs. However, in AC planning, the algorithm only determines the system structure and the type of buses and lines that are fixed AC.

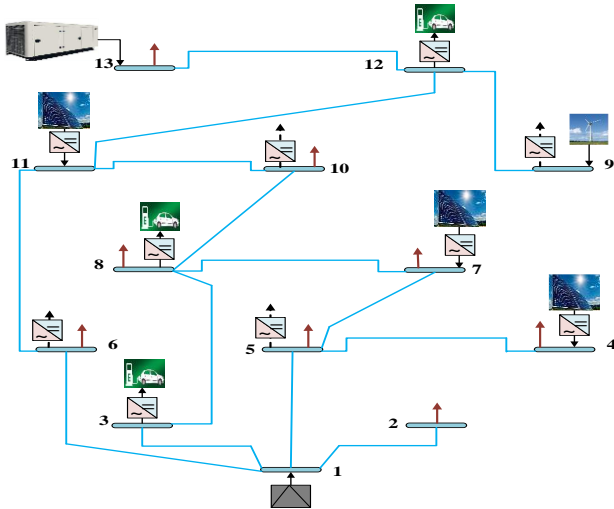


Figure 9. The optimal structure of AC distribution system under case 3

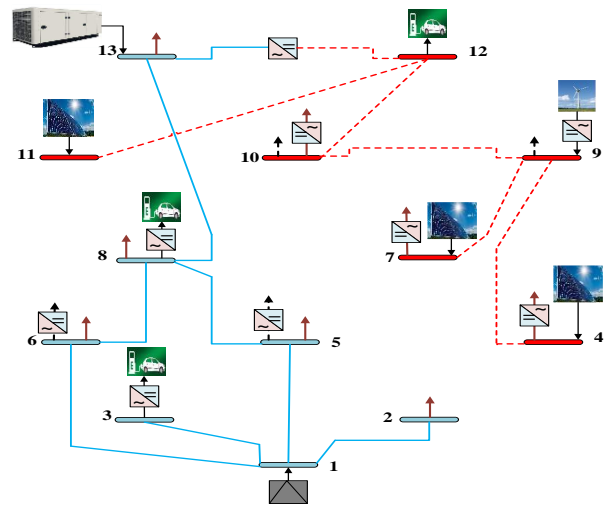


Figure 10. The optimal structure of AC/DC distribution system under case 3

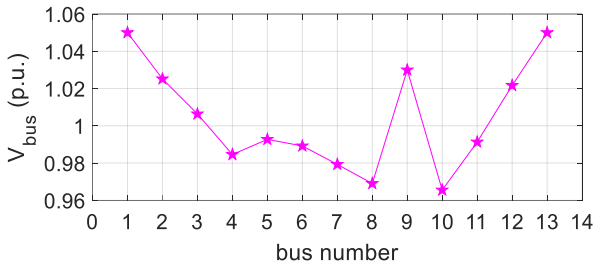


Figure 11. Bus voltage profile for AC distribution system under case 3

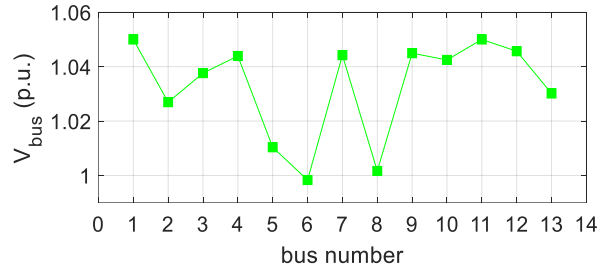


Figure 12. Bus voltage profile for AC/DC distribution system under case 3

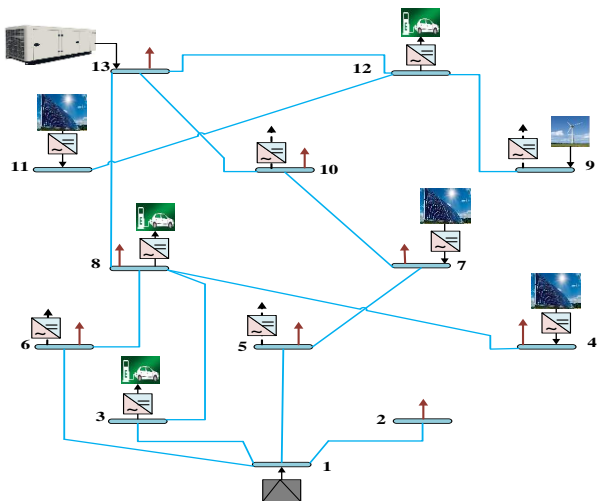


Figure 13. The optimal structure of AC distribution system under case 4

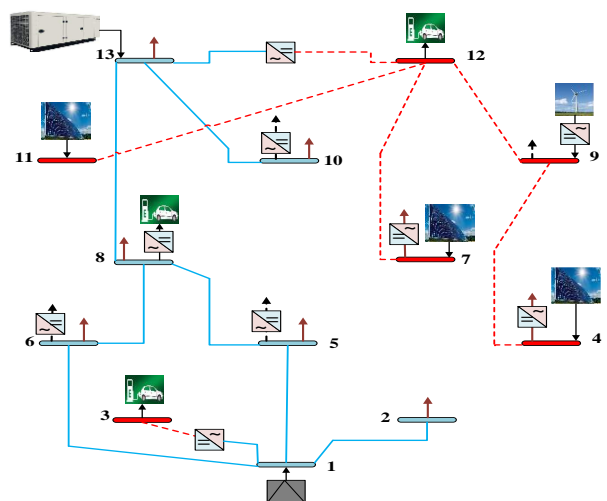


Figure 14. The optimal structure of AC/DC distribution system under case 4

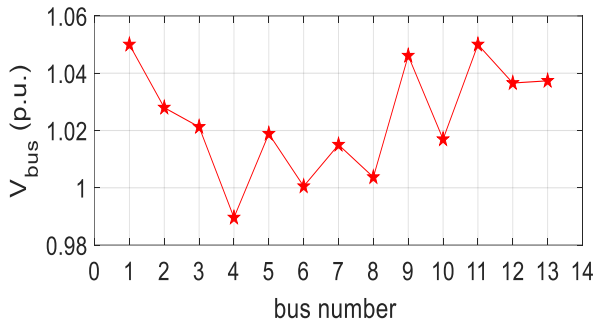


Figure 15. Bus voltage profile for AC distribution system under case 4

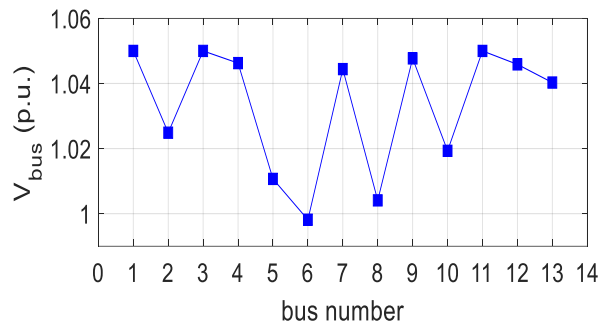


Figure 16. Bus voltage profile for AC/DC distribution system under case 4

In this paper, the planning problem is implemented under 4 cases that include planning without considering risk, considering risk less than 20%, less than 10%, and zero risk. In the first case, the planning results are compared with the mentioned reference results, and the correctness of the proposed method has been demonstrated. In cases 2 to 4, the planning problem has been implemented by reducing risk value. As shown in Figures 17 to 19, planning costs have increased with the reduction of risk. On the other hand, in all implemented cases, the minimum cost is related to AC/DC system planning. Therefore, optimal planning can be achieved by AC/DC planning under different risk levels.

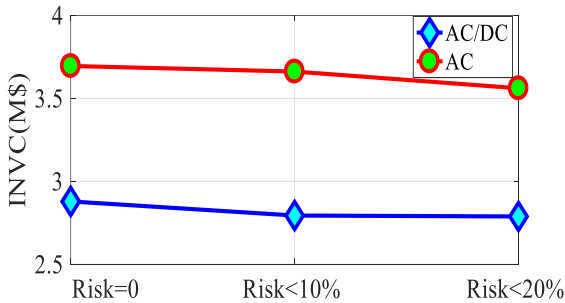


Figure 17. Planning results of investment costs under different risk levels

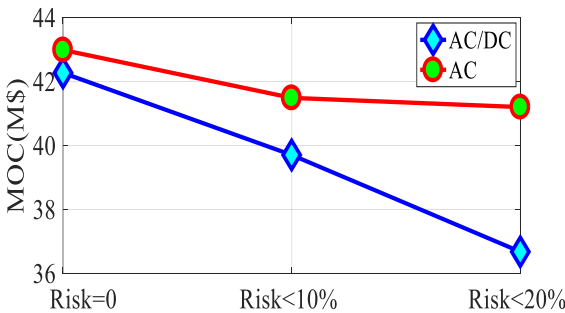


Figure 18. Planning results of maintenance and operation costs under different risk levels

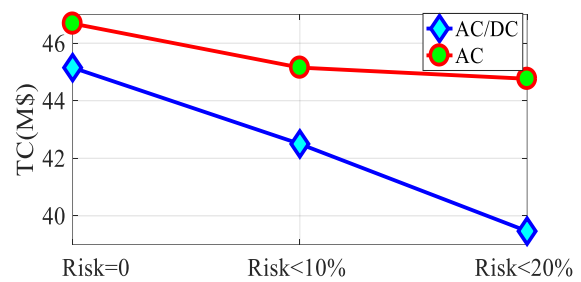


Figure 19. Planning results of total costs under different risk levels

TABLE 3. Values of random variables for a scenario

Type	a	b
Load Demand	54.14 %	48.57 %
EV Demand	44.08 %	37.53 %
Wind-DG Power	84.73 %	84.69 %
PV-DG Power	14.79 %	13.41 %

5. CONCLUSION

Today, in traditional distribution systems (of AC type), the multiplicity of loads and energy sources of DC type has made it uneconomical to continue in this system. Therefore, a solution can be to switch to an AC/DC distribution system due to the presence of various loads and energy sources. In this paper, the AC/DC distribution system planning is discussed. On the other hand, the uncertainties related to the forecasting of load demand and renewable DG output power cause the possible behavior of the distribution system. This behavior leads to risk in the distribution system. The K-means clustering method has been used to model the uncertainties in the problem. The goal of the problem is to minimize the investment and operation costs of the plan under possible risks to the network. The proposed mathematical model has been solved in the MATLAB/GAMS hybrid space. The effectiveness of the proposed model is demonstrated

by applying it to a distribution test system. In this paper, the planning problem has been tested under 4 cases. In the first case, the goal is the correctness of the proposed method. In cases 2 to 4, planning has been done by reducing the value of risk. According to the results obtained from these cases, it can be concluded that reducing the value of risk leads to an increase in planning costs. The results of AC/DC system planning show that due to AC and DC buses and lines in this system, optimal planning can be achieved with the goal of minimum planning costs. The results of numerical studies show that changes in the value of risk impact the planning problem.

6. REFERENCES

- Shahnia F, Arefi A, Ledwich G. Electric distribution network planning: Springer; 2018.
- Zhang L, Liang J, Tang W, Li G, Cai Y, Sheng W. Converting AC distribution lines to DC to increase transfer capacities and DG penetration. *IEEE Transactions on Smart Grid*. 2018;10(2):1477-87. <https://doi.org/10.1109/TSG.2017.2768392>
- Liu X, Liu Y, Liu J, Xiang Y, Yuan X. Optimal planning of AC-DC hybrid transmission and distributed energy resource system: Review and prospects. *CSEE Journal of Power and Energy Systems*. 2019;5(3):409-22. <https://doi.org/10.17775/CSEEJPES.2019.00540>
- Wang L, Yuan M, Zhang F, Wang X, Dai L, Zhao F. Risk assessment of distribution networks integrating large-scale distributed photovoltaics. *IEEE Access*. 2019;7:59653-64. <https://doi.org/10.1109/ACCESS.2019.2912804>
- Bhuiyan MZA, Anders GJ, Philhower J, Du S. Review of static risk-based security assessment in power system. *IET Cyber-Physical Systems: Theory & Applications*. 2019;4(3):233-9. <https://doi.org/10.1049/iet-cps.2018.5080>
- Wawrzyniak K, Urresti Padrón E, Gomulski K, Korab R, Jaworski W. Methodology of risk assessment and decomposition in power grid applications. *IET Generation, Transmission & Distribution*. 2018;12(15):3666-72. <https://doi.org/10.1049/iet-gtd.2017.1731>
- Ahmed HM, Eltantawy AB, Salama MM. A planning approach for the network configuration of AC-DC hybrid distribution systems. *IEEE Transactions on Smart Grid*. 2016;9(3):2203-13. <https://doi.org/10.1109/TSG.2016.2608508>
- Ahmed HM, Eltantawy AB, Salama M. A reliability-based stochastic planning framework for AC-DC hybrid smart distribution systems. *International Journal of Electrical Power & Energy Systems*. 2019;107:10-8. <https://doi.org/10.1016/j.ijepes.2018.11.003>
- Wang C, Ding Z, Zhang X, He Z, Liu H, Xu Z, editors. Bi-level Programming of AC/DC Hybrid Distribution System. 2021 IEEE/IAS Industrial and Commercial Power System Asia (I&CPS Asia); 2021: IEEE.
- Wang Z, Zhong L, Pan Z, Yu T, Qiu X. Optimal double Q AC-DC hybrid distribution system planning with explicit topology-variable-based reliability assessment. *Applied Energy*. 2022;322:119438. <https://doi.org/10.1016/j.apenergy.2022.119438>
- Huang L, Chen Z, Cui Q, Zhang J, Wang H, Shu J. Optimal planning of renewable energy source and energy storage in a medium-and low-voltage distributed AC/DC system in China. *The Journal of Engineering*. 2019;2019(16):2354-61. <https://doi.org/10.1049/joe.2018.8546>
- Sabzian-Molae Z, Rokrok E, Doostizadeh M. An optimal master-slave model for stochastic planning of AC-DC hybrid distribution systems. *Journal of Renewable Energy and Environment*. 2023;10(2):27-38. <https://doi.org/10.30501/jree.2022.323167.1309>
- Sabzian-Molae Z, Rokrok E, Doostizadeh M. An optimal planning model for AC-DC distribution systems considering the converter lifetime. *International Journal of Electrical Power & Energy Systems*. 2022;138:107911. <https://doi.org/10.1016/j.ijepes.2021.107911>
- Wang J, Zhao H, Hu E, Zhang Z, Shen Z, Zhao G, et al., editors. Distributed Generation Capacity Planning Method of AC/DC Hybrid Distribution Network Based on Different Functions of Energy Storage. 2020 IEEE 4th Conference on Energy Internet and Energy System Integration (EI2); 2020: IEEE.
- Yin D, Mei F, Zheng J. An AC/DC distribution network DG planning problem: A genetic-ant colony hybrid algorithm approach. *Applied Sciences*. 2019;9(6):1212. <https://doi.org/10.3390/app9061212>
- Wu X, Wang Z, Ding T, Li Z. Hybrid AC/DC microgrid planning with optimal placement of DC feeders. *Energies*. 2019;12(9):1751. <https://doi.org/10.3390/en12091751>
- Sun Z, Yan Z, Sharen G, Liang T, Liu X, Yin H, editors. Network Planning of AC/DC hybrid microgrid with Power Electronic Transformers. 2020 12th IEEE PES Asia-Pacific Power and Energy Engineering Conference (APPEEC); 2020: IEEE.
- Rezaei O, Mirzapour O, Panahzari M, Gholami H. Hybrid AC/DC provisional microgrid planning model considering converter aging. *Electricity*. 2022;3(2):236-50. <https://doi.org/10.3390/electricity3020014>
- Ghiasi M. Detailed study, multi-objective optimization, and design of an AC-DC smart microgrid with hybrid renewable energy resources. *Energy*. 2019;169:496-507. <https://doi.org/10.1016/j.energy.2018.12.083>
- Yang Y, Pei W, Huo Q, Sun J, Xu F. Coordinate planning of multiple microgrids and distribution network with mixed AC/DC interconnection method. *Energy Procedia*. 2018;145:313-8. <https://doi.org/10.1016/j.egypro.2018.04.057>
- Rousis AO, Konstantelos I, Strbac G. A planning model for a hybrid AC-DC microgrid using a novel GA/AC OPF algorithm. *IEEE Transactions on Power Systems*. 2019;35(1):227-37. <https://doi.org/10.1109/TPWRS.2019.2924137>
- Wu Z, Liu P, Gu W, Huang H, Han J. A bi-level planning approach for hybrid AC-DC distribution system considering N-1 security criterion. *Applied energy*. 2018;230:417-28. <https://doi.org/10.1016/j.apenergy.2018.08.110>
- Shen Y, Wu G, Zheng H, Deng J, Shi P, editors. Research on key technology of planning and design for AC/DC hybrid distribution network. *AIP Conference Proceedings*; 2018: AIP Publishing.
- Wu Z, Sun Q, Gu W, Chen Y, Xu H, Zhang J. AC/DC hybrid distribution system expansion planning under long-term uncertainty considering flexible investment. *IEEE Access*. 2020;8:94956-67. <https://doi.org/10.1109/ACCESS.2020.2990697>
- de Barros HF, Alvarez-Herault M-C, Raison B, Tran QT. Optimal AC/DC Distribution Systems Expansion Planning from DSO's Perspective Considering Topological Constraints. *IEEE Transactions on Power Delivery*. 2023. <https://doi.org/10.1109/TPWRD.2023.3277089>
- Liu P, Wu Z, Gu W, Lu Y, Yang X, Sun K, et al. Security-constrained AC-DC hybrid distribution system expansion planning with high penetration of renewable energy. *International Journal of Electrical Power & Energy Systems*. 2022;142:108285. <https://doi.org/10.1016/j.ijepes.2022.108285>
- Fan H, Wang C, Liu L, Li X. Review of uncertainty modeling for optimal operation of integrated energy system. *Frontiers in energy*

- research. 2022;9:641337.
<https://doi.org/10.3389/fenrg.2021.641337>
28. Sheikhhahmadi P, Bahramara S, Moshtagh J, Damavandi MY. A risk-based approach for modeling the strategic behavior of a distribution company in wholesale energy market. *Applied energy*. 2018;214:24-38.
<https://doi.org/10.1016/j.apenergy.2018.01.051>
29. Hemmati M, Mohammadi-Ivatloo B, Ghasemzadeh S, Reihani E. Risk-based optimal scheduling of reconfigurable smart renewable energy based microgrids. *International Journal of Electrical Power & Energy Systems*. 2018;101:415-28.
<https://doi.org/10.1016/j.ijepes.2018.04.005>
30. Gholami M, Sanjari MJ. Optimal Operation of Multi-Microgrid System Considering Uncertainty of Electric Vehicles. *International Journal of Engineering*. 2023;36(8).
<https://doi.org/10.5829/ije.2023.36.08b.01>
31. Galvani S, Choogan M. Data clustering based probabilistic optimal power flow in power systems. *IET Generation, Transmission & Distribution*. 2019;13(2):181-8.
<https://doi.org/10.1049/iet-gtd.2018.5832>
32. Khanalizadeh Eimi M, Mirhosseini Moghadam M, Tavakoli A, Alizadeh B. Stability Analysis of AC/DC Microgrids in Island Mode. *International Journal of Engineering*. 2021;34(7):1750-65.
<https://doi.org/10.5829/ije.2021.34.07a.20>
33. Hamad AA, Nassar ME, El-Saadany EF, Salama M. Optimal configuration of isolated hybrid AC/DC microgrids. *IEEE Transactions on Smart Grid*. 2018;10(3):2789-98.
<https://doi.org/10.1109/TSG.2018.2810310>

COPYRIGHTS

©2024 The author(s). This is an open access article distributed under the terms of the Creative Commons Attribution (CC BY 4.0), which permits unrestricted use, distribution, and reproduction in any medium, as long as the original authors and source are cited. No permission is required from the authors or the publishers.



Persian Abstract

چکیده

حرکت رو به رشد استفاده از تولیدات پراکنده و بارهای الکتریکی از نوع DC، منجر به تغییرات قابل توجهی در سمت تولید و تقاضا در شبکه‌ی توزیع انرژی الکتریکی گردیده است. از اینرو به دلیل حضور منابع انرژی و بارها از نوع DC و AC ادامه دادن در شبکه توزیع AC مقرون به صرفه نمی‌باشد. بنابراین برنامه‌ریزی شبکه‌ی توزیع AC/DC گزینه مناسبی است که به یک برنامه‌ریزی اقتصادی، مطمئن و ایمن در حضور تنوع بارها و منابع انرژی می‌توان دست یافت. از طرفی عدم قطعیت‌های موجود در پیش‌بینی تقاضای بار و توان تولیدی منابع انرژی باعث رفتار احتمالی شبکه‌ی توزیع می‌گردد. این رفتار، شبکه‌ی توزیع را در معرض ریسک قرار می‌دهد. در مقاله پیش‌رو به برنامه‌ریزی شبکه‌ی توزیع ترکیبی AC/DC مبتنی بر ریسک پرداخته شده است. برای مدل‌سازی عدم قطعیت‌های موجود در مسأله از روش خوشه‌بندی K-means استفاده شده است. همچنین مسأله برنامه‌ریزی در قالب مدل بهینه‌سازی با هدف کاهش هزینه‌های طرح تحت ریسک ناشی از عدم قطعیت‌ها در فضای hybrid MATLAB/GAMS فرموله‌بندی ریاضی و حل شده است. کارایی روش بیان شده با انجام مطالعات عددی بر روی شبکه‌ی توزیع نمونه نشان داده شده است.



Investigation and Analysis of Dual Metal Gate Overlap on Drain Side Tunneling Field Effect Transistor with Spacer in 10nm Node

S. Howldar, B. Balaji*, K. Srinivasa Rao

Department of Electronics and Communication Engineering, Koneru Lakshmaiah Education Foundation, Green Fields, Vaddeswaram, Andhra Pradesh, India

PAPER INFO

Paper history:

Received 07 September 2023

Received in revised form 28 November 2023

Accepted 12 December 2023

Keywords:

On Current

Off Current

Hafnium Oxide

Gate Oxide

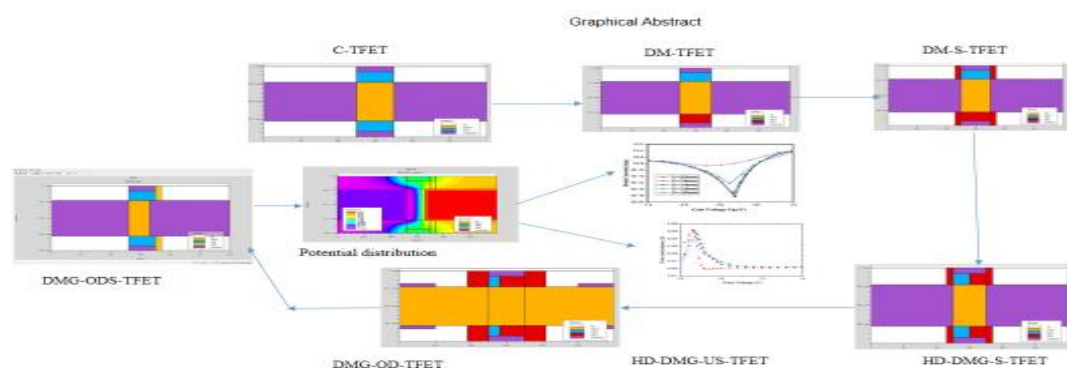
Channel Length

ABSTRACT

This paper investigates the electrical behavior and performance of a Dual Metal Gate Overlap on Drain Side Tunnel Field Effect Transistor with Spacer (DMG-ODS-TFET) in 10 nanometer technology. In this design, the utilization of two different metals to create the gate effectively maintains electrostatics and minimizes gate leakage current. This structure is formed by silicon dioxide and hafnium oxide as dielectric materials. The drain current characteristics such as subthreshold swing, on-state current, off-state leakage current, and transconductance are calculated for the proposed device using the available two-dimensional numerical device simulator silvaco tool. The characteristics of the proposed device vary with changes in channel length, doping concentrations of the drain and source, and the thickness of the oxide layer. This structure shows a lower off current, and better on-to-off current ratio with improved drain current. Consequently, the proposed design effectively balances gate control and leakage current, resulting in superior to conventional and dual metal gate devices. Based on improved performance parameters, this proposed structure is suitable for high-frequency applications.

doi: 10.5829/ije.2024.37.05b.07

Graphical Abstract



NOMENCLATURE

t_{ox}	Oxide thickness	SiO_2	Silicon dioxide
V_{ds}	Drain to source voltage	HfO_2	Hafnium oxide
I_d	Drain Current	V_{gs}	Gate to source voltage
I_{on}	On state current	I_{off}	Off state current

*Corresponding Author Email: vahividi@gmail.com (B. Balaji)

Please cite this article as: Howldar S, Balaji B, Srinivasa Rao K. Investigation and Analysis of Dual Metal Gate Overlap on Drain Side Tunneling Field Effect Transistor with Spacer in 10nm Node. International Journal of Engineering, Transactions B: Applications. 2024;37(05):887-95.

1. INTRODUCTION

The Metal Oxide-Semiconductor Field-Effect Transistor (MOSFET), is a fundamental electronic device used in a wide range of applications, from digital and analog circuits to power electronics. It serves and gives the crucial building block in modern electronic systems, allowing for the control and amplification of electrical signals. MOSFETs are the basic foundation of modern digital integrated circuits (ICs) such as microprocessors and memory chips (1). They are used in various analog applications, including amplifiers, voltage regulators, and analog switches. MOSFETs are employed in high-power applications like motor control, voltage inverters, and switching power supplies. RF MOSFETs are used in wireless communication devices and RF amplifiers. However, due to limited voltage handling capabilities compared to other devices, Tunnel Field Effect Transistor (TFET) have come up in to the semiconductor industry (2). For over five decades, the semiconductor industry has relied on the miniaturization of circuits through the downsizing the length of MOSFET as its primary device (3). However, conventional MOSFETs have limitations, such as a sub-threshold slope limited to 70 mV/decade and strict power constraints after scaling down the devices. Consequently, extensive research has sought alternatives for nano integrated circuits, leading to the adoption of highly energy-efficient TFETs for future applications. TFETs exhibit a sub-threshold slope of less than 70 mV/decade, making them ideal for commercial low-power uses (4).

As the semiconductor industry continues to advance towards smaller nodes and, the development of modern novel transistor designs becomes imperative to maintain performance gains while mitigating power consumption. Therefore, TFETs have garnered significant attention due to their potential to provide steep subthreshold slopes, reduced leakage current, and improved energy efficiency compared to conventional MOSFETs. In this work, the device modelling and the impact of dual metal gate overlap on the drain side of Tunnel Field Effect Transistor (DMG-ODS-TFET) with spacer technology is implemented in 10nm node (5). Both MOSFETs and TFETs are important semiconductor devices used in electronic circuits. While MOSFETs are widely established and versatile, TFETs offer unique characteristics that make them promising devices for specific applications, particularly in low-power and high-frequency domains (6). The choice between these two transistors depends on the specific requirements of the electronic system being designed. The TFET is an advanced semiconductor device that operates based on the principle of quantum mechanical tunneling. It offers unique properties and advantages, making it a promising device in the field of electronics. Researchers continue to

explore and develop TFETs to harness their full potential in future electronic systems (7).

The TFETs are emerging as the most promising devices for low-power applications, offering several advantages over MOSFETs. However, a significant limitation of TFETs is their low ON current. Therefore, researchers are actively working on enhancing the ION current in TFETs. One approach involves using high-k dielectric materials to improve mobility and ION current (8). The higher permittivity of these dielectric materials reduces gate dielectric leakage, and metal gates effectively control electrons within the high-k dielectric (9). This addition of high-permittivity dielectric materials enhances carrier mobility in the channel region and increases the ON current of TFETs. In TFETs, the implementation of multiple gate structures provides better control over the channel potential and increases the effective tunneling area, resulting in improved ON current (10). The primary tunneling area in TFETs is at the source-channel junction, and employing multiple gate structures effectively enlarges this tunneling area. Combining multi-material and double-gate TFET devices results in a high ON current. Additionally, increasing the source doping concentration enhances the ON current. To further suppress ambipolar effects and increase the ON current, lower band gap materials are employed. Hetero-junction devices are also used to achieve a lower effective band gap at the source-channel junction (11).

In the evolving field of the semiconductor industry, the rigorous pursuit of miniaturization and improved performance has led to the development of advanced transistor structures (12). Among these innovations, the DMG-ODS-TFET has gained prominence in the 10nm technology node. This device explores into the investigation and analysis of a crucial aspect of the proposed device. The rigorous demand for faster and more energy-efficient electronic devices has spurred continuous innovation in semiconductor manufacturing. As silicon technology advances into the 10nm node and beyond, transistor design has become increasingly complex. One notable development in this pursuit of performance optimization is the spacer technology (13).

The advanced DMG-OD-TFET addresses the limitations of traditional TFET designs and enhances performance device parameters in submicron technology (14). This innovative design comprises two components such as a dual metal gate (DMG) and spacer material on the drain side. The hetero dielectric gate stack employs two distinct dielectric materials high-k dielectric material, specifically hafnium oxide (HfO_2), and low-k dielectric material, such as silicon dioxide (SiO_2). By incorporating these dielectric materials into the design, it can optimize the electric field distribution, resulting in improved electrostatic control (15). This enhanced and

improvement will control effectively mitigates ambipolar conduction and significant challenge in TFETs, and enables efficient modulation of advanced device's on/off characteristics. Additionally, the integration of advanced gate overlap on the drain side into the TFET structure with HfO₂. This overlap physically separates the source and channel regions, thereby reducing direct source-to-drain tunneling current, a major contributor to off-state leakage in TFETs. Through the minimization of this leakage current, the underlap spacer enhances the on/off current ratio and overall device performance. However, a comprehensive analysis is essential to understand the impact of these design modifications on various metric devices.

The TFET offers several advantages, including a sub-60 mV/dec subthreshold swing (SS) at room temperature and reduced leakage current. This makes it a promising alternative to traditional MOSFETs for low-power applications. Various techniques have been explored to enhance TFET performance, such as employing graded Silicon and Germanium heterojunction TFETs through bandgap engineering and using dual spacer dielectrics SiO₂ and HfO₂. Additionally, reducing leakage current and subthreshold swing has been achieved by employing a very lightly doped drain material (with $N_D \approx 2 \times 10^{18} \text{ cm}^{-3}$) with a low density of states, such as Indium Gallium Arsenide. In this design, the length of the lightly doped drain should be limited to around 10 nm. Recent research has demonstrated that TFET performance can be further improved by introducing a non-uniform body thickness (16). In this paper, the two-dimensional cross sectional view and simulations of DMG-OD-TFET with low leakage current and low ON-to-OFF ratio is presented and introduced a new phenomenon called gate overlap on the drain side and demonstrate the presence of off-state current as the channel length is reduced to 10nm.

The DMG-OD-TFET is a promising device for advanced integrated circuits due to its ability to mitigate short-channel effects and improve device performance (17). Spacer technology, which involves the use of dielectric materials around the gate electrode, further enhances transistor performance by reducing leakage currents and improving electrostatic control. The overlap region, where the gate material extends beyond the gate dielectric, plays a pivotal role in device performance (18). It shows directly impacts device characteristics such as threshold voltage, subthreshold swing, and drain-induced barrier lowering (DIBL) (19).

The DMG-ODS-TFET in 10nm Node refers to an advanced semiconductor technology that plays a crucial role in enhancing the performance and energy efficiency of new transistors in the 10-nanometer semiconductor manufacturing process. This technology leverages a DMG design and spacer integration to address drain-induced barrier lowering (DIBL) and improve the overall proposed transistor characteristics in the 10nm node. The

10nm semiconductor manufacturing process in this proposed device signifies a high level of miniaturization and a substantial increase in transistor density compared to previous nodes. This design is crucial for optimizing transistor performance and mitigating various electrical characteristics, drain current, analog characteristics, and RF characteristics. The gate structure extends slightly beyond the drain region of the transistor. This extension is strategically engineered to address issues like DIBL, where the control of the proposed TFET behavior is affected by the voltage at the drain terminal. The proposed DMG-ODS-TFET relies on quantum tunneling for its operation, offering potential advantages in terms of reduced power consumption and improved drain current characteristics compared to conventional TFETs. Spacer materials SiO₂ and HfO₂ are the insulating materials around the gate structure to fine-tune the transistor characteristics and mitigate unwanted electrical effects.

2. DEVICE STRUCTURE AND SIMULATION PARAMETERS

The DMG-ODS-TFET leverages quantum tunneling for electron transport, making it a promising device for low-power applications. In the context of this proposed structure, it has two different gate materials, often used to control different aspects of device performance (20). The proposed device typically consists of a source, a drain, a channel, and a dual gate. The gate is usually separated from the channel by a thin insulating layer, and the gate materials can vary (21). A spacer material was added to this structure to enhance the device characteristics. The 10-nanometer node allows for more transistors per unit area and can offer improved performance and power efficiency. The overlap can impact the device's characteristics, such as threshold voltage and subthreshold swing, which are crucial for TFET performance (22). In this device, electrons tunnel through a thin insulating barrier between the source and the channel, which is different from traditional transistors like MOSFETs, where electrons move through a conductive channel as shown in Figure 1.

The mesh and two-dimensional cross-sectional view of the proposed device and its electric field distribution and potential distributions as shown in Figures 2, 3 and 4.

The TFET technology with other innovations, such as three-dimensional integration and advanced packaging techniques, could lead to enhanced overall system performance. Controlling the doping profiles in the TFET structure, especially in the drain region, can impact the tunneling process. Optimizing the doping concentration and distribution can contribute to better device characteristics.

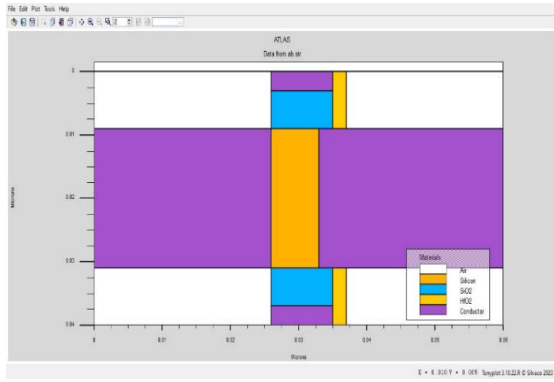


Figure 1. 2 D cross-sectional view of proposed Dual Material Gate Overlap on Drain Side TFET with spacer

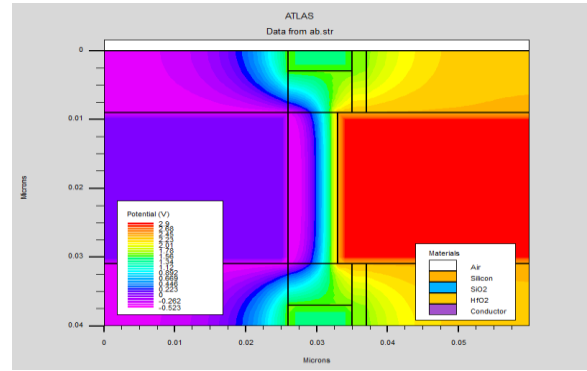


Figure 4. Potential distribution of proposed device

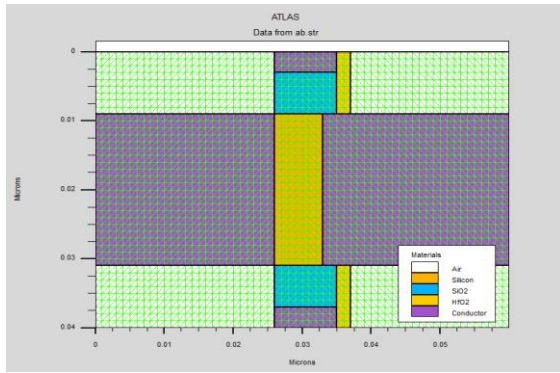


Figure 2. Mesh View of proposed device

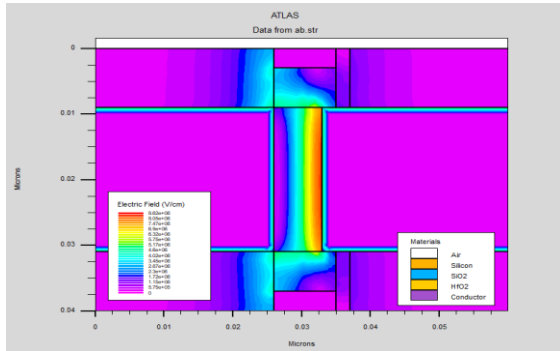


Figure 3. Electric field distribution of proposed device

The simulation work is carried out with three different drain doping concentrations ($N_d = 1 \times 10^{18} \text{ cm}^{-3}$, $2 \times 10^{18} \text{ cm}^{-3}$, and $3 \times 10^{19} \text{ cm}^{-3}$) for the proposed device. Table 1 presents the values of the gate work function, gate-on-drain overlap work function, and equivalent oxide thickness beneath the gate-on-drain

overlap for each of these drain doping concentrations (23). The channel length for all structures was set at 10 nanometers. The same gate work functions were utilized in the remaining three configurations. In these proposed structures, the selected a gate-on-drain overlap length of

TABLE 1. Parameter used for the simulation proposed device

Used Parameter	DMG-ODS-TFET
Device Length (W_L)	60 nm
Gate Length (L_G)	10 nm
Source Length (L_S)	25nm
Drain Length (L_D)	25nm
Channel Length (L_C)	10nm
Doping of Source (D_S)	$1 \times 10^{20} \text{ cm}^{-3}$
Doping of Drain (D_D)	$1 \times 10^{18} \text{ cm}^{-3}$
Doping of Channel (D_C)	$1 \times 10^{17} \text{ cm}^{-3}$
Metal Gate Work Function (W_F)	4.8eV

20 nm, which was found to be optimal for reducing ambipolar current in DMG-OD-TFET (24). Importantly, the introduction of the gate-on-drain overlap did not have an adverse impact on the AC performance of the device through increased gate-drain capacitance.

The on state current and off state current for different doping concentrations are summarized in Tables 2, 3 and 4.

3. RESULTS AND DISCUSSION

The drain current (I_d) versus gate-to-source voltage (V_{gs}) characteristics for a proposed device, investigating

TABLE 2. On current and off current at $N_d = 1 \times 10^{18} \text{ cm}^{-3}$

Gate Length	$I_{on}(A/\mu m)$	$I_{off}(A/\mu m)$	I_{on}/I_{off}
L=22nm	$4.2174e^{-6}$	$1.08069e^{-17}$	$3.90247e^{+11}$
L=18nm	$1.514e^{-5}$	$1.00242e^{-17}$	$1.51032e^{+12}$
L=14nm	$5.435e^{-5}$	$1.08069e^{-17}$	$5.02921e^{+12}$
L=12nm	$8.1414e^{-5}$	$9.21128e^{-18}$	$8.83853Ee^{+12}$
L=10nm	$8.1618e^{-4}$	$9.21128e^{-18}$	$4.9189e^{+14}$

TABLE 3. On current and off current at $N_d = 2 \times 10^{18} \text{ cm}^{-3}$

Gate Length	$I_{on}(A/\mu\text{m})$	$I_{off}(A/\mu\text{m})$	I_{on}/I_{off}
L=22nm	$4.1233e^{-5}$	$4.98288e^{-19}$	$8.27504e^{+13}$
L=18nm	$6.4603e^{-5}$	$2.24135e^{-18}$	$2.88231e^{+13}$
L=14nm	$7.1246e^{-5}$	$1.01878e^{-17}$	$1.54046e^{+13}$
L=12nm	$8.9812e^{-5}$	$6.67237 e^{-15}$	$2.68791e^{+13}$
L=10nm	$6.1735e^{-4}$	$2.15899 e^{-9}$	$2.98498e^{+13}$

TABLE 4. On current and off current at $N_d = 3 \times 10^{18} \text{ cm}^{-3}$

Gate Length	$I_{on}(A/\mu\text{m})$	$I_{off}(A/\mu\text{m})$	I_{on}/I_{off}
L=22nm	$4.0162e^{-6}$	$1.00224e^{-18}$	$4.00719e^{+13}$
L=18nm	$7.9799 e^{-6}$	$2.20201e^{-17}$	$3.62393e^{+11}$
L=14nm	$1.0376e^{-6}$	$5.45632e^{-14}$	$3.74891e^{+11}$
L=12nm	$9.4744e^{-6}$	$3.87088e^{-14}$	$3.98756e^{+11}$
L=10nm	$9.4892e^{-6}$	$1.1615e^{-9}$	$2.12042e^{+11}$

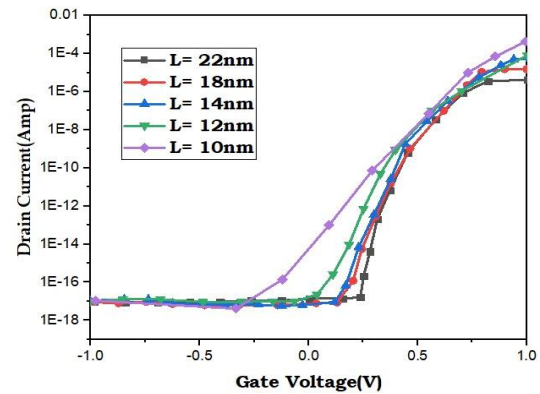
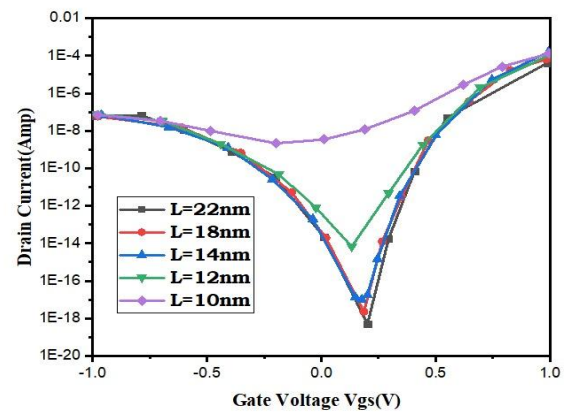
the behavior of this proposed transistor under different operating conditions (25). The dual metal gate overlap on the drain (DMG-OD) side can help to reduce the tunneling barrier and improve electron injection from the source to the channel (26). This can lead to a higher on-state current (I_{on}) compared to traditional TFET designs. Consequently, the I_d and V_{gs} curve should show an increased current level for a given V_{gs} , indicating improved device performance in the on-state (27). While DMG overlap can enhance gate control i.e. impact on gate leakage. Any unintended leakage current through the gate can affect the device's off-state performance. Depending on the materials and fabrication used, there may be variations in gate leakage current that are reflected in Figure 5.

The proposed device ability to achieve subthreshold swings below 60 mV/decade compared to conventional MOSFETs (28). With a DMG-OD side, the improvement in the subthreshold swing is due to enhanced gate control over the channel. A steeper subthreshold slope indicates better performance in the subthreshold region (29). The DMG structure allows for more precise control over the threshold voltage (V_{th}). By adjusting the work function of the metals or the gate length, can tune the V_{th} to this specific design requirements (30). This can be observed in the I_d vs. V_{gs} characteristics, with shifts in the threshold voltage for different device configurations. As with any semiconductor device, there are likely trade-offs associated with this design. For instance, the overlap of the gate on the drain side may affect other device parameters such as transconductance, drain conductance, off state leakage current and lower breakdown voltage. The proposed device exhibits temperature-sensitive behavior due to the tunneling mechanism. The I_d and V_{gs}

characteristics of the proposed device is analyzed at different temperatures to understand how the DMG overlap on drain side will show and influences the device's temperature dependence as shown in Figure 6.

The proposed device is validated and analyzed with potential equations as shown in Equations 1-3.

To achieve the highest drain current for both the conventional device and the proposed structure when the gate voltage is at zero, they should operate in depletion mode. Consequently, in the 10nm technology, the maximum current for the proposed device occurs when $V_G=0$. Notably, the drain current experiences a significant increase as the drain voltage varies while the gate voltage is held at zero. In TFET, the upper region of the channel needs to be depleted due to the gate channel bias. This depletion results in the movement of carriers towards the bottom of the channel, which in turn leads to the flow of drain current. As a result, the drain current predominantly flows in the lower area of the channel. This proposed device is expected to exhibit maximum velocity, the highest electron density, an effective

**Figure 5.** Drain current with gate voltage of proposed device at doping concentration $N_d = 1 \times 10^{18} \text{ cm}^{-3}$ **Figure 6.** Drain current with gate voltage of proposed device at doping concentration $N_d = 2 \times 10^{18} \text{ cm}^{-3}$

channel depth, and improved drain current flow as shown in Figure 7.

$$f_T = \frac{g_m}{2\pi(C_{gs} + C_{gd})} \tag{1}$$

$$f_r = \frac{g_m}{2\pi C_{gg}} \tag{2}$$

where C_{gs} -Gate to source capacitance

C_{gd} -Gate to drain capacitance

C_{gg} -Total gate capacitance

In the subthreshold region, drain conductance and drain voltage exhibits a steep increase in conductance with increasing drain voltage. This behavior signifies the proposed device ability to achieve a low subthreshold swing. In the saturation region, drain conductance may rapid continues to increase but gradually increase with increasing drain voltage. This is indicative of the device's ability to maintain a controlled and stable on-state current, which is essential for various applications. The DMG-OD side influences the drain conductance. It may affect the electric field distribution, gate control, and tunneling mechanism, all of which can directly impact conductance. The proposed TFET should exhibits a subthreshold swing and its performance significantly below the 60 mV/decade limit seen in traditional MOSFETs. Analyzing drain conductance for a proposed device is essential for understanding its electrical behavior, subthreshold characteristics, temperature sensitivity, radio frequency and overall suitability for various applications. Experimental measurements and device simulations are crucial for obtaining real-world data and validating the expected behavior of the device as shown in Figure 8.

$$I_d = zb(x)qn(x)v(x) \tag{3}$$

where z= channel width

b(x)=effective depth of the channel

q=electron charge

n(x)=electron density

v(x)=electron velocity

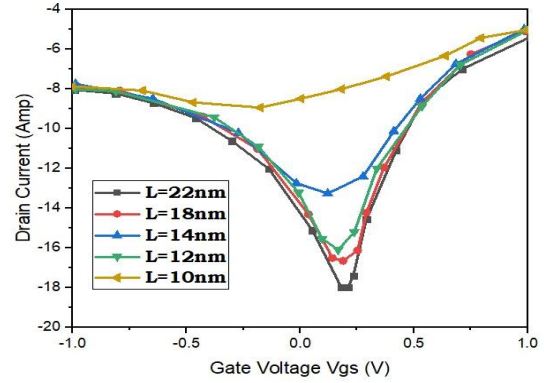


Figure 7. Drain current with a gate voltage of proposed device at doping concentration $N_d = 3 \times 10^{18} \text{ cm}^{-3}$

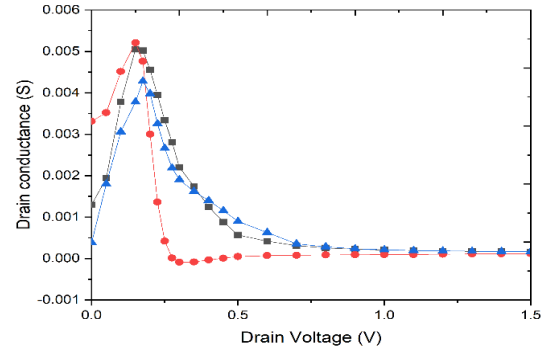


Figure 8. Drain conductance with a drain voltage of proposed device

The performance characteristics of different devices are evaluated in comparison to the proposed structure, as presented in Table 5. According to the comparison results, the proposed device exhibits and shows enhanced performance parameters when compared to existing devices and Table 6 shows the existing device

In semiconductor technology, TFETs are an advanced transistor designed to operate at lower power consumption compared to traditional MOSFETs. The dual metal gate overlap on the drain side to a feature in the TFET design that influences its performance.

TABLE 5. Performance Parameters Comparison comparison

Parameters	C TFET	SG TFET	DG TFET	HD-DG TFET	HD-DMG-TFET	DMG-OD-TEFT (18nm)	DMG-OD-TEFT (12nm)	DMG-OD-TEFT (10nm)
Ion(A/μm)	3.12	3.94	4.3	4.6	8.01	8.1	8.12	9.48
Ioff(A/μm)	9.40e ⁻¹¹	8.99e ⁻¹¹	4.50 e ⁻¹¹	4.22e ⁻¹¹	1.34	1.12	1.14	1.16
Ion/Ioff	1.69	1.70	1.88	1.84	1.9	2.1	2.11	2.12
Gm(S/mm)	1.34	1.38	1.42	1.46	1.41	1.55	1.88	3.1
Gd(S/mm)	0.32	0.39	0.419	0.45	0.452	0.46	0.61	0.71
Ron(Ωmm)	1.41	1.61	1.32	0.88	0.6	0.71	0.72	0.51

TABLE 6. Comparison with existed devices

Parameters	C TFET	SG TFET	DG TFET	HD-DG TFET	Proposed device
Ion(A/ μm)	2.12	2.9	3.1	4.5	6.78
Ioff(A/ μm)	9.01	8.08	7.6	7.58	7.55
Ion/Ioff	2.12	1.07	1.6	1.72	3.21

possibly affecting the current leakage and switching speed. To improve or fill gaps in the design of a proposed TFET, experimenting with different semiconductor materials and metal combinations for the gates can significantly impact the device's performance. Novel materials may offer improved electrical characteristics, better control over the tunneling process and reduced leakage. The optimization of the gate dielectric material can affect the tunneling characteristics and overall transistor behavior. Innovations in dielectric materials may help in reducing leakage currents and enhancing device performance. Fine-tuning the manufacturing processes, such as the deposition and etching techniques, can improve the precision and quality of the Dual Metal Gate Overlap. Optimizing these processes can enhance the transistor's reliability and performance. Advanced computer modeling and simulation techniques can help researchers understand the behavior of the TFET at a fundamental level. This understanding can guide the refinement of the Dual Metal Gate Overlap design.

The proposed device demonstrates superior drain conductance associated with the use of HfO_2 and SiO_2 dielectric materials. This elevated drain conductance plays a pivotal role in enabling the device to attain the highest packing density, primarily due to the augmented current flow within the device. As a result, the structural advantage inherent in the proposed device leads to a significant enhancement in advanced transconductance characteristics. A robust transconductance is crucial for achieving optimal device gain. However, the pursuit of reducing the subthreshold slope, though desirable, introduces a trade-off by causing an upturn in off-current and power dissipation within the device.

4. CONCLUSION

In this work, a Dual Metal Gate (DMG) Overlap on Drain Side Tunneling Field Effect Transistor (TFET) with spacer technique is investigated in 10nm technology. This proposed device achieving the highest drain current at zero gate voltage, while operating in depletion mode, is crucial for optimizing the proposed device functionality. HfO_2 holds significant potential as a semiconductor material for high-voltage and high-frequency applications, including cosmic cells and

energy devices. In this work, the design, analysis and calculation of performance parameters of both DC and RF properties, for a unique advanced device designed for the 10nm technology node using Silvaco TCAD. The proposed structure, utilizing Silvaco TCAD in the context of 10nm innovations, enhances various electrical properties such as on current (Ion), off current (Ioff), Ion/Ioff ratio, as well as RF properties including drain conductance (Gd) and on-resistance (Ron). The main analysis presented in this article demonstrates the ability to achieve exceptional performance in the proposed structure. This device incorporates a hetero-junction created by merging silicon materials with hafnium oxide at the drain-channel junction. Furthermore, it employs a hetero-dielectric gate stack consisting of SiO_2 and HfO_2 , with HfO_2 dielectric showing significant potential as a semiconductor material for applications requiring high voltage and high frequency range. These findings include maintaining an average subthreshold swing of this proposed device is less than 60 mV/dec (approximately 45 mV/dec), achieving a low OFF-state current of around $10^{-09}\text{A}/\mu\text{m}$, and attaining an impressive ION/IOFF ratio of approximately 10^{11} , even when using high drain doping concentrations up to $N_D = 3 \times 10^{18}\text{cm}^{-3}$. These results provide strong motivation for researchers to pursue experimental implementations of TFETs with enhanced performance. As a result, this advanced structure is well-suited for high-frequency applications.

5. REFERENCES

1. Krishnamurthy A, Reddy DV, Radhammac E, Jyothirmayeed B, Raoc DS, Agarwale V, et al. Design and Performance Analysis of 6H-SiC Metal-Semiconductor Field-Effect Transistor with Undoped and Recessed Area under Gate in 10nm Technology. *International Journal of Engineering, Transactions C: Aspects.* 2023;36(12):2264-71. [10.5829/ije.2023.36.12c.16](https://doi.org/10.5829/ije.2023.36.12c.16)
2. Meshkin R. An Extended-Source Tunneling-FET with Gate-Overlapped n+-Doped Pocket. *Journal of Electronic Materials.* 2023;1-7. <https://doi.org/10.1007/s11664-023-10524-5>
3. Radhama E, Vemana Chary D, Krishnamurthy A, Venkatarami Reddy D, Sreenivasa Rao D, Gowthami Y, et al. Performance analysis of high-k dielectric heterojunction high electron mobility transistor for rf applications. *International Journal of Engineering, Transactions C: Aspects.* 2023;36(9):1652-8. [10.5829/ije.2023.36.09c.09](https://doi.org/10.5829/ije.2023.36.09c.09)
4. Gowthami Y, Balaji B, Srinivasa Rao K. Performance Analysis and Optimization of Asymmetric Front and Back Pi Gates with Dual Material in Gallium Nitride High Electron Mobility Transistor for Nano Electronics Application. *International Journal of Engineering, Transactions A: Basics* 2023;36(7):1269-77. [10.5829/ije.2023.36.07a.08](https://doi.org/10.5829/ije.2023.36.07a.08)
5. Talukdar J, Rawat G, Singh K, Mummaneni K. Comparative analysis of the effects of trap charges on single-and double-gate extended-source tunnel FET with δp^+ SiGe pocket layer. *Journal of Electronic Materials.* 2020;49:4333-42. <https://doi.org/10.1007/s11664-020-08151-5>

6. Wangkheirakpam VD, Bhowmick B, Pukhrabam PD. Investigation of a dual MOSCAP TFET with improved vertical tunneling and its near-infrared sensing application. *Semiconductor Science and Technology*. 2020;35(6):065013. <https://doi.org/10.1088/1361-6641/ab8172>
7. Gowthami Y, Balaji B, Rao KS. Design and performance evaluation of 6nm hemt with silicon sapphire substrate. *Silicon*. 2022;14(17):11797-804. <https://doi.org/10.1007/s12633-022-01900-7>
8. Kumar PK, Balaji B, Rao KS. Performance analysis of sub 10 nm regime source halo symmetric and asymmetric nanowire MOSFET with underlap engineering. *Silicon*. 2022;14(16):10423-36. <https://doi.org/10.1007/s12633-022-01747-y>
9. Howldar S, Balaji B, Srinivasa Rao K. Design and Qualitative Analysis of Hetero Dielectric Tunnel Field Effect Transistor Device. *International Journal of Engineering, Transactions C: Aspects* 2023;36(6):1129-35. 10.5829/ije.2023.36.06c.11
10. Saravanan M, Parthasarathy E. Impact of Pocket Layer on Linearity and Analog/RF Performance of InAs-GaSb Vertical Tunnel Field-Effect Transistor. *Journal of Electronic Materials*. 2023;52(4):2772-9. <https://doi.org/10.1007/s11664-023-10239-7>
11. Dixit A, Gupta N. A compact model of gate capacitance in ballistic gate-all-around carbon nanotube field effect transistors. *International Journal of Engineering, Transactions A: Basics*. 2021;34(7):1718-24. 10.5829/IJE.2021.34.07A.16
12. Gopal G, Varma T. Impact of Temperature on the Reliability of UTB-DG-FE-TFETs and Their RF/Analog and Linearity Parameter Dependence. *Journal of Electronic Materials*. 2023;52(9):6293-307. <https://doi.org/10.1007/s11664-023-10556-x>
13. Chakrabarty R, Roy S, Pathak T, Kumar Mandal N. Design of Area Efficient Single Bit Comparator Circuit using Quantum dot Cellular Automata and its Digital Logic Gates Realization. *International Journal of Engineering, Transactions C: Aspects*. 2021;34(12):2672-8. 10.5829/ije.2021.34.12c.13
14. Gopal G, Varma T. Simulation-based analysis of ultra thin-body double gate ferroelectric TFET for an enhanced electric performance. *Silicon*. 2022;14(12):6553-63. <https://doi.org/10.1007/s12633-021-01428-2>
15. Venkatesh M, Balamurugan N. Influence of threshold voltage performance analysis on dual halo gate stacked triple material dual gate TFET for ultra low power applications. *Silicon*. 2021;13:275-87. <https://doi.org/10.1007/s12633-020-00422-4>
16. Dharmender, Nigam K. Low-K dielectric pocket and workfunction engineering for DC and analog/RF performance improvement in dual material stack gate oxide double gate TFET. *Silicon*. 2021;13:2347-56. <https://doi.org/10.1007/s12633-020-00822-6>
17. Hoonan Mehrabani A, Fattah A, Rahimi E. Design and simulation of a novel hetero-junction bipolar transistor with gate-controlled current gain. *International Journal of Engineering, Transactions C: Aspects* 2023;36(3):433-40. 10.5829/ije.2023.36.03c.01
18. Rafiee A, Nickabadi S, Nobarian M, Tagimalek H, Khatami H. Experimental investigation joining al 5083 and high-density polyethylen by protrusion friction stir spot welding containing nanoparticles using taguchi method. *International Journal of Engineering, Transactions C: Aspects*. 2022;35(6):1144-53. 10.5829/ije.2022.35.06c.06
19. Bera PK, Kar R, Mandal D. Modelling and Analysis of Dual Material Gate Charge Plasma Based Vertical t-shaped TFET. *Silicon*. 2021;1-10. <https://doi.org/10.1007/s12633-021-01518-1>
20. Kumar A, Sharma K. Investigation of dielectric properties of Ni/N-TiO₂/P-Si/Al heterojunction in wide range of temperature and voltage. *International Journal of Engineering, Transactions A: Basics*. 2022;35(4):698-705. 10.5829/ije.2022.35.04A.09
21. Balaji B, Srinivasa Rao K, Girija Sravani K, Bindu Madhav N, Chandrhas K, Jaswanth B. Improved drain current characteristics of hfo₂/sio₂ dual material dual gate extension on drain side-tfet. *Silicon*. 2022;14(18):12567-72. <https://doi.org/10.1007/s12633-022-01955-6>
22. Kumar PK, Balaji B, Rao KS. Halo-Doped Hetero Dielectric Nanowire MOSFET Scaled to the Sub-10 nm Node. *Transactions on Electrical and Electronic Materials*. 2023;1-11. <https://doi.org/10.1007/s42341-023-00448-6>
23. Emami N, Kuchaki Rafsanjani M. Extreme learning machine based pattern classifiers for symbolic interval data. *International Journal of Engineering, Transactions B: Applications*. 2021;34(11):2545-56. 10.5829/IJE.2021.34.11B.17
24. Fouladinia F, Gholami M. Decimal to excess-3 and excess-3 to decimal code converters in QCA nanotechnology. *International Journal of Engineering, Transactions C: Aspects*. 2023;36(9):1618-25. 10.5829/ije.2023.36.09c.05
25. Gowthami Y, Balaji B, Rao KS. Design and Analysis of a Symmetrical Low-κ Source-Side Spacer Multi-gate Nanowire Device. *Journal of Electronic Materials*. 2023;52(4):2561-8. <https://doi.org/10.1007/s11664-023-10217-z>
26. Tiwari S, Saha R. Optical Performance of Split-Source Z-Shaped Horizontal-Pocket and Hetero-Stacked TFET-Based Photosensors. *Journal of Electronic Materials*. 2023;52(3):1888-99. <https://doi.org/10.1007/s11664-022-10140-9>
27. Gupta AK, Raman A. Design, investigation, and sensitivity analysis of a biosensor based on an optimized electrostatically doped nanotube TFET. *Journal of Electronic Materials*. 2021;50:5462-71. <https://doi.org/10.1007/s11664-021-09072-7>
28. Sadeghi E, Ebrahimi E. Ultra Low Power Temperature Compensated Complementary Metal Oxide Semiconductor Ring Oscillator in Subthreshold. *International Journal of Engineering, Transactions A: Basics*. 2023;36(1):108-18. 10.5829/ije.2023.36.01a.13
29. Kwatra P, Nigam K, Singh SV. Design and Performance Evaluation of a Novel Dual Tunneling based TFET Considering Trap Charges for Reliability Improvement. *Silicon*. 2023;15(5):2407-25. <https://doi.org/10.1007/s12633-022-02188-3>
30. Howldar S, Balaji B, Srinivasa Rao K. Design and Analysis of Hetero Dielectric Dual Material Gate Underlap Spacer Tunnel Field Effect Transistor. *International Journal of Engineering, Transactions C: Aspects*. 2023;36(12):2137-44. 10.5829/ije.2023.36.12c.01

COPYRIGHTS

©2024 The author(s). This is an open access article distributed under the terms of the Creative Commons Attribution (CC BY 4.0), which permits unrestricted use, distribution, and reproduction in any medium, as long as the original authors and source are cited. No permission is required from the authors or the publishers.



Persian Abstract

چکیده

این مقاله به بررسی رفتار الکتریکی و عملکرد یک همپوشانی دروازه فلزی دوگانه روی ترانزیستور اثر میدان تونل سمت تخلیه با Spacer (DMG-ODS-TFET) در فناوری ۱۰ نانومتری می‌پردازد. در این طرح، استفاده از دو فلز مختلف برای ایجاد گیت، الکترواستاتیک را به طور موثر حفظ می‌کند و جریان نشتی گیت را به حداقل می‌رساند. این ساختار توسط دی اکسید سیلیکون و اکسید هافنیوم به عنوان مواد دی الکتریک تشکیل شده است. ویژگی‌های جریان تخلیه مانند نوسان زیرآستانه، جریان در حالت، جریان نشتی خارج از حالت، و رسانایی برای دستگاه پیشنهادی با استفاده از ابزار شبیه‌ساز دستگاه عددی دو بعدی موجود silvaco محاسبه می‌شود. ویژگی‌های دستگاه پیشنهادی با تغییر در طول کانال، غلظت دوپینگ درین و منبع، و ضخامت لایه اکسید متفاوت است. این ساختار جریان خاموش کمتر و نسبت جریان روشن به خاموش بهتر با جریان تخلیه بهبود یافته را نشان می‌دهد. در نتیجه، طرح پیشنهادی به طور موثر کنترل گیت و جریان نشتی را متعادل می‌کند و در نتیجه نسبت به دستگاه‌های دروازه فلزی معمولی و دوگانه برتری دارد. بر اساس پارامترهای عملکرد بهبود یافته، این ساختار پیشنهادی برای کاربردهای فرکانس بالا مناسب است.



Relaxation Process in Crude Oil after Ultrasonic Treatment

G. F. Baimukhametov^{*a}, A. V. Dengaev^b, E. U. Safiullina^c, A. A. Kayumov^a, I. M. Drozdov^b, V. V. Shishulin^b, A. Boushra^b, A. V. Vakhin^a, B. V. Sargin^d, M. S. Sidibe^b

^a Institute of Geology and Petroleum Technologies, Kazan Federal University, Kazan, Russia

^b Department of Petroleum Engineering, Gubkin National University of Oil and Gas, Moscow, Russia

^c Oil and Gas Faculty, Saint Petersburg Mining University, St. Petersburg, Russia

^d LLC "Volna", Moscow, Russia

PAPER INFO

Paper history:

Received 25 November 2023

Received in revised form 15 January 2024

Accepted 23 January 2024

Keywords:

Ultrasound

Cavitation

Asphaltenes

Aromatic and Resin Analysis

Sonochemistry

Viscosity

ABSTRACT

This paper presents an investigation on changes in viscosity and group composition of heavy oil samples after ultrasonic upgrading process. Heavy oil samples correspond to different oilfields (located in Russia) were processed under various ultrasonic mode, the cavitation consequence of which was controlled by acoustic method. The viscosity of samples was measured just after ultrasonic treatment, 10 minutes, and 1-34 days. The saturate, aromatic, resin and asphaltene (SARA) analysis was carried out after ultrasonic treatment with 34 days of relaxation and the achieved results were compared with the SARA fractions of original crude oil. The results of viscosity measurement showed viscosity reduction after the ultrasonic treatment. However, the viscosity was regressed after 1-4 days of relaxation with further reduction in 7 days. The degree of viscosity increase after 34 days was only 10% in contrast to viscosity of original crude oil. The power and the sonication time did not influence the relaxation process. In conclusion, attention was drawn to the results of SARA analysis, the content of saturates decreased and the relative content of heavy fragments such as resins and asphaltenes was increased, which determines the degree of viscosity increase after relaxation period.

doi: 10.5829/ije.2024.37.05b.08

Graphical Abstract

Average oil viscosity after ultrasonic treatment



Group composition of oil after ultrasonic treatment and relaxation



*Corresponding Author Email: baimukhametovi@mail.ru (G. F. Baimukhametov)

Please cite this article as: Baimukhametov GF, Dengaev AV, Safiullina EU, Kayumov AA, Drozdov IM, Shishulin VV, Boushra A, Vakhin AV, Sargin BV, Sidibe MS. Relaxation Process in Crude Oil after Ultrasonic Treatment. International Journal of Engineering, Transactions B: Applications. 2024;37(05):896-903.

1. INTRODUCTION

Due to growing interests in the heavy oil reservoirs (1-3), enhanced oil recovery methods became more popular (4-6). Ultrasound-assisted heavy oil upgrading is one of the methods of enhanced oil recovery. It allows to reduce viscosity of oil and paraffins and asphaltenes sedimentation (7-9). It is widely used during oil recovery and processing (10-12).

Asphaltenes are the heaviest molecules of oil and they mainly determine the viscosity of crude oil. However, the asphaltenes have a tendency to precipitate and aggregate. The size of the last depends mainly on its concentration. It is well known, that asphaltene molecules are present in toluene at concentrations less than 1 mg/l as monomers and above 5 mg/l as dimers and trimmers, etc. With increasing concentration, asphaltenes are present as supermolecules and solid-like aggregates (13-15).

The presence of large structures leads to non-Newtonian behavior of fluids. In such fluids, viscosity depends on the aggregate size, shape, interactions between structures, flexibility of aggregate elements, etc. (16). In heavy crude oils, asphaltenes structure, size and interaction can change due to external conditions, such as temperature and pressure (17-19). Thus, the ultrasound energy can be employed to destruct the aggregation of the asphaltenes, which significantly reduces the viscosity of the fluid (20-22). However in some cases, it has been reported that viscosity of crude oil can be increased up to the untreated levels or even more after sonification (23-25). Others argue that this phenomenon is due to the formation of new molecular structure in normal conditions (26, 27).

Relaxation phenomenon in chemistry is related to the delay between the external effect and system response. After an abrupt change of pressure or temperature it takes time for the molecular or atomic structure to re-equilibrate under new conditions. This effect can be caused by the redistribution of energy among electronic, nuclear, rotational and vibrational molecular energy states or by a shift in the ration of the number of product molecules to reactant molecules in chemical reactions. The relaxation time depends on the atomic and molecular structure, on the rate and mechanisms of chemical reactions (28).

Relaxation phenomenon in crude oil and similar organic fluids have been studied in several where magnetic field influence on the oil viscosity was investigated. It was concluded, that viscosity changes due to ferromagnetic aggregates destruction in the alternating magnetic field. Volkova et al. (29) investigated the destruction of polymers after sonification. It was observed that destructed polymer chains recombined after sonification. Cavitation process highly increases heat production during sonification (30, 31).

The aim of this study is to reveal the influence of ultrasonic relaxation on viscosity and group composition of heavy oil. Moreover, the light fragments were evaluated in detail by GC-MS analytical tool. The cavitation intensity was controlled using an acoustic method.

2. MATERIALS AND METHODS

Two crude oil samples were used in this study, one of which was isolated from Ashal'chi oil reservoir (Republic of Tatarstan, Russia) and the second one from North Komsomol oil reservoir (Yamalo-Nenetsk Autonomous Region, Russia).

LLC «VOLNA» (Moscow, Russia) developed the experimental set-up for the sonification of samples. This set-up allows to control the acoustic multifrequency fields at the given amplitude (32, 33). The schematic drawing of the set up is illustrated in Figure 1. The reactor (3) is connected to the thermostat (1), which allows it to maintain constant temperature. 100 mL of crude oil sample was maintained at temperature of 40°C for 1 hour before the sonification. The temperature of the samples during ultrasonic treatment is controlled by thermocouples (6). Temperature controlled reactor has a piezoceramic transducer mounted at the bottom (4) to produce the ultrasonic field.

The generator (9) was used to apply the high frequency signal to the transducer, it allows to regulate the amplitude of the waves by adjusting the power of the electric signal. Transformer (5) and oscilloscope (8) was used to detect and monitor the applied signal. The frequency of acoustic signal in the sample during sonification was also monitored using the hydrophone (7). Monitor for observation of data acquisition system (10) was used to record the signal processing. The spectrum of applied signal is shown in Figure 2. The main harmonics of the applied signal was 20 kHz.

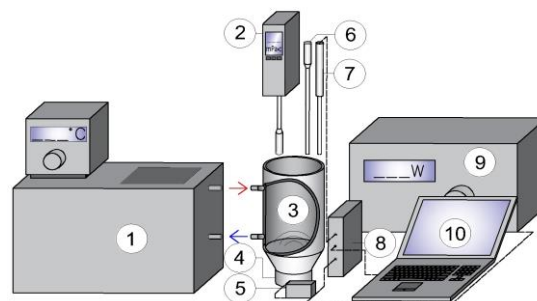


Figure 1. Experimental set-up for ultrasonic processing of oil 1. thermostat 2. viscosimeter 3. temperature-controlled reactor 4. piezoceramic ultrasonic transducer 5. current transformer 6. thermometer 7. hydrophone 8. digital oscilloscope 9. electric signal generator UZG-22 10. workstation

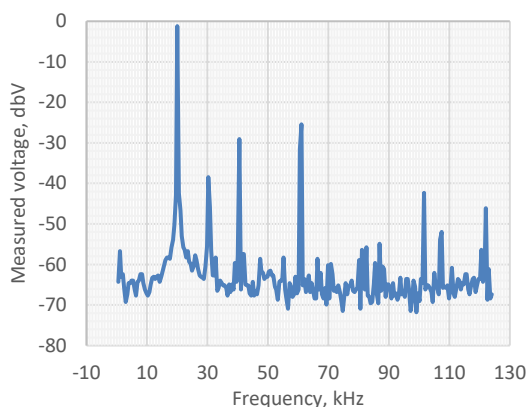


Figure 2. Applied signal spectrum

To determine viscosity changes during sonification PCE-RVI 2 viscosimeter was used. It was immersed into the reactor filled with crude oil immediately after sonification for the viscosity control during thermal conditioning. The viscosity of crude oil during viscosity relaxation was determined using a Fungilab Alpha L viscosimeter at 20 °C, 40 °C and 60 °C.

SARA analysis method was used to investigate the composition of crude oil after ultrasound treatment and relaxation. 40 ml of hexane was used to preipitate the asphaltene fraction from a gram of oil sample. The maltenes (de-asphalted oil sample) were extracted in Soxhlet extractor from the precipitate after filtration. The liquid adsorption chromatography in aluminum oxide was used to separate maltenes. The chromatography column had a diameter and length of 20 × 500 mm. Neutral aluminum oxide calcined at temperature of 450 °C for 3 h (as per TU 6-09-3916) was used to fill the column. After that maltenes were poured into the column and washed with hexane, toluene and toluene and methanol mixture to obtain saturates, aromatics and resins. All of the fractions were recovered from the solvents by distillation.

After SARA analysis saturates and aromatics were analyzed using Gas Chromatography and Mass Spectroscopy (GC-MS) in a Chromatec-Crystall 5000.2 chromatograph ("Chromatec", Yoshkar-Ala, Russia) and Mass-spectrometer 214.2.840.083-10 (ions source ADVIS). NIST (National Institute of Standards and Technology) library and relevant literature sources were used for the identification of molecules and compounds.

3. RESULTS AND DISCUSSION

An acoustic method of cavitation control was used during this study. Acoustic spectra for different oils during ultrasound treatment is shown in Figure 3, measured voltage is corrected for the ease of reading.

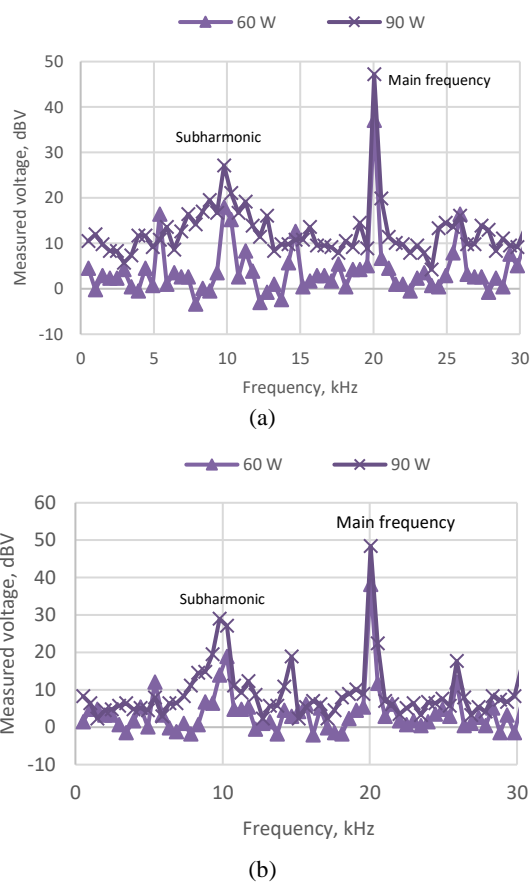


Figure 3. Acoustic spectra during sonification in: a) Ashal'chi crude oil, b) North-Komsomol crude oil

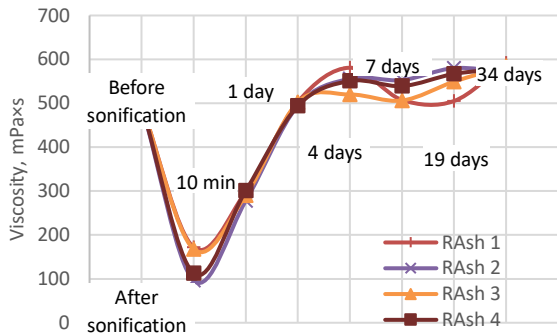
The highest peak on the spectra corresponds to the ultrasound signal (20 kHz). Subharmonic peak (10 kHz) corresponds to the intensity of cavitation process (34). Subharmonic peak appears at the power of ultrasound of 60 W. Due to the results of spectra measurements it was decided to perform all the tests in the range of 60-90 W. Treatment conditions are summarized in Table 1. It was decided to include the treatment duration of 10 min with pauses to avoid sample heating. Total duration of sonification in this case was 10 min.

Table 1 demonstrates that the biggest amount of heat was generated during the treatment at 90 W for 3 min. Pauses during the treatment allow significantly reduce heating.

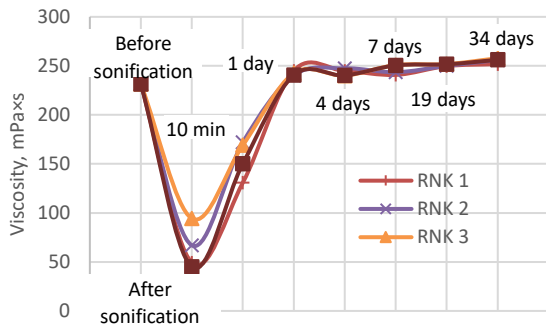
The viscosity measurements were performed before the treatment, after the treatment, 10 min after treatment and conditioning, and after 1, 4, 7, 19 and 34 days of relaxation at the temperature of 20 °C, 40 °C and 60 °C. During the relaxation samples were kept at ambient temperature of 20 °C. Measurement results are presented in Figure 4. Viscosity measurement temperature immediately after the treatment corresponds to the temperature in Table 1.

TABLE 1. Ultrasound treatment conditions.

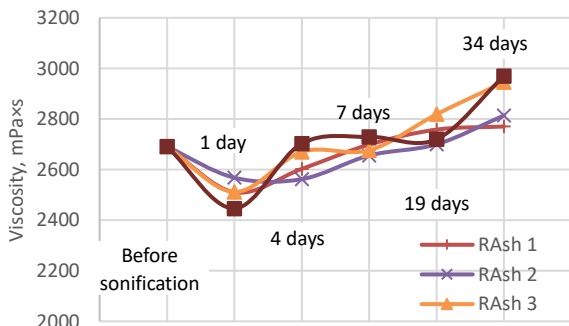
Sample	Crude oil	Ultrasound power	Duration	Temperature at the end of treatment
RAsh 1	Ashal'chi	60 W	3 min	43.4 °C
RAsh 2		90 W	3 min	53.4 °C
RAsh 3		60 W	10 min with 1 min pause every minute	46.3 °C
RAsh 4		60 W	10 min	50.3 °C
RNK 1	North-Komsomol	60 W	3 min	43.1 °C
RNK 2		90 W	3 min	54.9 °C
RNK 3		60 W	10 min with 1 min pauses every minute	46.6 °C
RNK 4		60 W	10 min	52.3 °C



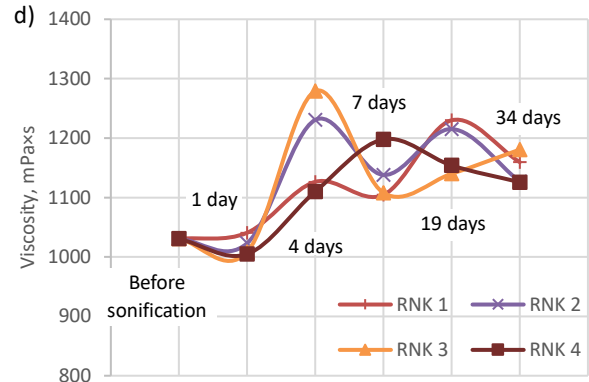
(a)



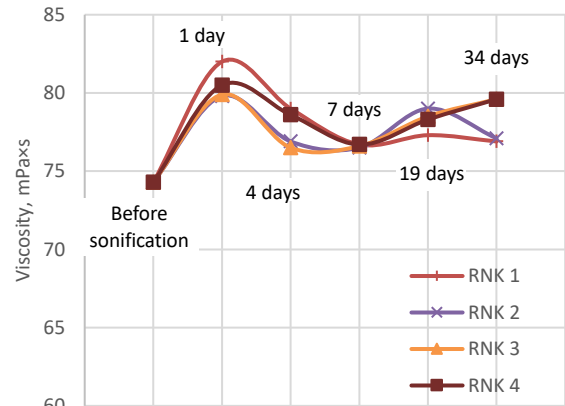
(b)



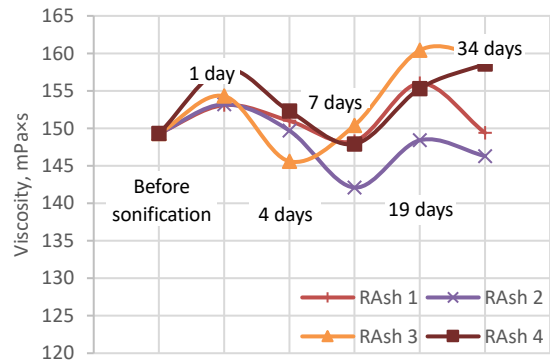
(c)



(d)



(e)



(f)

Figure 4. Crude oil viscosity after sonification: a) Ashal'chi 40 °C, shear rate 6.6 c-1, b) North-Komsomol 40 °C, shear rate 15.84 c-1, c) Ashal'chi 20 °C, shear rate 1.32 c-1, d) North-Komsomol 20 °C, shear rate 3.3 c-1, e) Ashal'cha 60 °C, shear rate 26.4 c-1, f) North-Komsomol 60 °C, shear rate 39.6 c-1

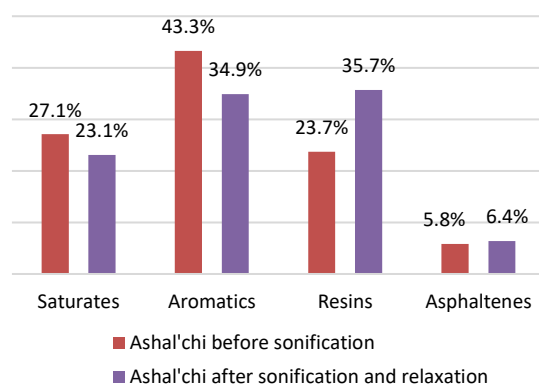
According to Figure 4, oil viscosity after 34 days increases to bigger level than before treatment, average increase is equal to 10% regardless of the treatment conditions. In the case of Figure 4, a, d, e, f an increase

of viscosity after 1-4 days can be seen. That effect can take place due to the formation of unstable temporary structure in the oil, which increases the oil viscosity. Ultrasound treatment itself can significantly reduce oil viscosity due to the oil heating and sonochemical destruction of the molecular structures and molecules, the viscosity of oil is significantly less after the treatment and conditioning than before the treatment. The viscosity reduction is equal to 80% after the treatment and 40% after the treatment and conditioning.

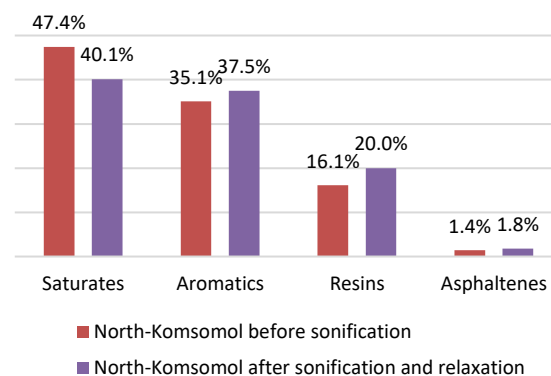
Measurement results indicate the possible molecular and aggregate structure destruction in crude oil after ultrasound treatment, which leads to the viscosity reduction. However, those changes are temporary, since molecular structure is tended to recover. During this process, temporary viscosity increase occurs, which indicates an unstable molecular structure appearance. After 7 days that temporary structures became more stable, making the oil less viscous, however viscosity is still higher than before the treatment due to the new molecular structure, which is formed under normal conditions. This new structure differs from an old structure, which was formed under the reservoir conditions.

The treatment conditions did not affect the viscosity changes significantly, that means that 3 minute and 60 W treatment is sufficient for the viscosity reduction of 100 mg of the crude oil.

After 34 days of relaxation SARA analysis of the samples exposed to 10 min of ultrasound without pauses was performed. The results are shown in Figure 5. Ultrasound treatment and relaxation lead to the increase of the polar components of oil and the reduction of saturates (Figure 5). Aromatics fraction is decreased in the case of Ashal'cha crude oil and increased in the case North-Komsomol crude oil. That means, during sonification and relaxation different parallel processes in the aromatic compounds occur. The reduction of saturates mean its destruction and association with the polar compounds, resins and asphaltenes.



(a)



(b)

Figure 5. SARA results before and after sonification and relaxation

The chromatogram of Ashal'chi crude oil before and after the ultrasound treatment and relaxation is shown in Figure 6. After the treatment and relaxation C25-C29 alkanes are appeared on the chromatogram.

Figure 7 presents the chromatogram of alkanes of North-Komsomol crude oil before and after an ultrasound treatment and relaxation. After the treatment and relaxation naphtenes peaks are increased as well as C14H30 and C17H36 alkanes.

In Figure 8, spectra of aromatics fraction of Ashalcha heavy oil sample before and after ultrasonic treatment and relaxation are presented. New peaks were observed on the specter after ultrasonic treatment, which corresponds to the benzenes with C12-C13 alkyl substitutes. Moreover, the intensity of the peaks corresponding to the benzene-thiophenes with C10H10S and C11H12S alkyls and 1,1-diphenylethane C14H14 was reduced.

In Figure 9, we illustrated the spectra of aromatics fractions isolated from the heavy oil samples of North-Komsomol field before and after sonification. We

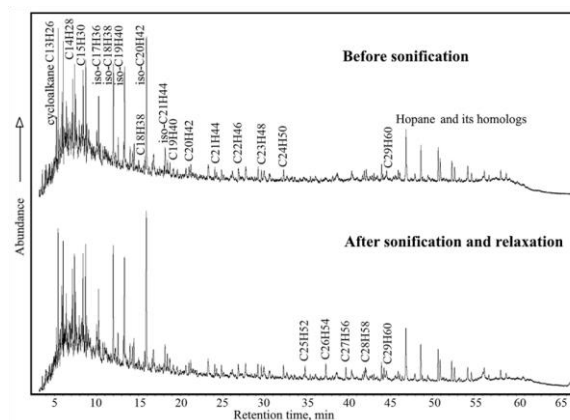


Figure 6. GC-MS spectra of saturates ($m/z=57$) isolated from Ashal'chi heavy oil samples

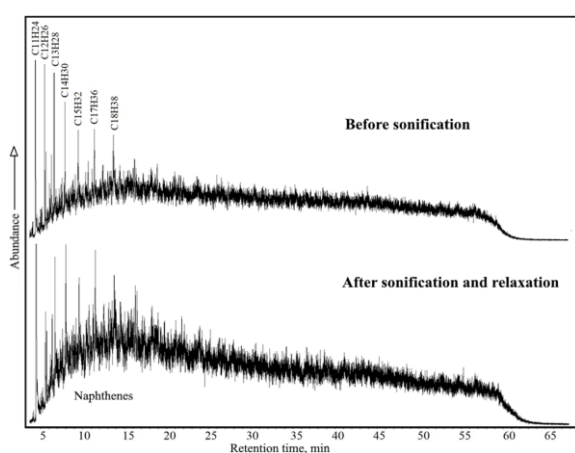


Figure 7. GC-MS spectra of saturates ($m/z=57$) isolated from North-Komsomol heavy oil samples

identified the new peaks corresponding to alkyl-tetrahydro-naphthalenes and alkylbenzenes with the composition of $C_{13}H_{16}$.

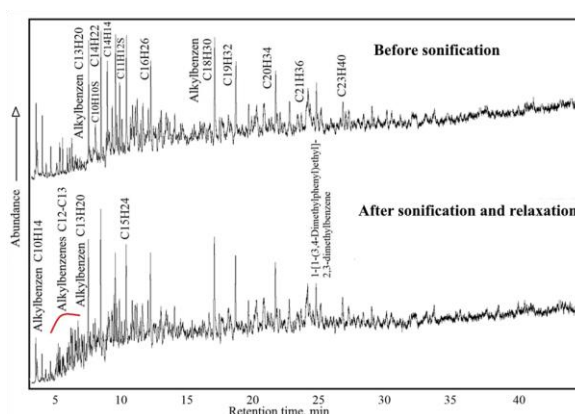


Figure 8. GC-MS spectra of aromatics isolated from Ashal'chi heavy oil samples

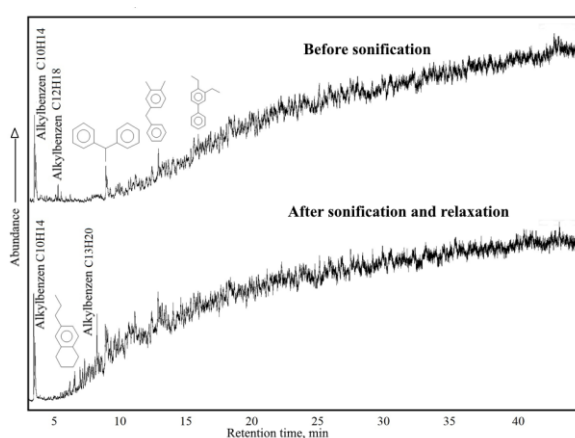


Figure 9. GC-MS spectra of aromatics isolated from North-Komsomol heavy oil samples

4. CONCLUSION

Ultrasonic treatment is a promising upgrading method to unlock the heavy oil production, transportation and refinery drawbacks. However, the long ultrasonic relaxation time can lead to the viscosity increase and decrease of light oil components. The following concluding remarks were achieved:

1. Ultrasonic treatment leads to instant heating of oil and a decrease in its viscosity, which is probably due to the destruction of its supramolecular structures.
2. A significant increase in viscosity after the relaxation period of 1-4 days, was observed, which may indicate the formation of large unstable supramolecular structures.
3. Stabilization of the structure and hence, viscosity was achieved after 7 days. However, the different power and sonication time under similar conditions did not have a noticeable effect on these processes.
4. Ultrasonic treatment of heavy oil with the long relaxation time contributed to the decrease in saturates and increase in heavy fragments such as resins and asphaltenes. The content of aromatics fraction was decreased in the composition of Ashal'cha heavy oil sample, while in case of North-Komsomol sample, it was increased. GC-MS results do not show significant changes of saturates and aromatics composition after ultrasonic treatment and relaxation.

In general, the results suggest that ultrasonic treatment can cause significant structural changes in oil and leads to a significant decrease in viscosity for the short period of time. This study expands the understanding of the behaviour of heavy oils with high resins and asphaltenes content after and during ultrasonic treatment in contrast to existing researches, where only short term effects were studied.

5. REFERENCES

1. Dvoynikov MV, Budovskaya ME. Development of a hydrocarbon completion system for wells with low bottomhole temperatures for conditions of oil and gas fields in Eastern Siberia. *Записки Горного института*. 2022;253:12-22. 10.31897/PMI.2022.4
2. Karpikov A, Aliev R, Babyr N, editors. An analysis of the effectiveness of hydraulic fracturing at YS1 of the Northern field. IOP Conference Series: Materials Science and Engineering; 2020: IOP Publishing. 10.1088/1757-899X/952/1/012036
3. Martuyshvili DA. Improving the geological and hydrodynamic model of a carbonate oil object by taking into account the permeability anisotropy parameter. *Записки Горного института*. 2020;243:313-8. 10.31897/PMI.2020.3.313
4. Ilyushin P, Vyatkin K, Kozlov A. Development of a method for estimating thermal conductivity of organic deposits on the wax flow loop laboratory installation. *International Journal of Engineering, Transactions C: Aspects*. 2022;35(6):1178-85. 10.5829/IJE.2022.35.06C.09
5. Askari Lasaki S. Oil Reservoirs Classification Using Fuzzy Clustering (RESEARCH NOTE). *International Journal of*

- Engineering, Transactions C: Aspects. 2017;30(9):1391-400. 10.5829/idosi.ije.2017.30.09c.12
6. Pemmadi VR, Patel J, Nagar A. Enhanced Oil Recovery. 10.22214/ijraset.2023.48875
 7. Raupov I, Rogachev M, Sytnik J. Design of a Polymer Composition for the Conformance Control in Heterogeneous Reservoirs. *Energies*. 2023;16(1):515. 10.3390/en16010515
 8. Lekomtsev A, Ilyushin PY, Stepanenko I, Mekhanoshina O, Bakaneev V, Korobov GY, et al. Technology of Stable Water-Oil Emulsion Breaking by Magnetic Impact. *Chemical and Petroleum Engineering*. 2021;57:98-105. 10.1007/s10556-021-00901-4
 9. Korolev M, Rogachev M, Tananykhin D. Regulation of filtration characteristics of highly watered terrigenous formations using complex chemical compositions based on surfactants. *Journal of Applied Engineering Science*. 2020;18(1):147-56. 10.5937/jaes18-24542
 10. Korobov GY, Parfenov DV, Van TN. MECHANISMS OF THE FORMATION OF ASPHALT-RESIN AND PARAFFIN DEPOSITS AND FACTORS INFLUENCING THEIR INTENSITY. Томского политехнического университета 2023. 2023:114. 10.18799/24131830/2023/4/3940
 11. Malarev V, Kopteva A, Koptev V, Gotsul Y. Improvement of efficiency of steam-thermal treatment of high-viscous oil formations using downhole electric steam generators. *Journal of Ecological Engineering*. 2021;22(2):17-24. 10.12911/22998993/130630
 12. Grigorev BM, Tananykhin SD, Poroshin AM. Sand management approach for a field with high viscosity oil. *Journal of Applied Engineering Science*. 2020;18(1):64-9. 10.5937/jaes18-24541
 13. Tananykhin D, Grigorev M, Simonova E, Korolev M, Stecyuk I, Farrakhov L. Effect of Wire Design (Profile) on Sand Retention Parameters of Wire-Wrapped Screens for Conventional Production: Prepack Sand Retention Testing Results. *Energies*. 2023;16(5):2438. DOI: 10.3390/en16052438
 14. Hemmati-Sarapardeh A, Dabir B, Ahmadi M, Mohammadi AH, Husein MM. Toward mechanistic understanding of asphaltene aggregation behavior in toluene: The roles of asphaltene structure, aging time, temperature, and ultrasonic radiation. *Journal of Molecular Liquids*. 2018;264:410-24. 10.1016/j.molliq.2018.04.061
 15. Evdokimov IN, Fesan AA, Losev AP. Asphaltenes: Absorbers and scatterers at near-ultraviolet-visible-near-infrared wavelengths. *Energy & Fuels*. 2017;31(4):3878-84. 10.1021/acs.energyfuels.7b00114
 16. Matveenko V, Kirsanov E. The viscosity and structure of dispersed systems. *Moscow University Chemistry Bulletin*. 2011;66:199-228. 10.3103/S0027131411040079
 17. Hasan MA, Shaw JM. Rheology of reconstituted crude oils: Artifacts and asphaltenes. *Energy & fuels*. 2010;24(12):6417-27. 10.1021/ef101185x
 18. Hassanzadeh M, Abdouss M. A comprehensive review on the significant tools of asphaltene investigation. Analysis and characterization techniques and computational methods. *Journal of Petroleum Science and Engineering*. 2022;208:109611. 10.1016/j.petrol.2021.109611
 19. Vasilyev V, Salamatova E, Maidanova N, Kalinin M, Strakhov V. Change in properties of roadmaking bitumen on oxidation. *Coke and Chemistry*. 2020;63(6):307-14. 10.3103/S1068364X20060083
 20. Krasnikov P, Gavrilo M, Efimenko K, Egorov A, Nikitchenko N, Tyukilina P, et al. Investigation of the Effect of Ultrasonication on the Properties of Feedstock for Production of Compounded Road Asphalts. *Petroleum Chemistry*. 2018;58:646-50. 10.1134/S0965544118080133
 21. Wang Z, Xu Y, Gu Y. Lithium niobate ultrasonic transducer design for enhanced oil recovery. *Ultrasonics Sonochemistry*. 2015;27:171-7. 10.1016/j.ultrsonch.2015.05.017
 22. Rahimi MA, Ramazani SA A, Alijani Alijanvand H, Ghazanfari MH, Ghanavati M. Effect of ultrasonic irradiation treatment on rheological behaviour of extra heavy crude oil: A solution method for transportation improvement. *The Canadian Journal of Chemical Engineering*. 2017;95(1):83-91. 10.1002/cjce.22676
 23. Qiao J, Song W, Wang W, Yuan X, Li L, editors. Experimental study of aging oil viscosity reduction caused by ultrasound. *Proceedings of Meetings on Acoustics*; 2017: AIP Publishing. 10.1121/2.0000695
 24. Lv S, Peng S, Zhang R, Guo Z, Du W, Zhang J, et al. Viscosity reduction of heavy oil by ultrasonic. *Petroleum Chemistry*. 2020;60:998-1002. 10.1134/S0965544120090194
 25. Abramov VO, Abramova AV, Bayazitov VM, Mullakaev MS, Marnosov AV, Ildiyakov AV. Acoustic and sonochemical methods for altering the viscosity of oil during recovery and pipeline transportation. *Ultrasonics sonochemistry*. 2017;35:389-96. 10.1016/j.ultrsonch.2016.10.017
 26. Mullakaev M, Volkova G, Gradov O. Effect of ultrasound on the viscosity-temperature properties of crude oils of various compositions. *Theoretical Foundations of Chemical Engineering*. 2015;49:287-96. 10.1134/S0040579515030094
 27. Kadyirov A, Karaeva J. Ultrasonic and heat treatment of crude oils. *Energies*. 2019;12(16):3084. 10.3390/en12163084
 28. Hague D. *Chemical relaxation*. Nature Publishing Group UK London; 1977.
 29. Volkova G, Anufriev R, Yudina N. Effect of ultrasonic treatment on the composition and properties of waxy high-resin oil. *Petroleum Chemistry*. 2016;56:683-9. 10.1134/S0965544116080193
 30. Hassanjani-Roshan A, Vaezi M, Koohestani H, Cheraghi F. Investigating the effect of ultrasound intensity on the magnetic properties of magnetite nanostructures synthesized by sonochemical method. *International Journal of Engineering, Transactions C: Aspects*. 2023;36(6):1034-9. 10.5829/IJE.2023.36.06C.01
 31. EL-Wazery M, Mabrouk O, Khafagy S, R El-sissy A. Mechanical and Microstructural Evaluation of AA6082-T61 Joints Produced by Ultrasonic Vibration Assisted Friction Stir Welding Process. *International Journal of Engineering, Transactions C: Aspects*. 2022;35(12):2297-304. 10.5829/ije.2022.35.12c.04
 32. Kuryakov V, editor Influence of ultrasonic treatment on kinetic of asphaltene aggregation in toluene/heptane mixture. *Journal of Physics: Conference Series*; 2021: IOP Publishing. 10.1088/1742-6596/1942/1/012035
 33. Dengaev AV, Kayumov AA, Getalov AA, Aliev FA, Baimukhametov GF, Sargin BV, et al. Chemical Viscosity Reduction of Heavy Oil by Multi-Frequency Ultrasonic Waves with the Main Harmonics of 20–60 kHz. *Fluids*. 2023;8(4):136. 10.3390/fluids8040136
 34. Hasanzadeh H, Mokhtari-Dizaji M, Bathaie SZ, Hassan ZM. Evaluation of correlation between chemical dosimetry and subharmonic spectrum analysis to examine the acoustic cavitation. *Ultrasonics sonochemistry*. 2010;17(5):863-9. 10.1016/j.ultrsonch.2010.02.009

COPYRIGHTS

©2024 The author(s). This is an open access article distributed under the terms of the Creative Commons Attribution (CC BY 4.0), which permits unrestricted use, distribution, and reproduction in any medium, as long as the original authors and source are cited. No permission is required from the authors or the publishers.



Persian Abstract

چکیده

در این مقاله به بررسی تغییرات ویسکوزیته و ترکیب گروهی نمونه های نفت سنگین پس از فرآیند ارتقاء اولتراسونیک می پردازیم. نمونه های نفت سنگین مربوط به میدین نفتی مختلف) واقع در روسیه (تحت حالت های مختلف اولتراسونیک پردازش شدند که پیامد کاویتاسیون آن با روش آکوستیک کنترل شد. ویسکوزیته نمونه ها بلافاصله پس از درمان اولتراسونیک، 10 دقیقه و 1-34 روز اندازه گیری شد. تجزیه و تحلیل SARA پس از درمان اولتراسونیک با 34 روز آرامش انجام شد و نتایج به دست آمده با فراکسیون SARA نفت خام اصلی مقایسه شد. نتایج اندازه گیری ویسکوزیته کاهش ویسکوزیته را پس از درمان اولتراسونیک نشان داد. با این حال، ویسکوزیته پس از 1-4 روز آرامش با کاهش بیشتر در 7 روز پسرقت شد. درجه افزایش ویسکوزیته پس از 34 روز تنها 10 درصد در مقایسه با ویسکوزیته نفت خام اصلی بود. قدرت و زمان فراصوت بر روند آرامش تأثیری نداشت. با توجه به نتایج تجزیه و تحلیل SARA، محتوای اشیاع کاهش یافته و محتوای نسبی قطعات سنگین مانند رزین ها و آسفالتین ها افزایش یافته است که تعیین کننده درجه افزایش ویسکوزیته پس از دوره آرامش است.



Comprehensive Review of Demulsifiers based on Magnetic Nanoparticles for Oil-water and Water-oil Separation

Y. Rozhkova^a, A. Lekomtsev^{*b}, V. Lisin^b, V. Poilov^a, E. Safiullina^c, D. Efremenko^c, A. Dengaev^d, W. Kang^e, Z. Li^e, H. Yang^e

^a Faculty of Chemical Technology, Perm National Research Polytechnic University, Perm, Russia

^b Mining and Oil Faculty, Perm National Research Polytechnic University, Perm, Russia

^c Oil and Gas Faculty, Saint Petersburg Mining University, St. Petersburg, Russia

^d Department of Petroleum Engineering, Gubkin National University of Oil and Gas, Moscow, Russia

^e School of Petroleum Engineering, China University of Petroleum (East China), Qingdao, Shandong, China

PAPER INFO

Paper history:

Received 03 December 2023

Received in revised form 16 January 2024

Accepted 20 January 2024

Keywords:

Magnetic Demulsifier

Water-in-oil Emulsion

Oil-in-water Emulsion

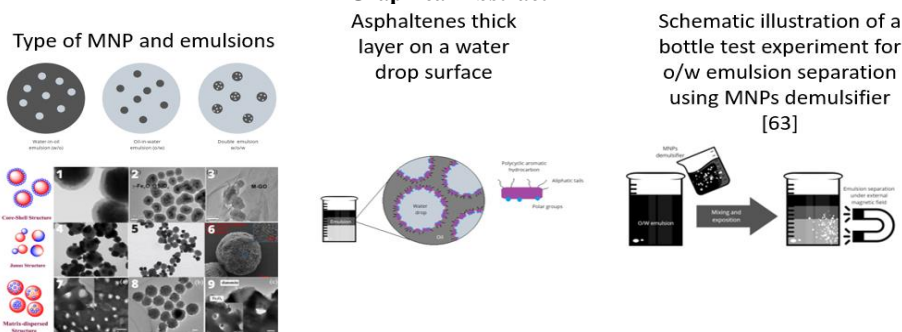
Emulsion Separation

A B S T R A C T

Oil-water emulsion causes a wide range of problems, one of which is the emergence of significant decreases in pressure in flow lines resulting in higher pumping and transportation costs. The most widely developed trend among oil/water separation technologies is using demulsifiers based on magnetic nanoparticles (MNPs). MNPs have specific chemical and mechanical properties, providing unique opportunities to solve oil production issues. The key features of such magnetic nanoparticles for their sustainable application are their reusability and stability; the opportunity of remote manipulation using external magnetic fields gives them a singular benefit in transport operations. The main objective of the study is the systematization of MNPs researches for effective oil and water emulsion separation. This review provides MNP demulsifier characteristics, Oil-water emulsions (OWE) separation mechanism, and factors influencing oil-water emulsions efficiency disruption by MNP demulsifier. The relevance of this study is that oil-water emulsions are often encountered in practice during field development. To solve this problem, the use of demulsifiers based on magnetic nanoparticles is proposed. The novelty of the work lies in the fact that the work collects several factors affecting demulsification at once and describes the impact of each factor. Among these factors, the most influential are: emulsion characteristics, water salinity, pH, reservoir temperature, addition of chemical surfactants, time and magnetic field. The mechanism of formation of oil-water emulsions of various types is also described, and negative consequences of emulsion formation are discussed. The results showed that the magnetic nanoparticles need a protective layer and the demulsifier should have good wettability by the continuous phase of the emulsion.

doi: 10.5829/ije.2024.37.05b.09

Graphical Abstract



*Corresponding Author Email: lav@pstu.ru (A. Lekomtsev)

Please cite this article as: Rozhkova Y, Lekomtsev A, Lisin V, Poilov V, Safiullina E, Efremenko D, Dengaev A, Kang W, Li Z, Yang H, Comprehensive Review of Demulsifiers based on Magnetic Nanoparticles for Oil-water and Water-oil Separation. International Journal of Engineering, Transactions B: Applications. 2024;37(05):904-19.

NOMENCLATURE

H	Strength of the applied magnetic field	χ_a	Linear component of the susceptibility
M_0	Saturation magnetization of superparamagnetic nanoparticles	V	Volume of magnetic nanoparticle
$L(x) = \coth x - 1/x$	Langevin function	M	Magnetization of magnetic nanoparticle
x	Langevin parameter	∇H	Gradient of magnetic field
μ_p	Average magnetic moment of each superparamagnetic nanoparticle	μ_0	Magnetic permeability in vacuum
T	Temperature		

1. INTRODUCTION

The oil industry faces the continuing challenge of improving operating well efficiency. This acquires particular relevance in the development of anomalous oil deposits, where well operation is complicated by high oil viscosity, asphalt-resin-paraffin deposits, and stable oil-water emulsions (OWE) in the form of intermediate emulsion layers during crude oil production and preparation. The large deposits of the Volga-Ural region are represented by the anomalous oils in the Devonian and Carboniferous deposits that are currently the region's main development targets. The operating features of such deposits include low reservoir and wellhead temperatures, high water cut, and high viscosity in the phase inversion sites typical for most of the fields located in the Perm Territory. Such problems are especially relevant during the well production of crude oil with water cut in the 60-70% range (1). The instability of the in-line demulsification process and oil treatment at on-site facilities leads to the production of poor-quality products and ultimately to a decrease in the latter's consumer cost. Maintaining the required oil conditions and processing off-grade oily fluids using affordable and economically-justified thermal, physical, and chemical methods at all stages of collection, transportation, and preparation are among the most important tasks of full-production-cycle oil companies. Oilfield experience shows that complex emulsion separation methods are considered more effective at the current stage of the development of cross-functional and end-to-end technologies. Among them, the application of magnetic nanoparticle (MNP) demulsifier is the most perspective technology for the intensification of in-line OWE demulsification due to its unique properties, particularly quick response, easy separation from the oil-water system under a magnetic field, and reusability even in complex field conditions. This systematic review presents an analysis of MNP research cases for the separation of crude material which is presented by oil – water (o/w and w/o) emulsion starting 2015, and provides information about the types, methods of particle synthesis, and demulsification test results. The authors hope that this article will help the novice researcher quickly grasp the main aspects of the MNP application.

2. MATERIALS AND METHODS

There are several approaches to preparing a review research (2). One most commonly used model is the PICO(S) model, which is mostly used for medical reviews (3, 4). The researcher must consider several questions when performing a literature review: problem, intervention, comparison, and outcomes. We decided to apply this approach for the article. As such, this article is divided into sections in accordance with the questions suggested by the PICO(S) model. The first section of the article declares the problem and formation mechanism of crude OWE. The second section presents a short review of modern approaches to OWE separation. The following sections are devoted to MNP demulsifiers, their characteristics, mechanisms and factors influencing OWE demulsification efficiency. At the end of the article, the outcomes impacting the effectiveness and prospective of magnetic demulsifiers application are represented.

The comprehensiveness of the literature research is provided by the quality of research data. All references to articles were taken from Science Direct, ACS Publications, and One Petro databases.

Analysis of search results for the request “magnetic crude oil demulsifier” on Science Direct gave 279 results, and 161 research articles were published from 1988 to 2022. Figure 1 shows a well-established trend of an increase in the number of articles, which is evident of a constant increase of researchers' interest in the study and development of magnetic demulsifiers. In this review, we

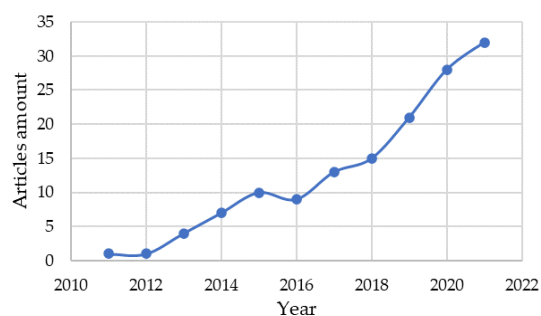


Figure 1. The growth in the number of articles since 2010 on the topic of magnetic demulsifiers for crude oil

will mainly consider research articles published since 2015.

3. OWE DAMAGE AND FORMATION MECHANISMS

OWE formation is a very undesirable and inevitable process in the petroleum industry. OWE can cause problems such as the appearance of high pressure drops in flow lines and higher pumping and transportation costs; an escalated corrosion rate; a lower oil API gravity (5). Hydrocarbon field development over 1-3 years inevitably leads to emulsion formation in the reservoir before its appearance on the surface onsite facilities. The emulsion is broken into two phases before transportation and treatment, the specific water and salt residual standard must be met, and the water content must be less than 1% (6). Several reviews describe crude oil/brine formation mechanisms (7, 8). In this section of the article, we will shortly consider several types of oil and water emulsions; mechanisms, and reasons for their formation.

Emulsion is a two-phase system consisting of several immiscible liquids one of which (the dispersed phase) is constantly dispersed in the form of balls in the second phase (solid phase) under the action of emulsifiers (9, 10). It is known three types of emulsion: water in oil (W/O), oil in water (O/W), and multiple (complex or double) emulsions (see Figure 2) (11, 12). Crude oil and reservoir water contain components contributing to emulsion formation and stabilization, that is, natural emulsifiers. These emulsions can be highly sustained due to the appearance of interfacially active compounds such as naphthenic acids, resins, asphaltenes, or solids (13, 14). For better understanding, the MNP demulsification mechanism, in this section, we will consider basic crude oil emulsifier-components, their structure, and their impact on emulsion formation.

3. 1. Asphaltenes Asphaltenes are represented by a non-homogeneous fraction consisting of polyfunctional molecules of crude oil that are insoluble in n-alkanes (typically heptane and etc.) and soluble in toluene (15). This fraction has the lowest H/C ratio among all crude oil components (16). It concentrates the majority of heteroatoms like oxygen, sulfur, and nitrogen (see Figure 3) and metallic elements like vanadium and nickel (15, 16). Asphaltenes contain both acid (e.g. phenolic functions) and basic (e.g. derivatives of pyridines) functionalities. Different models describe the asphaltene structure. One is the archipelago model, which views asphaltenes as small polyaromatic parts linked together by aliphatic or naphthenic moieties. The other is the continental model, which considers asphaltenes as single polyaromatic rings (polycyclic aromatic hydrocarbon) with connected aliphatic or naphthenic chains (15). A recently research has demonstrated that asphaltenes are small molecules mainly containing a polycyclic aromatic

group made of about 7 rings with linear attached hydrocarbon chains. The molecule has a molecular weight of 750 Da (16). The main properties of asphaltenes are self-association in solution and the ability to adsorb at interfaces (both the solid/liquid and liquid/liquid) (15-17). These properties allow asphaltenes to stabilize water/oil emulsions by leading to the difficulty of water droplets coalescence through organizing a thick layer on its surface (Figure 4) (15, 17). Asphaltenes adsorb at the liquid/liquid (water/oil) interface as shown by interfacial tension measurements. It has been discovered that asphaltenes form a rigid film at the interface of both phases - water and oil.

3. 2. Resins Resins have structural similarity with typical surfactant molecules: One part of chain is hydrophilic with polar functional groups; the other part of chain is hydrophobic and consists of alkyl chains. The stability of the emulsion maintained by asphaltenes is due to the highly viscoelastic films surrounding the water droplets, while resins enhance stability by replacing asphaltenes when the bond of asphaltenes decreases for a certain period (6).

3. 3. Naphthenic Acids The group of aliphatic organic carboxylic acids that contain one or more rings, such as monocyclic and polycyclic carboxylic acids and small amounts of acyclic and aromatic acids, includes naphthenic acids (18). The chemical formula of naphthenic acid is $C_nH_{2n}+ZO_2$, where n denotes the number of carbon atoms and Z is zero or a negative (in the event of a lack of hydrogen due to ring formation or double bonds) (19, 20). Naphthenic acids can be described mainly as C10–C50 compounds with 0–6 rings (21). The possible structures of naphthenic acids are represented in Figure 5. Naphthenic acid concentration in crude oil can reach as high as 4 wt.% (19). The naphthenic acids properties depend on the ionization degree, i.e., the pH of the produced water. They can react with cations (such as Ca^{2+} and Na^+) forming active surfactants (15, 21, 22). Together with asphaltenes, naphthenic acids take part in the stabilization of water/oil emulsion. The stabilization mechanism of emulsion may differ depending on the acid structure. In particular, unsaturated monocarboxylic acids co-adsorb at the water/oil interface together with asphaltenes; dicarboxylic acids form naphthenic salts and then create

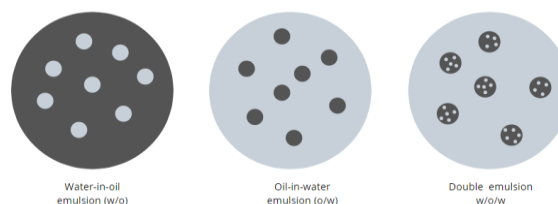


Figure 2. Types of emulsion

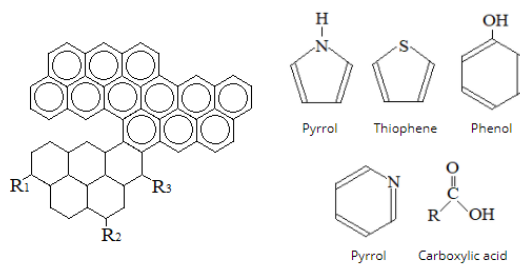


Figure 3. Typical asphaltene molecules

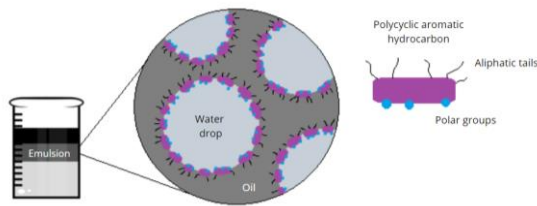


Figure 4. Asphaltenes thick layer on a water drop surface

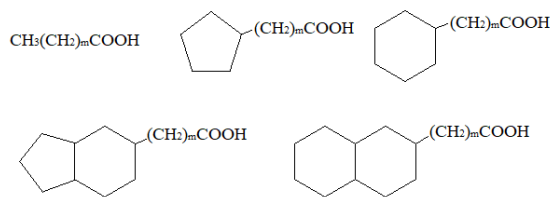


Figure 5. Structures of naphthenic acids

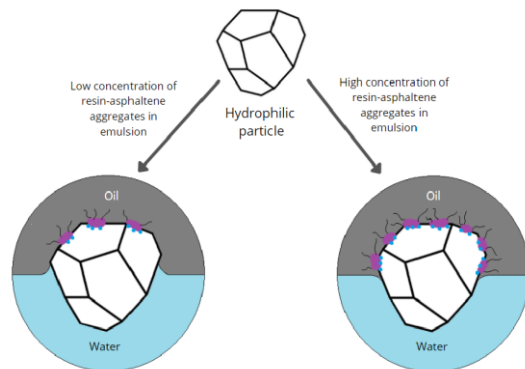


Figure 6. Resin and asphaltene aggregates adsorption onto a hydrophilic particle surface

the first layer on the water drop, which favors asphaltene adsorption (23).

3. 4. Inorganic Particles (Clay, Sand, Minerals)

Emulsions stabilized by solid particles are called Pickering emulsions. The type of emulsion depends on the wettability of solid particles at the interface of oil and

water: the liquid with better wetting properties to solid particles becomes the continuous phase, while the other (with worse wetting properties) becomes the dispersed one (24). Particles with a contact angle of $\theta < 90^\circ$ (water-wet particles) are effective in stabilizing oil-in-water (O/W) emulsions, while those with a contact angle of $\theta > 90^\circ$ (oil-wet particles) are effective in stabilizing water-in-oil (O/W) emulsions. If the particles are too hydrophobic (high θ) or too hydrophilic (low θ), they will be dispersed in the aqueous or oil phase, leading to emulsion separation (25).

The hydrophobicity of inorganic particles present in reservoirs can be caused by long-term contact with the oil. These results show a change in particle wettability due to the accumulation of particles at interfaces caused by the adsorption of asphaltenes and resins from crude oil. (see Figure 6) (26). By increasing particle concentration raises emulsion stability (26-28).

3. 5. Tertiary EOR Methods Contribution to Oil and Water Emulsification

Basic tertiary EOR methods contributing to OWE formation are alkaline, surfactant, polymer flooding and their combinations (for example, alkaline-surfactant-polymer flooding) (29-31). Several mechanisms have been identified that facilitate oil recovery in the alkaline process: interfacial tension lowering; oil emulsification; and changes of the rock formation wettability. In the case of alkaline flooding, emulsion formation becomes the oil recovery enhancement mechanism. The higher the acid number of oil, the more reactive it will be and the more readily it will form surfactants (27). Surfactant formation is the reason for OWE stabilization.

In addition, divalent cations existing in clays and water interact with alkali and precipitates (scale problems) and the large amounts of alkali lead to the stable emulsion formation. Therefore, the alkali is mostly combined with the polymer and surfactant for a higher oil recovery factor (28). However, Li et al. (29) explored the effect of partially hydrolyzed polyacrylamide (HPAM) on the formation of oil/water emulsion. The research establishes that HPAM may be adsorbed at the interface and increase the strength of the interfacial film and the absolute value of Zeta potential (29).

Li et al. (30) described a field case of alkaline-surfactant-polymer flooding using sodium hydroxide as the alkali component to enhance oil recovery on on-shore oil fields at Daqing in China. The alkali injected into the reservoir formed a stable W/O emulsion, although the crude oil was represented predominantly by a paraffinic fraction. They explained emulsion creation through interfacially-active soap molecule formation from carboxylic acids of the Daqing crude oil. These formed interfacially-active molecules are responsible for providing stability to the W/O emulsion (30).

4. MODERN APPROACHES TO CRUDE OIL-WATER EMULSION SEPARATION

Emulsion stability is ensured by the absence of a disperse-phase droplet coalescence (21, 26). This process occurs in the following steps: aggregation (the distance between dispersed liquid droplets is reduced; of the droplets drops are deformed, a thin film forms between them); and coalescence (the film breaks and the droplets coalesce) (9, 31). There are several mechanisms that resist coalescence: the Marangoni-Gibbs effect; steric repulsion; electrostatic repulsion, which retards film drainage; and thin film stabilization (26). Demulsification can be achieved using four main approaches: mechanical (filtration, membrane separation), electrical (voltage application), thermal, chemical (pH adjustment, treatment by demulsifier) and their combinations (6, 22). Several reviews exist that cover the physical and chemical approach for oil/water emulsion separation, particularly mechanical, thermal, electric, microwave, and other approaches (32-34). However, chemical demulsification is still the most widespread method because the application of the chemical is a cost-effective solution that saves energy and time (9, 35). Raya et al. (2), Grenoble and Trabelsi (31) gathered most of the above approaches to chemical demulsifier composition formulation. There are different types of surfactants functioning as demulsifiers like block co-polymeric of polypropylene and polyethylene oxide (pluronic surfactants) (36, 37) and its amine derivatives (like poloxamines), alkylamines, quaternized ammonium based cationic surfactants, zwitterionic demulsifiers (betaine-type), polysiloxane-polyether copolymer, unconventional surfactants like ionic liquid derivatives. A comparative test of such compounds as amie demulsifiers, polyhydric alcohol (PEGs, ethylene and propylene glycols), acid (sulphonate group), and polymeric demulsifiers (oilyethelen oxides and other) were conducted (38). The test results showed that reagents containing amino groups are more effective compared to demulsifiers containing hydroxyl and carboxyl functional groups (38). It was demonstrated that ionic liquids and polymers are more effective than traditional nonionic and anionic surfactants. Adewunmi and Kamal (39) presented studies of demulsifiers based on phosphonium-type ionic liquids with anionic components (including chloride, decanoate, and dicyanamide ions). In addition, imidazole-based ionic liquids (40), quaternary ammonium compound salts (N-alkyltriethylammonium bromide), and others can be used as demulsifiers (41). Among biodemulsifiers, such substances as ethyl cellulose, ethoxylated cocoamine, and α -amylase are considered (33). Detailed studies of α -amylase are presented by Jiang et al. (42). It has been shown that α -amylase is an effective biodemulsifier for W/O emulsion even at room temperature. However,

chemical demulsifiers must meet the following requirements: full removal of water and salts in small consumption per ton of oil; accessibility; low cost; must be environmentally friendly and meet the requirements of environmental standards and regulations (9, 43). One more highly developed trend in oil/water separation is demulsifiers based on magnetic nanoparticles (MNPs). MNPs have specific chemical and mechanical properties, and therefore offer unique opportunities for solving well production issues in new ways. The key features of such magnetic nanoparticles for their sustainable application are their reusability and stability (44); the possibility of remote manipulation by external magnetic fields which give them a special benefit in transport operation (45, 46). The main objective of this study is a systematization of MNPs research cases for effective oil and water emulsion separation.

5. MNP DEMULSIFIERS AND THEIR MAIN CHARACTERISTICS

MNP demulsifiers are chemical structures made by combining MNPs with other substances that perform a protective function, surface hydrophobization, or hydrophilization, and other functions.

The core exhibits superparamagnetic or ferromagnetic properties, which facilitates directional migration and magnetic induction heating under various magnetic fields. The reactive groups of the species degraded from the shell can be conjugated to specific molecules and thus functionalized. Therefore, functionalized MNPs possess the characteristics of magnetic particles and shell materials, which helps to improve the demulsification effect (45-48).

MNP magnetic cores can be made from iron oxides $\text{Fe}_2\text{O}_3/\text{Fe}_3\text{O}_4$, pure metals Fe and Co, and spinel-type ferromagnetics MgFe_2O_4 , MnFe_2O_4 , or CoFe_2O_4 (45, 47, 48). A number of materials, such as propyleneoxide-ethyleneoxide, block polyether, oleic acid, chitosan, N-isopropylacrylamide, sodium methacrylate, graphene oxide, tetraethyl orthosilicate, and other substances have been used for MNP surface modification (see Table 1). The quality of MNPs coated by modification material is estimated using the zeta potential. For example, the zeta potential of Fe_3O_4 nanoparticles in mmol/L KCl aqueous solutions was positively charged with a mean 22.07 mV. After its surface modification by SiO_2 , the MNPs became negatively charged with a mean zeta potential of -53.13 mV. This result also confirmed a full surface coverage of silica films on the MNPs (49).

Magnetite (Fe_3O_4) is an ideal magnetic material because of its low cytotoxicity and good biocompatibility (46). The synthesized Fe_3O_4 MNPs exhibited good demulsification performance. However, they are oxidized in the atmosphere and corroded in acidic

TABLE 1. Systematization of available cases of developed MNP-demulsifiers since 2015

Substance code	Method of synthesis and MNP's type	MNP's size, nm	The saturation magnetization, emu/g	Type of emulsion	Concentration	Effectiveness, %	Test temperature, C	Period of demulsification	pH	Recycle test (cycles)	Source
Fe ₃ O ₄ @OA	Chemical co-precipitation, Fe ₃ O ₄ with oleic acid (OA). OA molecules formed a single layer coating on the Fe ₃ O ₄ surface	12–14	No data	O/W	30 g/L	80	25	3 h	6.3–9.5	6	(46)
Fe ₃ O ₄ @OA	Chemical co-precipitation, Fe ₃ O ₄ with oleic acid. Spherical shape	12–14	24.07	O/W	100 g/L	97	25	12 h	4.0–7.5	5	(50)
PEMN	Solvothermal reaction, propyleneoxide-ethyleneoxide block polyether was endowed with the magnetism by reacting with iron (III) acetylacetonate. Core shell structure	11,41	9.08	W/O	0,625 g/L	100	70	30 min	No data	3	(51)
M-DMEA	Fe ₃ O ₄ @SiO ₂ nanoparticles covered by (3-glycidoxypropyl) trimethoxysilane, block copolymer of ethylene oxide (EO) and propylene oxide (PO) prepared by using N,N-dimethylethanolamine and 4-dimethylaminopyridine. Irregular shape with a core-shell structure	251	55.20	O/W	2,5 g/L	92,3	65	No data	No data	3	(49)
M-GO	Amino-functional Fe ₂ O ₃ @SiO ₂ (coded like c-Fe ₂ O ₃ @SiO ₂ -NH ₂) were anchored on the surface of GO matrix dispersed structure. Nearspherical core-shell nanoparticles where grinded on the GO particles	GO particles 100-1500 nm; amino-functional Fe ₂ O ₃ @SiO ₂ 100 nm	8.70	O/W	0,04-0,25 wt%	98,3-99,98	No data	5 min	2.0-4.0	6–7	(52)
Fe ₃ O ₄ @APFS-G-CS	Fe ₃ O ₄ MNPs were synthesized by using a solvothermal method with further coating of aminopropyl-functionalized silica (APFS) to form a surface for further grafting of chitosan molecular chains. Coreshell structure	350	30.5	O/W	0,4 g/L	90	25	30 min	pH 4.0 and 7.0	7	(53)
Fe ₃ O ₄ @AEAPFS MNPs	Fe ₃ O ₄ MNPs were synthesized by using a solvothermal method, AEAPFS layer was formed through a sol-gel process involving the hydrolysis and condensation of TEOS and N-(aminoethyl)-aminopropyl triethoxy silane (AEAPTES, 96%). Nearly spherical in shape, coreshell structure	360	51.9	O/W	650-800 mg/L depending on pH	99,9	no data	No data	various pH levels	5	(54)

Samples codes varies from S2 to S6	Fe ₃ O ₄ @SiO ₂ -MPS modified by N-isopropylacrylamide (NIPAM) and sodium methacrylate (SMA). Globular shape, core-shell structure	200	42.90-33.60	O/W	for S2 - 200 mg/L	99.9% at pH 6.0	30	No data	different	5	(55)
EP@APTE S-Fe ₃ O ₄	The expanded perlite (EP) was firstly modified by 3-aminopropyl triethoxysilane (APTES) to form the EP@APTES, and then magnetic Fe ₃ O ₄ nanoparticles (NPs) were further grafted onto the surface of EP@APTES. Globular shape, core-shell structure	200–300	46.30-34.10	O/W	500 mg/L	89-93% (pH ≤6)	No data	60 sec	pH 4.0-6.0	4	(56)
M-MWCNTs	Fe ₃ O ₄ @SiO ₂ -APTES particles are grafted onto the multi-walled carbon nanotubes amphiphilic surfactant. The type of structure is not clear, look like Janus particles	200–300	12.80	O/W	400 mg/L	93.3-94.2,	No data	No data	pH 2.0-6.0	5	(57)
P(MMA-AA-DVB)/Fe ₃ O ₄	Micro scale Poly(methylmethacrylate-acrylic acid-divinylbenzene) iron oxide Janus magnetic submicronic particles were prepared through soap free emulsion polymerization with methylmethacrylate and acrylic acid as a monomer, divinylbenzene as a cross-linker and potassium peroxy sulphate as initiator. Janus magnetic submicronic particles, raspberry like surface morphology	250	25.0	W/O	500 ppm	98%	60	1 h	pH 7.0-13.0	5	(58-60)
MAG-CMC-EC or M-CMC-EC	Fe ₃ O ₄ subsequently coated with carboxymethyl cellulose (CMC) (electrostatic force and hydrogen bonding), ethyl cellulose (EC) (esterification reaction). Core-shell structure	100	71.0	W/O		92%	25	3 h with magnetic field	No data	3	(44, 61)
M-Janus	Fe ₃ O ₄ subsequently coated with carboxymethyl cellulose (CMC) (electrostatic force and hydrogen bonding), ethyl cellulose (EC) (esterification reaction) and again CMC Janus magnetic particles	145	69.7	W/O, O/W		95% for W/O, 90% for O/W	No data	2 h without magnet, 30 min after setting strong magnet	No data	5	(44)
Fe ₃ O ₄ @PD A-PDMAPS (FPPM)	MNPs coated by Poly{3-[dimethyl(2-methacryloyloxyethyl) ammonio] propanesulfonate}. Core-shell magnetic microspheres	216	No data	W/O	0,85%-1%	no data	23	3 h without a magnet, then 68 hours on magnet	No data	No data	(62)
M-DM	Deatomite coated by (3-aminopropyl)-triethoxysilane, MNPs of Fe ₃ O ₄ , and polyethylenimine. Matrix dispersed structure	200–300	36.6	O/W	450 mg/L	95.3	25	60 sec	broad pH levels	5	(53)
MJ NPs	Fe ₃ O ₄ subsequently coated with carboxymethyl cellulose (CMC), ethyl cellulose (EC) and wax and again CMC. Core-shell structure	no data	No data	W/O	0,50%	78	25	15 min	No data	6	(63)

PEDHA- Fe ₃ O ₄	Synthesized through the covalent functionalization of magnetite (Fe ₃ O ₄) nanoparticles with Polyester bis-MPA dendron, 2-hydroxyl, 1-azide dendrimer. Core-shell structure	63.913 and 39.559 emu/g depending on the funct. layer thickness	W/O	15 mg/L	~78	60	50 h	No data	2	(64)	
Fe ₃ O ₄ @SiO ₂ @C	Fe ₃ O ₄ particles were first coated by dense silica through hydrolysis of tetraethyl orthosilicate (TEOS) at room temperature. Hydrophobic carbon could adsorb the air within their surroundings to form air film. Near-spherical, core-shell structure	464.4±19.85	no data	W/O	1%	100	25	5 days	No data	6	(65)
Fe ₃ O ₄ -SiO ₂	Preparation of Fe ₃ O ₄ -SiO ₂ by modified Stober process at room temperature. Sphere-shaped particles with clear-core shell structure	28.0 ± 3	42.3 ± 0.3	O/W	10 mg/L	93%-94.9%	25	10 min under the external magnetic fields	94-98	9	(66)
A-MNPs	Co-precipitation (co-ppt) method was used to synthesize MNPs, the MNPs surface has been consistently coated by 3-amino propyltriethoxysilane (3-APTES), sphere-shaped particles	21 to 255 nm	90	O/W	0.875 g/L	99.9 %	25	0.2 to 20 h, depending on the particle size	No data	No data	(67)

conditions. To protect it from corrosion, the surface of Fe₃O₄ MNPs is modified. Usually, the MNPs are first coated with a silica shell to prepare Fe₃O₄@SiO₂ MNPs, and then some functional macromolecular chains are imposed (54). MNPs prepared on the basis of Fe₃O₄ can generally be classified into four types according to their structures: Fe₃O₄@SiO₂@compounds particles, Fe₃O₄@compounds particles, compounds of cross-linked polymers and Fe₃O₄, and magnetic amphiphilic composites (51).

Adewunmi et al. (68), Wunet al. (69) presented MNP synthesis methods like: co-precipitation synthesis, solvothermal synthesis, sol-gel synthesis, redox synthesis, microemulsion, hydrothermal, sonochemical, and chemical vapor deposition. Zhu et al. (70), considered the advantages and disadvantages of MNP synthesis methods. For example, they considered the co-precipitation method to be a simple and efficient technique; however, unlike other methods, co-precipitation does not allow to control particle size distribution. The microemulsion method allowed controlling particle size, but the synthesis takes a lot of time and large amounts of solvent (70).

MNP-demulsifier type and size depending on the synthesis method. There are three basic types of MNP-demulsifier structures: core-shell, matrix-dispersed, and Janus structure (45). We selected photographs (mostly made by transmission electron microscopy, TEM) of different types of magnetic nanoparticles from different sources (see Figure 7).

All the cases that we analyzed show a wide range of examples of MNPs with a core shell structure, a few examples with a Janus structure, and only one with a matrix-dispersed structure. There is an opinion that the magnetic properties of nanoparticles can be affected by the type of MNP (14, 47).

MNPs with core-shell structures are considered less efficient demulsifiers due to the possibility of their desorption from the interface under an external magnetic force (11). Janus MNPs have a unique surfactant-like structure and, consequently, an asymmetric surface

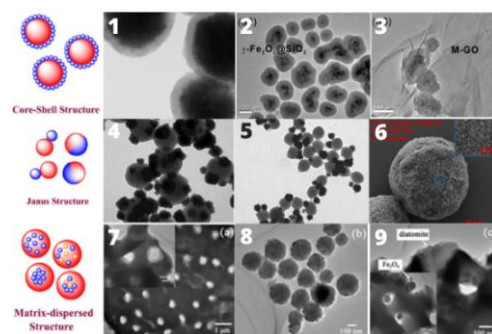


Figure 7. Typical structures of MNPs. The basic visual structures of MNPs were taken from (left column). 1-9 pictures were taken as real MNP examples from the following sources: 1 - Fe₃O₄@PDA-PDMAPS (FPPM); 2 - γ -Fe₂O₃@SiO₂; 3 - M-GO; 4 - P(MMA-AA-DVB)/Fe₃O₄, raspberry like structure (version of Janus like MNPs); 5-6 - M-Janus MNPs; 7-9 - M-DM MNPs

wettability. These types of MNPs can perform higher interfacial tension than conventional core-shell MNPs and demonstrate a stronger deposition on a water or oil droplet surface, as they require higher energy to desorb from the interface (22). However, Janus MNPs are better applied to O/W emulsions due to their high hydrophilicity (22-25). In fact, it is quite difficult to establish any correlation between MNP structure and demulsification efficiency: according to the data in Table 1, a high demulsification efficiency is typical of all three types of particles.

In Table 1, we collected data on available cases of MNP-demulsifiers that were developed basically since 2015. MNP-demulsifier size may vary from 12-14 nm (46, 50) to 465 nm (46). MNP-demulsifiers are made using magnetite nanoparticles of size about 200-300 nm.

The physical properties of magnetic nanoparticles and their magnetometric property are considered in detail in the reviews (45, 48). MNP-demulsifiers considered in this article (Table 1) have supermagnetic properties. This means that in the presence of an external magnetic field, a single domain of superparamagnetic MNPs aligns with the applied magnetic field. In the absence of an external field, superparamagnetic MNPs will exhibit no magnetization. Superparamagnetic MNP magnetization describes by the modified Langevin function (Equation 1) (48, 51).

$$M = M_0 L\left(\frac{\mu_p H}{k_B T}\right) + \chi_a H \quad (1)$$

One more important characteristic is the magnetic force (F) acting on the MNPs (Equation 2):

$$F = \mu_0 VM \nabla H \quad (2)$$

According to this equation, the ability of MNPs to move under an external magnetic field depends on particle magnetization: the greater the particle magnetization value, the easier the movement in the magnetic field. Practical research data for MNPs made on the basis of Fe_3O_4 represented in Table 1 shows that the larger the MNP diameter (i.e., the thicker the modified layer), the less the magnetization. It is important for magnetic materials to retain their superparamagnetic properties for them to be effectively separated from a complex multiphase system (49).

Further, in the article we will analyze the mechanism of O/W and W/O emulsion separation by MNP demulsifiers.

6. MECHANISM OF DEMULSIFICATION BY MNPs

Crude oil is usually produced in the form of a water-in-oil (W/O) or oil-in-water (O/W) emulsion (50). The emulsified water, crude oil, and bitumen are highly undesirable, as they may lead to problems of oil

transportation and catalyst deactivation in refinery operations (48).

For both types of emulsions (W/O and O/W), researchers connect the MNP demulsification activity with two basic factors: 1) ability of increasing the oil and water interfacial tension and 2) ability to interact with resins, naphthenic acids, asphaltenes and at the interface between oil and water (56, 57). The main reason for the stability of W/O emulsions is the "skin-like" asphaltene protective layer surrounding the water droplet phase. The broken asphaltene layer significantly increases the probability of water droplet coalescence and promotes demulsification (62). MNPs may exhibit demulsifying activity both independently and under a magnetic field. The demulsification process is shortened under a magnetic field (61, 63, 66). This is due to their easy separation from multiphase systems in the presence of external magnetic field. MNPs accumulate at oil-water interfaces of dispersed droplets, impart the magnetic properties to them, and then magnetically tagged droplets can rapidly coalesce and be isolated from the continuous phase (53, 55, 61, 67, 71-73).

The ability of MNPs to increase the interfacial tension is because of their amphiphilic structure. The structures of the hydrophobic and hydrophilic parts of MNPs are responsible for particle wettability. MNP wettability is the main difference between W/O and O/W demulsifiers. MNPs have to be wettable by the continuous phase of emulsion for better dispersion: a low contact angle for O/W emulsions and a high contact angle for W/O emulsion (26). The wettability of synthesized MNPs ($Fe_3O_4@AEAPFS$) was studied by Lü et al. (54). They studied the distribution behavior of MNPs between oil phase and water phase. The gravity effect makes $Fe_3O_4@AEAPFS$ -MNP pass through the oil-water interface and enter the aqueous phase. This is because the MNPs are surrounded by water and cannot fully come into contact with the diesel fuel. These MNPs have a large hydrophilic part (Fe_3O_4) and a small hydrophobic part ($EP@APTES$), so the particles are easily dispersed in the aqueous phase and reach the oil-water interface (56).

There are some examples of how researchers explain the mechanism of O/W demulsification by the developed MNPs (see Table 1). The demulsification of wastewater produced from flooding is considered in the article (49). The process was investigated under an optical microscope.

These M-DMEA particles accumulated at the O/W interface, enhancing the coalescence of oil droplets. After M-DMEA treatment, a clean aqueous phase without visible oil droplets was finally obtained. This work attributed the phenomenon to the interaction between N,N-dimethylethanolamine of MNPs and the surfactants of the emulsion such as asphaltenes, resins, and polymer residues (49).

Xu et al. (57) considered the demulsification mechanism of M-MWCNTs MNPs ($\text{Fe}_3\text{O}_4@SiO_2$ -APTES modified multi-walled carbon nanotubes), which have a similar structure to amphiphilic surfactants: hydrophobic carbon skeleton and hydrophilic MNPs. Partial $\text{Fe}_3\text{O}_4@SiO_2$ -APTES. MNPs show excellent interfacial activity and ability to adsorb asphaltenes. MNP surface functional groups ($-\text{NH}_2$, $-\text{OH}$ and $-\text{COOH}$) can serve as electron donors to form π - π bonds with aromatic molecules. Xu et al. (53), Lü et al. (71) also developed P(MMA-AA-DVB)/ Fe_3O_4 MNPs demulsification efficiency with the presence of carboxyl groups on the MNPs surface, which makes them interfacially active (53, 71). Vega et al. (72) used graphene oxide (GO) for MNPs surface modification (M-GO). Non-covalent interaction analysis attributed the strong affinity between M-GO and asphaltenes/resins to the π - π interactions.

Ko et al. (67) developed A-MNPs with a positive surface charge (amine group, $-\text{NH}_2$). The experiment results show that oil droplets are successfully separated negatively-charged oil droplets using cationic surfactant-coated MNPs (Figure 8). Xu et al. (53) described M-DM MNPs with a matrix dispersed structure based on diatomite (DM) coated by (3-aminopropyl)-triethoxysilane (APTES), MNPs of Fe_3O_4 , and polyethylenimine (PEI). The M-DM surface has a large number of amino groups. The asphaltene molecules are composed of aromatic rings and polar functional groups, such as hydroxyl, carboxyl, and epoxy. They considered that amino groups from the M-DM surface can form the hydrogen bonds with the hydroxyl groups derived from asphaltenes (53).

The MNP demulsifiers for W/O emulsions have to be wetted by oil fraction. For example, $\text{Fe}_3\text{O}_4@SiO_2@C$ MNPs are easily wetted by toluene, so they can easily transfer to the interface of the W/O emulsion and decrease the surface tension of water and ultimately lead to the coalescence of water droplets and separation of two phases (65, 74). Another example is PEMN MNPs received by solvothermal reaction propyleneoxide-ethyleneoxide block polyether with iron (III) acetylacetonate. A confocal microscope was used to observe the water droplets in W/O emulsions. After PEMN was added, the water droplets started to coalesce with each other and become bigger, making the emulsions more unstable. They supposed that PEMN MNPs could adsorb on the O/W interface by replacing some natural surfactants (51).

Lü et al. (71) explained that MNPs were synthesized: $\text{Fe}_3\text{O}_4@APFS$ (magnetite coated by aminopropyl-functionalised silica (APFS)) and $\text{Fe}_3\text{O}_4@APFS$ -G-CS (previous one MNPs coated by chitosan molecular chains). The zeta potential of these two types of MNPs was analyzed for the prediction of demulsification

efficiency. These nanoparticles have slightly different zeta potential: under pH 7.0, the potential of $\text{Fe}_3\text{O}_4@APFS$ was 18.2 mv, and of $\text{Fe}_3\text{O}_4@APFS$ -G-CS was 17.6 mv. This means that the positive charge intensity of the second type of MNPs was less than the first. Based on this fact, the authors assumed that for $\text{Fe}_3\text{O}_4@APFS$ MNPs, the electrostatic attraction of asphaltenes, resins, and naphthenic acids and demulsification efficiency could be higher. However, $\text{Fe}_3\text{O}_4@APFS$ -G-CS attracted negatively-charged oil droplets more effectively: the formation of aggregates of oil droplets and magnetic flocs was very fast and its size could reach 100 μm . They authors consider that the efficiency of demulsification by the $\text{Fe}_3\text{O}_4@APFS$ -G-CS is the consequence of hydrophobic interaction between grafted CS and oil droplets.

The demulsification mechanism for both W/O and O/W emulsions is practically the same: MNP demulsifiers disperse in a continuous medium of emulsion, interact with asphaltenes and other compounds of droplets' surface of dispersion medium, the shell is destroyed, and the droplets merge. MNP interaction with asphaltenes can be achieved mainly through Van der Waals interactions and Coulomb interactions. Many studies have been conducted on the zeta potential of asphaltenes under different conditions. Their main conclusion is that the surface of asphaltenes can be both positively and negatively charged (72, 73). Parra-Barrazaa et al. (73) reported that the anionic and the cationic surfactants adsorbing on the asphaltenes through the electrostatic interactions are able to reverse the zeta potential sign. In the research cases that we studied in this article, this conclusion is also true for MNP demulsifiers. The observed removal efficiency can be connected to the effect of MNP demulsifiers on the zeta potential of dispersed phase droplets in the continuous phase that leads to a decrease in electrostatic repulsion between droplets and enhancement of the removal efficiency (66).

This property of MNP-demulsifiers makes them an ideal reusable instrument for solving the problem of oil and water emulsion formation. In the following section, we collected factors affecting MNP demulsification efficiency.

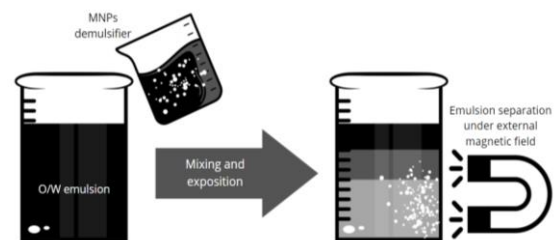


Figure 8. Schematic illustration of a bottle test experiment for O/W emulsion separation using MNPs demulsifier [63]

7. FACTORS AFFECTING MNP DEMULSIFICATION EFFICIENCY

Functional effectiveness of MNPs depends on three key environmental parameters: pH value, temperature, and ionic strength of water (55). However, the literature review hereunder showed that the demulsification efficiency of MNPs also depends on the characteristics of the emulsion and the MNP demulsifier itself. The aim of this section is to collect practical examples of factors that, according to the researcher's opinion, potentially influence the functional effect of modified MNPs.

7. 1. Emulsion Characteristics In preparing this review, we studied many examples of MNP demulsifiers that were developed for both O/W and W/O emulsions. We have collected some cases where authors discuss the properties of emulsion that have an influence on MNP demulsification effectiveness.

One characteristic of water and oil emulsion is viscosity. Liang et al. (50) revealed that emulsion viscosity is not the factor that significantly influences the demulsification capability of MNPs. Developed $\text{Fe}_3\text{O}_4@OA$ MNPs (Fe_3O_4 modified by oleic acid) were tested on two O/W emulsions with similar viscosities 1.68 and 1.43 mPa.s. In the experiment on the demulsification of MNPs at a concentration of 30 g/L, the separation effectiveness differed twice (36% and 80%, respectively). Microscopic analysis of the emulsion showed that droplet size was three times different (262 nm and 76 nm) (50). They concluded that the smaller the droplet size of O/W emulsion, the more difficult the demulsification process (50).

Another example of unexpected results of MNP testing on emulsions (W/O) with different API densities has been described by Ali et al. (58). $\text{P(MMA-AA-DVB)/Fe}_3\text{O}_4$ MNPs (polymethylmethacrylate-acrylic acid-divinylbenzene) showed high coalescence efficiency at a concentration of 600 ppm, at 60° C for 1 hour and effective separation of water from a stable emulsion with viscosity 35.95 API (7 wt.% asphaltenes) and 16.66 API having a higher asphaltens content (15 wt.% asphaltenes). Despite the significant difference in viscosity, the demulsification efficiency was high in both cases: 99 and 95%, respectively (58). They attributed this phenomenon to the high asphaltene content contributing to the adsorption of the MNP demulsifier on the interface between the water and oil.

One more important emulsion characteristic that can influence MNP demulsification efficiency is the emulsion phase volume ratio.

According to literature (52, 58-60, 64, 75-82) the water content in W/O emulsion is one of the primary factors that affects demulsification efficiency or emulsion stability. Stable emulsions require water content in addition to asphaltenes, resin, and paraffin

content. In their experiments, the researchers demonstrated that demulsification efficiency increases with an increase in water content from 30% to 50% using 500 ppm $\text{P(MMA-AA-DVB)/Fe}_3\text{O}_4$ MNP as demulsifiers; additionally, MNPs exhibit excellent efficiency and separation time optimization at half the water content.

7. 2. Water Mineralization Lü et al. (54) discovered a remarkable increase in the efficiency of separating O/W emulsion after adding NaCl or CaCl_2 within the concentration range of 0-0.15 mol/L. During their study on $\text{Fe}_3\text{O}_4@APFS$ MNPs at pH 7.0, they observed that MNPs exhibited attractive electrostatic interaction with oil droplets. The addition of salt weakened this electrostatic attraction due to electrostatic screening. However, as the ionic strength increased, the hydrophobicity of $\text{Fe}_3\text{O}_4@APFS$ MNPs improved, promoting their sorption at the surface of oil droplets. Consequently, the separation efficiency of oil was significantly enhanced (54).

The demulsification efficiency of MNPs described by Lü et al. (55) ($\text{Fe}_3\text{O}_4@SiO_2$ -MPS modified by N-isopropylacrylamide (NIPAM) and sodium methacrylate (SMA)) was significantly enhanced by increasing water ionic strength. They explained this phenomenon by the fact that cations partly shielded the MNPs surface negative charge that concentrated on sodium methacrylate monomers and the charge repulsion was therefore reduced; salt addition also enhanced the MNP hydrophobicity. Increasing ionic strength in this case was also favorable for MNP accumulation on the oil droplet surface.

7. 3. Influence of pH The pH value is an important factor to consider during demulsification by MNPs. Depending on the compounds used for MNP modification, the magnetic particles are able to change their performance at different pH levels. For example, MNPs modified by the co-polymer of sodium methacrylate (SMA) and N-isopropylacrylamide (NIPAM) became pH-sensitive due to the acid comonomer (55). MNP separation efficiency decreased with an increase in pH; the influence of pH on its separation efficiency became more significant with an increasing amount of SMA in coverage of MNPs. The authors explain these phenomena as due to the ionization of SMA under higher pH levels leading to an increase in MNPs hydrophilic properties. As a result, the repulsive forces between nanoparticles and oil droplets increased (55).

Another example of pH sensitive MNPs is M-GO sample (amino-functional $\text{Fe}_2\text{O}_3@SiO_2$ anchored on the surface of GO) (52). It was found that the M-GO maintained a good demulsification performance in an acidic condition. They attributed this phenomenon to the

ionization of the alcohol and carboxyl functional groups on the M-GO MNPs under the acid condition, which makes them less hydrophilic (52).

Successful examples of magnetic nanoparticles (MNPs) have been adapted to a wide range of pH values, as described Lü et al. (54) where Fe_3O_4 MNPs were modified by TEOS and N-(aminoethyl)-aminopropyl triethoxy silane (AEAPTES). The demulsification efficiency of these MNPs is achieved through different mechanisms under different pH values. At pH 4.0 and 7.0, the positively charged Fe_3O_4 @AEAPTES MNPs utilize both electrostatic attraction and interfacial activity to promote the sorption of MNPs onto the surface of oil droplets. However, at pH 10.0, the negatively charged Fe_3O_4 @AEAPTES MNPs repel the oil droplets through electrostatic interactions. Nevertheless, hydrophobic forces can still overcome the electrostatic repulsion, allowing the MNPs to successfully attach to the emulsified oil droplets. The synthesized Fe_3O_4 @AEAPTES MNPs demonstrate satisfactory separation performance at various pH levels, although their efficiency slightly declines with an increase in pH.

The pH value has a significant impact not only on functional groups of MNP demulsifiers, but also on the functional groups of asphaltenes. Under high or low pH, asphaltenes become charged, which increases their surface activity and hydrophilic behavior. In this condition, charged asphaltenes move to the oil-water interface and accumulate more easily. At acidic conditions, this property of asphaltenes is more pronounced due to the large number of carbocyclic groups in the structure. The stability W/O emulsion increases at pH below 7.0, as water drops do not merge well (60, 64, 74-86). In this case, the cationic type MNP demulsifier is preferable.

7. 4. Influence of Temperature Temperature also plays a crucial role in demulsification. Several examples discussed by Xu et al. (53) and Lü et al. (55) illustrated the influence of temperature on MNP demulsification efficiency. Xu et al. (53) have found that an increase in temperature from 15 to 60°C resulted in an increase in demulsification efficiency. This is mainly due to enhanced thermodynamic movement of interface molecules and decreased interfacial viscosity at higher temperatures, leading to emulsion instability. Meanwhile, Lü et al. (55) showed that the efficiency of an MNP demulsifier significantly decreased once the temperature was above the lower critical solution temperature (LCST) due to a hydrophobicity transition (55).

Ali et al. (58, 59) presented an example of W/O emulsion separation under 60°C covered different periods of time from 20 to 60 min. It was described that P(MMA-AA-DVB)/ Fe_3O_4 MNPs showed effective

demulsification efficiency for very stable W/O in 60 min at 60° C.

7. 5. Addition of Chemical Surfactants

Elmobarak and Almomani (66) organized MNP testing in combination with ordinary surfactants. Tests were carried out under three different surfactant concentrations of 0.05, 0.1 and 0.5 g/L at a constant concentration 10 mg/L of Fe_3O_4 - SiO_2 MNPs. It was found that demulsification efficiency slightly decreased by increasing the surfactant concentration in O/W emulsions. It was reported earlier that MNPs can attach to oil droplets in O/W emulsion as a result of the attractive force. The authors consider that surfactant added to emulsion increases the hydrophobicity of the oil droplets; the electrostatic repulsion between oil droplets becomes less pronounced and the interaction between oil droplets and the MNPs becomes worse. In addition, the anionic surfactants can interfere with acidic components in the oil and generate new compounds that can increase the density of the negative charge on the surface of oil droplets and enhance their stability (66). Nevertheless, we consider the influence of this factor as poorly understood. The right combination of surfactants will perhaps improve the demulsification efficiency.

7. 6. Time Ko et al. (67) described the results of experiments for studying the influence of mixing time on demulsification efficiency. They conclude that as the mixing time increases, the probability of collision between free MNPs and between free MNPs and MNP-oils increases. As a result, the particles might get more aggregated, and magnetic separation time gets shorter.

7. 7. Presence of Magnetic Field During MNP demulsifier application, a magnetic field can be applied with two aims: for MNP collection and for intensification of its activity. A magnetic field promotes quick and high demulsification efficiency and can compensate long time required for ordinary settling. For example, the experiments described by Elmobarak and Almomani (66) required 2 h settling time with a dose of 163 mg/L to achieve 94.9% demulsification, while this efficiency can be achieved in 8 min at a 10 mg/L concentration under a magnetic field.

The magnetic field influenced not only the MNP demulsifier, but also the OWE itself. The research findings conducted by Romanova et al. (75) showed that a magnetic field, constant and alternating electromagnetic fields applied to emulsion samples (W/O) of different composition lead to the destruction of the emulsion with 99 wt.% demulsification efficiency. However, the mechanism of that phenomena remains unclear. Khajeh et al. (76) have found that a magnetic field decreases the interfacial tension in the system of

water-toluene-asphaltenes and the number of hydrogen bonding between water and asphaltene molecules (76).

8. CONCLUSIONS

Interest in MNP demulsification technology is constantly growing. This review summarizes the research cases of MNP modification and testing for the demulsification of both types of OWEs (O/W and W/O). The range of bottle tests that were studied confirmed that MNP demulsifiers demonstrate excellent demulsification efficiency.

During the development of MNP demulsifiers, it is important to take it into account the following factors:

1. MNPs need a protective layer to avoid oxidation and corrosion.
2. The functional modification of MNPs have to be made in accordance with the type of emulsion and emulsifier characteristics (basically asphaltene). MNP demulsifier must have good wettability by continuous phase of emulsion.
3. It is also necessary to analyze the target OWE emulsifier characteristics (basically zeta potential of asphaltene). The functional groups of the MNP demulsifier must provide the necessary zeta-potential for electrostatic interaction with asphaltene.

This research experience proves MNPs as prospective substances for field application. The undoubted advantages of MNPs over conventional demulsifiers are their safety for the environment and reusability.

9. REFERENCES

1. Vyatkin K, Kochnev A, Lekomtsev A. Evaluation of oil viscosity expansion and property investigation of oil-water emulsion in Perm region. *Expos Oil Gas*. 2017;2:89-93.
2. Raya SA, Mohd Saaid I, Abbas Ahmed A, Abubakar Umar A. A critical review of development and demulsification mechanisms of crude oil emulsion in the petroleum industry. *Journal of Petroleum Exploration and Production Technology*. 2020;10:1711-28. <https://doi.org/10.1007/s13202-020-00830-7>
3. Gupta S, Rajiah P, Middlebrooks EH, Baruah D, Carter BW, Burton KR, et al. Systematic review of the literature: best practices. *Academic radiology*. 2018;25(11):1481-90. <https://doi.org/10.1016/j.acra.2018.04.025>
4. Aromataris E, Fernandez R, Godfrey C, Holly C, Khalil H, Tungpunkom P. Summarizing systematic reviews: methodological development. 2015. <https://doi.org/10.1097/XEB.0000000000000055>
5. O'Connor A, Anderson K, Goodell C, Sargeant J. Conducting systematic reviews of intervention questions I: writing the review protocol, formulating the question and searching the literature. *Zoonoses and public health*. 2014;61:28-38. <https://doi.org/10.1111/zph.12125>
6. Abduldredha MM, Aslina HS, Luqman CA. Overview on petroleum emulsions, formation, influence and demulsification treatment techniques. *Arabian Journal of Chemistry*. 2020;13(1):3403-28. <https://doi.org/10.1016/j.arabjc.2018.11.014>
7. Moeini F, Hemmati-Sarapardeh A, Ghazanfari M-H, Masihi M, Ayatollahi S. Toward mechanistic understanding of heavy crude oil/brine interfacial tension: The roles of salinity, temperature and pressure. *Fluid phase equilibria*. 2014;375:191-200. <http://dx.doi.org/doi:10.1016/j.fluid.2014.04.017>
8. Lashkarbolooki M, Riazi M, Ayatollahi S, Hezave AZ. Synergy effects of ions, resin, and asphaltene on interfacial tension of acidic crude oil and low-high salinity brines. *Fuel*. 2016;165:75-85. <http://dx.doi.org/10.1016/j.fuel.2015.10.030>
9. Saad M, Kamil M, Abdurahman N, Yunus RM, Awad OI. An overview of recent advances in state-of-the-art techniques in the demulsification of crude oil emulsions. *Processes*. 2019;7(7):470. <https://doi.org/10.3390/pr7070470>
10. Norrman K, Olesen KB, Zimmermann MS, Fadhel R, Vijn P, Sjølling TI. Isolation and Characterization of Surface-Active Components in Crude Oil—Toward Their Application as Demulsifiers. *Energy & Fuels*. 2020;34(11):13650-63. <https://dx.doi.org/10.1021/acs.energyfuels.0c02329>
11. Yang F, Tchoukov P, Qiao P, Ma X, Pensini E, Dabros T, et al. Studying demulsification mechanisms of water-in-crude oil emulsions using a modified thin liquid film technique. *Colloids and Surfaces A: Physicochemical and Engineering Aspects*. 2018;540:215-23. <https://doi.org/10.1016/j.colsurfa.2017.12.056>
12. Hart A. A review of technologies for transporting heavy crude oil and bitumen via pipelines. *Journal of Petroleum Exploration and Production Technology*. 2014;4:327-36. <https://doi.org/10.1007/s13202-013-0086-6>
13. Mohyaldinn ME, Hassan AM, Ayoub MA. Application of emulsions and microemulsions in enhanced oil recovery and well stimulation. *Microemulsion-a Chemical Nanoreactor*. 2019. <https://doi.org/10.5772/intechopen.84538>
14. Rodionova G, Strand M, Øye G. Potential applications of magnetic nanoparticles within separation in the petroleum industry. 2018. <https://doi.org/10.1016/j.petrol.2018.02.048>
15. Sjöblom J, Simon S, Xu Z. Model molecules mimicking asphaltene. *Advances in colloid and interface science*. 2015;218:1-16. <https://doi.org/10.1016/j.cis.2015.01.002>
16. Langevin D, Argillier J-F. Interfacial behavior of asphaltene. *Advances in colloid and interface science*. 2016;233:83-93. <http://dx.doi.org/10.1016/j.cis.2015.10.005>
17. Rahham Y, Rane K, Goual L. Characterization of the Interfacial Material in Asphaltene Responsible for Oil/Water Emulsion Stability. *Energy & Fuels*. 2020;34(11):13871-82. <https://dx.doi.org/10.1021/acs.energyfuels.0c02656>
18. Wu C, De Visscher A, Gates ID. On naphthenic acids removal from crude oil and oil sands process-affected water. *Fuel*. 2019;253:1229-46. <https://doi.org/10.1016/j.fuel.2019.05.091>
19. Headley JV, Peru KM, Barrow MP, Derrick PJ. Characterization of naphthenic acids from Athabasca oil sands using electrospray ionization: the significant influence of solvents. *Analytical Chemistry*. 2007;79(16):6222-9. <https://doi.org/10.1021/ac070905w>
20. Barros EV, Dias HP, Pinto FE, Gomes AO, Moura RR, Neto AC, et al. Characterization of naphthenic acids in thermally degraded petroleum by ESI (-)-FT-ICR MS and 1H NMR after solid-phase extraction and liquid/liquid extraction. *Energy & Fuels*. 2018;32(3):2878-88. <https://doi.org/10.1021/acs.energyfuels.7b03099>
21. Ese MH, Kilpatrick PK. Stabilization of water-in-oil emulsions by naphthenic acids and their salts: model compounds, role of pH, and soap: acid ratio. *Journal of Dispersion Science and Technology*. 2004;25(3):253-61. <http://dx.doi.org/10.1081/DIS-120038634>
22. Hurtevent C, Ubbels S, editors. Preventing naphthenate stabilised emulsions and naphthenate deposits at ekoundou oil field in

- cameroon. SPE International Oilfield Scale Symposium; 2006: OnePetro.
23. Pauchard V, Sjöblom J, Kokal S, Bouriat P, Dicharry C, Müller H, et al. Role of naphthenic acids in emulsion tightness for a low-total-acid-number (TAN)/high-asphaltenes oil. *Energy & Fuels*. 2009;23(3):1269-79. <https://doi.org/10.1021/ef800615e>
 24. Yang Y, Fang Z, Chen X, Zhang W, Xie Y, Chen Y, et al. An overview of Pickering emulsions: solid-particle materials, classification, morphology, and applications. *Frontiers in pharmacology*. 2017;8:287. <https://doi.org/10.3389/fphar.2017.00287>
 25. Ali N, Bilal M, Khan A, Ali F, Yang Y, Khan M, et al. Dynamics of oil-water interface demulsification using multifunctional magnetic hybrid and assembly materials. *Journal of Molecular Liquids*. 2020;312:113434. <https://doi.org/10.1016/j.molliq.2020.113434>
 26. Sullivan AP, Kilpatrick PK. The effects of inorganic solid particles on water and crude oil emulsion stability. *Industrial & engineering chemistry research*. 2002;41(14):3389-404. <https://doi.org/10.1021/ie010927n>
 27. Speight J. General methods of oil recovery. *Introduction to Enhanced Recovery Methods for Heavy Oil and Tar Sands*. 2016:253-322. <http://dx.doi.org/10.1016/B978-0-12-849906-1.00006-0>
 28. Mahdavi E, Zebarjad F. Screening criteria of enhanced oil recovery methods. *Fundamentals of Enhanced Oil and Gas Recovery from Conventional and Unconventional Reservoirs* Amsterdam: Elsevier. 2018:41-59. <https://doi.org/10.1016/B978-0-12-813027-8.00002-3>
 29. Li M, Xu M, Lin M, Wu Z. The effect of HPAM on crude oil/water interfacial properties and the stability of crude oil emulsions. *Journal of dispersion science and technology*. 2007;28(1):189-92. <https://doi.org/10.1080/01932690600992829>
 30. Li M, Lin M, Wu Z, Christy AA. The influence of NaOH on the stability of paraffinic crude oil emulsion. *Fuel*. 2005;84(2-3):183-7. <https://doi.org/10.1016/j.fuel.2004.09.001>
 31. Grenoble Z, Trabelsi S. Mechanisms, performance optimization and new developments in demulsification processes for oil and gas applications. *Advances in colloid and interface science*. 2018;260:32-45. <https://doi.org/10.1016/j.cis.2018.08.003>
 32. Abed S, Abdurahman N, Yunus R, Abdulbari H, Akbari S, editors. *Oil emulsions and the different recent demulsification techniques in the petroleum industry-A review*. IOP Conference Series: Materials Science and Engineering; 2019: IOP Publishing.
 33. Kokal S. Crude-oil emulsions: A state-of-the-art review. *SPE Production & facilities*. 2005;20(01):5-13. <https://doi.org/10.2118/77497-MS>
 34. Li B, Fan Y, Sun Z, Wang Z, Zhu L. Effects of high-frequency pulsed electrical field and operating parameters on dehydration of SAGD produced ultra-heavy oil. *Powder Technology*. 2017;316:338-44. <http://dx.doi.org/10.1016/j.powtec.2017.03.024>
 35. Raynel G, Marques DS, Al-Khabaz S, Al-Thabet M, Oshinowo L. A new method to select demulsifiers and optimize dosage at wet crude oil separation facilities. *Oil & Gas Science and Technology-Revue d'IFP Energies nouvelles*. 2021;76:19. <https://doi.org/10.2516/ogst/2020096>
 36. Long ZJ, Fu YR, Li DQ, Fu LX, Fu Q. Research on Low-Temperature Dehydration of Crude Oil Based on Paraffin-Based Demulsifier. *Advanced Materials Research*. 2012;361:414-8. <https://doi.org/10.4028/www.scientific.net/AMR.361-363.414>
 37. Tubuke Mwakasala B, Kang W, Yin X, Geng J, Zhao Y, Yang H. Demulsifier performance at low temperature in a low permeability reservoir. *Petroleum Science and Technology*. 2016;34(23):1905-12. <http://dx.doi.org/10.1080/10916466.2016.1240691>
 38. Nour H, Yunus RM, Jemaat Z. Chemical demulsification of water-in-crude oil emulsions. *Journal of Applied Sciences*. 2007;7(2):196-201. <https://doi.org/10.3923/jas.2007.196.201>
 39. Adewunmi AA, Kamal MS. Demulsification of water-in-oil emulsions using ionic liquids: Effects of counterion and water type. *Journal of Molecular Liquids*. 2019;279:411-9. <https://doi.org/10.1016/j.molliq.2019.02.008>
 40. Jabbari M, Izadmanesh Y, Ghavidel H. Synthesis of ionic liquids as novel emulsifier and demulsifiers. *Journal of Molecular Liquids*. 2019;293:111512. <https://doi.org/10.1016/j.molliq.2019.111512>
 41. Guzmán-Lucero D, Flores P, Rojo T, Martínez-Palou R. Ionic liquids as demulsifiers of water-in-crude oil emulsions: study of the microwave effect. *Energy & Fuels*. 2010;24(6):3610-5. <https://doi.org/10.1021/ef100232f>
 42. Jiang J, Wu H, Lu Y, Ma T, Li Z, Xu D, et al. Application of α -amylase as a novel biodemulsifier for destabilizing amphiphilic polymer-flooding produced liquid treatment. *Bioresource technology*. 2018;259:349-56. <https://doi.org/10.1016/j.biortech.2018.03.069>
 43. Shehzad F, Hussein IA, Kamal MS, Ahmad W, Sultan AS, Nasser MS. Polymeric surfactants and emerging alternatives used in the demulsification of produced water: A review. *Polymer Reviews*. 2018;58(1):63-101. <http://dx.doi.org/10.1080/15583724.2017.1340308>
 44. He X, Liang C, Liu Q, Xu Z. Magnetically responsive Janus nanoparticles synthesized using cellulose materials for enhanced phase separation in oily wastewaters and water-in-crude oil emulsions. *Chemical Engineering Journal*. 2019;378:122045. <https://doi.org/10.1016/j.cej.2019.122045>
 45. Zhou K, Zhou X, Liu J, Huang Z. Application of magnetic nanoparticles in petroleum industry: A review. *Journal of Petroleum Science and Engineering*. 2020;188:106943. <https://doi.org/10.1016/j.petrol.2020.106943>
 46. Liang J, Li H, Yan J, Hou W. Demulsification of oleic-acid-coated magnetite nanoparticles for cyclohexane-in-water nanoemulsions. *Energy & fuels*. 2014;28(9):6172-8. <https://doi.org/10.1021/ef501169m>
 47. Lu AH, Salabas EeL, Schüth F. Magnetic nanoparticles: synthesis, protection, functionalization, and application. *Angewandte Chemie International Edition*. 2007;46(8):1222-44. <https://doi.org/10.1002/anie.200602866>
 48. Akbarzadeh A, Samiei M, Davaran S. Magnetic nanoparticles: preparation, physical properties, and applications in biomedicine. *Nanoscale research letters*. 2012;7:1-13. <https://doi.org/10.1186/1556-276X-7-144>
 49. Duan M, Xu Z, Zhang Y, Fang S, Song X, Xiong Y. Core-shell composite nanoparticles with magnetic and temperature dual stimuli-responsive properties for removing emulsified oil. *Advanced Powder Technology*. 2017;28(5):1291-7. <http://dx.doi.org/10.1016/j.apt.2017.02.017>
 50. Liang J, Du N, Song S, Hou W. Magnetic demulsification of diluted crude oil-in-water nanoemulsions using oleic acid-coated magnetite nanoparticles. *Colloids and Surfaces A: Physicochemical and Engineering Aspects*. 2015;466:197-202. <http://dx.doi.org/10.1016/j.colsurfa.2014.11.050>
 51. Fang S, Chen B, Chen T, Duan M, Xiong Y, Shi P. An innovative method to introduce magnetism into demulsifier. *Chemical Engineering Journal*. 2017;314:631-9. <http://dx.doi.org/10.1016/j.cej.2016.12.023>
 52. Liu J, Wang H, Li X, Jia W, Zhao Y, Ren S. Recyclable magnetic graphene oxide for rapid and efficient demulsification of crude

- oil-in-water emulsion. *Fuel*. 2017;189:79-87. <http://dx.doi.org/10.1016/j.fuel.2016.10.066>
53. Xu H, Wang J, Ren S. Removal of oil from a crude oil-in-water emulsion by a magnetically recyclable diatomite demulsifier. *Energy & Fuels*. 2019;33(11):11574-83. <https://doi.org/10.1021/acs.energyfuels.9b02440>
54. Lü T, Qi D, Zhang D, Lin S, Mao Y, Zhao H. Facile synthesis of N-(aminoethyl)-aminopropyl functionalized core-shell magnetic nanoparticles for emulsified oil-water separation. *Journal of Alloys and Compounds*. 2018;769:858-65. <https://doi.org/10.1016/j.jallcom.2018.08.071>
55. Lü T, Qi D, Zhang D, Fu K, Li Y, Zhao H. Fabrication of recyclable multi-responsive magnetic nanoparticles for emulsified oil-water separation. *Journal of Cleaner Production*. 2020;255:120293. <https://doi.org/10.1016/j.jclepro.2020.120293>
56. Xu H, Jia W, Ren S, Wang J. Novel and recyclable demulsifier of expanded perlite grafted by magnetic nanoparticles for oil separation from emulsified oil wastewaters. *Chemical Engineering Journal*. 2018;337:10-8. <https://doi.org/10.1016/j.cej.2017.12.084>
57. Xu H, Jia W, Ren S, Wang J. Magnetically responsive multi-wall carbon nanotubes as recyclable demulsifier for oil removal from crude oil-in-water emulsion with different pH levels. *Carbon*. 2019;145:229-39. <https://doi.org/10.1016/j.carbon.2019.01.024>
58. Ali N, Zhang B, Zhang H, Zaman W, Li X, Li W, et al. Interfacially active and magnetically responsive composite nanoparticles with raspberry like structure; synthesis and its applications for heavy crude oil/water separation. *Colloids and Surfaces A: Physicochemical and Engineering Aspects*. 2015;472:38-49. <http://dx.doi.org/10.1016/j.colsurfa.2015.01.087>
59. Ali N, Zhang B, Zhang H, Li W, Zaman W, Tian L, et al. Novel Janus magnetic micro particle synthesis and its applications as a demulsifier for breaking heavy crude oil and water emulsion. *Fuel*. 2015;141:258-67. <http://dx.doi.org/10.1016/j.fuel.2014.10.026>
60. Zaman H, Ali N, Gao X, Zhang S, Hong K, Bilal M. Effect of pH and salinity on stability and dynamic properties of magnetic composite amphiphilic demulsifier molecules at the oil-water interface. *Journal of Molecular Liquids*. 2019;290:111186. <https://doi.org/10.1016/j.molliq.2019.111186>
61. Liang C, He X, Liu Q, Xu Z. Adsorption-based synthesis of magnetically responsive and interfacially active composite nanoparticles for dewatering of water-in-diluted bitumen emulsions. *Energy & Fuels*. 2018;32(8):8078-89. <https://doi.org/10.1021/acs.energyfuels.8b01187>
62. Mao X, Gong L, Xie L, Qian H, Wang X, Zeng H. Novel Fe₃O₄ based superhydrophilic core-shell microspheres for breaking asphaltene-stabilized water-in-oil emulsion. *Chemical Engineering Journal*. 2019;358:869-77. <https://doi.org/10.1016/j.cej.2018.10.089>
63. He X, Liu Q, Xu Z. Cellulose-coated magnetic Janus nanoparticles for dewatering of crude oil emulsions. *Chemical Engineering Science*. 2021;230:116215. <https://doi.org/10.1016/j.ces.2020.116215>
64. Umar AA, Saaid IM, Halilu A, Sulaimon AA, Ahmed AA. Magnetic polyester bis-MPA dendron nanohybrid demulsifier can effectively break water-in-crude oil emulsions. *Journal of Materials Research and Technology*. 2020;9(6):13411-24. <https://doi.org/10.1016/j.jmrt.2020.09.074>
65. Xie H, Wu Z, Wang Z, Lu J, Li Y, Cao Y, et al. Facile fabrication of acid-resistant and hydrophobic Fe₃O₄@ SiO₂@ C magnetic particles for valid oil-water separation application. *Surfaces and Interfaces*. 2020;21:100651. <https://doi.org/10.1016/j.surfin.2020.100651>
66. Elmobarak WF, Almomani F. Application of Fe₃O₄ magnetite nanoparticles grafted in silica (SiO₂) for oil recovery from oil in water emulsions. *Chemosphere*. 2021;265:129054. <https://doi.org/10.1016/j.chemosphere.2020.129054>
67. Ko S, Kim ES, Park S, Daigle H, Milner TE, Huh C, et al. RETRACTED ARTICLE: Amine functionalized magnetic nanoparticles for removal of oil droplets from produced water and accelerated magnetic separation. *Journal of Nanoparticle Research*. 2017;19:1-14. <https://doi.org/10.1007/s11051-017-3826-6>
68. Adewunmi AA, Kamal MS, Solling TI. Application of magnetic nanoparticles in demulsification: A review on synthesis, performance, recyclability, and challenges. *Journal of Petroleum Science and Engineering*. 2021;196:107680. <https://doi.org/10.1016/j.petrol.2020.107680>
69. Wu W, Wu Z, Yu T, Jiang C, Kim W-S. Recent progress on magnetic iron oxide nanoparticles: synthesis, surface functional strategies and biomedical applications. *Science and technology of advanced materials*. 2015;16(2):023501. <https://doi.org/10.1088/1468-6996/16/2/023501>
70. Zhu N, Ji H, Yu P, Niu J, Farooq M, Akram MW, et al. Surface modification of magnetic iron oxide nanoparticles. *Nanomaterials*. 2018;8(10):810. <https://doi.org/10.3390/nano8100810>
71. Lü T, Chen Y, Qi D, Cao Z, Zhang D, Zhao H. Treatment of emulsified oil wastewaters by using chitosan grafted magnetic nanoparticles. *Journal of Alloys and Compounds*. 2017;696:1205-12. <http://dx.doi.org/10.1016/j.jallcom.2016.12.118>
72. Vega SS, Urbina RH, Covarrubias MV, Galeana CL. The zeta potential of solid asphaltene in aqueous solutions and in 50: 50 water+ ethylene glycol (v/v) mixtures containing ionic surfactants. *Journal of Petroleum Science and Engineering*. 2009;69(3-4):174-80. <https://doi.org/10.1016/j.petrol.2009.08.014>
73. Parra-Barraza H, Hernández-Montiel D, Lizardi J, Hernández J, Urbina RH, Valdez MA. The zeta potential and surface properties of asphaltene obtained with different crude oil/n-heptane proportions☆. *Fuel*. 2003;82(8):869-74. [https://doi.org/10.1016/S0016-2361\(03\)00002-4](https://doi.org/10.1016/S0016-2361(03)00002-4)
74. Dvornikov MV, Budovskaya ME. Development of a hydrocarbon completion system for wells with low bottomhole temperatures for conditions of oil and gas fields in Eastern Siberia. *Записки Горного института*. 2022;253:12-22. 10.31897/PMI.2022.4
75. Romanova YN, Maryutina TA, Musina NS, Yurtov EV, Spivakov BY. Demulsification of water-in-oil emulsions by exposure to magnetic field. *Journal of petroleum science and engineering*. 2019;179:600-5. <https://doi.org/10.1016/j.petrol.2019.05.002>
76. Khajeh K, Aminfar H, Mohammadpourfard M. Molecular dynamics simulation of the magnetic field influence on the oil-water interface. *Fluid Phase Equilibria*. 2020;522:112761. <https://doi.org/10.1016/j.fluid.2020.112761>
77. Grigorev BM, Tananykhin SD, Poroshin AM. Sand management approach for a field with high viscosity oil. *Journal of Applied Engineering Science*. 2020;18(1):64-9. 10.5937/jaes18-24541
78. Tananykhin D, Korolev M, Stecyuk I, Grigorev M. An investigation into current sand control methodologies taking into account geomechanical, field and laboratory data analysis. *Resources*. 2021;10(12):125. <https://doi.org/10.3390/resources10120125>
79. Tananykhin D, Grigorev M, Simonova E, Korolev M, Stecyuk I, Farrakhov L. Effect of Wire Design (Profile) on Sand Retention Parameters of Wire-Wrapped Screens for Conventional Production: Prepack Sand Retention Testing Results. *Energies*. 2023;16(5):2438. <https://doi.org/10.3390/en16052438>

80. Podoprigora D, Byazrov R, Sytnik J. The comprehensive overview of large-volume surfactant slugs injection for enhancing oil recovery: Status and the outlook. *Energies*. 2022;15(21):8300. <https://doi.org/10.3390/en15218300>
81. Raupov I, Rogachev M, Sytnik J. Design of a Polymer Composition for the Conformance Control in Heterogeneous Reservoirs. *Energies*. 2023;16(1):515. <https://doi.org/10.3390/en16010515>
82. Islamov S, Bondarenko A, Mardashov D. A selection of emulsifiers for preparation of invert emulsion drilling. *Topical Issues of Rational Use of Natural Resources, Volume 2*. 2019:487. 10.1201/9781003014638-2
83. Nguyen VT, Pham TV, Rogachev MK, Korobov GY, Parfenov DV, Zhurkevich AO, et al. A comprehensive method for determining the dewaxing interval period in gas lift wells. *Journal of Petroleum Exploration and Production Technology*. 2023;13(4):1163-79. 10.1007/s13202-022-01598-8
84. Вотинов А, Середин В, Колычев И, Галкин С. Возможности учета трещиноватости каширо-верейских карбонатных объектов при планировании пропантного гидроразрыва пласта. *Записки Горного института*. 2021;252:861-71. 10.31897/PMI.2021.6.8
85. Aneke F, Adu J. Adsorption of heavy metals from contaminated water using leachate modular tower. *Civil Engineering Journal*. 2023;9(6):1522-41. 10.28991/CEJ-2023-09-06-017
86. Ismail WNW, Syah MIAI, Abd Muhet NH, Bakar NHA, Yusop HM, Samah NA. Adsorption behavior of heavy metal ions by hybrid inulin-TEOS for water treatment. *Civil Engineering Journal*. 2022;8(9):1787-98. <https://doi.org/10.28991/CEJ-2022-08-09-03>

COPYRIGHTS

©2024 The author(s). This is an open access article distributed under the terms of the Creative Commons Attribution (CC BY 4.0), which permits unrestricted use, distribution, and reproduction in any medium, as long as the original authors and source are cited. No permission is required from the authors or the publishers.

**Persian Abstract****چکیده**

امولسیون نفت-آب طیف وسیعی از مشکلات را ایجاد می کند که یکی از آنها کاهش قابل توجه فشار در خطوط جریان است که منجر به افزایش هزینه های پمپاژ و حمل و نقل می شود. گسترده ترین روند توسعه یافته در میان فناوری های جداسازی نفت/آب، استفاده از دمولسیفایرهای مبتنی بر نانوذرات مغناطیسی (MNPs) است. MNP ها خواص شیمیایی و مکانیکی خاصی دارند و فرصت های منحصر به فردی را برای حل مسائل تولید نفت فراهم می کنند. ویژگی های کلیدی چنین نانوذرات مغناطیسی برای کاربرد پایدار آنها قابلیت استفاده مجدد و پایداری آنهاست. فرصت دستکاری از راه دور با استفاده از میدان های مغناطیسی خارجی به آنها یک مزیت منحصر به فرد در عملیات حمل و نقل می دهد. هدف اصلی این مطالعه، نظام بندی تحقیقات MNPs برای جداسازی موثر امولسیون روغن و آب است. این بررسی ویژگی های امولسیفایر MNP، مکانیسم جداسازی امولسیون های روغن-آب (OWE) و عوامل مؤثر بر اختلال در کارایی امولسیون های روغن-آب توسط دمولسیفایر MNP را ارائه می کند. ارتباط این مطالعه این است که امولسیون های نفت-آب اغلب در عمل در طول توسعه میدان با آن مواجه می شوند. برای حل این مشکل، استفاده از دمولسیفایرهای مبتنی بر نانوذرات مغناطیسی پیشنهاد شده است. تازگی کار در این واقعیت نهفته است که کار چندین عامل موثر بر دامولسیفکاسیون را به طور همزمان جمع آوری می کند و تأثیر هر عامل را توصیف می کند. از میان این عوامل، مهمترین آنها عبارتند از: ویژگی های امولسیون، شوری آب، PH، دمای مخزن، افزودن سورفکتانت های شیمیایی، زمان و میدان مغناطیسی. مکانیسم تشکیل امولسیون های روغن-آب در انواع مختلف نیز توضیح داده شده است و پیامدهای منفی تشکیل امولسیون مورد بحث قرار می گیرد. نتایج نشان داد که نانوذرات مغناطیسی نیاز به لایه محافظ دارند و دمولسیفایر باید ترشوندگی خوبی در فاز پیوسته امولسیون داشته باشد.



Heat Transfer Augmentation for Impingement of Steady Air Jet under Exponential Heat Flux Boundary Condition

A. M. Rathod^a, N. P. Gulhane^a, U. M. Siddique^{*b}

^a Department of Mechanical Engineering, Veermata Jijabai Technological Institute, Mumbai, India

^b Department of Production Engineering, Veermata Jijabai Technological Institute, Mumbai, India

PAPER INFO

Paper history:

Received 15 September 2023

Received in revised form 14 November 2023

Accepted 13 December 2023

Keywords:

Nusselt Number

Exponential Varying Heat Flux

Cooling Rate

Slope

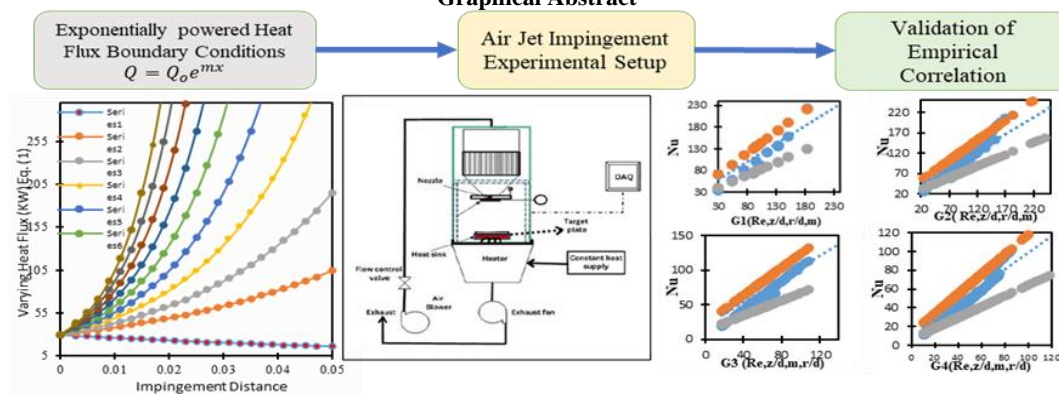
Heat Transfer

ABSTRACT

The cooling rate under impingement of air jet finds massive application in electronic packaging, material processing industries and cooling of gas turbine. The conventional cooling of heat sinks is till date carried out using a fan and pump. Recently, the momentous impingement of air has been found to produced 1.5 times the cooling rate, as compared with conventional method, under same pumping power. Previously, attractive amount of Research is carried out in observing the cooling rate for constant heat flux boundary condition, and less are available for constant wall temperature. The present research provides an in-depth numerical investigation for such jet impinged heat sinks, with a heat flux boundary condition. The exponential variation of heat flux magnitude with radial distance (Away from impingement point), is observed to be a generic alternate of constant wall temperature boundary condition. The numerical computation for heat transfer of such exponentially powered heat flux sink is carried out using FLUENT (ANSYS 2023R1). An orthogonal 2-D mesh computational domain with a compactible SST and K-Omega turbulence model is simulated for various inlet velocity and nozzle-target spacing. The impingement of jet and local cooling of target surface is defined using a well know non-dimensional Reynolds and Nusselt number, respectively. The exponential power for non-uniformly heated sinks can be readily selected (0.1-1) to replicate the present non-uniform heating or constant wall temperature boundary condition. Non-uniform heating has gained lots of attention of heat transfer researcher across the globe. The computation results extracted for various impinging Reynolds number and nozzle-target spacing, were closely best fitted using regression and validated with referred previous literature results. Tight dependency of slope parameter, over Reynolds number and z/d is observed in local cooling rate. These dependencies are judged based on the power of exponents. The semi – empirical correlations are defined separately for and stagnation, transition, and wall jet regions, separately. Such correlation can plan the design of cooling system, under non-uniform heating conditions

doi: 10.5829/ije.2024.37.05b.10

Graphical Abstract



*Corresponding Author Email: u.i.siddiqui@gmail.com (U. M. Siddique)

Please cite this article as: Rathod AM, Gulhane NP, Siddique UM, Heat Transfer Augmentation for Impingement of Steady Air Jet under Exponential Heat Flux Boundary Condition. International Journal of Engineering, Transactions B: Applications. 2024;37(05):920-30.

NOMENCLATURE

Re	Reynolds number	m	The slope of heat flux	$G1, G2, G3 \& G4$	Functions
Pr	Prandtl number	Nu	Nusselt number	Greek Symbols	
GR	Growth rate	ΔT	Temperature difference	ρ	Density of air
z	Nozzle exit to target surface spacing	z/d	Nozzle target spacing	α	Thermal Diffusivity
h	Heat transfer coefficient	C	Non-dimensional constant	ω	Specific Dissipation rate
Q and Q_o	Heat flux (w/m^2)	t	Geometric thickness	μ	Dynamic viscosity
\bar{T}_s	Average surface temperature	\bar{T}_f	Mean Bulk Fluid Temperature	C_p	Specific heat

1. INTRODUCTION

The continuous demand in cooling rate for efficient working of work station, electronic packaging system and material processing industries, is continuously being investigated by heat transfer researcher and postdoc. The conventional method of cooling using fan immensely demands for higher pumping power, increasing the running cost of system. Jet impingement using heat transfer, resulting in around 150% increase in cooling rate with same pumping power, was observed in early 1990's. Till date the steady jet impingement heat transfer is almost completely investigated and sufficient empirical correlations are readily available for design of cooling system. The air jet impingement over a hot target surface is a study partially in line with external force convection. Ricou et al. (1) for the first time investigated the entrainment effect of atmospheric air in suppressing the overall cooling rate for a fully developed laminar impingement. The Nusselt profile (Nu vs $\frac{r}{d}$) for the isothermal impinging jet was found to have the same velocity gradient over target surface as that of the one with higher/ lower temperature as that of target surface. The fully developed turbulent impingement is more of mixed convection and very less ($\pm 2\%$) natural convection (1). Hoogendoorn (2) investigated the heat transfer near stagnation zone, using liquid crystal technique. It was observed for the nozzle target spacing ($\frac{z}{d} > 5$) the stagnant point heat transfer is equivalent to that of the flow past the cylinder, provided the cylinder is five times the diameter as that of target surface. The fully developed turbulent impingement is majorly observed to possess a turbulence intensity greater than 1%. The turbulence intensity is the measure of root mean square velocity at nozzle exit. Pamadi and Belov (3) observed the secondary peak in the Nusselt profile near transition and far jet region ($r/d > 2.5$). Such peaks are more prone to happen with lower nozzle target spacing ($\frac{z}{d} < 1$) (4). Using finite difference technique of Kolmogorov-Prandtl hypothesis, secondary peaks were even bound to observed in stagnation zone due to some turbulence palpitation. Kataoka (5) observed the fluid density variation for free jets of burned gas and CO_2 air mixture. The potential core of impinging jet as observed by Behera et al. (6), is the core length of velocity at nozzle exits. This core of impinging jet is least affected by entrainment

effect and has poor cross diffusion of momentum. The potential core of temperature development was correlated with inlet temperature by Behera (6). A generalize model for logarithmic mean temperature difference in terms of core length conveys an exponential decay in Nusselt profile with respect to radial distance. The radial distance is measured from the point of impingement to the extreme of target surface. Shadlesky (7) investigated the existence of critical range of Stanton number for fully developed potential core of impinging jet. The developed potential core is highly sensitive to the nature of development of velocity at nozzle exit. Between 0.57 and 0.763 (St), the flow exit the nozzle carries a fully developed potential core. With a temperature difference $0^\circ C < \Delta T < 60^\circ C$, an overall difference of 15% – 25 % was observed with overall cooling rate proposed by Hollworth and Gero (8), the Nusselt number magnitude empirical correlation as summation of heat transfer due to turbulence and heat transfer due to temperature difference as, $q_s = h\Delta T_1 + h\phi\Delta T$. The heat transfer due to turbulence is majorly due to adverse pressure gradient at the point of impingement. Zumbrennen et al. (9) investigated the transient heat transfer cooling rate for pulse impingement air jet. The data points were recorded for before and after the renewal/vanish of thermal boundary layer. Empirical relation for water jet impingement ($Nu_{wt} = Re_w^m \cdot Pr^{0.4}, 60 - 90\%$) at stagnation point was found to independent of pulse rate. Major enhancements were attributed to the turbulence jet intensity and vorticity amplification. A 25% uncertainty with turbulent impingement and 11% for laminar was observe by Zumbrennen et al. (9). Goldstein and Seol (10) investigated the average cooling rate for the row of impinging circular and square shape jet, with a fully developed velocity profile at outlet of nozzle. The $\frac{Nu}{Re^{0.7}}$ against the span wise position of target surface under constant heat flux was investigated for $1 < \frac{z}{d} < 6$ and $10000 < Re < 25000$. The cooling rate at stagnation region was found to dominate over the other local position. In line with the previous literature, less significant change in Nusselt profile and overall cooling rate for variation in span wise distribution spacing of nozzle ($1 < \frac{s}{d} < 4$), was observed. This is due to the poor mixing of potential core of consecutive impinging jet. The research work concluded the higher area averaged cooling rate for closely spaced impinging

nozzle. The premixing of potential core of optimally spaced nozzle induces higher turbulence over the target surface. With nozzle target spacing less than 1. Lytle and Webb (11) observed a significant increase in stagnation point heat transfer and few secondary peaks. These secondary peaks observed in $\left(1 < \frac{r}{d} < 2.5\right)$, is the recovery effect for the continuity equation. The secondary peaks $\left(\frac{z}{d} > 1\right)$ shifts radially out with increase in Reynolds number from 5100 to 23000. Behnia (12) reported the computational results for $v^2 - f$ turbulence model for predicting the flow over the target surface for a confined impingement of jet. This enhancement due to the confinement of jet was observed for $30000 < Re < 70000$. The degree of confinement is determined with the premixing of potential core of impinging jet with atmospheric air. Garimella and Schroeder (13) investigated the impingement of multi-jet and its effect on overall cooling rate. With 2×2 and 6×6 sets of impinging nozzles, the stagnant heat transfer secondary peaks were observed distinguished for $\left(\frac{z}{d} > 4\right)$ (9). Up till, here it can be well concluded that utilization of pumping power of impinging jet in the form of heat transfer is much challenging for single jet. The impingement of multi-jet reflects some secondary peaks to dissolve its pumping power, through some turbulence mixing. The present study proposed few such empirical correlation of $Nu = f_1\left(Re, \frac{z}{d}, \frac{r}{d}\right)$. Han and Goldstein (14) gave a summary review of crossflow diffusion and angle of impingement against the overall cooling rate. With impingement angle of 90° , the Nusselt profile against the radial distance was observed to be perfectly symmetrical (mirror image). Not much deviation in overall cooling rate (10% – 25%) with variation in angle of impingement was observed. Katti and Prabhu (4) investigated local heat transfer distribution between a smooth flat surface and impinging of air from a circular straight pipe nozzle. Three vital heat transfer region were observed, stagnation $\left(\frac{r}{d} = 0\right)$, transition $\left(1 < \frac{r}{d} < 2.5\right)$ and wall jet $\left(\frac{r}{d} > 2.5\right)$ for fully developed impingement. The local heat transfer characteristics were estimated for varying Reynolds numbers between 12000 and 28000 and nozzle-target spacing of 0.5 - 8 nozzle diameters. Sagot et al. (15) validated the SST K-omega turbulence model for the impingement of gas at a temperature greater than that of the target surface, demonstrating the heating application of impingement heat transfer. Good validation with Dittus-Boelter equation with $Pr^{0.4}$ was observed, Sagot et al. (15) reported the robustness of SST K-omega in predicting the heat transfer rate within $\pm 10\%$ uncertainty with general equation of internal forced convection (16). Alimohammadi et al. (17) numerically predicted the local heat transfer coefficients of an unconfined steady impinging air jet

with a constant temperature boundary condition. The secondary peak was observed by coupling the SST turbulence model with Gamma-Theta transition model. Maximum of 5% deviation in local, area-averaged and stagnation Nusselt number for $\frac{H}{D} = 1$ and $Re = 14000$ was observed. Guo et al. (18) investigated the transient heat transfer due to the impingement of a 6mm diameter circular jet and reported the event of steadiness in cooling, after 80s of start of impingement. The numerical validation of an ICFM-CFD-3D meshed computational domain was computed with fluent solver to observe the velocity contour at different time step (before 80s). The numerical work was validated against the experimental results within $\pm 10\%$ accuracy of Nusselt number, with previous literature work. The author reported a significant increase in cooling rate with increase in nozzle target spacing $\left(4 < \frac{z}{d} < 8.5\right)$ for the jet impinging at $Re = 34000$. Luhar et al. (19) reported the set of algebraic equation used in determining temperature coefficients and proposed analytical model. This analytical model was constructed using finite different scheme. Sundaram and Venkatesan (20) studied heat transfer characteristics over the pin fin surface using RNG Turbulence model. It was observed that temperature decreases with the number of perforation of pin. Umair and Gulhane (21) observed Nusselt profile variation with the emergence of secondary peaks at lower nozzle target spacing $\left(\frac{r}{d} < 1\right)$.

These variations were attributed to the presence of turbulence flow near stagnation region. In line with the previous literature, Umar et al. (22) proposed semi empirical correlation with low nozzle target spacing $\left(\frac{r}{d} < 1\right)$. These correlation established a power law relation across four specific regions: stagnation, near wall, far wall and jet region. Umair and Gulhane (23) reported the non-uniformity in cooling characteristics of target surface. Thermal diffusivity (property variation) and geometric thickness (target surface) were studied for the occurrences of unevenness in Nusselt profile. The author reported a critical dependency of non-uniformity (Nusselt Profile) for air flow rate, below $59.33 - 66.76 \text{ mm}^3/\text{s}$. Siddique et al. (24) also investigated the effect of target surface thickness in inducing the unevenness to the profile cooling. Well clarified semi empirical correlation for $Pr \times \frac{t}{d} < 0.012$ and $Pr \times \frac{t}{d} < 0.012$ was reported. The work future recommended the existence of the Nusselt number correlation as function of $Pr, \frac{t}{d}, \frac{z}{d}, Re$ & $\frac{r}{d}$ which take care of such non-uniformity/ unevenness. Umair et al. (23) experimental readings were validated with the coupled SST and Gamma - theta transition model in CFX. The Standard deviation in Nusselt profile converge with the increase in the value of constant $c = \frac{Re}{z/d} > 6000$. Recently, Siddique

et al. (25) numerically investigated the modification in transitional semi empirical correlation of Nusselt number with linearly varying heat flux. The article carried the numerical work with unevenness in Nusselt profile, considering the slope parameter (m). Husain and Ariz (26) studied the effect of design parameter using 3D computational model to enhance heat transfer with effusion holes. Aminzadeh et al. (27) numerically examined the impact of inlet flow rate and temperature differences (0, 100, and 300K) on the behavior of a self-excited oscillating jet with Reynolds number 1000 and 3000. $\pm 10\%$ deviation in overall cooling rate was observed. The effect of viscous dissipation on heat transfer coefficient in laminar, non-Newtonian flows studied by Manglik and Prusa (28). The Nusselt number correlation with wall temperature gradient in transition region was proposed. Lu and Cheng (29) analyzed the friction factor and Nusselt number for viscous compressible flow in a tube. The turbulence friction factor was observed to be a strong function of velocity gradient and varies with impinging temperature. Wang et al. (30) experimentally investigated forced convection over NACA-63421 airfoil, for different temperature of streamed impinging jet, ranging from -30°C to 20°C . At $Re \geq 5 \times 10^5$, the average Nusselt number fluctuation was observed to be greater for a cylinder a compared with flat plate airfoil. The value of Nusselt density varying Reynold number (0 to $2 \frac{g}{m^3}$) for multiphase flow was proposed in terms of local Nusselt number. The uncertainty of Nusselt number was observed to lie within 7.34 %. Wang et al. (31) proposed a new non-dimensional correlation of heat transfer coefficient with impinging droplet on NACA airfoil at different angle of attack. The present work is actually inclined with a non – uniform heat flux boundary condition, and the degree of local unevenness is considered using a slope parameter (m). The average and local Nusselt number were found to vary with angle of attack. Extensive and massive work is carried out for predicting the externa flow heat transfer coefficient (Nusselt number) for impinging jet and sufficient correlations are available in terms of Reynold, Prandtl number and nozzle target spacing ($\frac{z}{d}$). It is true that the experimental arrangement for constant wall temperature boundary condition, in order to determine the heat transfer coefficient is difficult, hence current work, tries to propose a unique form of a varying heat flux. Such exponentially varying heat flux boundary condition and its inverse are some of the similar keens of constant temperature boundary conditions.

The objective of the current study is to establish and correlate the slope (m) of non-uniform heat flux, input velocity, nozzle –target spacing and heat transfer rate. The computations were performed using SST-K omega turbulence. In the later part the article proposes few empirical correlation, correlating the Nusselt number

with $Re, \frac{z}{d}$ and slope (m). Local Nusselt profile r/d is the local parameter incorporate.

2. NUMERICAL METHODOLOGY

2. 1. Computational Approches

The computational domain as shown in Figure 1 consist of flexible nozzle target spacing ($2 < \frac{z}{d} < 6$). Exponentially varying heat flux boundary condition is implemented for heating purpose. The numerical simulations are carried out using fluent and SST-K omega as solver and primary turbulence model, respectively. The Reynolds Number varies between 2000 to 14000 . Katti and Prabhu [4], proposed the correlation for Nusselt number magnitude for Reynolds number range 12000 to 28000.

The impingement was carried out, using straight smooth nozzle of 7.35 mm diameter. Sajad et. al. [17], proposed the stagnation Nusselt number correlation for Reynolds number range of 6000 – 14000. The air impinging nozzle was 13 mm in diameter and $L = 32D$. The diameter of impinging nozzle is selective, since the present study classifies the stagnation ($\frac{r}{d} \leq 0$), transition ($1 < \frac{r}{d} < 2.5$) and wall jet region ($\frac{r}{d} > 2.5$), separately.

The present study is carried out for the range of impinging Reynolds number, 2000 – 14000 under impinging nozzle of 8 mm. The air velocity at exit of the nozzle at inlet temperature ranges from 2 m/s to 15 m/s (For the current range of Reynolds number) The velocity of air is calculated using $Re = \frac{\rho V d}{\mu}$. The air velocity ranges from 2 m/s to 15 m/s. The nozzle diameter is chosen as 8 mm (4). The nozzle target spacing z/d varies between 2 – 6.

$$Q = Q_0 \times e^{mx} \quad (1)$$

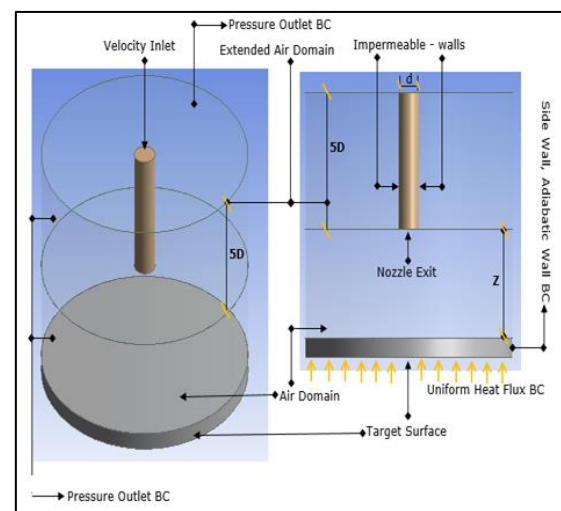


Figure 1. Computational Domain

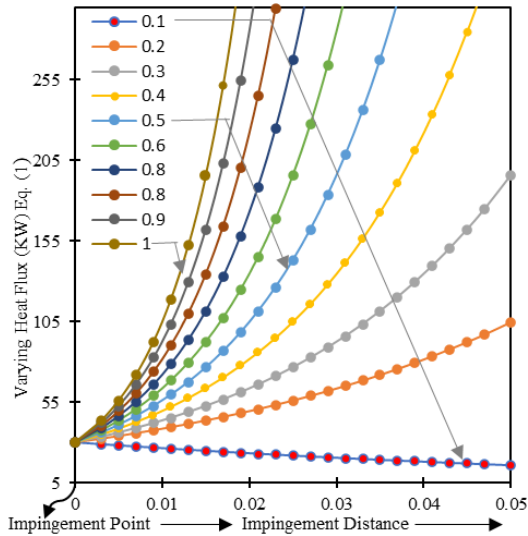


Figure 2. Exponential Varying Heat Flux condition

The heat flux boundary condition that changes exponentially from the stagnation point to far end region of the plate is mapped in Figure 2. Equation 1 defines the boundary condition as a ramping heat flux input, and Q_0 denotes the constant heat flux magnitude, m represents the slope of exponentially varying heat flux. The heat transfer rate for a fully developed impingement causes a forced convection. The heat transfer rate for forced convection is given in Equation 2 (16).

$$Q = h A_s (\bar{T}_s - \bar{T}_f) \tag{2}$$

The governing equation for Continuity, momentum and the energy are solved simultaneously in ANSYS FLUENT by using second order upwind method. The value of turbulence intensity at nozzle exit is set to 1-3% and turbulence Prandtl number as 0.7 (22).

$$\frac{\partial u_i}{\partial x_i} = 0 \tag{3}$$

$$\frac{\partial(\rho u)}{\partial t} + \rho u_j \frac{\partial u_i}{\partial x_j} = -\frac{\partial p}{\partial x_i} + \frac{\partial}{\partial x_j} (2\mu S_{ij} - \rho \overline{u'_i u'_j}) \tag{4}$$

$$\frac{\rho(\partial T)}{\partial t} + \rho u_j \frac{\partial T}{\partial x_j} = \frac{\partial}{\partial x_j} \left(\frac{k}{C_p} \frac{\partial T}{\partial x_j} - \rho \overline{u'_i T} \right) \tag{5}$$

where, S_{ij} is mean strain rate and C_p, μ & k are specific heat, viscosity and Thermal conductivity. Shear Stress Transport model, combining the effect of free stream and near wall region, gave satisfactory results for constant Heat Flux and Constant Temperature Boundary Condition. The four-equation turbulence model equation of SST and Gamma - Theta is summarized with Equation.

$$\frac{\partial k}{\partial t} + U_j \frac{\partial k}{\partial x_j} = P_k - \beta * k\omega + \partial/\partial x_j \left[\frac{(\vartheta + \sigma_k \vartheta_t) \partial k}{\partial x_j} \right] \tag{6}$$

$$\frac{\partial \omega}{\partial t} + U_j \frac{\partial \omega}{\partial x_j} = \alpha S^2 - \beta \omega^2 + \partial/\partial x_j \left[\frac{(\vartheta + \sigma_w \vartheta_t) \partial \omega}{\partial x_j} \right] + 2(1 - F_1) \sigma_{w2} \frac{1}{\omega} \frac{\partial k}{\partial x_i} \frac{\partial \omega}{\partial x_i} \tag{7}$$

In Equations 6 & 7 k represents the turbulent kinetic energy and ω represents the specific dissipation rate. $(\vartheta + \sigma_k \vartheta_t)$ and $(\vartheta + \sigma_w \vartheta_t)$ represents the effective diffusivities of k and ω respectively. αS^2 is cross diffusion term. Sajad Alimohammadi et al. (17) validated the SST and transition Gamma - Theta turbulence model, with CFX solver. Zhang et al. (32) validated the use of SST K - Omega turbulence model for constant Heat Flux Boundary Condition. The computation time with use of SST + K - Omega was found to be far less (60%), as compared with CFX (22).

2. 2. Grid Independence Test

An adaptive mesh with different growth rate along X and Y axis are generated using Mesh modeler of Ansys pack 2023R1. Growth rate are kept adaptive, in order to generated optimal number of nodes and cell size. The mesh shown in Figure 3, is orthogonal unstructured, with skewness in range of 0.9-1 The heat transfer highly relies on quality and density of grid and number of nodes and structure of computational domain. Hence, to ensure that the grid independence result and optimistic time of computation. Grid independence is carried out by varying the number of nodes of 2-D computational domain. The grid independence is carried out at $\frac{z}{a} = 4$ & $Re = 12000$. The distance of first cell from wall, in combination with post computing multiple, defines a non-dimensional y^+ . As per Nikuradse (33), this value is maintained much less than 1, throughout the domain. Figure 4 shows the Nusselt number distribution for various grid sizes.

In order to get optimum grid size, number of divisions are varied along the radial and axial directions, ranging from 240 to 480 and 280 to 520, respectively. However, it is advisable to adjust the number of divisions according

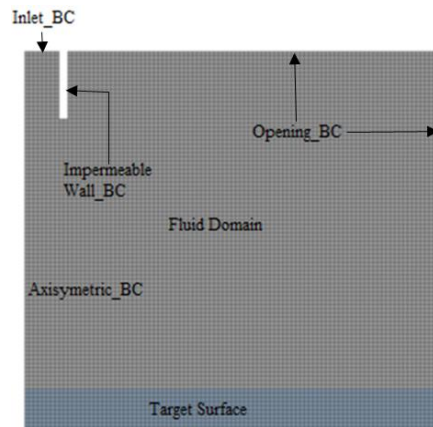


Figure 3. Schematic diagram of grid

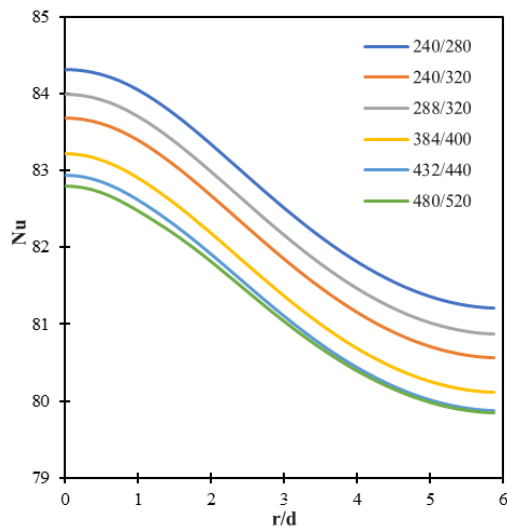


Figure 4. Nusselt profile for various number of division over radial/axial direction at $z/d=4$ & $Re=12000$

to changes in the $(\frac{z}{d})$ value. Thus, mesh size containing 480 the number of divisions on radial and 520 number of division on axial edge is found to give the results within $\pm 1\%$ of previous grid size.

2. 3. Validation of Turbulence Model As per the literature study, especially for impingement of jet, it is very crucial to accurately compute the heat transfer in both the near wall and far wall regions, which majorly dependence on the choice of appropriate turbulence model. A graphical comparative study is carried out at $\frac{z}{d} = 4$ and Reynolds number 12000. Figure 5 illustrates the result of heat transfer, in form of Nusselt profile for different turbulence model. The adverse pressure gradient effect makes the k -epsilon turbulence model fails to predict the heat transfer. On the other hand, the k -omega turbulence model provides an accurate profile but deviates significantly, In near jet and far jet region. This is due its especially in predicting the flow behavior in near wall region for 'Internal Forced Convection'. The discrepancy arises for the model choice and its ability to predict turbulence vortices generated, due to impingement. Menter (34) strongly justifies the use of SST turbulence model for estimating turbulence heat transfer with air jet. The SST turbulence model incorporates an additional term that effectively predicts the production and termination of local turbulence vortices, the turbulence production term (p_k). Not only that the latest study by Alimohammadi et al. (17) and Umair et al. (35) strongly recommend the use of SST-K omega and SST-Gamma Theta for accurately mapping the turbulence behavior for the case of impingement. The current work is inclined towards measurement of heat transfer for ranges of Reynolds number (Re), nozzle

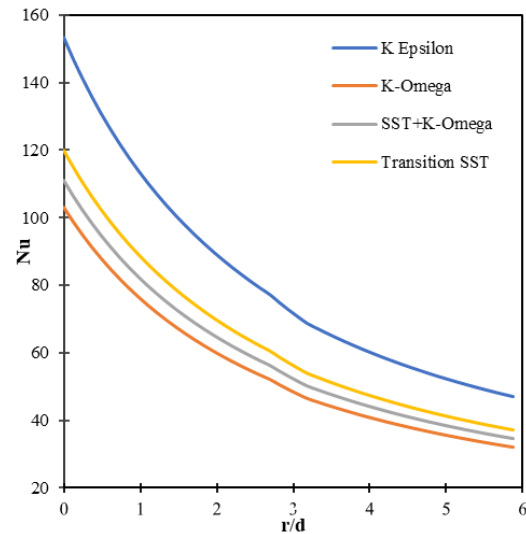


Figure 5. Nusselt profile for different Turbulence Models at $z/d=4$ & $Re=12000$

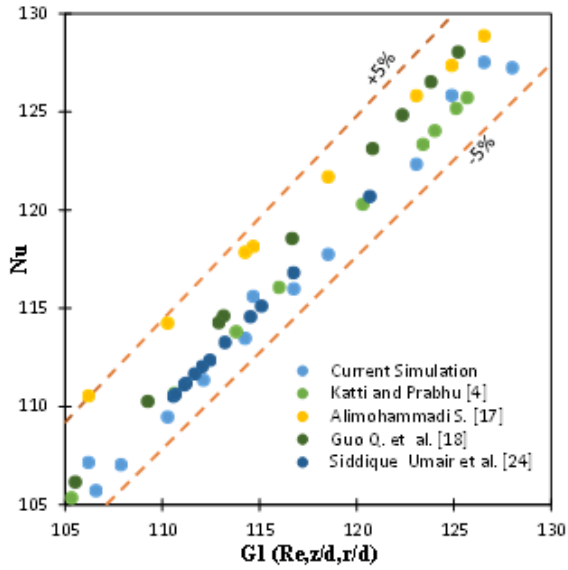
target spacing $(\frac{z}{d})$ and slope parameter (m) against radial distance $(\frac{r}{d})$. Figures 6(a) & 6(b) represent the validation of current grid size and turbulence model with the results of Katti and Prabhu (4). The proposed correlation at stagnation $(0 < \frac{r}{d} < 1)$ and transition region $(1 < \frac{r}{d} < 2.5)$, digitized and compared in Figures 7(a) & 7(b). Validations are carried out for $\frac{z}{d} = 4$ and Reynolds number of 10000, 12000 and 14000 which are shown in Figures 6(a) & 6(b). The approximate percentage error of present computation with Katti and Prabhu (4) results lies within $\pm 10\% \sim \pm 15\%$. The underestimation of heat transfer results with FLUENT, as in present case, is due to the lack of constraints in mapping the turbulence vortices and its timely changed behavior with different boundary condition.

2. 4. Overall and Local Cooling Rate for Different Reynolds Number

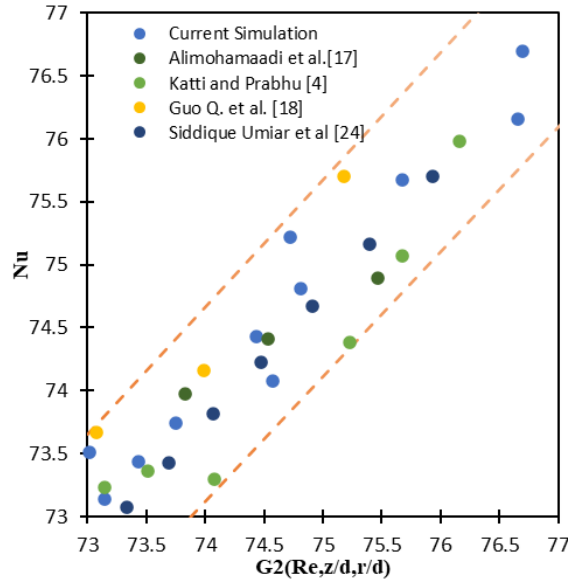
Figure 7 shows the Nusselt number magnitude distribution with varying Reynold number at constant nozzle target spacing of 4 and slope of 0.5. In the present study Reynolds number is varied from 2000 – 14000. With an increase in Reynolds number the local Nusselt magnitude increases along, locally. The average Nusselt magnitude increases with an increase in Reynolds number. The stagnation increase is due to the adverse pressure gradient and radial increase is due to higher velocity gradient. At higher velocity, the heat carried away quickly and thus forced convection renders better heat transfer coefficient, with impingement.

2. 5. Overall and Local Cooling Rate for Different Nozzle Target Spacing (z/d)

Figure 8 represents



(a) Stagnation Region



(b) Transition Region

Figure 6 (a) & (b). Turbulence model validation at stagnation and transition region

the variation of nozzle target spacing ($\frac{z}{d}$) at a constant Reynold number of 12000. The Nusselt profile exhibit a consistent slope value of 0.5. As the distance between nozzle and target surface increases, the local Nusselt magnitude decrease. However, this trend is not applicable for a nozzle target spacing less than 1 ($\frac{z}{d} < 1$). This is due to the under- development of the potential core and lack of computational model availability. At a Reynold number of 12000, the potential core is well developed for nozzle target spacing values greater than 4 resulting a smooth Nusselt profile.

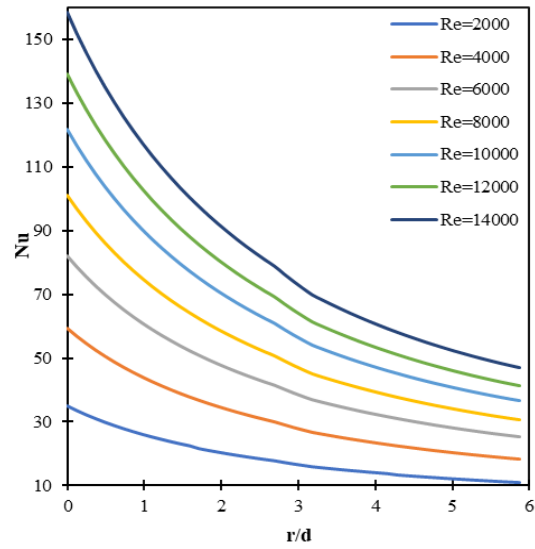


Figure 7. Nusselt Profile at different Reynold number

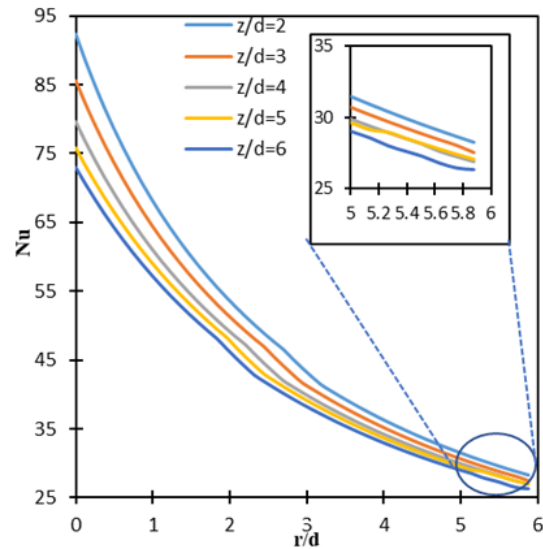


Figure 8. Nusselt profile at varying z/d

2. 6. Overall and Local Cooling Rate for Different Slope of Varying Heat Flux

Figure 9 represents the Nusselt profile with a Reynold number of 12000 and $z/d=4$ at various slope (m) parameter of Input heat flux. The observation from Figure 9 indicate the heat dissipation to be more at lower slope ($m < 0.5 - 0.6$). The heat transfer rate from the impinging fluid to the target surface reduces as the slope of heat flux increases. The local Nusselt number is reduced for higher slopes of heat input, and the overall distribution of the Nusselt profile under non-uniformity heat flux boundary conditions is Affected. Such non-uniformity is of practical importance in electronic packaging system.

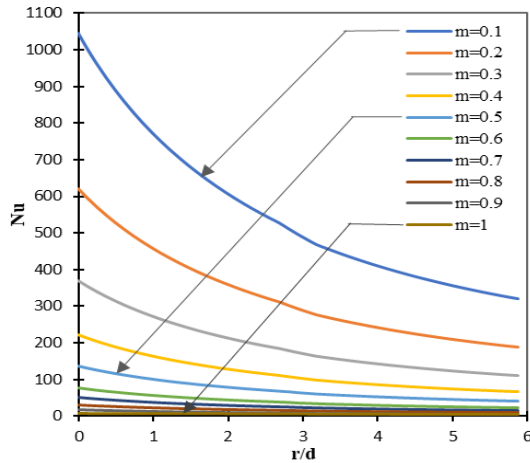


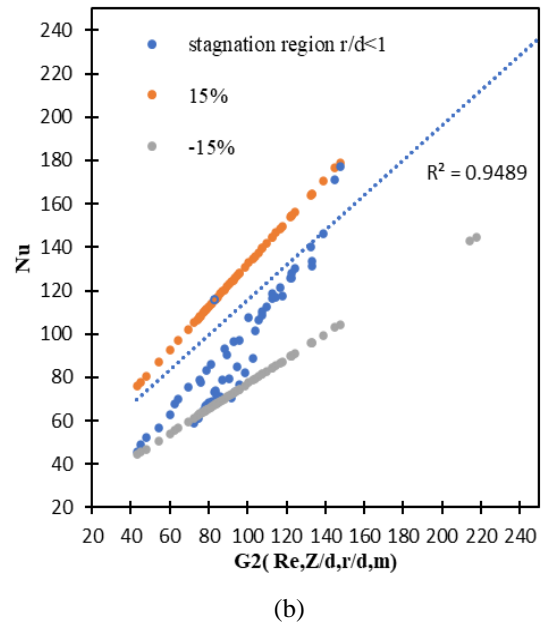
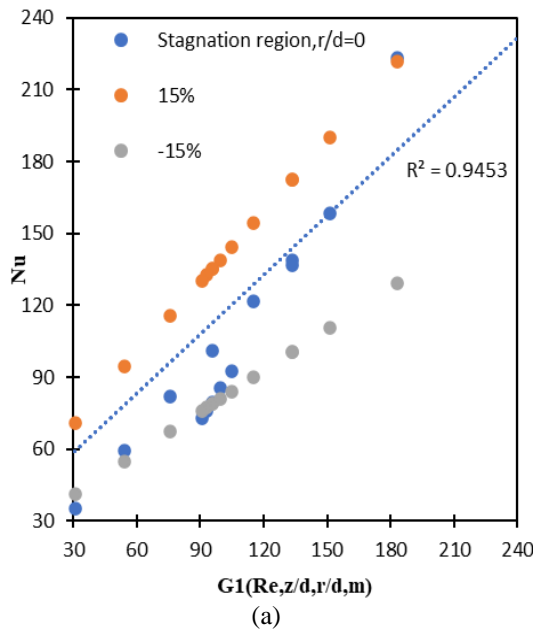
Figure 9. Nusselt Profile at different slope of input

2. 7. Semi-empirical Correlations Representing Nusselt Profile

In the current simulation the Nusselt number empirical relation is proposed for various regions at stagnation region ($\frac{r}{d} = 0$) & ($0 < \frac{r}{d} < 1$), transition region ($1 < \frac{r}{d} < 2.5$) and wall jet regions ($\frac{r}{d} > 2.5$). The empirical correlations are formed using regression analysis by sampling the data of different heat transfer results of varying Reynolds (Re), $\frac{z}{d}$ & m . Table 1 shows the corresponding correlation for every individual region. The correlations proposed in Table 1, is within $\pm 15\%$ error, and should be applicable for practical problems of non-uniform heat flux. The error of $\pm 15\%$ as shown in Figure 10 is well in line with external forced convection of , Cenjal (16).

TABLE 1. Proposed Correlation for Local Nusselt Number at Different Regions

Region	Function	Semi-empirical relation
Stagnation region ($\frac{r}{d} = 0$)	$G1\left(Re, \frac{z}{d}, m, \frac{r}{d}\right)$	$Nu = 0.0282 \times (Re)^{0.815} \left(\frac{z}{d}\right)^{-0.131} (m)^{-1.425}$
Stagnation region ($0 < \frac{r}{d} < 1$)	$G2\left(Re, \frac{z}{d}, m, \frac{r}{d}\right)$	$Nu = 0.0212 \times (Re)^{0.815} \left(\frac{z}{d}\right)^{-0.104} (m)^{-1.419} \left(\frac{r}{d}\right)^{-0.119}$
Transition region ($1 < \frac{r}{d} < 2.5$)	$G3\left(Re, \frac{z}{d}, m, \frac{r}{d}\right)$	$Nu = 0.0254 \times (Re)^{0.788} \left(\frac{z}{d}\right)^{-0.078} (m)^{-1.419} \left(\frac{r}{d}\right)^{-0.382}$
Wall jet region ($\frac{r}{d} > 2.5$)	$G4\left(Re, \frac{z}{d}, m, \frac{r}{d}\right)$	$Nu = 0.192 \times (Re)^{0.79} \left(\frac{z}{d}\right)^{-0.202} (m)^{-1.328} \left(\frac{r}{d}\right)^{-0.584}$



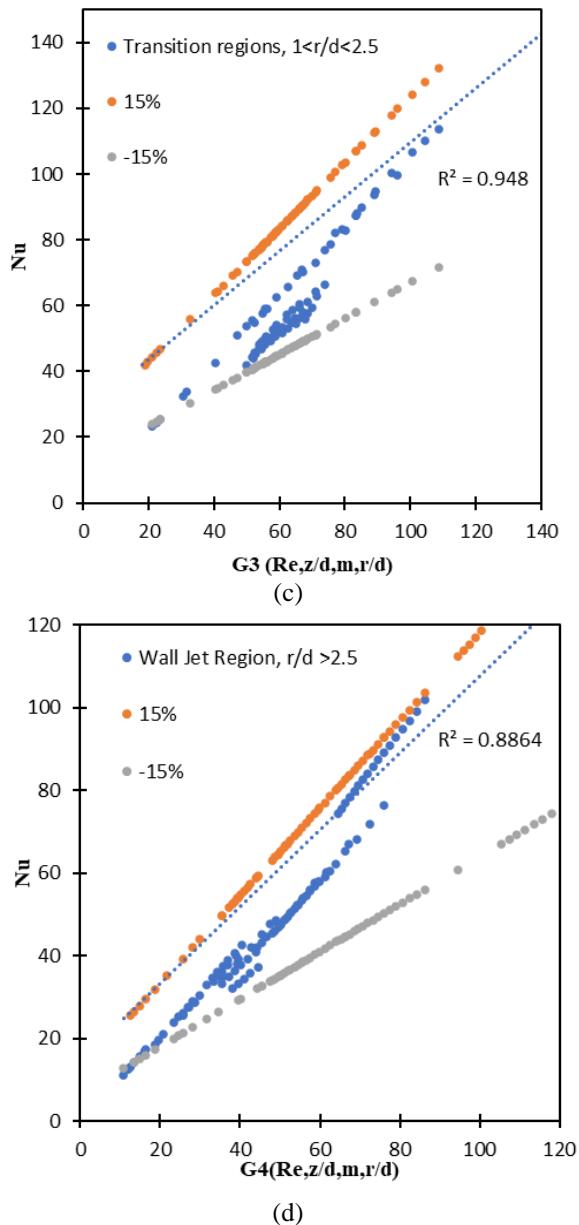


Figure 10. Validation of G1, G2, G3 & G4 function with local Nusselt number

3. CONCLUSION

The present work investigated using exponentially varying heat flux boundary, inevitably justifies the dependency of impinging Reynolds number (pumping power) and nozzle-target surface spacing, as that of constant heat flux boundary condition literature. The extended robustness of SST coupled K-Omega turbulence model in computing the flow field for non-uniform boundary condition is observed. The local cooling profile (Nu Vs G (Re, z/d, m, r/d)) for non-uniform exponent of 0.1 – 1, is found to replicate the constant wall temperature boundary condition. The

customized exponentially powered heat flux boundary condition can be taken as the substitute for constant wall temperature boundary condition computation purpose. Many commercial computing software like FLUENT, OpenFOAM, MATLAB. is less responsive to such constant wall temperature boundary condition.

4. SCOPE OF FUTURE WORK

Constant wall temperature boundary condition is seamless problem for young researchers, specially when it is simulation in FLUENT. As per the most authoritative textbooks, the constant wall temperature boundary condition, is achieved with wall hot water circulation. Such traditional arrangement in FLUENT, will require extra computational effort and time. The novel exponentially powered heat flux boundary condition renders a similar result as that of constant temperature. The choice of exponent magnitude, as per the available non – uniform heat flux or uniform temperature, can be easily replicated with exponent magnitude. The generic profile of exponential heat flux boundary condition can be further investigated more to its equivalency for constant temperature BC. The exponential slope parameter can even be use for defining the cooling in various material processing industries, to forecast the type of strength desired.

5. ACKNOWLEDGMENTS

The experimental setup received financial support from Technical Education Quality Improvement Program-II (TEQIP-II/MH2G03/204)/778) at Veermata Jijabai Technological Institute under the guidance of Prof. N P Gulhane. Prof. Nitin P Gulhane is currently acting as a supervisor and Dr. Siddique Umair is the co-supervisor. Mr. Avinash–M. Rathod (First Author) has received Research Fellowship for investigating Jet Impingement Heat Transfer from Mahatma Jyotiba Phule Research & Training Institute (MAHAJYOTI-Fellowship 2022_198).

6. REFERENCES

1. Ricou FP, Spalding D. Measurements of entrainment by axisymmetrical turbulent jets. *Journal of fluid mechanics.* 1961;11(1):21-32. <https://doi.org/10.1017/S0022112061000834>
2. Hoogendoorn C. The effect of turbulence on heat transfer at a stagnation point. *International Journal of Heat and Mass Transfer.* 1977;20(12):1333-8. [https://doi.org/10.1016/0017-9310\(77\)90029-1](https://doi.org/10.1016/0017-9310(77)90029-1)
3. Pamadi B, Belov I. A note on the heat transfer characteristics of circular impinging jet. *International Journal of Heat and Mass Transfer.* 1980;23(6):783-7. [https://doi.org/https://doi.org/10.1016/0017-9310\(80\)90032-0](https://doi.org/https://doi.org/10.1016/0017-9310(80)90032-0)

4. Katti V, Prabhu S. Experimental study and theoretical analysis of local heat transfer distribution between smooth flat surface and impinging air jet from a circular straight pipe nozzle. *International Journal of Heat and Mass Transfer*. 2008;51(17-18):4480-95. <https://doi.org/10.1016/j.ijheatmasstransfer.2007.12.024>
5. KATAOKA K, SHUNDOH H, MATSUO H. A generalized model of the development of nonisothermal, axisymmetric free jets. *Journal of Chemical Engineering of Japan*. 1982;15(1):17-22. <https://doi.org/DOI:10.1252/JCEJ.15.17>
6. Behera RC, Dutta P, Srinivasan K. Numerical study of interrupted impinging jets for cooling of electronics. *IEEE Transactions on Components and Packaging Technologies*. 2007;30(2):275-84. <https://doi.org/10.1109/TCAPT.2007.898353>
7. Shadlesky P. Stagnation point heat transfer for jet impingement to a plane surface. *AIAA Journal*. 1983;21(8):1214-5. <https://doi.org/10.2514/3.8231>
8. Hollworth B, Gero L. Entrainment effects on impingement heat transfer: part II—local heat transfer measurements. 1985. <https://doi.org/https://doi.org/10.1115/1.3247520>
9. Zumbrennen D, Incropera F, Viskanta R. Convective heat transfer distributions on a plate cooled by planar water jets. 1989. <https://doi.org/https://doi.org/10.1115/1.3250802>
10. Goldstein R, Seol W. Heat transfer to a row of impinging circular air jets including the effect of entrainment. *International journal of heat and mass transfer*. 1991;34(8):2133-47. [https://doi.org/https://doi.org/10.1016/0017-9310\(91\)90223-2](https://doi.org/https://doi.org/10.1016/0017-9310(91)90223-2)
11. Lytle D, Webb B. Air jet impingement heat transfer at low nozzle-plate spacings. *International Journal of Heat and Mass Transfer*. 1994;37(12):1687-97. [https://doi.org/10.1016/0017-9310\(94\)90059-0](https://doi.org/10.1016/0017-9310(94)90059-0)
12. Behnia M, Parneix S, Shabany Y, Durbin P. Numerical study of turbulent heat transfer in confined and unconfined impinging jets. *International Journal of Heat and Fluid Flow*. 1999;20(1):1-9. [https://doi.org/https://doi.org/10.1016/S0142-727X\(98\)10040-1](https://doi.org/https://doi.org/10.1016/S0142-727X(98)10040-1)
13. Garimella SV, Schroeder VP. Local heat transfer distributions in confined multiple air jet impingement. *J Electron Packag*. 2001;123(3):165-72. <https://doi.org/10.1115/1.1371923>
14. Han B, Goldstein RJ. Jet-impingement heat transfer in gas turbine systems. *Annals of the New York Academy of Sciences*. 2001;934(1):147-61. <https://doi.org/https://doi.org/10.1111/j.1749-6632.2001.tb05849.x>
15. Sagot B, Antonini G, Christgen A, Buron F. Jet impingement heat transfer on a flat plate at a constant wall temperature. *International Journal of Thermal Sciences*. 2008;47(12):1610-9. <https://doi.org/10.1016/j.ijthermalsci.2007.10.020>
16. Çengel YA, Ghajar AJ. *Heat and Mass Transfer: Fundamentals [and] Applications*: McGraw-Hill Education; 2020.
17. Alimohammadi S, Murray DB, Persoons T. Experimental validation of a computational fluid dynamics methodology for transitional flow heat transfer characteristics of a steady impinging jet. *Journal of Heat Transfer*. 2014;136(9):091703. <https://doi.org/10.1016/j.ijheatmasstransfer.2016.09.048>
18. Guo Q, Wen Z, Dou R. Experimental and numerical study on the transient heat-transfer characteristics of circular air-jet impingement on a flat plate. *International Journal of Heat and Mass Transfer*. 2017;104:1177-88. <https://doi.org/10.1016/j.ijheatmasstransfer.2017.03.064>
19. Luhar S, Sarkar D, Jain A. Steady state and transient analytical modeling of non-uniform convective cooling of a microprocessor chip due to jet impingement. *International Journal of Heat and Mass Transfer*. 2017;110:768-77. <https://doi.org/10.5829/idosi.ije.2015.28.10a.14>
20. Muniyandi V. Heat transfer study of perforated fin under forced convection. *International Journal of Engineering, Transactions A: Basics*., 2015;28(10):1500-6. <https://doi.org/10.5829/idosi.ije.2015.28.10a.14>
21. GULHANE N, Siddique U. On numerical investigation of non-dimensional constant representing the occurrence of secondary peaks in the Nusselt distribution curves. *International Journal of Engineering, Transactions A: Basics*., 2016;29(10):1431-40. <https://doi.org/10.5829/idosi.ije.2016.29.10a.00>
22. Mohd Umair S, Gulhane N, Al-Robaian A, Khan SA. On numerical investigation of semi-empirical relations representing local nusselt number at lower nozzle-target spacing's. *International Journal of Engineering, Transactions A: Basics*., 2019;32(1):137-45. <https://doi.org/10.5829/ije.2019.32.01a.18>
23. Umair SM, Gulhane NP. On numerical investigation of nonuniformity in cooling characteristic for different materials of target surfaces being exposed to impingement of air jet. *International Journal of Modeling, Simulation, and Scientific Computing*. 2017;8(03):1750024. <https://doi.org/10.1142/S1793962317500246>
24. Siddique UM, Bhise GA, Gulhane NP. On numerical investigation of local Nusselt distribution between flat surface and impinging air jet from straight circular nozzle and power law correlations generation. *Heat Transfer—Asian Research*. 2018;47(1):126-49. <https://doi.org/10.1002/htj.21295>
25. Siddique Mohd U, Ansari E, Khan SA, Gulhane NP, Patil R. Numerical Investigation of Nondimensional Constant and Empirical Relation Representing Nusselt Profile Nonuniformity. *Journal of Thermophysics and Heat Transfer*. 2020;34(1):215-29. <https://doi.org/10.2514/1.T5828>
26. Husain A, Ariz M. Thermal performance of jet impingement with spent flow management. *International Journal of Engineering, Transactions A: Basics*., 2017;30(10):1599-608. <https://doi.org/10.5829/ije.2017.30.10a.22>
27. Aminzadeh M, Khadem J, Zolfaghari S, Omidvar A. Numerical Investigation on Oscillation Behavior of a Non-isothermal Self-excited Jet in a Cavity: The Effects of Reynolds Number and Temperature Differences. *International Journal of Engineering, Transactions C: Aspects*. 2022;35(6):1193-201.
28. Manglik R, Prusa J. Viscous dissipation in non-Newtonian flows—Implications for Nusselt number. *Journal of thermophysics and heat transfer*. 1995;9(4):733-42. <https://doi.org/10.2514/3.732>
29. Lu G, Cheng P. Friction factor and Nusselt number for thermoacoustic transport phenomena in a tube. *Journal of thermophysics and heat transfer*. 2000;14(4):566-73. <https://doi.org/10.2514/2.6558>
30. Wang X, Bibeau E, Naterer G. Experimental correlation of forced convection heat transfer from a NACA airfoil. *Experimental thermal and fluid science*. 2007;31(8):1073-82. <https://doi.org/10.1016/j.expthermflusci.2006.11.008>
31. Wang X, Naterer G, Bibeau E. Multiphase Nusselt Correlation for the Impinging Droplet Heat Flux from a NACA Airfoil. *Journal of thermophysics and heat transfer*. 2008;22(2):219-26. <https://doi.org/10.2514/1.32401>
32. Zhang Y, Li P, Xie Y. Numerical investigation of heat transfer characteristics of impinging synthetic jets with different waveforms. *International Journal of Heat and Mass Transfer*. 2018;125:1017-27. <https://doi.org/10.1016/j.ijheatmasstransfer.2018.04.120>
33. Williamson J. The laws of flow in rough pipes. *La Houille Blanche*. 1951(5):738-57. <https://doi.org/10.1051/lhb/1951058>
34. Menter FR. Influence of freestream values on k-omega turbulence model predictions. *AIAA journal*. 1992;30(6):1657-9. <https://doi.org/10.2514/3.11115>
35. Umair SM, Kolawale AR, Bhise GA, Gulhane NP. On numerical heat transfer characteristic study of flat surface subjected to variation in geometric thickness. *International Journal of Computational Materials Science and Engineering*. 2017;6(02):1750010. <https://doi.org/10.1142/S2047684117500105>

COPYRIGHTS

©2024 The author(s). This is an open access article distributed under the terms of the Creative Commons Attribution (CC BY 4.0), which permits unrestricted use, distribution, and reproduction in any medium, as long as the original authors and source are cited. No permission is required from the authors or the publishers.

**Persian Abstract****چکیده**

سرعت خنک کننده تحت برخورد جت هوا کاربرد گسترده ای در بسته بندی الکترونیکی، صنایع پردازش مواد و خنک سازی توربین گاز پیدا می کند. خنک سازی معمولی سینک های حرارتی تا به امروز با استفاده از فن و پمپ انجام می شد. اخیراً مشخص شده است که برخورد مهم هوا در مقایسه با روش معمولی، ۱.۵ برابر سرعت خنک سازی با قدرت پمپاژ یکسان تولید می کند. پیش از این، تحقیقات جذابی در مورد مشاهده سرعت خنک سازی برای شرایط مرزی شار حرارتی ثابت انجام شده است و کمتر برای دمای ثابت دیوار در دسترس است. تحقیق حاضر یک بررسی عددی عمیق را برای چنین سینک های حرارتی برخورد شده با جت، با شرایط مرزی شار حرارتی ارائه می دهد. تغییر نمایی بزرگی شار حرارتی با فاصله شعاعی (دور از نقطه برخورد)، به عنوان یک جایگزین عمومی از شرایط مرزی دمای دیواره ثابت مشاهده می شود. محاسبات عددی برای انتقال حرارت چنین سینک شار حرارتی با نیروی نمایی با استفاده از FLUENT (ANSYS 2023R1) انجام می شود. یک دامنه محاسباتی مش دوبعدی متعامد با مدل تلاطم **SST** و **K-Omega** فشرده برای سرعت ورودی و فاصله نازل-هدف مختلف شبیه سازی شده است. برخورد جت و خنک کننده موضعی سطح هدف به ترتیب با استفاده از عدد رینولدز و ناسلت غیربهدی شناخته شده تعریف می شود. توان نمایی برای سینک هایی که به طور یکنواخت گرم می شوند را می توان به آسانی انتخاب کرد (۰.۱-۱) برای تکرار گرمایش غیریکنواخت فعلی یا شرایط مرزی دمای دیوار ثابت. گرمایش غیریکنواخت توجه بسیاری از محققین انتقال حرارت را در سراسر جهان به خود جلب کرده است. نتایج محاسباتی استخراج شده برای عدد رینولدز مختلف و فاصله نازل-هدف، با استفاده از رگرسیون بهترین برازش را داشتند و با نتایج ادبیات قبلی ارجاع شده اعتبارسنجی شدند. وابستگی شدید پارامتر شیب به عدد رینولدز و Z/d در نرخ خنک سازی موضعی مشاهده می شود. این وابستگی ها بر اساس قدرت توان ها قضاوت می شوند. همبستگی های نیمه تجربی به طور جداگانه برای مناطق رکود، انتقال و جت دیواری به طور جداگانه تعریف می شوند. چنین همبستگی می تواند طراحی سیستم خنک کننده را در شرایط گرمایش غیر یکنواخت برنامه ریزی کند.



Basic Engineering Properties of Concrete with Refractory Brick as Coarse Aggregate: Compressive Stress-Time Relationship Assessment

U. Jureje, M. W. Tjaronge, M. A. Caronge*

Civil Engineering Department, Universitas Hasanuddin, Makassar, Indonesia

PAPER INFO

Paper history:

Received 15 August 2023

Received in revised 13 September 2023

Accepted 17 December 2023

Keywords:

Refractory Brick Aggregate

Compressive Strength

Compressive Stress-time Relationship

Toughness Index

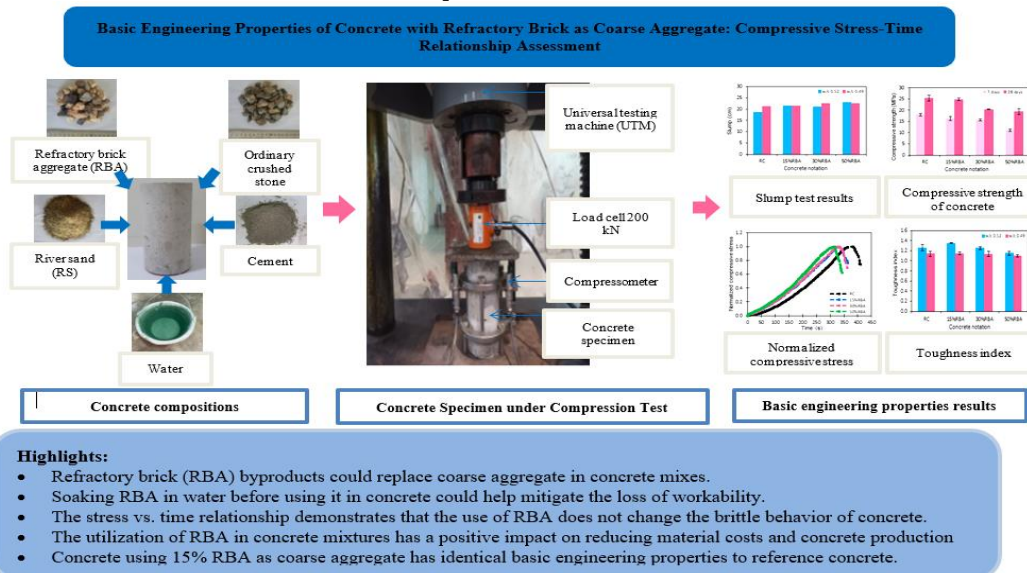
Sustainable Concrete

ABSTRACT

This study aims to investigate the use of refractory brick (RBA) by-products as a substitute for coarse aggregate in sustainable concrete production. Concrete mixes with water-to-binder (w/c) ratios of 0.52 and 0.49 and containing 0%, 15%, 30%, and 50% RBA as a partial replacement for ordinary crushed stone (OCS) were produced. The following properties were examined in this study: workability, compressive strength, stress-time relationship, toughness index, performance criteria, and cost analysis. The test results showed that an increase in the RBA percentage in the concrete mixtures positively contributed to concrete workability. Moreover, the compressive strength and all phases in the compressive stress and time relationship decreased as the percentage of RBA in the concrete mixture increased. However, at 15%RBA, the toughness index value was comparable to that of the reference concrete, whereas based on the performance criteria, the replacement of OCS with 15%RBA for both water-cement ratios met the minimum requirements. Meanwhile, cost comparison analysis discloses that material and production costs can be reduced by approximately 51.84% and 1.5–6.5%, respectively. Based on the analysis of all the test results, 15%RBA exhibited insignificant differences in value compared with the reference concrete. Thus, the use of 15%RBA as an OCS replacement is an acceptable and viable option for producing sustainable concrete.

doi: 10.5829/ije.2024.37.05b.11

Graphical Abstract



*Corresponding Author Email: ma-caronge@unhas.ac.id (M. A. Caronge)

1. INTRODUCTION

The large-scale construction of buildings and infrastructure in urban areas, which are mostly composed of concrete and mortar, requires large amounts of sand and naturally crushed stone or ordinary crushed stone (OCS). Concrete is manufactured with an aggregate proportion of approximately 60–75% of the overall volume, with approximately 45% coarse aggregate (1, 2). Each year, approximately 13.12 billion tons of aggregates are globally utilized (3). Related to the conditions mentioned above, it is necessary to keep abreast of major changes in reuse and recycling technology so as to significantly reduce the use of virgin materials as building materials and to provide added value to non-hazardous waste (4).

Refractory brick (RB) by-products are non-hazardous and non-toxic solid by-products that can be used as fire-resistant and high-temperature furnace walls. The number of RB by-products will continue to grow in line with the need for furnaces. Approximately 28 million tons of RB by-products are generated each year (5). In general, the utilization of RB by-products as aggregates or additives for concrete production has been extensively studied (6-9).

Efforts to add value to by-products and provide sustainable cement have encouraged cement manufacturers to adopt fly ash or pozzolanic materials from other by-products as cement substances to produce blended cement (10). Such cement recognized as sustainable cement and is available in the national market as Portland composite cement (PCC) and used to produce reliable concrete and mortar (11).

The robustness of concrete structures to compressive loads is characterized by the mechanisms of compressive failure that may occur, which depend on the constituent properties of the concrete. One of the qualitative assessments used to evaluate the failure mechanism is through the loading response time behaviour described in the scientific literatures (12, 13).

The investigational method utilized throughout this study to develop a link between stress and related time responses is proposed as a novel approach to the assessment of hardened concrete containing RB and blended cement under compressive load.

2. MATERIALS AND METHODS

2.1. Materials PCC blended cement that available on the market serves as the principal binder in the manufacture of all concrete mixtures in this study. The PCC cement used has a specific gravity of 3.07 and fulfills the Indonesian requirement for PCC.

Fine aggregate is natural sand mined from rivers and defined as river sand (RS). Ordinary stone spanning

numerous surfaces in the same nickel-obtaining location was crushed into a smaller, coarser shape and then regarded as coarse aggregate. In the present study, such aggregate was defined as ordinary crushed stone (OCS) in the process of producing regular concrete. The Refractory Brick Aggregate (RBA) used in this study was acquired from the kiln walls of a nickel slag ore furnace in Sorowako, Indonesia. The RBA were crushed manually and sieved to obtain the required size and amount to produce coarse-aggregate RBA with a size range of 10–28 mm.

The grain size distribution of RS, OCS, and RBA complies with the concrete mix gradation standard according to ASTM C33 (14). The grain size distribution of RS, OCS, and RBA is shown in Figure 1, and the physical appearance of RS, OCS, and RBA is shown in Figure 2. Meanwhile, the physical properties of RS, OCS, and RBA are listed in Table 1.

The primary chemical compound components of RBA are Al₂O₃ (17.52%), SiO₂ (35.11%), and Fe₂O₃ (19.55%), all of which can be characterized as reactive owing to their high combustion temperatures. Based on the physical properties listed in Table 1, RBA possesses lower specific gravity and higher water absorption than OCS. Such high water absorption was due to the presence of pores on the surface of the RBA. The property causes the RBA abrasion value greater than OCS, which is 36% for RBA and 17.5% for OCS, as summarized in Table 1.

Owing to the high water absorption of RBA, prior to their inclusion in the concrete mix, the RBA were pretreated by immersion in water for 4 hours and then air-dried until saturated surface dry (SSD) conditions. This

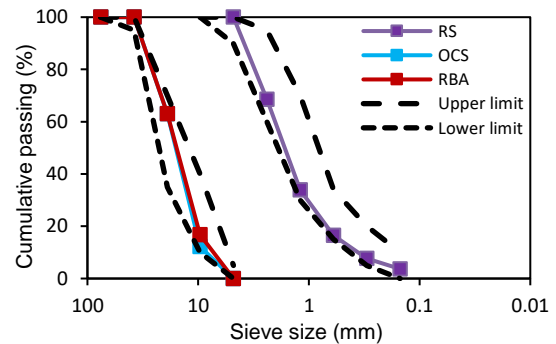


Figure 1. Gradation of aggregate grain size



(a) RS (b) OCS (c) RBA

Figure 2. Physical appearance of the aggregate

TABLE 1. Physical properties of aggregates

Item	Specific gravity	Water absorption (%)	Fineness modulus	Los angeles abrasion (%)
RS	3.02	0.45	3.70	-
OCS	3.13	0.36	7.25	17.50
RBA	2.92	2.91	7.20	36.00
Testing standard	ASTM C127 (15) and ASTM C128 (16)		ASTM C136 (17)	ASTM C131 (18)

approach is in accordance with the methodology applied by previous researchers (6). This approach mitigates the loss of water during mixing owing to the high water absorption of RBA.

2. 2. Mix Proportions and Specimen Preparation

The design of concrete mixture is carried out through the trial mix process to obtain a proportional mixture composition for the target concrete strength (f'c) of 21 MPa and 25 MPa with w/c of 0.52 and 0.49, respectively. Eight concrete mix compositions were prepared using the RBA by-product as a partial replacement for OCS at 0%, 15%, 30%, and 50% by aggregate volume. The concrete mix design is presented in Table 2, and concrete mixing is carried out based on ASTM C192 (19). The concrete sample was manufactured using a 75-liter mixer. Then, the fresh concrete mixture was poured into an iron cylinder mold with a diameter of 100 mm and a height of

200 mm and compacted for 60 s using a vibrator machine. The concrete mixture was then left for 24 hours before the mold was opened, and the concrete samples were soaked in fresh water at a constant temperature of 20±2 °C until the testing day.

2. 3. Fresh Concrete Test The slump test of fresh concrete was performed according to ASTM C143 (20). In this study, a target slump measuring 20±2 cm was used.

2. 4. Compressive Strength Test The compressive strength test was performed using a universal testing machine (UTM) with a capacity of 1000 kN, as depicted in Figure 3, based on ASTM C39 (21). The load is applied to the surface of the specimen at a speed of 0.25 MPa/second until the specimen is crushed. To provide a straightforward alignment between the time response and compressive stress, a load cell coupled with a set of computerized devices was used to capture the load value and linked time during the compressive testing process. A concrete compressive strength test was performed on three specimens of each concrete mixture, and the average values of the three samples were adopted for quantitative assessment.

2. 5. Toughness Index The toughness index is a parameter that describes the behaviour of a solid material

TABLE 2. The concrete mix designs

Notation	f'c = 21 MPa (w/c = 0.52)				f'c = 25 MPa (w/c = 0.49)			
	RC	15%RBA	30%RBA	50%RBA	RC	15%RBA	30%RBA	50%RBA
Water, (kg/m ³)	238	238	238	238	236	236	236	236
Cement, (kg/m ³)	458	458	458	458	487	487	487	487
RS, (kg/m ³)	755	755	755	755	743	743	743	743
OCS, (kg/m ³)	1132	962	793	566	1115	948	781	558
RBA, (kg/m ³)	0	159	318	531	0	157	314	523



Figure 3. Concrete specimen test setup

such as concrete at post-peak stress and indicates the energy capability of the concrete to resolve the fracture of the material.

As depicted in Figure 4, the toughness index is calculated by dividing the area under compressive stress against time with details of the initial stress area up to 80% post-peak stress divided by the area from initial stress to peak stress, where in this study the y axis is compressive stress and the x axis is time. This calculation is based on previous studies (22, 23).

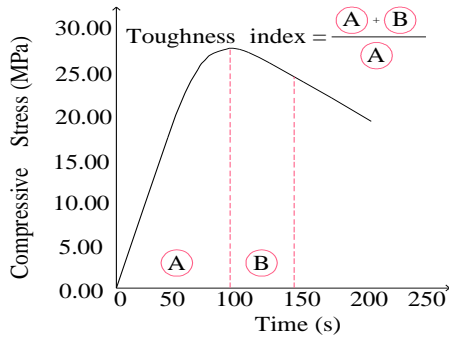


Figure 4. Definition of toughness index

3. RESULTS AND DISCUSSION

3.1. Workability According to Figure 5, it is clear that the slump values achieved by the RC and all RBA mixtures meet the slump design of 20 ± 2 cm, which indicates that the workability of fresh concrete can be easily handled in the field. Other studies also found that the use of brick waste as coarse aggregates in concrete mixes increases the slump (24). The visual observation depicted in Figure 6 revealed that bleeding and segregation did not occur. These qualitative results indicate good workability, which positively influences the pouring and compaction processes.

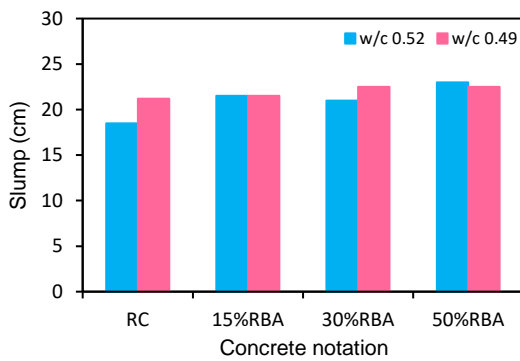


Figure 5. Slump values of the fresh concrete for different percentages of RBA



Figure 6. Visual observations of slump tests in fresh concrete

3.2. Compressive Strength Figures 7 and 8 depict the effect of using RBA on the compressive strength. The results implied that the compressive strength increased with increasing curing times of 7 and 28 days for all samples. A similar trend was also found in the use of ceramic waste (RBA belongs to the ceramic subgroup) as aggregate in concrete mixtures (25). Furthermore, the trend of declining values in compressive strength occurred with the addition of RBA in the concrete mixture as an OCS partial substitution.

A possible rational explanation for the declining values in compressive strength along with an increase in the substitution of RBA for OCS in the concrete mix is due to the consequence of RBA being more porous compared to OCS, as detailed in Table 1.

Similar findings were obtained by a previous researcher who used recycled brick as a partial substitute for natural coarse aggregate in concrete. An increase in the use of recycled brick aggregate in concrete mixes resulted in a decline in the compressive strength values as a consequence of high water absorption and the weaker strength of the recycled aggregate (26).

As shown in Figures 7 and 8, the use of 15%RBA as a substitute for coarse aggregate in concrete mixes with w/c 0.59 and w/c 0.49 results in the minimum loss of compressive strength among variations of concrete

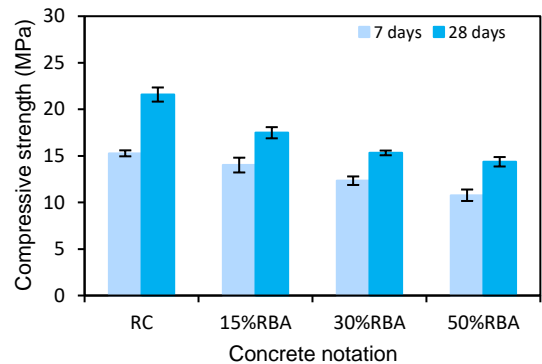


Figure 7. Compressive strength of concrete for w/c 0.59

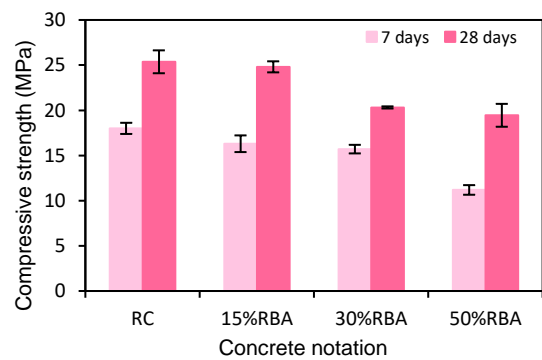


Figure 8. Compressive strength of concrete for w/c 0.49

mixtures modified with 30%RBA and 50%RBA when compared to RC.

3. 3. Compressive Stress and Time Pattern The findings shown in Figures 9 and 10 were obtained based on a compressive strength test that also measured the response time. As depicted in Figures 9 and 10, the pattern of the relationship between compressive stress and response time in all mixtures with and without RBA showed the same tendency. Two different phases can be clearly observed in all the mixtures: the rising phase, which shows a linear trend until it approaches the peak stress, and the declining phase of the post peak stress, which appears to immediately drop steeply.

This finding confirms that even though RBA is weaker than OCS, RBA has brittle properties that cause brittle behavior in concrete modified with RBA. So that the use of RBA in concrete mixtures in principle does not change the brittle behavior of the relationship between compressive stress and time. According to the cited literature, the coarse aggregate skeleton plays an essential role in carrying compressive loads. Hence, the quality of the coarse aggregate affects the brittle of concrete when carry compressive loads (2).

Furthermore, the relationship between the normalized compressive stress and response time was determined with the aim of thoroughly and quantitatively examining the action of compressive stress in attaining the elastic, peak, and ultimate phases of both RC and concrete containing RBA. The elastic and ultimate phases were specified in this study as stress at 40% peak stress and 80% post-peak stress, respectively.

3. 4. Elastic Phases According to Figures 9 and 10, because the quality of coarse aggregates affects the ability of concrete to control elastic deformation due to compressive loading, the response time in the elastic phase is heavily dependent on the coarse aggregate quality. The more rapid rate of reaching the elastic phase in all the RBA containing concretes was attributed to the declining robustness of the concrete with increasing RBA amounts, which was observed at 7 and 28 days of passage.

3. 5. Peak Phases According to Figures 9 and 10, it can be quantitatively determined that the difference in response time between the RC and RBA concrete after 28 days of passage was less than 17%. Such a finding is due to the fact that all concrete mixtures contain cement paste and mortar in the same amount. The response time did not differ significantly at this stage, indicating that the effort to sustain the inelastic phase owing to the current compressive load was controlled more by the mortar or cement paste, which bound the coarse aggregate to maintain the overall robustness of the concrete. These findings are corroborated by earlier scientific

investigations. In accordance with the relevant scientific literature, when subjected to compressive stresses, the specimen underwent lateral and vertical deformations, with the lateral deformation retained by the mortar and ITZ bonding the coarse aggregate. Consequently, the quantity and quality of the mortar and paste used control the ability of the concrete to endure a load in the inelastic phase up to the peak stress (27).

3. 6. Ultimate Phases According to the experimental results acquired after 28 days, as depicted in Figures 9 and 10, the difference in response time between the RC and RBA concrete did not exceed 20%. This result indicates that efforts to maintain the ultimate phase (i.e., post-peak stress) were more controlled by the mortar or cement paste, which bound the coarse aggregate to maintain the overall strength of the concrete.

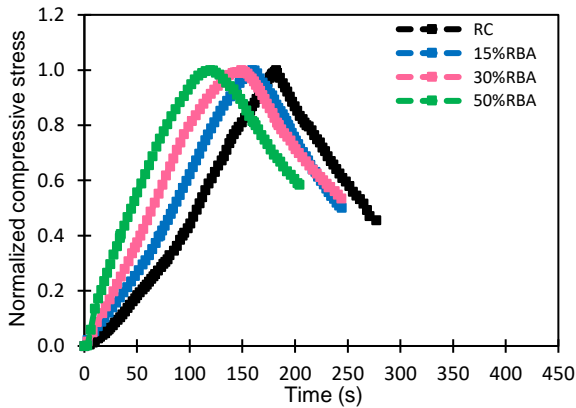
3. 7. Toughness Index According to the calculation of the toughness index depicted in Figure 11, 15%RBA disclosed a better energy capability of the concrete to resolve the failure of the material, which is 7.20% and 0.93% for w/c 0.52 and w/c 0.49, respectively, compared to RC values. Meanwhile, 30% and 50% RBA exhibited insignificant decreases in the toughness index values of 0.73% and 8.91% for w/c 0.52, and 0.12% and 3.64% for w/c 0.49, respectively, compared with RC. In accordance with the acquired toughness index values, 15%RBA exhibited comparable ductile behaviour to that of RC.

3. 8. Performance Criteria It is important to develop performance criteria for concrete containing RBA to ensure that they can be applied in actual construction work. This study proposes the acceptance of the RBA criteria as a coarse aggregate for concrete mixtures based on the performance of the relationship between compressive stress and response time. Such performance acceptance criteria are designed by adopting the principle used to accept pozzolanic waste as a partial replacement for cement. The strength activity index (SAI) was obtained from the results of the compressive strength test on the concrete after 28 days, with an adequate requirement of 75%, as established in ASTM C618 (28). The experimental findings in Table 3 demonstrate that all RBA mixtures for w/c 0.49 and 15% RBA for w/c 0.52 meet the minimum requirements for SAI. This indicates that for both water-cement ratios, the replacement of OCS with 15% RBA can be utilized in a concrete mixture.

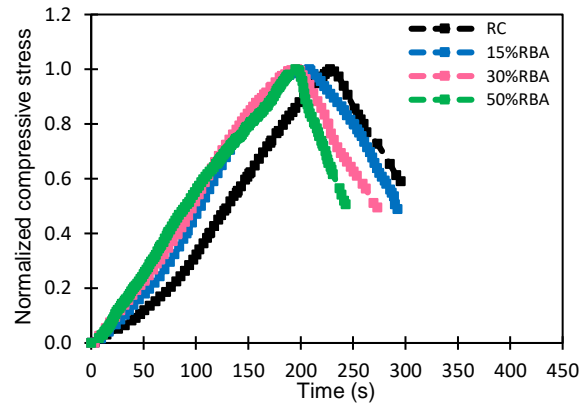
3. 9. Cost Comparison Analysis In addition to considering the mechanical properties aspect of the compressive stress-time assessment of the use of RBA, the comparison of the finished cost of new concrete with reference concrete is also evaluated. The findings presented in Table 4 compare the costs of handling,

processing, and transportation for RBA and natural coarse aggregate in the form of crushed stone (OCS). As can be seen, the acquisition costs for RBA processing are 29.34 \$/m³, which is 51.84% less expensive than the necessary expenditures when using OCS. These results

show that the use of RBA as a partial replacement for coarse aggregate in concrete mixes results in more economical concrete production costs compared to reference concrete (RC), as stated in Tables 5 and 6. The findings in Tables 5 and 6 demonstrate that the use of

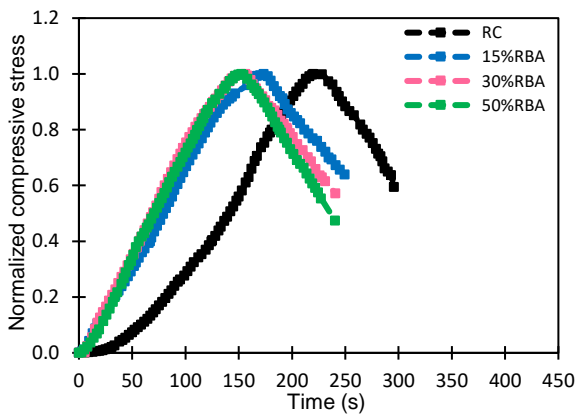


(a) Experimental at 7 days passed

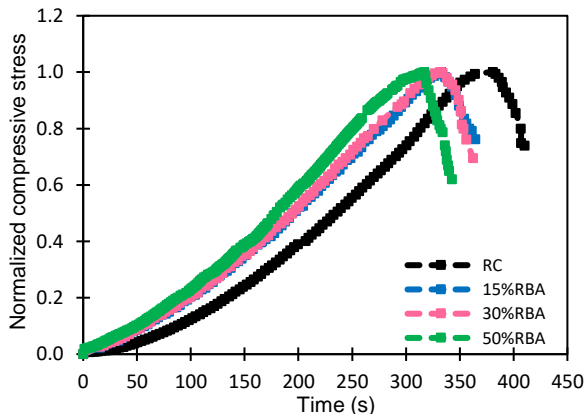


(b) Experimental at 28 days passed

Figure 9. Compressive stress and response time with w/c 0.52 for different percentages of RBA in concrete



(a) Experimental at 7 days passed



(b) Experimental at 28 days passed

Figure 10. Compressive stress and response time with w/c 0.49 for different percentages of RBA in concrete

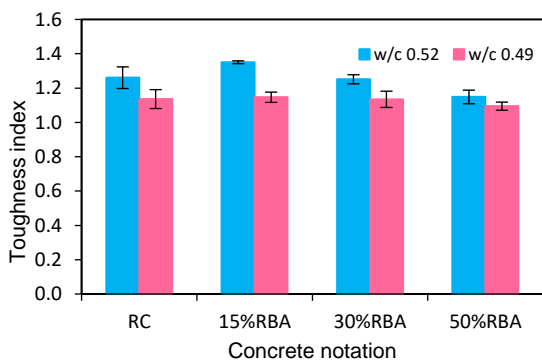


Figure 11. Toughness index for different percentages of RBA in concrete

TABLE 3. SAI of concrete mixture

Notation	RC	15%RBA	30%RBA	50%RBA
OCS, (%)	100	85	70	50
RBA, (%)	0	15	30	50
f _c for w/c 0.52, (MPa)	21.59	17.49	15.32	14.37
f _c for w/c 0.49, (MPa)	25.37	24.81	20.32	19.45
SAI for w/c 0.52, (%)	-	81.02	70.97	66.57
SAI for w/c 0.49, (%)	-	97.80	80.08	76.65

TABLE 4. Cost analysis of ordinary crushed stone (OCS) and RBA materials

No	Item	Quantity	Unit	Rate per unit (\$)*		Cost (\$)	
				OCS	RBA	OCS	RBA
A.	Materials						
	- Raw materials	1	m ³	18.99	0	18.99	0
	- Transportation (max. distance 20 km)	1	m ³	2.83	2.83	2.83	2.83
	- Wash water	2	m ³	1.86	1.86	3.72	3.72
B.	Labor						
	- Non-skilled labor	1	man/d	7.13	7.13	7.13	7.13
	- Skilled labor	1	man/d	11.64	11.64	11.64	11.64
C.	Tools and equipment						
	- Processing tools (2% of material cost)					0.51	0.13
	- Electricity (1% of material cost)					0.26	0.07
D.	Total cost (A+B+C)					45.08	25.52
E.	Overheads and profit (15% x D)					6.76	3.83
	<i>Cost per m³ of materials (D+E)</i>					51.84	29.34

*Prices according to the Makassar, Indonesia, local market as of May 2023

TABLE 5. Cost analysis of concrete w/c 0.52 with different RBA content

No	Item	Quantity (kg/m ³)				Rate per unit (\$)*	Actual cost (\$)			
		RC	15%RBA	30%RBA	50%RBA		RC	15%RBA	30%RBA	50%RBA
A.	Materials									
	- Water	238	238	238	238	0.0034	0.81	0.81	0.81	0.81
	- Cement	458	458	458	458	0.1668	76.39	76.39	76.39	76.39
	- RS	755	755	755	755	0.0134	10.12	10.12	10.12	10.12
	- OCS	1132	962	793	566	0.0168	19.02	16.16	13.32	9.51
	- RBA	0	159	318	531	0.0028	0.00	0.45	0.89	1.49
B.	Labor									
	- Non-skilled labor (man/d)						7.82	7.82	7.82	7.82
	- Skilled labor (man/d)						12.21	12.21	12.21	12.21
C.	Equipment and tools									
	- Tools and plants (2% of material cost)						2.13	2.08	2.03	1.97
	- Electricity (1% of material cost)						1.06	1.04	1.02	0.98
D.	Total cost (A+B+C)						129.56	127.08	124.61	121.30
E.	Overheads and profit (15% x D)						19.43	19.06	18.69	18.19
	<i>Cost per m³ of concrete modified with RBA (D+E)</i>						148.99	146.14	143.30	139.49

*Prices according to the Makassar, Indonesia, local market as of May 2023

TABLE 6. Cost analysis of concrete w/c 0.49 with different RBA content

No	Item	Quantity (kg/m ³)				Rate per unit (\$)*	Actual cost (\$)			
		RC	15%RBA	30%RBA	50%RBA		RC	15%RBA	30%RBA	50%RBA
A.	Materials									
	- Water	236	236	236	236	0.0034	0.80	0.80	0.80	0.80
	- Cement	487	487	487	487	0.1668	81.23	81.23	81.23	81.23
	- RS	743	743	743	743	0.0134	9.96	9.96	9.96	9.96
	- OCS	1115	948	781	558	0.0168	18.73	15.93	13.12	9.37
	- RBA	0	157	314	523	0.0028	0.00	0.44	0.88	1.46
B.	Labor									
	- Non-skilled labor (man/d)						7.82	7.82	7.82	7.82
	- Skilled labor (man/d)						12.21	12.21	12.21	12.21
C.	Equipment and tools									
	- Tools and plants (2% of material cost)						2.21	2.17	2.12	2.06
	- Electricity (1% of material cost)						1.11	1.08	1.06	1.03
D.	Total cost (A+B+C)						134.07	131.64	129.20	125.94
E.	Overheads and profit (15% x D)						20.11	19.75	19.38	18.89
	<i>Cost per m³ of concrete modified with RBA (D+E)</i>						154.18	151.38	148.58	144.84

*Prices according to the Makassar, Indonesia, local market as of May 2023

RBA as a partial replacement for coarse aggregate is effective in reducing concrete production costs. With details for w/c 0.52 and 0.49, the cost savings achieved for mixture variations of 15%RBA, 30%RBA, and 50% RBA as compared to reference concrete (RC) are 1.5–2.0%, 3.5–4.0%, and 6.0–6.5%, respectively. This acquisition indicates that, in addition to providing economic benefits, the use of RBA helps minimize degradation of the environment. As a result, the inclusion of RBA in the concrete mix will support sustainable concrete movement.

4. CONCLUSIONS

This paper evaluates the basic engineering properties of waste refractory brick as a coarse aggregate through compressive stress-time relationship assessment. The following conclusions were drawn from the experimental results of this study.

1. The presence of RBA of 15%–50% at w/c 0.49 and 0.52 is able to interact well with natural aggregate and mortar so as to produce good workability.
2. The presence of 15% RBA provides comparable performance at both w/c 0.49 and 0.52 related to

compressive strength and toughness index based on compressive stress and time relationship.

3. Referring to the SAI analysis, concrete with 15%–50% RBA at w/c 0.49 meets the minimum requirement, while at w/c 0.52, only concrete with 15% RBA meets the requirements.
4. The utilization of RBA as a partial replacement for coarse aggregate in concrete mixtures has a positive impact on reducing material costs and concrete production by approximately 51.84% and 1.5–6.5%, respectively.

5. ACKNOWLEDGMENT

All activities were carried out at Eco Materials Laboratory of the Civil Engineering Department, Universitas Hasanuddin, Indonesia.

6. REFERENCES

1. Cachim PB. Mechanical properties of brick aggregate concrete. *Construction and Building Materials*. 2009;23(3):1292-7. <https://doi.org/10.1016/j.conbuildmat.2008.07.023>

2. Meddah MS, Zitouni S, Belâabes S. Effect of content and particle size distribution of coarse aggregate on the compressive strength of concrete. *Construction and building materials*. 2010;24(4):505-12. <https://doi.org/10.1016/j.conbuildmat.2009.10.009>
3. Mohammed TU, Hasnat A, Awal MA, Bosunia SZ. Recycling of brick aggregate concrete as coarse aggregate. *Journal of Materials in Civil Engineering*. 2015;27(7):B4014005. [https://doi.org/10.1061/\(asce\)mt.1943-5533.0001043](https://doi.org/10.1061/(asce)mt.1943-5533.0001043)
4. Hristova T, Savov N, Yanev N. MUNICIPAL SOLID WASTE AND NON-HAZARDOUS WASTE PROCESSING FOR SUSTAINABLE CIRCULAR ECONOMY THROUGH BLOCKCHAIN. *Journal of Chemical Technology & Metallurgy*. 2023;58(3).
5. Horckmans L, Nielsen P, Dierckx P, Ducastel A. Recycling of refractory bricks used in basic steelmaking: A review. *Resources, Conservation and Recycling*. 2019;140:297-304. <https://doi.org/10.1016/j.resconrec.2018.09.025>
6. Khattab M, Hachemi S. Performance of recycled aggregate concrete made with waste refractory brick. *International Journal of Engineering Research in Africa*. 2021;57:99-113. <https://doi.org/https://doi.org/10.4028/www.scientific.net/JERA.57.99>
7. Khattab M, Hachemi S, Al Ajlouni M. Evaluating the physical and mechanical properties of concrete prepared with recycled refractory brick aggregates after elevated temperatures' exposure. *Construction and Building Materials*. 2021;311:125351. <https://doi.org/10.1016/j.conbuildmat.2021.125351>
8. Hachemi S, Khattab M, Benzetta H. The effects of recycled brick and water/cement ratios on the physical and mechanical performance of recycled aggregates concrete. *Innovative Infrastructure Solutions*. 2022;7(4):270. <https://doi.org/10.1007/s41062-022-00868-y>
9. Nematzadeh M, Baradaran-Nasiri A. Residual properties of concrete containing recycled refractory brick aggregate at elevated temperatures. *Journal of materials in civil engineering*. 2018;30(1):04017255. [https://doi.org/10.1061/\(asce\)mt.1943-5533.0002125](https://doi.org/10.1061/(asce)mt.1943-5533.0002125)
10. Caronge MA, Tjaronge M, Rahim IR, Irmawaty R, Lopian FE. Feasibility study on the use of processed waste tea ash as cement replacement for sustainable concrete production. *Journal of Building Engineering*. 2022;52:104458. <https://doi.org/10.1016/j.jobe.2022.104458>
11. Tjaronge M, Irmawaty R, Amiruddin A, editors. Early Age of Volume Weight, Indirect Tensile Strength and Tensile Elastic Modulus of Foam Concrete Containing Blended Cement. *IOP Conference Series: Earth and Environmental Science*; 2022: IOP Publishing.
12. Kim Y-R, De Freitas FA, Jung JS, Sim Y. Characterization of bitumen fracture using tensile tests incorporated with viscoelastic cohesive zone model. *Construction and Building Materials*. 2015;88:1-9. <https://doi.org/10.1016/j.conbuildmat.2015.04.002>
13. Ming F, Li D, Zhang M, Zhang Y. A novel method for estimating the elastic modulus of frozen soil. *Cold Regions Science and Technology*. 2017;141:1-7. <https://doi.org/10.1016/j.coldregions.2017.05.005>
14. ASTM C. Standard specification for concrete aggregates. Philadelphia, PA: American Society for Testing and Materials. 2003. https://doi.org/10.1520/C0033_C0033M-18
15. Astm A. Standard test method for relative density (specific gravity) and absorption of coarse aggregate. ASTM West Conshohocken, PA. 2015. <https://doi.org/10.1520/C0127-15>
16. ASTM A. Standard test method for density, relative density (specific gravity), and absorption of fine aggregate. 2012. <https://doi.org/10.1520/C0128-22>
17. Astm C. Standard test method for sieve analysis of fine and coarse aggregates. ASTM C136-06. 2006. https://doi.org/10.1520/C0136_C0136M-19
18. ASTM C. Standard test method for resistance to degradation of small-size coarse aggregate by abrasion and impact in the Los Angeles machine. ASTM International, West Conshohocken, PA. 2006. https://doi.org/10.1520/C0131_C0131M-20
19. International A. ASTM C192/C192M-19, Standard Practice for Making and Curing Concrete Test Specimens in the Laboratory. American Society of Testing Materials; 2019.
20. International A. ASTM C143/C143M-20, Standard Test Method for Slump of Hydraulic-Cement Concrete. ASTM International West Conshohocken; 2009.
21. ASTM A. C39/C39M-21. Standard Test Method for Compressive Strength of Cylindrical Concrete Specimens; ASTM International: West Conshohocken, PA, USA. 2021. https://doi.org/10.1520/C0039_C0039M-21
22. Gao Y, Wang B, Liu C, Hui D, Xu Q, Zhao Q, et al. Experimental investigation on static compressive toughness of steel fiber rubber concrete. *Reviews on Advanced Materials Science*. 2022;61(1):576-86. <https://doi.org/10.1515/rams-2022-0260>
23. Pasra M, Tjaronge M, Caronge M, Djaluddin A, Lopian F, Tumpu M. Influence of Tensile Load on Bonding Strength of Asphalt Concrete Containing Modified Buton Asphalt and Polyethylene Terephthalate Waste: A Case Study of Indonesian Roads. *International Journal of Engineering, Transactions C: Aspects*. 2022;35(9):1779-86. <https://doi.org/10.5829/ije.2022.35.09c.14>
24. Liu X, Wu J, Zhao X, Yan P, Ji W. Effect of brick waste content on mechanical properties of mixed recycled concrete. *Construction and Building Materials*. 2021;292:123320. <https://doi.org/10.1016/j.conbuildmat.2021.123320>
25. Yasin Mousavi S, Tavakkoli A, Jahanshahi M, Dankoub A. Performance of high-strength concrete made with recycled ceramic aggregates (research note). *International Journal of Engineering, Transactions C: Aspects*. 2020;33(6):1085-93. <https://doi.org/10.5829/ije.2020.33.06c.05>
26. González JS, Gayarre FL, Pérez CL-C, Ros PS, López MAS. Influence of recycled brick aggregates on properties of structural concrete for manufacturing precast prestressed beams. *Construction and building materials*. 2017;149:507-14. <https://doi.org/10.1016/j.conbuildmat.2017.05.147>
27. Song H, Yao J, Xiang J. The role of aggregate and cement paste in the deterioration of the transitional interface zone of pervious concrete during freeze-thaw cycles. *Case Studies in Construction Materials*. 2022;16:e01086. <https://doi.org/10.1016/j.cscm.2022.e01086>
28. Standard A. C618-12a, Standard Specification for coal fly ash and raw or calcined natural Pozzolan for use in concrete. 2012 Annual Book of ASTM Standards. 2012. <https://doi.org/10.1520/C0618-12a>

COPYRIGHTS

©2024 The author(s). This is an open access article distributed under the terms of the Creative Commons Attribution (CC BY 4.0), which permits unrestricted use, distribution, and reproduction in any medium, as long as the original authors and source are cited. No permission is required from the authors or the publishers.

**Persian Abstract****چکیده**

هدف این مطالعه بررسی استفاده از محصولات جانبی آجر نسوز (RBA) به عنوان جایگزینی برای سنگدانه درشت در تولید بتن پایدار است. مخلوط‌های بتنی با دو نسبت آب به بایندر 0.52 (w/c) و ۰.۴۹ و حاوی ۰، ۱۵، ۳۰ و ۵۰ درصد RBA به عنوان جایگزینی جزئی برای سنگ‌های خرد شده معمولی (OCS) تولید شد. خواص زیر در این مطالعه مورد بررسی قرار گرفت: کارایی، مقاومت فشاری، رابطه تنش-زمان، شاخص چقرمگی، معیارهای عملکرد و تحلیل هزینه. نتایج آزمایش نشان داد که افزایش درصد RBA در مخلوط‌های بتن به طور مثبتی به کارایی بتن کمک می‌کند. علاوه بر این، با افزایش درصد RBA در مخلوط بتن، مقاومت فشاری و تمام مراحل در تنش فشاری و رابطه زمانی کاهش یافت. با این حال، در ۱۵٪ RBA، مقدار شاخص چقرمگی با بتن مرجع قابل مقایسه بود، در حالی که بر اساس معیارهای عملکرد، جایگزینی OCS با ۱۵٪ RBA برای هر دو نسبت آب به سیمان حداقل الزامات را برآورده کرد. در همین حال، تجزیه و تحلیل مقایسه هزینه نشان می‌دهد که هزینه‌های مواد و تولید را می‌توان به ترتیب تقریباً ۵۱.۸۴٪ و ۶.۵-۱.۵٪ کاهش داد. بر اساس تجزیه و تحلیل تمام نتایج آزمایش، ۱۵٪ RBA تفاوت‌های ناچیزی در ارزش در مقایسه با بتن مرجع نشان داد. بنابراین، استفاده از ۱۵٪ RBA به عنوان جایگزین OCS یک گزینه قابل قبول و قابل قبول برای تولید بتن پایدار است.



A Multi-product Humanitarian Supply Chain Network Design Problem: A Fuzzy Multi-objective and Robust Optimization Approach

A. Fallahi^a, A. Pourghazi^b, H. Mokhtari^{*c}

^a Department of Industrial Engineering, Sharif University of Technology, Tehran, Iran

^b Department of Management and Entrepreneurship, Faculty of Humanities, University of Kashan, Kashan, Iran

^c Department of Industrial Engineering, Faculty of Engineering, University of Kashan, Kashan, Iran

PAPER INFO

Paper history:

Received 08 August 2023

Received in revised form 10 September 2023

Accepted 11 September 2023

Keywords:

Relief Logistics

Product Differentiation

Multi-Objective Optimization

Robust Optimization

Fuzzy Programming

ABSTRACT

In today's dynamic and unpredictable world, the planning and management of humanitarian supply chains hold paramount importance. Efficient logistics management is crucial for effectively delivering essential aid and resources to affected areas during disasters and emergencies, ensuring timely support and relief to vulnerable populations. In this research, we addressed a novel humanitarian supply chain network design problem that considers product differentiation and demand uncertainty. Specifically, we simultaneously incorporate non-perishable, perishable, and blood products as critical components of the network. The problem is formulated as a multi-objective mixed-integer linear programming model aiming to minimize the total cost and total traveled distance of products by making location, allocation, and production decisions. To enhance realism, we account for demand uncertainty in affected areas. To tackle this challenging problem, we proposed a two-phase solution methodology. Firstly, we employed a robust optimization approach to establish a deterministic counterpart for the stochastic model. Subsequently, an efficient fuzzy programming-based approach reformulates the model into a single-objective form, effectively accommodating decision-makers' preferences. Numerical instances are solved to investigate the performance of the model and solution methodologies. The results demonstrate the effectiveness of our fuzzy approach in finding non-dominated solutions, enabling decision-makers to explore trade-offs. Also, sensitivity analyses were conducted to provide more insights. Finally, some suggestions are presented to extend the current work by feature researchers.

doi: 10.5829/ije.2024.37.05b.12

NOMENCLATURE

Sets

I	The set of suppliers for non-perishable relief products	O	The set of non-perishable relief products
S	The set of suppliers for perishable relief products	M	The set of perishable relief products
D	The set of donor groups	Q	The set of quality levels for perishable relief products
P	The set of fixed blood collection centers	G	The set of blood products
A	The set of mobile blood collection centers	J	The set of potential warehouses
C	The set of capacity levels for mobile blood collection centers	N	The set of packages
L	The set of blood processing centers	K	The set of affected regions

Parameters

CNS_i	The fixed contract cost of non-perishable relief products supplier i	WLC_j	The establishment cost of warehouse j
CPS_s	The fixed contract cost of perishable relief products supplier s	BEW_{gj}	The equipment cost of warehouse j for blood product g
NCP_i	The capacity of supplier i to supply non-perishable relief products	CRW_j	The capacity of warehouse j
PCP_s	The capacity of supplier s to supply perishable relief products	WMN	The maximum number of warehouses
MNS	The maximum number of suppliers for non-perishable relief products	NNP_{qno}	The number of non-perishable relief product o at quality level q in package n

*Corresponding Author Email: Mokhtari_ie@kashanu.ac.ir (H. Mokhtari)

Please cite this article as: Fallahi A, Pourghazi A, Mokhtari H, A Multi-product Humanitarian Supply Chain Network Design Problem: A Fuzzy Multi-objective and Robust Optimization Approach. International Journal of Engineering, Transactions B: Applications. 2024;37(05):941-58.

MPS	The maximum number of suppliers for perishable relief products	NPP_{nm}	The number of perishable relief product m in package n
TPW_{ijm}	The transportation cost of perishable relief product m from supplier i to warehouse j	NBP_{ng}	The quantity of blood product g in package n
TNW_{sjoq}	The transportation cost of non-perishable relief product o at quality level q from supplier s to warehouse j	PPW_{jn}	The production cost of package n in warehouse j
BDC_d	The blood donation capacity of donor group d	TWA_{jkn}	The transportation cost of package n from warehouse j to affected region k
MLC_{ac}	The location cost of mobile blood collection center a at capacity level c	DMN_{kn}	The demand of package n in affected region k
NRM	The number of required mobile blood collection centers	DST	The minimum percentage of demand satisfaction
BDF_{dp}	The donation cost of donor group p in fixed blood collection center d	PCW_o	The perishability cost of product o
BDM_{da}	The donation cost of donor group p in mobile blood collection center a	PRL_{oq}	The perishability rate of product o at quality level q
FBC_p	The capacity of fixed blood collection center p	ECA_{nk}	The cost of a packaging error for package n in affected region k
FBM_{ac}	The capacity of mobile blood collection center a at capacity level c	ERP_{nj}	The package production fault for package n in warehouse j
CUS	The wastage rate of blood in collection centers	DNW_{ij}	The distance between the non-perishable relief products supplier i and warehouse j
TMP_{al}	The transportation cost of blood from mobile blood collection center a to blood processing center l	DPW_{sj}	The distance between the perishable relief products supplier s and warehouse j
TFP_{pl}	The transportation cost of blood from the fixed blood collection center p to the blood processing center l	DMR_{al}	The distance between the mobile blood collection center a and the blood processing center l
CBP_l	The capacity of blood processing center l	DLR_{pl}	The distance between the fixed blood collection center p and blood processing center l
PRC_{lg}	The production cost of blood product g in blood processing center l	DRW_{lj}	The distance between the blood processing center l and warehouse j
PUS	The wastage rate of blood in blood processing centers	DWA_{jk}	The distance between the warehouse j and affected region k
TBW_{lgj}	The transportation cost of blood product g from blood processing center l to warehouse j	ϕ	A big number
Variables			
qnw_{ijm}	The quantity of transported non-perishable relief product m from supplier i to warehouse j	sps_s	A binary decision variable; 1 if supplier s for perishable products is selected and 0, otherwise
qpw_{sjoq}	The quantity of transported perishable product o at level q from supplier s to warehouse j	lmc_{ac}	A binary decision variable; 1 if mobile blood collection center a at capacity level c is located and 0, otherwise
qsw_{jo}	The quantity of spoiled product o in warehouse j	lwh_j	A binary decision variable; 1 if warehouse j is established and 0, otherwise
qbm_{da}	The quantity of blood donation by donor group d in mobile collection center a	ecw_{gj}	A binary decision variable; 1 if warehouse j is equipped to holding infrastructures of product g and 0, otherwise
qbf_{dp}	The quantity of blood donation by donor group d in fixed collection center p	pbv_{jn}	A binary decision variable; 1 if warehouse j produce the package type n and 0, otherwise
qmp_{al}	The quantity of transported blood from mobile blood collection center a to blood processing center l	dam_{da}	A binary decision variable; 1 if donor group d is assigned to mobile blood collection center a and 0, otherwise
qfp_{pl}	The quantity of transported blood from fixed blood collection center p to blood processing center l	daf_{dp}	A binary decision variable; 1 if donor group d is assigned to fixed blood collection center p and 0, otherwise
qbw_{glj}	The quantity of transported blood product g from blood processing center l to warehouse j	amp_{al}	A binary decision variable; 1 if mobile blood collection center a is assigned to blood processing center l and 0, otherwise
qpp_{jn}	The quantity of produced packages of type n in warehouse j	apf_{pl}	A binary decision variable; 1 if fixed collection center p is assigned to blood processing center l and 0, otherwise
tqa_{jkn}	The number of transported package type n from warehouse j to affected region k	bsw_{glj}	A binary decision variable; 1 if blood processing center l is assigned to warehouse j for transformation of product g and 0, otherwise
sns_i	A binary decision variable; 1 if supplier i for non-perishable relief products is selected and 0, otherwise		

1. INTRODUCTION

Disaster events have always been on human life paths. Various crises, such as earthquakes, floods, storms, terrorist attacks, etc., have impacted people's lives in the past years (1). Since the beginning of 21st century, around 22,000 natural and man-made disasters have occurred worldwide (2). The September 11th terrorist attack, the Kermanshah earthquake in Iran, the Japan

Tsunami, and the Pakistan flood are some of the disasters in the recent century. Regarding the severity, the possible consequences of disaster events might be catastrophic. Physical injuries and economic and environmental problems are examples of such negative results of disasters (3). During the terrorist attack of September 11th, almost 3,000 people lost their lives, and more than 6,000 were injured. The 2010 flood in Pakistan left over 300,000 dead and missing people, billions of lost

property, and more than 20 millions homeless (4). According to the reports on Japan's tsunami, more than 24,000 people were dead or missing, more than 76,000 houses were destroyed, and people suffered a lot of damage. In 2017, during the Kermanshah earthquake in Iran, more than 10,000 people were injured, 600 people died, and many others became homeless (5). Also, a list of recent statistic shown in Figure 1 indicates that about 24.5 million people have been displaced due to disasters worldwide during the past 15 years¹. In this situation, governments and humanitarian organizations must be prepared for the crisis events and respond to them efficiently by providing medical aid, food, and shelter to the victims (6). Here, humanitarian supply chain (HSC) planning is of great importance. HSC planning is defined as a process of planning, implementation, efficient control, and managing flows in the storage of crisis-related goods and services to reduce the suffering of vulnerable people (7, 8). The importance of HSC planning prompted researchers to focus on this problem in recent years.

One of the main features of HSCs is the demand for multiple product types, which are totally different in their nature. In general, there are three categories of items in HSCs: non-perishable, perishable, and blood products (9, 10). As the first category, the non-perishable relief products include the prevailing items such as tents, blankets, sleeping bags, etc. The main feature of these products is that they do not lose their properties over time and can be stored long, and there is no special storage requirement. Perishable products are the second category of products in HSCs. Unlike non-perishable products, they require special storage infrastructures, such as air circulation systems or low-temperature environments, to maintain quality. The lack of these types of equipment and conditions results in the degradation of the products. Alcohol, medicine, etc., are some examples of perishable products. Finally, blood products are the third category of products in HSCs. Although, blood products are inherently perishable, several factors distinguish blood

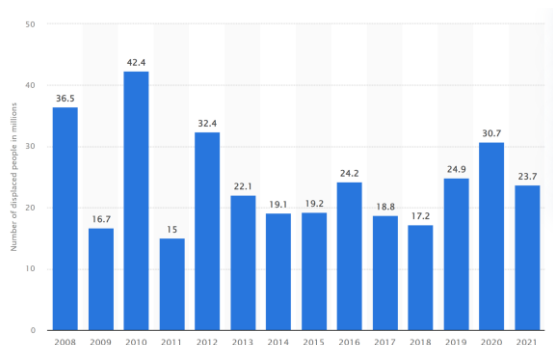


Figure 1. Number of people displaced from 2008 to 2021

¹ www.statista.com

from other products, even similar perishable products. While non-perishable and perishable products can be purchased from companies and retailers at a purchasing cost, humans are the suppliers of blood, and blood donation is a volunteer activity. Therefore, the blood supply is very limited. In addition, the donated blood can not be directly used in the affected region. The whole blood should be tested, processed, and decomposed into subproducts, including red blood cells, platelets, and plasma. The resulting subproducts are also different in their properties; each has a particular shelf life and storage condition, which are totally different. Finally, the results of blood shortage in HSCs differ from other products and may cause human death (11).

To the best of the authors' knowledge, no paper in the literature addresses the HSC design problem considering these products and the related features. More specifically, the recent work by Abazari, Aghsami (9) is one of the closest works to this research, which addresses the non-perishable and perishable products in an HSC. However, they ignored the presence of blood products in the HSC system. This research aims to design an HSC network considering three types of non-perishables, perishables, and blood products. In this problem, total cost and total traveled distance were considered objective functions to cover the network's economic and emergency response goals. As the first part of the solution methodology, we present an efficient fuzzy programming approach to establish a trade-off between these conflictive objectives and establish the single-objective counterpart model. Since the demand of affected regions in HSCs is violated during the crisis period, the product demand uncertainty is also considered to present a more realistic framework. In this direction, a robust optimization approach will be provided in the second part of the solution methodology to consider the demand uncertainty. The performance of the developed model and proposed methodologies will be investigated through extensive analysis of numerical examples. Briefly, the main contribution of this work can be summarized as follows:

- Developing a multi-objective HSC design problem considering three categories of non-perishable, perishable, and blood products under demand uncertainty.
- Developing a mixed-integer linear programming (MILP) mathematical model for the problem.
- Presenting an efficient fuzzy programming approach to deal with the conflicts of objectives.
- Presenting a robust optimization approach to deal with the demand uncertainty.
- Solving several numerical examples to investigate the performance of the developed model and solution methodologies.

The rest of the paper is organized as follows. Section 2 provides a review of the related studies in the literature. Section 3 provides the problem definition and a multi-objective mixed-integer linear mathematical model for the defined problem. Section 4 presents a two-part solution methodology for the problem. First, a fuzzy-programming approach is proposed to handle the objectives' conflicts. Then, a robust optimization approach is discussed to address the uncertainty. Section 5 explores the performance model of the model and solution methodologies by solving several numerical examples. Section 6 presents managerial insights based on the computational results. Finally, section 7 provides a conclusion to the paper and some direction for future works.

2. RELATED STUDIES

As pointed out before, the proper planning of operations is very important in disaster conditions. Therefore, the HSC planning problems have been investigated from different viewpoints in recent years. Researchers have tried to define several strategic, tactical, and operational problems for HSC networks. In these problems, optimal decision-making frameworks for various decisions, such as facility location, flow allocation, inventory planning, production, etc., have been addressed. In this section, we reviewed the relevant studies to this paper in the literature. Interested readers can study the review papers in the literature, such as the works by Kovács and Spens (12) and Balcik, Bozkir (13).

A significant portion of studies in the field of HSC planning has been focused on network design problems with location-allocation decisions. Zhan and Liu (14) studied a multi-objective HSC design problem that simultaneously minimizes the unmet demand and service time. They utilized a goal programming approach to address the conflict of objectives. Murali, Ordóñez (15) developed a new model to determine the optimal location of facilities in an HSC. In this paper, the goal is to maximize the number of served people. Bozorgi-Amiri, Jabalameli (16) addressed the uncertainty in the HSC design problem by considering uncertainty in demand, capacities, and cost parameters. The model was solved using a PSO algorithm. Khayal, Pradhananga (17) studied a location planning problem for impermanent distribution centers of HSC. A dynamic resource allocation approach for these facilities was also presented. Hasani and Mokhtari (18) presented some strategies for designing and redesigning an HSC. In this paper, a rolling horizon planning method was used to address the uncertainty and dynamics of the network. In another research, Hasani and Mokhtari (19) studied a multi-objective HSC and employed the fault tree analysis (FTA) method for risk assessment of the network. The

objective functions were the minimization of total cost and risk and the maximization of population coverage. Wang and Nie (20) tried to improve the transportation operations of an HSC and developed a location-allocation model considering traffic congestion. Aghajani, Torabi (21) utilized the option contract for coordination in an HSC. The results prove that this contract can improve the responsiveness and cost-efficiency of the network. Mansoori, Bozorgi-Amiri (22) considered evacuating injured people from the affected region. They proposed a multi-objective model to minimize unmet demand and the number of non-evacuate homeless people. Nezhadroshan, Fathollahi-Fard (23) focused on a robust humanitarian logistics problem for disaster response, aiming to address operational and disruption uncertainties. They introduced a novel scenario-based possibilistic-stochastic programming approach to address uncertainty in a network with central warehouses and distribution centers. Recently, Mahtab, Azeem (24) proposed a multi-objective robust-stochastic model for humanitarian logistics, focusing on pre- and post-disaster decisions. The authors addressed facility location, pre-positioning, distribution scheduling, and equity in supply distribution. Their model incorporated uncertainties in demand, transportation, and supply condition, with a real flood case study. Akbari, Valizadeh (25) developed a model for integratig service provider collaboration in HSC. The authors used cooperative game theory approaches to solve this problem. Foroughi, Moghaddam (26) presented a resilient HSC with multiple disasters in their paper. The resilience parameters were obtained using the best-worst multi-criteria decision-making method.

The importance of transportation and inventory decisions in HSCs motivated researchers to develop models focusing on these problems. Ukkusuri and Yushimito (27) suggested inventory preposition as an effective strategy for increasing the responsiveness of HSC. They presented the idea as a location-routing problem. Kutanoglu and Mahajan (28) developed a model for inventory management of an HSC. The network included a central warehouse and several local warehouses. The authors also considered the possibility of transshipment between the local warehouses. Campbell and Jones (29) developed a new model to determine the location of HSC suppliers in predisaster conditions. Their model also incorporated inventory decisions. Ahmadi, Seifi (30) developed a multi-depot vehicle routing-location problem for an HSC network. They considered the failure of the network and stochastic travel times. Bozorgi-Amiri and Khorsi (31) developed a multi-objective location-routing problem for an HSC under the risk of disruption. The model aimed to minimize unsatisfied demand, total cost, and travel time. Sabouhi, Bozorgi-Amiri (32) presented a transportation planning problem for an HSC that included location,

routing, and scheduling decisions. The authors formulated the disruption of routes, and the objective function was minimizing the expected arrival time of relief vehicles. Tofighi, Torabi (33) worked on a two-level HSC network, which included warehouses and distribution centers. The uncertainty in supply, demand, and availability levels of the transportation routes were taken into account, and the problem was formulated using a two-stage stochastic programming model.

As pointed out, several types of products are in demand in HSCs. Some of the previous studies aimed to address these products and their features in disasters. Zhang and Jiang (34) investigated the pharmacy management problem in an HSC as a perishable product and tried simultaneously minimizing the system's total cost and servicing time. Akbarpour, Torabi (35) also presented a model for pharmacy supply chain planning during disasters. In this research, an option contract is proposed for coordination with suppliers. Some other works investigated the planning of blood flow in the outbreak of crisis events. Jabbarzadeh, Fahimnia (36) proposed a new problem for blood supply chain design under disaster scenarios. In this paper, the demand uncertainty was addressed by a robust optimization approach. Khalilpourazari, Soltanzadeh (10) presented a blood supply chain planning problem to respond to the earthquake disaster. They considered the possibility of helicopter usage to transport blood and injured people. Fallahi, Mousavian Anaraki (37) developed a new model for supply chain planning of regular and convalescent plasma during the COVID-19 pandemic. The authors suggested using motivational programs and a transshipment strategy to increase the efficiency of the supply chain. Haghjoo, Tavakkoli-Moghaddam (38) suggested a reliable approach to address the disruption of the blood supply chain during the disaster. In this study, the impact level of disruption on facilities depends on the initial investment level. Kamyabniya, Noormohammadzadeh (39) presented an integrated model for the flow management of platelet blood products. They assumed ABO/Rh(d)-compatibility and difference in age of products to establish a more realistic problem. Recently, Hong (40) introduced a weighted goal programming model to optimize an HSC configuration while accounting for emergency response facility disruptions. By employing a two-stage network data envelopment analysis (DEA) approach, the proposed method consistently identifies efficient configurations, offering valuable insights for disaster response planning. Modarresi and Maleki (41) developed a two-stage stochastic model for efficient humanitarian relief supply chain design, integrating pre- and post-disaster decisions to enhance disaster management. The model encompasses quantity flexibility contracts, equitable relief goods distribution, warehouse location, inventory planning, and various post-disaster activities.

The approach effectively reduces inventory levels pre-disaster and mitigates supply risks post-disaster, as demonstrated in the context of a potential earthquake in Iran.

Table 1 presents a comprehensive comparison of the key features and contributions of our current work in contrast to previous research efforts. This table serves as a valuable reference to highlight the distinct advantages and novel aspects of our study compared to the prior state-of-the-art. As can be seen in the literature, there are several papers on optimizing HSCs. Also, some papers in other research areas studied the supply chain planning of particular perishable products such as blood and pharmacy in disaster situations. However, none of the previous papers investigated an HSC design problem considering three types of non-perishable, perishable, and blood products. This research aims to cover this gap by developing a new MILP multi-objective model for the problem. The total cost and total traveled distance of products are considered as the objective functions to provide flexibility for decision-makers to make trade-offs between economic and emergency response aspects. The conflicts of these objectives will be handled by presenting an efficient fuzzy programming approach. Moreover, the uncertainty in product demand is another assumption of this research, which will be addressed by a robust optimization approach.

3. PROBLEM DEFINITION AND MODELING

In this section, we describe the new problem for designing an HSC network under three categories of non-perishable, perishable, and blood relief products. First, the problem definition is presented. Then, the MILP mathematical model is developed by presenting notations, objective functions, and constraints.

3. 1. Problem Definition Natural and human disasters have always been a part of human life. Today, crisis management is very effective in preventing damage from these disasters. One of the crisis management mechanisms is the design of the HSC network, which greatly reduces the damages after the disaster. This paper considers a multi-echelon HSC that includes perishable, non-perishable, and blood products as three types of relief items (9, 10). The main echelons are the suppliers of perishable and non-perishable relief products, the blood donor groups, fixed and mobile blood collection centers, blood processing centers, warehouses, and affected regions. The perishable and non-perishable relief products are purchased from a set of available suppliers and directly transported into warehouses. The location of warehouses should be determined from a set of potential locations. Regarding the perishable nature, we assumed that perishable relief products are available

TABLE 1. The novelties of the current research against the previous work in the literature

Research	Year	Product types			Objective numbers		Uncertainty	Solution approach		Case study
		Non-perishable	Perishable	Blood	Single	Multiple		Exact	(Meta) heuristic	
Zhan and Liu (14)	2011	✓	✗	✗	✗	✓	✓	✗	✗	
Murali, Ordóñez (15)	2012	✓	✗	✗	✓	✗	✓	✓	✓	
Bozorgi-Amiri, Jabalameli (16)	2012	✓	✗	✗	✓	✗	✓	✗	✓	
Zhang and Jiang (34)	2014	✗	✓	✗	✗	✓	✓	✓	✓	
Jabbarzadeh, Fahimnia (36)	2014	✗	✗	✓	✓	✗	✓	✓	✓	
Ahmadi, Seifi (30)	2015	✓	✗	✗	✓	✗	✓	✓	✓	
Khayal, Pradhananga (17)	2015	✓	✗	✗	✓	✗	✗	✓	✓	
Bozorgi-Amiri and Khorsi (31)	2016	✓	✗	✗	✗	✓	✓	✓	✓	
Tofighi, Torabi (33)	2016	✓	✗	✗	✗	✓	✓	✓	✓	
Hasani and Mokhtari (18)	2018	✓	✗	✗	✗	✓	✓	✓	✓	
Wang and Nie (20)	2019	✓	✗	✗	✓	✗	✓	✓	✓	
Aghajani, Torabi (21)	2020	✓	✗	✗	✗	✓	✓	✓	✓	
Khalilpourazari, Soltanzadeh (10)	2020	✗	✗	✓	✓	✗	✗	✓	✓	
Akbarpour, Torabi (35)	2020	✗	✓	✗	✗	✓	✓	✓	✓	
Mansoori, Bozorgi-Amiri (22)	2020	✓	✗	✗	✗	✓	✓	✓	✓	
Haghjoo, Tavakkoli-Moghaddam (38)	2020	✗	✗	✓	✓	✗	✓	✓	✓	
Nezhadroshan, Fathollahi-Fard (23)	2021	✓	✗	✗	✗	✓	✓	✓	✓	
Kamyabniya, Noormohammadzadeh (39)	2021	✗	✗	✓	✗	✓	✓	✓	✓	
Sabouhi, Bozorgi-Amiri (32)	2021	✓	✗	✗	✓	✗	✓	✓	✓	
Mahtab, Azeem (24)	2022	✓	✗	✗	✗	✓	✓	✓	✓	
Akbari, Valizadeh (25)	2022	✓	✗	✗	✓	✗	✓	✗	✓	
Fallahi, Mousavian Anaraki (37)	2022	✗	✗	✓	✗	✓	✗	✓	✓	
Foroughi, Moghaddam (26)	2022	✓	✗	✗	✗	✓	✗	✗	✓	
Modarresi and Maleki (41)	2023	✓	✗	✗	✓	✗	✓	✓	✓	
Hong (40)	2023	✓	✗	✗	✗	✓	✗	✓	✓	
This paper	2023	✓	✓	✓	✗	✓	✓	✓	✗	

in different quality levels. There is a set of donor groups who volunteer to donate blood. We consider a set of fixed blood collection centers and mobile blood collection centers to receive the whole blood from these volunteer groups. The location of fixed blood collection centers is prespecified. However, mobile blood collection centers should be located in the network.

Also, each mobile blood collection center has a set of

collection capacity levels, and the optimal capacity level for each center should be determined. The collected whole blood should be transported into processing centers for testing and production of subproducts. A portion of blood in collection and processing centers cannot be used and is lost.

After processing, different subproducts, e.g. red blood cells, platelets, and plasma, are obtained from

whole blood. Then, the produced blood subproducts are sent to the warehouses. Different blood products need different holding equipment. Therefore, the decisions for inventory holding equipment of warehouses are also taken into account in the problem. The received non-perishable, perishable, and blood products are packaged and grouped in the warehouse to transport to affected regions (42). A portion of perishable relief products may expire or spoil based on a perishability rate while being stored in warehouses and cannot be included in relief packages. Each type of package contains a prespecified amount of each product. We consider the possibility of human fault in the packaging of products, and a portion of packages may not be used in affected regions due to these faults (42). Depending on the package type, these faults impose a cost in each affected region.

Note that each facility can service another facility if they are within servicing distance. There is a service level constraint, and a minimum level of demand for each affected region should be satisfied (43). The goal is to determine the optimal location, allocation, blood production, and packaging decisions so that the objective functions are optimized. The economic aspects are considered in the first objective, where the goal is to minimize the total cost of the HSC. To improve the responsiveness of the network, the second objective function aims to minimize the total traveled distance of products in the network. Figure 1 demonstrates the structure of the studied HSC network.

3. 2. Mathematical Modelling Considering the above-described components, the total cost objective can be expressed as follows:

$$\begin{aligned} \text{Min } Z_1 = & \sum_{i=1}^I \text{CNS}_i \text{sns}_i + \sum_{s=1}^S \text{CPS}_s \text{sps}_s + \\ & \sum_{a=1}^A \sum_{c=1}^C \text{MLC}_{ac} \text{lmc}_{ac} + \\ & \sum_{d=1}^D \sum_{p=1}^P \text{BDF}_{dp} \text{qbf}_{dp} + \end{aligned} \tag{1}$$

$$\begin{aligned} & \sum_{d=1}^D \sum_{a=1}^A \text{BDM}_{da} \text{qbm}_{da} + \\ & \sum_{a=1}^A \sum_{l=1}^L \text{TMP}_{al} \text{qmp}_{al} + \\ & \sum_{a=1}^A \sum_{l=1}^L \text{TMP}_{al} \text{qmp}_{al} + \\ & \sum_{g=1}^G \sum_{l=1}^L \sum_{j=1}^J \text{PRC}_{gl} \text{qbw}_{glj} + \\ & \sum_{g=1}^G \sum_{l=1}^L \sum_{j=1}^J \text{TBW}_{glj} \text{qbw}_{glj} + \sum_{j=1}^J \text{WLC}_{jl} \text{wh}_j + \\ & \sum_{g=1}^G \sum_{j=1}^J \text{BEW}_{gj} \text{ecw}_{gj} + \\ & \sum_{i=1}^I \sum_{j=1}^J \sum_{m=1}^M \text{TPW}_{ijm} \text{qnw}_{ijm} + \\ & \sum_{o=1}^O \sum_{q=1}^Q \sum_{s=1}^S \sum_{j=1}^J \text{TNW}_{sjoq} \text{qpws}_{joq} + \\ & \sum_{p=1}^P \sum_{l=1}^L \text{TFP}_{pl} \text{qfp}_{pl} + \sum_{j=1}^J \sum_{n=1}^N \text{PPW}_{jn} \text{qpp}_{jn} + \\ & \sum_{j=1}^J \sum_{n=1}^N \text{PPW}_{jn} \text{qpp}_{jn} + \\ & \sum_{j=1}^J \sum_{k=1}^K \sum_{n=1}^N \text{TW}_{A_{jkn}} \text{tqa}_{jkn} + \\ & \sum_{j=1}^J \sum_{k=1}^K \sum_{n=1}^N \text{ECA}_{nk} \text{ERP}_{nj} \text{tqa}_{jkn} + \\ & \sum_{o=1}^O \sum_{j=1}^J \text{PCW}_o \text{qsw}_{jo} \end{aligned}$$

The total cost of the presented HSC network includes the fixed contract cost of non-perishable relief products, the fixed contract cost of perishable products, the location cost of mobile blood collection centers, the blood donation cost at fixed blood collection centers, the blood donation cost at mobile blood collection centers, the blood transportation cost from mobile blood collection centers to blood processing facilities, the blood transportation cost from fixed blood collection centers to blood processing facilities, the production cost of blood products in blood processing facilities, the establishment cost of warehouses, the equipment cost of warehouses for blood products, the transportation cost of non-perishable relief products from suppliers to warehouses, the transportation cost of perishable products from suppliers to warehouses, the transportation cost of blood products from blood processing centers to warehouses, the production cost of packages in warehouses, the transportation cost of packagers from warehouses to affected regions, the exceed cost, and the total perishability cost.

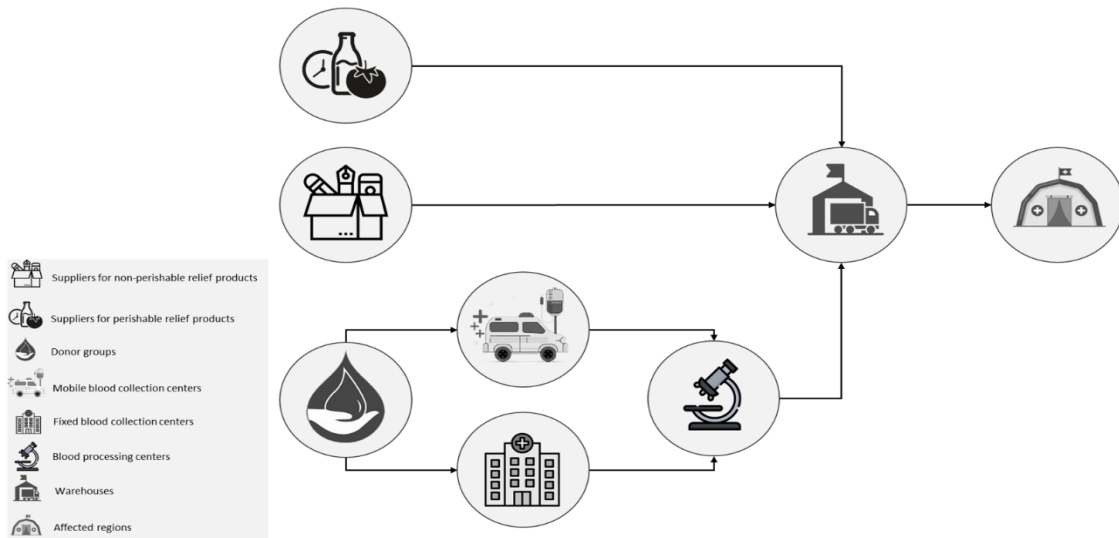


Figure 1. A schematic illustration of the studied network

$$\begin{aligned}
 \text{Min } Z_2 = & \\
 & \sum_{i=1}^I \sum_{j=1}^J \sum_{m=1}^M DNW_{ij} qn w_{ijm} + \\
 & \sum_{o=1}^O \sum_{q=1}^Q \sum_{s=1}^S \sum_{j=1}^J DPW_{sj} qp w_{sjoq} + \\
 & \sum_{p=1}^P \sum_{l=1}^L DLR_{pl} qf p_{pl} + \\
 & \sum_{a=1}^A \sum_{l=1}^L DMR_{al} qmp_{al} + \\
 & \sum_{g=1}^G \sum_{l=1}^L \sum_{j=1}^J DRW_{lj} qb w_{glj} + \\
 & \sum_{j=1}^J \sum_{k=1}^K \sum_{n=1}^N DW A_{jk} BP_{jk}^n
 \end{aligned} \tag{2}$$

In addition, the second objective function minimizes the total traveled distance of products, including non-perishable relief products, perishable products, whole blood, blood subproducts, and the produced packages. The objective functions is subjected to the following constraints:

Establishment constraints

$$\sum_{m=1}^M \sum_{i=1}^I qn w_{ijm} \leq \phi l w h_j \quad \forall j \in J \tag{3}$$

$$\sum_{m=1}^M \sum_{j=1}^J qn w_{ijm} \leq \phi s n s_i \quad \forall i \in I \tag{4}$$

$$\sum_{j=1}^J \sum_{o=1}^O \sum_{q=1}^Q qp w_{sjoq} \leq \phi s p s_s \quad \forall s \in S \tag{5}$$

$$\begin{aligned}
 a p m_{al} \leq \sum_{c=1}^C l m c_{ac} & \quad \forall a \in A, \\
 & \quad \forall l \in L \tag{6}
 \end{aligned}$$

$$\sum_{n=1}^N p b v_{jn} = l w h_j \quad \forall j \in J \tag{7}$$

$$\sum_{n=1}^N \sum_{k=1}^K t q a_{jkn} \leq \phi l w h_j \quad \forall j \in J \tag{8}$$

$$\begin{aligned}
 q p p_{jn} \leq \phi p b v_{jn} & \quad \forall j \in J, \\
 & \quad \forall n \in N \tag{9}
 \end{aligned}$$

Constraints 3 to 5 limit product flow to the established warehouses and selected suppliers. Constraints 6 limit the flow of blood between the established mobile blood collection centers and blood processing centers. Constraints 7 guarantee that one package type is produced in each established warehouse. Constraints 8 limit the outflow of packages to the established warehouses. Constraints 9 limit the production of package types to the determined facilities for each package type.

Capacity constraints

$$\sum_{j=1}^J \sum_{m=1}^M qn w_{ijm} \leq N C P_i \quad \forall i \in I \tag{10}$$

$$\sum_{o=1}^O \sum_{q=1}^Q \sum_{j=1}^J qp w_{sjoq} \leq P C P_s \quad \forall s \in S \tag{11}$$

$$\sum_{a=1}^A q b m_{da} + \sum_{p=1}^P q b f_{dp} \leq B C D_d \quad \forall d \in D \tag{12}$$

$$\sum_{d=1}^D q b f_{dp} \leq F B C_p \quad \forall p \in P \tag{13}$$

$$\sum_{d=1}^D q b m_{da} \leq \sum_{c=1}^C F B M_{ac} l m c_{ac} \quad \forall a \in A \tag{14}$$

$$\sum_{c=1}^C l m c_{ac} \leq 1 \quad \forall a \in A \tag{15}$$

$$\begin{aligned}
 \sum_{a=1}^A q m p_{al} + \sum_{p=1}^P q f p_{pl} \leq C B P_l & \quad \forall a \in A, \\
 & \quad \forall l \in L \tag{16}
 \end{aligned}$$

$$\sum_{n=1}^N q p p_{jn} \leq C R W_j \quad \forall j \in J \tag{17}$$

Constraints 10 and 11 are the limitations on suppliers' capacity for non-perishable and perishable relief products. Constraints 12 consider the donation capacity of each donor group. Constraints 13 and 14 are the capacity constraints of fixed and mobile collection centers, respectively. Constraints 15 guarantee that each mobile blood collection center is worked with one capacity level. The capacity limitation of blood processing centers is considered by Constraints 16. Constraints 17 consider the package production capacity of the warehouses.

Facility numbers constraints

$$\sum_{i=1}^I s n s_i \leq M N S \tag{18}$$

$$\sum_{s=1}^S s p s_s \leq M P S \tag{19}$$

$$\sum_{a=1}^A \sum_{c=1}^C l m c_{ac} \leq N R M \tag{20}$$

$$\sum_{j=1}^J l w h_j \leq W M N \tag{21}$$

Constraints (18) and (19) limit the number of suppliers to the specified threshold. Constraints (20) limit the number of mobile blood collection centers to the specified threshold. The maximum number of located warehouses is taken into account by constraints (21).

Network balance constraints

$$(1 - C U S) \sum_{d=1}^D q b f_{dp} = \sum_{l=1}^L q f p_{pl} \quad \forall p \in P \tag{22}$$

$$\begin{aligned}
 (1 - C U S) \sum_{d=1}^D q b m_{da} = & \\
 \sum_{l=1}^L q m p_{al} & \quad \forall a \in A \tag{23}
 \end{aligned}$$

$$\begin{aligned}
 (1 - P U S) (\sum_{a=1}^A q m p_{al} + \\
 \sum_{p=1}^P q f p_{pl}) = \sum_{g=1}^G \sum_{j=1}^J q b w_{glj} & \quad \forall l \in L \tag{24}
 \end{aligned}$$

$$\begin{aligned}
 q p p_{jn} N P P_{mn} \leq \sum_{i=1}^I q n w_{ijm} + \\
 \phi (1 - p b v_{jn}) & \quad \forall m \in M, \\
 & \quad \forall j \in J \tag{25}
 \end{aligned}$$

$$\begin{aligned}
 & \forall j \in J, & \forall a \in A, & qmp_{al} \geq apm_{al} & \forall l \in L & (36) \\
 & \forall o \in O, & & & & \\
 & \forall q \in Q, & & & & \\
 & \forall n \in N, & & & & \\
 & \forall j \in J, & & & & \\
 & \forall g \in G, & & & & \\
 & \forall n \in N, & & & & \\
 & \forall j \in J, & & & & \\
 & \forall o \in O, & & & & \\
 & \forall j \in J, & & & & \\
 & \forall n \in N, & & & & \\
 & \forall j \in J, & & & & \\
 & \forall n \in N, & & & & \\
 & \forall g \in G, & & & & \\
 & \forall j \in J, & & & & \\
 & \forall l \in L, & & & & \\
 & \forall g \in G, & & & & \\
 & \forall j \in J, & & & & \\
 & \forall l \in L, & & & & \\
 & \forall g \in G, & & & & \\
 & \forall j \in J, & & & & \\
 & \forall g \in G, & & & & \\
 & \forall j \in J, & & & & \\
 & \forall k \in K, & & & & \\
 & \forall n \in N, & & & & \\
 & \forall m \in M, & & & & \\
 & \forall j \in J, & & & & \\
 & \forall d \in D, & & & & \\
 & \forall p \in P, & & & & \\
 & \forall p \in P, & & & & \\
 & \forall d \in D, & & & & \\
 & \forall a \in A, & & & & \\
 & \forall l \in L, & & & &
 \end{aligned}$$

$$qpp_{jn}NBP_{qno} \leq \sum_{s=1}^S \left((1 - PRL_{oq})qpws_{joq} \right) + \phi(1 - pbv_{jn}) \quad (26)$$

$$qpp_{jn}NBP_{ng} \leq \sum_{l=1}^L qbw_{glj} + \phi(1 - pbv_{jn}) \quad (27)$$

$$qsw_{jo} = \sum_{s=1}^S \sum_{q=1}^Q PRL_{oq}qpws_{joq} \quad (28)$$

$$\sum_{k=1}^K tqa_{jkn} \leq qpp_{jn} \quad (29)$$

The flow constraints of blood in fixed collection centers, mobile collection centers, and processing centers are formulated in constraints (22) to (24), respectively. Constraints (25) to (27) ensure that each warehouse produces one type of package and limit the inflow and outflow of facilities based on the production quantity. Constraints (28) determine the quantity of spoiled perishable products in warehouses. Constraints (29) ensure that the total flow of packages from the warehouses to affected regions is less than or equal to the quantity of produced packages.

Facilities assignment constraints

$$\sum_{a=1}^A dam_{da} + \sum_{p=1}^P daf_{dp} \leq 1 \quad \forall d \in D \quad (30)$$

$$qbm_{da} \leq \phi dam_{da} \quad \forall d \in D, \forall a \in A \quad (31)$$

$$qbm_{da} \geq dam_{da} \quad \forall d \in D, \forall a \in A \quad (32)$$

$$qbf_{dp} \leq \phi daf_{dp} \quad \forall d \in D, \forall p \in P \quad (33)$$

$$qbf_{dp} \geq daf_{dp} \quad \forall p \in P, \forall d \in D \quad (34)$$

$$qmp_{al} \leq \phi apm_{al} \quad \forall a \in A, \forall l \in L \quad (35)$$

$$qfp_{pl} \leq \phi apf_{pl} \quad \forall p \in P, \forall l \in L \quad (37)$$

$$qfp_{pl} \geq apf_{pl} \quad \forall p \in P, \forall l \in L \quad (38)$$

$$qbw_{glj} \leq \phi bsw_{glj} \quad \forall g \in G, \forall j \in J \quad (39)$$

$$qbw_{glj} \geq bsw_{glj} \quad \forall l \in L, \forall g \in G, \forall j \in J \quad (40)$$

$$\sum_{l=1}^L qbw_{glj} \leq \phi ecw_{gj} \quad \forall g \in G, \forall j \in J \quad (41)$$

Each donor group should be assigned to a fixed or mobile blood collection center, and constraints (30) ensure this. Constraints (31) to (40) limit the flow of products only to the assigned facilities. Constraints (41) limit blood product flow to warehouses with the required holding equipment.

Demand satisfaction constraints

$$\sum_{j=1}^J (1 - ERP_{nj})tqa_{jkn} \geq DMN_{kn}DST \quad \forall k \in K, \forall n \in N, \forall m \in M, \forall j \in J \quad (42)$$

Constraints (42) ensure the minimum level of demand satisfaction in each affected region.

4. SOLUTION APPROACH

The section addresses the presented two-phase solution methodology for the problem. The goal is to simultaneously handle the objectives conflicts and the models's uncertainty. First, a robust optimization approach is presented to deal with the demand uncertainty of the HSC system. Afterward, a fuzzy

programming approach is described that handles the conflicts of the objective functions and provides a single-objective counterpart of the MILP model.

4. 1. Robust Optimization Approach Considering the above-described components, the total cost objective can be expressed as follows:

Several approaches have been presented in the literature to address the uncertainty in optimization problems. A well-known way to deal with uncertainty is stochastic programming. However, this approach needs historical data to estimate probability mass/density functions. In addition, constraint violation may occur in stochastic programming. Therefore, a robust optimization approach was developed in the literature to address these problems. Robust optimization aims to develop a feasible solution for all realizations of unknown parameters. Unlike stochastic programming, the robust optimization approach can deal with both hard constraints and interval uncertainty. In this procedure, an interval uncertainty is considered for the stochastic parameters.

As mentioned, we considered the uncertainty in demand for packages in affected regions. It is difficult to estimate the demand of the HSC systems using a probability distribution function. We use the proposed approach by Bertsimas and Sim (44) as one of the most well-known approaches in the literature (45). Consider the following optimization problem:

$$\begin{aligned}
 & \text{Max } cx \\
 & \text{S.t} \\
 & \sum_{j \in J_i} \tilde{a}_{ij} x_j + \sum_{j \in N \setminus \{J_i\}} \tilde{a}_{ij} x_j \leq \mu_i(x) \quad \forall i \in I \quad (43) \\
 & x \in F(x) \quad \forall \tilde{a}_{ij} \in J_i
 \end{aligned}$$

where \tilde{a}_{ij} is the uncertain parameter of the system and is in the interval $[\bar{a}_{ij} - \hat{a}_{ij}, \bar{a}_{ij} + \hat{a}_{ij}]$. In this interval, \bar{a}_{ij} and \hat{a}_{ij} are the nominal value and deviation. In addition, J_i is the set of uncertain parameters in row i . This approach considers a parameter, denoted by Γ_i , for each i , which is referred to as the budget of uncertainty. This parameter allows for control over the level of conservatism in the solution and can take on integer values in the range of $(0, |J_i|)$. The budget of uncertainty ensures that the solution remains feasible even when multiple parameters are changed simultaneously. The reformulation of the problem using the budget of uncertainty is as follows:

$$\begin{aligned}
 & \text{Max } cx \\
 & \text{S.t} \\
 & \quad \quad \quad \forall i \in I, \quad (44)
 \end{aligned}$$

$$\sum_{j \in N} a_{ij} x_j + \max_{\{S_i | S_i \in J_i, |S_i| = \Gamma_i\}} \{\sum_{j \in S_i} \hat{a}_{ij} x_j\} \leq b_i \quad \forall \tilde{a}_{ij} \in J_i$$

$$x \in F(x) \quad \forall \tilde{a}_{ij} \in J_i$$

However, the above model is in a nonlinear form, which can be linearized as follows:

$$\begin{aligned}
 & \text{Max } cx \\
 & \text{S.t} \\
 & z_i \Gamma_i + \sum_{j \in J_i} p_{ij} + \sum_{j \in N} a_{ij} x_j \leq b_i \quad \forall i \in I \\
 & z_i + p_{ij} \geq \tilde{a}_{ij} x_j \quad \forall i \in I, \quad (45) \\
 & \quad \quad \quad j \in J_i \\
 & z_i, p_{ij} \geq 0 \quad \forall i \in I, \\
 & \quad \quad \quad \forall j \in J \\
 & x \in F(x) \quad \forall \tilde{a}_{ij} \in J_i
 \end{aligned}$$

where z_i and p_{ij} are two auxiliary variables. Considering the explained procedure, the robust formulation of the presented problem substitutes Equation (42) with the following constraints:

$$\sum_{j=1}^J (1 - ERP_{nj}) tqan_{jk} \geq \quad \forall k \in K \quad (46)$$

$$\begin{aligned}
 & (D\overline{MN}_{kn} + P_k^n + Z_k^n \Gamma) DST \quad \forall n \in N \\
 & P_k^n + Z_k^n \geq D\overline{MN}_{kn} \quad \forall k \in K, \quad (47) \\
 & \quad \quad \quad \forall n \in N
 \end{aligned}$$

4. 1. Fuzzy Programming Multi-objective Approach

Several approaches have been developed in the literature to address the conflicts of objectives in multi-objective optimization problems. Among these approaches, fuzzy techniques are becoming more popular due to their ability to determine the satisfaction level of any objective function directly (46, 47). This allows decision-makers to calculate Pareto solutions depending on their choices (i.e., the relative degree of importance of objectives). Zimmermann (48) developed the first approach for multi-objective based on fuzzy theory, which was the max-min method. The main deficiency of this method is that it does not ensure the calculation of Pareto solutions. Considering this problem, Lai and Hwang (49) developed the augmented max-min method. The SO and LZL methods were some other approaches that were developed in subsequent years by Selim and Ozkarahan (50) and Li, Zhang (51), respectively. In this paper, we utilize the TH method, which was developed by Torabi and Hassini (52), to

handle the conflict between total cost and total traveled distance of products. This approach guarantees the calculation of Pareto solutions and includes the following phase:

Phase I: In this phase, the positive ideal solution and negative ideal solutions of each objective function are calculated. Consider a bi-objective problem. The positive best solutions (PBS) of each objective function, PBS_{Z_1} and PBS_{Z_2} are obtained through the separate optimization of the model for each objective function. In addition, the negative best solution (NBS) is obtained as follows:

$$NBS_{Z_1} = Z_1(x_{PBS_{Z_2}}) \tag{48}$$

$$NBS_{Z_2} = Z_2(x_{PBS_{Z_1}}) \tag{49}$$

Phase II: In this phase, for each objective function, a linear membership function is established as follows:

$$\mu_1(x) = \begin{cases} 1 & Z_1 \leq PBS_{Z_1} \\ \frac{NBS_{Z_1} - Z_1}{NBS_{Z_1} - PBS_{Z_1}} & PBS_{Z_1} \leq Z_1 \leq NBS_{Z_1} \\ 0 & Z_1 \geq NBS_{Z_1} \end{cases} \tag{50}$$

$$\mu_2(x) = \begin{cases} 1 & Z_2 \leq PBS_{Z_2} \\ \frac{NBS_{Z_2} - Z_2}{NBS_{Z_2} - PBS_{Z_2}} & PBS_{Z_2} \leq Z_2 \leq NBS_{Z_2} \\ 0 & Z_2 \geq NBS_{Z_2} \end{cases} \tag{51}$$

Phase III: In this phase, the single-objective equivalent problem is established using the aggregation function of TH method as below:

$$Min \lambda(x) = \beta \lambda_0 + (1 - \beta) \sum_i w_i \mu_i(x)$$

S.t:

$$\lambda_0 \leq \mu_i(x) \quad \forall i = 1,2 \tag{52}$$

$$x \in F(x)$$

$$\lambda_0, \lambda \in [0,1]$$

5. COMPUTATIONAL EXPERIMENTS

In this section, we validate the developed model and provide insights by solving several numerical examples. The data of numerical examples are mostly adopted from the works by Abazari, Aghsami (9) and Khalilpourazari, Soltanzadeh (10). Table 2 presents the details of the data.

To explore the performance of the problem, the model is coded in GAMS programming software, and the CPLEX solver is used to solve each problem. The examples are randomly generated and run on a personal

laptop with 8 GB of RAM, Intel Core i7, and CPU 2.6 GHz. As previously highlighted, there exist inherent conflicts between the objectives, making it challenging to optimize both objective functions simultaneously. This inherent trade-off implies that enhancing one objective may come at the expense of the other. Table 3 provides a comprehensive summary of our findings. The values presented in the third and fourth columns of the table quantitatively illustrate the nature of these conflicts. When efforts are made to improve the total traveling distance, the optimization process tends to favor the selection of closer facilities. However, this preference may lead to increased costs for the healthcare system. Consequently, in this scenario, the model tends to allocate less attention to minimizing the location cost of the facilities. Conversely, when the focus is on improving the total cost, the optimization process shifts towards selecting facilities that minimize location costs and other cost components.

TABLE 2. The considered ranges for the data of numerical examples

Parameter	Value	Parameter	Value
NCP_i	Rand(40000,7000)	PRL_{oq}	Rand(0.1,0.2)
PCP_s	Rand(2000,3000)	MLC_{ac}	Rand(5000,50000)
BDC_d	Rand(100,3000)	BDF_{dp}	Rand(0.5,3)
WLC_j	Rand(1000,3000)	BDM_{da}	Rand(0.05,3)
CNS_i	Rand(20000,40000)	TMP_{at}	Rand(0.05,2)
CRW_j	Rand(7000,18000)	TFP_{pt}	Rand(0.25,2)
CPS_s	Rand(20000,50000)	TBW_{lgj}	Rand(0.02,1.5)
PCW_o	Rand(200,500)	PRC_{lg}	Rand(0.05,1.75)
FBC_p	Rand(500,2000)	FBM_{ac}	Rand(100,1000)
CBP_t	Rand(500,2000)	DPW_{sj}	Rand(10,350)
MNS	RandI(1,3)	DNW_{ij}	Rand(10,1000)
WMN	RandI(2,5)	DMR_{al}	Rand(1,600)
MPS	RandI(1,3)	DLR_{pt}	Rand(50,550)
NRM	RandI(1,5)	DRW_{ij}	Rand(8,1000)
CUS	Rand(0.1,0.2)	DWA_{jk}	Rand(50,600)
PUS	Rand(0.05,0.15)	BEW_{gj}	Rand(20,700)
DST	Rand(0.85,0.95)	PPW_{jn}	Rand(0.15,1.5)
TPW_{ijm}	Rand(0.2,2)	ERP_{nj}	Rand(0.05,2)
TWA_{jkn}	Rand(0.01,2)	NNP_{qno}	RandI(0,40)
\overline{DMN}_{kn}	RandI(0,10)	NPP_{nm}	RandI(0,50)
\widehat{DMN}_{kn}	Rand(0.05,0.2)	NBP_{ng}	RandI(0,50)
TNW_{sjoq}	Rand(0.05,1.5)		

In this continuing, the analysis of sensitivity is performed to provide more insights into the behavior of the model. Sensitivity analysis is a systematic approach to investigate the impact of variation on the input of parameters to the outputs of the model. We carry out the sensitivity analysis on model parameters and problem parameters. First, we are going to analyze the sensitivity of results based on variations in the price of robustness, as the main parameter of the proposed robust optimization methodology. The obtained computational results in different levels of price of robustness are summarized in Table 3. The conducted sensitivity analysis on the price of robustness provides crucial and illuminating findings for the multi-objective optimization problem in HSC planning. The results reveal that both the total cost and total traveled distance objectives are highly responsive to changes in the price of robustness. As the price of robustness increases, there is a clear and significant upward trend in both cost and distance metrics, highlighting the trade-off between achieving cost efficiency and ensuring robustness in the network design.

This pivotal insight emphasizes the necessity of carefully selecting an appropriate price of robustness, as it directly impacts the delicate balance between minimizing expenses and guaranteeing a robust supply

chain in unpredictable contexts. Understanding the trade-off allows decision-makers to make informed choices that align with their priorities and strategic objectives. Moreover, the analysis demonstrates that CPU time remains stable and unaffected by variations in the price of robustness. This stability is of immense practical importance, as it enables decision-makers to explore a diverse range of robustness values without compromising the optimization process's computational speed. The ability to efficiently examine different robustness levels empowers planners to make timely and well-informed decisions even under time constraints.

In this part, we evaluate the impact of changes in some parameters on the objective functions of the studied HSC. The supplier's capacity, demand, and blood wastage rate are selected as three important parameters for sensitivity analysis. The sensitivity analysis of the objective functions to variations in the nominal value of the demand rate has been thoroughly investigated, and the findings are depicted in Figure 2. Understanding the sensitivity of the objective functions to demand variations offers invaluable insights for supply chain decision-makers. By recognizing the intricate relationship between demand rates and cost and distance metrics, planners can proactively adapt their strategies to cope with dynamic demand scenarios effectively.

TABLE 3. The results of the problem based on the degree of importance of objective functions

(w_1, w_2)	Γ	β	z_1	z_2	μ_{z_1}	μ_{z_2}	%Gap	CPU time (S)
(0.0,1.0)	0.5	0.3	242267.64	322693.05	0.441	0.965	0.00	1.41
(0.2,0.8)	0.5	0.3	242382.33	282957.99	0.724	0.832	0.00	1.62
(0.4,0.6)	0.5	0.3	242382.96	282957.99	0.724	0.832	0.00	1.40
(0.2,0.8)	0.5	0.3	242382.96	282957.99	0.780	0.731	0.00	1.52
(1.0,0.0)	0.5	0.3	251491.01	222314.23	0.780	0.731	0.00	1.44

TABLE 4. The results of the problem based on the variation in the price of robustness

(w_1, w_2)	Γ	β	z_1	z_2	μ_{z_1}	μ_{z_2}	%Gap	CPU time (S)
(0.8,0.2)	0.00	0.3	239863.75	272809.46	0.736	0.792	0.00	1.47
(0.8,0.2)	0.10	0.3	240367.59	274844.88	0.736	0.791	0.00	1.53
(0.8,0.2)	0.20	0.3	240871.44	276880.31	0.736	0.791	0.00	1.52
(0.8,0.2)	0.30	0.3	241375.28	278915.73	0.735	0.791	0.00	1.49
(0.8,0.2)	0.40	0.3	241879.12	280951.15	0.735	0.791	0.00	1.53
(0.8,0.2)	0.50	0.3	242382.96	282986.58	0.735	0.791	0.00	1.47
(0.8,0.2)	0.60	0.3	242886.81	285022.00	0.735	0.791	0.00	1.47
(0.8,0.2)	0.70	0.3	243390.65	287057.42	0.734	0.791	0.00	1.48
(0.8,0.2)	0.80	0.3	243894.49	289092.85	0.734	0.791	0.00	1.49
(0.8,0.2)	0.90	0.3	244398.34	291128.27	0.734	0.791	0.00	1.45
(0.8,0.2)	1.00	0.3	244902.18	293163.69	0.734	0.792	0.00	1.46

Implementing appropriate demand management and response mechanisms can lead to more resilient and cost-efficient supply chain networks, ensuring timely and optimal delivery of humanitarian aid and resources to those in need. As expected, the results reveal a clear and consistent negative impact of increasing demand rates on both objective functions. This behavior is intuitively understandable, as higher demand necessitates a greater flow of products within the supply chain network. Consequently, an increase in product flow leads to a rise in both the total cost and total traveled distance objectives. The amplified demand significantly affects the overall transportation and distribution processes, resulting in higher costs incurred and longer distances traveled. These observations underscore the critical importance of managing and responding to fluctuating demand patterns in HSC planning. Notably, the sensitivity analysis highlights that the total traveled distance objective exhibits a higher degree of sensitivity compared to the total cost. This finding suggests that changes in demand rates have a more pronounced impact on the transportation aspect of the supply chain network, which directly influences the total distance traveled by products.

In the investigation of the second parameter, we analyzed the sensitivity of the objective functions concerning the wastage rate of blood products, as illustrated in Figure 3. Understanding the sensitivity of the objective functions to the wastage rate of blood products empowers supply chain decision-makers to design more robust and cost-effective networks. By strategically managing blood product utilization and implementing waste reduction measures, organizations can enhance their responsiveness to emergencies and humanitarian crises, ensuring a reliable supply of blood products to those in need. As anticipated, the results exhibit a clear and consistent negative correlation between increasing wastage rates of blood products and the performance of the objective functions. This negative impact is expected, as higher wastage rates imply a higher percentage of blood products that become unsuitable for use or are discarded, resulting in inefficiencies in the supply chain network. To mitigate the adverse effects of increased wastage rates, the network's donation and processing of blood must be strategically increased to satisfy demand efficiently. By bolstering the blood flow through the network, the system can better meet the demand for blood products. However, the analysis reveals that such increases in blood flow come at a cost, as they lead to higher total cost and total traveled distance objectives. These findings underscore the significance of minimizing wastage rates and optimizing the blood supply facilities to ensure efficient allocation and utilization of blood products. Effective waste management strategies and enhanced

processing and distribution procedures can play a pivotal role in reducing wastage rates and associated costs while improving overall supply chain performance.

In our latest phase of investigation, we are delving into a sensitivity analysis of the objective functions, regarding variations in supplier capacity, as vividly depicted in Figure 4. This critical analysis serves as a powerful tool for supply chain decision-makers, providing them with valuable insights for making informed and strategic choices. This strategic approach to supplier capacity planning ensures the timely and efficient delivery of essential goods and resources; thus, enhancing the network's responsiveness in effectively addressing humanitarian crises and emergency scenarios.

Our sensitivity analysis has unveiled intriguing and contrasting behaviors exhibited by the objective functions in response to changes in supplier capacity. One noteworthy revelation is that increases in supplier capacity do not significantly impact the overall performance of the supply chain network. This finding suggests that the network is inherently equipped to

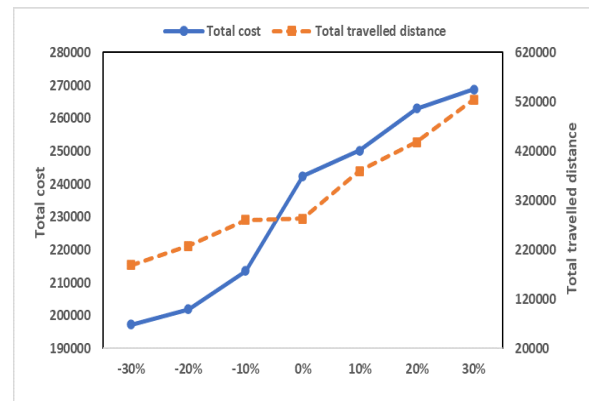


Figure 2. Sensitivity analysis of objectives with respect to the demand for packages

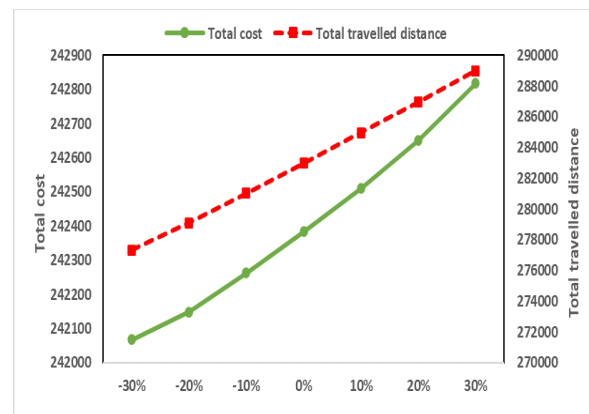


Figure 3. Sensitivity analysis of objectives with respect to blood wastage rate

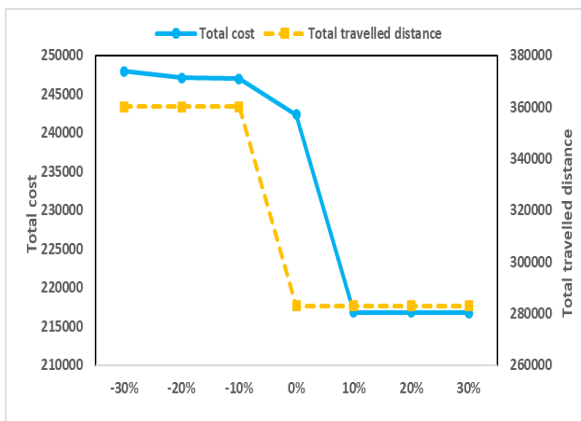


Figure 4. Sensitivity analysis of objectives with respect to the capacity of suppliers

accommodate higher supplier capacities without incurring substantial adverse effects on the total cost and total traveled distance objectives. On the flip side, when supplier capacity experiences reductions, it triggers a remarkable and noteworthy ripple effect throughout the network's performance. This leads to a substantial increase in both the total cost and total traveled distance, emphasizing the critical role of prudent supplier capacity management in optimizing supply chain performance.

While our analysis indicates that augmenting supplier capacity may not necessarily yield substantial improvements, it underscores the paramount importance of maintaining adequately calibrated capacities. This proactive approach helps mitigate the risk of cost escalations and operational inefficiencies. Additionally, addressing reductions in supplier capacity in a timely and proactive manner is crucial to preempt potential disruptions and ensure the seamless operation of the supply chain.

6. MANAGERIAL INSIGHTS

Our computational experiments offer valuable insights for supply chain decision-makers in the context of HSC management. By analyzing various scenarios and conducting sensitivity analyses, we unveil critical considerations for optimizing HSC networks. Here are the key managerial insights:

Balancing conflicting objectives: In HSC planning, there exists a fundamental trade-off between minimizing total cost and reducing total traveled distance. As demonstrated in Table 3, varying the importance of each objective function affects the network's performance. When prioritizing one objective, such as minimizing total traveling distance, it results in selecting nearer facilities but potentially increases costs. Conversely, minimizing total costs involves selecting facilities that reduce location costs and other cost components, which may

lead to longer distances traveled. Managers must carefully consider this trade-off to align network design with specific priorities and operational constraints.

- **Robustness of network:** The sensitivity analysis of the price of robustness, as depicted in Table 4, highlights a critical managerial decision. Both total cost and total traveled distance objectives are highly responsive to changes in the price of robustness. Decision-makers should strategically select an appropriate price of robustness, as it directly impacts the balance between cost efficiency and network robustness. This choice influences the network's ability to adapt to uncertainties without incurring substantial cost increases. Moreover, the stability of CPU time allows planners to explore different robustness levels efficiently, even under time constraints, enabling informed decisions in dynamic environments.
- **Managing demand variations:** Understanding the sensitivity of objective functions to demand variations, as shown in Figure 2, is pivotal for HSC managers. Higher demand rates significantly impact both total cost and total traveled distance, necessitating proactive demand management strategies. To enhance network resilience and cost-effectiveness, managers should implement demand forecasting and response mechanisms. This enables the efficient allocation of resources and ensures timely aid delivery during fluctuating demand scenarios.
- **Minimizing Blood Wastage:** The sensitivity analysis related to blood wastage rates, which is provided in Figure 3, emphasizes the importance of waste reduction strategies in blood product supply chains. Increasing wastage rates negatively affect both cost and distance objectives. To mitigate these effects, organizations should focus on optimizing blood supply facilities, enhancing processing and distribution procedures, and minimizing waste. Efficient waste management strategies can lead to cost savings while improving overall supply chain performance.
- **Supplier Capacity Management:** Analyzing the sensitivity of objective functions to changes in supplier capacity, which is presented in Figure 4, reveals the significance of prudent supplier capacity management. Increasing supplier capacity does not substantially impact overall network performance, indicating room for accommodating higher capacities without incurring significant cost or distance penalties. However, reducing supplier capacity has a noteworthy negative impact. To optimize supply chain performance, managers should maintain well-calibrated capacities, proactively address reductions, and ensure smooth operations, particularly in humanitarian crises and emergency situations.

This paper can be extended in several ways by future research. From the problem development viewpoint, resiliency is of great importance for HSCs. One of the potential directions is to consider the resiliency objectives and improve the power of the network in facing disruptions (26). Furthermore, some other important decisions, such as the inventory and routing decisions, also have the potential to be incorporated in the presented model by considering proper coordination agreements such as VMI (53). From the solution methodology perspective, we employed the CPLEX commercial solver, a powerful optimization tool known for its ability to handle MILP mathematical models. CPLEX allowed us to find non-dominated solutions for the studied multi-objective HSC network design problem. However, it's essential to acknowledge that as the problem size scales up, the computational costs associated with solving it can become quite substantial regarding the NP-hard complexity of the problem. Researchers and practitioners should be mindful of these computational challenges. Therefore, the exact or metaheuristic algorithms such as can be designed in future research to consider this issue. Some examples are different variants of Lagrangian relaxation, fast fireworks (54), memetic (55-57), hybrid multi-objective evolutionary (58), tabu search (59-61), differential evolution (62, 63), ant-based (64), multi-objective profitable severity and delay reduction (65), particle swarm optimization (66) algorithms. In addition, the machine learning approaches, such as unsupervised learning methods, can be used to cluster the packages, and improve the performance of the system (67).

7. CONCLUSION

In this research, we developed a new humanitarian supply chain network design problem under product differentiation and demand uncertainty. For the first time, non-perishable, perishable, and blood products were simultaneously considered as three important products of the network. The problem was formulated using a MILP multi-objective mathematical model. The model aims to minimize the total cost and total traveled distance of products by determining location, allocation, and production decisions. To provide a more realistic problem, the uncertainty in demand of affected areas was also taken into account.

A two-phase solution methodology was suggested to solve this problem. First, a robust optimization approach was presented to establish the deterministic counterpart of the stochastic model. Next, an efficient fuzzy programming-based approach was designed to reformulate the model in a single-objective form. The model's performance and solution methodologies were investigated by solving numerical instances. The results

showed that the proposed fuzzy approach can successfully find non-dominated solutions for the problem considering the decision-maker's preferences. The choice of the price of robustness significantly influences the balance between cost efficiency and network robustness, highlighting the importance of strategic decision-making for this parameter. Sensitivity analyses reveal the impact of demand variations on both cost and distance objectives, emphasizing the need for proactive demand management strategies. Furthermore, minimizing blood wastage rates and prudent supplier capacity management emerge as crucial factors for cost savings and network responsiveness.

8. REFERENCES

1. Javadian N, Modares S, Bozorgi A. A bi-objective stochastic optimization model for humanitarian relief chain by using evolutionary algorithms. *International Journal of Engineering*. 2017;30(10):1526-37. 10.5829/ije.2017.30.10a.14
2. Batta R, Peng J, Smith JC, Greenberg HJ. *Leading Developments from INFORMS Communities*: INFORMS; 2017.
3. Cotes N, Cantillo V. Including deprivation costs in facility location models for humanitarian relief logistics. *Socio-Economic Planning Sciences*. 2019;65:89-100. 10.1016/j.seps.2018.03.002
4. Barzinpour F, Esmaili V. A multi-objective relief chain location distribution model for urban disaster management. *The International Journal of Advanced Manufacturing Technology*. 2014;70:1291-302. 10.1007/s00170-013-5379-x
5. Omrani H, Najafi I, Bahrami K, Najafi F, Safari S. Acute kidney injury following traumatic rhabdomyolysis in Kermanshah earthquake victims; a cross-sectional study. *The American journal of emergency medicine*. 2021;40:127-32. 10.1016/j.ajem.2020.01.043
6. Charles A, Lauras M, Van Wassenhove LN, Dupont L. Designing an efficient humanitarian supply network. *Journal of Operations Management*. 2016;47:58-70. 10.1016/j.jom.2016.05.012
7. Malmir B, Zobel CW. An applied approach to multi-criteria humanitarian supply chain planning for pandemic response. *Journal of Humanitarian Logistics and Supply Chain Management*. 2021;11(2):320-46. 10.1108/JHLSCM-08-2020-0064
8. Nikkhoo F, Bozorgi-Amiri A. A procurement-distribution coordination model in humanitarian supply chain using the information-sharing mechanism. *International Journal of Engineering*. 2018;31(7):1057-65. 10.5829/ije.2018.31.07a.08
9. Abazari SR, Aghsami A, Rabbani M. Prepositioning and distributing relief items in humanitarian logistics with uncertain parameters. *Socio-Economic Planning Sciences*. 2021;74:100933. 10.1016/j.seps.2020.100933
10. Khalilpourazari S, Soltanzadeh S, Weber G-W, Roy SK. Designing an efficient blood supply chain network in crisis: neural learning, optimization and case study. *Annals of Operations Research*. 2020;289:123-52. 10.1007/s10479-019-03437-2
11. Fallahi A, Mokhtari H, Niaki STA. Designing a closed-loop blood supply chain network considering transportation flow and quality aspects. *Sustainable Operations and Computers*. 2021;2:170-89. 10.1016/j.susoc.2021.07.002
12. Kovács G, Spens KM. Humanitarian logistics in disaster relief operations. *International Journal of Physical Distribution &*

- Logistics Management. 2007;37(2):99-114. 10.1108/09600030710734820
13. Balcik B, Bozkir CDC, Kundakcioglu OE. A literature review on inventory management in humanitarian supply chains. *Surveys in Operations Research and Management Science*. 2016;21(2):101-16. 10.1016/j.sorms.2016.10.002
 14. Zhan S-l, Liu N, editors. A multi-objective stochastic programming model for emergency logistics based on goal programming. 2011 fourth International Joint Conference on Computational Sciences and Optimization; 2011: IEEE.
 15. Murali P, Ordóñez F, Dessouky MM. Facility location under demand uncertainty: Response to a large-scale bio-terror attack. *Socio-Economic Planning Sciences*. 2012;46(1):78-87. 10.1016/j.seps.2011.09.001
 16. Bozorgi-Amiri A, Jabalameli MS, Alinaghian M, Heydari M. A modified particle swarm optimization for disaster relief logistics under uncertain environment. *The International Journal of Advanced Manufacturing Technology*. 2012;60:357-71. 10.1007/s00170-011-3596-8
 17. Khayal D, Pradhananga R, Pokharel S, Mutlu F. A model for planning locations of temporary distribution facilities for emergency response. *Socio-Economic Planning Sciences*. 2015;52:22-30. 10.1016/j.seps.2015.09.002
 18. Hasani A, Mokhtari H. Redesign strategies of a comprehensive robust relief network for disaster management. *Socio-Economic Planning Sciences*. 2018;64:92-102. 10.1016/j.seps.2018.01.003
 19. Hasani A, Mokhtari H. An integrated relief network design model under uncertainty: A case of Iran. *Safety Science*. 2019;111:22-36. 10.1016/j.ssci.2018.09.004
 20. Wang Q, Nie X. A stochastic programming model for emergency supply planning considering traffic congestion. *IIEE Transactions*. 2019;51(8):910-20. 10.1080/24725854.2019.1589657
 21. Aghajani M, Torabi SA, Heydari J. A novel option contract integrated with supplier selection and inventory prepositioning for humanitarian relief supply chains. *Socio-Economic Planning Sciences*. 2020;71:100780. 10.1016/j.seps.2019.100780
 22. Mansoori S, Bozorgi-Amiri A, Pishvaei MS. A robust multi-objective humanitarian relief chain network design for earthquake response, with evacuation assumption under uncertainties. *Neural Computing and Applications*. 2020;32:2183-203. 10.1007/s00521-019-04193-x
 23. Nezhadroshan AM, Fathollahi-Fard AM, Hajiaghaci-Keshteli M. A scenario-based possibilistic-stochastic programming approach to address resilient humanitarian logistics considering travel time and resilience levels of facilities. *International Journal of Systems Science: Operations & Logistics*. 2021;8(4):321-47. 10.1080/23302674.2020.1769766
 24. Mahtab Z, Azeem A, Ali SM, Paul SK, Fathollahi-Fard AM. Multi-objective robust-stochastic optimisation of relief goods distribution under uncertainty: a real-life case study. *International Journal of Systems Science: Operations & Logistics*. 2022;9(2):241-62. 10.1080/23302674.2021.1879305
 25. Akbari F, Valizadeh J, Hafezalkotob A. Robust cooperative planning of relief logistics operations under demand uncertainty: a case study on a possible earthquake in Tehran. *International Journal of Systems Science: Operations & Logistics*. 2022;9(3):405-28. 10.1080/23302674.2021.1914767
 26. Foroughi A, Moghaddam BF, Behzadi MH, Sobhani FM. Developing a bi-objective resilience relief logistic considering operational and disruption risks: a post-earthquake case study in Iran. *Environmental Science and Pollution Research*. 2022;29(37):56323-40. 10.1007/s11356-022-18699-w
 27. Ukkusuri SV, Yushimito WF. Location routing approach for the humanitarian prepositioning problem. *Transportation research record*. 2008;2089(1):18-25. 10.3141/2089-03
 28. Kutanoglu E, Mahajan M. An inventory sharing and allocation method for a multi-location service parts logistics network with time-based service levels. *European Journal of Operational Research*. 2009;194(3):728-42. 10.1016/j.ejor.2007.12.032
 29. Campbell AM, Jones PC. Prepositioning supplies in preparation for disasters. *European Journal of Operational Research*. 2011;209(2):156-65. 10.1016/j.ejor.2010.08.029
 30. Ahmadi M, Seifi A, Tootooni B. A humanitarian logistics model for disaster relief operation considering network failure and standard relief time: A case study on San Francisco district. *Transportation Research Part E: Logistics and Transportation Review*. 2015;75:145-63. 10.1016/j.tre.2015.01.008
 31. Bozorgi-Amiri A, Khorsi M. A dynamic multi-objective location-routing model for relief logistic planning under uncertainty on demand, travel time, and cost parameters. *The International Journal of Advanced Manufacturing Technology*. 2016;85:1633-48. 10.1007/s00170-015-7923-3
 32. Sabouhi F, Bozorgi-Amiri A, Vaez P. Stochastic optimization for transportation planning in disaster relief under disruption and uncertainty. *Kybernetes*. 2021;50(9):2632-50. 10.1108/K-10-2020-0632
 33. Tofighi S, Torabi SA, Mansouri SA. Humanitarian logistics network design under mixed uncertainty. *European Journal of Operational Research*. 2016;250(1):239-50. 10.1016/j.ejor.2015.08.059
 34. Zhang Z-H, Jiang H. A robust counterpart approach to the bi-objective emergency medical service design problem. *Applied Mathematical Modelling*. 2014;38(3):1033-40. 10.1016/j.apm.2013.07.028
 35. Akbarpour M, Torabi SA, Ghavamifar A. Designing an integrated pharmaceutical relief chain network under demand uncertainty. *Transportation Research Part E: Logistics and Transportation Review*. 2020;136:101867. 10.1016/j.tre.2020.101867
 36. Jabbarzadeh A, Fahimnia B, Seuring S. Dynamic supply chain network design for the supply of blood in disasters: A robust model with real world application. *Transportation Research Part E: Logistics and Transportation Review*. 2014;70:225-44. 10.1016/j.tre.2014.06.003
 37. Fallahi A, Mousavian Anaraki SA, Mokhtari H, Niaki STA. Blood plasma supply chain planning to respond COVID-19 pandemic: a case study. *Environment, Development and Sustainability*. 2022;1-52. 10.1007/s10668-022-02793-7
 38. Haghjoo N, Tavakkoli-Moghaddam R, Shahmoradi-Moghaddam H, Rahimi Y. Reliable blood supply chain network design with facility disruption: A real-world application. *Engineering Applications of Artificial Intelligence*. 2020;90:103493. 10.1016/j.engappai.2020.103493
 39. Kamyabniya A, Noormohammadzadeh Z, Sauré A, Patrick J. A robust integrated logistics model for age-based multi-group platelets in disaster relief operations. *Transportation Research Part E: Logistics and Transportation Review*. 2021;152:102371. 10.1016/j.tre.2021.102371
 40. Hong J-D. Design of humanitarian supply chain system by applying the general two-stage network DEA model. *Journal of Humanitarian Logistics and Supply Chain Management*. 2023;13(1):74-90. 10.1108/JHLSCM-06-2022-0069
 41. Modaresi SA, Maleki MR. Integrating pre and post-disaster activities for designing an equitable humanitarian relief supply chain. *Computers & Industrial Engineering*. 2023;181:109342. 10.1016/j.cie.2023.109342

42. Vaillancourt A. Kit management in humanitarian supply chains. *International Journal of Disaster Risk Reduction*. 2016;18:64-71. 10.1016/j.ijdr.2016.06.002
43. Noham R, Tzur M. Designing humanitarian supply chains by incorporating actual post-disaster decisions. *European Journal of Operational Research*. 2018;265(3):1064-77. 10.1016/j.ejor.2017.08.042
44. Bertsimas D, Sim M. The price of robustness. *Operations Research*. 2004;52(1):35-53. 10.1287/opre.1030.0065
45. Kaviyani-Charati M, Heidarzadeh Souraki F, Hajiaghahi-Keshтели M. A robust optimization methodology for multi-objective location-transportation problem in disaster response phase under uncertainty. *International Journal of Engineering*. 2018;31(11):1953-61. 10.5829/ije.2018.31.11b.20
46. Fallahi A, Shahidi-Zadeh B, Niaki STA. Unrelated parallel batch processing machine scheduling for production systems under carbon reduction policies: NSGA-II and MOGWO metaheuristics. *Soft Computing*. 2023;1-29. 10.1007/s00500-023-08754-0
47. Amani Bani E, Fallahi A, Varmazyar M, Fathi M. Designing a sustainable reverse supply chain network for COVID-19 vaccine waste under uncertainty. *Computers & Industrial Engineering*. 2022;174:108808. 10.1016/j.cie.2022.108808
48. Zimmermann H-J. Fuzzy programming and linear programming with several objective functions. *Fuzzy Sets and Systems*. 1978;1(1):45-55. 10.1016/0165-0114(78)90031-3
49. Lai Y-J, Hwang C-L. A new approach to some possibilistic linear programming problems. *Fuzzy Sets and Systems*. 1992;49(2):121-33. 10.1016/0165-0114(92)90318-X
50. Selim H, Ozkarahan I. A supply chain distribution network design model: an interactive fuzzy goal programming-based solution approach. *The International Journal of Advanced Manufacturing Technology*. 2008;36:401-18. 10.1007/s00170-006-0842-6
51. Li X-q, Zhang B, Li H. Computing efficient solutions to fuzzy multiple objective linear programming problems. *Fuzzy Sets and Systems*. 2006;157(10):1328-32. 10.1016/j.fss.2005.12.003
52. Torabi SA, Hassini E. An interactive possibilistic programming approach for multiple objective supply chain master planning. *Fuzzy Sets and Systems*. 2008;159(2):193-214. 10.1016/j.fss.2007.08.010
53. Asadkhani J, Fallahi A, Mokhtari H. A sustainable supply chain under VMI-CS agreement with withdrawal policies for imperfect items. *Journal of Cleaner Production*. 2022;376:134098. 10.1016/j.jclepro.2022.134098
54. Chen M, Tan Y. SF-FWA: A Self-Adaptive Fast Fireworks Algorithm for effective large-scale optimization. *Swarm and Evolutionary Computation*. 2023;80:101314. 10.1016/j.swevo.2023.101314
55. Dulebenets MA. An Adaptive Polyploid Memetic Algorithm for scheduling trucks at a cross-docking terminal. *Information Sciences*. 2021;565:390-421. 10.1016/j.ins.2021.02.039
56. Dulebenets MA. A Diffused Memetic Optimizer for reactive berth allocation and scheduling at marine container terminals in response to disruptions. *Swarm and Evolutionary Computation*. 2023;80:101334. 10.1016/j.swevo.2023.101334
57. Keshavarz T, Salmasi N, Varmazyar M. Minimizing total completion time in the flexible flowshop sequence-dependent group scheduling problem. *Annals of Operations Research*. 2015;226:351-77. 10.1007/s10479-014-1667-6
58. Pasha J, Nwodu AL, Fathollahi-Fard AM, Tian G, Li Z, Wang H, et al. Exact and metaheuristic algorithms for the vehicle routing problem with a factory-in-a-box in multi-objective settings. *Advanced Engineering Informatics*. 2022;52:101623. 10.1016/j.aei.2022.101623
59. Seydanlou P, Sheikhalishahi M, Tavakkoli-Moghaddam R, Fathollahi-Fard AM. A customized multi-neighborhood search algorithm using the tabu list for a sustainable closed-loop supply chain network under uncertainty. *Applied Soft Computing*. 2023;110495. 10.1016/j.asoc.2023.110495
60. Varmazyar M, Akhavan-Tabatabaei R, Salmasi N, Modarres M. Operating room scheduling problem under uncertainty: Application of continuous phase-type distributions. *IISE Transactions*. 2020;52(2):216-35. 10.1080/24725854.2019.1628372
61. Varmazyar M, Salmasi N. Sequence-dependent flow shop scheduling problem minimising the number of tardy jobs. *International Journal of Production Research*. 2012;50(20):5843-58. 10.1080/00207543.2011.632385
62. Fallahi A, Mahnam M, Niaki STA. A discrete differential evolution with local search particle swarm optimization to direct angle and aperture optimization in IMRT treatment planning problem. *Applied Soft Computing*. 2022;131:109798. 10.1016/j.asoc.2022.109798
63. Fallahi A, Amani Bani E, Niaki STA. A constrained multi-item EOQ inventory model for reusable items: Reinforcement learning-based differential evolution and particle swarm optimization. *Expert Systems with Applications*. 2022;207:118018. 10.1016/j.eswa.2022.118018
64. Singh E, Pillay N. A study of ant-based pheromone spaces for generation constructive hyper-heuristics. *Swarm and Evolutionary Computation*. 2022;72:101095. 10.1016/j.swevo.2022.101095
65. Singh P, Pasha J, Moses R, Sobanjo J, Ozguven EE, Dulebenets MA. Development of exact and heuristic optimization methods for safety improvement projects at level crossings under conflicting objectives. *Reliability Engineering & System Safety*. 2022;220:108296. 10.1016/j.res.2021.108296
66. Keshavarz T, Salmasi N, Varmazyar M. Flowshop sequence-dependent group scheduling with minimisation of weighted earliness and tardiness. *European Journal of Industrial Engineering*. 2019;13(1):54-80. 10.1504/EJIE.2019.097920
67. Kochakshani F, Kayvanfar V, Haji A. Supply chain planning of vaccine and pharmaceutical clusters under uncertainty: The case of COVID-19. *Socio-Economic Planning Sciences*. 2023;87:101602. 10.1016/j.seps.2023.101602

COPYRIGHTS

©2024 The author(s). This is an open access article distributed under the terms of the Creative Commons Attribution (CC BY 4.0), which permits unrestricted use, distribution, and reproduction in any medium, as long as the original authors and source are cited. No permission is required from the authors or the publishers.

**Persian Abstract****چکیده**

در محیط پویا و غیرقابل پیش‌بینی دنیای امروز، برنامه‌ریزی و مدیریت زنجیره‌های تامین بشردوستانه از اهمیت بسیار بالایی برخوردار است. در این راستا مدیریت لجستیک کارا سبب می‌شود تا کالاها و منابع ضروری در شرایط قابل قبول و در زمان مناسب به نواحی بحران‌زده تحویل گردند و در نهایت پشتیبانی لازم از جمعیت آسیب‌دیده به عمل آید. در این پژوهش، یک مسئله‌ی طراحی شبکه‌ی زنجیره تامین بشردوستانه با در نظر گرفتن تمایز میان اقلام و همچنین شرایط عدم قطعیت تقاضا مورد بررسی قرار می‌گیرد. به‌صورت دقیق‌تر، سه دسته‌ی کلی کالاهای فسادناپذیر، کالاهای فسادپذیر و خون به عنوان سه دسته کالای اساسی در شبکه‌ی زنجیره تامین بشردوستانه در مسئله‌ی طراحی شبکه لحاظ می‌شوند. مسئله در قالب یک مدل برنامه‌ریزی ریاضی چندهدفه عددصحیح-خطی فرموله می‌شود. اهداف مسئله‌ی ارائه‌شده، حداقل‌سازی مجموع هزینه و مجموع مسافت طی شده‌ی کالاها می‌باشند. به‌منظور نزدیک‌تر نمودن فرضیات پژوهش به شرایط دنیای واقعی، عدم قطعیت در پارامتر تقاضای محصولات نیز لحاظ می‌گردد. یک متدولوژی دو مرحله‌ی به عنوان روش حل مسئله ارائه می‌شود. در ابتدا، یک رویکرد بهینه‌سازی استوار جهت فرموله‌سازی مدل هم‌ارز قطعی مسئله مورد بحث قرار می‌گیرد. در مرحله‌ی دوم، یک روش کارای مبتنی بر برنامه‌ریزی فازی جهت تبدیل مسئله‌ی دوهدفه به یک مسئله‌ی تک‌هدفه تشریح می‌شود. عملکرد مدل ریاضی توسعه‌داده شده و متدولوژی پیشنهادی از طریق حل مثال‌های عددی مختلف مورد تجزیه و تحلیل قرار می‌گیرند. نتایج محاسباتی بیانگر این هستند که روش فازی پیشنهادی قادر است تا مجموعه جواب‌های نامغلوب برای مسئله را با در نظر گرفتن ترجیحات تصمیم‌گیرنده ایجاد نماید. همچنین تحلیل حساسیت بر روی پارامترهای ورودی مسئله با هدف ایجاد بینش بیشتر انجام می‌شود. در انتها پیشنهاداتی برای تحقیقات آتی جهت توسعه‌ی پژوهش فعلی ارائه می‌شود.



Performance Evaluating Energy, Economic and Environmental Performance with an Integrated Approach of Data Envelopment Analysis and Game Theory

M. Mohammadzadeh, M. Navabakhsh*, A. Hafezalkotob

Department of Industrial Engineering, Islamic Azad University, South Tehran Branch, Iran

PAPER INFO

Paper history:

Received 31 December 2023
 Received in revised form 11 February 2024
 Accepted 18 February 2024

Keywords:

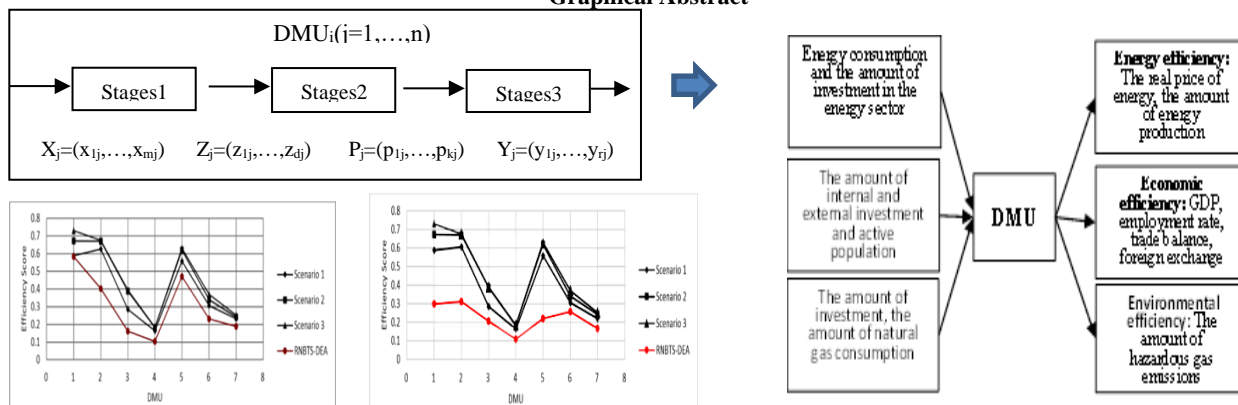
Performance Evaluation
 Economic
 Energy
 Environmental
 Game Theory
 Data Envelopment Analysis

A B S T R A C T

This research has been carried out with the aim of evaluating the energy, economic and environmental performance of selected countries that export energy resources with the integrated approach of data envelopment analysis (DEA) and game theory. The methodology of this research, including super-efficiency and cross-efficiency methods have also been used to rank efficient countries before the cooperation phase. Then, in the cooperation phase, each country is investigated using the method of cooperative games theory and Shapley's value. The resulting model was implemented and the rank of the efficient countries was compared with each other in the super-efficiency and cross-efficiency method (before cooperation) and the Shapley's value method (after cooperation). The results showed that Qatar and Yemen have the highest, Lebanon and Jordan the lowest energy efficiency; Kuwait, Qatar and Turkmenistan have the highest economic efficiency, Iran and Turkey have the lowest economic efficiency; UAE and Qatar have the highest, Iran and Jordan the lowest environmental efficiency.

doi: 10.5829/ije.2024.37.05b.13

Graphical Abstract



NOMENCLATURE

BR	v	U	Horizontal components of velocity (m/s)
C_c	Cunningham correction factor	V	Vertical components of velocity (m/s)
C_k	Discrete lattice velocity in direction (k)	U_i, U_j	Random numbers between 0 and 1
C_s	Speed of sound in Lattice scale	Greek Symbols	
d^p	Particle diameter (μm)	ρ	Density (kg/m^3)
f_k^{eq}	Equilibrium distribution function	τ	Lattice relaxation time

*Corresponding Author Email: m_navabakhsh@azad.ac.ir (M. Navabakhsh)

Please cite this article as: Mohammadzadeh M, Navabakhsh M, Hafezalkotob A, Performance Evaluating Energy, Economic and Environmental Performance with an Integrated Approach of Data Envelopment Analysis and Game Theory. International Journal of Engineering, Transactions B: Applications. 2024;37(05):959-73.

1. INTRODUCTION

Energy consumption is an indispensable aspect of production processes across all stages, as it is imperative for the production process to function. It is impossible to carry out any production activity without the use of energy. Economic growth models that neglect the significance of energy in driving economic growth suffer imperfections. Numerous scholarly works have examined the relationship between economic growth and energy consumption, while comparatively a few studies have delved into the effects of energy on product growth (1). Energy consumption and all economic activities exert direct and indirect impacts on the environment; meaning that the process of energy production, from extraction to production, and consumption, can significantly harm the environment (2). The correlation between economic development and the environment is a major and convoluted economic concern. Energy consumption is an essential component of any economic activity. It plays a vital role in driving economic growth and enhancing the overall quality of human life while leading to the generation of environmental pollutants (3). Energy is widely acknowledged as a major constituent in the establishment and advancement of industrial societies (4). In that light, the level of access to various energy sources serves as an indicator of the political and economic development and influence of countries. The combination of high energy prices and the significant investment required in the capital sector, along with the rapid expansion of industrialization and the increasing energy demands of societies, has prompted the adoption of policies to optimize energy consumption (5). These policies aim to prevent uncontrolled and inefficient energy usage while reducing production costs and enhancing public welfare (6). Therefore, given the great importance of energy and the reduction of fossil energy sources and the increasing fuel price in production and services, as well as environmental issues, the improvement of consumption status and efficiency has given much attention as possible in its use (7). Enhancing energy efficiency is a widely used cost-effective approach to the enhancement of energy security; the promotion of industrial competitiveness, and the mitigation of climate change repercussions (8). Furthermore, with the rise in population growth and energy dependence, there has been a corresponding increase in the consumption of fossil fuels, leading to environmental challenges (9). As a result, there is a growing necessity for politicians to engage with experts and opinion leaders to formulate and execute policies that promote energy efficiency and reduce overall energy consumption (10). A significant number of developing countries are undergoing raised energy consumption as a result of economic growth and subsequent better living standards (11). Besides, this increasing trend cannot

continue to rise as the available resources are limited. This is while energy security and environmental crises are other issues that have raised serious concerns. In addition, the utilization of energy often requires substantial investments, which are frequently limited in developing countries (12). Moreover, energy consumption in these nations tends to contribute to elevated levels of environmental pollution and energy inefficiency when compared to more developed countries. Consequently, improving energy, economic, and environmental efficiency emerges as a feasible solution (13).

In spite of the extensive endeavors made in developed nations to enhance awareness, adopt environmentally friendly technologies, and increase energy efficiency; the rapid pace of economic development has resulted in a substantial surge in energy consumption (14). Consequently, this has given rise to multiple environmental challenges, including the international emission of greenhouse gases. Each year, state-level meetings are convened to address environmental risks, promote stability, and mitigate greenhouse gas emissions (15, 16). Based on a comprehensive analysis of these conventions, certain countries demonstrably lack a definitive stance toward effectively attaining the objectives outlined in these conventions, evidently shunning the principle of responsibility (17). These conventions serve countries as an opportunity to be able to align their policy-making with global CO₂ emission reduction policies while interacting with credible international institutions. In recent conventions, a legally binding regime aimed at reducing emissions for all countries has been approved, indicating that in order to achieve the objectives of emission reduction, it is imperative for both developed and developing countries to establish robust policy frameworks (18). To effectively utilize emission reduction permits as a means to regulate pollution levels and align them with socially optimal standards, an exhaustive constraint has been imposed on the overall emission levels within a given region (19). This restriction enables the evaluation and allocation of permits to countries that have actively participated in the program. This limited availability serves as a driving force behind the trade and exchange of licenses (20). To ensure the efficiency of these licenses several criteria must be thoroughly examined: responsibility, qualification, equality, effectiveness, and sustainable development. In order to determine the optimal emission rate in countries to create a win-win situation in terms of environmental impact and efficiency in the study area, permits were efficiently allocated while taking into account the social and economic aspects (21, 22). To establish an appropriate setting for the achievement of Pareto optimal conditions, it is feasible to ensure that all countries are placed in a favorable position

once the efficiency frontier outlined in the employed model is attained (23).

The evaluation of energy and environmental performance holds significant importance for policymakers and economists. This interest stems from two key factors: the escalating levels of greenhouse gas emissions and the limited availability of energy resources. These factors are integral in shaping the behavior of energy consumers and how they respond to energy programs. In certain instances, consumers exhibit complete responsiveness, while in others, they pose challenges to policy packages (24). In light of the escalating energy consumption and environmental pollution, and subsequently their adverse impact on health, it has become imperative to prioritize the optimization of existing resources and prevent energy waste (25). This directs the attention of energy policymakers toward the necessity of optimally exploiting energy sources. Unmistakably, relevant decision-making and planning require a full grasp of the current and final consumption of energy carriers in terms of efficiency (26). The unchecked surge in energy consumption across developing nations has made it imperative to adopt energy optimization strategies (27). As a result, in conjunction with other production factors, the efficiency and optimization of energy is a determining constituent of the economic pulse of nations (28). Accordingly, economic developments have progressively increased the significance of energy efficiency and optimization. As environmental concerns continue to rise, it is crucial to consider the negative impacts and pollutants that arise from economic activities when evaluating the efficiency of businesses at both the micro and macro levels. This is especially important in energy-intensive industries and at the macro level where pollutants can have a significant impact on the environment (29).

Besides, other methods are also available to measure efficiency. DEA has become increasingly popular in recent years as a method for measuring efficiency. It is based on mathematical programming that allows for measuring the relative efficiency of the units using the possible production set (PPS) formed by all units. This method has many significant advantages: Its main advantage is its ability to compute the efficiency of units with multiple inputs and outputs. Additionally, it does not make any assumptions about the production frontier shape or the internal structure of decision-making units (30).

In the past, classic DEA models regarded systems as a black box and to some extent ignored their internal structures. That is to say, models with network structures were treated as a single unit. This approach failed to account for the fact that real-world problems in telecommunications, such as power distribution and transportation, often have a network structure. Over the

past few years, there have been advancements in the development of models that also incorporate the network structure of decision-making units. It is crucial to acknowledge that in problems with a network structure, the collaboration among subsystems leads to an increase in the overall efficiency of the system. Consequently, models should be able to effectively take this collaboration into account. Game theory is a viable methodology that can facilitate the achievement of this objective. The approach mentioned has gained popularity in recent years and is commonly referred to as centralized models in the field of data envelopment analysis. One of the main issues with these models is their inability to provide a distinct performance value for each subunit (31). It should be noted that certain researchers have adopted the leader-follower approach or the concept of achieving maximum efficiency. However, it is important to recognize that this approach is at odds with the principles of the cooperative gameplay concept. In classical DEA models, it is commonly assumed that data is certain. As a result, these models lack the capability to handle data uncertainties. In the real world, certain data are inherently inaccurate, ambiguous, and uncertain. Therefore, it is crucial to adopt approaches that can effectively manage this uncertainty during the modeling process. Numerous methods have been proposed for controlling uncertainty in optimization problems. In recent years, there has been a significant focus on approaches to addressing complex problems, such as fuzzy set theory, random programming, and optimization. These methods have proven to be effective in tackling a wide range of challenges and have garnered significant attention from researchers. It is worth noting that previous investigations into the implementation of these approaches in DEA have primarily focused on issues with simple and non-network structures. However, there is a dearth of quantitative research on the use of uncertainty control approaches in network-structured issues. It is important to mention that the existing studies are restricted to the use of fuzzy approaches, ignoring other approaches. The objective of this study is to address the aforementioned issues by first introducing a DEA model based on the Nash bargaining game, a technique in game theory. Then, in order to effectively control the uncertainty of the proposed model, three approaches are employed: fuzzy set theory, random programming, and robust optimization. In conclusion, various numerical examples and case studies were used to validate the proposed models and estimate their efficiency.

Gabriel et al. (1) reported that energy service companies face limited resources. The companies are centralized using the DEA method. The DEA model is used to limit the efficient use of resources. The results of the study demonstrated that this method demonstrated good effectiveness in improving energy consumption in energy service companies in Spain.

Amani and Bagherzadeh Valami (32) studied a thorough examination of sustainable development and sustainability using DEA analysis. They suggested that these concepts have been at the core of policy-making within multilateral agreements at a wide range of levels. Despite their importance, both concepts have been defined ambiguously. Data envelopment analysis is an increasingly used method for measuring sustainability. This paper is a review of the body of research published between 2017 and 2020 and explores the extent to which DEA has been applied to measuring sustainability. Previous research demonstrated that social capital remains a key factor in measuring sustainability. Furthermore, process indicators are also being treated as an alternative measure. Despite their significance, these measures fail to fully capture the multidimensional nature of sustainability and sustainable development. The findings of this research reveal that the majority of programs are focused on Asian countries or Chinese regions, while it seems to be a significant research gap in European territories.

Maddi et al. tried to analyze and forecast the relative efficiency of multiple branches of the Social Security Organization throughout Iran. A framework was developed in this study to estimate the future value of unit efficiency using artificial neural networks. This research delves into the measurement of cost and technical efficiency in a two-tier supply chain under both stable and unstable price conditions. To achieve this, we utilized the non-parametric method of DEA and game theory. By doing so, we were able to address research gaps in this field and provide valuable insights. First, branch efficiency was assessed using the DEA method, followed by the classification of the efficiency level. We used time series functions to predict the future efficiencies of units based on their previous efficiencies and cost-efficiency calculations over several consecutive years. By analyzing historical data and using advanced forecasting techniques, we were able to accurately predict the future efficiencies of these units. The findings of this research suggest that managers must implement a data collection and processing system and consistently perform clustering and efficiency prediction for upcoming months and years based on whose results they must concentrate on enhancing and optimizing inputs and outputs.

Amani and Bagherzadeh Valami (32) report that DEA is a linear programming-based approach utilized in economics to measure the efficiency of decision-making units. In classical models of data envelopment analysis, the efficiency of a system is typically calculated by treating the entire system as a decision-making unit (DMU) and disregarding the inter-process relationships within the system. However, the internal relationships of different parts of a DMU may have diverse structures that can complicate the evaluation of its efficiency. A

network perspective is a viable solution to model inter-unit relationships (33). The relationship between subunits in a DMU may occur in series, parallel, or mixed states. The objective of this study is to address the aforementioned issues by introducing a DEA model based on the Nash bargaining game, a technique in game theory. In the next stage, in order to effectively control uncertainty, three approaches are employed: fuzzy set theory, random programming, and robust optimization.

1. 1. Research Questions

1. What is the energy efficiency of the selected countries?
2. What is the economic efficiency of the selected countries?
3. What is the environmental efficiency of the selected countries?
4. What is the integrated efficiency rate of selected countries in cooperative game conditions?

1. 2. Research Objectives

1. Design a model to overcome the limitations of standard DEA analysis
2. Application of the game theory method and how to integrate them with the DEA model
3. Determine factors influencing energy, economic, and environmental efficiency

2. METHODOLOGY

This is a development-oriented study in which the main approach is based on mathematical modeling. This research paper proposes a parametric linear mathematical programming model to analyze a three-stage data envelope problem with a series structure. The proposed model is based on game theory and the system identifies uncertainties. Additionally, various approaches were employed to control uncertainty. The data in this study is quantitative-qualitative. The data were collected using the library survey method. The library method was used for general data collection. The employed data analysis methods are stated as follows:

1. Data coverage analysis: to identify units whose decision-making is carried out effectively. This article estimates efficiency using linear programming dual. The dual problem imposes a minimum requirement on the quantities of inputs, which is conditioned by specific amounts of the product, as outlined below:

$$MIN = \theta_0 - \varepsilon \left(\sum_{i=1}^m s_i^- + \sum_{r=1}^s s_r^+ \right)$$

Provided that the "DEA model" is its returns to scale structure, which includes:

$$\sum_{j=1}^n x_{ij} \lambda_j + s^-_i = \theta_0 x_{i0}$$

$$\sum_{j=1}^n y_{rj} \lambda_j - s_r^+ = y_{r0}$$

$$\lambda_j \geq 0 \quad s_r^+ \geq 0 \quad s_i^- \geq 0$$

- The CCR constant returns of scale;
- The BCC variable returns of scale;

The proposed robust bargaining model is based on the scenario-based discrete robust optimization approach. Another feature of this model is that it uses the proposed solution to improve inefficient units and achieve the efficiency frontier. These solutions include input-oriented DEA and output-oriented DEA models.

The selection between an input-oriented or output-oriented perspective is contingent upon the level of management control over the inputs or outputs. When management lacks control over the outputs and their quantity is predetermined and fixed, the reduction in input quantity is regarded as a managerial viewpoint. Consequently, the model is approached as an input-oriented model. Conversely, if management lacks control over the inputs and their quantity is predetermined and fixed, the reduction in output quantity is considered a managerial viewpoint. In this case, the model is approached as an output-oriented model.

2. Collaborative Game Theoretical Model: In non-cooperative games, players may adopt a strategy that ultimately results in the least possible outcome, based on the opponent's chosen strategy, in order to maximize their own outcome. Therefore, in peer games, players try to cooperate with the player or other players of the game to achieve more benefits. In this case, a set of singles, duets, or multiple players is called a coalition. In cooperative game theory, the primary emphasis is on the formation of feasible coalitions and the calculation of surplus that accrues to the set of players in each coalition. Next, the obtained surplus must be allocated among the players, which is mentioned in cooperative games with transferable utility. The allocation of surplus encourages players to join feasible coalitions. The cooperative game is displayed as (N, v) . In every specific game and per coalition T , the security level can be defined with respect to $(T)v$. It is referred to as the characteristic function game (CFG). The characteristic function is assumed to have no information asymmetry. Per each coalition T , T can be defined as the function $(T)v$. This demonstrates the total surplus that the coalition members receive through cooperation regardless of the strategies adopted by the players outside the coalition. In a cooperative game, for the selected action of coalition members and the complementary coalition, the outcome of the coalition T versus those outside equals the sum of the

outcomes of each coalition member. It is calculated as follows:

$$u(T) = \sum_{i \in T} u_i(a_1, a_2, \dots, a_k), \quad i = 1, 2, \dots, n$$

3. The Nash product: Suppose there will be increased mutual benefits resulting from cooperation between two countries in reducing energy consumption and CO₂ emissions. When the level of cooperation is strong, the interests of both countries will significantly increase. Conversely, if the level of cooperation is low, the impact on their interests will be minimal. The Nash product, which represents the product of the multiplication of their combined additional benefits, is derived from their collaborative efforts. Due to the assumption that cooperation between the two sides will generate additional interests, the interests of both countries exceed their individual interests at the point of threat. The disparity between the interests at the threat point and the interests resulting from mutual cooperation leads to the acquisition of supplementary interests. The Nash product is obtained by utilizing the coordinate system. As depicted below, moving from point A upwards along line AB increases the value of the country's interests. However, in a competitive scenario, the value of the interests of the first country remains constant. Similarly, moving from point A to the right along line AC enhances the value of the first country's interests, while the value of the second country's interests remains unaltered in the competitive state. The interests of the second country under a competitive state is shown in Figure 1.

In the event of competitive conditions and lack of cooperation between two countries, their interests can be demonstrated by A. However, if these countries choose cooperation over competition, they can enjoy additional interests beyond point A. For instance, at point N, both countries can agree on the amount of energy consumption and emissions, resulting in increased interest for each country. The value of these benefits can be represented as V1 and W1, respectively. By agreeing to cooperate, both countries can increase their interests.

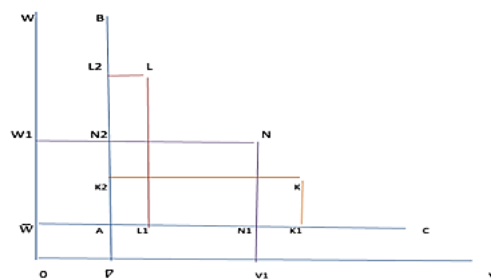


Figure 1. The interests of the second country under a competitive state

The increase in interests is equal to N_1 for the first country and N_2 for the second country. The level of cooperation can be determined by comparing the interests of cooperation to those of competitive conditions.

4. The relationship between DEA and game theory: DEA is a non-parametric method used to evaluate the relative efficiency of decision-making units. DEA is a powerful tool that uses all collected observations to measure efficiency and optimizes each observation in comparison to the optimal efficient frontier, unlike regression analysis, which obtains the best performance available in the study set of units by averaging. In regression analysis, the performance of each unit is estimated relative to an optimized regression equation, while in DEA, the performance of units is examined by constructing and solving n models.

The primary DEA model is founded on the principles of inclusive observations, convexity, constant returns to scale, feasibility, and minimal extrapolation. The concept of production possibility set is essential in this analysis, as it should comprise all inputs and corresponding outputs that are realistically feasible. Additionally, this set should generally include the set of observations of the units under evaluation. The problem can be posited mathematically as follows:

Suppose X is the input vector for a decision-making unit and Y is its output vector. Then, the production possibility set is introduced as follows:

$$T = \{(X, Y) | \text{Non - negative } x \text{ can produce non - negative } y.\}$$

To establish a comprehensive set of principles, we acknowledge these principles that are at the core of data coverage analysis models.

The principle I is based on the argument that the inputs received are aligned with the desired outputs. This principle is widely accepted. To put it differently, it serves as the real production possibility of the society. Mathematically, this principle can be represented as $(X_j, Y_j) \in T; j = 1, \dots, n$, where n represents the number of units.

(Principle II) Feasibility: It states that if $(X, Y) \in T$, then X has the ability to produce Y. This means that any input greater than X can also result in the production of Y, and any output less than Y can still be produced from X. The principle can be expressed mathematically as follows:

$$\forall (X, Y) \forall \bar{X} \forall \bar{Y} \{ (X, Y) \in T \& \bar{X} \geq X \& \bar{Y} \leq Y \} \Rightarrow (\bar{X}, \bar{Y}) \in T$$

(Principle III) Convexity: It states that if $(\hat{X}, \hat{Y}) \in T, (X, Y) \in T$, then we will have:

$$[\lambda(X, Y) + (1 - \lambda)(\hat{X}, \hat{Y})] \in T \quad 0 \leq \lambda \leq 1$$

According to the convexity principle, if Y, X produce \hat{Y}, \hat{X} , then, the input $\lambda X + (1 - \lambda)\hat{X}$ can generate an output of $\lambda Y + (1 - \lambda)\hat{Y}$, where $0 \leq \lambda \leq 1$.

(Principle IV) Constant scale return: It states that if X is added with a coefficient of λ , the value of Y will also grow with the same coefficient λ .

(Principle V) Minimal extrapolation T: This set is taken as the smallest set of values that satisfy the first four principles.

In DEA, units strive to determine the optimal weight combination for measuring their performance. The efficiency measurement method in this analysis is based on the minimal distances of each unit from the production set frontier. This approach is essentially a form of minimization, which is a subset of optimization

In this section of the article, the primary approach under consideration is the integration of the bargaining game with DEA. It is worth noting that the solutions derived from the bargaining game exhibit Pareto optimality. These principles can be subject to modification depending on various assumptions. The model is outlined as follows:

$$T = (K, L, E, GDP, CO_2): (K, L, E) \xrightarrow{\quad} (GDP, CO_2)$$

As the data results in the production of limited outputs, T is regarded as the production function. The objective of this study was to employ a methodology that aligns with production theory concepts while simultaneously minimizing undesirable outputs and maximizing desirable outputs. Mathematically, the representation of robust data access and desired outputs is as follows:

$$(K, L, E, GDP, CO_2) \in T \text{ (or } (K, L, E, \check{G}DP, CO_2) \in T)$$

$$\text{If } (K, L, E, GDP, CO_2) \in T \text{ and } (\check{K}, \check{L}, \check{E}) \geq (K, L, E) \text{ (or } \check{G}DP \leq GDP)$$

In 1951, Nash introduced the Nash Equilibrium, also known as the Nash Solution, which outlines three essential features for resolving any problem. These conditions include:

- Pareto efficiency
- the independence of solutions from alternative options
- symmetry

In order to obtain the Nash solution of the bargaining game, it is necessary for the solution space to be compact, convex, and inclusive of the payoff vectors. These payoff vectors should ensure that the payoffs for each player exceed the values of their corresponding breakpoints. Suppose utility functions $v(x)$ and $U(x)$ for actors 1 and 2, respectively. In the context of the bargaining game, if we assume V and U, the logical decision would be to maximize the product of the multiplication of the difference between the utility functions and the breakpoint values for each actor. In simpler terms, the following conditions must be met:

$$\text{Maximize } |U(x) - u_d| |V(y) - v_d|$$

The solution acquired is called Nash solution and the product of the multiplication is called Nash product. The Nash relation can be extended to more than two actors. Now, if it is assumed that $U_i(x)$ is the utility function for

the i^{th} player and U_i is the value of the breakpoint for the i^{th} player -when they have not entered the game; then:

$$\text{Maximize } \Pi_{i=1}^n |u_i(x) - u_i(d)|$$

Below is an illustration of a PSTS process model. As shown, each DMU j comprises three interconnected series stages. Furthermore, the outputs generated by each stage serve as the sole inputs for the subsequent stage. This implies that stages 1 and 2 do not produce any external outputs, while stages 2 and 3 do not receive any external inputs. Figure 2 shows DMU of three interconnected stages in series.

Return to scale represents the link between changes in inputs and outputs of a system.

2. 1. Research Findings

In this part, in order to demonstrate the efficiency and applicability of the proposed models, various numerical examples and case studies are utilized, and their results are thoroughly examined and analyzed.

In the field of choosing appropriate indicators to evaluate energy, economic and environmental performance of countries, some researchers have put forward suggestions that are mentioned in the second part. Based on them, Figure 3 shows the impact of input variables on specified efficiencies and their selected indicators was prepared, which is stated as follows:

2. 1. 2. The Answers to Questions 1 to 3 are Explained below

The data presented in this article pertains to a comprehensive evaluation of selected countries (Azerbaijan, Kuwait, Qatar, Turkey, Yemen, Emirates, Lebanon, Saudi Arabia, Turkmenistan, Jordan, Iran, and Bahrain) from 2014 to 2019. The data was carefully analyzed using energy, economic, and environmental input data, taking into account similar

conditions. The entire data is presented in the following. The efficiency values for energy, economics, and the environment were calculated for each DMU. Table 1 specifies the results.

Overall, it can be stated that most countries have a high level of efficiency, averaging around 50%, and none of the DMUs have completely undesirable efficiency. In other words, DMUs have been able to achieve relatively desirable outcomes from their inputs. It can be

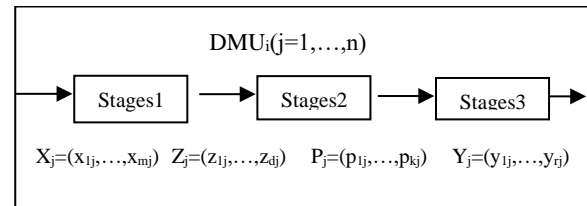


Figure 2. DMU of three interconnected stages in series

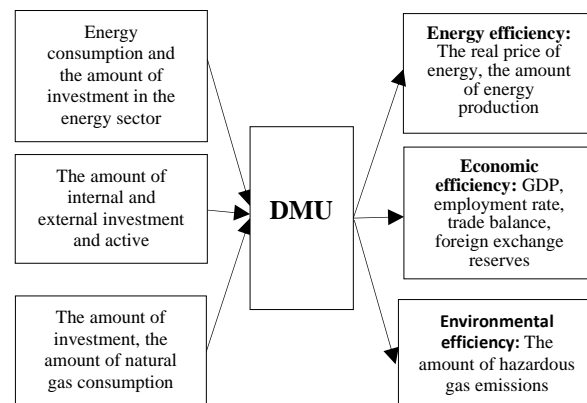


Figure 3. Selected inputs and outputs

TABLE 1. The energy, economic, and environmental efficiency scores of DMUs

DMU	Energy efficiency, %	Economic efficiency, %	Environmental efficiency, %	Total efficiency
Azerbaijan	82.1	84	66.41	77.5
Kuwait	91	100	74.4	88.4
Qatar	100	100	79	93
Türkiye	80	86	62	76
Yemen	100	93	71.3	88.1
United Arab Emirates	92.8	96	83.8	90.8
Lebanon	78.5	83	71.4	77.6
Saudi Arabia	93	98.9	78.9	90.2
Turkmenistan	94.6	100	72.6	89
Jordan	73.2	89	61.2	74.4
Iran	90.7	86	58.6	78.4
Bahrain	91	100	63.3	84.7

acknowledged that these DMUs have prevented resource and input waste and have had proper management of their outputs and inputs. On the other hand, the values obtained for each of the lines represent the economic scale compared to the constant efficiency. These values indicate the economies of scale of each DMU in terms of CRS, increasing efficiency to scale (IRS), and decreasing efficiency to scale (DRS). In simpler terms, if $\sum_{j=1}^n \lambda_j^* = 1$, the economies of scale of lines will be constant, if $\sum_{j=1}^n \lambda_j^* > 1$, the economies of scale will be decreasing, and if $\sum_{j=1}^n \lambda_j^* < 1$, the economies of scale will be increasing. Table 2 displays the λ values obtained for each company.

As shown in Table 2, DMUs 3 and 11 exhibit a constant return to scale, indicating a linear relationship between institutions and outputs. On the other hand, DMUs 2, 8, and 10 demonstrate an increasing return to scale, where an increase in inputs results in a relatively greater increase in outputs. Conversely, DMUs 1, 4, 6, 7, 9, 12, and 5 display diminishing returns to scale, meaning that increasing inputs by one unit leads to a smaller relative increase in output.

Computational results of the NBTS-DEA model under uncertainty conditions

In this section, the validity and accuracy of the NBTS-DEA model are assessed under uncertain conditions. This analysis is based on the following relationship:

$$MAX F_{so} = \left(\sum_i \theta_i X_i + \sum_i \theta_i W_i + \sum_r \theta_r U_r \right)$$

TABLE 2. The λ values of DMUs

DMU	$\sum_{j=1}^n \lambda_j^*$
DMU1	3.462
DMU2	0.854
DMU3	1
DMU4	3.531
DMU5	0
DMU6	2.077
DMU7	3.723
DMU8	0.861
DMU9	3.112
DMU10	0.915
DMU11	1
DMU12	2.058

where x represents the decision-making unit, W denotes the computational efficiency value, and U represents the estimated efficiency value under future uncertainty conditions. Table 3 summarizes the efficiency values obtained from the centralized model and the Nash bargaining model at breakpoints (0.0.0), $(\theta^1_{min}, \theta^2_{min}, \theta^3_{min})$.

According to the findings presented in Table 3, the outcomes of the centralized model are nearly identical to those of the bargaining model at (0.0.0) breakpoint. As it is anticipated that the NBTS-DEA model at breakpoint (0.0.0) will exhibit similar behavior to the centralized

TABLE 3. The results of the centralized model versus the Nash bargaining model

DMU	Centralized Model				Ba rgaining Model Brealodown Point (0.0.0)				Ba rgaining Model Brealodown Point $(\theta^1_{min}, \theta^2_{min}, \theta^3_{min})$			
	Energy efficiency	Economic efficiency	Enviornmental efficiency	Total efficiency	Energy efficiency	Economic efficiency	Enviornmental efficiency	Total efficiency	Energy efficiency	Economic efficiency	Enviornmental efficiency	Total efficiency
1	0.906	1.000	0.572	0.518	0.906	1.000	0.572	0.518	0.906	1.000	0.572	0.518
2	1.000	1.000	1.000	1.000	1.000	1.000	1.000	1.000	1.000	1.000	1.000	1.000
3	0.515	0.392	0.501	0.100	0.516	0.388	0.497	0.099	0.517	0.348	0.549	0.099
4	0.666	0.505	0.425	0.143	0.667	0.504	0.425	0.143	0.669	0.502	0.425	0.143
5	0.769	0.191	1.000	0.147	0.769	0.191	1.000	0.147	0.769	0.191	1.000	0.147
6	1.000	0.206	0.468	0.096	1.000	0.206	0.468	0.096	1.000	0.206	0.468	0.096
7	1.000	0.219	1.000	0.219	1.000	0.220	0.997	0.219	1.000	0.224	0.979	0.219
8	0.693	0.172	0.832	0.099	0.690	0.172	0.832	0.099	0.690	0.172	0.832	0.099
9	0.467	0.594	0.862	0.239	0.467	0.592	0.863	0.239	0.466	0.570	0.897	0.238
10	0.356	1.000	0.738	0.262	0.356	1.000	0.737	0.262	0.381	0.907	0.738	0.255
11	0.637	0.174	0.835	0.092	0.629	0.174	0.835	0.091	0.629	0.174	0.835	0.091
12	1.000	0.241	0.726	0.175	1.000	0.240	0.728	0.175	1.000	0.212	0.819	0.174

model. The congruence of the results between these two models, particularly in terms of overall efficiency and the efficiency of each stage, validates the proposed model. That DMU 2 is the only efficient entity across all parts in both models.

Based on the analysis of Table 3, it can be inferred that the total efficiency scores derived from the centralized model are nearly identical to those of the Nash bargaining model at breakpoint $(\theta^1_{min}, \theta^2_{min}, \theta^3_{min})$ for all DMUs. Consequently, it can be deduced that the Nash bargaining model proposed offers the same benefits as the centralized model in assessing the overall efficiency of the process. Furthermore, as shown that the efficiency scores of stages II and III in DMUs 3, 9, and 12, as well as the efficiency scores of stages I and II in DMU 10, calculated by the centralized model, differ from the efficiency scores calculated by the proposed non-parametric model. Additionally, in the centralized model, stage II of DMU 10 is efficient, whereas it is inefficient in the non-parametric model at breakpoint $(\theta^1_{min}, \theta^2_{min}, \theta^3_{min})$. It should be noted that, unlike the centralized model, the non-parametric model provides a fair and unique decomposition of overall performance scores into component efficiencies.

2. 2. Results of NBTS-DEA Model under Robust Conditions

To assess the efficiency of the supply chain depicted in Figure 4, analysis was conducted using two models: the centralized model and the proposed Nash bargaining game model. The objective was to calculate the total efficiency values and the efficiency of each component of the DMUs for each scenario at the (0.0.0) breakpoint and $\epsilon = 0.001$ step size. The total efficiency scores of all DMUs using both the centralized model and the Nash bargaining game model at breakpoint (0.0.0) are nearly identical. This outcome serves as an indication of the validity of the proposed Nash bargaining game model. The results of centralized scenario model are summarized in Table 4.

Here, the method of DMU which involves constructing the most anti-ideal DMU, was employed to identify breakpoints (see Table 5 for the breakpoints obtained in each stage of the process and scenario).

These breakpoints are utilized in the proposed robust bargaining model to determine the total efficiency scores and the efficiency of the process components for each scenario (see Table 6 for the results). As shown, the total efficiency scores were decomposed into the components

TABLE 4. The results of centralized scenario model

DMUs	Scenario 1				Scenario 2				Scenario 3			
	Step 1	Step 2	Step 3	All system	Step 1	Step 2	Step 3	All system	Step 1	Step 2	Step 3	All system
1	1.000	0.589	1.000	0.589	1.000	0.672	1.000	0.672	1.000	0.731	1.000	0.731
2	0.975	0.880	0.730	0.626	0.859	0.990	0.787	0.670	0.898	1.000	0.751	0.675
3	0.808	0.699	0.505	0.286	0.764	0.816	0.622	0.388	0.665	0.926	0.640	0.394
4	1.000	0.660	0.249	0.164	1.000	0.697	0.261	0.182	1.000	0.724	0.254	0.184
5	0.948	0.967	0.609	0.558	0.920	0.938	0.717	0.619	0.833	0.929	0.817	0.632
6	0.787	1.000	0.389	0.307	0.693	1.000	0.490	0.340	0.755	1.000	0.490	0.370
7	0.825	0.579	0.487	0.232	0.729	0.647	0.515	0.243	0.678	0.678	0.548	0.252
8	0.832	0.172	0.693	1.000	0.219	0.979	0.224	1.000	0.219	0.997	0.220	1.000
9	0.862	0.594	0.467	0.690	0.099	0.832	0.172	0.690	0.099	0.832	0.172	0.690
10	0.738	1.000	0.356	0.467	0.238	0.897	0.570	0.466	0.239	0.863	0.592	0.467
11	0.835	0.174	0.637	0.356	0.255	0.738	0.907	0.381	0.262	0.737	1.000	0.356
12	0.726	0.241	1.000	0.629	0.091	0.835	0.174	0.629	0.091	0.835	0.174	0.629

TABLE 5. The breakpoints of each step for each scenario

Step	Scenario		
	1	2	3
1	0.566	0.573	0.543
2	0.529	0.619	0.638
3	0.154	0.175	0.166

uniquely and equitably. This highlights one of the key advantages of the proposed bargaining model.

In order to utilize the proposed DEA RNBS model, its parameters should be configured. These parameters should be set in a manner that does not impact the overall problem and aligns with the specific constraints. The values for these parameters are specified in Table 7.

TABLE 6. The results of the NBTS DEA model

DMUs	Scenario 1				Scenario 2				Scenario 3			
	Step 1	Step 2	Step 3	All system	Step 1	Step 2	Step 3	All system	Step 1	Step 2	Step 3	All system
1	1.000	0.588	1.000	0.588	1.000	0.672	1.000	0.672	1.000	0.730	1.000	0.730
2	0.974	0.937	0.664	0.606	0.861	0.988	0.787	0.670	0.898	1.000	0.751	0.675
3	0.781	0.722	0.505	0.285	0.764	0.816	0.622	0.388	0.691	0.882	0.640	0.390
4	1.000	0.659	0.249	0.164	1.000	0.696	0.261	0.182	1.000	0.724	0.254	0.184
5	0.975	0.939	0.609	0.558	0.921	0.937	0.717	0.619	0.832	0.927	0.817	0.630
6	0.787	1.000	0.389	0.306	0.693	1.000	0.490	0.340	0.755	1.000	0.490	0.370
7	0.729	0.651	0.466	0.221	0.728	0.646	0.515	0.242	0.678	0.678	0.548	0.252
8	1.000	0.340	1.000	0.340	1.000	0.763	1.000	0.763	1.000	0.550	1.000	0.550
9	0.986	0.945	0.897	0.540	0.931	0.943	0.767	0.606	0.823	0.931	0.807	0.604
10	0.778	1.000	0.345	0.301	0.687	1.000	0.487	0.324	0.766	1.000	0.487	0.369
11	1.000	0.567	0.234	0.165	1.000	0.767	0.245	0.165	1.000	0.870	0.202	0.168
12	0.890	0.701	0.499	0.276	0.756	0.818	0.640	0.390	0.689	0.878	0.650	0.387

TABLE 7. The values of the RNBTS-DEA model parameters

Parameters	W_1	W_6	W_7^+	W_7^-	W_8^+	W_8^-	W_9^+	W_9^-	W_{10}^+	W_{10}^-	λ
Amounts	1	8	1	8	1	8	2	8	2	8	0.4

In Table 7, Columns 2 to 6 display the weighted average efficiency scores for each stage, as well as the total efficiency score and rank for each DMU in the DEA model of the Nash bargaining game at breakpoint (0.0.0). Similarly, in Table 8, Columns 7 to 11 present the

efficiency scores for each step, the total efficiency score, and the rank for each DMU in the RNBTS-DEA model at breakpoint (0.0.0). Table 8 also summarizes the results for the same breakpoint ($\theta^1_{min}, \theta^2_{min}, \theta^3_{min}$), as shown in Table 8.

TABLE 8. Weighted average results of the NBTS-DEA model under the scenario versus the results of the RNBTS-DEA model

DMUs	Weighted average results of the VBTS-DEA model under the scenario					RENBS-DEA Model				
	Step 1	Step 2	Step 3	All system	Rank	Step 1	Step 2	Step 3	All system	Rank
1	1.000	0.666	1.000	0.666	1	0.945	0.647	0.954	0.583	1
2	0.891	0.971	0.764	0.660	2	0.596	0.874	0.772	0.402	3
3	0.744	0.821	0.598	0.364	4	0.406	0.743	0.537	0.162	6
4	1.000	0.694	0.256	0.178	7	0.761	0.634	0.215	0.104	7
5	0.913	0.934	0.715	0.607	3	0.830	0.759	0.748	0.471	2
6	0.732	1.000	0.465	0.339	5	0.635	0.859	0.423	0.231	4
7	0.740	0.637	0.516	0.242	6	0.661	0.591	0.480	0.188	5
8	1.000	0.659	0.249	0.164	9	1.000	0.770	0.202	0.102	8
9	1.000	0.567	0.261	0.132	11	0.504	0.436	0.453	0.101	9
10	1.000	0.659	0.254	0.146	10	0.406	0.438	0.221	0.098	10
11	1.000	0.567	0.234	0.165	8	0.346	0.548	0.201	0.095	12
12	0.165	1.000	0.567	0.121	12	0.254	0.387	0.168	0.097	11

The above tables illustrate that the per breakpoints (0.0.0) and $(\theta^1_{min}, \theta^2_{min}, \theta^3_{min})$, total efficiency scores of all DMUs in the RNBS-DEA model are lower compared to the total efficiency scores obtained from the weighted average of the NBTS-DEA model in the study scenarios. This discrepancy arises due to the inclusion of the 2nd moment of the NBTS-DEA model and a penalty for deviating from the limits in the RNBS-DEA model, in addition to the weighted average of the NBTS-DEA model in the given scenarios. The tables also suggest that the robust optimization model presented exhibits a significant sensitivity to breakpoints. Consequently, both the efficiency scores and the ranking of DMUs have experienced considerable fluctuations with the alteration of breakpoints from (0.0.0) to $(\theta^1_{min}, \theta^2_{min}, \theta^3_{min})$. Figure 4 visually represents the overall performance scores acquired from the RNBS-DEA model and the NBTS-DEA model for each scenario at breakpoint (0.0.0). The figure above illustrates the identical observations at breakpoint $(\theta^1_{min}, \theta^2_{min}, \theta^3_{min})$.

As shown in Figures 4 and 5, the efficiency scores obtained from the RNBS-DEA model are less than or equal to the NBTS-DEA model for all DMUs and in all scenarios. It should be noted that the results obtained from the RNBS-DEA model are robust in terms of both feasibility and optimality.

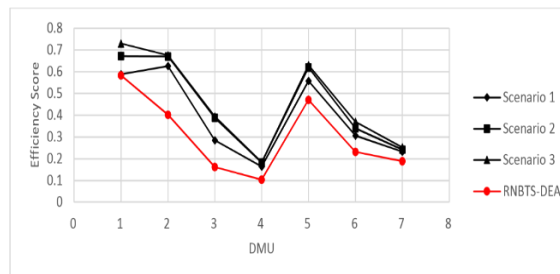


Figure 4. Total efficiency scores of the proposed NBTS-DEA model under different scenarios versus the proposed RNBS-DEA model at breakpoint (0.0.0)

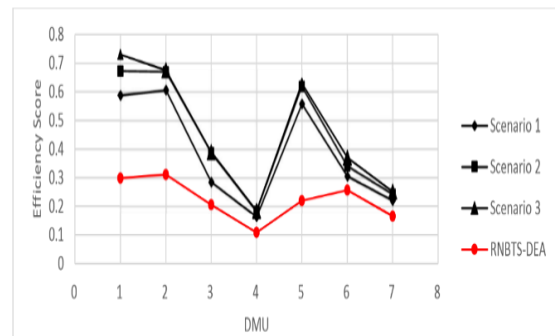


Figure 5. Total efficiency scores of the proposed NBTS-DEA model under different scenarios versus the proposed RNBS-DEA model at breakpoint (0.0.0)

2. 4. Answer to Question 4 it is Explained below

The evaluation of countries' efficiencies indicated that only Azerbaijan, Kuwait, Qatar, and Turkey have demonstrated level 1 efficiency and are acknowledged as such among the 12 countries evaluated. As a result, a collaborative game theory is developed for the mentioned countries.

2. 4. 1. First Step: Formation of Coalitions

The first step in the process is to establish coalitions. Each efficient country is assigned a unique symbol based on Table 8. There will be as many as P possible coalitions equal to 1 to 4. Coalition formation is stated in Table 9. Formation of the coalition and the resulting cohesive efficiency stated in Table 10.

TABLE 9. Coalition formation

Türkiye	Qatar	Kuwait	Azerbaijan	Country
D	C	B	A	Symbol

2. 4. 2. Step Two: Calculating the Profit of Coalitions

TABLE 10. Formation of the coalition and the resulting cohesive efficiency

Integrated functionality, %	Profit	Coalition	Integrated functionality, %	Profit	Coalition	Integrated functionality, %	Profit	Coalition
95	1.211	A-D	73	0.677	A-C	40	0.458	A-B
99	1.415	A-C-D	39.5	0.452	A-B-D	62	0.622	A-B-C
25	0.365	B-C	27	0.205	B-C	90.5	1.012	B-A
16	0.225	B-C-D	36.5	0.384	B-A-D	46	0.514	B-A-C
86	0.921	C-D	89	0.941	C-B	80.5	0.717	C-A
27	0.415	C-B-D	92	1.124	C-A-D	89	1.009	C-A-B
12	0.112	D-C	75.5	0.696	D-B	93.5	1.201	D-A
60.5	0.620	D-B-C	76	0.709	D-A-C	70	0.650	D-A-B

2. 4. 3. Step Three: Calculating the Shapley value

Based on the evaluation of coalition values, the value of decision-making units in each coalition was evaluated and calculated using the Shapley value formula (Table 11).

Therefore, the countries were compared and evaluated based on the obtained Shapley value achieved through different coalitions using the cross-efficiency and super-efficiency methods (Table 12).

3. DISCUSSION

The 2025 Vision Document positions Iran as a developed, active, and influential participant in the global economy. To achieve the goals outlined in the document, Iran must have substantial economic growth. However, economic growth and development in any country are inextricably linked to energy consumption, which has negative environmental impacts. Therefore, it is crucial to consider technical, economic, and environmental factors when setting energy production and consumption patterns. By doing so, Iran can ensure sustainable economic growth while minimizing its environmental footprint. This research investigates the relationship between economic activities, carbon dioxide emissions, and energy consumption during the production process. Using the data envelopment analysis method, the study measures the level of energy efficiency in Iran and neighboring countries from 2012 to 2019. Additionally, the study evaluates the extent to which the goals outlined in the vision document for energy efficiency have been achieved. By analyzing these factors simultaneously, in response to the questions of the thesis, the findings

showed that among the 12 selected countries (Azerbaijan, Kuwait, Qatar, Turkey, Yemen, UAE, Lebanon, Saudi Arabia, Turkmenistan, Jordan, Iran and Bahrain), the highest energy efficiency is related to the countries of Qatar and Yemen and the lowest The efficiency is related to Lebanon and Jordan; The highest environmental efficiency is related to the UAE and Qatar and the lowest efficiency is related to Iran and Jordan; The highest economic efficiency is related to the countries of Kuwait, Qatar and Turkmenistan, and the lowest efficiency is related to Iran and Turkey.

The findings related to the efficiency rating of 5 countries of Qatar, UAE, Saudi Arabia, Turkmenistan, Kuwait and Yemen are more efficient. Kuwait, UAE and Qatar have been the same in the assessment of super-efficiency and alliance, and the changes are related to the countries of Saudi Arabia and Turkmenistan. This case shows that the efficiency score of each decision-making country in the super-efficiency method does not necessarily cause its rank after the cooperation phase.

The findings of this work showed that the country of Qatar with the highest efficiency also has the most effect in the coalition and its rank remains unchanged, but the efficiency score of the country of Saudi Arabia is lower than that of Turkmenistan, but its impact on the coalition is greater, so the score of Saudi Arabia in the Shapley method is increased and Its ranking has been improved compared to the ranking in the super performance method. Also, the country of Turkmenistan, which was higher than Saudi Arabia in the super efficiency method, has decreased in the Shapley method.

The research aims to provide a comprehensive understanding of the energy efficiency landscape in the region. The results of this research demonstrate that the current state of energy efficiency in Iran is suboptimal. Therefore, Iran must implement programs aimed at enhancing energy efficiency. This will not only enable the country to expand its economic development capabilities but also ensure the preservation of existing resources and prevent any harm to the environment and human health. As data coverage analysis is a comparative approach, it is recommended that future studies in Iran should include a comparison with developed countries. This will help portray a more accurate picture of energy efficiency.

In recent years, DEA researchers have shown great interest in developing models to calculate the efficiency of network-structured processes. Classical models have proven inadequate in this regard, prompting the seeking of new DEA models to overcome this weakness. One such model is the multi-stage structure - a particular type of network structure - where the outputs of each stage serve as inputs for the next stage. The most widely used type of model developed in this field is the two-stage data DEA model. These models are able to calculate the

TABLE 11. The calculated Shapley value after the cooperation and coalition phase

Türkiye	Qatar	Kuwait	Azerbaijan	Country
0.236	0.222	0.325	0.125	P=1
0.333	0.625	0.229	1.425	P=2
0.620	0.632	0.111	0.425	P=3
0.659	0.325	0.222	0.701	P=4
1.848	1.807	0.887	1.676	Shapley value

TABLE 12. The calculated Shapley value after the cooperation and coalition phase

Türkiye	Qatar	Kuwait	Azerbaijan	Country
0.938	0.800	0.857	0.947	Super efficiency
0.960	0.927	0.934	0.900	Cross-functionality
1.848	1.807	0.887	1.676	Shapley value
1	2	4	3	Ranking

efficiency scores of each step in addition to the total efficiency score. The network structure known as the three-stage process is a unique and prevalent phenomenon in the real world, with multiple applications. A three-level supply chain consisting of suppliers, manufacturers, and distributors can exemplify these processes.

There are different methods available for modeling three-stage processes, which are derived from generalizing the approaches used in two-stage process modeling. The game theory approach, also used here, is one of the most commonly used such approaches. This approach mainly involves non-cooperative and cooperative games. The first category of models is known as leader-follower or decentralized models, and the second category of models is known as centralized models. In centralized models, the system's overall efficiency is prioritized before evaluating the efficiency of individual components. This is while decentralized models prioritize the efficiency of the most significant or leading component, followed by the subordinate components and ultimately determine the overall system efficiency. Centralized and decentralized models have different assumptions regarding the importance of components. In centralized models, all components are considered equally important, while in decentralized models, components have equal priority. In real-world problems with network structures, calculating the overall efficiency of the process is more important than calculating the efficiency of the components. Therefore, methods based on this approach attract more attention from company managers. However, in non-collaborative models, the leader component is more important than the follower components, and calculating the efficiency of the components has a higher priority than determining the efficiency of the overall process. This approach is less favored by managers. Non-collaborative models can be used in specific cases where the value of the components is not equal, such that the leader has more power than the other component (follower), and the follower has no control over the leader. The sub-process under the leader determines the optimal weights related to intermediate criteria (optimal strategy), making it a useful approach in certain scenarios. In centralized models, a serious challenge is the fair and unique decomposition of the overall efficiency score into component efficiency scores. However, many developed models have struggled to provide a satisfactory solution. To address this issue, a data envelopment analysis model is necessary. This model should calculate overall and three-stage process component efficiency scores while preserving the advantages of previous models and providing a fair and unique decomposition of component efficiency.

A DEA model based on the game theory approach is considered a viable choice for this objective. In this study, the overall efficiency and efficiency of the

components of the three-stage processes with a net structure, in which the outputs of each stage are used as the only inputs of the next stage, were calculated. To that end, we used a three-stage data envelopment analysis model based on the non-cooperative game theory approach. The proposed model is able to provide a fair and unique decomposition of overall efficiency into component efficiencies while maintaining the advantages of cooperative games. As game theory models are generally nonlinear, finding global optimal solutions in such difficult models can be challenging. Hence, multiple transformations were used to convert the aforementioned nonlinear game theory model into a linear parametric programming model.

To identify the breaking points of each stage, the study utilized an anti-ideal DMU approach. The values of breaking points can significantly impact the optimal solutions of bargaining models, and selecting inappropriate values can render the model infeasible. Therefore, here, various scenarios were developed to perform a sensitivity analysis on breaking point values and the extent to which they impact the proposed model. This analysis provides valuable insights into the optimal selection of breaking point values for slicing models.

DEA models rely on the efficiency frontier formed by the available data to calculate the efficiency of DMUs. In that light, any uncertainty can threaten the validity of the efficiency scores calculated. To overcome this uncertainty challenge, three approaches were employed: fuzzy set theory, robust optimization, and stochastic optimization.

The optimization approach used in this study is based on the stable scenario method. To achieve the objective, several scenarios with specified probable occurrence values were applied to a case study of a cement supply chain consisting of the supplier, producer, and distributor. The proposed robust DEA model was solved for each scenario with different breakpoints. The results were compared with the centralized model. The total efficiency scores obtained from both methods for all DMUs were almost equal, indicating the validity of the proposed model in an uncertain state. Finally, the proposed robust DEA model was implemented on the dataset of the study supply chain, and its results were analyzed.

The α -cuts method was utilized in the fuzzy approach to develop two bargaining DEA models in the fuzzy form. These models are used to calculate the lower and upper bounds of the efficiency of the three pure development process stages. These models were converted into a linear form. For the random state, the stochastic programming approach was employed, using the proposed random bargaining model to evaluate the efficiency of the three-stage processes with random outputs.

4. CONCLUSION AND FUTURE RESEARCH

In the following, to check the validity and efficiency of the proposed models, some numerical examples were presented, and the results were analyzed. The results indicate the energy efficiency of Azerbaijan, Kuwait, Qatar, Turkey, Yemen, UAE, Lebanon, Saudi Arabia, Turkmenistan, Jordan, Iran, and Bahrain as follows: 82.1%, 85.7%, 100%, 83.5%, 100%, 90.8%, 78.5%, and 87.3%.

The future research suggestions are proposed in the following section:

The focus here is on models that operate under constant return-to-scale conditions. However, it is worth exploring the potential for developing models that can accommodate variable return-to-scale conditions in future research endeavors. The proposed model cannot be utilized for general three-stage processes that involve the presence of external outputs for Stages 1 and 2, or external inputs for Stages 2 and 3. Hence, it is recommended to develop a modeling approach for assessing processes with such structures as a foundation for future research.

In this study, the fuzzy, stable, and random approaches were employed to address the data uncertainty of PSTS processes. Since each approach was implemented individually, future research could explore the potential benefits of combining them to enhance the management of uncertainty in real-world problems.

It is suggested to develop the proposed models to evaluate processes with unfavorable data.

The robust bargaining model proposed in this research is based on the discrete robust optimization approach (scenario-based). Future research can address the use of robust continuous approaches.

Another avenue for future research is the development of a stochastic bargaining model that can effectively handle uncertainty in all PSTS process data.

5. REFERENCES

- Villa G, Lozano S, Redondo S. Data envelopment analysis approach to energy-saving projects selection in an energy service company. *Mathematics*. 2021;9(2):200.
- Wang C-N, Dang T-T, Wang J-W. A combined Data Envelopment Analysis (DEA) and Grey Based Multiple Criteria Decision Making (G-MCDM) for solar PV power plants site selection: A case study in Vietnam. *Energy Reports*. 2022;8:1124-42.
- Tsaples G, Papathanasiou J. Data envelopment analysis and the concept of sustainability: A review and analysis of the literature. *Renewable and Sustainable Energy Reviews*. 2021;138:110664. <https://doi.org/10.1016/j.rser.2020.110664>
- Arouri MEH, Youssef AB, M'henni H, Rault C. Energy consumption, economic growth and CO2 emissions in Middle East and North African countries. *Energy policy*. 2012;45:342-9. <https://doi.org/10.1016/j.enpol.2012.02.042>
- Singh G, Singh P, Sodhi G, Tiwari D. Energy auditing and data envelopment analysis (DEA) based optimization for increased energy use efficiency in wheat cultivation (*Triticum aestivum* L.) in north-western India. *Sustainable Energy Technologies and Assessments*. 2021;47:101453. <https://doi.org/10.1016/j.seta.2021.101453>
- Bampatsou C, Papadopoulos S, Zervas E. Technical efficiency of economic systems of EU-15 countries based on energy consumption. *Energy Policy*. 2013;55:426-34. <https://doi.org/10.1016/j.enpol.2012.12.021>
- DeBenedictis LF, Giles DE, Policy P, Branch L. *Diagnostic Testing in Econometrics: Variable Addition, RESET, and Fourier Approximations*: Department of Economics, University of Victoria; 1996.
- Ren J, Gao B, Zhang J, Chen C. Measuring the energy and carbon emission efficiency of regional transportation systems in China: chance-constrained DEA models. *Mathematical Problems in Engineering*. 2020;2020:1-12. <https://doi.org/10.1155/2020/9740704>
- Chen C-K. CONSTRUCT MODEL OF THE KNOWLEDGE-BASED ECONOMY INDICATORS. *Transformations in Business & Economics*. 2008;7(2).
- Ito K. CO2 emissions, renewable and non-renewable energy consumption, and economic growth: Evidence from panel data for developing countries. *International Economics*. 2017;151:1-6. <https://doi.org/10.1016/j.inteco.2017.02.001>
- Chen CK. Causal modeling of knowledge-based economy. *Management Decision*. 2008;46(3):501-14. <https://doi.org/10.1108/00251740810863915>
- Fukuyama H, Matousek R. Modelling bank performance: A network DEA approach. *European Journal of Operational Research*. 2017;259(2):721-32. <https://doi.org/10.1016/j.ejor.2016.10.044>
- Huang D, Li G, Chang Y, Sun C. Water, energy, and food nexus efficiency in China: a provincial assessment using a three-stage data envelopment analysis model. *Energy*. 2023;263:126007. <https://doi.org/10.1016/j.energy.2022.126007>
- Collard F, Fève P, Portier F. Electricity consumption and ICT in the French service sector. *Energy Economics*. 2005;27(3):541-50. <https://doi.org/10.1016/j.eneco.2004.12.002>
- Kamarudin F, Sufian F, Nassir AM, Anwar NAM, Hussain HI. Bank efficiency in Malaysia a DEA approach. *Journal of Central Banking Theory and Practice*. 2019. 10.2478/jcbtp-2019-0007
- Li F, Zhu Q, Liang L. Allocating a fixed cost based on a DEA-game cross efficiency approach. *Expert Systems with Applications*. 2018;96:196-207. <https://doi.org/10.1016/j.eswa.2017.12.002>
- Antonakakis N, Cunado J, Filis G, Gabauer D, de Gracia FP. Oil and asset classes implied volatilities: Investment strategies and hedging effectiveness. *Energy Economics*. 2020;91:104762. <https://doi.org/10.1016/j.eneco.2020.104762>
- Odhiambo NM. Energy consumption, prices and economic growth in three SSA countries: A comparative study. *Energy policy*. 2010;38(5):2463-9. <https://doi.org/10.1016/j.enpol.2009.12.040>
- Liu H, Zhang R, Zhou L, Li A. Evaluating the financial performance of companies from the perspective of fund procurement and application: New strategy cross efficiency network data envelopment analysis models. *Energy*. 2023;269:126739. <https://doi.org/10.1016/j.energy.2023.126739>
- Zhou W, Chen Q, Luo D, Jiang R, Chen J. Global energy consumption analysis based on the three-dimensional network model. *IEEE Access*. 2020;8:76313-32. 10.1109/ACCESS.2020.2989186

21. Lu C-C, Lin I-F, Lin T-Y, Chiu Y-h. Two-stage dynamic data envelopment analysis measuring the overall efficiency and productivity changes of industry and agriculture in EU countries. *Journal of Cleaner Production*. 2023;382:135332.
22. Narayan PK, Narayan S. Estimating income and price elasticities of imports for Fiji in a cointegration framework. *Economic Modelling*. 2005;22(3):423-38. <https://doi.org/10.1016/j.econmod.2004.06.004>
23. Leng Y-J, Zhang H. Comprehensive evaluation of renewable energy development level based on game theory and TOPSIS. *Computers & Industrial Engineering*. 2023;175:108873. <https://doi.org/10.1016/j.cie.2022.108873>
24. Toloo M, Nalchigar S, Sohrabi B. Selecting most efficient information system projects in presence of user subjective opinions: a DEA approach. *Central European Journal of Operations Research*. 2018;26:1027-51. <https://doi.org/10.1007/s10100-018-0549-4>
25. Wu J, Liang L, Yang F, Yan H. Bargaining game model in the evaluation of decision making units. *Expert Systems with Applications*. 2009;36(3):4357-62. <https://doi.org/10.1016/j.eswa.2009.05.001>
26. Shi X. Environmental efficiency evaluation of Chinese industry systems by using non-cooperative two-stage DEA model. *Mathematical Problems in Engineering*. 2019;2019:1-10. <https://doi.org/10.1155/2019/9208367>
27. Halkos GE, Tzeremes NG. Oil consumption and economic efficiency: A comparative analysis of advanced, developing and emerging economies. *Ecological Economics*. 2011;70(7):1354-62.
28. Yanqing X, Mingsheng X. A 3E Model on Energy Consumption, Environment Pollution and Economic Growth---An Empirical Research Based on Panel Data. *Energy Procedia*. 2012;16:2011-8. <https://doi.org/10.1016/j.egypro.2012.01.306>
29. Zuo Y, Shi Y-l, Zhang Y-z. Research on the sustainable development of an economic-energy-environment (3E) system based on system dynamics (SD): A case study of the Beijing-Tianjin-Hebei Region in China. *Sustainability*. 2017;9(10):1727. <https://doi.org/10.3390/su9101727>
30. Zhang X-P, Cheng X-M, Yuan J-H, Gao X-J. Total-factor energy efficiency in developing countries. *Energy Policy*. 2011;39(2):644-50. <https://doi.org/10.1016/j.enpol.2010.10.03>
31. Zhou P, Ang B, Han J. Total factor carbon emission performance: a Malmquist index analysis. *Energy Economics*. 2010;32(1):194-201. <https://doi.org/10.1016/j.eneco.2009.10.003>
32. Amani N, Bagherzadeh Valami H. Efficiency Evaluation of regional electronic companies in Iran by Network DEA: A based on the Conversion of the Structures into a uniform structure. *Journal of decisions and operations research*. 2018;3(3):249-80. <https://doi.org/10.22105/dmor.2018.81213>
33. Wu Y, Li K, Fu X. An integrated zero-sum game and data envelopment analysis model for efficiency analysis and regional carbon emission allocation. *Decision Analytics Journal*. 2024;10:100387. <https://doi.org/10.1016/j.dajour.2023.100387>

COPYRIGHTS

©2024 The author(s). This is an open access article distributed under the terms of the Creative Commons Attribution (CC BY 4.0), which permits unrestricted use, distribution, and reproduction in any medium, as long as the original authors and source are cited. No permission is required from the authors or the publishers.

**Persian Abstract****چکیده**

هدف: این پژوهش با هدف ارزیابی عملکرد انرژی، اقتصاد و زیست محیطی کشورهای منتخب صادر کننده منابع انرژی با رویکرد یکپارچه تحلیل پوششی داده‌ها و نظریه بازی انجام شده است. روش‌شناسی پژوهش: روش ابرکارایی و کارایی متقاطع نیز به منظور رتبه‌بندی کشورهای کارآمد قبل از فاز همکاری مورد استفاده قرار گرفته است. سپس در فاز همکاری، هر کشور با استفاده از روش نظریه بازی‌های همکارانه و ارزش شاپلی مسئله مورد بررسی قرار می‌گیرد. یافته‌ها: نتایج نشان داد که قطر و یمن بیشترین و لبنان و اردن کمترین کارایی انرژی؛ کویت، قطر و ترکمنستان بیشترین و به ایران و ترکیه کمترین کارایی اقتصادی؛ امارات و قطر بیشترین و ایران و اردن کمترین کارایی زیست محیطی را دارند.



Behavior of Reinforced Geopolymer Concrete Beams under Repeated Load

H. Raad Shaker*, W. AlSaraj, L. A. AL-Jaberi

Civil Engineering Department, College of Engineering, Mustansiriyah University, Baghdad, Iraq

PAPER INFO

Paper history:

Received 04 November 2023

Received in revised form 11 December 2023

Accepted 24 December 2023

Keywords:

Geo-polymer

Glass fiber Reinforced Polymer

Polyvinyl Alcohol

Steel Fiber

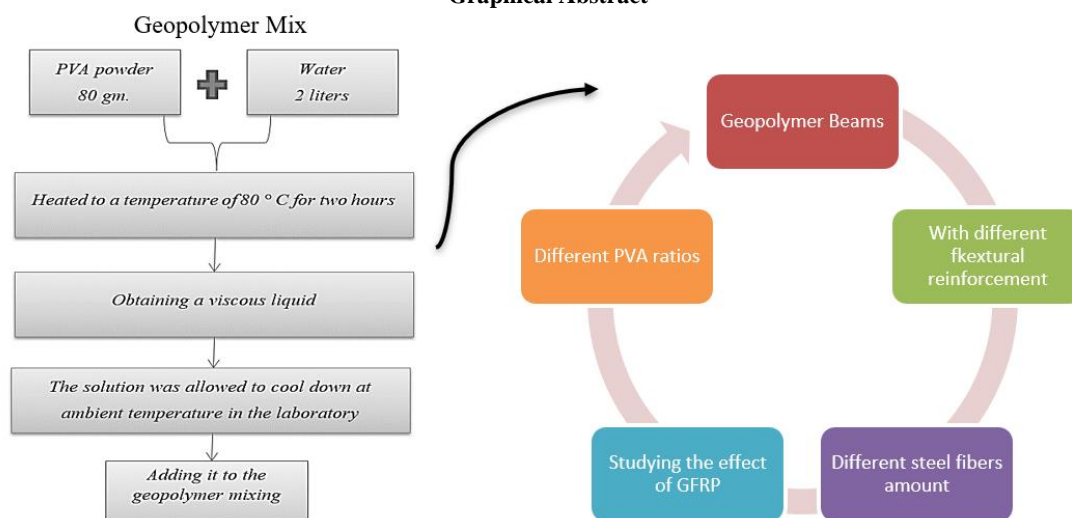
Repeated Load

ABSTRACT

Finding an alternative material for building constructions is an essential topic nowadays after the weather pollution which caused by cement production factories, at the same time, the engineers thinking to find such material from environments wastes to minimize the earth pollutions. Geopolymer is very important material which satisfy such purpose, because it is minimizes the need to concrete production and overcome the environment from many slags. Geopolymer beams were casted and tested under repeated load to study the possibility of using them as structural members exposing to repeated loads. The beams also strengthen by steel fibers and glass fiber reinforced polymer (GFRP) to investigate their effect on such new structural member. It was concluded that, it has been observed that the structural behavior of geo-polymer concrete beams tends to be more flexible when compared to that of ordinary concrete beams. Also, the geopolymer members showed an improvement in strength when using the steel fibers and GFRP, which what was observed on conventional concrete.

doi: 10.5829/ije.2024.37.05b.14

Graphical Abstract



1. INTRODUCTION

Concrete is a broadly used construction material and the construction industry exploit the natural resources (1).

Ordinary Portland Cement (OPC) plays a vital function in the production of concrete and the manufacturing of cement involves burning of huge quantities of fuel and breakdown of limestone, which results in large emission

*Corresponding Author Email: hussein.shaker@qu.edu.iq
(H. Raad Shaker)

of carbon dioxide to the atmosphere (2). The production of one ton of Portland cement causes the release of approximately one ton of carbon dioxide into the environment and the consumption of 1.5 tons of raw materials in manufacturing one ton of cement (3). Another essential reason pushed the engineers to look for another construction material which is a catastrophic fires occurs in France in 1973, which led Davidovits to think in another non-flammable and non-combustible material (4). Davidovits (5) prepared the geopolymer to replace OPC by activating active aluminosilicate materials with high alkali solution. Geopolymer can be produced from industrial wastes and geological sources including fly ash (FA), blast furnace slag, bottom ash, metakaolin (MK), and so on (6). Both ordinary concrete and geopolymer concrete are weak under tensile stresses and for this reason; the concrete in tension is neglected in many international codes and depends in totally on the strength of steel reinforcement to resist the tensile strength in structural members. While plain concrete tensile strength enhanced significantly by adding steel fibers to the concrete mix (7). The use of geopolymer cement can reduce carbon dioxide emissions by 44-64% compared to Portland cement (8).

Geopolymer concrete (GPC) is environmentally friendly, is energy saving, and also has similar or better mechanical properties than OPC concrete (OPCC) [10]. Compared to OPCC, GPC has better bond strength under similar compressive strength, higher early strength, and faster speed of strength development (9). Besides, the fire resistance of GPC is much better than the traditional concrete. As a result, GPC can be used in repairing and strengthening of existing structures, such as bridge structures, pavement structures, building structures, and so on. The rapid repaired strength can be obtained.

Geopolymer concrete have an enhanced mechanical and chemical properties when comparing with the normal conventional concretes, such as higher compressive, tensile and flexural strengths (10), faster hardening (10), longer durability (10), resistance to fire, and high temperature (11).

Many researchers studied the effect of concrete beam under repeated loads (12-14), but there is no research in the literature studied the behavior of Geopolymer beams under repeated loads. So, it is a novelty to investigate such topic for filling up the gap of literature for such essential case.

It was concluded that, from the previous research, a magnitude of residual deflection formed at the final of each loading stage after the unloading cycle due to the microcracks merging and the residual applied stresses. Also, the concrete beam which exposed to repeated load losses a magnitude of its failure load capacity when comparing with the static load due to the multi repeating cycles of loading and unloading stages (12, 15).

Repeated load may be subjected on structural

members by a periodic of series loads which may cause due to vehicle passing on bridges. These repeating loads causing deflections in each single passing on the beam and may cracked the beam with several micro cracks, or helps the creep and shrinkage cracks to be matching and developing after a period of time till cause failure. This phenomenon called as fatigue, the capacity of beam to overcome the repeated load after several periodic loadings.

Loads which applied on any structure classified into three basic categories, which are: static, dynamic and the repeated load. The static loads neither accelerates the beam nor effects on the velocity of it, so the first two items from the dynamic load equations (Equation 1) were neglected at static loading. In contrast to the the dynamic loading, which effects on beam velocity and acceleration so all items in the equation will be considered. But in the case of repeated load, and since the load is too slow, the inertia effect ignored (has no effect on the mass) (16-18). The study investigated the behaviour of Geopolymer beams under the effect of fatiage loading.

$$m\ddot{u} + c\dot{u} + ku = F(t) \quad (1)$$

2. EXPERIMENTAL WORK

Nine reinforced concrete beams designed to fail by flexural stresses were casted and test under repeated loads. Nine beams casted by geo-polymer concrete, and one beam made of normal concrete to compare with the geo-polymer concrete. The difference between the geopolymer beams relenting to the geopolymer mixture itself are shown in Tables 1 and 2. The first group includes four reinforced geo-polymer concrete beams made of the first mix, the second group includes four reinforced geo-polymer concrete beams made of the second mix, and the third group includes a reinforced concrete beam made of normal concrete has a w/c ratio equals 0.42. The difference between the first and second mixture is the percentage of PVA content.

All beams have the same dimension 1600 mm length, 250mm depth, and 150 mm width as shown in Figure 1. The beams denoted by mixture type, type of fiber which used, reinforcement presence, and the amount of fibers which used, as explain in Figure 2.

The beams were subjected to a successive cycle of loading and unloading (repeated loading) (7). Through this type of loading, as shown in Figure 3.

Usually, in the laboratories works, the designers tested the beam to loading equals the service load (70% of the ultimate service load (P_s)) and then unloaded it to get a repeated load cycle. Two cycles exposing quarter the service load, then two cycles of exposing half of the service load, the next three cycles applying the third-quarter service load and the final next cycles applying

TABLE 1. The mixing proportion for three mixing

The mixing proportion 1 st mixing.							
Type of concrete	Slag	Sand	Glass Sand	NaoH (8 mol)	Na2Sio3	Steel Fiber	PVA 0.2%
Geopolymer	520	962	78	119	297	60	2.6
The mixing proportion 2 nd mixing							
Type of concrete	Slag	Sand	Glass Sand	NaoH (8 mol)	Na2Sio3	Steel Fiber	PVA 0.75%
Geopolymer	520	962	78	119	297	60	9.75
The mixing proportion 3 rd mixing							
Type of concrete	Cement	Sand	Gravel	Water	Sp N211		
Normal concrete	390	515	1185	235	1.1		

TABLE 2. The steel proportion for beams

No.	Symbol	Type mixing	Type of longitudinal reinforcement	Top reinforcement	Bottom reinforcement
1 st	GSRA5	1 st	steel	2φ12	2φ12
2 nd	GSRB6	1 st	steel	2φ12	2φ16
3 rd	GGRA7	1 st	GFRP	2φ10	2φ10
4 th	GGRB8	1 st	GFRP	2φ10	2φ14
5 th	GSRA13	2 nd	steel	2φ12	2φ12
6 th	GSRB14	2 nd	steel	2φ12	2φ16
7 th	GGRA15	2 nd	GFRP	2φ10	2φ10
8 th	GGRB16	2 nd	GFRP	2φ10	2φ14
9 th	RCR18	3 rd	Steel	2φ12	2φ12

fully service load. Such increment in the applied load is called a rainfall style of repeating load, as explain in Figure 3.

3. MATERIAL PROPERTIES

The steel Fibers used is hooked end with a length of 30 mm and a diameter of 0.51mm and its specifications are Bright and clean wire, the density is 7800 kg/m³, the Tensile strength is 1200 MPa and aspect ratio (L/d) is 60.

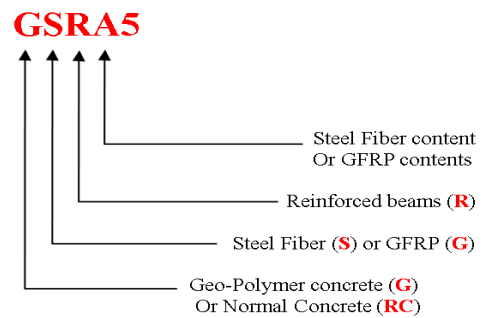


Figure 2. Bems symbol definations

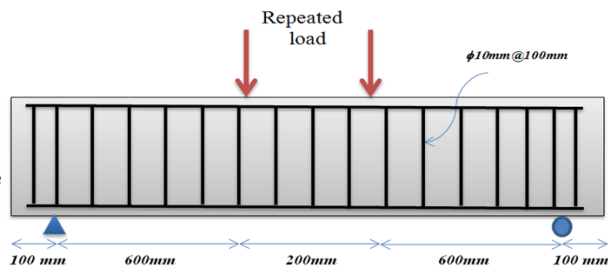


Figure 1. Beam Specimens

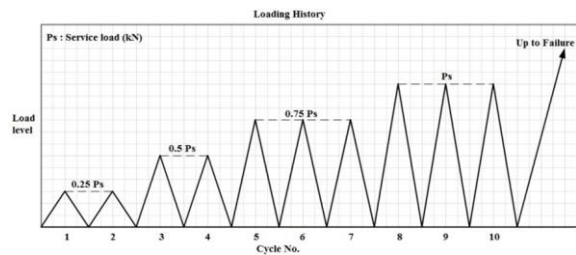


Figure 3. Proposed Repeated Loading History of Specimens

The tested properties of concrete and geopolymer were listed in Figure 6.

3. 1. Cement Portland cement (Al-Jeser) was used in the experimental study. It complies with the Iraqi Standard (I.Q.S) NO.5 of 1984.

3. 2. Fine and Course Aggregat In concrete mix used naturally sand and gravel. This sand was tested according to Iraqi Standard Specification (I.Q.S NO 45 of 1984), and gravel was tested according to Iraqi Standard Specification (I.Q.S NO 45 of 1984).

3. 3. Reinforced Bars As explained in Table 3, the samples were reinforced with two types of longitudinal reinforcement, steel and GFRP, with different diameters:
 - STEEL bars: a diameter of 12 mm was used where the

yield stress was 524 Mpa while ultimate stress was 655 Mpa, and a steel bar with a diameter of 16 mm where the yield stress was 560 Mpa while ultimate stress was 659 Mpa.

- GFRP bars: a diameter of 10 mm was used where the tensile strength was 895 Mpa and a steel bar with a diameter of 14 mm where the tensile strength was 1169 Mpa.

For transverse reinforced a diameter of steel bar 10 mm was used for all beams where the yield stress was 508 Mpa while ultimate stress was 635 Mpa.

3. 4. Preparation Alkaline Solution for Geopolymer and Poly (Vinyl Alcohol) (PVA) Preparation of alkaline solution for geopolymer is shown in Figure 4, and preparation of PVA is shown in Figure 5. The tested mechanical properties are illustrated in Figure 6.

TABLE 3. Reinforcement properties

No	Normal Bar Diameter (mm)	Bar Type	Description of bar	Yeild stress (MPa)	Ultimate Stress (MPa)	Bending result at 180°
1	10	Steel	Deformed	508	635	Successful
2	12	Steel	Deformed	524	655	Successful
3	16	Steel	Deformed	560	659	
No.	Normal bar Diameter	Bar Type	Description of bar	Tensile strength (MPa)		Bending result at 180°
4	10	GFRP	Deformed	895		Successful
5	14	GFRP	Deformed	1169		Successful

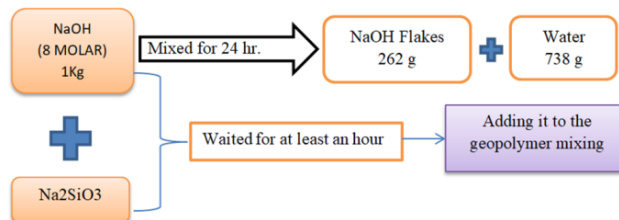


Figure 4. Preparation Of Alkaline Solution For Geopolymer

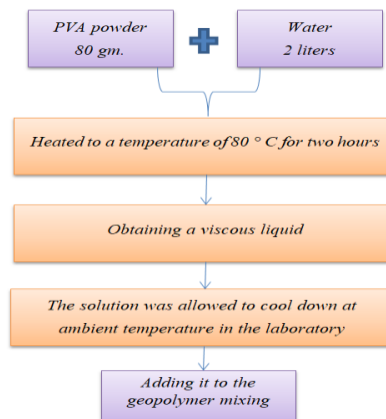


Figure 5. Preparation Of PVA

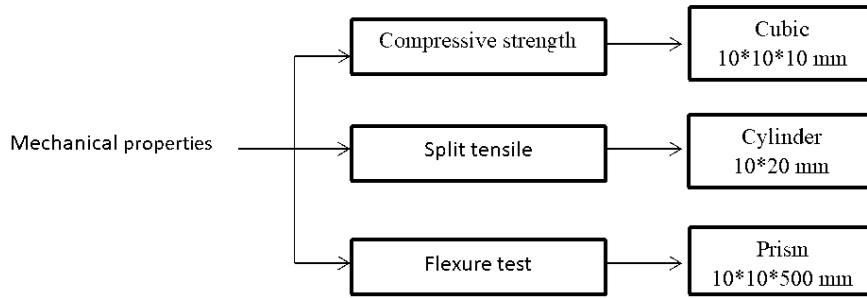


Figure 6. Mechanical Properties.

4. EXPERIMENTAL TEST RESULTS

Experimental results including mechanical properties of mixtures and results from tested beam specimens. The mechanical properties including compressive strength, tensile strength and flexural strength. are shown in Figures 7 to 11, Tables 4 and 5. It can be concluding that,

increasing PVA within the mix deteriorated the concrete compressive strength because it is working on incrementing the water amount in the mix. The same behavior was observed for the flexural strength and there is no significant influence observed for the tensile strength.

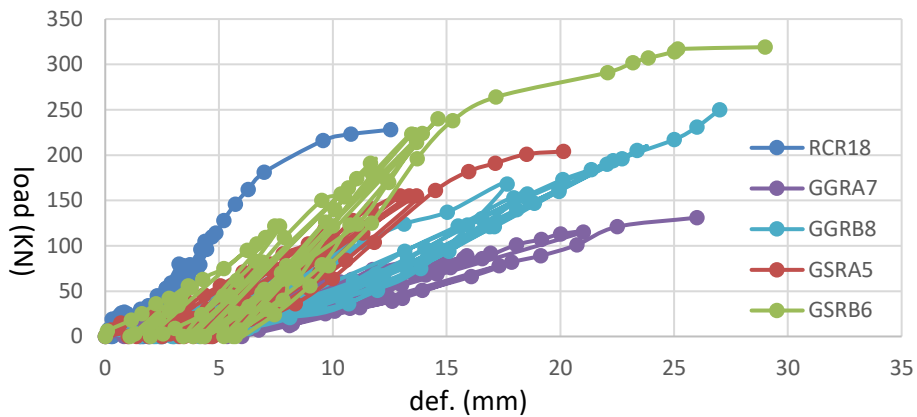


Figure 7. Comparison The Load-Deflection Curve Between Beams In The 1st & 3rd Group

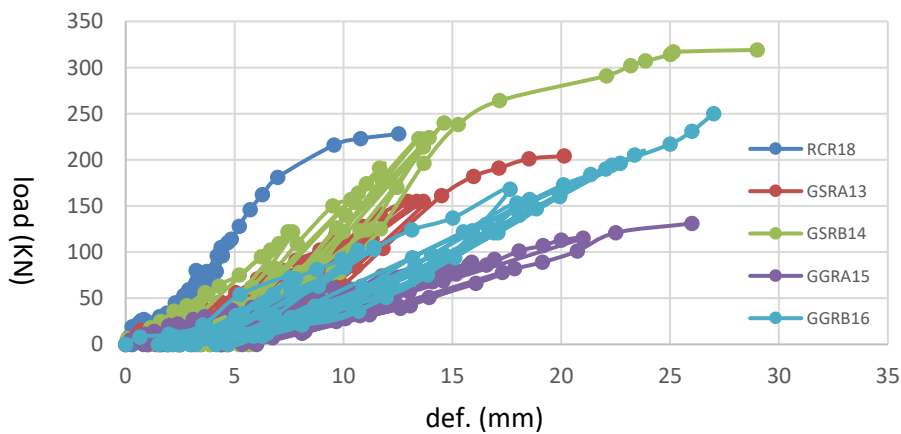


Figure 8. Comparison The Load-Deflection Curve Between Beams In The 2nd & 3rd Group

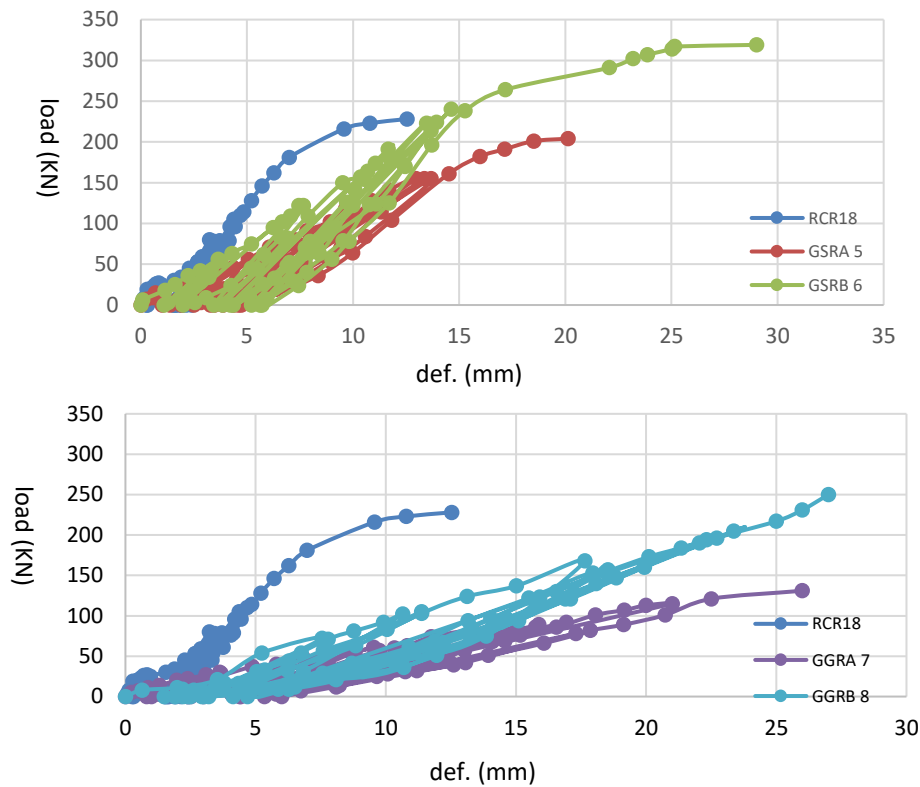


Figure 9. Comparison The Load-Deflection Curve in 1st Group Between Beams Which Have The Same Properties

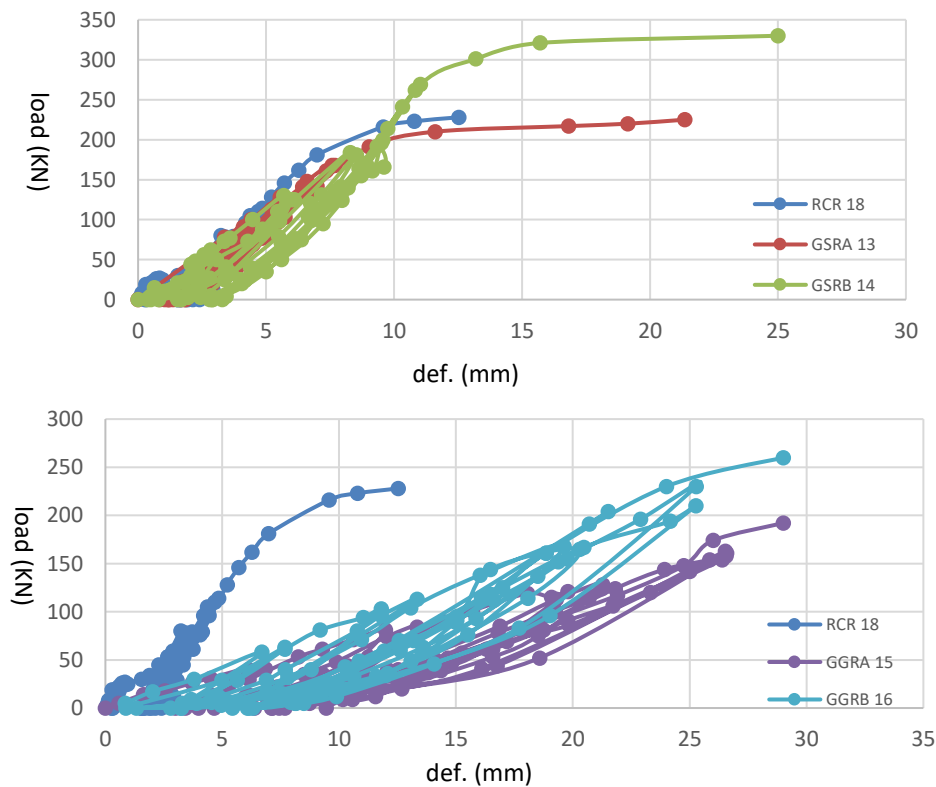


Figure 10. Comparison The Load-Deflection Curve in 2nd Group Between Beams Which Have The Same Properties



Figure 11. Crack patterns for all tested beams

After testing the specimens experimentally, it was observed that, all beams' types failed by flexural stresses in spite of their different types; which may indicate that,

the failure criteria of (geopolymer or concrete) beams; still yielding to their theoretical design (which was planned before to be flexural) even it was reinforced by

steel fiber, GFRP or even casted by geopolymer material. Ultimate loads, cracking loads and increasing of ultimate load for all beams are provided in Table 5.

From the obtained results, when comparing between the first two geopolymer beams (GSRA5 and GSRB6) it can be concluded that, the increment of steel ratio from (5 to 6) enhance the final capacity of beams by 56.37% , and 90.8% for GFRP samples after increasing the steel ratio from 7% to 8%, all for the same mixes properties (the first mix).

For the second mix, the resistance of beam developed by 46.7% after incrementing the steel ratio from 13% to 14%, while for GFRP samples, the ultimate capacity of beams increased by 32.6% when developing the steel ratio from 15% to 16%, as shown in Table 4.

As a conclusion, it can be stated that, as the steel fiber and EFRB working on developing the concrete strength, it is also effective to enhance the properties of geopolymer mixed against the applied loads and enhance the overall resistance (such as flexural resistance, as well as all the others properties).

The value of the deflection occurring in the geopolymer samples compared to the applied load is higher than the deflection occurring in normal concrete.

By increasing the percentage of reinforcing steel, noticed that a delay in the appearance of the initial crack in all geopolymer beams when comparing the beam of the symbol “A”, which represents the minimum steel percentage, with the beam of symbol “B”, which represents an increase in the steel percentage.

The structural behavior of geo-polymer concrete beams tends to be more flexible when compared to that of ordinary concrete beams .

From Figure 7, in which the results of load versus deflection of the first group specimens were listed. It can be concluded that, the behavior of concrete beam appears more brittleness than the geopolymer samples. The deflection at the same loading stage seems to be larger in geopolymer specimens comparing with the concrete. This case appears again when observing the GFRP specimens at the same Figure 7. The GFRP shows more ductility than the normal concrete and geopolymers beams.

From Figure 8, it can be clearly noticed that, the same behavior involved the ductility of conventional concrete and the brittleness of GFRP was observed .

By following the crack patterns which listed in Figure 11, it can be seen the flexural cracks formed clearly beneath the loaded points, which is described to be vertical passing through the neutral axes of beams.

It can be concluded from Table 6 that, the residual deflection after a cycle of load increases gradually due to micro cracks merging from the previous loadings besides shrinkage cracks. Also, the residual deflection minimizes when increasing the steel reinforcement ratio.

TABLE 4. Mechanical Properties Results.

Mixing No. (MPa)	First mixing	Second mixing	Third mixing
Compressive strength	47	40	38
Tensile strength	4.7	4.5	2.3
Flexure strength	4.92	3.207	3.1

TABLE 5. Ultimate Loads And Cracking Loads For All Beams

Beams No.	Beams Symbol	First crack loading (KN)	Ultimate deflection (mm)	Ultimate load (KN)
9 th	RCR18	45	12.53	228
1 st	GSRA5	91	20.13	204
2 nd	GSRB6	150	29	319
3 rd	GGRA7	80	26	131
4 th	GGRB8	142	27	250
5 th	GSRA13	95	21.35	225
6 th	GSRB14	155	25	330
7 th	GGRA15	85	29	196
8 th	GGRB16	120	29	260

TABLE 6. Residual deflection at the end of each cycle

		Residual deflection (mm)									
Beams	Cycle	1	2	3	4	5	6	7	8	9	10
	G.S.R.A 5		1	1.36	1.9	2.49	3.46	3.87	3.28	4.36	4.72
G.S.R.B 6		1.09	1.27	1.98	3.42	4.21	3.85	4.35	5.61	5.2	5.71

G.G.R.A 7	0.82	1	2.51	2.4	3	3.4	4.39	4.43	5.34	6
G.G.R.B 8	1.49	1.91	2.22	2.42	3.2	2.93	2.5	4.14	4.69	3.02
G.S.R.A 13	0.85	1.14	1.03	1.2	1.22	1.36	1.81	1.66	1.85	2
G.S.R.B 14	0.49	0.37	0.79	1.68	1.55	2	2.8	2.9	2.89	3.28
G.G.R.A 15	3	3.42	3.98	4.65	6.38	7.1	7.68	7.43	9.45	7.14
G.G.R.B 16	0.88	2.79	3.25	3.22	6.08	6.15	6.31	5.44	4.2	1.33
R.C.R 18	0.31	0.26	1.55	1.52	1.88	1.63	1.67	1.95	2.39	2.13

7. CONCLUSIONS

1. The compressive strength increased by 24% for the first mixture when compared with the third mixture and by 5% when compared with the second mixture.
2. The tensile strength increased by 104% for the first mixture when compared with the third mixture and by 96% when compared with the second mixture.
3. The flexural strength increased by 59% for the first mixture when compared with the third mixture and by 3% when compared with the second mixture.
4. The optimal ratio of PVA in mixture represents 0.2 %.
5. When comparing beams made of geo-polymer concrete with ordinary concrete, the best percentage of increase in ultimate strength was observed for beam NO.6 (GSRB14) (45%) which reinforced by steel bars 2 ϕ 12mm at top and 2 ϕ 16mm at bottom.
6. All the beams that were reinforced with the minimum reinforcement gave less resistance than the beam made of concrete under repeated load, which is beam No.1, beam No.3, beam No.5, and beam No.7 where the percentage of decrease was -11%,-43%, -1.3%, and -14% respectively.
7. The percentage of increase in the ultimate strength when compared with ordinary concrete was for beam No. 2 is 40%, beam No.4 is 10% and beam No.8 is 14%.
8. It has been observed that the structural behavior of geo-polymer concrete beams tends to be more flexible when compared to that of ordinary concrete beams.
9. The maximum deflection in all samples was high compared with the normal concrete, where the ultimate deflection reached 29 mm, while in the normal concrete it was 12.53mm.
10. Noticed that the first crack was delayed in appearing in the geopolymer samples compared to the normal concrete, due to the presence of steel fiber and PVA.

8. REFERENCES

1. Mehta PK. Greening of the concrete industry for sustainable development. *Concrete international*. 2002;24(7):23-8.
2. Kong DL, Sanjayan JG. Damage behavior of geopolymer composites exposed to elevated temperatures. *Cement and Concrete Composites*. 2008;30(10):986-91. <https://doi.org/10.1016/j.cemconcomp.2008.08.001>
3. Esparham A, Mehrdadi N. Effect of combined different sources of alumina silicate on mechanical properties and carbonation depth of environmentally friendly geopolymeric composite based on metakaolin. *International Journal of Engineering, Transactions A: Basics*. 2023;36(7). 10.5829/ije.2023.36.07a.18
4. Malhotra V. Making concrete" greener" with fly ash. *Concrete international*. 1999;21(5):61-6. <https://www.concrete.org/publications/internationalconcreteabstractportal/m/details/id/248>
5. Davidovits J. Geopolymers and geopolymeric materials. *Journal of thermal analysis*. 1989;35:429-41. <https://doi.org/doi.org/10.1007/BF01904446>
6. Chu Y-S, Davaabal B, Kim D-S, Seo S-K, Kim Y, Ruescher C, et al. Reactivity of fly ashes milled in different milling devices. *Reviews on Advanced Materials Science*. 2019;58(1):179-88. <https://doi.org/doi:10.5829/ije.2022.35.10a.19>
7. Goaz HA, Shamsaldeen HA, Abdulrehman MA, Al-Gasham T. Evaluation of steel fiber reinforced geopolymer concrete made of recycled materials. *International Journal of Engineering*. 2022;35(10):2018-26.
8. Mithun B, Narasimhan M, Nitendra P, Ravishankar A. Flexural fatigue performance of alkali activated slag concrete mixes incorporating copper slag as fine aggregate. *Selected Scientific Papers-Journal of Civil Engineering*. 2015;10(1):7-18. <https://doi.org/doi.org/10.1515/sspjce-2015-0001>
9. Arenas C, Luna-Galiano Y, Leiva C, Vilches L, Arroyo F, Villegas R, et al. Development of a fly ash-based geopolymeric concrete with construction and demolition wastes as aggregates in acoustic barriers. *Construction and Building Materials*. 2017;134:433-42. <https://doi.org/doi.org/10.1016/j.conbuildmat.2016.12.119>
10. Yu Q, Li S, Li H, Chai X, Bi X, Liu J, et al. Synthesis and characterization of Mn-slag based geopolymer for immobilization of Co. *Journal of Cleaner Production*. 2019;234:97-104. <https://doi.org/10.1016/j.jclepro.2019.06.149>
11. Rajamma R, Labrincha JA, Ferreira VM. Alkali activation of biomass fly ash–metakaolin blends. *Fuel*. 2012;98:265-71. <https://doi.org/10.1016/j.fuel.2012.04.006>
12. Radhy ZH, Neamah MW, Makki OM, Al-Mutairee HM, editors. Experimental and statistical capacity of rubberized continuous deep beams under monotonic and repeated load. *IOP Conference Series: Earth and Environmental Science*; 2023: IOP Publishing.
13. Salmi A, Bousshine L, Lahlou K. A new model of equivalent modulus derived from repeated load cbr test. *International Journal of Engineering, Transactions A: Basics*. 2020;33(7):1321-30. 10.5829/ije.2020.33.07a.19
14. Hassan SA, Ali MK. behavior of hybrid reinforced concrete deep beams with web openings under repeated loading. *Journal of Engineering and Sustainable Development*. 2019;23(4):52-75. <https://doi.org/10.31272/jeasd.23.4.4>
15. Almahmood H, Ashour A, Sheehan T. Flexural behaviour of hybrid steel-GFRP reinforced concrete continuous T-beams. *Composite Structures*. 2020;254:112802.

16. Penzien J. Dynamics of structures 1995.
17. Mukhopadhyay M. Structural Dynamics: Springer; 2021.
18. Dhundasi A, Khadiraikar R, Momin A. Stress-strain characteristics of reactive powder concrete under cyclic loading. International Journal of Engineering, Transactions A: Basics. 2022;35(1):172-83. 10.5829/ije.2022.35.01a.16

COPYRIGHTS

©2024 The author(s). This is an open access article distributed under the terms of the Creative Commons Attribution (CC BY 4.0), which permits unrestricted use, distribution, and reproduction in any medium, as long as the original authors and source are cited. No permission is required from the authors or the publishers.



Persian Abstract

چکیده

یافتن مصالح جایگزین برای ساخت و سازه‌های ساختمانی امروزه پس از آلودگی هوا ناشی از کارخانجات حفاظ سیمان موضوعی ضروری است و در عین حال مهندسان به فکر یافتن چنین موادی از زباله‌های محیطی برای به حداقل رساندن آلودگی‌های زمین هستند. ژئوپلیمر ماده بسیار مهمی است که چنین شرایطی را برآورده می‌کند، زیرا نیاز به تولید بتن را به حداقل می‌رساند و از بسیاری از سرباره‌ها پر محیط غلبه می‌کند. تیرهای ژئوپلیمری تحت بارهای مکرر ریخته‌گری و آزمایش شدند تا امکان استفاده از آنها به عنوان اعضای سازه‌ای در معرض بارهای مکرر بررسی شود. تیرها همچنین توسط الیاف فولادی و GFRP تقویت می‌شوند تا تأثیر آنها بر چنین اعضای ساختاری جدیدی بررسی شود. نتیجه‌گیری شد که مشاهده شده است که رفتار ساختاری تیرهای بتنی ژئوپلیمری در مقایسه با تیرهای بتنی معمولی انعطاف پذیرتر است. همچنین، اعضای ژئوپلیمر در هنگام استفاده از الیاف فولادی و GFRP، بهبود مقاومت را نشان دادند، چیزی که در بتن معمولی مشاهده شد.



CNN-based Approach for Enhancing Brain Tumor Image Classification Accuracy

A. Muis^a, S. Sunardi^{*b}, A. Yudhana^b

^a Graduate Program of Informatics, Universitas Ahmad Dahlan, Indonesia

^b Department of Electrical Engineering, Universitas Ahmad Dahlan, Indonesia

PAPER INFO

Paper history:

Received 29 October 2023

Received in revised form 13 December 2023

Accepted 28 December 2023

Keywords:

Accuracy

Brain Tumor

Convolutional Neural Network

Machine Learning

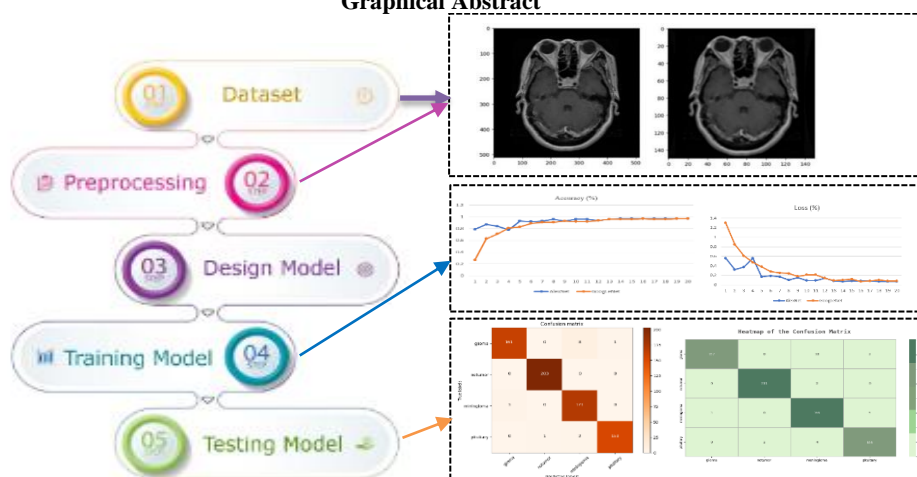
Magnetic Resonance Image

ABSTRACT

Brain tumors are one of the deadliest diseases in the world. This disease can attack anyone regardless of gender or certain age groups. The diagnosis of brain tumors is carried out by manually identifying images resulting from Computerized Tomography Scan or Magnetic Resonance Imaging, making it possible for diagnostic errors to occur. In addition, diagnosis can be made using biopsy techniques. This technique is very accurate but takes a long time, around 10 to 15 days and involves a lot of equipment and medical personnel. Based on this, machine learning technology is needed which can classify based on images produced from MRI. This research aims to increase the accuracy of previous research in the classification of brain tumors so that errors do not occur in the diagnosis of brain tumors. The method used in this research is Convolutional Neural Network using the AlexNet and Google Net architectures. The results of this research obtained an accuracy of 98% for the AlexNet architecture and 96% for GoogleNet. This result is higher when compared with previous research. This finding can reduce the computational burden during model training. The results of this research can help physicians diagnose brain tumors quickly and accurately.

doi: 10.5829/ije.2024.37.05b.15

Graphical Abstract



1. INTRODUCTION

Brain tumors are considered one of the most dreaded diseases by humans. It is a life-threatening condition that can occur in individuals regardless of age, gender, or

specific groups (1). Essentially, brain tumors can grow and develop in parts of the body surrounding the brain (2). Brain tumors are characterized by the uncontrolled growth of cells, which continue to proliferate in the affected area of the body. This excessive cell growth is

*Corresponding Author Email: sunardi@mti.uad.ac.id (S. Sunardi)

unnecessary for the body or any specific organ. Instead, it disrupts the body's metabolism and can impair the function of nearby organs surrounding the tumor (3). Brain tumors are tumors that develop and grow in the vicinity of the skull. Based on their growth characteristics, brain tumors can be classified into two types benign brain tumors and malignant brain tumors. Benign brain tumors have a slow growth rate and do not spread to surrounding tissues, but they can still damage the brain. On the other hand, malignant tumors exhibit rapid growth and can invade surrounding tissues. Brain tumors are considered one of the most dangerous diseases in the world. This disease is one of the deadliest diseases, posing a significant threat to individuals affected by them (4). Only about one third of patients with this disease survive for five years after diagnosis.

Doctors diagnose brain tumors in patients using several methods. First, they assess the patient's physical condition and medical history, including examining the neural tissues within the skull to determine if they are intact or compromised. Second, they employ scanning machines such as CT Scan and Magnetic Resonance Imaging (MRI) to aid in the diagnosis (5). CT Scan is performed using X-ray machines to provide doctors with a clearer view of the patient's condition, including body structures and blood cells. On the other hand, MRI differs from CT Scan as it does not involve radiation and can generate clear images of the skull, allowing for diagnosis based on the MRI scan results. MRI scans produce detailed images of the body's organs using a magnetic field, but this technique often requires a longer duration (6, 7). The third method is the collection of body tissues for examination by a neuropathologist. This technique is called a biopsy. Biopsy can also assist doctors in diagnosing the type of brain tumor, whether it is benign or malignant, present in the patient. The biopsy process can indeed be time-consuming as the collected tissue samples need to be sent to the laboratory for examination. However, it is crucial to diagnose this disease quickly and accurately to ensure appropriate treatment. Therefore, early detection technology is needed for brain tumor diagnosis in patients. Additionally, monitoring the progression of brain tumors in affected patients is essential for effective management of the disease (8). Machine learning techniques can indeed be utilized to detect brain tumors by leveraging brain images obtained from MRI scans. This highlights the significant impact of machine learning development in the field of healthcare, enabling effective detection and classification of specific diseases, including brain tumors (9-12). The aim is to facilitate prompt and accurate treatment or therapy for patients diagnosed with brain tumors, considering that the treatment process can be lengthy (13).

Machine learning is a branch of Artificial Intelligence (AI) that involves designing and developing algorithms with the goal of enabling computers to learn from data

provided to them. The data can be in the form of binary data, images, videos, or even sound, and can be learned by the technology. machine learning can also recognize handwriting (14). This capability assists humans in solving image processing problems. Image processing is highly valuable in the field of healthcare as it aids in detecting diseases within the human body by utilizing medical images generated from CT or MRI scans. The classification of medical images using deep learning is an important research topic because it has broad applications in the diagnosis of various diseases (15-19). Images from MRI scans are extracted to generate new image data based on created algorithms. The most commonly used algorithm for image extraction and classification using deep learning is Convolutional Neural Network (CNN) (20, 21).

CNN has emerged as the leading algorithm for performing classification of medical images in recent years (22-25). CNN is capable of efficiently classifying a large number of images (26). Essentially, the CNN algorithm consists of two main stages in the classification process following the input of an image feature extraction and classification. CNN can decrease the count of trainable network parameters by leveraging a blend of characteristics sourced from multiple layers to enhance the overall accuracy (27). The feature extraction stage comprises convolutional layers and pooling, while the classification stage involves fully connected layers and the output layer (28). Figure 1 is a general feature extraction stage in CNN.

Figure 1 shows that the input image measuring 150x150 is convolved using a 3x3 kernel with ReLU activation and using Maxpooling size 2x2. The convolutional layer is a crucial component of the CNN algorithm as it generates new images after convolving the input image. This process involves applying filters to extract features from the input image. The filters used are typically matrices of sizes 1x1, 3x3, 5x5, or 7x7. The filter operation produces a feature map by altering the values of each feature map. After the feature map is obtained, pooling is performed. Pooling is not conducted until the convolutional layer generates a new feature map from the input image. Pooling is a process of reducing the size of the image while retaining important information. The commonly used pooling layers are max pooling and average pooling. Max pooling involves selecting the highest value within each filter to generate a new image,

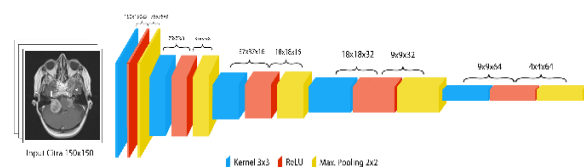


Figure 1. CNN Algorithm

while average pooling calculates the average value of each matrix passed through the filter. The pooling filter size is often 2x2. The output obtained from pooling is converted into a vector and fed into the fully connected layer, which is the last layer in the CNN algorithm. The layers from the previous stage are connected to the neurons in the subsequent layer, similar to a typical artificial neural network (11). In this layer, activation functions such as sigmoid or softmax are used to determine the classification of the image displayed in the output. The output represents the result of the fully connected layer, where it classifies the input image into specific labels or classes. The output assigns the input image to its corresponding class based on the similarity or similarity to the learned data.

CNN has gained popularity as a powerful algorithm for classifying images in various domains, including medical imaging. Whether it's brain images or other types of medical images, CNN has demonstrated its effectiveness in accurately classifying and analyzing them (29). Its ability to learn and capture intricate patterns in images has made it a popular choice for image classification tasks in the field of medical technology.

Ismael and Abdel-Qader (30) conducted a study to classify brain tumor diseases using a neural network. This research utilized brain tumor images obtained from MRI scans. The dataset employed in the study consisted of 3064 samples, including three classes: glioma, meningioma, and pituitary. Figure 2 in the study reveals that the classification technique employed a multilayer neural network comprising three layers: input, hidden, and output. The input layer consisted of 270 neurons, one hidden layer contained 90 neurons, and the output layer comprised 3 neurons. The study achieved an accuracy of 96% for the meningioma class, 96.29% for glioma, and 95.66% for pituitary, resulting in an overall accuracy of 91.9%. The study conducted by Pashaei et al. (23) examined the CNN and Extreme Learning Machines (ELM) methods for brain tumor classification. This research utilized MRI images of meningioma, glioma, and pituitary tumors, with a total dataset of 3064 samples. The study employed 4 convolutional layers, 4 pooling layers, and 1 fully connected layer. They presented the results of the confusion matrix analysis to determine the precision, recall, and F-measure values using the CNN algorithm, where the pituitary class achieved the highest percentages of 98.3%, 100%, and 99.1% respectively. The study yielded the highest accuracy of 93.68% using CNN [23]. Anaraki et al. (31) conducted a study on the classification of MRI images using neural networks and the Genetic algorithm. The dataset used in this research consisted of 600 brain tumor images, classified into three classes: glioma, meningioma, and pituitary. In their study illustrated the implementation of CNN architecture, which includes two case studies. In the first case study, 4x4 convolutional layer was used, followed by max

pooling with size of 2x2. The final convolutional layer had a size of 6x6, resulting in a total of 96 feature maps for case study one. In the second case study, a 6x6 convolutional layer was used, along with max pooling of size 2x2. The final convolutional layer had size of 4x4, generating 384 feature maps. The study achieved an accuracy of 94.2% (31). These results demonstrate that the employed methods are highly effective in classifying brain tumors based on MRI images. Baranwal et al. conducted a performance analysis of the classification methods CNN and Support Vector Machine (SVM) using brain MRI images. The aim of this study was to classify brain tumor diseases, including meningioma, glioma, and pituitary tumors. Figure 3 in the study presents a CNN architecture, consisting of 5 convolutional layers with max pooling. Each image resulted in 1024 feature maps, which were classified into their respective classes. The classification results were analyzed to determine the best method for classification. The study achieved an accuracy of 94% using the CNN algorithm and 81% using SVM (32). These results demonstrate that CNN is more effective and accurate compared to the SVM algorithm. The classification conducted by Deepak et al. focused on common brain tumors, namely glioma, meningioma, and pituitary tumors. The research method employed CNN with the GoogLeNet architecture. In their study presented a comparison with previous similar research studies. The conclusion drawn after comparing the results with prior studies indicates that the algorithm used in this research outperforms the previous findings in terms of accuracy. The study achieved a high accuracy of 98% (33). Research on brain tumors with the highest accuracy of 98.76% was obtained using the ResNet algorithm, but this research used data on 233 brain tumor patients plus 980 without brain tumors (34). In addition, edge detection of images affected by brain tumors has been carried out, but still obtains low accuracy, namely 86.59% (35). Edge detection is the most important part in knowing where the tumor is. Research using the AlexNet and GoogLeNet architectures carried out previously obtained an accuracy of 95.77% for the AlexNet-Conv5 architecture and 95.44 for GoogLeNet-inception-4e (36). This research has differences with the model proposed in this research. that research uses the original input image while this research reduces the input image to reduce the computational load.

Previous research studies have often utilized the CNN algorithm for image classification, as CNN has shown success in solving classification problems (37). The images used in these studies are brain images obtained from MRI scans, including both images with brain tumors and images without brain tumors. Several studies have achieved high accuracy in classifying brain tumor images.

This research aims to improve the accuracy of previous studies by utilizing advanced CNN-based

algorithms that have been developed (38). The technique used in this research starts by changing the input image to a smaller size. The input image is tested using the AlexNet and GoogLeNet algorithms. Before testing, the dataset is divided into test data and testing data. Test data is further divided into test data and validation data. This aims to test the model during the training process. During the training process, the Callback function used is ReduceLRonPlateau. The function helps adjust the learning rate used so that the training process is stable and prevents overfitting. Next, testing is carried out using testing data to produce a confusion matrix which is analyzed to determine the level of accuracy obtained.

2. METHOD

The research methodology begins with the collection of brain tumor data obtained from MRI scans. The dataset then undergoes a preprocessing stage to clean and organize the data. Following that, a model is designed for classifying the dataset. Before conducting the classification, the created model undergoes training using a training dataset to improve its performance. Once the model is trained, it is then tested using a separate dataset to evaluate its classification capabilities. This process aims to assess the model's ability to accurately classify new datasets. Figure 2 illustrated the proposed research methods.

Figure 2 is the proposed method which starts from the search stage for brain tumor image datasets, the data preparation stage to be used as training and testing data, the model design stage according to the proposed model, the model training stage using training data, the model testing stage to test the proposed model.

2.1. Datasets Dataset is a collection of data that can be in the form of numbers, images, or other formats, containing information relevant to the research. In this particular study, the dataset consists of brain images obtained from MRI scans, as MRI images are well-suited



Figure 2. Research method

for extracting image features using CNN (32). The MRI brain images downloaded for this study are categorized into four classes: glioma tumor, meningioma tumor, no tumor, and pituitary tumor. The dataset used in this research includes 7023 brain images, which are divided into 6320 for training the model and 703 for testing the model.

2.2. Preprocessing Preprocessing is a stage of preparing the dataset so that the data can be processed by machine learning architectures (39). Preprocessing the data can also enhance the performance of the application in extracting features from images (40). The preprocessing techniques used in this research include resizing and grayscale conversion. Resizing is the process of adjusting the size of input images to a uniform size before classification using the CNN algorithm.

Based on Figure 3, it is observed that the images before preprocessing have a size of 500x500. This large image size can pose challenges for the model in performing classification as it requires more time to extract image features (41). Therefore, resizing is performed to ensure that the dataset used has consistent size. In this research pixel size of 150x150 is used. Although the image size used is significantly different from the original size, it does not compromise the image information. Grayscale is the process of converting the color image to grayscale image. The brain images used in this research consist of three color channels (RGB), hence grayscale is performed to convert the three channel image into two channel image, enabling better classification by the employed architecture.

2.3. Design Model This stage involves the creation of a model or architecture for classifying the dataset. In this research, two CNN architectures, namely AlexNet and GoogLeNet, are utilized. AlexNet is a neural network architecture developed by Alex Krizhevsky. The AlexNet input image size that we proposed is 150x150. This size is different from the original AlexNet input image size, which is 227x227 with three different filters. This size is extracted in the convolution layer until it reaches a fully connected layer with a number of

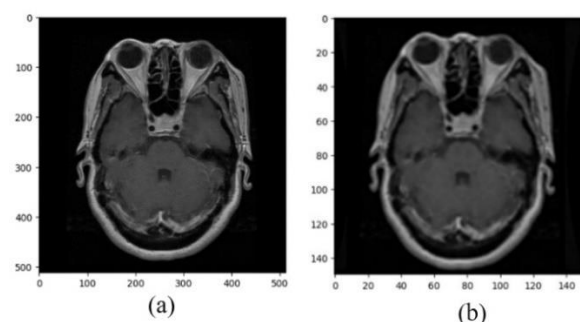


Figure 3. Preprocessing image (a) before (b) after

parameters 2304. The output results are different from the output results in the original AlexNet architecture, namely 9216 parameters. This difference is due to the input size of the image used, namely 150x150. Next, a fully connected layer with 4096 parameters is added until it is activated using the softmax function with four class output. Both architectures were developed to participate in the ImageNet LSVRC-2010 competition, which involved classifying images with a large number of classes. AlexNet emerged as the winner in 2012, while GoogLeNet claimed the top spot in 2014, surpassing AlexNet's performance. In this research, both architectures are employed to enhance the accuracy of classifying brain images from MRI scans.

The CNN architecture is a deep learning architecture in machine learning that consists of feature extraction and fully connected layers (42). In the feature extraction stage, there are several layers that are responsible for extracting features from images, transforming them into new images known as feature maps. The fundamental steps in feature extraction are the convolution and pooling layers. Convolution involves the multiplication of two matrices followed by summation.

Equation to calculate convolution in the feature extraction stage of CNN architecture is stated as follows.

$$C(i,j)=\sum_m\sum_n I(i+m,j+n) \cdot K(m,n) \tag{1}$$

The value of C(i,j) represents the convolution result at pixel location (i,j) in the feature map. I(i+m,j+n) denotes the pixel value in the input image at location (i+m,j+n), K(m,n) represents the value in the convolution kernel at location (m,n), and $\sum_m\sum_n$ indicates the summation operation over variables m and n according to the kernel size. Furthermore, the convolutional results can pass through activation functions such as ReLU (Rectified Linear Unit) to introduce non-linearity to the extracted features. After the convolutional stage, a pooling layer is applied, which aims to reduce the spatial dimensions of the feature map while preserving important information. One commonly used type of pooling is max pooling, where the maximum value within each pooling window is retained. The feature extraction process in CNN architecture is repeated with multiple convolutional and pooling layers to generate increasingly complex and abstract features from the input image.

Another equation that can be used to calculate convolution is as follows.

$$a.b = \sum_{i=1}^n a_i b_i = a_1 b_1 + a_2 b_2 + \dots + a_n b_n \tag{2}$$

The values of a and b represent the values in the kernel used, with a kernel size of 2x2. If using a 3x3 kernel, the kernel values will not only include a and b but also an additional value, c. An example implementation of Equation 1 using a 2x2 kernel, a 3x3 image size, employing zero padding, stride 1, and the following

values for the kernel: a1=1, a2=2, b1=3, and b2=4 as in Figure 4.

Figure 4 show values in the kernel are multiplied by the values in the 2x2 image matrix, resulting in a1=0, a2=0, b1=0, and b2=4. Therefore, the sum of these values is 4. Consequently, the initial value in the feature map matrix is 4. This operation is performed until the entire matrix has been traversed by the kernel.

The convolutional stage produces new images or feature maps derived from overlapping pixels of the input image, resulting in multiple feature maps when the input image is convolved multiple times. The feature map generated for each image can be calculated using the following equation.

$$n_{out} = \left\lfloor \frac{n_{in} + 2p - k}{s} \right\rfloor + 1 \tag{3}$$

The value of n_out represents the resulting feature map size after each convolution operation, n_in represents the input layer size or the size of the image being used, p represents the padding size applied, k represents the size of the kernel used, and S represents the stride value, indicating the movement of the kernel both horizontally and vertically. In this study, the feature maps generated after each convolution operation can be calculated. The study utilizes input images of size 150x150, applies zero padding, uses a 3x3 filter size, and employs a stride of one for kernel movement.

The resulting new features from one convolutional step are as follows.

$$n_{out} = \left\lfloor \frac{150 + 2 \times 1 - 3}{1} \right\rfloor + 1$$

Based on that, the resulting feature map will have the same size as the input image, which is 150 pixels. This is because of the use of zero padding. To determine important information within the image, one can create a histogram of the image. An image histogram is a graph that represents the distribution of pixel values in an image. The histogram can reveal a lot about the brightness and contrast of an image. Therefore, the histogram is a valuable tool for both qualitative and quantitative image processing. Mathematically, the image histogram can be calculated using the following equation.

$$h_i = \frac{n_i}{n} \tag{4}$$

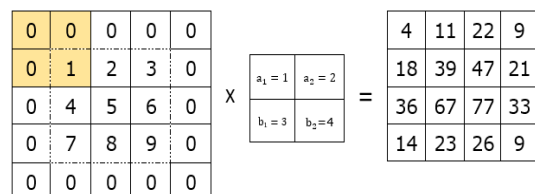


Figure 4. Convolutional layer

The value of n_i represents the number of pixels that have a certain gray level in the image, while n represents the total number of pixels in the image. As an example, Figure 5 displays the binary extraction result of brain tumor images, represented in matrix form.

Figure 5 displays the result of image extraction in the form of a binary data matrix that can be used to generate a histogram. Figure 5 shows an image with a size of 150x150, which means that the value of n is 22,500 pixels. To determine the value of n_i the number of occurrences of each binary data needs to be known. Figure 6 represents the histogram generated from processing the binary data of brain tumor images.

The difference in the proposed architectural model lies in the use of the input image size which uses a size of 150x150 for AlexNet and GoogLeNet respectively. The actual input image size of AlexNet is 227x227 while GoogLeNet is 224x224. The size of 150x150 is proposed because it will reduce the computational load and the model training process is relatively fast.

2. 4. Training Model A training dataset for image in machine learning is a collection of image data used to train models or algorithms to learn visual patterns. This dataset plays a crucial role in tasks such as image recognition, object detection, segmentation, and various other image processing tasks. Essentially, each image in

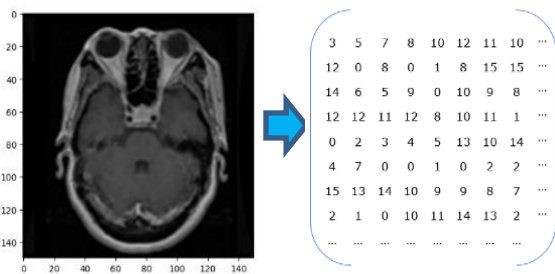


Figure 5. Binary data of brain image

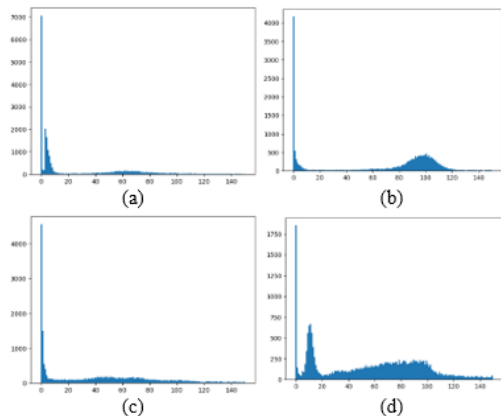


Figure 6. Histogram image (a) glioma (b) notumor (c) meningioma (d) pituitary

the training dataset is considered as an input consisting of a pixel matrix that represents the light intensity at each point in the image. The pixel values are typically represented on a scale of 0-255, where 0 represents the color black and 255 represents the color white. In addition, labels or annotations are also an integral part of a training dataset for images. These labels serve to provide information about the class or category represented by each image in the dataset. For example, in a face recognition dataset, each image would be assigned a label indicating the identity of the person depicted in the image. These labels are necessary to train the model to recognize and differentiate between different objects or classes. In the context of this study, the labels represent the classes of the dataset, which include glioma, notumor, meningioma, and pituitary.

The training of the model is an essential step in the experimentation process before conducting model testing. The initially created model may not classify images accurately since it hasn't learned from the dataset. Therefore, the training phase is crucial as the model needs to learn to recognize patterns in the given dataset (43). The model is first trained using the training data, which consists of 6,320 (90%) images out of the total 7,023 brain MRI dataset. This allows the model to learn from the provided dataset. Before training, the training data is divided into 32 batches (batch size). The training process is carried out for 20 iterations (epochs). Each model used in this research is trained with a scenario of batch size 32, 20 epochs, a learning rate of 0.001, and the Adam optimization algorithm, which is known to perform better than other optimization algorithms (31).

2. 5. Testing Model This stage is performed after the model is trained using the training data. The purpose of this stage is to test the created model's ability to classify brain images using data that the model has never seen before. The testing data consists of 703 (10%) images from the total 7,023 brain MRI dataset. The results of the testing phase using the testing data are presented in the form of a confusion matrix for further analysis. A confusion matrix is a tool that displays and compares the actual values or ground truth values with the predicted values generated by the model. The results from the confusion matrix can be used to calculate evaluation metrics such as precision, recall, and F1-score. Additionally, the confusion matrix allows for the calculation of the accuracy of each model.

Figure 7 displays the confusion matrix obtained from the model testing. The confusion matrix includes the values TP (True Positive), TN (True Negative), FP (False Positive), and FN (False Negative). TP represents the correctly predicted data for each class. For example, the TP value for the glioma class is A1, for the meningioma class is B2, for the notumor class is C3, and for the pituitary class is D4. TN is the sum of all values in the

A1	A2	A3	A4
B1	B2	B3	B4
C1	C2	C3	C4
D1	D2	D3	D4

Figure 7. Confusion matrix

matrix excluding the values from the corresponding row and column of the class. For example, the TN value for the glioma class includes B2, B3, B4, C2, C3, C4, D2, D3, and D4. FP is the sum of each column in the class excluding the TP values. For example, the FP value for the glioma class includes B1, C1, and D1. FN is the sum of each row excluding the TP values. For example, the FN value for the glioma class includes A2, A3, and A4. The obtained results from the confusion matrix are processed to calculate the accuracy percentage for each model created. The processing of the confusion matrix results is performed using the following equation (44, 45).

$$Precision = \frac{TP}{TP+FP} \quad (5)$$

$$Recall = \frac{TP}{TP+FN} \quad (6)$$

$$F1 - Score = 2 \times \frac{Precision \times Recall}{Precision + Recall} \quad (7)$$

$$Accuracy = \frac{\sum TP}{Total Data} \quad (8)$$

Precision is the ratio of TP (True Positive) to the total number of data predicted as positive. A smaller value of FP (False Positive) will increase the precision value. Recall is the ratio of TP to the total number of data actually positive. A smaller value of FN (False Negative) will increase the recall value. F1-Score is the harmonic mean of precision and recall. The best F1-Score value is 1.0, and the worst value is 0. Accuracy measures the correctness of the predicted values compared to the true values. Model testing uses accuracy to evaluate the performance of a model in classification. Each model used in this study was tested using the same testing scenario. After going through all the aforementioned steps, the next step is to examine the best test results based on the accuracy percentage of each model used in classifying brain tumor images based on their labels.

Additionally, attention is also given to the training time required based on the number of iterations performed.

3. RESULT AND DISCUSSION

This study was conducted by reviewing several previous research papers. Some of the studies found related to this research achieved high accuracy, with an average accuracy above 90% (23, 28-30). This presents a challenge in conducting research to improve the accuracy using the same method (CNN) and the same object of study (brain tumor images).

3. 1. Result This research was conducted using the same dataset, which is the dataset of human brain MRI scans, to perform classification using two different architectures. Although this study employs the same method, the difference lies in the feature extraction stage, where the feature extraction is performed using the AlexNet and GoogLeNet architectures. Prior to inputting the images into these architectures, the data undergoes preprocessing to ensure consistency with other datasets. The research yields two main results: the training model results and the testing model results.

3. 1. 1. Training Model The training process is carried out using the Adam optimization, which assists the model in training. Adam aims to iteratively update the weights based on the training data. Adam optimization is a method that computes different learning rates for each parameter. In this research, the dataset consists of 7023 brain image data, which would require a significant amount of time if all the data were trained together due to the limitations of computer memory. To address this, parameters such as Batch Size and Epoch are utilized. Batch Size is a parameter used to divide the dataset into smaller groups, allowing the computer to process them one by one and update the obtained values at the end of each training data. The batch size value used in this study is 32, meaning the model will train on 32 groups of data and update the obtained values at the end of training.

The model training is performed iteratively to allow the model to learn the data accurately, as the previously learned data is revisited. Misclassifications or erroneous classifications of brain image datasets during the initial training process are learned again, enabling the second training to be correct. This helps reduce the model's errors in performing classification tasks. The model training process is conducted with 20 epochs, where each model undergoes 20 iterations. There is another parameter used in this study, called ReduceLRonPlateau, which reduces the learning rate if the model fails to show progress in learning based on the current learning rate during an epoch. After the completion of model training,

the results of each model experiment are saved in the .h5 format for future use in training. The training results of the dataset using the AlexNet and GoogLeNet architectures can be seen in Table 1.

Table 1 shows the results of the training data with 20 iterations. The first iteration of the AlexNet model took 111 seconds and achieved an accuracy of 0.79 with a loss of 0.56. This result is relatively low because the model is initially learning from new data, so subsequent iterations are needed to further improve its learning. On the other hand, the GoogLeNet model achieved an accuracy of 0.27 and a loss of 1.3 in the first iteration, taking a total of 156 seconds. This result is lower compared to the first iteration of the AlexNet model.

In the second iteration, there is an improvement in accuracy for both models, accompanied by a decrease in the training time. The AlexNet model achieved an accuracy of 0.87 and a loss of 0.32. This demonstrates that AlexNet is capable of improving accuracy, reducing loss values, and reducing the time required for iterations. On the other hand, the GoogLeNet model achieved an accuracy of 0.63 and a loss of 0.85. This indicates a significant increase in accuracy from 0.27 in the first iteration to 0.63 in the second iteration. Moreover, there

TABLE 1. Training result

Epoch	AlexNet		GoogLeNet	
	Loss	Accuracy	Loss	Accuracy
1	0.56	0.79	1.3	0.27
2	0.32	0.87	0.85	0.63
3	0.37	0.84	0.61	0.71
4	0.56	0.78	0.47	0.81
5	0.17	0.93	0.38	0.83
6	0.19	0.92	0.28	0.89
7	0.17	0.93	0.25	0.91
8	0.1	0.96	0.24	0.91
9	0.15	0.93	0.18	0.93
10	0.09	0.96	0.21	0.92
11	0.09	0.96	0.21	0.92
12	0.14	0.94	0.14	0.94
13	0.08	0.96	0.09	0.96
14	0.07	0.97	0.1	0.96
15	0.08	0.97	0.12	0.96
16	0.08	0.97	0.07	0.97
17	0.08	0.97	0.08	0.96
18	0.07	0.97	0.1	0.96
19	0.07	0.97	0.08	0.97
20	0.07	0.97	0.08	0.97

was a significant decrease in the loss value from 1.3 to 0.27. The training time also decreased in the second iteration, with 111 seconds decreasing to 110 seconds for the AlexNet model and 156 seconds decreasing to 148 seconds for the GoogLeNet model. Figure 8 represents the accuracy graph of the training results for the dataset using the AlexNet and GoogLeNet models.

Figure 8 shows that the average results obtained initially had low values, but there was an improvement in accuracy in subsequent iterations. This indicates that both models are capable of learning the data effectively, and as the iterations progress, the accuracy increases. This improvement in accuracy also influences the loss values obtained. Figure 9 represents the graph of the loss values obtained during the training process.

Figure 9 illustrates a decreasing trend in the loss value with each iteration. This indicates that the models are able to reduce errors and learn the brain tumor dataset effectively. The decreasing loss values signify that the models are improving their ability to make accurate predictions and minimize the discrepancy between predicted and actual values in the dataset.

3.1.2. Testing Model The dataset used for training consists of 90% of the data, while 10% is used for testing the model. The purpose of testing the model is to determine its accuracy or performance. The model that was trained on the training data is used again for testing

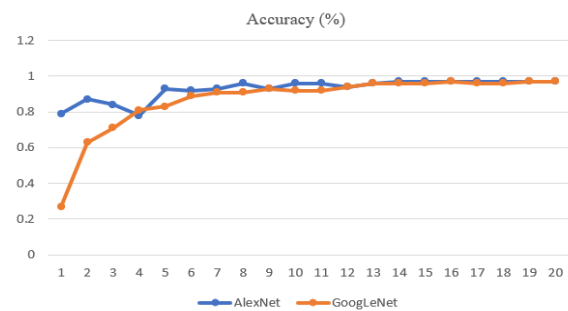


Figure 8. Accuracy training result

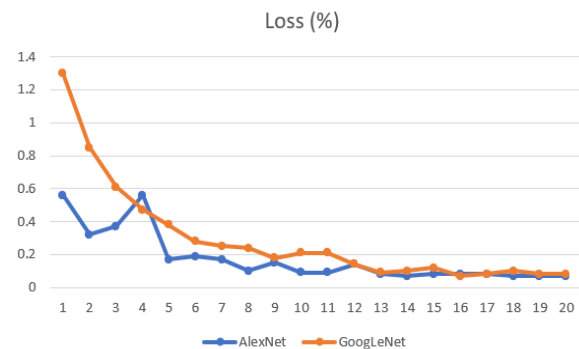


Figure 9. Loss training result

by providing a dataset that has not been previously seen by the model. This allows the model to classify the data according to what it has learned before. The results are visualized in the form of a confusion matrix, which consists of correctly classified and misclassified data for each image class. A total of 703 images are used, including 170 images of the glioma class, 203 images of the non-tumor class, 174 images of the meningioma class, and 156 images of the pituitary class. Figures 10 and 11 show the classification results visualized in the form of a confusion matrix for both the AlexNet and GoogLeNet models.

Figure 10 represents the classification results using the AlexNet model. Based on Figure 7, it is visualized in Table 2.

Table 2 shows that the highest classification result is achieved in the notumor class, where 100% of the images are correctly classified according to their classes. On the other hand, the lowest accuracy is obtained in the glioma class, with an accuracy of 95%. Despite being the lowest, this accuracy is still considered very high. The data from the confusion matrix is used in the accuracy formula to calculate the accuracy percentage. The confusion matrix resulting from the testing of the model using AlexNet achieved an accuracy of 98%, indicating that 688 images were correctly classified according to their respective classes. However, there were 15 misclassified images, accounting for a 2% error rate.

The GoogLeNet algorithm performed classification using a 10% subset of the total dataset, similar to how the dataset was used for testing the AlexNet model. One of the methods employed in GoogLeNet was image reduction, which aimed to reduce the input images while preserving crucial information. Figure 11 displays the confusion matrix obtained from evaluating the GoogLeNet model. The confusion matrix provides a visual representation of the classification results for each class. The analysis of the confusion matrix reveals the

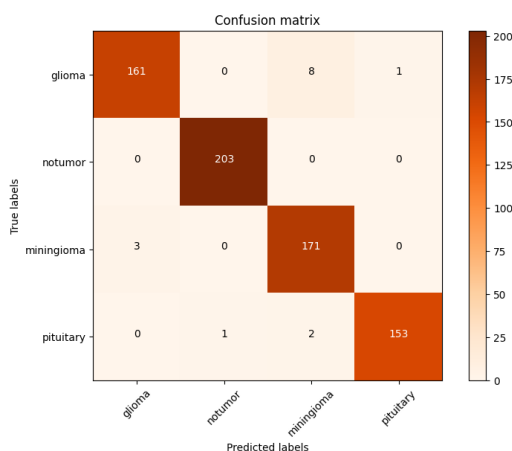


Figure 10. Confusion matrix result using AlexNet architecture

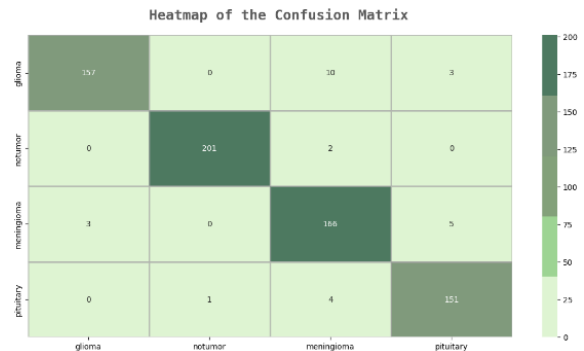


Figure 11. Confusion matrix result using GoogLeNet

TABLE 2. Classification result using AlexNet architecture

Class	Classification True	Dataset size	Accuracy (%)
Glioma	161	170	95
Notumor	203	203	100
Meningioma	171	174	98
Pituitary	153	156	98

performance of the GoogLeNet model in classifying the images.

Figure 11 displays the confusion matrix obtained from testing the pre-trained GoogLeNet architecture using a dataset of 6,335 images. The model was evaluated using a set of 703 images. The results of the testing, as shown in the confusion matrix, are visualized in Table 3.

Table 3 shows that the highest accuracy in the testing results is achieved in the "notumor" class, with a percentage of 99%. Out of a total of 203 "notumor" images, 201 of them were correctly classified. To examine the misclassified data, we can refer to the confusion matrix in Figure 11. The confusion matrix reveals that 2 misclassified data points in the "notumor" class were incorrectly classified as "meningioma". On the other hand, the lowest percentage is observed in the "glioma" class, where 157 out of 170 total "glioma" images were correctly classified. Although the accuracy is the lowest among the four classes in the dataset, it still achieves a high accuracy rate of 92%. Based on these results, the testing of the GoogLeNet architecture yields an accuracy percentage of 96%, with a total of 675 out of

TABLE 3. Testing result using GoogLeNet architecture

Class	Classification True	Dataset size	Accuracy (%)
Glioma	157	170	92
Notumor	201	203	99
Meningioma	166	174	95
Pituitary	151	156	97

703 test images being correctly classified into their respective classes. However, 28 images, accounting for 4% of the total test data, are still misclassified.

The obtained confusion matrix results from the dataset testing can be processed to evaluate the model's performance in correctly identifying specific classes by determining the values of Precision (P), Recall (R), and F1-Score (F1S). Here is Table 4 displaying the results obtained from the confusion matrix.

Based on Table 4, the obtained precision values are 0.98 for the AlexNet architecture and 0.96 for the GoogLeNet architecture. The "notumor" class achieves an excellent precision score as it obtains a value of 1.0 in both algorithms. This indicates that the algorithms can effectively identify images with and without tumors. Meanwhile, the Recall value for the AlexNet algorithm is 0.98, which is better than the GoogLeNet value of 0.96. F1-Score is calculated from the Precision and Recall values, where it represents the harmonic mean of precision and recall. It indicates the balance between correctly identifying positive results and the proportion of false negatives. The obtained F1-Score values are 0.98 for the AlexNet architecture and 0.96 for the GoogLeNet architecture. The F1-Score values obtained for both architectures indicate that the classification models have good precision and recall.

This research shows that the use of appropriate input images greatly influences the accuracy in classifying medical images of brain tumors. Apart from that, this research also succeeded in reducing the computational load when training the model because the image size has been changed to be smaller.

3. 2. Discussion This study was conducted to test the architectures used in classifying brain images into four classes with a dataset of 7023 images. The highest accuracy was obtained for the "notumor" class, both using the AlexNet and GoogLeNet architectures. Meanwhile, the lowest accuracy was obtained for the glioma class, with 94% accuracy for the AlexNet architecture and 92% accuracy for the GoogLeNet architecture.

The results obtained in this study showed an accuracy of 98% for the AlexNet architecture and 96% for the GoogLeNet architecture. These accuracy percentages can

TABLE 4. Processed results of confusion matrix

Class	AlexNet			GoogLeNet		
	P	R	F	P	R	F
Glioma	0.98	0.95	0.96	0.98	0.92	0.95
Notumor	0.32	0.87	110	0.85	0.63	148
Meningioma	0.37	0.84	109	0.61	0.71	148
pituitary	0.56	0.78	121	0.47	0.81	146

be categorized as very high compared to previous studies on brain tumor classification using CNN architectures. Table 5 presents the accuracy results obtained in previous research using brain tumor images.

Based on Table 5, it can be observed that the previous research achieved the highest accuracy of 94.2%. This result is lower than the accuracy obtained in this study, both using the AlexNet and GoogLeNet architectures. Table 5 shows that from 2018, research related to brain image classification using CNN achieved an accuracy of 91.9%. In the following year, there was an improvement in accuracy with the same research achieving 93.68%. Similarly, from 2019 to 2020, the accuracy reached 94%.

This research achieved a higher accuracy compared to previous studies, demonstrating that it can improve upon previous results using the same images and methodology. This improvement can be attributed to several factors. Firstly, the dataset used in this research consists of 7,023 brain images, while the previous study utilized only 3,064 images. The larger dataset allows for a more comprehensive training of the model and can lead to better accuracy. Another factor contributing to the increased accuracy is the use of the same architecture, CNN, as in the previous study. However, in this research, the CNN architecture was enhanced by incorporating additional feature extraction stages that differ from the previous study. Feature extraction plays a crucial role in improving accuracy, as more filters used in the process result in more feature maps generated. Additionally, employing multiple convolutional stages generates a greater number of image models, which serve as the basis for classification in the fully connected layer.

TABLE 5. Comparison with some previous studies

Author	Year	Dataset Size	Accuracy (%)
Ismael and Qader (30)	2018	3064	91.9
Pashaei et al. (23)	2018	3064	93.68
Anaraki et al. (31)	2019	600	94
Baranwal et al. (32)	2020	3064	94
Our Studies (AlexNet)	2023	7023	98
Our Studies (GoogLeNet)	2023	7023	96

4. CONCLUSION

This research succeeded in increasing the classification accuracy of medical images of brain tumors by utilizing the AlexNet and GoogLeNet architectures. Both architectures make changes to the input image using a size of 150x150. This size is much smaller than the original size of the input image in AlexNet and GoogLeNet. However, the input image has been proven

to increase accuracy and be able to speed up the computing process due to its smaller size. The AlexNet architecture achieved higher accuracy compared to the GoogLeNet architecture. Both architectures demonstrated higher accuracy compared to several previous studies. These results suggest that the AlexNet and GoogLeNet architectures in CNN can improve the accuracy percentage for brain tumor image classification. Based on these findings, the AlexNet and GoogLeNet architectures can diagnose brain tumor diseases based on MRI images. The accuracy obtained in the "notumor" class using the AlexNet algorithm was able to identify all the datasets that did not have brain tumor diseases. Patients with brain images from MRI scans can be diagnosed without having to consult a doctor, reducing the cost of expensive consultations. Additionally, this diagnosis can be conducted rapidly without waiting for laboratory examinations such as biopsy, which can take 10 to 15 days.

We hope that in future research, there will be ways to further increase the accuracy compared to this study, to minimize errors in diagnosing brain tumor diseases using machine learning. This would ensure that patients receive prompt and accurate treatment.

5. ACKNOWLEDGMENTS

This work is supported by the Ministry of Education, Culture, Research, and Technology of the Republic of Indonesia based on Contract number: 181/E5/PG.02.00.PL/2023. The authors also gratefully acknowledge the helpful comments and suggestions of the reviewers, which have improved the presentation.

6. REFERENCES

- Nawaz SA, Khan DM, Qadri S. Brain tumor classification based on hybrid optimized multi-features analysis using magnetic resonance imaging dataset. *Applied Artificial Intelligence*. 2022;36(1):2031824. 10.1080/08839514.2022.2031824
- Nanda SJ, Gulati I, Chauhan R, Modi R, Dhaked U. A K-means-galactic swarm optimization-based clustering algorithm with Otsu's entropy for brain tumor detection. *Applied Artificial Intelligence*. 2019;33(2):152-70. 10.1080/08839514.2018.1530869
- Angeli S, Emblem KE, Due-Tonnessen P, Stylianopoulos T. Towards patient-specific modeling of brain tumor growth and formation of secondary nodes guided by DTI-MRI. *NeuroImage: Clinical*. 2018;20:664-73. 10.1016/j.nicl.2018.08.032
- Miller KD, Ostrom QT, Kruchko C, Patil N, Tihan T, Cioffi G, et al. Brain and other central nervous system tumor statistics, 2021. *CA: a cancer journal for clinicians*. 2021;71(5):381-406. 10.3322/caac.21693
- Le D-N, Parvathy VS, Gupta D, Khanna A, Rodrigues JJ, Shankar K. IoT enabled depthwise separable convolution neural network with deep support vector machine for COVID-19 diagnosis and classification. *International journal of machine learning and cybernetics*. 2021:1-14. 10.1007/s13042-020-01248-7
- Hamghalam M, Wang T, Lei B. High tissue contrast image synthesis via multistage attention-GAN: application to segmenting brain MR scans. *Neural Networks*. 2020;132:43-52. 10.1016/j.neunet.2020.08.014
- Arunachalam S, Sethumathavan G. An effective tumor detection in MR brain images based on deep CNN approach: i-YOLOV5. *Applied Artificial Intelligence*. 2022;36(1):2151180. 10.1080/08839514.2022.2151180
- Badr CE, Silver DJ, Siebzehrubel FA, Deleyrolle LP. Metabolic heterogeneity and adaptability in brain tumors. *Cellular and Molecular Life Sciences*. 2020;77:5101-19. 10.1007/s00018-020-03569-w
- Qu Z, Cao C, Liu L, Zhou D-Y. A deeply supervised convolutional neural network for pavement crack detection with multiscale feature fusion. *IEEE transactions on neural networks and learning systems*. 2021;33(9):4890-9. 10.1109/TNNLS.2021.3062070
- Amjoud AB, Amrouch M. Object Detection Using Deep Learning, CNNs and Vision Transformers: A Review. *IEEE Access*. 2023. 10.1109/ACCESS.2023.3266093
- Chahal PK, Pandey S, Goel S. A survey on brain tumor detection techniques for MR images. *Multimedia Tools and Applications*. 2020;79:21771-814. 10.1007/s11042-020-08898-3
- Takahashi M, Miki S, Fujimoto K, Fukuoka K, Matsushita Y, Maida Y, et al. Eribulin penetrates brain tumor tissue and prolongs survival of mice harboring intracerebral glioblastoma xenografts. *Cancer Science*. 2019;110(7):2247-57. 10.1111/cas.14067
- Li Q, Liu X, He Y, Li D, Xue J. Temperature guided network for 3D joint segmentation of the pancreas and tumors. *Neural Networks*. 2023;157:387-403. 10.1016/j.neunet.2022.10.026
- Zohrevand A, Imani Z. Holistic persian handwritten word recognition using convolutional neural network. *International Journal of Engineering*. 2021;34(8):2028-37. 10.5829/ije.2021.34.08b.24
- Siddique MAB, Arif RB, Khan MMR, editors. *Digital image segmentation in matlab: A brief study on otsu's image thresholding*. 2018 international conference on innovation in engineering and technology (ICIET); 2018: IEEE. 10.1109/CIET.2018.8660942
- Mulyadi R, Islam AA, Murtala B, Tammase J, Hatta M, Firdaus M. Diagnostic yield of the combined Magnetic Resonance Imaging and Magnetic Resonance Spectroscopy to predict malignant brain tumor. *bmj*. 2020;9:1486. 10.15562/bmj.v9i1.1486
- Isaieva K, Laprie Y, Turpault N, Houssard A, Felblinger J, Vuissoz P-A. Automatic tongue delineation from mri images with a convolutional neural network approach. *Applied Artificial Intelligence*. 2020;34(14):1115-23. 10.1080/08839514.2020.1824090
- Shamrat FJM, Azam S, Karim A, Ahmed K, Bui FM, De Boer F. High-precision multiclass classification of lung disease through customized MobileNetV2 from chest X-ray images. *Computers in Biology and Medicine*. 2023;155:106646. 10.1016/j.compbiomed.2023.106646
- Nawaz A, Rehman AU, Ali TM, Hayat Z, Rahim A, Uz Zaman UK, et al. A Comprehensive Literature Review of Application of Artificial Intelligence in Functional Magnetic Resonance Imaging for Disease Diagnosis. *Applied Artificial Intelligence*. 2021;35(15):1420-38. 10.1080/08839514.2021.1982185
- Khan AI, Wani MA. Patch-based segmentation of latent fingerprint images using convolutional neural network. *Applied*

- Artificial Intelligence. 2019;33(1):87-100. 10.1080/08839514.2018.1526704
21. Zhao X, Wu Y, Song G, Li Z, Zhang Y, Fan Y. A deep learning model integrating FCNNs and CRFs for brain tumor segmentation. *Medical image analysis*. 2018;43:98-111. 10.1016/j.media.2017.10.002
 22. Li Z, Liu F, Yang W, Peng S, Zhou J. A survey of convolutional neural networks: analysis, applications, and prospects. *IEEE transactions on neural networks and learning systems*. 2021. 10.1109/TNNLS.2021.3084827
 23. Pashaei A, Sajedi H, Jazayeri N, editors. Brain tumor classification via convolutional neural network and extreme learning machines. 2018 8th International conference on computer and knowledge engineering (ICCKE); 2018: IEEE. 10.1109/ICCKE.2018.8566571
 24. Oyewola DO, Dada EG, Misra S, Damaševičius R. A novel data augmentation convolutional neural network for detecting malaria parasite in blood smear images. *Applied Artificial Intelligence*. 2022;36(1):2033473. 10.1080/08839514.2022.2033473
 25. Niepceron B, Nait-Sidi-Moh A, Grassia F. Moving medical image analysis to GPU embedded systems: Application to brain tumor segmentation. *Applied Artificial Intelligence*. 2020;34(12):866-79. 10.1080/08839514.2020.1787678
 26. Billah ME, Javed F. Bayesian convolutional neural network-based models for diagnosis of blood cancer. *Applied Artificial Intelligence*. 2022;36(1):2011688. 10.1080/08839514.2021.2011688
 27. Rohani M, Farsi H, Mohamadzadeh S. Deep Multi-task Convolutional Neural Networks for Efficient Classification of Face Attributes. *International Journal of Engineering, Transactions B: Applications*. 2023;36(11):2102-11. 10.5829/ije.2023.36.11b.14
 28. Arabahmadi M, Farahbakhsh R, Rezazadeh J. Deep learning for smart Healthcare—A survey on brain tumor detection from medical imaging. *Sensors*. 2022;22(5):1960. <https://doi.org/10.3390/s22051960>
 29. Xie Y, Zaccagna F, Rundo L, Testa C, Agati R, Lodi R, et al. Convolutional neural network techniques for brain tumor classification (from 2015 to 2022): Review, challenges, and future perspectives. *Diagnostics*. 2022;12(8):1850. 10.3390/diagnostics12081850
 30. Ismael MR, Abdel-Qader I, editors. Brain tumor classification via statistical features and back-propagation neural network. 2018 IEEE international conference on electro/information technology (EIT); 2018: IEEE. 10.1109/EIT.2018.8500308
 31. Anaraki AK, Ayati M, Kazemi F. Magnetic resonance imaging-based brain tumor grades classification and grading via convolutional neural networks and genetic algorithms. *biocybernetics and biomedical engineering*. 2019;39(1):63-74. 10.1016/j.bbe.2018.10.004
 32. Baranwal SK, Jaiswal K, Vaibhav K, Kumar A, Srikantaswamy R, editors. Performance analysis of brain tumour image classification using CNN and SVM. 2020 Second International Conference on Inventive Research in Computing Applications (ICIRCA); 2020: IEEE. 10.1109/ICIRCA48905.2020.9183023
 33. Deepak S, Ameer P. Brain tumor classification using deep CNN features via transfer learning. *Computers in biology and medicine*. 2019;111:103345. 10.1016/j.compbiomed.2019.103345
 34. Daniel MC, Ruxandra LM, editors. Brain Tumor Classification Using Pretrained Convolutional Neural Networks. 2021 16th International Conference on Engineering of Modern Electric Systems (EMES); 2021: IEEE. 10.1109/EMES52337.2021.9484102
 35. Emadi M, Jafarian Dehkordi Z, Iranpour Mobarakeh M. Improving the accuracy of brain tumor identification in magnetic resonance imaging using super-pixel and fast primal dual algorithm. *International Journal of Engineering, Transactions A Basics*.. 2023;36(3):505-12. 10.5829/ije.2023.36.03c.10
 36. Rehman A, Naz S, Razzak MI, Akram F, Imran M. A deep learning-based framework for automatic brain tumors classification using transfer learning. *Circuits, Systems, and Signal Processing*. 2020;39:757-75. 10.1007/s00034-019-01246-3
 37. Alem A, Kumar S. End-to-End Convolutional Neural Network Feature Extraction for Remote Sensed Images Classification. *Applied Artificial Intelligence*. 2022;36(1):2137650. 10.1080/08839514.2022.2137650
 38. M. Alqhtani S. BreastCNN: a novel layer-based convolutional neural network for breast cancer diagnosis in DMR-thermogram images. *Applied Artificial Intelligence*. 2022;36(1):2067631. 10.1080/08839514.2022.2067631
 39. Agrawal R, Sharma M, Singh BK. Performance evaluation of automated brain tumor detection systems with expert delineations and interobserver variability analysis in diseased patients on magnetic resonance imaging. *Applied Artificial Intelligence*. 2018;32(7-8):670-91. 10.1080/08839514.2018.1504500
 40. Hasan MM, Ali H, Hossain MF, Abujar S, editors. Preprocessing of continuous bengali speech for feature extraction. 2020 11th International Conference on Computing, Communication and Networking Technologies (ICCCNT); 2020: IEEE. 10.1109/ICCCNT49239.2020.9225469
 41. Pitak L, Saengprachatanarug K, Laloon K, Posom J. Predicting the true density of commercial biomass pellets using near-infrared hyperspectral imaging. *Artificial Intelligence in Agriculture*. 2022;6:266-75. 10.1016/j.aiaa.2022.11.004
 42. Alamri NMH, Packianather M, Bigot S. Deep learning: Parameter optimization using proposed novel hybrid bees Bayesian convolutional neural network. *Applied Artificial Intelligence*. 2022;36(1):2031815. 10.1080/08839514.2022.2031815
 43. Augusto Costa J, Carmona Cortes O. A Convolutional Neural Network for Detecting Faults in Power Distribution Networks along a Railway: A Case Study Using YOLO. *Applied Artificial Intelligence*. 2021;35(15):2067-86. 10.1080/08839514.2021.1998974
 44. Alzughabi S, El Khediri S. A Cloud Intrusion Detection Systems Based on DNN Using Backpropagation and PSO on the CSE-CIC-IDS2018 Dataset. *Applied Sciences*. 2023;13(4):2276. 10.3390/app13042276
 45. Tri Handoyo A, Kusuma GP. Severity Classification of Diabetic Retinopathy Using Ensemble Stacking Method. *Revue d'Intelligence Artificielle*. 2022;36(6). 10.18280/ria.360608

COPYRIGHTS

©2024 The author(s). This is an open access article distributed under the terms of the Creative Commons Attribution (CC BY 4.0), which permits unrestricted use, distribution, and reproduction in any medium, as long as the original authors and source are cited. No permission is required from the authors or the publishers.



Persian Abstract

چکیده

تومورهای مغزی یکی از کشنده ترین بیماری ها در جهان هستند. این بیماری می تواند هر فردی را بدون در نظر گرفتن جنسیت یا گروه های سنی خاص مورد حمله قرار دهد. تشخیص تومورهای مغزی با شناسایی دستی تصاویر حاصل از اسکن توموگرافی کامپیوتری یا تصویربرداری تشدید مغناطیسی انجام می شود و امکان بروز خطاهای تشخیصی را فراهم می کند. علاوه بر این، تشخیص را می توان با استفاده از تکنیک های بیوپسی انجام داد. این تکنیک بسیار دقیق است، اما زمان زیادی طول می کشد، حدود 10 تا 15 روز و شامل تجهیزات و پرسنل پزشکی زیادی است. بر این اساس، فناوری یادگیری ماشینی مورد نیاز است که بتواند بر اساس تصاویر تولید شده از MRI طبقه بندی کند. هدف این تحقیق افزایش دقت تحقیقات قبلی در طبقه بندی تومورهای مغزی است تا در تشخیص تومورهای مغزی خطا رخ ندهد. روش مورد استفاده در این تحقیق شبکه عصبی کانولوشن با استفاده از معماری AlexNet و GoogLeNet است. نتایج این تحقیق برای معماری AlexNet 98% و برای GoogLeNet 96% به دست آورد. این نتیجه در مقایسه با تحقیقات قبلی بیشتر است. این یافته می تواند بار محاسباتی را در طول آموزش مدل کاهش دهد. نتایج این تحقیق می تواند به پزشکان در تشخیص سریع و دقیق تومورهای مغزی کمک کند.



Machine Learning Models for Mechanical and Micro Structural Properties of Recycled Fine Aggregate Concrete Using Different Mixing Approaches

A. Ranjith^{*a}, M. K. Yashwanth^b, B. M. Kiran^c, V. R. Ananda^d

^a Department of Civil Engineering, Nitte (Deemed to be University), NMAM Institute of Technology, Nitte, Karnataka, India

^b Department of Civil Engineering, Maharaja Institute of Technology Mysore, Mandya, Karnataka, India

^c Department of Civil Engineering, AdiChunchanagiri Institute of Technology, Chikmagalur, Karnataka, India

^d Department of Civil Engineering, Vivekananda College of Engineering and Technology, Puttur, Karnataka, India

PAPER INFO

Paper history:

Received 09 November 2023

Received in revised form 13 December 2023

Accepted 30 December 2023

Keywords:

Recycled Aggregate Concrete

Recycled Fine Aggregate

Particle Packing

Compressive Strength

Micro Structure

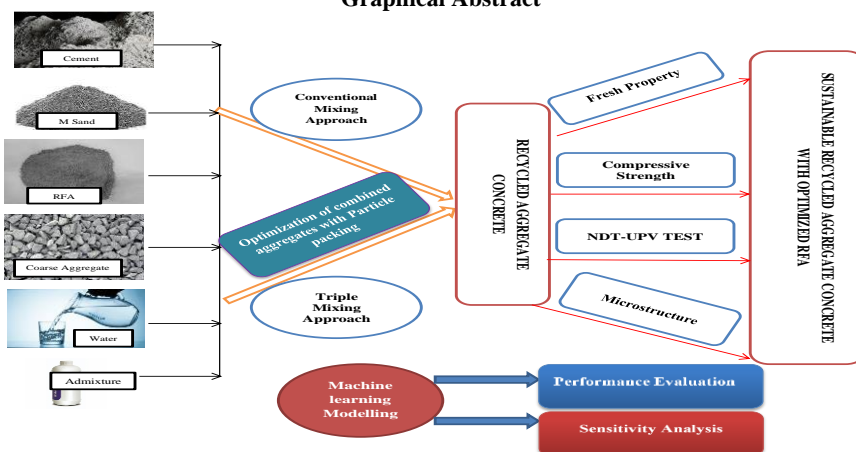
Machine Learning

ABSTRACT

The construction industry is primarily responsible for the depletion of natural resources and the disruption of environmental equilibrium due to unregulated mining activities. In this particular context, the utilization of recycled fine aggregate (RFA) derived from construction and demolition (C&D) waste presents itself as a viable solution. The conventional method of mix proportioning for RFA in concrete is not applicable in this case. The main innovation of our research lies in the fulfilment of one of the principles of circular economy, namely the reduction of carbon emissions, through the recycling of locally collected concrete waste. To tackle this issue, a novel triple mix-proportioning approach has been developed using the concepts of maximum packing density and minimum paste theory. The fresh and hardened properties were evaluated and microstructural characterization was carried out for the newly formulated mixes incorporating RFA with optimized combined aggregates. The compressive strength of concrete with recycled fine aggregate increases by 5.04% for 25% and, 21.69% for 50% replacement, and decreases by 35.44% for 100% replacement as compared to controlled concrete at the age of 28 days using the triple mixing approach. The findings indicate that replacing approximately 50% of sand with RFA is the optimal amount, as further replacement leads to a decrease in compressive strength, particularly at 100% replacement due to the presence of adhered mortar in RFA. In this study, the performance evaluation of RFA concrete has been conducted by comparing six established ML regression models and sensitivity analysis was performed to assess the variable's performance.

doi: 10.5829/ije.2024.37.05b.16

Graphical Abstract



*Corresponding Author Email: ranjith.anand70@gmail.com (A. Ranjith)

Please cite this article as: Ranjith A, Yashwanth MK, Kiran BM, Anand VR, Machine Learning Models for Mechanical and Micro Structural Properties of Recycled Fine Aggregate Concrete Using Different Mixing Approaches. International Journal of Engineering, Transactions B: Applications. 2024;37(05):997-1011.

1. INTRODUCTION

Recently, there has been an increase in the utilization of recycled aggregate in concrete owing to its potential in curbing environmental pollution and conserving natural resources. Over the period of 2005-2013, India generated an estimated 165-175 million tons of construction and demolition (C&D) debris on an annual basis (1). The deposit of this waste material in a landfill has had detrimental effects on the ecosystem. India has put forth a series of policies aimed at promoting the use of recycled aggregates as a substitute for natural aggregates in various applications (2). The mining of M sand from rocks or quarries has also contributed to environmental hazards. The utilization of recycled coarse aggregates (RCA) in concrete has undergone extensive research in various countries and has been implemented on a global scale (3). In contemporary society, there is a growing apprehension regarding the escalating magnitude of Construction and Demolition (C&D) substances as well as the significant fraction of refuse amassing in landfills (4). Within the realm of construction, a substantial portion of refuse originates from the demolition of edifices. The exorbitant expenses associated with disposal, which encompass dumping fees and landfill taxes, coupled with the limited accessibility of disposal sites, present an opportunity for the advancement of high-performance concrete (HPC) that incorporates refuse substances as a viable alternative (5).

India has recently garnered attention for its efforts to promote sustainable materials in the construction sector. The utilization of recycled concrete brings forth a multitude of notable advantages, fostering environmental sustainability and enhancing efficiency within the industry. Primarily, it diminishes the need for natural aggregates; thereby conserving crucial resources such as gravel and sand, all while mitigating the adverse environmental effects associated with quarrying and extraction processes. Furthermore, the recycling of concrete diverts construction and demolition waste away from landfills, resulting in reduced waste and the cultivation of a circular economy approach. Additionally, the incorporation of recycled concrete as a partial substitute for natural aggregates facilitates energy conservation during concrete production, predominantly in the realm of cement manufacturing, thereby contributing to improved energy efficiency. It is also worth noting that adequately processed and integrated recycled concrete fortifies the mechanical properties of high strength concrete, culminating in structures that are more resilient and enduring.

The product's strength can be attributed to the fact that when water is added to the recycled sand, it activates some of the binding properties that the cementitious material, which had not been hydrated previously, possesses. Fine recycled concrete aggregates (RFAs)

include not only the original river sand, but also a significant amount of old cement matrix. This matrix can exist either as fine particles with a high-absorption capacity or as mortar adhered to the surface of the river sand particles. The presence of this adhering cement matrix has resulted in the RFAs having a lower density, greater water absorption, and reduced hardness and strength compared to natural fine aggregates (6, 7).

The existing literature has documented that the performance of concrete is adversely affected as the proportion of recycled fine aggregate (RFA) in the concrete increases (8-10). Nevertheless, studies have demonstrated that the introduction of superplasticizers or mineral admixtures yields more favorable outcomes (11-13). For the incorporation of RFA exceeding 20%, it becomes necessary to pre-soak the aggregates in order to attain the desired workability of the concrete (14).

Relatively limited research has been conducted on concrete made with recycled fine aggregates (RFAs) due to the notable porosity and substantial water absorption of the RFAs. The elevated porosity of the preexisting cement paste results in unfavorable properties of the interfacial transition zone (ITZ) (15). The water absorption rate of the RFAs was found to be 11-13% (11, 16), which exceeded that of the natural fine aggregate, further highlighting their high porosity.

In their study, Kumar et al. (16) found that the compressive and splitting tensile strengths of the concrete were reduced by 16% and 7.0%, respectively. When using recycled fine aggregates (RFA) in high strength concrete, the reduction in compressive strength ranged from 4% to 12%, while the reduction in splitting tensile strength was 24% for concrete containing 100% RFA (11, 17). Previous studies on RFA concrete (11, 18) showed that most slump values fell within the range of 80-134 mm. However, Yang et al. (19) investigated the use of high slump RFA concrete, with a slump range of 175-200 mm, but they focused solely on normal strength RFA concrete.

The conventional method of mix proportioning for RFA concrete does not improve the concrete's performance in the absence of additives or admixtures (20). On the other hand, different mixing approaches have enhanced the performance of concrete containing recycled coarse aggregates (RCA) (21). By incorporating RCA into the concrete mix, construction companies can effectively reduce their carbon footprint and contribute to the conservation of natural resources (22). Unfortunately, there have been limited studies on the suitable mix proportioning of concrete using RFA.

Recently, an assessment was conducted on the laboratory properties of recycled aggregate concrete. Moreover, constitutive relationships were established by simulating the experimental outcomes (23) and stress-strain characteristics (24) of developed beams, utilizing the ABAQUS software. To evaluate the torsional

capacity of both natural aggregate concrete (NAC) and recycled aggregate concrete (RAC) beams under pure torsion, an experimental investigation was conducted. The obtained results were subsequently validated by simulating them in the ATENA-3D simulation software (25). These types of studies demonstrate the increasing potential of recycled aggregate concrete for its structural applications (23, 25).

This necessitates the implementation of a sustainable and environmentally conscious strategy for the utilization of Recycled Fine Aggregate (RFA) in concrete. Within this framework, it is imperative to employ suitable techniques for the formulation of concrete mixes in order to maximize the efficient utilization of RFA as a substitute for river sand. The traditional method of mixing utilized in recycled aggregate concrete fails to enhance the performance of RAC. In order to address this issue, alternative mixing techniques such as the two-stage mixing approach (TSMA) and triple mixing (TM) have been implemented (26, 27). Thus, to promote sustainability and conserve natural resources, we have opted to partially substitute natural fine aggregates with recycled fine aggregates at varying levels of replacement, utilizing different mixing approaches in the preparation of concrete.

Furthermore, the results obtained for a specific recycled substance may rely on the geographic location and origin of the waste. Therefore, in order to incorporate a particular recycled fine aggregate in novel concrete mixtures for structural purposes, a thorough examination of multiple batches of the substance is necessary due to its variability and sensitivity to its source. The aim of this investigation is to assess the characteristics of locally produced RFA and explore the potential of substituting natural fine sand in concrete with recycled fine concrete aggregate. This is accomplished by considering various loading conditions through experimentation and by comparing the mechanical properties of concrete made with recycled fine aggregate to those of concrete made with natural sand.

The effectiveness of the recently formulated RFA concrete mixes is subsequently contrasted with the traditional concrete formulated according to IS 10262 (28). In this investigation, the assessment of RFA concrete performance has been carried out by comparing six well-established individual ML regression models. Moreover, statistical indicators have been utilized to compare the models. The findings imply that the ML approach shows significant potential in accurately forecasting performance. Additionally, a sensitivity analysis was conducted to evaluate the performance of the variable.

1. 1. Novelty and Research Significance

Concrete derived from recycled aggregate provides support for numerous sustainability initiatives due to its ability to conserve landfill space, manage construction

waste in a more environmentally friendly manner, diminish the necessity for aggregate extraction, and mitigate pollution caused by the mining of natural aggregate. Nonetheless, the utilization of recycled aggregate concrete (RAC) remains limited as a result of insufficient advancements in the realm of testing and specifications pertaining to its production. Consequently, there is a pressing demand for further investigation and enhancements in this field.

The bulk of previous research conducted on recycled concrete aggregates (RCA) has predominantly concentrated on coarse RCA (CRCA), while significantly less progress has been made in regards to the utilization of fine RCA particles (RFA).

The primary novelty of our investigation resides in fulfilling one of the principles of circular economy, namely, the reduction of the carbon footprint, through the recycling of locally collected concrete waste. In the current study, we endeavor to overcome the drawbacks of various mix design methods, thus introducing a maximum packing density with minimal paste design concept to enhance the performance parameters of RAC in a straightforward manner. This article presents an innovative approach to the proportioning of concrete, aiming to effectively utilize RFA by replacing different percentages of river sand with a combined gradation of RFA, intermediate (10 mm) aggregate, and coarse aggregate (20 mm). Machine learning models were employed to assess the performance evaluation of formulated RFA concrete mixtures, and the conducted sensitivity analysis reveals the most significant parameter ingredient. Figure 1 shows the visual appearance of materials used in experimental program.

2. MATERIALS AND METHODS

2. 1. Material Characterization Prior to utilization of any substance in the fabrication of recycled aggregate concrete, it is imperative to perform a comprehensive characterization. Therefore, experimental investigations were undertaken to ascertain the pertinent physical properties.

2. 1. 1. Cement The Portland Pozzolona Cement (PPC), which was utilized in this project and obtained from a local supplier, was manufactured by Maha cement and is compliant with the IS: 1489 (Part 1) (29) standards. The characteristics of the aforementioned PPC have been enumerated in Table 1.

2. 1. 2. Natural Coarse Aggregate The concrete utilized hard gravel that was crushed to a maximum size of 20mm. The fractions of aggregates used were divided into two categories: 20mm passing and 10mm retained at 60%, and 10mm passing and 4.75mm retained at 40%. This selection of aggregates adheres to IS: 383-2016 (30). Table

2 illustrates the properties of NCA. The coarse aggregate's sieve analysis is depicted in Figure 2.

2. 1. 3. Natural Fine Aggregates (NFA) Throughout our study, natural fine aggregate was replaced with Manufactured sand (M-sand) obtained from a local vendor. In accordance with IS: 383-2016 (30), M-sand complies

with Zone-II. Table 3 summarized the characteristics and physical properties of natural fine aggregate.

2. 1. 4. Recycled Fine Aggregate (RFA) Recycled fine aggregate (RFA) is procured through the pulverization of construction and demolition (C&D) waste into dimensions similar to those of natural fine aggregate. RFA adheres to the standards of Zone-II as

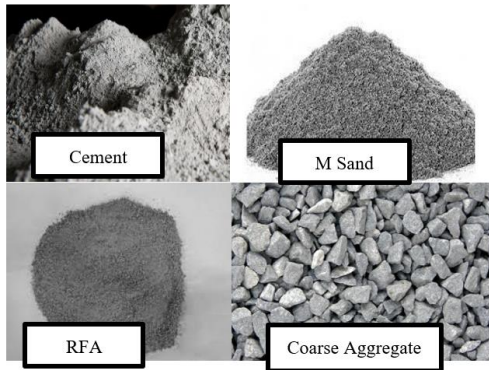


Figure 1. Visual Appearance of materials used in Experimental Program

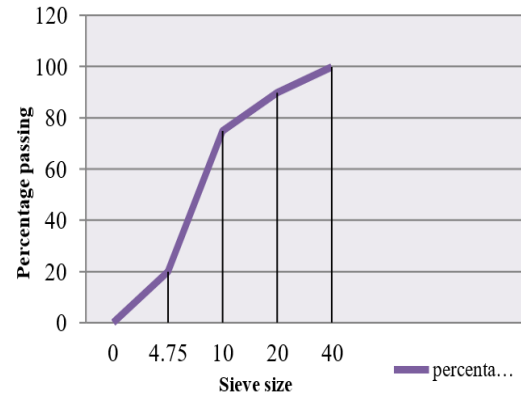


Figure 2. Sieve analysis of coarse aggregate

TABLE 1. Physical properties of cement (PPC Grade)

Sl. No.	Parameters	Test Results	Requirements as per IS:1489(part 1) (29)	Test code
1	Consistency	31		IS 4031(part 4):1988 (30)
2	Initial setting time (min)	240	Min 30 mins	IS 4031(part 5):1989 (31)
3	Final setting time (min)	270	Max 600 mins	IS 4031(part 5):1989 (31)
4	Soundness (mm)		10mm	IS:4031(part 3)-1988 (32)
5	Specific gravity	3.05	3 to 4	IS 4031-(part 3):1999 (33)
6	Fineness by Blaine's (m ² /kg)	366	Min 300	IS:4031(part 2)-1996 (34)
Compressive Strength				
7	3 days (MPa)	23	16	IS 4031-6:1988 (35)
	7 days (MPa)	33	22	(35)

TABLE 2. Physical properties of natural coarse aggregate

Sl No.	Parameters	Test Results	Requirements as per IS:383-2016	Test IS code
1.	Specific gravity	2.8	-	IS: 2386 (Part 3) (35)
2.	Water absorption	0.5%	-	IS: 2386 (Part 3) (35)
3.	Shape test Flakiness Index Elongation Index	23.5% 16.89%	< 30%	IS: 2386(Part 1)-1963 (36)
4.	Crushing value	27.45%	<45%	IS: 2386(Part 4)-1963 (37)
5.	Angularity Number	4.9	0 to 11	IS: 2386(Part 1)- 1963 (36)
Bulk density kg/m ³ (20mm passing-10mm retained)				
		1.59 g/ cm ³		
6.	Compacted Loosely Packed	1.51 g/ cm ³	-	IS: 2386(Part 3) (35)
(10mm passing-4.75mmretained) Compacted				
		1.55g/ cm ³ 1.51g/ cm ³	-	
Loosely packed				

TABLE 3. Physical properties of natural fine aggregate (NFA)

SI No.	Parameters	Test Results	Test code
1	Specific gravity	2.61	IS: 2386(Part 3) (35)
2	Fineness modulus	3.01	IS: 2386(Part 1) (36)
3	Sieve Analysis	Zone-II	IS: 2386(Part 1) (36)
4	Water Absorption	7 %	IS: 2386(Part 3) (35)
5	Loose Bulk Density	1.481g/ cm ³	IS: 2386(Part 3) (35)
6	Compacted Bulk Density	1.744 g/cm ³	IS: 2386(Part 3) (35)

outlined by IS: 383-2016 (38). The attributes of RFA are outlined in Table 4. Furthermore, a mineralogical analysis of the RFA was carried out through X-Ray diffraction (XRD) analysis. The XRD graph depicted in Figure 3 clearly exhibits the presence of silica, as indicated by the hump observed between 20-352θ.

2. 1. 5. Particle Size Analysis of NFA And RFA

The analysis of particle size for NFA, 25RFA+75NFA, 50NFA+50RFA, and RFA is appropriately delineated in Figure 4. It is noteworthy to mention that all specimens fall within zone II, as prescribed by IS: 383-2016 (38).

TABLE 4. Physical properties of recycled fine aggregate (RFA)

SI No.	Parameters	Test Results	Test code
1	Specific gravity	2.50	IS:2386(Part3) (35)
2	Fineness modulus	2.71	IS:2386(Part1) (37)
3	Sieve Analysis	Zone-II	IS:2386(Part1) (37)
4	Water Absorption	31.25%	IS:2386(Part3) (35)
5	Loose Bulk Density	1.24g/cc	IS:2386(Part3) (35)
6	Compacted Bulk Density	1.408 g/cc	IS:2386(Part3) (35)

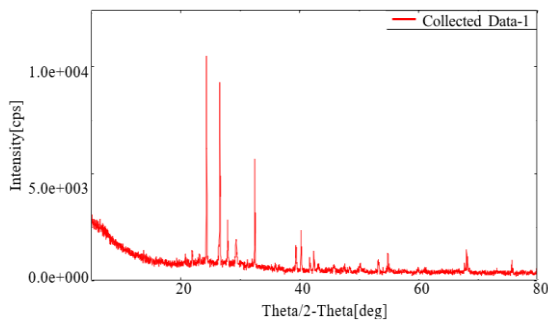


Figure 3. X-ray diffraction analysis of RFA

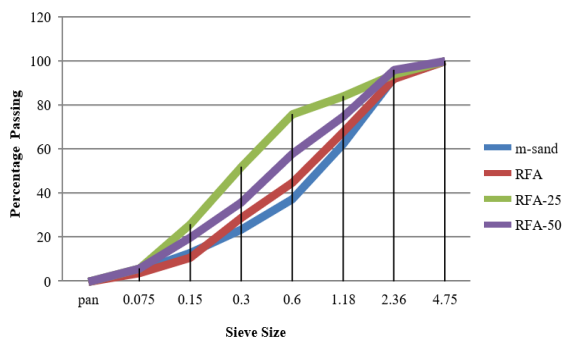


Figure 4. Particle size distribution of m sand, RFA, various replacement levels of RFA with msand

2. 1. 6. Chemical Admixture

The present study utilizes a chemical admixture known as Smart Care Maximo Plast PC-200, a superplasticizer based on polycarboxylic ether.

The properties of the aforementioned chemical admixture can be found in Table 5.

2. 1. 7. Concrete Mix Proportion

The concrete formulations were devised for M30 classification in compliance with IS: 10262-2019 (28), and the composition ratios are delineated in Table 6.

3. MIX APPROACH

3. 1. Conventional Mixing

The present study has incorporated conventional mixing as one of the mixing

TABLE 5. Properties of chemical admixture

Parameters	Properties
Appearance	Yellow to brown liquid
Specific Gravity@27°C	1.03 to 1.08
pH	Min 6
Chloride Content	< 0.5 % by weight as per BS5075:Part1

TABLE 6. Mix proportions of controlled and recycled fine aggregate concrete mixes

Mixing Approach	Designation	Cement (kg/m ³)	M-sand (kg/m ³)	RFA (kg/m ³)	NCA (kg/m ³)		Water(kg)	Chemical Admixture	W/C
					10 mm	20 mm			
Conventional	Controlled Concrete	345	727	0	884	346	148	3.45	0.43
Triple mixing with optimized combined aggregate concept	RFA 25	326	545.25	181.75	936	365	132	2.95	0.40
	RFA 50	326	363.5	363.5	936	365	132	2.95	0.40
	RFA 100	326	0	727	936	365	132	2.95	0.40

approaches. Conventional mixing involves a sequential addition of ingredients to create a proper dry mix. Initially, half of the coarse aggregate is introduced into the mixer, followed by the addition of the dry mix and mixed for a minimum of two minutes.

Cement, fine aggregate, and the remaining coarse aggregate. The components are then thoroughly mixed to achieve a homogenous mixture. Subsequently, water and chemical admixture, such as superplasticizers, are added to the dry mix and mixed for a minimum of two of two minutes. The procedure of conventional mixing is visually represented in Figure 5.

3.2. Triple Mixing with Optimization of Combined Aggregates

Triple mixing, a novel mixing

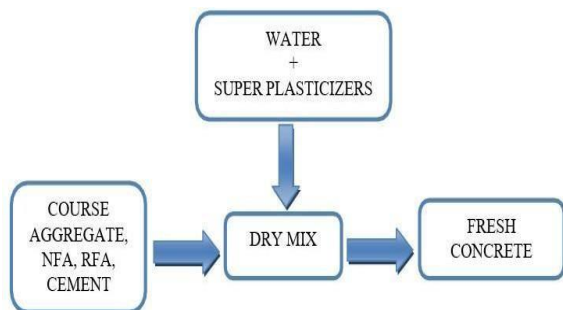


Figure 5. Conventional mixing approach

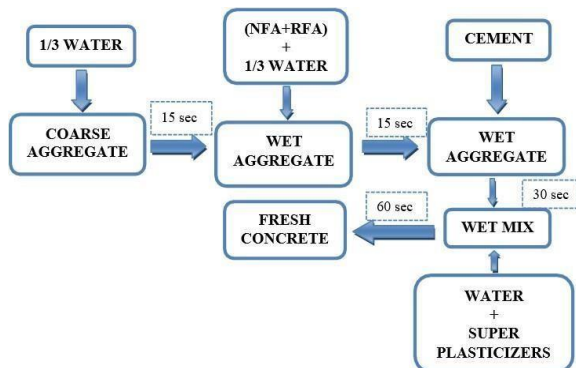


Figure 6. Triple mixing approach

methodology in the construction industry, was employed in our research (39). Despite its lack of widespread usage, this approach presents a promising alternative to traditional mixing techniques. In this research, a new approach is proposed for the optimal mixture design of concrete to efficiently utilize recycled fine aggregate (RFA) as a substitute for river sand. The proposed approach involves a combination of RFA, intermediate aggregate (10 mm), and coarse aggregate (20 mm) to achieve a well-packed particle arrangement with minimal paste content. The experimental procedure for achieving maximum packing density of aggregates is depicted in Figure A.1 (Provided in Appendix). The proportions of fine aggregate (FA), intermediate aggregate (IA), and coarse aggregate (CA) are determined as 40:42:18 according to the guidelines specified in IS 456 (BIS 2000), ensuring that the total percentage of aggregates adds up to 100.

To assess the effectiveness of different fine aggregates, the percentage of fine aggregate is varied from 0% to 100% in a systematic manner. For instance, if the fine aggregate constitutes 10%, the remaining 90% is divided into 63% for the intermediate aggregate and 27% for the coarse aggregate (FA + IA + CA = 10 + 63 + 27 = 100). Similarly, data sets are gathered by altering the percentage of intermediate aggregate and coarse aggregate as well. The process commences with the mixing of coarse aggregate and 1/3-part water for 15 seconds, followed by the addition of fine aggregate and RFA, which is mixed for an additional 15 seconds. Finally, cement is introduced to the wet aggregate and mixed for 30 seconds. The ultimate step in the concrete preparation process involves blending the remaining one-third portion of water with a chemical admixture and incorporating it into the wet mixture. This amalgamation must be mixed for a duration of 60 seconds to ensure optimal results. The ultimate fresh concrete product is generated after two minutes of preparation. This method of blending has proven to yield superior hardened properties, such as compressive strength, in recycled aggregate concrete when compared to traditional mixing techniques. Figure 6 depicts the triple mixing approach utilized in this process.

4. RESULT AND DISCUSSION

4. 1. Fresh Property Slump

The concrete formulations were formulated to attain a target slump of 75mm. Upon examination of Figure 7, it is evident that the consistency of the mixture, as indicated by the slump measurement, varied from 90-110mm for both the controlled concrete and recycled aggregate concrete mixtures in both the traditional and triple mixing methods. This desired degree of slump was achieved by incorporating 1% super plasticizer with an unvarying W/C of 0.43 in all the formulations.

Although the workability of RAC was marginally reduced in comparison to controlled concrete in the conventional mixing method due to the existence of surface pores and rough surface texture in RFA which necessitates more water, negligible variations were noted in the triple mixing approach for both controlled concrete and recycled aggregate concrete.

4. 2. Hardened Property: Compressive Strength

The concrete mixtures were formulated with the aim of achieving a compressive strength of 30Mpa. Upon analysis of Figure 8 and Table 7, it is evident that the compressive strength of recycled aggregate concrete (RAC) experiences a decrease of 27.89% for 25% replacement, 21.58% for 50% replacement, and 63.02% for 100% replacement of recycled fine aggregate (RFA) in comparison to controlled concrete at 7 days. Figure 9 and Table 7 illustrates that the compressive strength of RAC increases by 10.51% for 25% replacement, 10.67% for 50% replacement, and experiences a decrease of 38.71% for 100% replacement in comparison to controlled concrete at the age of 28 days, following conventional mixing approach. Notably, the compressive strength of recycled aggregate concrete increases by 5.04% for 25% replacement, 21.69% for 50% replacement, and experiences a decrease of 35.44% for 100% replacement in comparison to controlled concrete at the age of 28 days, following triple mixing approach.

The observed enhancement in compressive strength can be attributed to the particle packing of RFA. A portion of the RFA was found to be finer than natural fine aggregate, resulting in a more compact and dense concrete (40). However, a reduction in compressive strength occurs beyond a 50% replacement rate, particularly at 100% replacement, due to the presence of attached old cement mortar in RFA. The decrease in compressive strength of RAC at all replacement levels after 7 days and the increase in compressive strength of RAC at all replacement levels after 28 days can be attributed to the internal curing effect of RFA. This effect allows for the water initially absorbed inside the pores of RFA to be available at later stages for cement hydration (41, 42).

4. 3. Quality Assessment: Ultrasonic Plus Velocity

(UPV) Test

The non-destructive UPV test is employed as a method for evaluating the quality of concrete. The direct approach is utilized to determine

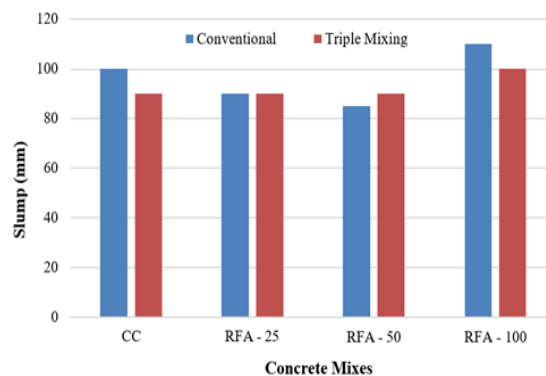


Figure 7. Slump test results of various concrete mixes

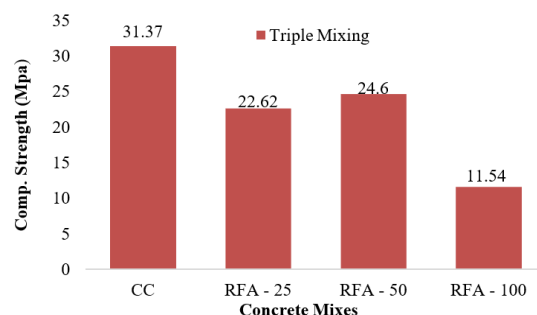


Figure 8. Graphical representation of compressive strength test results of concrete mixes at the age of 7

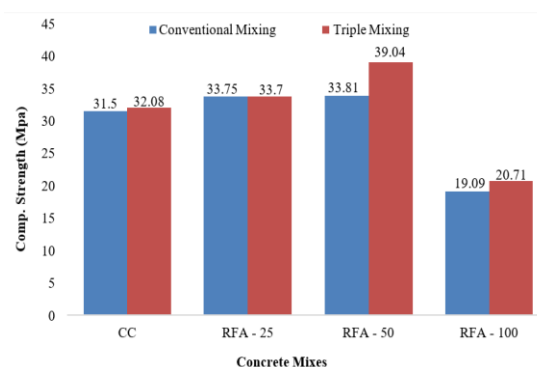


Figure 9. Graphical representation of compressive strength test results of concrete mixes at the age of 28 days

TABLE 7. Compressive strength test results of concrete mixes

Specimen	Triple Mixing 7 days (MPa)	Triple Mixing 28 days (MPa)
CC	31.37	31.15
RFA 25%	22.62	33.75
RFA 50%	24.60	33.81
RFA 100%	11.54	19.09

UPV values for various concrete mixes. Table 8 illustrate the UPV results of all specimens that were cured for 28 days. The UPV values ranged from 9500 to 10000 m/sec, regardless of whether the concrete was made with controlled or recycled aggregates, and whether conventional or triple mixing approaches were employed.

It was observed that the UPV values increased as the RFA content increased, regardless of age. These findings demonstrate that the UPV value falls within the excellent category, as prescribed in Table 1 IS 516 (Part 5)/(section1):2018 (43).

4. 4. Micro Structural Analysis Microstructural analysis was conducted on all concrete mixes of 28-day

cured specimens. Subsequently, the cured specimens underwent compression testing, and the ruptured specimens were examined using a scanning electron microscope.

4. 4. 1. Micro Structural Analysis of Controlled Concrete

Figures 11a and 11b serve to depict the microstructure of controlled concrete through the utilization of conventional mixing and triple mixing methods. The former figure showcases the formation of hydrated calcium silicate hydrate (CSH) gel and the rupture of concrete specimen occurring through the aggregate. Similarly, Figure 11b demonstrates the formation of hydrated CSH gel in contrast to Figure 10a.



Figure 10. Salient process involved in the experimental program

TABLE 8. Ultrasonic pulse velocity test results of concrete mixes

Sample	Ultrasonic Pulse Velocity at 28 days age for		Grading
	Conventional Mixing (m/s)	Triple Mixing (m/s)	
CC	9500	9750	Excellent
RFA25	9709	9417.6	Excellent
RFA50	10000	10000	Excellent
RFA 100	10000	10000	Excellent

It is worth noting that the formation of CSH gel plays a pivotal role in the enhancement of cube specimen strength.

4. 4. 2. Micro Structural Analysis of Recycled Aggregate Concrete at 25% Replacement of RFA

Figures 11a and 11b depict the microstructure of Recycled Aggregate Concrete (RAC) at a 25% replacement of Recycled Fine Aggregate (RFA) by means of the conventional mixing approach and the triple mixing approach, respectively. The formation of Calcium

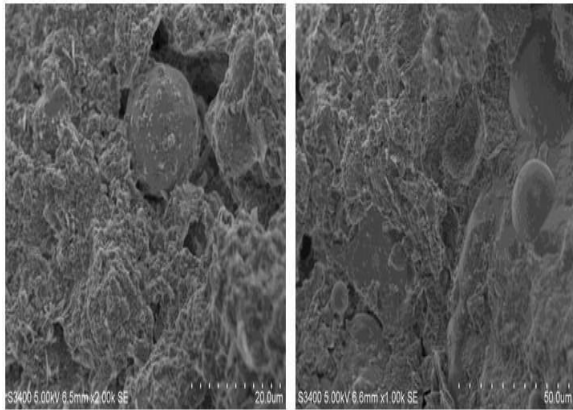


Figure 11a. Microstructure of controlled concrete by conventional mixing

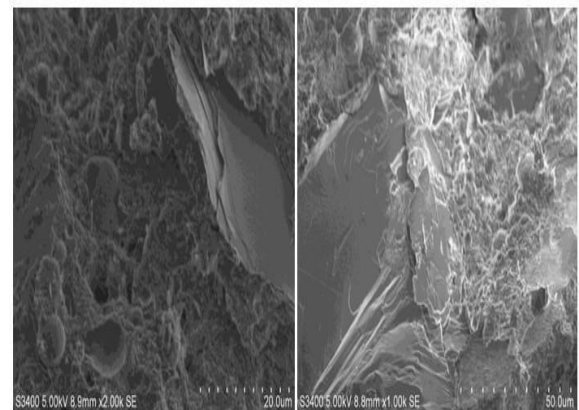


Figure 12a. Micro structure of recycled aggregate concrete with 25% RFA by conventional mixing

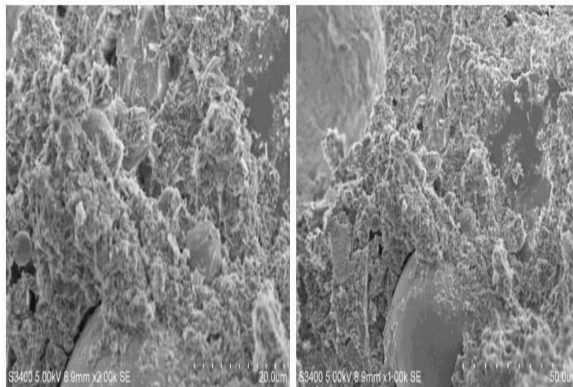


Figure 11b. Microstructure of controlled concrete by triple mixing

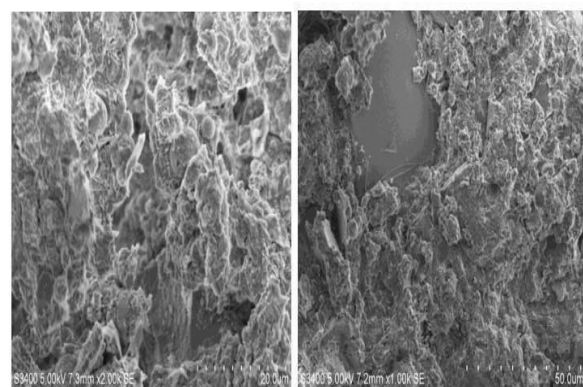


Figure 12b. Microstructure of recycled aggregate concrete with 25% RFA by triple mixing

Silicate Hydrate (CSH) gel was observed in both Figures 12a and 12b, along with the observation of hexagonal platelets of calcium hydroxide in both conventional and triple mixing approach specimens. A denser microstructure was observed in Figures 12a and 12b in comparison to the controlled concrete illustrated in Figures 11a and 11b. This denser microstructure is the reason for the increase in strength observed in RAC in comparison to controlled concrete for both mixing approaches.

4. 4. 3. Micro Structural Analysis of Recycled Aggregate Concrete at 50% Replacement of RFA

Figures 13a and 13b depict the microstructure of Recycled Aggregate Concrete (RAC) at 50% replacement of Recycled Fine Aggregate (RFA) in both conventional and triple mixing approaches, respectively. It is noteworthy that the formation of hydrated Calcium Silicate Hydrate (CSH) gel is more pronounced in RAC at 50% RFA replacement in comparison to conventional concrete, as evidenced by Figures 11a and 11b. Moreover, a denser microstructure was observed in RAC

at 50% RFA replacement, which surpasses that of other concrete mixes, including recycled aggregate concrete at 25% replacement, as shown in Figures 12a and 12b. The analysis of the microstructure is in alignment with the compressive strength results obtained.

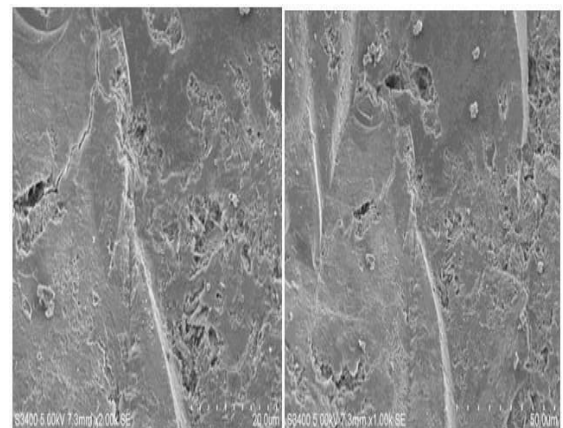


Figure 13a. Microstructure of recycled aggregate concrete with 50% RFA by conventional mixing

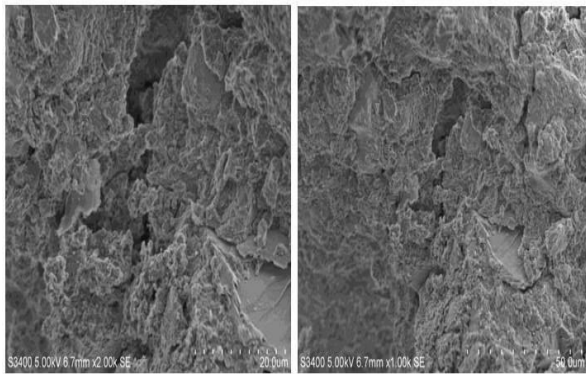


Figure 13b. Microstructure of recycled aggregate concrete with 50% RFA by triple mixing

5. 6. Proposed Machine Learning Models

Six machine learning (ML) methodologies have been integrated to optimize the RFA concrete for relationship modeling. The six ML algorithms utilized in this study (44), include Support Vector Regression (SVR), Decision Tree Regression (DTR), Gradient Boosting Regression (GBR), Artificial Neural Network (ANN), Bayesian Ridge Regression (BRR), and Kernel Ridge Regression (KRR).

Typical network structure of SVR is represented in Figure 14 (44).

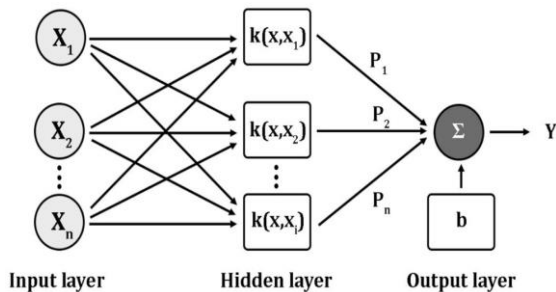


Figure 14a. Network of support vector machine (44)

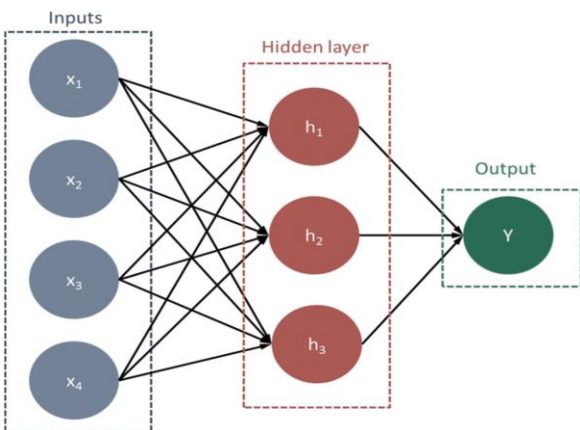


Figure 14b. Function of ANN (38)

5. 6. 1. Dataset

The implementation of the prediction utilizes a dataset collected from 423 specimens, each with distinct influencing variables. In order to facilitate the training process, this dataset is divided into two separate subsets: a training set and a testing set. The training set is utilized to train the machine learning models and adjust the hyper-parameters, while the testing set is reserved for performance evaluation (44, 45). The training set is selected at random and the remaining data comprises the testing set. It is noteworthy that the same training set is employed in all six machine learning models presented in this paper, with the testing set being consistent across each model as well. Specifically, 70% of the entire dataset is allocated to the training set, with the remaining 30% being assigned to the testing set (46, 47).

5. 6. 2. Comparison of Integrated ML Approaches

In this section, a total of six Machine Learning (ML) techniques that have been integrated are analyzed and their predictive performance on the testing set is thoroughly compared and discussed. The evaluation of performance is carried out utilizing the Mean Squared Error (MSE) value and the R value (47).

Figure 15 presents the Mean Squared Error (MSE) and R value of six Machine Learning (ML) models on the testing set. Analysis of Figure 15(a) indicates that Gradient Boosting Regression (GBR) is the optimal prediction model in terms of MSE. When GBR is utilized, the MSE values of the training and testing sets

TABLE 9. Dataset for performance prediction

Particular	Concrete type	Input Variables	Size	Output variable
Dataset	RFA Concrete	Cement, Water, Fine aggregate, Coarse aggregate, Admixture	423	Compressive strength

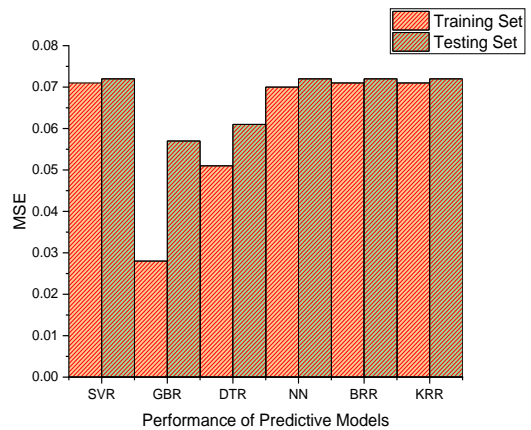


Figure 15a. Predictive performance of models – MSE

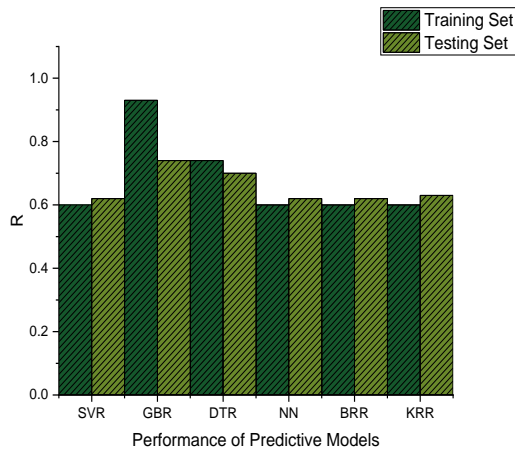


Figure 15b. Predictive performance of models - R

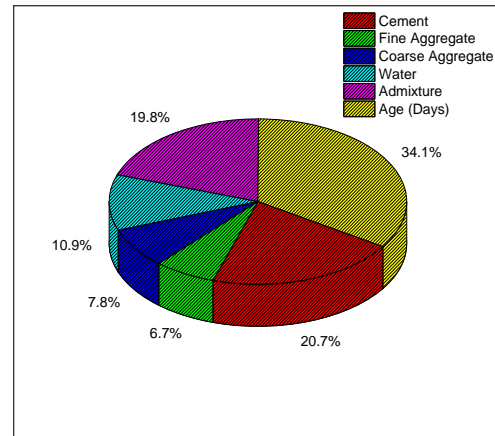


Figure 16. Sensitivity analysis of all datasets

are 0.028 and 0.057, respectively. Meanwhile, Decision Tree Regression (DTR) also exhibits commendable performance, with the training and testing MSE values of 0.051 and 0.061, respectively. The remaining four models demonstrate a comparable MSE of approximately 0.7. In Figure 15(b), GBR surpasses the other five models with respect to R value.

The training set and testing set exhibit R values of 0.93 and 0.74, respectively. DTR also showcases a favorable predictive ability with R values of 0.74 and 0.7 for training and testing sets, respectively. The remaining four models have R values that are approximately 0.6. SVR, NN, BRR, and KRR exhibit a testing set R value that is slightly higher than their respective training set R values. In contrast, the performance of BRR is comparatively inadequate when evaluated using MSE and R values, as opposed to DTR and GBR. Based on Figure 15, it is evident that DTR and GBR are more effective in predicting the effective performance of the RFA concrete.

5. 6. 3. Sensitivity Analysis Sensitivity analysis was conducted utilizing equation number 1 in order to comprehend the relative contribution of input parameters towards the compressive strength. Within the equation, $f_{max}(y_i)$ and $f_{min}(y_i)$ represent the highest and lowest values of predicted parameter, respectively, corresponding to the i^{th} domain. It is important to note that all input variables were maintained as constants, utilizing their mean values (48-50).

$$S = \frac{f_{max}(y_i) - f_{min}(y_i)}{\sum_{n=1}^j N_i} \tag{1}$$

Equation 1 is employed to all the datasets to estimate the sensitivity of input variable on the predictor. The parameter such as SP, Cement Content, Water content, age of the specimens was found to have higher influence on compressive strength compared to other materials

used as depicted in Figure 16. The least sensitive variable is fine aggregate and coarse aggregate.

6. CONCLUSION

This manuscript delineates an innovative technique for determining the appropriate mixture proportions of recycled fine aggregate concrete. This technique employs a combined particle packing method, resulting in a refined performance of the concrete that is based on recycled fine aggregate.

(1) The physical properties of Recycled Fine Aggregate (RFA) are akin to those of natural fine aggregate, albeit with a notable distinction in water absorption. Specifically, the water absorption of RFA is 6.25% greater than that of M sand.

(2) The mix proportioning that has been developed displays a negligible impact on the workability of concrete. The workability of concrete experiences a decline as the percentage of RFA content increases, as a result of the presence of previously adhered mortar.

(3) At the age of 7 days, an increase in the percentage of replacement of RFA resulted in a decrease in the compressive strength of RAC, in comparison to controlled concrete.

(4) As the proportion of RFA increases, there is a corresponding decrease in the mechanical characteristics. Nevertheless, this decline in properties can be mitigated by incorporating specific additives into the concrete blends through the utilization of this recently developed mixture ratio. In the triple mixing approach, the compressive strength of RAC increased with a proportional increase in the percentage of replacement of RFA, up to 50%, in contrast to controlled concrete.

(5) The compressive strength of recycled aggregate concrete increases by 5.04% for 25% replacement,

21.69% for 50% replacement and decreases by 35.44% for 100% replacement as compared to controlled concrete at the age of 28 days for triple mixing approach. This increase in compressive strength was attributed to the filler effect of RFA, part of which was finer than natural fine aggregate, making concrete more compact and denser. But beyond 50%, there is reduction in compressive strength particularly at 100% replacement due to the presence of adhered mortar in RFA.

(5) According to IS: 516 (Part 5)/(section1):2018, the UPV test values for both controlled concrete and RAC are classified as excellent.

(6) The utilization of 50% replacement of recycled fine aggregate (RFA) in concrete, through the triple mixing approach, resulted in the observation of the formation of a hydrated calcium silicate hydrate (CSH) gel and a highly compact microstructure. This was in contrast to the other concrete mixes studied.

(7) The verification of the optimal Machine Learning (ML) model's performance is conducted through the utilization of Mean Squared Error (MSE) and the R value, resulting in the attainment of minimum MSE values for all six ML models. The findings indicate that the ML approach has immense potential for the accurate prediction of performance. The optimal Gradient Boosting Regression (GBR) model exhibits commendable performance on both the training and testing sets. The achievement of a low MSE and high R value between the predicted CCP values and the experimental results on both the training and testing sets signifies that the optimal GBR model outperforms the other five models in terms of accurate prediction.

(8) Sensitivity analysis has demonstrated that the variables, such as Superplasticizer, Cement, Water, and Age (day), exert a substantial influence on compressive strength, subsequently followed by the pozzolan material. The variable displaying the lowest sensitivity is fine aggregate, along with coarse aggregate.

The article serves as a basic framework for the proper utilization of C& D waste for the development of sustainable concrete which solves environmental issues. With the methodology adopted here, minimum paste and maximum packing density concept will be an answer for reduced carbon footprint in the days to come.

Limitations: The article emphasizes the advantageous utilization of concrete based on RFA (Recycled Fine Aggregate) through the application of a unique mix proportioning technique. This technique allows for a 50% replacement of RFA in the concrete, resulting in enhanced performance when combined with the inclusion of mineral admixtures. Subsequent research endeavors should explore the potential contributions and efficiencies of alternative cementitious binders when employing RFA concrete. Also, cost effectiveness of this novel mixing method should also be explored in future studies.

Our study can be utilized as a fundamental framework for furthering the implementation of RCA in the process of preparing concrete for the purpose of sustainable construction.

Future Research

The authors acknowledge the significance of additional investigation pertaining to the topic in order to establish a logical framework for specifying recycled aggregate and concrete. To enumerate a handful of prospective domains, there exists a necessity to formulate procedures for designing concrete mixtures, analyze recycled concrete at the micro-structural level, and scrutinize the enduring capacity of said concrete, especially in arduous surroundings.

7. ACKNOWLEDGEMENTS

The authors would like to thank Maharaja Institute of Technology Mysore for providing us the laboratory facilities and Rock crystal for providing us recycled fine aggregate to conduct experimental investigation on recycled aggregate concrete.

8. REFERENCES

- Jain S, Singhal S, Jain NK. Construction and demolition waste (C&DW) in India: generation rate and implications of C&DW recycling. *International Journal of Construction Management*. 2021;21(3):261-70.
- Kirthika S, Singh S. Durability studies on recycled fine aggregate concrete. *Construction and Building Materials*. 2020;250:118850. <https://doi.org/10.1016/j.conbuildmat.2020.118850>
- Evangelista L, De Brito J. Durability performance of concrete made with fine recycled concrete aggregates. *Cement and Concrete Composites*. 2010;32(1):9-14. <https://doi.org/10.1016/j.cemconcomp.2009.09.005>
- Shaaban M, Edris WF, Odah E, Ezz MS, Al-Sayed AA-KA. A Green Way of Producing High Strength Concrete Utilizing Recycled Concrete. *Civil Engineering Journal*. 2023;9(10):2467-85. <https://doi.org/10.28991/cej-2023-09-10-08>
- Al Mashhadani D, Wong LS, Kong SY, Al-Zand AW, Midhin MA. An evaluative review of recycled waste material utilization in high-performance concrete. *Civil Engineering Journal*. 2023;9(11):2927-57. <https://doi.org/10.28991/cej-2023-09-11-020>
- Evangelista L, De Brito J. Concrete with fine recycled aggregates: a review. *European Journal of Environmental and Civil Engineering*. 2014;18(2):129-72. <https://doi.org/10.1080/19648189.2013.851038>
- Evangelista L, Guedes M, De Brito J, Ferro AC, Pereira M. Physical, chemical and mineralogical properties of fine recycled aggregates made from concrete waste. *Construction and building materials*. 2015;86:178-88. <https://doi.org/10.1016/j.conbuildmat.2015.03.112>
- Poon C-s, Kou S-c. Properties of cementitious rendering mortar prepared with recycled fine aggregates. *Journal of Wuhan University of Technology-Mater Sci Ed*. 2010;25:1053-6. <https://doi.org/10.1007/s11595-010-0148-2>

9. Etxeberria M, Vegas I. Effect of fine ceramic recycled aggregate (RA) and mixed fine RA on hardened properties of concrete. *Magazine of concrete research*. 2015;67(12):645-55. <https://doi.org/10.1680/mac.14.00208>
10. Fan C-C, Huang R, Hwang H, Chao S-J. The effects of different fine recycled concrete aggregates on the properties of mortar. *Materials*. 2015;8(5):2658-72. <https://doi.org/10.3390/ma8052658>
11. Pereira P, Evangelista L, De Brito J. The effect of superplasticisers on the workability and compressive strength of concrete made with fine recycled concrete aggregates. *Construction and Building Materials*. 2012;28(1):722-9. <https://doi.org/10.1016/j.conbuildmat.2011.10.050>
12. Kou S-C, Poon C-S. Effects of different kinds of recycled fine aggregate on properties of rendering mortar. *Journal of Sustainable Cement-Based Materials*. 2013;2(1):43-57. <https://doi.org/10.1080/21650373.2013.766400>
13. Anastasiou E, Filikas KG, Stefanidou M. Utilization of fine recycled aggregates in concrete with fly ash and steel slag. *Construction and Building Materials*. 2014;50:154-61. <https://doi.org/10.1016/j.conbuildmat.2013.09.037>
14. González-Taboada I, González-Fonteboa B, Eiras-López J, Rojo-López G. Tools for the study of self-compacting recycled concrete fresh behaviour: Workability and rheology. *Journal of Cleaner Production*. 2017;156:1-18. <https://doi.org/10.1016/j.jclepro.2017.04.045>
15. Gómez-Soberón JM. Porosity of recycled concrete with substitution of recycled concrete aggregate: An experimental study. *Cement and concrete research*. 2002;32(8):1301-11. [https://doi.org/10.1016/s0008-8846\(02\)00795-0](https://doi.org/10.1016/s0008-8846(02)00795-0)
16. Kumar R, Gurram SCB, Minocha AK. Influence of recycled fine aggregate on microstructure and hardened properties of concrete. *Magazine of Concrete Research*. 2017;69(24):1288-95. <https://doi.org/10.1680/jmacr.17.00030>
17. Santos SA, Da Silva PR, De Brito J. Mechanical performance evaluation of self-compacting concrete with fine and coarse recycled aggregates from the precast industry. *Materials*. 2017;10(8):904. <https://doi.org/10.3390/ma10080904>
18. Pedro D, De Brito J, Evangelista L. Structural concrete with simultaneous incorporation of fine and coarse recycled concrete aggregates: Mechanical, durability and long-term properties. *Construction and Building Materials*. 2017;154:294-309. <https://doi.org/10.1016/j.conbuildmat.2017.07.215>
19. Yang K-H, Chung H-S, Ashour AF. Influence of Type and Replacement Level of Recycled Aggregates on Concrete Properties. 2008. <https://doi.org/10.14359/19826>
20. Kirthika S, Singh S, Chourasia A. Performance of recycled fine-aggregate concrete using novel mix-proportioning method. *Journal of Materials in Civil Engineering*. 2020;32(8):04020216. [https://doi.org/10.1061/\(ASCE\)MT.1943-5533.0003289](https://doi.org/10.1061/(ASCE)MT.1943-5533.0003289)
21. McGinnis MJ, Davis M, de la Rosa A, Weldon BD, Kurama YC. Strength and stiffness of concrete with recycled concrete aggregates. *Construction and Building Materials*. 2017;154:258-69. <https://doi.org/10.1016/j.conbuildmat.2017.07.015>
22. Kryeziu D, Selmani F, Mujaj A, Kondi I. Recycled concrete aggregates: a promising and sustainable option for the construction industry. *Journal of Human, Earth, and Future*. 2023;4(2):166-80. <https://doi.org/10.28991/hef-2023-04-02-03>
23. Pawar AJ, Patel M, Suryawanshi S. Finite Element Modelling of Laboratory Tests on Reinforced Concrete Beams Containing Recycled Aggregate Concrete. *International Journal of Engineering, Transactions B: Applications*. 2023;36(5):991-9. <https://doi.org/10.5829/ije.2023.36.05b.15>
24. Pawar AJ, Suryawanshi S. Comprehensive analysis of stress-strain relationships for recycled aggregate concrete. *International Journal of Engineering, Transactions B: Applications*. 2022;35(11):2102-10. <https://doi.org/10.5829/ije.2022.35.11b.05>
25. Masne N, Suryawanshi S. Analytical and experimental investigation of recycled aggregate concrete beams subjected to pure torsion. *International Journal of Engineering, Transactions A: Basics*. 2022;35(10):1959-66. <https://doi.org/10.5829/ije.2022.35.10a.14>
26. Evangelista L, De Brito J. Mechanical behaviour of concrete made with fine recycled concrete aggregates. *Cement and concrete composites*. 2007;29(5):397-401. <https://doi.org/10.1016/j.cemconcomp.2006.12.004>
27. Nedeljković M, Visser J, Šavija B, Valcke S, Schlangen E. Use of fine recycled concrete aggregates in concrete: A critical review. *Journal of Building Engineering*. 2021;38:102196. <https://doi.org/10.1016/j.jobe.2021.102196>
28. 10262: I. Concrete Mix Proportioning–Guidelines (second revision). IS: 10262, Bureau of Indian Standards New Delhi, India; 2019.
29. IS 1489 (Part-1) – 2015, Portland Pozzolana Cement-Specification, Bureau of Indian Standards New Delhi India. 2015.
30. IS40314:1988 (Reaffirmed 2005), Methods of physical test for hydraulic cement part-4: Determination of consistency of standard cement paste, Bureau of Indian standards New Delhi India 2005.
31. IS40315:1989 (Reaffirmed 2005), Methods of physical test for hydraulic cement part-5: Determination of initial and final setting times, Bureau of Indian standards New Delhi India. 2005.
32. IS4031-3:1988 (Reaffirmed 2005), Methods of physical test for hydraulic cement part-3: Determination of Soundness, Bureau of Indian standards New Delhi India, 2005.
33. IS40312:1999 (Reaffirmed 2004), Methods of physical test for hydraulic cementpart-2: Determination of specific gravity by Blaine Air Permeability Method, Bureau of Indian standards New Delhi India. 2004.
34. IS4031-1:1996 (Reaffirmed 2004), Methods of physical test for hydraulic cementpart-1 Determination of fineness, Bureau of Indian standards New Delhi India. 2004.
35. IS 2386-3:1963 (Reaffirmed 2002), Methods of test for aggregates for concrete part- 3: Specific gravity, Density, Voids, Absorption and Bulking, Bureau of Indian Standards New Delhi India. 2002.
36. IS23864:1963 (Reaffirmed 2002), Mechanical Properties, Bureau of Indian Standards New Delhi India. 2002.
37. IS 2386-1:1963 (Reaffirmed 2002), Methods of test for aggregates for concrete part- 1: Particle size and shape, Bureau of Indian Standards New Delhi India. 2002.
38. IS B. 383 Coarse and Fine Aggregate for Concrete—Specification (Third Revision). Bureau of Indian Standards: New Delhi, India. 2016.
39. IS: Methods of physical tests for hydraulic cement—Part 6: Determination of compressive strength of hydraulic cement other than masonry cement,(first revision). Bureau of Indian Standards, New Delhi. 2005:1-3.
40. Khatib JM. Properties of concrete incorporating fine recycled aggregate. *Cement and concrete research*. 2005;35(4):763-9. <https://doi.org/10.1016/j.cemconres.2004.06.017>
41. Tam VW, Tam CM. Diversifying two-stage mixing approach (T SMA) for recycled aggregate concrete: T SMAs and T SMAsc. *Construction and building Materials*. 2008;22(10):2068-77. <https://doi.org/10.1016/j.conbuildmat.2007.07.024>
42. Yashwanth M, Kumar BN, Kumar DS. Potential of bagasse ash as alternative cementitious material in recycled aggregate concrete. *International Journal of Innovative Technology and Exploring Engineering*. 2019;8(11):271-5. 10.35940/ijitee.K1319.0981119

43. IS516:1959 (Reaffirmed 2004), Methods of test for Strength of concrete, Bureau of Indian Standards New Delhi India. 2004.
44. Zendejboudi A, Baseer MA, Saidur R. Application of support vector machine models for forecasting solar and wind energy resources: A review. *Journal of cleaner production*. 2018;199:272-85. <https://doi.org/10.1016/j.jclepro.2018.07.164>
45. Song H, Ahmad A, Farooq F, Ostrowski KA, Maślak M, Czamecki S, et al. Predicting the compressive strength of concrete with fly ash admixture using machine learning algorithms. *Construction and Building Materials*. 2021;308:125021. <https://doi.org/10.1016/j.conbuildmat.2021.125021>
46. Chaabene WB, Flah M, Nehdi ML. Machine learning prediction of mechanical properties of concrete: Critical review. *Construction and Building Materials*. 2020;260:119889. <https://doi.org/10.1016/j.conbuildmat.2020.119889>
47. Huang X, Wasouf M, Sresakoolchai J, Kaewunruen S. Prediction of healing performance of autogenous healing concrete using machine learning. *Materials*. 2021;14(15):4068. <https://doi.org/10.3390/ma14154068>
48. IS456 ISC. Plain and reinforced concrete—code of practice (fourth revision). Bureau of Indian Standards, Manak Bhavan. 2000;9.
49. IS 650:1991 (Reaffirmed 2008), Standard sand for testing cement- Specification, Bureau of Indian Standards New Delhi India. 2008.
50. IS1199:1959 (Reaffirmed 2004), Methods of sampling and analysis of concrete, Bureau of Indian Standards New Delhi India. 2004.

COPYRIGHTS

©2024 The author(s). This is an open access article distributed under the terms of the Creative Commons Attribution (CC BY 4.0), which permits unrestricted use, distribution, and reproduction in any medium, as long as the original authors and source are cited. No permission is required from the authors or the publishers.



Persian Abstract

چکیده

صنعت ساخت و ساز در درجه اول مسئول کاهش منابع طبیعی و برهم زدن تعادل زیست محیطی به دلیل فعالیت های غیرقانونی معدن است. در این زمینه خاص، استفاده از سنگدانه های ریزبازافتی (RFA) که از ضایعات ساخت و ساز و تخریب (D&C) به دست می آید خود را به عنوان یک راه حل مناسب نشان می دهد. روش مرسوم تناسب مخلوط برای RFA در بتن در این مورد قابل اجرا نیست. نوآوری اصلی تحقیقات ما در تحقق یکی از اصول اقتصاد دایره ای، یعنی کاهش انتشار کربن، از طریق بازیافت زباله های بتن جمع آوری شده محلی است. برای مقابله با این موضوع، یک رویکرد جدید نسبت مخلوط سه گانه با استفاده از مفاهیم حداکثر چگالی بسته بندی و تئوری خمیر حداقل توسعه داده شده است. خواص تازه و سخت شده ارزیابی شد و خصوصیات ریزساختاری برای مخلوط های تازه فرموله شده حاوی RFA با سنگدانه های ترکیبی بهینه سازی شده انجام شد. مقاومت فشاری بتن با سنگدانه های ریزبازافتی ۵/۰۴ درصد برای ۲۵ درصد و ۲۱/۶۹ درصد برای ۵۰ درصد جایگزینی افزایش می یابد و ۳۵/۴۴ درصد برای جایگزینی ۱۰۰ درصد در مقایسه با بتن کنترل شده در سن ۲۸ روز با استفاده از رویکرد اختلاط سه گانه کاهش می یابد. یافته ها نشان می دهد که جایگزینی تقریباً ۵۰ درصد ماسه با RFA مقدار بهینه است، زیرا جایگزینی بیشتر منجر به کاهش مقاومت فشاری، به ویژه در جایگزینی ۱۰۰ درصد به دلیل وجود ملات چسبیده در RFA می شود. در این مطالعه، ارزیابی عملکرد بتن RFA با مقایسه شش مدل رگرسیون ML انجام شده و تحلیل حساسیت برای ارزیابی عملکرد متغیر انجام شد.

Appendix

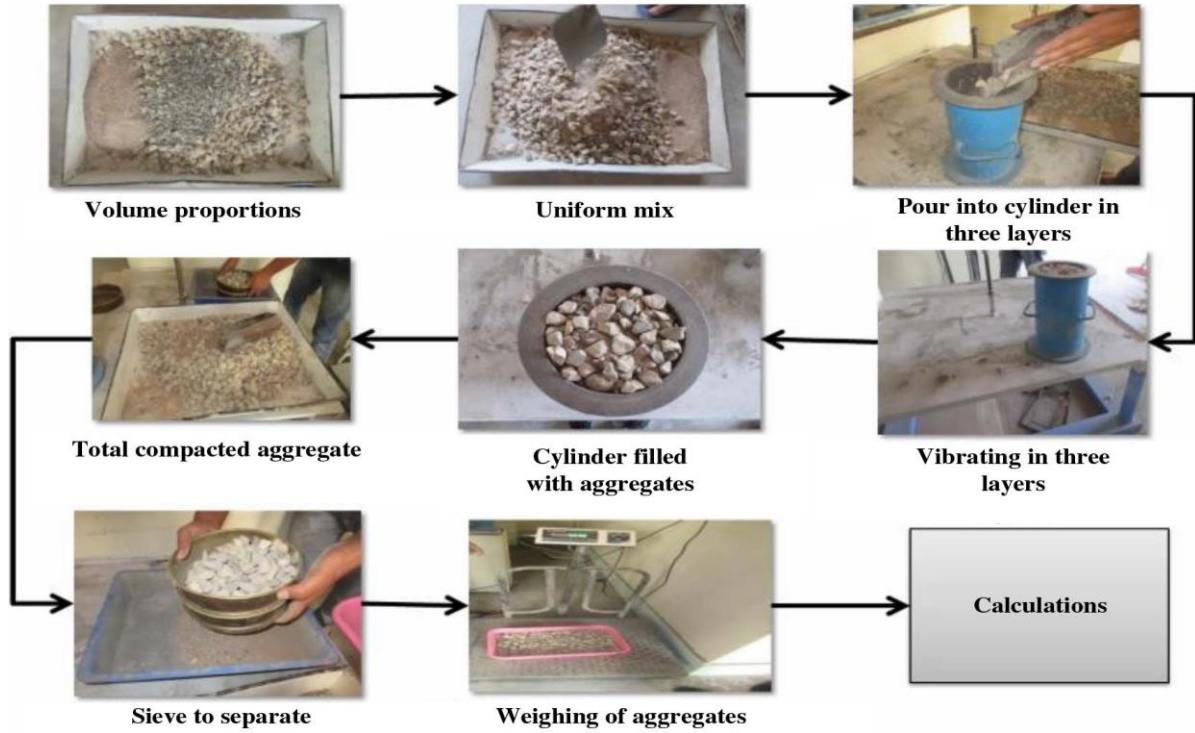


Figure A.1. Experimental procedure to determine particle packing density [33]



Thermodynamic Simulation of an Efficient Flash Ironmaking Technology for Chadormalu Mining and Industrial Company

F. Firouzi, S. K. Sadrnezhad*

Department of Materials Science and Engineering, Sharif University of Technology, Tehran, Iran

PAPER INFO

Paper history:

Received 21 June 2023

Received in revised form 16 October 2023

Accepted 27 October 2023

Keywords:

Flash Ironmaking

Chadormalu Concentrate

Thermodynamic Simulation

Heat and Material Balances

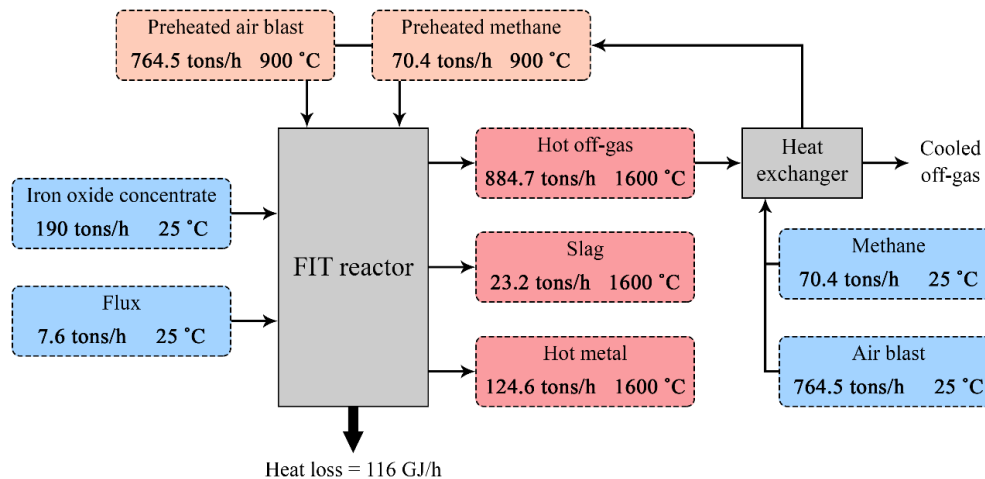
CO₂ Emission

ABSTRACT

The Flash Ironmaking Technology (FIT) utilizing methane (CH₄) and air blast (containing 21% oxygen) has been exclusively simulated and calculated for the Chadormalu Mining and Industrial Company (CMIC). The obtained results based on thermodynamic simulation and heat and material balance calculations of the FIT have revealed that a total rate of 70.405 tons/h preheated CH₄ is required for the annual production of one million tons of hot metal with 95% metallization. 47% of the methane acts as a reducing agent, and the rest burns with 764.489 tons/h preheated air blast (including 20% excess) to provide 1078 GJ/h energy for running the process at 1600 °C (1873 K). Accordingly, 193.134 tons/h carbon dioxide (CO₂) is emitted through the process, equivalent to 1.550 tons for every ton of produced hot metal. It indicates that the simulated FIT is eco-friendlier than the blast furnace and coal-based direct reduction ironmaking processes while eliminating coke-making, pelletization or gas-reforming units.

doi: 10.5829/ije.2024.37.05b.17

Graphical Abstract



1. INTRODUCTION

Crude steel is the most consuming construction material, with a worldwide production of 1885 million tons in 2022 (1). Despite the development of different ironmaking technologies, the blast furnace is still the

most dominant, supplying about 75% of the world's iron (2). The rest includes direct reduction processes, categorized into gas- and coal-based types (3). In 2022, over 127 million tons of direct reduced iron (DRI) were produced all over the world, about 70% of them via gas-based reduction processes, such as MIDREX (57.8%)

*Corresponding Author: sadrnez@sharif.edu (S. K. Sadrnezhad)

and HYL/Energiron (12.1%). Rotary kiln and PERED are coal-based processes that accounted for 27.9% and 2.2% of the total DRI production, respectively (4).

The blast furnace benefits from coke, reducing agents' supplier and fuel for achieving high temperatures. Despite its dominance, ironmaking via the blast furnace method has many drawbacks. The process is strongly dependent on good quality coke, which its short supply has made it expensive all around the world. Establishing a coke oven and pelletization/sintering plants are also required for blast furnace ironmaking (5-8). On the other hand, various technologies developed for DRI production utilize lower-temperature operations (9, 10). These processes, however, suffer from some technical and operational problems. Freshly produced DRI is highly reactive and extremely susceptible to oxidation in the ambient atmosphere. Hence, its handling and storage are always a great concern of direct reduction plants (11, 12). Unintentional sticking and agglomeration of iron ore pellets during reduction, mainly due to building up of low melting eutectic phase and partial sintering, disturbs the continuous operation (13, 14). The employed aluminosilicate refractories are vulnerable to destruction by steam, H₂, and CO attack, and carbon deposition in the liner pores (15). Furthermore, emissions of carbon oxides from all discussed ironmaking processes are significant, which leads to serious environmental problems, primarily global warming (16-19). Considering the technical shortcomings of current methods and global environmental issues, more energy-efficient and eco-friendly ironmaking technologies need to be developed.

A novel flash ironmaking technology (FIT) has recently been developed, similar to the copper flash smelting processes (20). FIT is based on directly reducing iron oxide concentrate by a gaseous reducing agent (such as hydrogen or natural gas) through a gas-solid suspension reaction (21-23). As schematically depicted in Figure 1, fine iron oxide concentrate and flux particles are sprinkled into the flash ironmaking reactor with preheated feed gas and oxygen. A part of the feed gas burns with oxygen to sustain the reactor temperature of 1500-1600 °C (1773-1873 K). The rest reduces input iron oxides in the presence of flux, producing molten iron (hot metal) and fused slag of oxide constituents. They are given enough time to undergo a gravitic separation among the settlement region. Moreover, hot off-gas (containing H₂, H₂O, CO, and CO₂) is directed toward the heat exchanger to preheat the feed gas (24-26).

The novel FIT directly utilizes the fine particles of iron oxide concentrate (<100 μm) without further treatment, resulting in very high reaction rates. Hence, high metallization degrees can be achieved within a few seconds of the residence time (27-29). The process is flexible with a wide variety of gaseous reducing agents, including natural gas (23, 24), hydrogen (H₂) (27-30), carbon monoxide (CO) (31-33), methane (CH₄) (34) or

their mixture. Although pure oxygen or oxygen-enriched air is regularly used for fuel combustion to reduce emissions (24, 34), the process can utilize air blast instead, which is more economical. In addition, highly problematic coke-making, pelletization/sintering, and gas-reforming units would be eliminated (24-26). A typical FIT process is reported to emit less than 0.98 tons of CO₂ and consumes about 8.68 GJ energy for every ton of hot metal produced, which are believed to be, respectively, about 39% and 32% lower than the average amounts corresponding to the conventional blast furnace ironmaking process (24).

This study aims to implement a thermodynamic simulation of the FIT exclusively for iron oxide concentrate produced by the Chadormalu Mining and Industrial Company (CMIC), known as one of the leading suppliers of iron oxide concentrate in Iran and the Middle East (35). First, the process progression is predicted and discussed according to the simulated equilibrium compositions for the increasing input rate of methane as the only reducing agent. The rates of fuel and air blast (containing 21% oxygen, as a new option for fuel combustion in the FIT) are calculated based on the heat and material balances for achieving 95% metallization. Furthermore, the process emissions are calculated and compared with those of the conventional ironmaking processes.

2. METHODOLOGY

The FIT thermodynamic simulation and relevant calculations were performed based on the annual production of one million tons of hot metal. The chemical composition of the Chadormalu iron oxide concentrate and the intended flux are presented in Tables 1 and 2, respectively. The iron content of concentrate, coupled with 320 days of operation, resulted in its input rate of 190 tons/h. Furthermore, the input rate of flux was considered one-twenty-fifth of the concentrate rate (i.e., 7.6 tons/h).

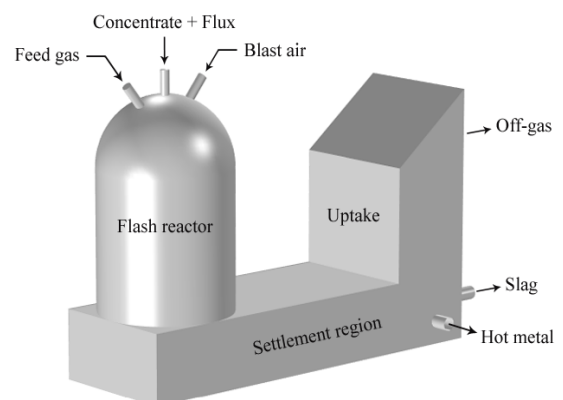


Figure 1. A schematic representation of the flash ironmaking technology (FIT)

TABLE 1. Chemical composition of the Chadormalu iron oxide concentrate (36)

Component	Content (wt.%)
Fe ₃ O ₄	72.1
Fe ₂ O ₃	24.1
SiO ₂	2.60
CaO	0.45
Al ₂ O ₃	0.40
MgO	0.35

TABLE 2. Chemical composition of the flux

Component	Content (wt.%)
MgO	72.1
CaO	24.1
SiO ₂	2.60

This study benefitted the HSC Chemistry 6.0 software for performing all thermodynamic simulations and relevant calculations based on the heat and material balances. The “Equilibrium Compositions” module was utilized to simulate the process by calculating the equilibrium value of compounds at a specific condition. First, the chemical system was defined by introducing the substances and potentially stable phases to be considered in the “Species” sheet calculations. The amounts of raw materials were inserted based on previously mentioned input rates and chemical compositions. Since investigating the role of methane in the FIT was desired, an initial input amount of 1E-16 Mmol (actually zero) and an incremental step of 0.015 Mmol were selected for this compound. At last, the equilibrium temperature of 1600 °C (1873 K), the total pressure of 1 bar (100 kPa), and 250 steps were applied in the “Options” sheet. It is worth mentioning that the temperature of raw materials did not affect the final equilibrium conditions.

In the next step, heat and material balances were performed to calculate the required amount of methane, air blast, and process emissions using the corresponding module. For this purpose, after selecting the intended equilibrium among 250 previously calculated ones, its corresponding initial value of reactants and equilibrium value of products (including unreacted reactants) were transferred to IN1 and OUT1 sheets of the “Heat and Material Balances” module, respectively. All input streams were at room temperature 25 °C (298 K), except the feed gas (methane) and air blast. Similar to previous works, these streams were justifiably set to be preheated to 900 °C (1173 K) by passing through a heat exchanger (21, 24). The temperature of all output streams would be 1600 °C (1873 K), i.e., the process temperature.

Moreover, a heat loss rate of 116 GJ/h was selected, according to the evident data given in the literature (24).

It is noteworthy to mention that previous calculations did not consider the constituents involved in fuel combustion. Thus, the amount of methane required for heat generation in the process and the combustion products were related to the molar value of air blast (containing 21% O₂ and 79% N₂) to satisfy the material balance. Excess air blast was also considered in calculations to ensure complete fuel combustion. The input value of the blast’s oxygen was the independent parameter that the module iterations would finally determine it to achieve the heat balance.

3. RESULTS AND DISCUSSION

3. 1. Process Progression Figure 2 represents different molar equilibrium compositions for the increasing rate of CH₄. Every set of points located on an imaginary vertical line represents an individual equilibrium for a specific input rate of CH₄. Therefore, the reduction progression can be described by putting together all 250 different equilibriums based on an operation time of one hour. Partial reductions start with converting hematite (Fe₂O₃) and magnetite (Fe₃O₄) in the feedstock to their relevant lower oxides. Therefore, the equilibrium value of Fe₂O₃ decreases continuously. However, simultaneous production and reduction of Fe₃O₄ result in a slight increase in its equilibrium value, followed by a descending trend.

Afterward, the equilibrium value of wustite (FeO) rises steeply, reaching a maximum of 2.135 Mmol for 0.390 Mmol of input CH₄. For this input amount of CH₄, metallic iron starts to be produced, and its equilibrium value gradually increases at the expense of FeO

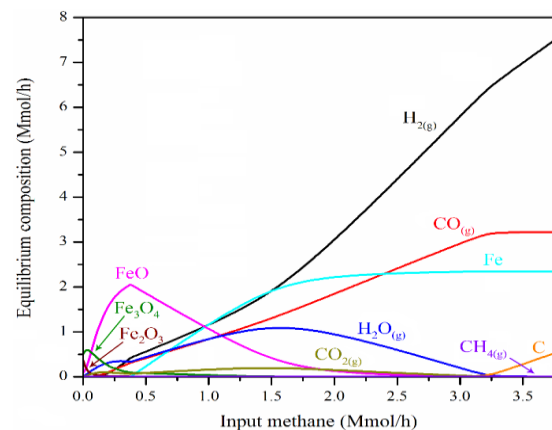
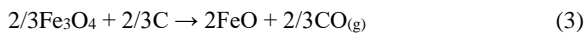
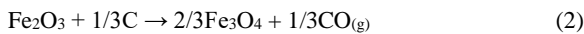


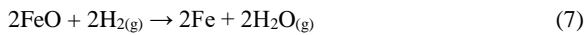
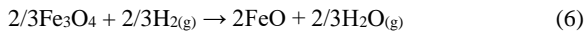
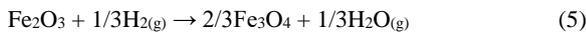
Figure 2. Different equilibrium compositions of the FIT for the increasing rate of methane at 1600 °C (1873 K). Each graph is obtained by putting together the results of 250 different equilibriums.

diminishing. Finally, the equilibrium value of molten iron reaches its maximum amount of 2.348 Mmol by completing FeO reduction (for 3.450 Mmol of input CH₄). Flux or other oxide constituents in concentrate (i.e., CaO, SiO₂, MgO, and Al₂O₃) do not affect the equilibrium processes. They are heated to the operating temperature and form a fused slag. Thus, their different contents in various operating units do not affect the discussed process progression.

It is also worth spending a few sentences on gaseous constituents to cognize the process better. Production of carbon oxides and water vapor through the process can be attributed to the reduction of iron oxides by the carbon and hydrogen contents of methane, respectively. A continuous increase in the equilibrium value of CO indicates that the carbon content of methane is thoroughly involved in all partial reductions, according to Reactions 1 to 4. This proposition is confirmed by considering negligible equilibrium values of CO₂ and stable carbon throughout the process, together with stable carbon (soot) formation for keeping methane feeding after the completion of reductions.



On the other hand, partial reductions by the hydrogen content of methane (produced through Reaction 1) occur according to Reactions 5 to 7. The variation trend of equilibrium H₂O reveals that for an increasing amount of input methane, the contribution of hydrogen in partial reductions increases gradually, reaching its maximum for 1.575 Mmol CH₄. Further increase in the input amount of methane gradually decreases the contribution of hydrogen in the reduction process.



Besides using fine particles of concentrate, the hydrogen contribution in reductions is another reason for high reaction rates in the FIT because it is well-known that iron oxide reduction by hydrogen is more favorable than by CO from thermodynamics and kinetics viewpoints. Unlike CO, hydrogen reduction of iron oxides are more endothermic and thermodynamically proceeds more efficiently at higher temperatures (37). On the other hand, smaller atomic size of hydrogen and higher diffusivity make H₂ a faster reducing agent comparing to CO (38). Hydrogen participation in partial reductions also improves the process eco-friendliness

through decreasing methane consumption, which lowers the subsequent carbon oxide emissions (27-30, 39).

3. 2. Heat and Material Balances The results of heat and material balances of the FIT are utilized for calculating the required feed gas, air blast, and carbon oxides emissions. For this purpose, the equilibrium representing 95% metallization for 2.07 Mmol/h of input CH₄ is selected among the others. As the “Equilibrium Compositions” module calculates the thermodynamic equilibrium condition, the calculated rate of input CH₄ is just the theoretical one needed for achieving the equilibrium. In such a case, the preliminary results (refer to supplementary Table S1) indicate that the lack of 1078 GJ/h energy (8.65 GJ per ton of hot metal) disturbs the heat balance of the process. Therefore, a further CH₄ is also needed as fuel to burn with air blast for heat generation through complete or incomplete combustion (Reactions 8 or 9, respectively). Complete fuel combustion through Reaction 9 can be achieved by introducing excess air blast. The fuel combustion may be considered an individual unit process rather than being coupled with partial reductions to avoid its involved gaseous constituents disrupt the equilibrium conditions of the primary FIT process.

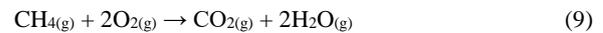


Table 3 represents the final results of heat and material balance calculations (also refer to supplementary Table S2 for complementary information). According to the

TABLE 3. The results of heat and material balances

Stream	T (°C)	Species	Rate ^a (tons/h)	Rate (Mmol/h)	Enthalpy ^b (GJ/h)
Iron oxide concentrate (Input)	25	Fe ₃ O ₄	136.990	0.592	-659.99
		Fe ₂ O ₃	45.790	0.287	-235.99
		SiO ₂	4.940	0.082	-74.89
		CaO	0.855	0.015	-9.68
		Al ₂ O ₃	0.760	0.007	-12.49
		MgO	0.665	0.016	-9.93
Flux (Input)	25	CaO	6.840	0.122	-77.44
		MgO	0.532	0.013	-7.94
		SiO ₂	0.228	0.004	-3.46
Feed gas (Input)	900	CH _{4(g)}	70.405	4.389	-98.68
Air blast (Input)	900	O _{2(g)}	178.063	5.564	160.32
		N _{2(g)}	586.426	20.934	569.48
Hot metal (Output)	1600	Fe	124.629	2.232	168.19

		FeO	8.354	0.116	-17.31
		CaO	7.695	0.137	-76.04
		SiO ₂	5.168	0.086	-68.84
Slag (Output)	1600	MgO	1.197	0.030	-15.51
		Al ₂ O ₃	0.760	0.007	-11.06
		Fe ₃ O ₄	0.037	0.000	-0.11
		Fe ₂ O ₃	0.005	0.000	-0.02
		CO _{2(g)}	107.769	2.449	-758.32
		CO _(g)	54.323	1.939	-113.23
		H ₂ O _(g)	99.938	5.547	-971.92
Off-gas	1600	H _{2(g)}	6.511	3.230	157.06
		O _{2(g)}	29.677	0.927	50.48
		N _{2(g)}	586.426	20.934	1079.94
		CH _{4(g)}	0.000	0.000	0.00
		C (Soot)	0.006	0.001	0.02
Heat loss		-	-	-	116.00

^a This column is used for material balance.

^b This column is used for heat balance. Each given enthalpy contains the heat of formation reaction and the required energy for heating up the compound from 298 K to the specified temperature as well as the values of the latent enthalpies (for possible phase transformations).

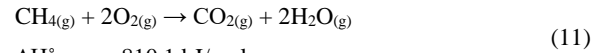
results, running the FIT for the Chadormalu iron oxide concentrate at defined operating conditions consumes 70.405 tons/h CH₄: 47% for iron oxide reductions, and 53% as fuel to provide the mentioned energy required to sustain the system temperature of 1600 °C (1873 K) (refer to electronic supplementary material). Accordingly, 764.489 tons/h air blast including 20% excess (178.063 tons/h O₂ + 586.426 tons/h N₂) is required for complete fuel combustion. Complementary data on different percentages of excess air blast are also presented in supplementary Figure S1.

From the environmental viewpoint, 107.769 tons/h CO₂ and 54.323 tons/h CO are emitted through the simulated FIT. As all CO would eventually be oxidized to CO₂, the process overallly emits 193.134 tons/h CO₂. Accordingly, this emission rate accounts for 1.550 tons of CO₂ per ton of hot metal (refer to electronic supplementary material), which implies that the simulated FIT can be categorized among the eco-friendly ironmaking processes. The calculated rate is lower than that of the blast furnace (about 1.700 tons of CO₂ per ton of hot metal) (38) and coal-based direct reduction ironmaking techniques such as rotary kiln (1.391 to 1.880 tons of CO₂ per ton of DRI) and coal gasifier (1.566 to 1.969 tons of CO₂ per ton of DRI) ones (39). This superiority can be generally attributed to the heat generation capacity of carbon (coal or coke) and methane. As Reactions 10 and 11 represent, combustion of each mole of carbon and CH₄ generates 396.2 and 808.9 kJ heat at the operational temperature of 1600 °C (1873 K), respectively. Therefore, elevating the

temperature of constituents consumes less carbon in the form of CH₄, and consequently, less amount of carbon oxide is generated.



$$\Delta H^{\circ}_{1873} = -396.5 \text{ kJ/mol}$$



$$\Delta H^{\circ}_{1873} = -810.1 \text{ kJ/mol}$$

The CO₂ emission of the simulated FIT is only higher than that of the gas-based direct reduction ironmaking techniques emitting 0.815 to 1.160 tons of CO₂ per ton of DRI for the natural gas reformer DRI process (39). However, one should consider the final product of the FIT (molten iron) in return for the solid sponge iron produced by various direct reduction processes which should be further melted by the electric arc furnaces for steelmaking. FIT also eliminates pelletization/sintering and gas-reforming required for DRI production. It is noteworthy that the total CO₂ emission of the intended FIT can be further reduced by substituting the air blast (containing 21% oxygen) with oxygen-enriched air. The more the oxygen content of the air blast is, the eco-friendlier the process would be. Accordingly, the CO₂ emission is reduced to 1.286 tons per ton of hot metal for using pure oxygen in the process (refer to supplementary Table S3). Energy saving strategies such as waste heat recovery and export gases for power generation can further improve the pollution index of the process.

4. CONCLUSIONS

The FIT has been simulated for iron production from the Chadormalu iron oxide concentrate by methane and air blast (containing 21% oxygen). The process eliminates coke-making, pelletization, and gas-reforming units. Based on heat and material balance calculations, 70.405 tons/h CH₄ and 764.489 tons/h air blast (including 20% excess) are required for the annual production of one million tons of hot metal with 95% metallization. Accordingly, methane plays a dual role: 47% as a reducing agent and 53% as fuel to sustain the reactor temperature of 1600 °C (1873 K). Furthermore, 193.134 tons/h CO₂ is emitted, and 1078 GJ/h energy is supplied. The values are equivalent to 1.550 tons of CO₂ and 8.65 GJ energy per ton of hot metal, respectively. Utilizing pure oxygen or oxygen-enriched air blast further improves the pollution index of the simulated FIT and puts it among eco-friendly ironmaking processes.

5. REFERENCES

1. Yearbook SS. World Steel Association: Brussels, Belgium; 2014.
2. Association WS. Fact sheet: energy use in the steel industry. Worldsteel Committee on Economic Studies Brussels, Brussels.

2016. <https://worldsteel.org/wp-content/uploads/Fact-sheet-Energy-use-in-the-steel-industry.pdf>
3. Anameric B, Kawatra SK. Properties and features of direct reduced iron. *Mineral processing and extractive metallurgy review*. 2007;28(1):59-116. <https://doi.org/10.1080/08827500600835576>
 4. World direct reduction statistics. 2023, Midrex Technologies Incorporation: New Jersey, USA. <https://www.midrex.com/wp-content/uploads/MidrexSTATSBook2022.pdf>
 5. Chen Y, Zuo H. Review of hydrogen-rich ironmaking technology in blast furnace. *Ironmaking & Steelmaking*. 2021;48(6):749-68. <https://doi.org/10.1080/03019233.2021.1909992>
 6. Wu X, Wang S, Fang H, Xu Z, Che P, Acquah AK. Study on semi-coke as an alternative fuel for blast furnace injection coal. *Energy Sources, Part A: Recovery, Utilization, and Environmental Effects*. 2022;44(2):5562-73. <https://doi.org/10.1080/15567036.2022.2027577>
 7. Xing X. Effects of coal interactions during cokemaking on coke properties under simulated blast furnace conditions. *Fuel Processing Technology*. 2020;199:106274. <https://doi.org/10.1016/j.fuproc.2019.106274>
 8. Helle H, Helle M, Saxen H. Nonlinear optimization of steel production using traditional and novel blast furnace operation strategies. *Chemical Engineering Science*. 2011;66(24):6470-81. <https://doi.org/10.1016/j.ces.2011.09.006>
 9. Sadrnezhad S. Direct Reduced Iron an Advantageous Charge Material for Induction Furnaces. *International Journal of Engineering*. 1990;3(1):37-48. https://www.ije.ir/article_71018.html
 10. Zare Ghadi A, Valipour M, Biglari M. Transient entropy generation analysis during wustite pellet reduction to sponge iron. *International Journal of Engineering, Transactions B: Applications*. 2018;31(8):1274-82. <https://doi.org/10.5829/ije.2018.31.08b.16>
 11. Paswan MK, Mukherjee C. Economic analysis of transportation directly reduced iron (dri) through ship. *International Journal of Services Technology and Management*. 2012;17(2-4):251-66. <https://doi.org/10.1504/IJSTM.2012.048540>
 12. Towhidi N. Reoxidation rate of sponge iron pellets, briquettes and iron powder compressed to various compressions in air. *International Journal of Engineering*. 1988;1(2):111-6. https://www.ije.ir/article_70983.html
 13. Komatina M, GUDENAU HW. The sticking problem during direct reduction of fine iron ore in the fluidized bed. *Metallurgical and Materials Engineering*. 2018. <https://doi.org/10.30544/378>
 14. Yi L, Huang Z, Jiang T. Sticking of iron ore pellets during reduction with hydrogen and carbon monoxide mixtures: behavior and mechanism. *Powder Technology*. 2013;235:1001-7. <https://doi.org/10.1016/j.powtec.2012.11.043>
 15. Chakraborty I, Sinha S. Refractories for Direct Iron Reduction Processes. https://www.researchgate.net/profile/Indra-Chakraborty-3/publication/344770108_OPTIMISATION_OF_BLAST_FURNACE_TROUGH_LINING_REFRACTORY_PERFORMANCE/links/614c1ee0519a1a381f796959/OPTIMISATION-OF-BLAST-FURNACE-TROUGH-LINING-REFRACTORY-PERFORMANCE.pdf
 16. Gielen D, Moriguchi Y. CO₂ in the iron and steel industry: an analysis of Japanese emission reduction potentials. *Energy policy*. 2002;30(10):849-63. [https://doi.org/10.1016/S0301-4215\(01\)00143-4](https://doi.org/10.1016/S0301-4215(01)00143-4)
 17. Li X, Sun W, Zhao L, Cai J. Material metabolism and environmental emissions of BF-BOF and EAF steel production routes. *Mineral Processing and Extractive Metallurgy Review*. 2018;39(1):50-8. <https://doi.org/10.1080/08827508.2017.1324440>
 18. Dahui XX, Wang. Reducing greenhouse gas emissions from energy consumption activities by the iron and steel industry in East China. *Energy sources*. 1999;21(6):541-6. <https://doi.org/10.1080/00908319950014669>
 19. Zhang X, Jiao K, Zhang J, Guo Z. A review on low carbon emissions projects of steel industry in the World. *Journal of cleaner production*. 2021;306:127259. <https://doi.org/10.1016/j.jclepro.2021.127259>
 20. Kemori N, Denholm W, Kurokawa H. Reaction mechanism in a copper flash smelting furnace. *Metallurgical and Materials Transactions B*. 1989;20:327-36. <https://doi.org/10.1007/BF02696985>
 21. Sohn HY, Mohassab Y. Development of a novel flash ironmaking technology with greatly reduced energy consumption and CO₂ emissions. *Journal of Sustainable Metallurgy*. 2016;2:216-27. <https://doi.org/10.1007/s40831-016-0054-8>
 22. Sohn HY, Fan D-Q, Abdelghany A. Design of novel flash ironmaking reactors for greatly reduced energy consumption and CO₂ emissions. *Metals*. 2021;11(2):332. <https://doi.org/10.3390/met11020332>
 23. Abdelghany A, Fan D-Q, Sohn H. Novel flash ironmaking technology based on iron ore concentrate and partial combustion of natural gas: a CFD study. *Metallurgical and Materials Transactions B*. 2020;51:2046-56. <https://doi.org/10.1007/s11663-020-01909-6>
 24. Pinegar H, Moats MS, Sohn H. Flowsheet development, process simulation and economic feasibility analysis for novel suspension ironmaking technology based on natural gas: Part 1—Flowsheet and simulation for ironmaking with reformerless natural gas. *Ironmaking & Steelmaking*. 2012;39(6):398-408. <https://doi.org/10.1179/1743281211Y.0000000053>
 25. Wang R-r, Zhang J-l, Liu Y-r, Zheng A-y, Liu Z-j, Liu X-l, et al. Thermal performance and reduction kinetic analysis of cold-bonded pellets with CO and H₂ mixtures. *International Journal of Minerals, Metallurgy, and Materials*. 2018;25:752-61. <https://doi.org/10.1007/s12613-018-1623-6>
 26. Yang Y, Bao Q, Guo L, Wang Z, Guo Z. Numerical simulation of flash reduction in a drop tube reactor with variable temperatures. *International Journal of Minerals, Metallurgy and Materials*. 2022;29(2):228-38. <https://doi.org/10.1007/s12613-020-2210-1>
 27. Chen F, Mohassab Y, Jiang T, Sohn HY. Hydrogen reduction kinetics of hematite concentrate particles relevant to a novel flash ironmaking process. *Metallurgical and Materials Transactions B*. 2015;46:1133-45. <https://doi.org/10.1007/s11663-015-0332-z>
 28. Elzohiery M, Fan D, Mohassab Y, Sohn H. Kinetics of hydrogen reduction of magnetite concentrate particles at 1623–1873 K relevant to flash ironmaking. *Ironmaking & Steelmaking*. 2021;48(5):485-92. <https://doi.org/10.1080/03019233.2020.1819942>
 29. Wang H, Sohn H. Hydrogen reduction kinetics of magnetite concentrate particles relevant to a novel flash ironmaking process. *Metallurgical and Materials Transactions B*. 2013;44:133-45. <https://doi.org/10.1007/s11663-012-9754-z>
 30. Qu Y, Xing L, Wang C, Shao L, Zou Z. Kinetic characterization of flash reduction process of hematite ore fines under hydrogen atmosphere. *International Journal of Hydrogen Energy*. 2020;45(56):31481-93. <https://doi.org/10.1016/j.ijhydene.2020.08.196>
 31. Fan D-Q, Elzohiery M, Mohassab Y, Sohn H. The kinetics of carbon monoxide reduction of magnetite concentrate particles through CFD modelling. *Ironmaking & Steelmaking*. 2021;48(7):769-78. <https://doi.org/10.1080/03019233.2020.1861857>
 32. Fan D, Elzohiery M, Mohassab Y, Sohn H. Rate-enhancement effect of CO in magnetite concentrate particle reduction by H₂+

- CO mixtures. *Ironmaking & Steelmaking*. 2021;48(9):1064-75. <https://doi.org/10.1080/03019233.2021.1915645>
33. Chen F, Mohassab Y, Zhang S, Sohn HY. Kinetics of the reduction of hematite concentrate particles by carbon monoxide relevant to a novel flash ironmaking process. *Metallurgical and Materials Transactions B*. 2015;46:1716-28. <https://doi.org/10.1007/s11663-015-0345-7>
34. Elzohiery M, Fan D, Mohassab Y, Sohn H. Experimental investigation and computational fluid dynamics simulation of the magnetite concentrate reduction using methane-oxygen flame in a laboratory flash reactor. *Metallurgical and Materials Transactions B*. 2020;51(3):1003-15. <https://doi.org/10.1007/s11663-020-01809-9>
35. (CMIC), C.M.a.I.C. Products of chadormalu mining and industrial co. 2020 <http://chadormalu.com/en-us/Products>
36. Tahari MNA, Salleh F, Saharuddin TST, Samsuri A, Samidin S, Yarmo MA. Influence of hydrogen and carbon monoxide on reduction behavior of iron oxide at high temperature: Effect on reduction gas concentrations. *International Journal of Hydrogen Energy*. 2021;46(48):24791-805. <https://doi.org/10.1016/j.ijhydene.2020.06.250>
37. Heidari A, Niknahad N, Iljana M, Fabritius T. A review on the kinetics of iron ore reduction by hydrogen. *Materials*. 2021;14(24):7540. <https://doi.org/10.3390/ma14247540>
38. Changqing H, Xiaowei H, Zhihong L, Zhang C. Comparison of CO₂ emission between COREX and blast furnace iron-making system. *Journal of environmental sciences*. 2009;21:S116-S20. [https://doi.org/10.1016/S1001-0742\(09\)60052-8](https://doi.org/10.1016/S1001-0742(09)60052-8)
39. Nduagu EI, Yadav D, Bhardwaj N, Elango S, Biswas T, Banerjee R, et al. Comparative life cycle assessment of natural gas and coal-based directly reduced iron (DRI) production: A case study for India. *Journal of Cleaner Production*. 2022;347:131196. <https://doi.org/10.1016/j.jclepro.2022.131196>

COPYRIGHTS

©2024 The author(s). This is an open access article distributed under the terms of the Creative Commons Attribution (CC BY 4.0), which permits unrestricted use, distribution, and reproduction in any medium, as long as the original authors and source are cited. No permission is required from the authors or the publishers.



Persian Abstract

چکیده

فرآیند تولید آهن به روش فن آوری فلش با استفاده از گاز متان و هوا (حاوی ۲۱٪ اکسیژن) به طور اختصاصی برای شرکت معدنی و صنعتی چادرملو شبیه سازی و محاسبه شده است. نتایج حاصل بر اساس شبیه سازی ترمودینامیکی و محاسبات مربوط به موازنه جرم و انرژی فرآیند فلش نشان می دهد که در مجموع ۷۰/۴۰۵ tons/h متان پیش گرم برای تولید سالانه یک میلیون تن آهن خام با ۹۵٪ احیاء مورد نیاز است. ۴۷٪ از این مقدار متان به عنوان عامل احیاء اکسیدهای آهن عمل کرده و مابقی با ۷۶۴/۴۸۹ tons/h هوای پیش گرم (با احتساب ۲۰٪ مقدار اضافی) می سوزد تا ۱۰۷۸ GJ/h انرژی مورد نیاز برای اجرای عملیات در دمای ۱۶۰۰ °C را تأمین کند. در همین راستا، ۱۹۳/۱۳۴ tons/h دی اکسید کربن طی فرآیند انتشار می یابد که معادل ۱/۵۵۰ تن به ازای تولید هر تن آهن خام است. این امر نشان می دهد که فرآیند فلش شبیه سازی شده، از لحاظ آلایندگی زیست محیطی، پاکیزه تر از روش های کوره بلند و احیاء مستقیم بر پایه زغال برای تولید آهن است که در عین حال، نیاز به استفاده از واحدهای کک سازی، گندله سازی یا ریفرمیگ گاز را برطرف می نماید.

Supplementary Material

NOTE: Original data files of mechanistic study and heat and material balances (MECHANISM.IGI and H&M.BAL) are also included in the ZIP Electronic Supplementary Materials. Use HSC CHEMISTRY version 6.0 or later for using them.

TABLE S1. The results of heat and material balances by ignoring the fuel combustion process

Type	Stream	Temperature (°C)	Species	Rate (tons/h)	Rate (Mmol/h)	Enthalpy* (GJ/h)
Input	Iron oxide concentrate	25	Fe ₃ O ₄	136.990	0.592	-659.99
			Fe ₂ O ₃	45.790	0.287	-235.99
			SiO ₂	4.940	0.082	-74.89
			CaO	0.855	0.015	-9.68
			Al ₂ O ₃	0.760	0.007	-12.49
			MgO	0.665	0.016	-9.93
	Flux	25	CaO	6.840	0.122	-77.44
			MgO	0.532	0.013	-7.94
	Feed gas	900	SiO ₂	0.228	0.004	-3.46
			CH ₄ (g)	33.208	2.070	-46.54
Total				230.808	3.208	-1138.35
Output	Hot metal	1600	Fe	124.629	2.232	168.19
			FeO	8.354	0.116	-17.31
			CaO	7.695	0.137	-76.04
	Slag	1600	SiO ₂	5.168	0.086	-68.84
			MgO	1.197	0.030	-15.51
			Al ₂ O ₃	0.760	0.007	-11.06
			Fe ₃ O ₄	0.037	0.000	-0.11
	Off-gas	1600	Fe ₂ O ₃	0.005	0.000	-0.02
			CO ₂ (g)	5.727	0.130	-40.30
			CO(g)	54.323	1.939	-113.23
			H ₂ O(g)	16.397	0.910	-159.47
			H ₂ (g)	6.511	3.230	157.06
			CH ₄ (g)	0.000	0.000	0.00
			C (Soot)	0.006	0.001	0.02
			<i>Heat loss</i>			116.00
Total				230.808	8.818	-60.62
Balance = Total_{Output} – Total_{Input}				0.000	5.610	1077.73

TABLE S2. Complementary results of heat and material balances

Type	Stream	Temperature (°C)	Rate (tons/h)	Enthalpy* (GJ/h)
Input	Concentrate	25	190.000	-1002.96
	Flux	25	7.600	-88.84
	Feed gas	900	70.405	-98.68
	Air blast	900	764.490	729.79
Total			1032.495	-460.67

	Hot metal	1600	124.629	168.19
	Slag	1600	23.216	-188.88
Output	Off-gas	1600	884.650	-555.98
			<i>Heat loss</i>	116.00
	Total		1032.495	-460.67
Balance = Total_{Output} – Total_{Input}			0.000	0.00

TABLE S3. The results of heat and material balances for using pure oxygen

Type	Stream	Temperature (°C)	Species	Rate (tons/h)	Rate (Mmol/h)	Enthalpy* (GJ/h)
Input	Iron oxide concentrate	25	Fe ₃ O ₄	136.990	0.592	-659.99
			Fe ₂ O ₃	45.790	0.287	-235.99
			SiO ₂	4.940	0.082	-74.89
			CaO	0.855	0.015	-9.68
			Al ₂ O ₃	0.760	0.007	-12.49
			MgO	0.665	0.016	-9.93
	Flux	25	CaO	6.840	0.122	-77.44
			MgO	0.532	0.013	-7.94
	Feed gas	900	SiO ₂	0.228	0.004	-3.46
			CH ₄ (g)	58.449	3.643	-81.92
Pure oxygen	900	O ₂ (g)	120.832	3.776	108.79	
	Total		376.881	8.557	-1064.94	
Output	Hot metal	1600	Fe	124.629	2.232	168.19
			FeO	8.354	0.116	-17.31
			CaO	7.695	0.137	-76.04
	Slag	1600	SiO ₂	5.168	0.086	-68.84
			MgO	1.197	0.030	-15.51
			Al ₂ O ₃	0.760	0.007	-11.06
			Fe ₃ O ₄	0.037	0.000	-0.11
			Fe ₂ O ₃	0.005	0.000	-0.02
			CO ₂ (g)	74.971	1.704	-527.54
	Off-gas	1600	CO(g)	54.323	1.939	-113.23
			H ₂ O(g)	73.087	4.057	-710.79
			H ₂ (g)	6.511	3.230	157.06
			O ₂ (g)	20.138	0.629	34.24
			CH ₄ (g)	0.000	0.000	0.00
			C (Soot)	0.006	0.001	0.02
			<i>Heat loss</i>		116.00	
	Total		376.881	14.168	-1064.94	
Balance = Total_{Output} – Total_{Input}			0.000	5.611	0.00	

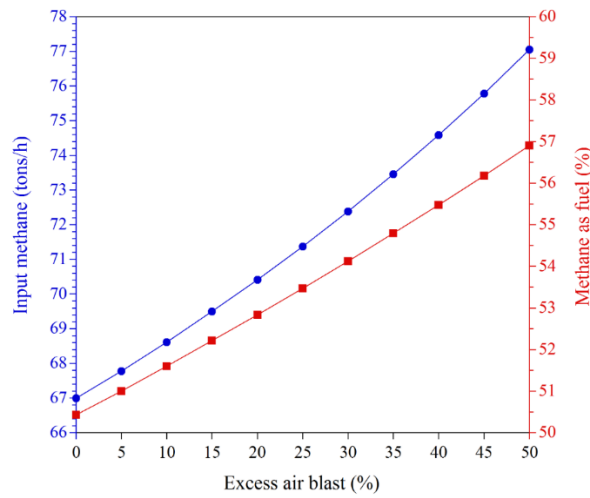


Figure S1. Effect of excess air blast on total input rate of methane (squares) and contribution of methane as fuel (circles)

Clarification of calculations (based on final heat and material balances):

- The degree of metallization $= \frac{n_{\text{Fe (produced)}}}{n_{\text{Fe (max)}}} = \frac{2.232}{2.348} \times 100 = 95\%$
- The methane's contribution as reducing agent $= \frac{n_{\text{CH}_4 \text{ (reducing agent)}}}{n_{\text{CH}_4 \text{ (total)}}} = \frac{2.07}{4.389} \times 100 = 47\%$
- The methane's contribution as fuel $= \frac{n_{\text{CH}_4 \text{ (fuel)}}}{n_{\text{CH}_4 \text{ (total)}}} = \frac{4.389 - 2.07}{4.389} \times 100 = 53\%$
- Energy for every ton of hot metal $= \frac{\text{total energy}}{m_{\text{Fe}}} = \frac{1078}{124.629} = 8.65 \text{ GJ / ton hot metal}$
- CO₂ emission for every ton of hot metal $= \frac{m_{\text{CO}_2} + \left(\frac{M_{\text{CO}_2}}{M_{\text{CO}}}\right)m_{\text{CO}}}{m_{\text{Fe}}} = \frac{107.769 + \left(\frac{44}{28}\right)54.323}{124.629} = 1.550 \text{ tons CO}_2 / \text{ton hot metal}$



Semantic Segmentation of Aerial Imagery: A Novel Approach Leveraging Hierarchical Multi-scale Features and Channel-based Attention for Drone Applications

E. Sahragard, H. Farsi*, S. Mohamadzadeh

Department of Electrical and Computer Engineering, University of Birjand, Birjand, Iran

PAPER INFO

Paper history:

Received 28 September 2023

Received in revised form 12 November 2023

Accepted 19 November 2023

Keywords:

Semantic Drone Segmentation

Hierarchical Multi-scale Feature Extraction

Efficient Channel-based Attention

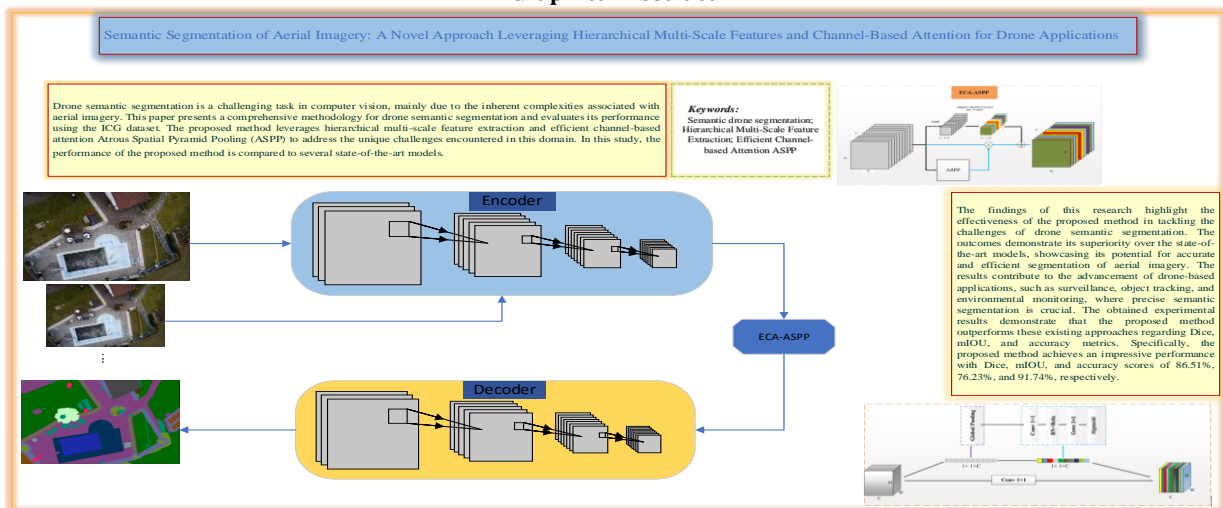
Atrous Spatial Pyramid Pooling

ABSTRACT

Drone semantic segmentation is a challenging task in computer vision, mainly due to inherent complexities associated with aerial imagery. This paper presents a comprehensive methodology for drone semantic segmentation and evaluates its performance using the ICG dataset. The proposed method leverages hierarchical multi-scale feature extraction and efficient channel-based attention Atrous Spatial Pyramid Pooling (ASPP) to address the unique challenges encountered in this domain. In this study, the performance of the proposed method is compared to several state-of-the-art models. The findings of this research highlight the effectiveness of the proposed method in tackling the challenges of drone semantic segmentation. The outcomes demonstrate its superiority over the state-of-the-art models, showcasing its potential for accurate and efficient segmentation of aerial imagery. The results contribute to the advancement of drone-based applications, such as surveillance, object tracking, and environmental monitoring, where precise semantic segmentation is crucial. The obtained experimental results demonstrate that the proposed method outperforms these existing approaches regarding Dice, mIOU, and accuracy metrics. Specifically, the proposed method achieves an impressive performance with Dice, mIOU, and accuracy scores of 86.51%, 76.23%, and 91.74%, respectively.

doi: 10.5829/ije.2024.37.05b.18

Graphical Abstract



*Corresponding Author Email: hfarsi@birjand.ac.ir (H. Farsi)

Please cite this article as: Sahragard E, Farsi H, Mohamadzadeh S. Semantic Segmentation of Aerial Imagery: A Novel Approach Leveraging Hierarchical Multi-scale Features and Channel-based Attention for Drone Applications. International Journal of Engineering, Transactions B: Applications. 2024;37(05):1022-35.

NOMENCLATURE

$x(i, j)$	Input feature map	$C1$	the weight of the first and second convolutions with kernel size 1
H	Height of the feature maps	TP	True positive
W	Width of the feature maps	FN	False-negative
IoU	Intersection over Union	FP	False positive
δ	ReLU activation function	σ	Sigmoid activation function

1. INTRODUCTION

Deep learning has emerged as a powerful technique in various domains, and it plays a crucial role in enabling drones to understand and accurately interpret their surroundings [1]. Semantic segmentation, a critical application, involves classifying objects or regions at the pixel level in drone images, enabling tasks such as aerial surveillance, infrastructure inspection, and precision agriculture(1). However, achieving accurate and reliable semantic segmentation for drone imagery poses significant challenges due to its unique characteristics (2),(3). The rapid advancement of drone technology has revolutionized industries by offering unprecedented capabilities for data acquisition and analysis (4). Drones, equipped with high-resolution cameras, provide a comprehensive aerial viewpoint, capturing valuable information that can be extracted through semantic segmentation. (5). This enables drones to make informed decisions based on their environmental understanding (6),(7). However, drone semantic segmentation encounters several challenges that must be addressed to achieve accurate results (8). The first challenge lies in the variability of scale and perspective inherent in aerial imagery. Objects of interest in drone images exhibit variations in distance, size, and orientation, making accurate segmentation challenging. Additionally, complex backgrounds often present in drone images, such as buildings, trees, and other objects, introduce occlusions and ambiguities in object boundaries, which further complicates the precise delineation from the surroundings. (9). The lack of readily available large-scale, diverse, and accurately annotated datasets poses a significant challenge when it comes to training robust semantic segmentation models that are specifically designed for drones. This limitation results in suboptimal performance and limited generalization capability. In this paper, we proposed a novel approach to address these challenges in drone semantic segmentation. Our method aims to improve the accuracy and robustness of semantic segmentation results by combining hierarchical multi-scale feature extraction with an efficient channel-based attention ASPP module. The proposed method contributes significantly to the field of drone semantic segmentation. Specifically, we introduced a hierarchical multi-scale feature extraction module that captures features at different scales and levels of granularity, enabling our model to handle scale and perspective

variations prevalent in drone imagery. We also incorporated an efficient channel-based attention ASPP module that selectively focuses on informative features while suppressing irrelevant ones. This attention-based approach enhances the discriminative power of the model and improves segmentation accuracy. Furthermore, we proposed a feature fusion and integration step that combines the attention-guided features with the hierarchical multi-scale features, leveraging their complementary information to further enhance segmentation performance. Overall, our proposed method addresses the challenges of scale and perspective variability, complex backgrounds, and limited training data in drone semantic segmentation. Combining hierarchical multi-scale feature extraction and efficient channel-based attention ASPP provides a robust and accurate solution for interpreting drone-captured scenes.

In the following sections, we will describe the methodology in detail, present experimental results, and discuss the significance and implications of our findings. We believe these revisions provide a more targeted and logical overview of the existing work while highlighting the novelty and contributions of our approach in drone semantic segmentation.

2. LITERATURE REVIEW

During the past decade, deep learning has witnessed significant advancements in diverse domains, including machine vision (10), object tracking (11), and segmentation (12), (13). Deep learning methods have revolutionized this field by leveraging their ability to automatically learn and extract meaningful representations from large-scale datasets (14). In this section, we present a thorough review of research conducted on semantic segmentation of aerial imagery, particularly emphasizing its application in drone-related tasks. We examined the methodologies, techniques, and approaches utilized in previous studies, with a focus on how deep neural networks have been employed to achieve accurate semantic segmentation of aerial images. This literature review critically analyzes the accomplishments, limitations, and advancements in the field, laying the foundation for the proposed method. Additionally, it identifies the gaps that the present study aims to address. Moreover, this study highlights the significance of the proposed approach, which utilizes

hierarchical multi-scale features and channel-based attention. These advancements contribute to pushing the boundaries of aerial imagery analysis for drone applications. This research aims to advance semantic segmentation in aerial imagery by addressing identified gaps and introducing novel techniques. The intended outcome is an improved understanding and interpretation of aerial scenes. As a result, this advancement will enhance the capabilities and effectiveness of drones in various applications and domains such as surveillance, environmental monitoring, urban planning, and disaster response. We specifically examine the methodologies, techniques, and approaches utilized in previous studies, with a focus on the advancements made by prominent methods. These methods have made significant contributions to the field of semantic segmentation and have been widely adopted in various computer vision tasks(15).

FCN revolutionized semantic segmentation with end-to-end pixel-wise segmentation, serving as a foundational method (16). However, it has limitations in capturing fine details and object boundaries in aerial imagery (17). UNet introduced an encoder-decoder structure with skip connections and brought groundbreaking advancements in medical imaging (18). Nevertheless, it's important to note that the symmetric pathways in question may not fully cater to scale variations. This observation suggests that further considerations may be required to address the issue effectively. UNet++ was developed as an enhancement to UNet, incorporating nested skip and dense connections to improve segmentation accuracy. However, the increased complexity of UNet++ limit its feasibility in resource-constrained drone applications (19). DeepLab effectively addresses the challenge of capturing global and local contextual information using atrous/dilated convolutions and multi-scale contextual information (20). It dramatically improves segmentation accuracy, especially for objects of different scales and complex backgrounds. However, the reliance on dense dilated convolutions in DeepLab increases memory consumption and inference times, potentially introducing artefacts in segmentation masks. Lin et al. (21) utilize a feature pyramid network (FPN) for multi-scale object detection and segmentation, capturing local and global context. A limitation of this approach is its reliance on predefined anchor scales, which may encounter difficulties in handling diverse scale variations present in aerial imagery.

The PSPNet method, proposed by Zhao et al. (22) employs spatial pyramid pooling and dilated convolutions to capture contextual information at different scales in drone imagery. It utilizes a CNN backbone, like ResNet or VGG, to extract feature maps, followed by pyramid pooling modules. However, the pooling operations in PSPNet can cause information

loss and reduced spatial resolution, leading to difficulties in accurately segmenting small objects and capturing fine details in aerial imagery.

By leveraging the insights and advancements from these methods, we propose a novel approach for semantic segmentation of aerial imagery in the context of drone applications. Our approach leverages hierarchical multi-scale features and channel-based attention mechanisms to enhance segmentation accuracy and improve the interpretability of aerial scenes. Through the integration of these innovative techniques, we aim to address the limitations and challenges faced in the field and contribute to the advancement of aerial imagery analysis for drone applications.

The following sections of this paper will provide a detailed description of our proposed method, including the architectural design, training strategies, and evaluation metrics. Additionally, we will present comprehensive experimental results to demonstrate the effectiveness and superiority of our approach compared to existing methods. Finally, we will discuss the implications of our findings and outline potential future research directions in the domain of semantic segmentation for drone applications.

3. PROPOSED METHOD

This section provides an overview of the methodology employed in this paper. We present a high-level description of the proposed method and explain its key components: hierarchical multi-scale feature extraction and efficient channel-based attention ASPP.

Furthermore, we discuss how these components effectively address the challenges encountered in drone semantic segmentation. The algorithm is introduced as follows:

Algorithm 1

1. **Input:** Drone image I, Ground truth segmentation map GT
2. **Preprocess** the input image I
3. **Define** the architecture of the proposed model, which includes the hierarchical multi-scale feature extraction and the Channel-based Attention ASPP module. The model consists of the following components:
 - Convolutional layers for feature extraction at different scales.
 - Efficient Channel-based Attention ASPP module for inter-channel dependencies.
 - Convolutional layers for refinement.
 - Up-sampling layers for restoring the original image size.
 - Softmax or sigmoid activation for obtaining pixel-wise predicted probabilities.
4. Initialize the model parameters.
5. Define the loss function, in this work as pixel-wise cross-entropy loss.
6. Set the number of training iterations and the learning rate for optimization.
7. Perform the training loop:
 - a. For each iteration:
 - Perform forward propagation through the model:
 - Obtain multi-scale feature maps

- Apply the Efficient Channel-based Attention ASPP module to the multi-scale feature maps
 - Fuse the multi-scale feature maps to generate a final feature representation.
 - Apply convolutional layers and activation functions to refine the feature representation.
 - Up-sample the refined feature representation to the original image size.
 - Apply softmax activation to obtain pixel-wise predicted probabilities P for each class.
 - Calculate the loss L between the predicted probabilities P and the ground truth segmentation map GT .
 - Perform backpropagation to compute and update the gradients of the model's parameters.
 - Update the model parameters using an optimizer with the defined learning rate.
- b. Repeat the training loop for the specified number of iterations.
8. Evaluate the trained model on validation or test data:
- Preprocess the validation/test images in the same way as the training images.
 - Perform forward propagation through the trained model to obtain predicted probabilities for the validation/test images.
 - Evaluate the segmentation performance using metrics such as intersection over union (IoU), Dice score and accuracy.
9. Output: Trained model for drone semantic segmentation.

The proposed method aims to improve the accuracy and robustness of drone semantic segmentation by combining hierarchical multi-scale feature extraction with efficient channel-based attention ASPP. The method influences the unique characteristics of aerial imagery and addresses the challenges posed by scale and perspective variability, complex backgrounds, and limited training data. The following explanation provides an overview of the components used in the proposed method.

3. 1. Hierarchical Multi-scale Feature Extraction

The hierarchical multi-scale feature extraction component captures features at multiple scales and levels of granularity (23), (24). It involves extracting features from different layers of the network architecture, allowing the model to incorporate information from various scales. By considering features at multiple scales, the model can handle the variations in object sizes, orientations, and perspectives often presented in drone imagery. This multi-scale feature extraction enables the model to capture both fine-grained details and global context, leading to improved segmentation accuracy. This component addresses the challenge of scale and perspective variability in drone imagery. The model can adapt to variations in object sizes, orientations, and perspectives by capturing features at different scales. This allows accurate segmentation of objects in aerial scenes, regardless of their scale or spatial arrangement. The use of multi-scale feature extraction in the model allows for the capture of both local details and global context. This, in turn, leads to improved segmentation accuracy, particularly when dealing with variations in scale.

In the proposed method, we utilize the ResNet-50 backbone, which is a widely used convolutional neural

network architecture known for its effectiveness in feature extraction. The hierarchical feature extraction process begins with the initial convolutional layer of the ResNet-50 backbone, which captures low-level features such as edges and textures. These features provide a basis for subsequent layers to extract more complex and informative features. The ResNet-50 backbone consists of several stages, each containing multiple residual blocks. The feature extraction layers at different scales are determined by the stages and blocks within the ResNet-50 architecture. In the ResNet-50 architecture, the first stage consists of a single convolutional layer that captures low-level features. The subsequent stages, each contains a varying number of residual blocks. These blocks consist of multiple convolutional layers, including bottleneck layers that reduce the spatial dimensions and increase the number of channels. The hierarchical multi-scale feature extraction process with the ResNet-50 backbone enables the capture of both local and global information in drone imagery. The earlier stages of the ResNet-50 capture local information and fine-grained details, which are crucial for segmenting small objects or objects with intricate textures. These features preserve object boundaries and capture local variations effectively. As the network progresses through the stages of the ResNet-50, the scale of the features increases, incorporating more global context. The later stages capture features at coarser scales, enabling the model to consider the relationships between objects and their surroundings. This global context is essential for accurately segmenting larger objects and handling complex scenes with multiple objects and backgrounds. The hierarchical multi-scale feature extraction process provides a comprehensive representation of the input scene by combining features from different stages of the ResNet-50 backbone. The model can leverage these multi-scale features to make informed decisions during the segmentation process, effectively addressing the challenges of scale and perspective variability in drone imagery.

3. 2. Efficient Channel-based Attention ASPP

The efficient channel-based attention Atrous Spatial Pyramid Pooling (ASPP) component incorporates an attention mechanism that selectively focuses on informative features while suppressing irrelevant ones. This attention-based approach enhances the discriminative power of the model by assigning attention weights to different channels of the feature maps. By emphasizing relevant features and de-emphasizing less informative ones, the model becomes more adept at discriminating objects from complex backgrounds and handling occlusions. The efficient channel-based attention ASPP enables the model to exploit local and global contextual information effectively, leading to enhanced segmentation accuracy.

A vital advantage of the ASPP module with efficient channel attention lies in its ability to model interdependencies among different channels of feature maps. The channels in feature maps represent various aspects or semantic features of objects in the image. However, not all channels contribute equally to the segmentation task. The incorporation of efficient channel attention resolves this issue by dynamically adjusting the importance of each channel through learned attention weights. By emphasizing informative channels and suppressing noise or low-value channels, the ASPP module ensures accurate and reliable segmentation results. The utilization of channel-level attention allows the model to leverage limited training data more efficiently, resulting in enhanced generalizability. This component tackles the challenges of complex backgrounds and limited training data in drone semantic segmentation. By applying an attention mechanism, the model can selectively focus on informative features while suppressing irrelevant ones. This attention-based approach aids in discriminating objects from complex backgrounds and handling occlusions, leading to improved segmentation accuracy. During the training process, the attention weights are learned through backpropagation, optimizing the model to attend to the most informative features for semantic segmentation. These weights are adjusted iteratively, allowing the module to adaptively focus on relevant channels depending on the specific characteristics of the input data. The dynamic adjustment of attention weights ensures that the module can adapt to different semantic segmentation tasks and handle variations in object appearance and context. It enables the model to effectively capture both local and global information while suppressing noise and irrelevant details. Different components of the module are explained in the following sub-sections.

3. 2. 1. ASPP Module In CNN architectures, the ASPP module plays a crucial role in capturing multi-scale contextual information within images effectively (20), (25). Its fundamental purpose is to aggregate features from distinct receptive fields of the CNN's convolution kernel, enabling the extraction of comprehensive multi-scale information from an image. The ASPP module consists of parallel branches that apply atrous spatial convolutions to the input image. Each branch operates at a specific dilation rate. The dilation rate determines the spacing between kernel elements, resulting in an expanded receptive field that enhances the ability of the model to capture contextual details while keeping the computational cost low (26). Figure 1 provides a visual illustration of the ASPP module, showcasing its architecture and functionality.

3. 2. 2. Efficient Channel-based Attention The attention module can be implemented using techniques like squeeze-and-excitation blocks (27), (28). These

techniques enable the model to learn and adaptively adjust the channel-wise attention weights based on the input data. Figure 2 illustrates the architecture of the Efficient Channel-based Attention module.

We can formulate the ECA module as follows: Let X represent the input feature maps with dimensions $H \times W \times C$, where H and W are the height and width of the feature maps, and C is the number of channels.

- Compression: Apply GAP to X to obtain a channel descriptor z of dimensions $1 \times 1 \times C$:

$$z(X) = \frac{1}{H \times W} \sum_{i=1}^H \sum_{j=1}^W x(i, j) \quad (1)$$

- Re-weighting: Apply a two-layer convolution with kernel size 1 to z to obtain an attention of weights s of dimensions $1 \times 1 \times C$:

$$s = F_{ex}(z, C1) = \delta(C1(\sigma C1(z))) \quad (2)$$

where δ is a ReLU activation function, and $C1$ is the weight of the first and second convolutions with kernel size 1, respectively. Besides, σ is a sigmoid activation function that scales the 1×1 conv output to the range $[0, 1]$, ensuring that the weights are positive and sum to 1.

- Scaling: Apply the weights s to the original feature maps X to obtain the scaled feature maps Y of dimensions $H \times W \times C$:

$$Y = s \otimes X \quad (3)$$

After performing the element-wise multiplication denoted by \otimes , the resulting scaled feature maps,

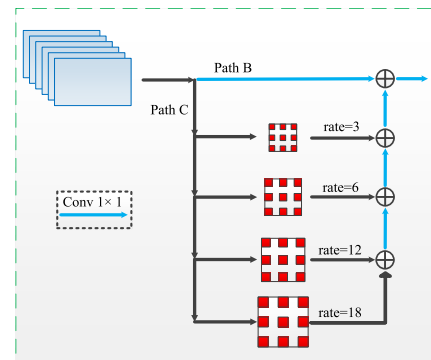


Figure 1. The details of the ASPP structure

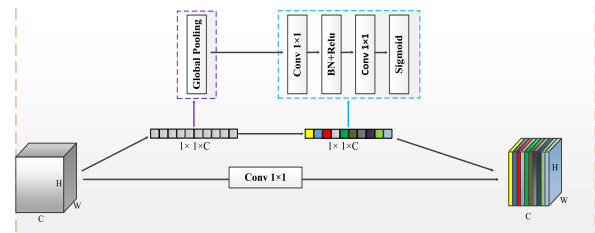


Figure 2. The details of the ECA structure

represented as Y , are subsequently passed to the next layer in the network. Using GAP to extract information from each channel of the input feature map, the ECA mechanism enabled the model to prioritize important features and enhance its overall performance. The resulting feature map utilized one-dimensional (1-D) convolutional cross-channel interaction instead of 1×1 convolutions to minimize the computational complexity of the model (29).

3. 2. 3. Efficient Channel-based Attention ASPP

We introduce the Efficient Channel-based Attention ASPP (ECA-ASPP) module as an innovative component within our proposed method, offering an alternative to the concatenation operation utilized in the DeepLab architecture. Figure 3 provides a visual representation of the various components and operations involved within the ECA-ASPP structure. These details are crucial for understanding how the architecture functions and how it leverages its unique features to enhance image analysis.

Our module focuses on modeling interdependencies between channels presented in feature maps, dynamically adjusting the importance of each channel using attention weights. By employing this attention mechanism, we enhance feature representation, resulting in improved discriminative power and more accurate segmentation. The main advantage of our method is that it is able to selectively focus on useful information channels while reducing the importance of less relevant channels. This selective attention enables the network to efficiently utilize features, leading to enhanced segmentation performance and improved efficiency compared to the traditional concatenation operation.

By combining hierarchical multi-scale feature extraction with the ECA-ASPP, the proposed method leverages the complementary strengths of both approaches. The multi-scale feature extraction captures a wide range of spatial details, while the channel attention module enhances the discriminative power of the extracted features. This integration aids the model in effectively handling the challenges of drone semantic segmentation, such as variations in object scales, complex backgrounds, and occlusions.

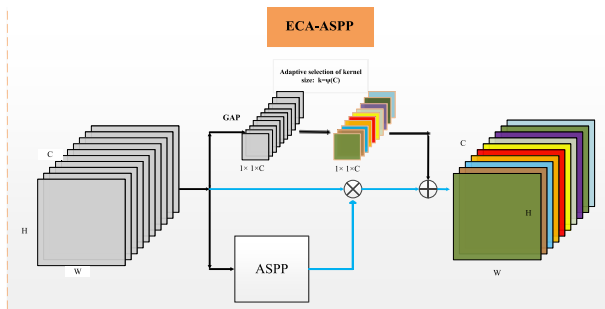


Figure 3. The details of ECA-ASPP structure

4. EXPERIMENTAL RESULT

4. 1. Datasets and Data Augmentation

The designers of the Semantic Drone Dataset have specifically aimed to enhance the safety of autonomous drone flight and landing procedures by focusing on a semantic understanding of urban scenes. The dataset comprises imagery of over 20 houses captured from a bird's eye view at heights ranging from 5 to 30 meters above the ground. The images were acquired using a high-resolution camera with a size of 6000×4000 pixels (24 megapixels). The dataset includes pixel-accurate annotations for semantic segmentation. Detailed labels for 20 classes are assigned to the training and test sets. These classes include various elements such as trees, grass, other vegetation, dirt, gravel, rocks, water, paved areas, pools, persons, dogs, cars, bicycles, roofs, walls, fences, fence poles, windows, doors, and obstacles. The complexity of the dataset is constrained to these 20 classes, allowing researchers to focus on the specific semantic understanding of urban scenes. This carefully annotated dataset provides a valuable resource for developing and evaluating algorithms in semantic segmentation in the context of autonomous drone flights (30).

4. 1. 1. Data Augmentation

In the proposed method, we utilize data augmentation techniques to improve the performance of our semantic segmentation model on the semantic drone dataset. Data augmentation is a widely used approach in computer vision tasks, including semantic segmentation, to address challenges such as limited labelled data and variations in environmental conditions. The data augmentation process involved applying a set of transformations to the original dataset, resulting in the creation of new and diverse training samples. These transformed samples facilitated an increase in quantity and variety of the training data, leading to improved model performance and generalization ability (31), (32). Specifically, we applied several standard data augmentation techniques to the semantic drone dataset:

- **Random Cropping:** This technique involves randomly selecting a portion of the image and using it as a new image. It aids in introducing variations in the position and composition of objects within the image. By cropping different parts of the image, the model can learn to recognize objects from various perspectives and locations.
- **Horizontal Flipping:** During horizontal flipping, the image undergoes a horizontal flip, creating a mirror image of the original. This technique is effective when the orientation of objects in the image does not affect their interpretation. It helps the model learn to recognize objects regardless of their left-right orientation.

- **Vertical Flipping:** Similar to horizontal flipping, vertical flipping involves flipping the image vertically, resulting in an upside-down version of the original image. It can be helpful in certain applications where the orientation of objects is not critical, such as text recognition or specific types of image classification.
- **Rotation:** This involves rotating the image to a certain degree. By applying the rotation, the model becomes more robust to changes in the orientation of objects in the image. It aids the model in learning to recognize objects from different angles and improves its ability to generalize to rotated images.
- **Random Brightness and Contrast Adjustments:** This technique involves randomly adjusting the brightness and contrast of the image. By modifying the brightness and contrast, the model can handle variations in lighting conditions. It helps the model become more resilient to changes in illumination and enhances its ability to generalize to images with different lighting levels.
- **Contrast-Limited Adaptive Histogram Equalization (CLAHE):** CLAHE is an image enhancement technique that improves the contrast of an image. It redistributes pixel intensities in a way that enhances details in both bright and dark regions of the image. The CLAHE aids the model in capturing fine-grained details and improves its performance in low-contrast images.
- **Grid Distortion:** Grid distortion applies a distortion effect to the image by manipulating a grid overlay. It introduces local deformations to the image, which can help the model learn to handle geometric transformations. The Grid distortion is particularly useful for tasks that require the model to be robust to deformations, such as object detection or image segmentation.
- **Optical Distortion:** Optical distortion simulates lens distortion effects in the image. It applies non-linear transformations to mimic the distortions introduced by different camera lenses. This technique is useful in scenarios where the images are captured by wide-angle lenses. By training the model with optically distorted images, it becomes more robust to lens distortions in real-world scenarios.

By applying these data augmentation techniques, we augmented the semantic drone dataset with transformed images, effectively expanding the size of the training dataset and introducing variations representative of real-world scenarios. This enabled our model to learn from a broader range of conditions and improved its ability to segment objects in unseen drone images accurately. Data augmentation played a crucial role in our semantic segmentation pipeline, enhancing the performance and generalization ability of our model on the semantic drone dataset.

Figure 4 shows the original image alongside four augmented versions generated from it. The original image serves as the base or reference image, while the four augmented images are created by applying augmentation techniques to the original image. Each augmented image has undergone a specific data augmentation technique. These techniques include random cropping, horizontal flipping, vertical flipping, rotation, random brightness, and contrast adjustments, contrast-limited adaptive histogram equalization, grid distortion, and optical distortion.

4. 2. Evaluation Metric

4. 2. 1. Intersection over Union

Semantic segmentation tasks commonly employ the Intersection over Union (IoU) metric as the primary evaluation measure (33). This widely adopted metric quantifies the quality of a predicted segmentation mask by calculating the ratio between the intersection and the union of the predicted and ground truth masks. The IoU metric yields a value between 0 and 1, where a score of 1 denotes a flawless segmentation. The IoU is mathematically defined as follows:

$$IoU = \frac{TP}{TP+FP+FN} \quad (4)$$

where TP stands for true positive (the number of correctly classified pixels), FP stands for false positive (the number of incorrectly classified pixels), and FN stands for false negative (the number of pixels that should have been classified as belonging to the class but were not). Mean Intersection over Union (mIoU) is a commonly used evaluation metric for semantic segmentation tasks, defined as the average IoU score across all classes:

$$meanIoU = \frac{1}{C} \sum_c IoU_c \quad (5)$$

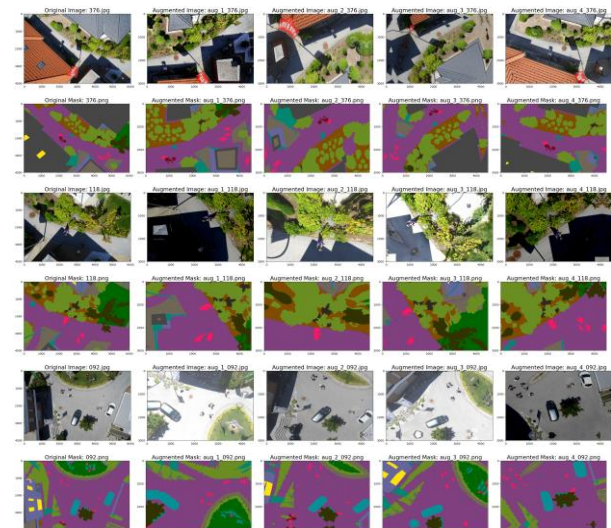


Figure 4. Examples of augmented images in the ICG dataset

The meanIoU (mIoU) score evaluates the overall accuracy of a segmentation model across all classes. A higher mIoU score signifies improved segmentation accuracy (34).

4. 2. 2. Dice Metric The Dice coefficient, also known as the Sørensen–Dice coefficient and F1 score, is a widely used metric for evaluating the performance of binary image segmentation models on a given dataset. It effectively captures the balance between false positives (FP) and false negatives (FN) (35). The Dice coefficient measures the degree of overlap between the predicted and ground truth segmentations. It ranges from 0 to 1, where 1 indicates a perfect overlap, and 0 specifies no overlap. The computation of the Dice coefficient relies on the counts of true positives (TP), false negatives (FN), and false positives (FP), which can be derived from the confusion matrix of the model's predicted outcomes. The TP count represents the number of correctly identified positive pixels, while the FN count reflects the number of incorrectly identified negative pixels. Conversely, the FP count denotes the number of pixels erroneously classified as positive. The Dice coefficient is mathematically defined as follows:

$$Dice = \frac{2|X \cap Y|}{|X| + |Y|} = \frac{2TP}{2TP + FP + FN} \quad (6)$$

The Mean Dice (mDice) coefficient represents the average Dice coefficient score across all classes within a dataset. We can calculate the Dice coefficient as follows, which provides a measure of overall segmentation performance:

$$mean\ Dice = \sum_c Dice_c \quad (7)$$

4. 2. 3. Pixel-wise Accuracy The evaluation of performance and accuracy in semantic segmentation models often involves utilizing the pixel-wise accuracy metric for pixel-level predictions. Pixel-wise accuracy calculates the ratio of correctly classified pixels to the total number of pixels in the image. To calculate this metric, we compare the model's estimated outcomes with the ground truth labels on a pixel-by-pixel basis. Each pixel in the predicted segmentation is compared to its corresponding pixel in the ground truth segmentation. If the predicted label matches the ground truth label, the pixel is classified correctly. Utilizing pixel-wise accuracy provides valuable insights into the overall performance of semantic segmentation models.

4. 3. Experimental Result Table 1 presents the experimental results for evaluating a semantic drone segmentation model. The metrics used for evaluation are IoU, Dice coefficient, and Accuracy. Each row is related to a specific class. Table 1 demonstrates the performance of the proposed method across different classes. The model achieves high IoU, Dice, and

TABLE 1. Performance Evaluation of Proposed Method Across Multiple Classes

Class	IoU	Dice	Acc
Unlabeled	50.14	66.7910	88.02
Paved-area	95	97.4359	97.42
Dirt	62.71	77.0819	79.26
Grass	93.04	96.3945	97.45
Gravel	79.98	88.8765	96.17
Water	92.35	96.0229	98.52
Rocks	85.89	92.4095	95.67
Pool	96.62	98.2809	98.54
Vegetation	74.4	85.3211	85.37
Roof	94.9	97.3833	97.66
Wall	84.85	91.8042	82.89
Window	69.28	81.8526	87.9
Door	47.03	63.9733	63.51
Fence	59.65	74.7260	73.93
Fence-pole	42.4	59.5506	60.86
Person	79.16	88.3679	89.72
Dog	68.05	80.9878	75.01
Car	94.25	97.0399	98.58
Bicycle	67.58	80.6540	75.83
Tree	78.17	87.7477	84.03
Bald-tree	79.99	88.8827	89.5
Ar-marker	88.17	93.7131	95.28
Obstacle	78.23	87.7854	93.46

Accuracy scores for several classes such as paved-area, grass, pool, and car.

These high scores indicate that the proposed model successfully captures the boundaries and details of these classes, resulting in accurate segmentation. However, it is worth noting that certain classes such as unlabeled, dirt, fence-pole, and door exhibit lower scores, indicating areas where the model faces challenges in achieving accurate segmentation. These classes may pose challenges due to their complex or ambiguous visual characteristics, resulting in lower performance than other classes. Figure 5 demonstrates the performance of the proposed method for drone semantic segmentation using augmented images from the ICG dataset. The figure comprises three columns, each providing crucial information about the segmentation process. The first column showcases the original images from the augmented ICG dataset. The drone captures these images, and we apply augmentation techniques such as rotation, scaling, flipping, or adding noise to enhance them.

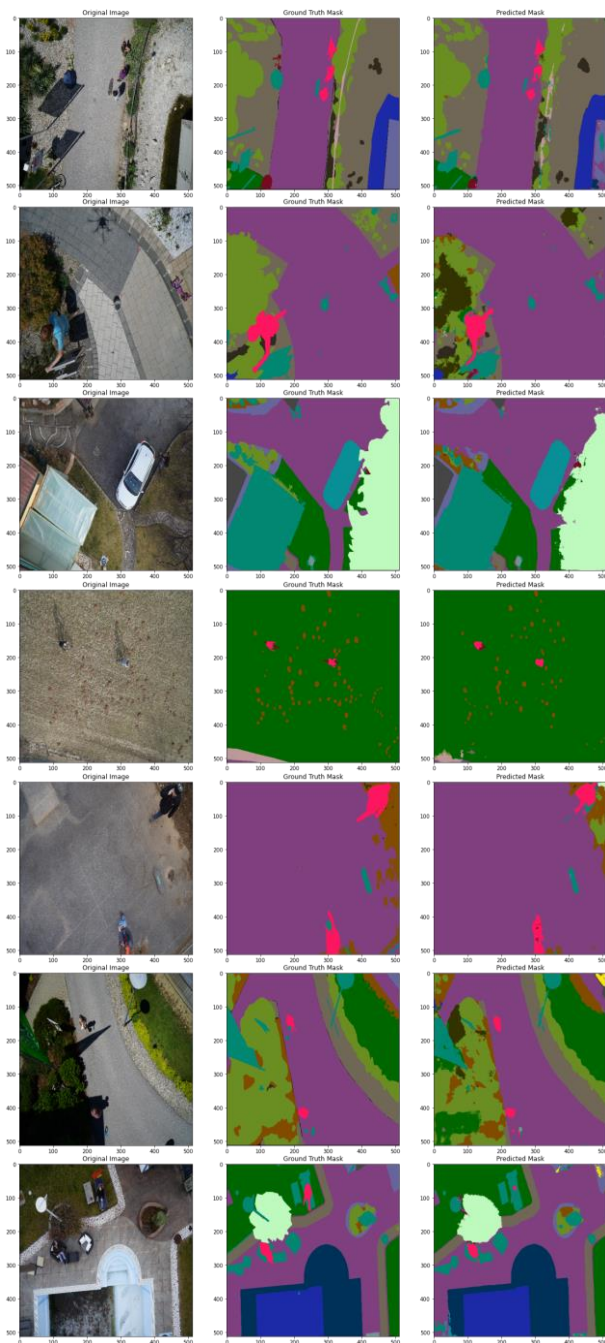


Figure 5. Qualitative results. From left to right: input, ground truth, our method on ICG

Augmenting the dataset enhances its diversity and enables the model to handle a broader range of real-world scenarios. The second column presents the ground truth annotations, which serve as the reference labels for each image pixel. These annotations are meticulously handcrafted masks, accurately outlining the boundaries and regions of interest in the augmented images. They represent the accurate segmentation information and provide a benchmark against which the

performance of the proposed method can be evaluated. The third column displays the predicted masks generated by the proposed method. These masks result from applying our trained model to the augmented images from the dataset. The experimental results indicate that the proposed method performs well in handling the augmented ICG dataset for drone semantic segmentation. The predicted masks exhibit a high degree of agreement with the ground truth annotations, suggesting that the proposed model successfully captures and classifies the objects in the augmented drone imagery. These results highlight the robustness and generalization capability of the proposed method, showcasing its potential for real-world applications. Figure 6 illustrates the accuracy of metrics' measurement results for all the compared methods obtained during the validation phases.

Figures 7 and 8 illustrate the measurement results of the Dice coefficient and mIOU metrics for all the compared methods during the training and validation phases. We obtained these results by training for 20 epochs. By analyzing the results in Figures 7 and 8, it is evident that the proposed method outperforms the other compared techniques in terms of both the Dice coefficient and mIOU metrics. The proposed method achieves significantly higher scores, indicating its superiority in accurately segmenting objects in the given dataset.

In our study on semantic segmentation, we employed the following hyperparameters to train and evaluate the models. These choices were made based on prior research in the field and empirical observations. We set the batch size to 8, determining the number of samples propagated through the network in each training iteration. This value strikes a balance between memory consumption and convergence speed. To complete one epoch, we used 200 steps per epoch. This value ensures that the model is exposed to a diverse

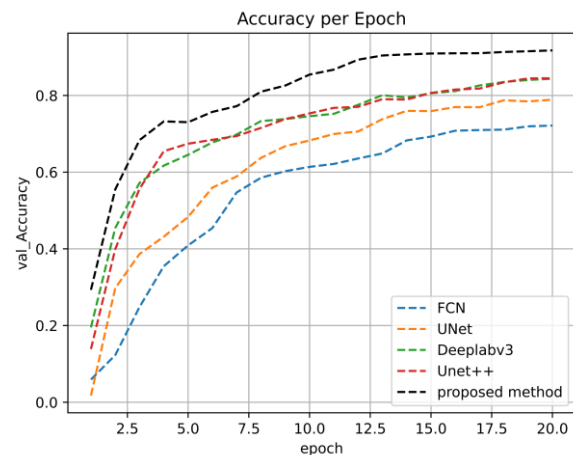


Figure 6. Comparison of accuracy for different methods validation phases

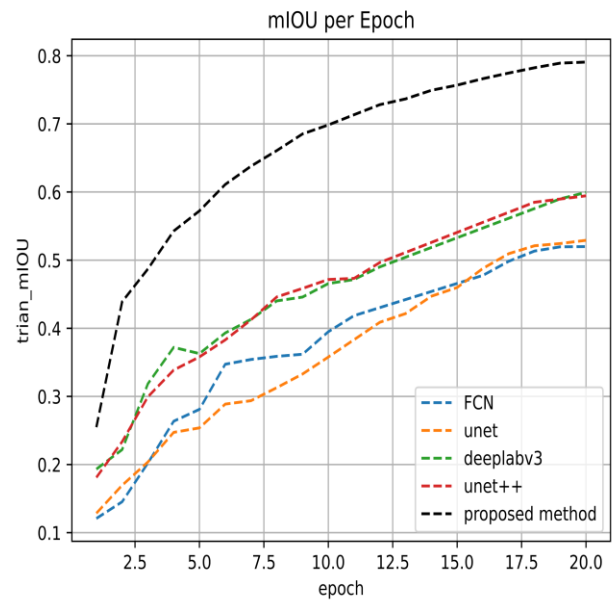
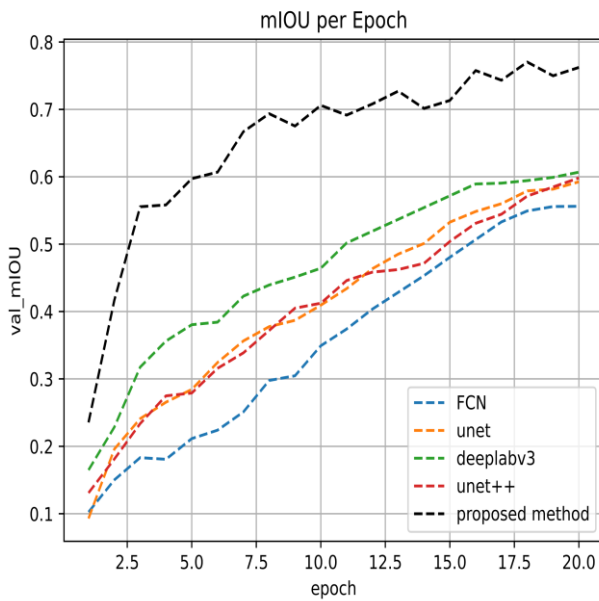


Figure 7. Comparison of mIOU metrics for different methods in training and validation phases

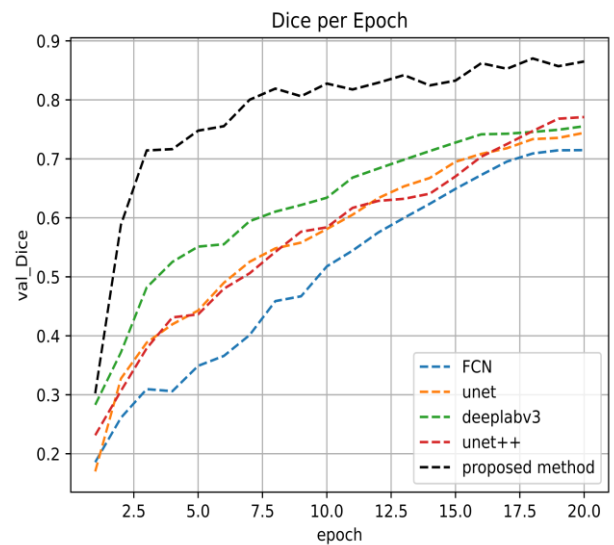
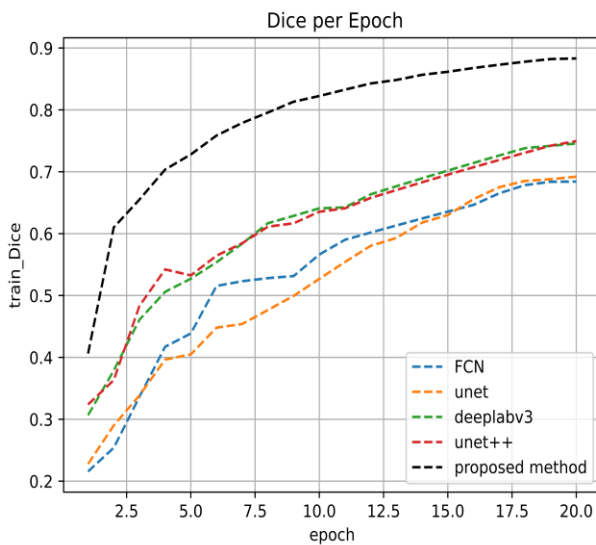


Figure 8. Comparison of dice metrics for different methods in training and validation phases

range of samples during training, facilitating better generalization. For validation, we utilized ten validation steps per epoch, allowing us to evaluate the performance of the model on a separate set of samples.

The input shape of images was (512, 512, 3). We initialized the learning rate to 0.0001, determining the step size during gradient descent optimization. We chose this initial learning rate to strike a balance between convergence speed and accuracy. To further refine the learning process, we employed an Exponential Decay Learning-Rate-Scheduler callback. This scheduler gradually reduced the learning rate over

time, aiding the model in refining its parameters effectively. The proposed model was trained for 20 epochs, allowing the model to learn from the dataset multiple times. The number of epochs affects both training time and the capacity of the model to generalize, which refers to its ability to accurately classify or predict unseen or new data that was not a part of the training set. A model with good generalization can effectively extrapolate patterns and provide an accurate prediction on unfamiliar data, indicating its robustness and ability to handle real-world scenarios.

Additionally, we utilized two callbacks during training: Model-Checkpoint and Early-Stopping. The Model-Checkpoint callback saved the best model weights based on a specified metric, enabling the retrieval of the best-performing model. The Early-Stopping callback monitored a specified metric and stopped training early if the metric did not improve for a certain number of epochs, preventing overfitting.

Table 2 provides information on the training schedule and time for a semantic segmentation model. The model was trained for 20 epochs, with a maximum (initial) learning rate of $10e4$ and a minimum learning rate of $1.12 \times 10e5$. The total training time for the model was 22981 seconds. Additionally, it is worth noting that the best weights were obtained at the 18th epoch, indicating the optimal point of model performance during training.

Table 3 presents the evaluation results of various semantic segmentation methods for drone images, including the proposed method. We assessed the performance using three metrics: Dice coefficient, mean Intersection over Union (mIOU), and accuracy. The proposed method achieved an impressive Dice coefficient of 86.51%, indicating a strong agreement between the predicted and ground truth segmentations. This demonstrates the accuracy of the proposed method in capturing the shapes and boundaries of objects in the drone images. Additionally, our method achieved an mIOU of 76.23%, showcasing its ability to represent the spatial extent of the objects accurately. The high mIOU suggests that the method effectively captures the overall

TABLE 2. Training schedule and time with learning rate (best weights at 18th epoch)

Epochs	Max. (Initial) LR	Min. LR	Total Training Time
20	$10e4$	$1.12 \times 10e5$	22981 s

TABLE 3. Comparative evaluation of semantic drone segmentation methods

	Dice	mIOU	Accuracy
FCN (36)	71.44	55.58	72.14
UNet-VGG16 (37)	74.80	59.70	78.44
UNet-ResNet50	75.01	60.01	78.91
FPN (21)	75.37	60.48	80.04
PspNet (22)	76.52	61.98	83.93
DeeplabV3-ResNet50 (20)	75.94	61.21	84.35
Unet++ (19)	77.06	62.68	84.48
DeeplabV3+VGG16 (38)	76.87	64.01	85.79
DeeplabV3+ResNet50 (38)	79.18	65.27	86.11
Proposed	86.51	76.23	91.74

quality of the segmentation output. Moreover, our method achieved an accuracy of 91.74%, indicating its effectiveness in correctly labelling pixels within the drone images. This showcases the reliability of the proposed method in accurately classifying the pixels. Comparing the proposed method to the other methods in the table, we outperformed them regarding Dice coefficient, mIOU, and accuracy.

The FCN method achieved a Dice coefficient of 71.44, an mIOU of 55.58, and an accuracy of 72.14. These results indicate that FCN performs reasonably well but has limitations in accurately capturing fine details and object boundaries in aerial imagery. The UNet-VGG16 method showed improvement with a Dice coefficient of 74.80, an mIOU of 59.70, and an accuracy of 78.44. This suggests that incorporating the VGG16 architecture in the UNet framework enhances the segmentation results. Further enhancing the UNet architecture with the ResNet50 backbone, the UNet-ResNet50 method achieved a Dice coefficient of 75.01, an mIOU of 60.01, and an accuracy of 78.91. This suggests that integrating a more advanced backbone network results in enhanced segmentation performance. The FPN method demonstrated even better performance with a Dice coefficient of 75.37, an mIOU of 60.48, and an accuracy of 80.04. This suggests that utilizing a feature pyramid network effectively captures multi-scale information and enhances segmentation accuracy. The PspNet method continued the trend of improvement, achieving a Dice coefficient of 76.52, an mIOU of 61.98, and an accuracy of 83.93. This indicates that the Pyramid Scene Parsing Network (PspNet) is effectively captures both local and global contextual information, leading to improved segmentation results. DeeplabV3-ResNet50 obtained a Dice coefficient of 75.94, an mIOU of 61.21, and an accuracy of 84.35. This suggests that the DeeplabV3 architecture, combined with the ResNet50 backbone, improves segmentation accuracy, particularly for objects of different scales and complex backgrounds. The Unet++ method improved the results with a Dice coefficient of 77.06, an mIOU of 62.68, and an accuracy of 84.48. combining incorporating nested skip and dense connections in the UNet architecture enhances segmentation accuracy. DeeplabV3+-VGG16 achieved a Dice coefficient of 76.87, an mIOU of 64.01, and an accuracy of 85.79. This suggests that utilizing the VGG16 architecture in the DeeplabV3+ framework improves segmentation accuracy, capturing finer details and object boundaries. DeeplabV3+-ResNet50 showed even better performance, with a Dice coefficient of 79.18, an mIOU of 65.27, and an accuracy of 86.11. This indicates that combining the DeeplabV3+ architecture with the ResNet50 backbone further enhances segmentation accuracy.

Finally, the proposed method outperformed all other methods, achieving a Dice coefficient of 86.51, an

mIOU of 76.23, and an accuracy of 91.74. These results demonstrate that the novel method proposed in this paper achieves the highest segmentation accuracy, showcasing its effectiveness and superiority over existing methods in semantic drone segmentation.

Our method outperforms other evaluated methods in accurately segmenting objects in drone images. It combines hierarchical multi-scale feature extraction with an Efficient Channel-based Attention ASPP module, capturing local and global information. The proposed method achieves significantly higher segmentation accuracy by focusing on relevant features. These findings contribute to advancing drone semantic segmentation techniques and offer insights for future research. Our method shows superior performance, promising improved accuracy and reliability in drone image segmentation.

5. CONCLUSION

In this study, we proposed a novel method for drone semantic segmentation that combines hierarchical multi-scale feature extraction and an Efficient Channel-based Attention ASPP module. The superior performance of our proposed method can be attributed to its ability to capture both local and global information while efficiently focusing on relevant features, resulting in accurate object segmentation in drone images. The evaluation results demonstrate that the proposed method outperforms other existing methods regarding segmentation accuracy. These findings validate the effectiveness of the hybrid approach and its potential to advance the field of drone semantic segmentation. Furthermore, our proposed method offers significant advancements in drone imagery applications. Improving the accuracy and reliability of segmentation algorithms provides valuable insights for various tasks such as object detection, tracking, and scene understanding in drone-based systems. Looking ahead, there are promising prospects for the suggested hybrid approach. One potential direction for future research is to explore the scalability and efficiency of the method for real-time or near-real-time applications. This could involve optimizing the computational efficiency of the approach to enable its deployment on resource-constrained platforms. Moreover, further investigations can be conducted to evaluate the proposed method on large-scale, diverse, and challenging datasets specific to drone imagery. This would provide a deeper understanding of its performance and generalization capabilities across different environmental conditions and object classes. The findings contribute to the existing body of knowledge and provide a foundation for future research and development in drone-based computer vision systems.

6. REFERENCES

1. Bhatnagar S, Gill L, Ghosh B. Drone image segmentation using machine and deep learning for mapping raised bog vegetation communities. *Remote Sensing*. 2020;12(16):2602. 10.3390/rs12162602
2. Lyu Y, Vosselman G, Xia G-S, Yilmaz A, Yang MY. UAVid: A semantic segmentation dataset for UAV imagery. *ISPRS journal of photogrammetry and remote sensing*. 2020;165:108-19.
3. Asgari Taghanaki S, Abhishek K, Cohen JP, Cohen-Adad J, Hamarneh G. Deep semantic segmentation of natural and medical images: a review. *Artificial Intelligence Review*. 2021;54:137-78. 10.48550/arXiv.1910.07655
4. Benjdira B, Bazi Y, Koubaa A, Ouni K. Unsupervised domain adaptation using generative adversarial networks for semantic segmentation of aerial images. *Remote Sensing*. 2019;11(11):1369.
5. Chakravarthy AS, Sinha S, Narang P, Mandal M, Chamola V, Yu FR. DroneSegNet: Robust Aerial Semantic Segmentation for UAV-Based IoT Applications. *IEEE Transactions on Vehicular Technology*. 2022;71(4):4277-86. 10.1109/TVT.2022.3144358
6. Zhang L, Wang M, Ding Y, Wan T, Qi B, Pang Y. FBC-ANet: A Semantic Segmentation Model for UAV Forest Fire Images Combining Boundary Enhancement and Context Awareness. *Drones*. 2023;7(7):456. 10.3390/drones7070456
7. Mahmudnia D, Arashpour M, Bai Y, Feng H. Drones and blockchain integration to manage forest fires in remote regions. *Drones*. 2022;6(11):331. 10.3390/drones6110331
8. Kumar S, Kumar A, Lee D-G. Semantic Segmentation of UAV Images Based on Transformer Framework with Context Information. *Mathematics*. 2022;10(24):4735. 10.3390/math10244735
9. Lobo Torres D, Queiroz Feitosa R, Nigri Happ P, Elena Cué La Rosa L, Marcato Junior J, Martins J, et al. Applying fully convolutional architectures for semantic segmentation of a single tree species in urban environment on high resolution UAV optical imagery. *Sensors*. 2020;20(2):563. 10.3390/s20020563
10. Sezavar A, Farsi H, Mohamadzadeh S. A Modified Grasshopper Optimization Algorithm Combined with CNN for Content Based Image Retrieval. *International Journal of Engineering*. 2019;32(7):924-30. 10.5829/ije.2019.32.07a.04 https://www.ije.ir/article_87122_c98ece12fa7377fe34ea6c8a5f519352.pdf
11. Feizi A. Convolutional Gating Network for Object Tracking. *International Journal of Engineering*. 2019;32(7):931-9. 10.5829/ije.2019.32.07a.05 https://www.ije.ir/article_87123_97e73a696cb75dc070dd2dced8875f7d.pdf
12. Hassanpour H, Mortezaie Z, Behgdadi A. Sensing Image Regions for Enhancing Accuracy in People Re-identification. *Iranian (Iranica) Journal of Energy & Environment*. 2022;13(3):295-304.
13. Habibi M, Hassanpour H. Splicing Image Forgery Detection and Localization Based on Color Edge Inconsistency using Statistical Dispersion Measures. *International Journal of Engineering*. 2021;34(2):443-51. 10.5829/ije.2021.34.02b.16 https://www.ije.ir/article_124931_7626c7eef9e9dc3ae8dfa8e6c6adf7ac.pdf
14. Sakimalla G, Chilukuri P, Jamuna A. Picture Segmentation using changing Artifacts Identification and Bias Modification. 2023. 10.36227/techrxiv.22362469.v1
15. Niu R, Sun X, Tian Y, Diao W, Feng Y, Fu K. Improving semantic segmentation in aerial imagery via graph reasoning and

- disentangled learning. *IEEE Transactions on Geoscience and Remote Sensing*. 2021;60:1-18.
16. Zagoruyko S, Komodakis N. Wide residual networks. *arXiv preprint arXiv:160507146*. 2016.
 17. Kestur R, Farooq S, Abdal R, Mehraj E, Narasipura O, Mudigere M. UFCN: A fully convolutional neural network for road extraction in RGB imagery acquired by remote sensing from an unmanned aerial vehicle. *Journal of Applied Remote Sensing*. 2018;12(1):016020-.
 18. Giang TL, Dang KB, Le QT, Nguyen VG, Tong SS, Pham V-M. U-Net convolutional networks for mining land cover classification based on high-resolution UAV imagery. *Ieee Access*. 2020;8:186257-73. 10.1109/ACCESS.2020.3030112
 19. Zhou Z, Siddiquee MMR, Tajbakhsh N, Liang J. Unet++: Redesigning skip connections to exploit multiscale features in image segmentation. *IEEE transactions on medical imaging*. 2019;39(6):1856-67. 10.48550/arXiv.1912.05074
 20. Chiu W-T, Lin C-H, Jhu C-L, Lin C, Chen Y-C, Huang M-J, et al., editors. Semantic segmentation of lotus leaves in UAV aerial images via U-Net and deepLab-based networks. 2020 International Computer Symposium (ICS); 2020: IEEE. 10.1109/ICSS1289.2020.00110
 21. Lin T-Y, Dollár P, Girshick R, He K, Hariharan B, Belongie S, editors. Feature pyramid networks for object detection. *Proceedings of the IEEE conference on computer vision and pattern recognition*; 2017.
 22. Zhao H, Shi J, Qi X, Wang X, Jia J, editors. Pyramid scene parsing network. *Proceedings of the IEEE conference on computer vision and pattern recognition*; 2017. 10.48550/arXiv.1612.01105
 23. Li S, Zhu X, Bao J. Hierarchical multi-scale convolutional neural networks for hyperspectral image classification. *Sensors*. 2019;19(7):1714. 10.3390/s19071714
 24. Huo X, Sun G, Tian S, Wang Y, Yu L, Long J, et al. HiFuse: Hierarchical Multi-Scale Feature Fusion Network for Medical Image Classification. *arXiv preprint arXiv:220910218*. 2022. 10.1016/j.bspc.2023.105534
 25. Megir V, Sfikas G, Mekras A, Nikou C, Ioannidis D, Tzovaras D, editors. Salient object detection with pretrained deeplab and K-means: Application to UAV-captured building imagery. *Pattern Recognition ICPR International Workshops and Challenges: Virtual Event, January 10-15, 2021, Proceedings, Part VII*; 2021: Springer. 10.1007/978-3-030-68787-8_35
 26. Liu Y, Wang L, Zhao L, Yu Z. *Advances in Natural Computation, Fuzzy Systems and Knowledge Discovery: Volume 1*: Springer Nature; 2019.
 27. Shaw P, Uszkoreit J, Vaswani A. Self-attention with relative position representations. *arXiv preprint arXiv:180302155*. 2018. 10.48550/arXiv.1803.02155
 28. Hu J, Shen L, Sun G, editors. Squeeze-and-excitation networks. *Proceedings of the IEEE conference on computer vision and pattern recognition*; 2018.
 29. Wang Q, Wu B, Zhu P, Li P, Zuo W, Hu Q, editors. ECA-Net: Efficient channel attention for deep convolutional neural networks. *Proceedings of the IEEE/CVF conference on computer vision and pattern recognition*; 2020. 10.48550/arXiv.1910.03151
 30. Semantic Drone Dataset. In: Technology GUo, editor. *Institute of Computer Graphics and Vision, Graz University of Technology*.
 31. Prakash S, Shah P, Agrawal A. Exploiting CNNs for Semantic Segmentation with Pascal VOC. *arXiv preprint arXiv:230413216*. 2023. 10.48550/arXiv.2304.13216
 32. Rebuffi S-A, Goyal S, Calian DA, Stimberg F, Wiles O, Mann TA. Data augmentation can improve robustness. *Advances in Neural Information Processing Systems*. 2021;34:29935-48. 10.48550/arXiv.2111.05328
 33. Gu Z, Cheng J, Fu H, Zhou K, Hao H, Zhao Y, et al. Ce-net: Context encoder network for 2d medical image segmentation. *IEEE transactions on medical imaging*. 2019;38(10):2281-92. 10.48550/arXiv.1903.02740
 34. Union GIO, editor A metric and a loss for bounding box regression. Rezaatofghi, N Tsoi, J Gwak, A Sadeghian, I Reid, S Savarese//*IEEE/CVF Conference on Computer Vision and Pattern Recognition (CVPR)*, Long Beach, CA, USA; 2019. 10.48550/arXiv.1902.09630
 35. Wu K, Du B, Luo M, Wen H, Shen Y, Feng J, editors. Weakly supervised brain lesion segmentation via attentional representation learning. *Medical Image Computing and Computer Assisted Intervention–MICCAI 2019: 22nd International Conference, Shenzhen, China, October 13–17, 2019, Proceedings, Part III 22*; 2019: Springer. 10.1007/978-3-030-32248-9_24
 36. Long J, Shelhamer E, Darrell T, editors. Fully convolutional networks for semantic segmentation. *Proceedings of the IEEE conference on computer vision and pattern recognition*; 2015.
 37. Ronneberger O, Fischer P, Brox T, editors. U-net: Convolutional networks for biomedical image segmentation. *Medical Image Computing and Computer-Assisted Intervention–MICCAI 2015: 18th International Conference, Munich, Germany, October 5-9, 2015, Proceedings, Part III 18*; 2015: Springer.
 38. Guo Z, Xu J, Liu A, editors. Remote sensing image semantic segmentation method based on improved Deeplabv3+. *International Conference on Image Processing and Intelligent Control (IPIC 2021)*; 2021: SPIE. 10.1117/12.2611930

COPYRIGHTS

©2024 The author(s). This is an open access article distributed under the terms of the Creative Commons Attribution (CC BY 4.0), which permits unrestricted use, distribution, and reproduction in any medium, as long as the original authors and source are cited. No permission is required from the authors or the publishers.

**Persian Abstract****چکیده**

تقسیم‌بندی معنایی پهپاد یک وظیفه چالش‌برانگیز در حوزه بینایی کامپیوتر است. این وظیفه به دلیل پیچیدگی‌های مرتبط با تصاویر هوایی، به ویژه دشوار است. در این مقاله، یک روش جامع برای تقسیم‌بندی معنایی پهپاد ارائه شده است و عملکرد آن با استفاده از مجموعه داده ICG مورد ارزیابی قرار می‌گیرد. روش پیشنهادی از استخراج ویژگی‌های چندمقیاس سلسله‌مراتبی و استفاده بهینه از توجه مبتنی بر کانال استفاده می‌کند. این روش به چالش‌های منحصربه‌فرد موجود در این حوزه پاسخ می‌دهد. در این مطالعه، عملکرد روش پیشنهادی با چندین مدل مدرن مقایسه شده است. نتایج آزمایشی نشان می‌دهند که روش پیشنهادی نسبت به این رویکردهای موجود با معیارهای mIOU, Dice و دقت عملکرد بهبود قابل توجهی دارد. به طور خاص، روش پیشنهادی با معیارهای mIOU, Dice و دقت به ترتیب ۸۶.۵۱٪، ۷۶.۲۳٪ و ۹۱.۷۴٪ عملکرد چشمگیری را به دست می‌آورد. یافته‌های این پژوهش نشان می‌دهند که روش پیشنهادی در مقابله با چالش‌های تقسیم‌بندی معنایی پهپاد مؤثر است. این نتایج به پیشرفت برنامه‌های مبتنی بر پهپاد، مانند نظارت، پیگیری اشیاء و نظارت محیطی که تقسیم‌بندی معنایی دقیق آنها ضروری است، کمک می‌کند.



Cyclic and Monotonic Behavior of Non-plastic Silts with the Presence of Initial Static Shear Stress Using Strain Energy Approach: A Case Study for a Tailings Dam

M. Abdollahi, J. Bolouri Bazaz*, A. Akhtarpour

Civil Engineering Department, Ferdowsi University of Mashhad, Mashhad, Iran

PAPER INFO

Paper history:

Received 08 October 2023

Received in revised form 21 November 2023

Accepted 26 November 2023

Keywords:

Triaxial

Static Shear Stress Ratio

Liquefaction

Strain Energy

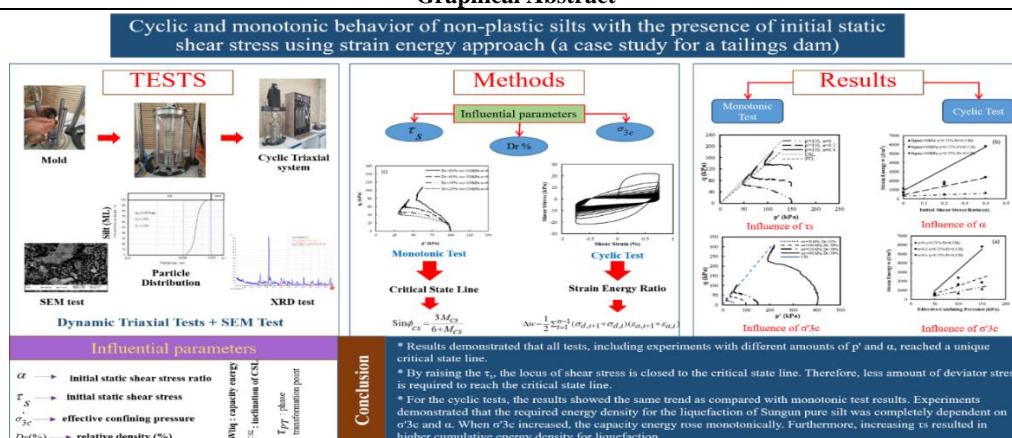
Non-plastic Silt

ABSTRACT

Mining Exploration, excavation, and construction are considered as mining activities which are recently growing dramatically. Therefore, utilizing the mining wastes with the least environmental damage is a significant concern. Tailings dams are one of the conventional solutions that store the extracted hazardous substances safely for water resources management and environmental protection. This research deals with the effects of monotonic and seismic loadings on silt-sized copper wastes existed in a tailings dam at Northwest Iran as a case study. Various values of initial static shear stress are performed using an automated cyclic triaxial system. Monotonic undrained compressive tests were performed with a relatively constant density and considering three values of 50, 100, and 150 kPa for mean effective stress. Depending on the first density of samples, applying a mean effective confining pressure of 100 kPa, increased the initial densities by 25 to 30% as compared to the initial condition. Moreover, the effect of initial shear stress ratio with three values of 0, 0.2, and 0.4 was evaluated. No peak point was observed for samples under $\alpha = 0$, whereas, samples with $\alpha = 0.4$ encountered a peak point before reaching to the phase transformation point. The results of cyclic experiments were used to evaluate capacity energy and residual pore pressure based on the strain energy approach. Cyclic tests on the samples were performed considering the shear amplitude of 0.75% and frequency of 0.3 Hz. It is shown that the most energy dissipation occurs at the first cycle possessing the highest stiffness. For $\alpha = 0$, energy density increased from 474 J/m³ to 1147.4 J/m³; however, a more intense increase was measured from 682 J/m³ to 5839 J/m³ when $\alpha = 0.4$. It is also found that applying initial shear stress has a pretty considerable influence on monotonic strength and the liquefaction resistance of silts. The increase of α from 0 to 0.4 yielded a linear increase in the shear strength of samples in the range of 20 kPa to 70 kPa. The results of this paper were then validated accurately through some previous studies.

doi: 10.5829/ije.2024.37.05b.19

Graphical Abstract



*Corresponding Author Email: bolouri@um.ac.ir (J. Bolouri Bazaz)

Please cite this article as: Abdollahi M, Bolouri Bazaz J, Akhtarpour A. Cyclic and Monotonic Behavior of Non-plastic Silts with the Presence of Initial Static Shear Stress Using Strain Energy Approach: A Case Study for a Tailings Dam. International Journal of Engineering, Transactions B: Applications. 2024;37(05):1036-49.

NOMENCLATURE

NOMENCLATURE		Greek Symbols	
q_s	Deviator stress at static loading	α	Initial static shear stress ratio
PT	Phase transformation point	τ_s	Initial static shear stress
CSL	Critical state line	σ'_{3c}	Effective confining pressure
r_u	Pore pressure ratio	σ_1	Maximum principal stress
CU	Consolidation-Undrained test (triaxial test)	σ_3	Minimum principal stress
W	Energy density	φ_{CSL}	Inclination of CSL, internal friction angle
W_{liq}	Capacity energy	τ_{PT}	Shear stresses at the phase transformation point
W/W_{liq}	Strain energy ratio		

1. INTRODUCTION

Tailings dam is one of the vital structures subjected to extensive failure under seismic loadings. It is crucial to note that tailings dam problems are not limited to design and construction. During the period of operation, tailings dams are known as a source of pollution alongside the human communities due to the production of a significant amount of contaminated materials (1). Consequently, destructive factors such as seepage, instability, and above all earthquake and dynamic loadings can lead to polluted surface and polluted groundwater. According to the USCOLD report (2), earthquake is the major cause of failure in tailing dams. This failure may occur if some parts of the tailings dam body is liquefied (2). Liquefaction is a challenging subject in geotechnical engineering problems, mostly in saturated loose sands and non-plastic silts. This phenomenon has been the cause of intensive failures in many earthquakes (3). The studies on the stability of tailings dams related to initial and final elevations of the dam crest under dynamic loading indicated that the liquefaction takes place for both dam body and impoundment, leading to the dam instability at the final elevation (4, 5). Some solutions such as vertical gravel column drains can reduce the liquefaction potential of a soft ground (6).

There are various techniques, including in-situ and experimental methods to assess the potential of liquefaction for several soils. For instance, based on spectral matching to a target spectrum, Hanindya et al. (7) developed an artificial time history of earthquake to study the liquefaction of a stratified ground and concluded that liquefaction potential reduces with increasing stiffness and depth of soil. Cone Penetration Test (CPT) results can also be employed to determine the liquefaction potential. For example, Latifi et al. (8) successfully analyzed the liquefaction problem for a zone in Morocco using CPT data. From a structural viewpoint, liquefaction potential of a ground can be assessed regarding physical characteristics of the subsurface structure determined based on two innovative geophysical approaches, including Rayleigh surface waves and electrical resistivities (9). In addition, the stress-based approach and strain energy-based method are two common experimental procedures in the literature (10-16). Among these methods, stress-based method has been more common among researchers for

liquefaction assessment (10, 17). In this procedure, the shear stress level, mean effective stress, and the number of cycles, are the critical parameters in estimating the liquefaction potential of cohesion-less soils. Although the stress-based approach is continually improved through recent attempts and increases in the number of studies on liquefaction, the uncertainty due to random loading needs to be addressed (18). However, the strain energy-based method is a relatively modern one to determine the silty soil liquefaction potential. Among those, the strain energy absorption model in soils for the liquefaction assessment is a new method recently considered by researchers (14, 16, 18, 19). In this method, the quantity of strain energy per unit volume dissipated in the deposit is utilized to assess the cyclic behavior of sands. In geomaterials subjected to cyclic loading, the cumulative area limited to the shear stress-strain loops indicates how strain energy density dissipates (14). In the past years, many researchers implied that the relationship between dissipated strain energy density and pore pressure buildup partially depends on the stress (14, 20, 21). The benefits of the strain energy method have led to additional research into the evaluation of potential liquefaction. The existence of a rational correlation among dissipated strain energy, residual pore pressure, and non-recoverable plastic deformation can be employed to develop energy-based pore pressure models through experimental results (14).

To assess the influences of initial static shear stress τ_s and mean effective stress p' , many researchers have conducted a wide range of laboratory tests on sands and silty sands (22-25) and FEM modeling for saturated sand (26). Furthermore, Iraj (27) analyzed finn-byrne model for liquefaction of quay and cantilevered retaining walls. Monotonic and cyclic loads are two conventional loading types in various geotechnical problems (28, 29). Previous attempts demonstrate that τ_s has a significant effect on shear resistance under monotonic and cyclic loading. For instance, it is concluded that the initial shear static ratio (α) is directly proportional to the number of cyclic shear stresses needed to initiate the liquefaction (30, 31). Besides, any increase or decrease in cyclic strength under initial static shear stress depends on the intensity of τ_s and the initial density of the soil (31). Under a given α , Hosono and Yoshimine (32) as well as Fakharian and Shabani (28) assessed the cyclic resistance of sand through numerous undrained cyclic triaxial tests. Their studies illustrated that the direction of the α has a

considerable impact on the cyclic strength of soil (28, 32).

The present research mainly investigates the influences of seismic loadings on pure silt related to the Sungun Copper tailings dam in Northwest Iran as a case study. This tailing dam was constructed using the upstream method. The evaluation of the liquefaction potential of saturated non-plastic silt is of particular importance. The monotonic and cyclic tests under different τ_s were performed using an automated cyclic triaxial system. A series of experimental tests was carried out using an automated cyclic triaxial system. The experiments on pure silt under monotonic loading revealed an unusual response for different densities from 25% to 80%. All tests demonstrated a relatively similar dilation rate, and their dilative trends were not remarkable for all ranges of densities from loose to dense conditions. In other words, there was no intensive strain hardening in stress-strain diagrams, even for very dense silty soils. For the cyclic condition, tests were conducted on silts using the strain-energy method. The experimental results indicated dramatic changes in the dissipated strain energy required for the liquefaction by changing the σ'_{3c} and τ_s .

2. MATERIAL AND SAMPLE PREPARATION

Sungun copper mine is one of the open pit mines situated in the northwestern region ($43^\circ 46'$ East and $38^\circ 42'$ North) of Iran, close to the Aras River (Figure 1). Metal minerals are widely present in the geological features of the Aras watershed. Sungun copper mine is very important in terms of industry and geological formations in the mentioned area. This mine started its activity in 1990 and is known as a productive reserve of almost 800 million tons of 0.67-grade copper ore. Hence, a minimum of 380 million tons of copper waste can be produced during 25 years (33).

From a geological viewpoint, the studied region is situated in the Oligocene volcanic area. It includes calc-



Figure 1. Sungun porphyry copper mine located in Iran

alkaline volcanic minerals, mainly trachy-andesite, andesite, and dacite containing basaltic lava (34). Sungun porphyry copper deposits are found in trachyandesite rocks that contain cool silver-colored porphyry latite of medium to high resistance and medium to severe weathering. The color of the areas influenced by the penetration of underground water changes to brown in some locations. Moreover, small amounts of sulfide minerals containing chalcopyrite and pyrite are observed in the lower depths. The material used in this study is non-plastic silt supplied from Sungun Porphyry copper mine with the characteristics given in Table 1. The simplified lithology map of Sungun copper mine is shown in Figure 2. The X-ray diffraction (XRD) test that was carried out on the materials as plotted in Figure 3. The results of XRD analysis include compound name, percent of each mineral, and chemical formula.

The distribution of particle size is presented in Figure 4. The magnified photos (SEM) of the silt sample are illustrated in Figure 5 with two different magnifications ($20 \mu\text{m}$ & $10 \mu\text{m}$). The magnified photos show angular particle shapes, and the surface of the particles looks relatively smooth.

Experiments were carried out on samples with diameter and height of 50 mm and 100 mm, respectively, using a monotonic/cyclic triaxial device. The moist tamping method is employed to prepare the samples (Figure 6). In moist tamping, the sand with 12% moist was tamped in 5 layers to achieve the desired void ratio.

TABLE 1. Characteristics of the Sungun copper tailings samples

(a) Quantitative X-ray diffraction (XRD) analysis		
Compound	Percent (%) (By atomic weight)	Chemical formula
Silicate	43.9	Si O ₂
Illite	34.3	Al ₂ H ₂ K O ₁₂ Si ₄
Kaolinite	8.7	Al ₂ H ₄ O ₉ Si ₂
Iron (II) duo-disulfide Marcasite	6.1	Fe S ₂
Quartz	1.6	O ₂ Si
Unidentified peak area		
(b) Geotechnical properties		
Parameter	Symbol	Value
Specific gravity	G _s	2.70-2.73
Internal friction angle (deg)	ϕ'	11.2-36.7
Liquid limit	LL	23.6-25.3
Minimum dry unit weight (kN/m ³)	$\gamma_{d(\text{min})}$	12.36
Maximum dry unit weight (kN/m ³)	$\gamma_{d(\text{max})}$	15.46

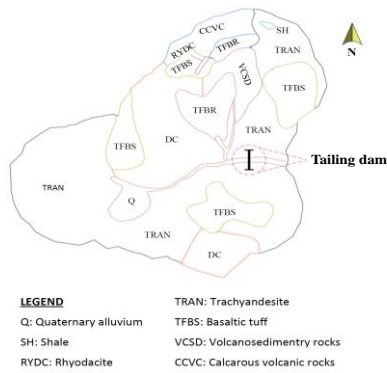
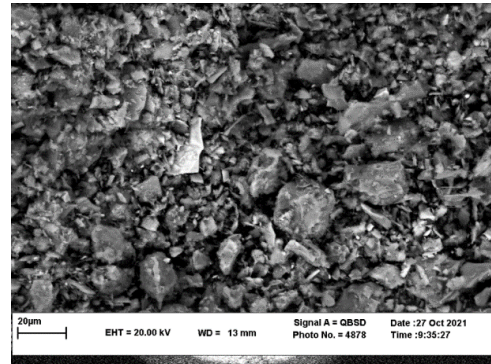


Figure 2. Simplified lithology map of Songgun copper mine



(b)

Figure 5. Microscopic scanning of pure silt (a) scale 20 µm (b) 10 µm

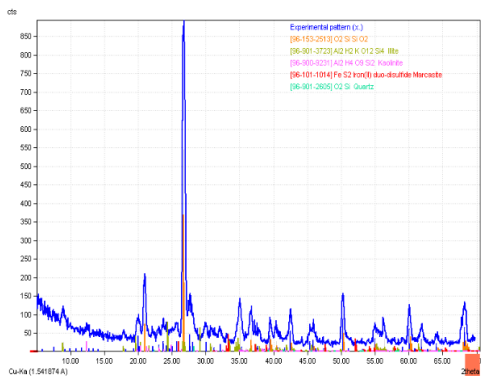


Figure 3. Experimental pattern of Sungun silt components

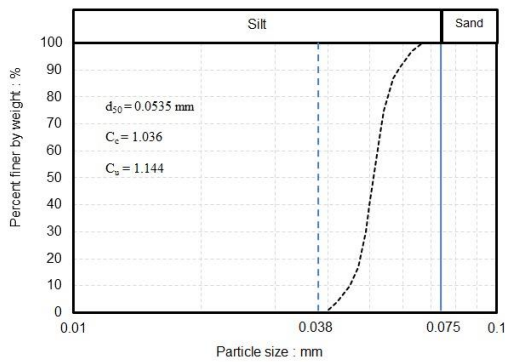
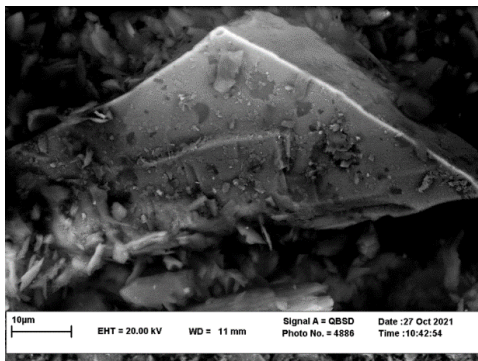


Figure 4. Particle size distribution



(a)



Figure 6. Sample preparation in Triaxial device

The weight and height of each layer were measured separately depending on the number of the layers using the moist tamping method suggested by Ladd (35). Carbon dioxide was initially circulated for 60 min, followed by passing de-aired water equivalent to double of sample volume, to ensure better saturation. By applying a 10 kPa cell pressure, sample disturbance during de-aired water circulation can be prevented. Fully saturated samples were achieved with Skempton's B-

values exceeding 0.95. After saturation, consolidation of the whole samples under the desired σ'_{3c} was performed. The duration for consolidation often took 2 h for pure silt samples.

3. TEST PROGRAM

In the current study, the critical state parameters and liquefaction potential of silty sand are evaluated through a wide range of laboratory monotonic and cyclic experiments. All tests were performed on samples with initial densities of 25, 45, 60, and 80%.

As the first phase, a set of monotonic tests was planned to determine the soil mechanical parameters as well as the critical state line (CSL). For all tests, three consolidation stress paths, including one isotropic and two anisotropic paths ($\alpha = 0, 0.2, \text{ and } 0.4$), were chosen (see Eq. 1). All monotonic tests (see Table 2) were carried out with three different effective mean stresses p' of 50, 100, and 150 kPa along with one test under p' of 400 kPa (only for comparison) to investigate isotropic and anisotropic consolidation. The values for α were selected as 0 (i.e., isotropic condition), 0.2, and 0.4, (i.e., anisotropic condition). The isotropic and anisotropic

stages of drained loading are applied respectively to meet the final magnitude of τ_s related to the consolidation part. After consolidation, monotonic tests were initiated by applying deviatoric stress and terminated when reaching 20 percent of shear strain.

In the second phase, nine cyclic tests (see Table 2) were conducted to assess the liquefaction potential of pure silt samples. The investigation into the influences of τ_s and σ'_{3c} on the cyclic behavior is also intended. All cyclic experiments were conducted by loading the samples under strain-controlled conditions to estimate capacity energy W_{liq} and residual pore pressure. Table 2 demonstrates the test programs, including p' , D_r , and α for monotonic and cyclic conditions.

4. MONOTONIC TEST RESULTS

4. 1. Influences of D_r and Σ'_{3c} The initial tests were conducted on non-plastic silt at 25, 45, 60, and 80% relative densities to assess the soil behavior. Saturated and consolidated samples were subjected to strain-controlled undrained shearing at a 0.05 mm/min deformation rate. Figures. 7a, 7b, and 7c demonstrate τ - γ , u_e - γ diagrams and the effective stress paths,

TABLE 2. Summary of triaxial tests schedule performed in the present research

Test Name	Confining pressure (kPa)	Relative final density (%)	Initial shear stress ratio (α)	Loading type	Shear strain amplitude (%)
T100-25-0m	100	25	0	monotonic	20
T100-45-0m	100	45	0	monotonic	20
T100-60-0m	100	60	0	monotonic	20
T100-80-0m	100	80	0	monotonic	20
T50-50-0m	50	45-50	0	monotonic	20
T100-50-0m	100	45-50	0	monotonic	20
T150-50-0m	150	45-50	0	monotonic	20
T400-50-0m	400	45-50	0	monotonic	20
T50-50-0.2m	50	45-50	0.2	monotonic	20
T100-50-0.2m	100	45-50	0.2	monotonic	20
T150-50-0.2m	150	45-50	0.2	monotonic	20
T50-50-0.4m	50	45-50	0.4	monotonic	20
T100-50-0.4m	100	45-50	0.4	monotonic	20
T150-50-0.4m	150	45-50	0.4	monotonic	20
T50-50-0c	50	45-50	0	cyclic	0.75
T100-50-0c	100	45-50	0	cyclic	0.75
T150-50-0c	150	45-50	0	cyclic	0.75
T50-50-0.2c	50	45-50	0.2	cyclic	0.75
T100-50-0.2c	100	45-50	0.2	cyclic	0.75
T150-50-0.2c	150	45-50	0.2	cyclic	0.75
T50-50-0.4c	50	45-50	0.4	cyclic	0.75

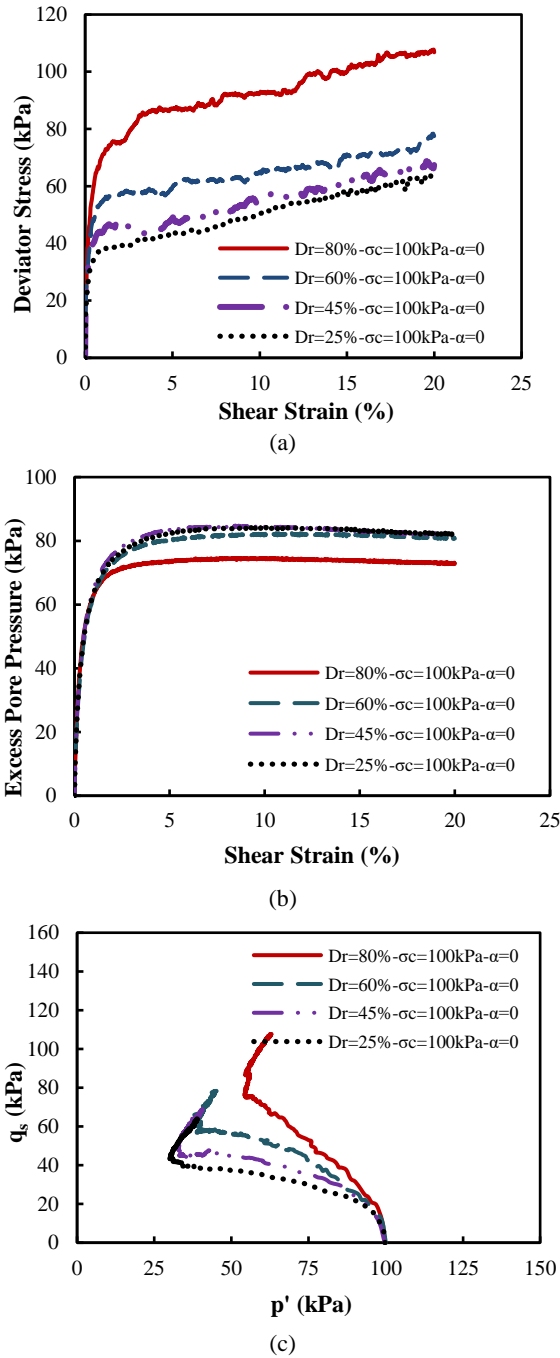


Figure 7. Monotonic behavior of pure silt for loose to dense samples - current study a) $q_s-\gamma$ b) $u_e-\gamma$ c) Stress paths

respectively. Clearly, all samples illustrate a slight strain-hardening behavior. In other words, samples are moderately dilated when axial strain is enhanced, even for the loosest conditions.

For medium to dense conditions, it is usually expected an intensive dilative response for non-cohesive soils, while in this study, a slight dilation was observed

even at 80% density. Karim and Alam (36) observed a similar response for loose and dense non-plastic silts. They compared the behavior of pure silt, clean sand, and different mixtures of sand and silt extensively. Figure 8 shows a highly dilated response of sand compared with a shallow dilative behavior of silt in the same density of 78% (36).

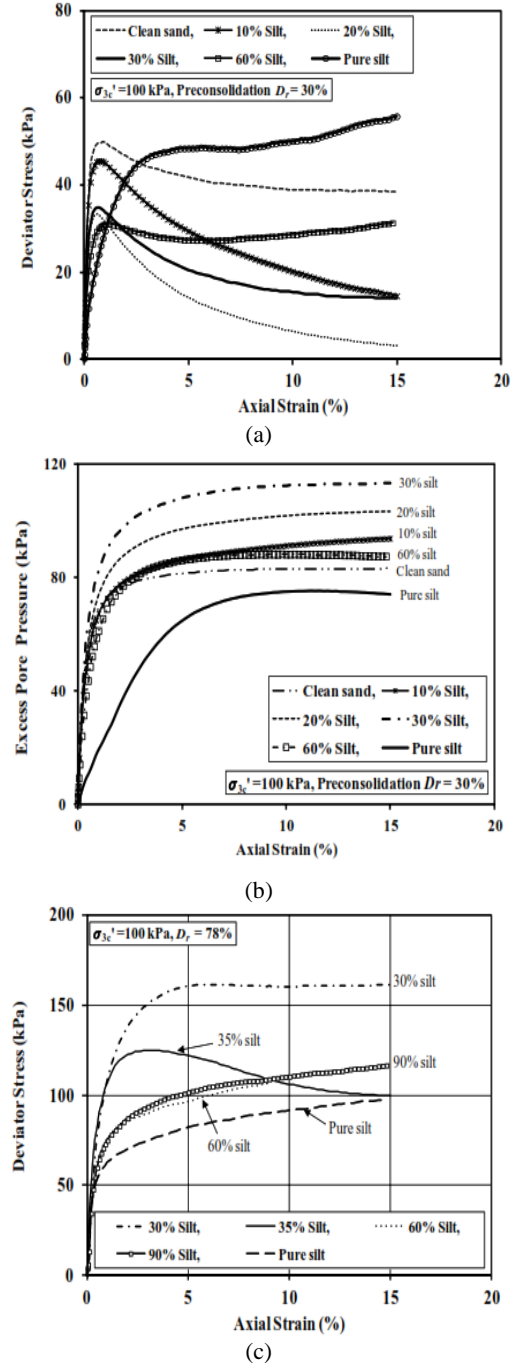


Figure 8. a) q_s and u_e versus axial strain ϵ for 30% density b) q_s versus ϵ for 78% density (36)

Similarly, the results in the present study support the observations mentioned above by Karim and Alam (36). This behavior of slight dilation in silty materials seemingly results from the small size of grains and their relatively smooth surface (as shown in Figure 5b). During current tests, applying a mean effective confining pressure of 100 kPa, increased the initial densities of samples by 25% to 30% as compared to the initial condition, depending on their first density. Several experiments were conducted with four σ'_{3c} values including 50 kPa, 100 kPa, 150 kPa, and 400 kPa to investigate the confining pressure impact on loose non-plastic silts. By increasing the σ'_{3c} , soils tend to show more contractive behavior. Thus, σ'_{3c} was increased up to 400 kPa so that contractive behavior was observed. The sample was prepared with 5% density initially and after applying $\sigma'_{3c} = 400$ kPa, the final density before applying shear loads reached 50%. Preparing the sample with negative density to achieve a looser sample (after consolidation) was impossible in this particular silt. As seen in Figure 9, irrespective of σ'_{3c} magnitude, all samples demonstrated contractive behavior (i.e., strain-softening) initially, and then followed by dilative behavior (i.e., strain-hardening) with increasing the axial strain even at high σ'_{3c} levels. This transition happened after reaching the phase transformation (PT) point. It was shown that at PT point, contractive behavior changes into dilative behavior while u_e experiences its maximum pressure within the test (37). Moreover, any complete loose state response or even flow liquefaction point (peak point) was not observed through the experiments.

4. 2. Influence of α In many geotechnical engineering, there are several situations in which the soil stratum is subjected to the in-situ τ_s . To examine this issue, the effect of τ_s in the sloping parts of the dam should be assessed. For this purpose, the adequate mean stresses of 50, 100, and 150 kPa were applied to samples to be isotropically consolidated first. Afterward, by applying τ_s to the sample in a drained condition, it was

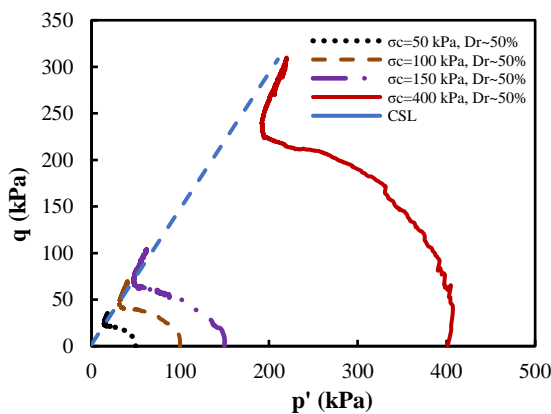


Figure 9. Influence of σ'_{3c} on Sungun silt behavior

consolidated anisotropically as shown in Figure 10. The initial static shear stress ratio is expressed as:

$$\alpha = \frac{\tau_s}{\sigma'_{3c}} \tag{1}$$

$$\tau_s = \frac{q_s}{2} = \frac{\sigma_1 - \sigma_3}{2} \tag{2}$$

Figure 11 illustrates three tests results considering three values for the α under a given mean effective stress of 150 kPa when $\alpha = 0, 0.2, \text{ and } 0.4$. Based on input data, the critical state line (CSL) and the phase transformation line (PTL) were drawn in this figure as well.

The friction angle of granular soils in the steady state is called the critical state friction angle of the soil and is indicated by ϕ_{CSL} . This friction angle is widely applied as a very important feature in geotechnical projects as well as in various behavioral models. The critical state line in the q - p' plane is reflected well by a straight line passing through the origin:

$$q = M_{CSL} \cdot p' \tag{3}$$

where M_{CS} is a constant equal to the stress ratio at critical state. The critical state friction angle ϕ_{CSL} in triaxial compression conditions can be obtained from the stress ratio at critical state using Equation 4:

$$\sin \phi_{CSL} = \frac{3M_{CSL}}{6+M_{CSL}} \tag{4}$$

The inclination of CSL (i.e., internal friction angle ϕ_{CSL}) was equal to 37° . Besides, it is worth noting that all ultimate points stand on a unique CSL regardless of the initial anisotropic condition. In other words, the loci of critical state lines are not governed by the τ_s . These results follow the findings concluded in a study based on the Discrete Element Method by Zhao et al. (38) in which no correlation between the mean effective stress and CSL was reported. By increasing the α , the effective stress state approaches the CSL (39). Thus, the strain-softening

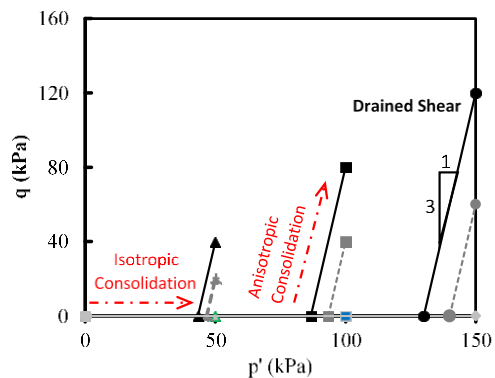
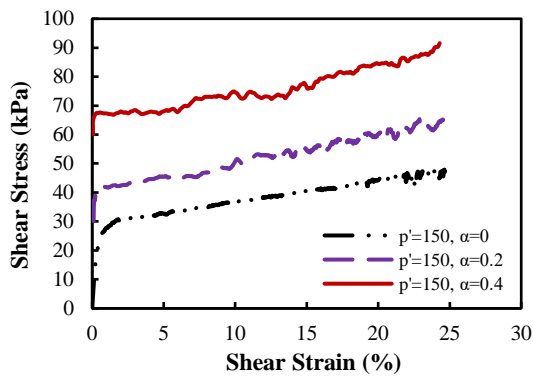
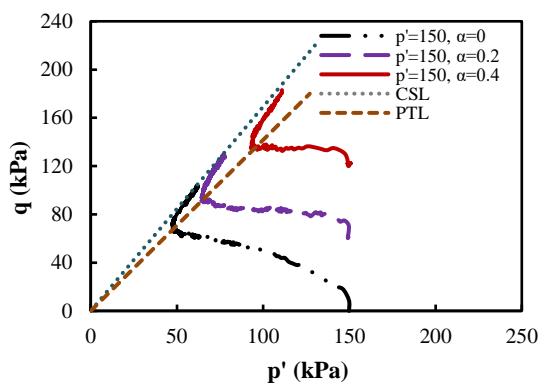


Figure 10. Drained stress path before monotonic and cyclic loadings



(a)



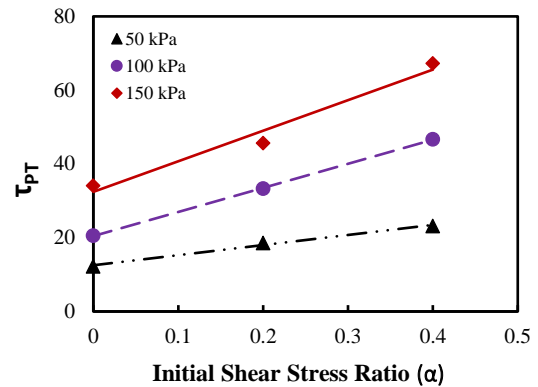
(b)

Figure 11. Influence of τ_s on Sungun silt response, a) τ - γ , b) Stress paths

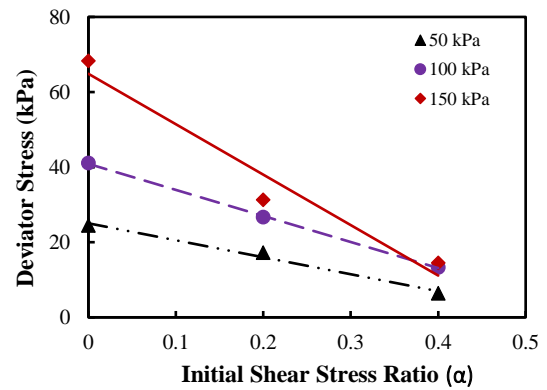
deformations might occur with a small trigger. Monotonic test results demonstrated in Figure 11 followed this trend. The stress path diagrams of 3 undrained tests for three values of the α parameter, including 0, 0.2, and 0.4 were presented in Figure 11. While a sample with no initial shear stress ratio (i.e., $\alpha = 0$) shows no peak point and subsequently strain-hardening behavior was seen in all phases of the test, samples under the τ_s of 0.4 experienced a partial strain-softening behavior and indicated a peak point before reaching to the phase transformation (PT) point.

From Figure 12, the increase of α from 0 to 0.4 will lead to a linear increase in the shear strength of samples. Therefore, the τ will experience a higher level of strength through the compressive loading. These findings have been shown in Figure 12a for shear stresses at phase transformation point (τ_{PT}) under the various amounts of σ'_{3c} as well as different amounts of τ_s values. As seen in this figure, an increase in both σ'_{3c} and τ_s changes the amount of phase transformation point and, consequently the shear stress level at PT (τ_{PT}). This behavior is in appliance with previous studies by Rasouli et al. (40).

Another parameter assessed in the current study was the deviator stress applied to the soil from the end of consolidation and the beginning of loading until the



(a)



(b)

Figure 12. Influence of τ_s on a) shear stress at PT , b) Required Deviator Stress at PT after anisotropic consolidation

phase transformation point. Variations of deviator stress versus the α value at 50, 100, and 150 kPa mean effective stresses are presented in Figure 12. Considering the test results for different values of α , the deviator stress required to reach the PT point is diminished with rising the intensity of τ_s . This decline is interpreted by the state of stresses associated with the critical state line. When the τ_s is exerted on the sample, the travel distance to the CSL decreases, and consequently, less shear loading is required for failure. It is evident that for the highest τ_s , the sample experiences a slight increase in deviator stress to achieve the phase transformation point. Moreover, as shown in Figure 12b, a more significant amount of mean effective stress will increase the shear stress level.

5. CYCLIC TEST RESULTS

Numerous laboratory experiments were carried out using a cyclic triaxial device to investigate the cyclic behavior of the Sungun non-plastic silt. The liquefaction resistance and pore pressure development were determined based on the strain energy approach using the results of various tests conducted with the strain control state. In this approach, the quantity of strain energy per unit volume

dissipated in the deposit (also called unit energy and energy density (41)) is utilized to assess the cyclic response of silt (14). The main parameters of the strain energy approach include energy density dissipated instantaneously (W), capacity energy (W_{liq}) and strain energy ratio (W/W_{liq}) (14, 18). It should be noted that in addition to soil and porous media, the approach is effectively applied to investigate the cyclic behavior of structural elements (e.g., steel plates (42); reinforced concrete (43); alloy beams (44)) under earthquake conditions. The achievement of a pore pressure ratio (r_u) of 1 is assumed an appropriate criterion for liquefaction occurrence. The tests can provide the clarification on how τ_s and σ'_{3c} affect the liquefaction response.

As stated in Section 2, the moist tamping method was used to prepare samples considering the under-compaction coefficient. The initial density of prepared samples was selected based on their σ'_{3c} as such final density after consolidation reached the relatively same amount of 45%. Undrained (CU) tests were performed on loose samples with three initial relative densities of 10%, 20%, and 25% under three σ'_{3c} values including 50 kPa, 100 kPa, and 150 kPa, respectively. While the consolidation of 50 kPa, 100 kPa, and 150 kPa were applied to the sample, the relative density of this non-plastic silt was somewhat increased by 20, 25, and 30%, respectively. An increase in density of the Sungun silt due to the application of σ'_{3c} seems to be more intense than what sand experienced during the consolidation process under the same conditions as reported by Karim and Alam (36).

5. 1. Influence of γ All cyclic tests were performed considering the shear amplitude of 0.75% and frequency of 0.3 Hz. Figure 13 shows loops of $u_e-\gamma$ and $\tau-\gamma$ for a cyclic test with a 100 kPa σ'_{3c} and 50 % density. It is evident that the most energy dissipation takes place at the first cycle having the highest stiffness. Besides, the maximum magnitude of u_e , the most reduction in shear modulus and stiffness, happened at the first cycle.

Variations of τ , γ , r_u , and W with the number of cycles N , are illustrated in Figures 14a to 14d, respectively. It is shown that applying the cyclic strain-control loading raises the u_e instantly, leading to a decrease in the shear stress capacity. In addition, W is monotonically increased with time until soil failure.

5. 2. Influences of τ_s and σ'_{3c} In this section, the impacts of in-situ τ_s and σ'_{3c} derived at sloping parts of the dam on pore pressure buildup, energy density and consequently, liquefaction potential of the current tailings dam are discussed. To this aim, a series of comparisons is provided to assess the role of τ_s .

First, variations of u_e versus W for the p' of 50 kPa, 100 kPa, and 150 kPa and three values for α , including 0, 0.2, and 0.4 were plotted in Figure 15. Clearly, there is a rational correlation between dissipated energy density

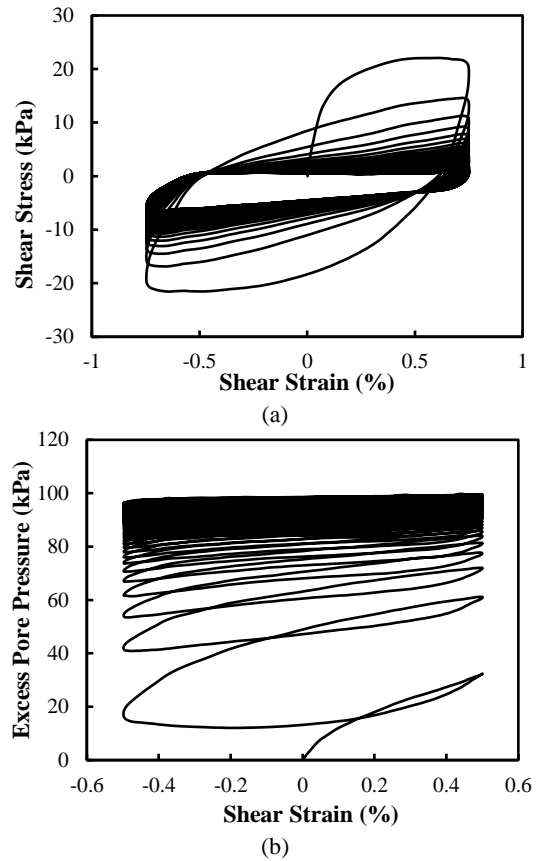
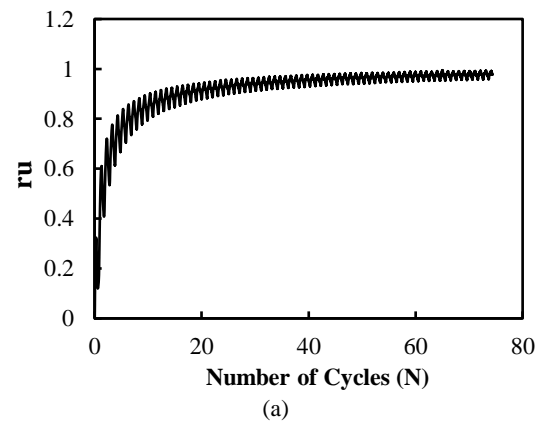
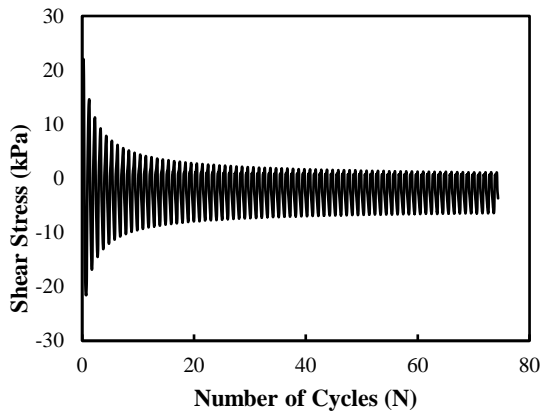


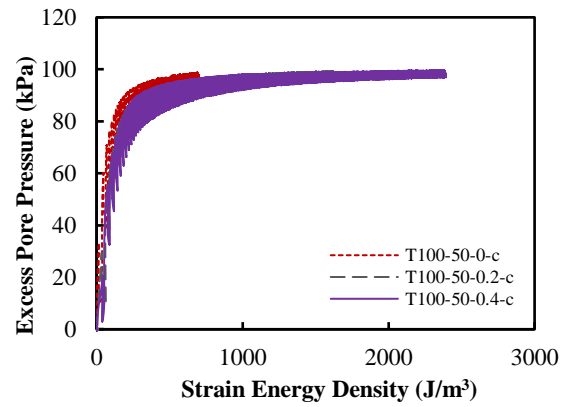
Figure 13. Results of cyclic tests in terms of the shear strain for Sungun silt when $D_r = 50\%$ and $\sigma'_{3c} = 100$ kPa

and pore pressure buildup in different conditions. The test results also implies that a considerable energy density is required for higher values of mean effective stress and α . In other words, the energy density necessitated at liquefaction time increases with p' and τ_s applied to the sample. As a result, mean effective stress and α have a significant impact on the Sungun pure silt from a viewpoint of liquefaction resistance. All tests were plotted until the corresponding liquefaction cycle number.

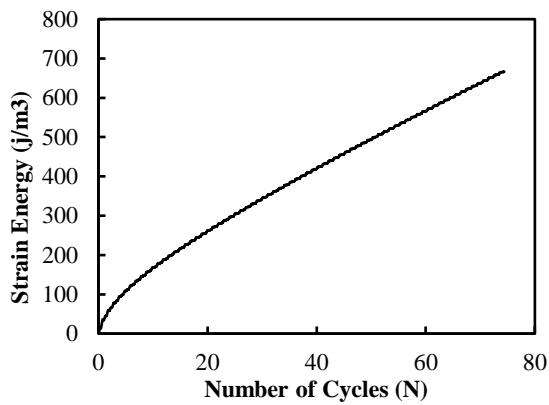




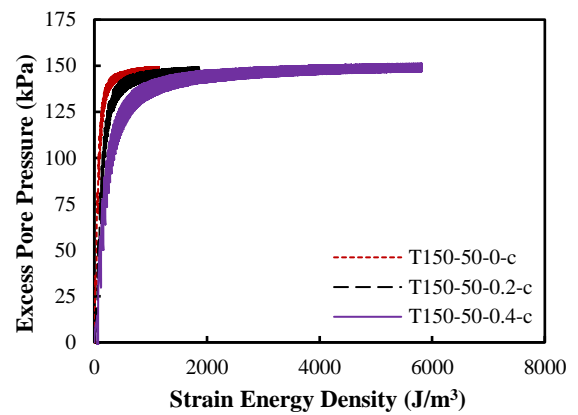
(b)



(b)



(c)



(c)

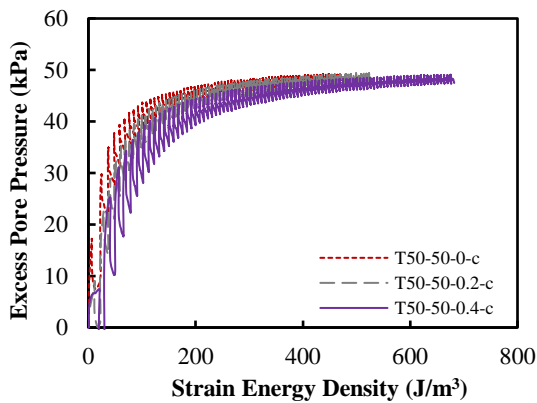
Figure 14. Results of cyclic tests in terms of the number of cycles for Sungun pure silt when $D_r=50\%$ and $\sigma_c=100$ kPa

Figure 15. Variations of u_e versus W at three σ'_{3c} values of 50,100 & 150 kPa, and α of 0, 0.2 & 0.4 on Sungun silts

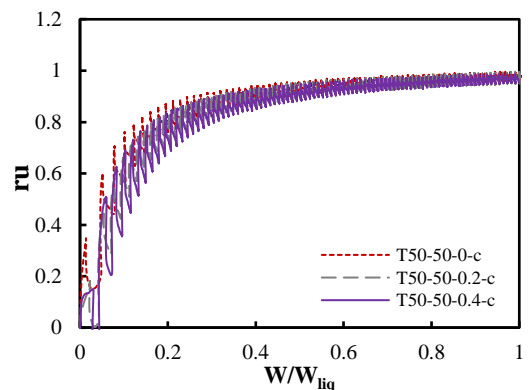
Figure 16 compares the impact of τ_s for three values of σ'_{3c} in terms of r_u-W/W_{liq} . As can be seen, there is no essential difference in the trends and magnitudes of all graphs. In other words, variation in τ_s reflects just a negligible impact on the r_u-W/W_{liq} relationship. This trend for the Sungun samples was roughly similar to that for Toyoura sand as concluded by Jafarian et al. (14). The similarity of r_u-W/W_{liq} curves could be a reflection of the

normalization of strain energy density (W) by capacity energy (W_{liq}). In other words, τ_s affects both strain energy and capacity energy simultaneously, and consequently, its influence is reduced essentially.

To indicate the impact of initial mean effective stress and τ_s (or adequate confining pressure σ'_{3c}) clearly, a set of diagrams compared the capacity energy of sample at the liquefaction time. As presented in Figure 17, the



(a)



(a)

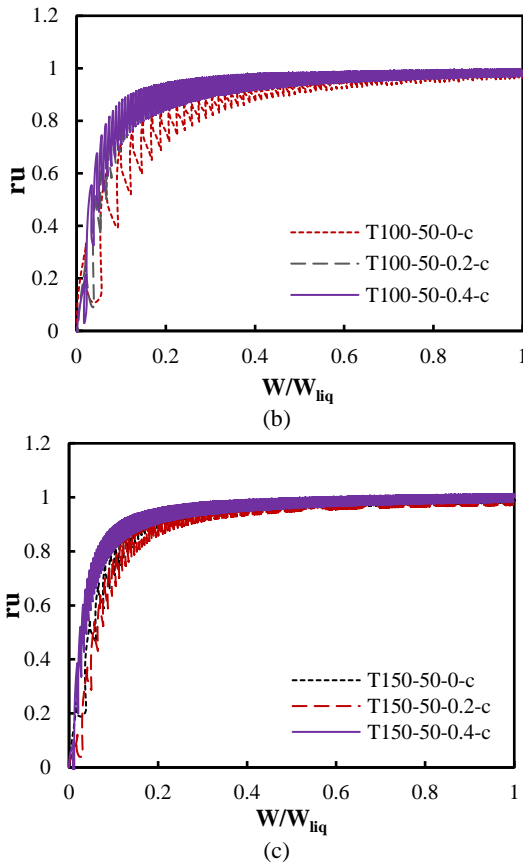


Figure 16. Variation of r_u against W/W_{liq} , at three σ'_{3c} values of 50,100 & 150 kPa, and α of 0, 0.2 & 0.4 on Sungu silt

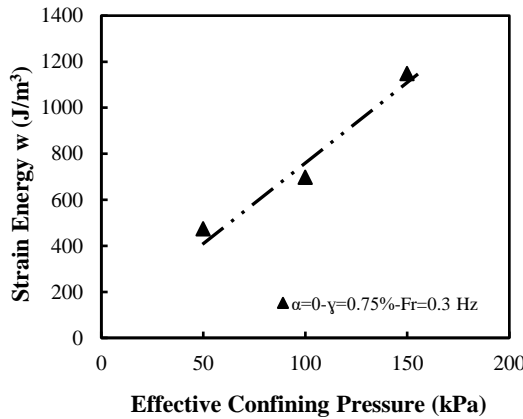


Figure 17. Variation of W required for liquefaction against σ'_{3c} in the current study

effect of σ'_{3c} is entirely evident in the amount of W . The more σ'_{3c} is applied, the further the level of W is gained. Thus, while two samples have a relatively similar density, the firmer one (with higher σ'_{3c}) requires greater energy density to be liquefied. This trend is in good agreement with that reported in some previous studies (14, 16, 30, 45) under both experimental and numerical modelings as shown in Figure 18.

Figure 19a presents three lines corresponding to three amounts considered for α . It should be noted that the rate of dissipated energy density dramatically increases with the α . For instance, the amount of energy density rises from 474 J/m³ to 1147.4 J/m³ for $\alpha = 0$, while it encounters a more intense increase from 682 J/m³ to 5839 J/m³ for $\alpha = 0.4$. Furthermore, Figure 19b illustrates the variation of dissipated W versus α . It is observed that the required energy for liquefaction rises with an increase in the α value. However, the increasing rate of energy

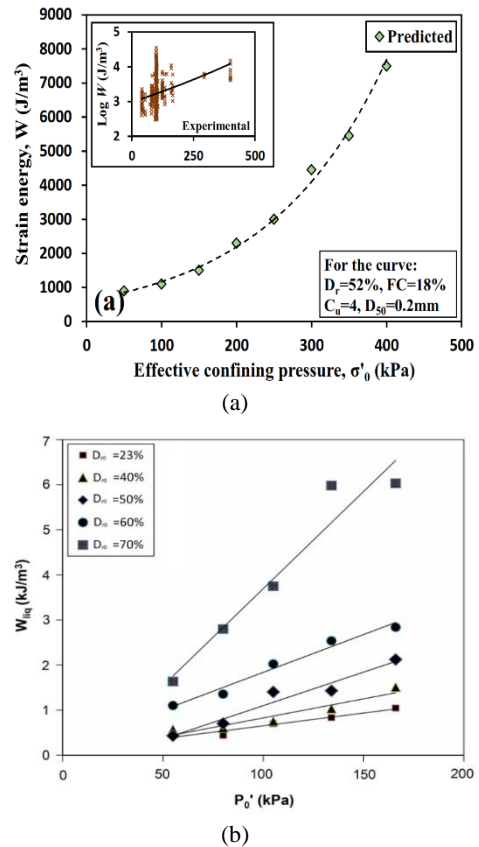
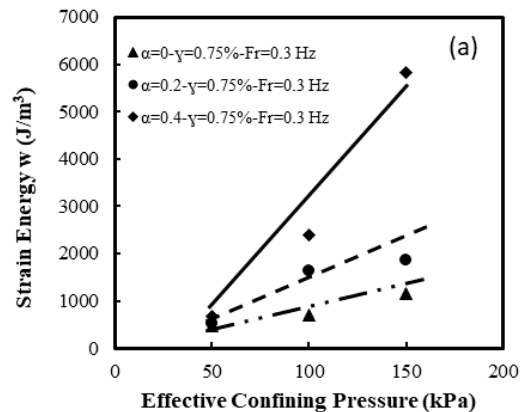


Figure 18. Variations of W against a) σ'_0 , Javdanian (45), b) σ'_{3c} , Jafarian et al. (14)



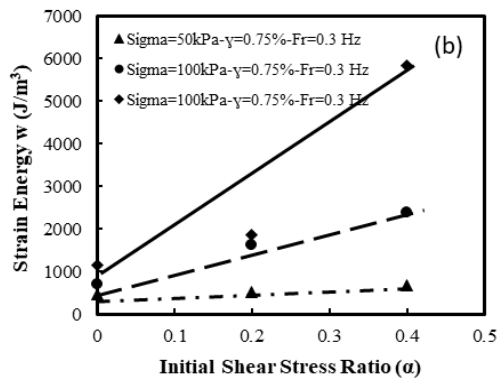


Figure 19. Variations of W against a) σ'_{3c} , b) α for pure silt in the current study

density is quite different for various σ'_{3c} . For example, under the lowest confining pressure (i.e., 50 kPa), when the τ_s was increased from 0 to 0.4, the growth of energy density was almost 204 J/m³, while increasing the σ'_{3c} up to 150 kPa, raised the growth of energy density to 4690 J/m³. This means that τ_s rather affects the energy dissipated for liquefaction, however, the increment rate strongly depends on the σ'_{3c} intensity.

6. CONCLUSION

The strain energy approach conventionally captures the simultaneous effects of stress and strain influence to assess the liquefaction phenomenon for clean sands or silty sand. Pure silt is found as a main part of tailings material extracted from the Sungun copper mine, which is susceptible to liquefaction. In this research, the liquefaction potential of silt-sized copper waste deposits behind the tailings dam was evaluated using the strain energy method. It considers the cyclic response of silt based on the quantity of strain energy per unit volume dissipated in the deposit. Several triaxial tests were conducted under different conditions to investigate the influences of effective mean stress p' (or confining pressure σ'_{3c}) and initial shear stress τ_s on the behavior of particular silts related to the Sungun copper tailings through monotonic and dynamic loadings.

Based on monotonic and cyclic test results obtained in the current research, the key findings may be drawn as follows:

1. Monotonic test results revealed a low tendency for a dilative response even at the dense states of Sungun silt. Density change after consolidation was moderately high even under low σ'_{3c} (e.g., 20% for 50 kPa), in contrast with that for granular materials reported in previous studies. The slight dilation in the dense samples stemming from the negligible reduction of pore pressure could attributed to the extremely small grains and the low roughness of the Sungun silt particles.

2. An increase of τ_s for monotonic tests led to a higher resistance in terms of shear stress.

3. A unique critical state line (CSL) was attained under different amounts of p' and α .

4. As the τ_s increased, the locus of shear stress approached the critical state line, and the deviator stress level required to reach the CSL was reduced.

5. Cyclic and monotonic test results showed the same trends. The energy density required for the liquefaction of Sungun pure silt was completely dependent upon σ'_{3c} and α . The capacity energy monotonically increased with σ'_{3c} . A sample with a higher D_r needed a greater energy density for the liquefaction. The cumulative energy density for liquefaction was directly proportional to τ_s .

6. The growth rate in capacity energy at higher σ'_{3c} was dramatically increased with τ_s . It rose sharply with any increase of σ'_{3c} at higher τ_s levels.

7. REFERENCES

1. Jafarzadeh Marandi M, Ghiasi V, Badv K. Numerical Evaluation of Two-dimensional Multi-layer Cover System to Regulate Acid Mine Drainage of Tailing Dams. *International Journal of Engineering, Transactions A: Basics*. 2023;36(10):1839-56. [10.5829/ije.2023.36.10a.10](https://doi.org/10.5829/ije.2023.36.10a.10)
2. USCOLD TDI. US Committee on Large Dams (USCOLD). Denver, Colorado. 1994.
3. Koketsu K, Miyake H. A seismological overview of long-period ground motion. *Journal of Seismology*. 2008;12(2):133-43. <https://doi.org/10.1007/s10950-007-9080-0>
4. Xu B, Wang Y. Stability analysis of the Lingshan gold mine tailings dam under conditions of a raised dam height. *Bulletin of Engineering Geology and the Environment*. 2015;74(1):151-61. <https://doi.org/10.1007/s10064-014-0602-z>
5. Naeini M, Akhtarpoor A. Numerical analysis of seismic stability of a high centerline tailings dam. *Soil Dynamics and Earthquake Engineering*. 2018;107:179-94. <https://doi.org/DOI:10.1016/j.soildyn.2018.01.019>
6. Hamed Sangari A, Marandi SM. Laboratory Studies on the Effect of Vertical Gravel Column Drains on Liquefaction Potential. *International Journal of Engineering*. 2011;24(3):209-26. https://www.ije.ir/article_71914_b325c15a6d012b938b1c9470f3233b11.pdf
7. Hanindya KA, Makrup L, Widodo, Paulus R. Deterministic Seismic Hazard Analysis to Determine Liquefaction Potential Due to Earthquake. *Civil Engineering Journal*. 2023;9(5):1203-16. [10.28991/CEJ-2023-09-05-012](https://doi.org/10.28991/CEJ-2023-09-05-012)
8. Latifi FE, Baba K, Ardouz G, Bouanani LE. Evaluation of Liquefaction Potential based on Cone Penetration Test (CPT) and Semi-empirical Methods. *Civil Engineering Journal*. 2023;9(2):423-36. [10.28991/CEJ-2023-09-02-013](https://doi.org/10.28991/CEJ-2023-09-02-013)
9. Özcan Çakır, Coşkun N. Dispersion of Rayleigh Surface Waves and Electrical Resistivities Utilized to Invert Near Surface Structural Heterogeneities. *Journal of Human, Earth, and Future*. 2022;3(1):1-16. [10.28991/HEF-2022-03-01-01](https://doi.org/10.28991/HEF-2022-03-01-01)
10. Seed HB, Idriss IM. Simplified procedure for evaluating soil liquefaction potential. *Journal of the Soil Mechanics and Foundations division*. 1971;97(9):1249-73. <https://doi.org/10.1061/JSFEAQ.0001662>

11. Ishihara K. Liquefaction and flow failure during earthquakes. *Geotechnique*. 1993;43(3):351-451. <https://doi.org/10.1680/geot.1993.43.3.351>
12. Vaid Y, Sivathayalan S. Static and cyclic liquefaction potential of Fraser Delta sand in simple shear and triaxial tests. *Canadian Geotechnical Journal*. 1996;33(2):281-9. <https://doi.org/10.1139/t96-007>
13. Nemat-Nasser S, Shokooch A. A unified approach to densification and liquefaction of cohesionless sand in cyclic shearing. *Canadian Geotechnical Journal*. 1979;16(4):659-78. <https://doi.org/10.1139/t79-076>
14. Jafarian Y, Towhata I, Baziar M, Noorzad A, Bahmanpour A. Strain energy based evaluation of liquefaction and residual pore water pressure in sands using cyclic torsional shear experiments. *Soil Dynamics and Earthquake Engineering*. 2012;35:13-28. <https://doi.org/10.1016/j.soildyn.2011.11.006>
15. Chen Y, Hsieh S, Chen J-W, Shih C. Energy-based probabilistic evaluation of soil liquefaction. *Soil Dynamics and Earthquake Engineering*. 2005;25(1):55-68. <https://doi.org/10.1016/j.soildyn.2004.07.002>
16. Baziar M, Sharafi H. Assessment of silty sand liquefaction potential using hollow torsional tests—An energy approach. *Soil Dynamics and Earthquake Engineering*. 2011;31(7):857-65. <https://doi.org/10.1016/j.soildyn.2010.12.014>
17. Whitman RV. Resistance of soil to liquefaction and settlement. *Soils and Foundations*. 1971;11(4):59-68. https://doi.org/10.3208/sandf1960.11.4_59
18. Baziar M, Jafarian Y. Assessment of liquefaction triggering using strain energy concept and ANN model: capacity energy. *Soil Dynamics and Earthquake Engineering*. 2007;27(12):1056-72. <https://doi.org/10.1016/j.soildyn.2007.03.007>
19. Zhang W, Goh AT, Zhang Y, Chen Y, Xiao Y. Assessment of soil liquefaction based on capacity energy concept and multivariate adaptive regression splines. *Engineering Geology*. 2015;188:29-37. <https://doi.org/10.1016/j.enggeo.2015.01.009>
20. Liang L. Development of an energy method for evaluating the liquefaction potential of a soil deposit: Case Western Reserve University; 1995.
21. Towhata I, Ishihara K. Shear work and pore water pressure in undrained shear. *Soils and foundations*. 1985;25(3):73-84. https://doi.org/10.3208/sandf1972.25.3_73
22. Boulanger RW, Seed RB. Liquefaction of sand under bidirectional monotonic and cyclic loading. *Journal of geotechnical engineering*. 1995;121(12):870-8. [https://doi.org/10.1061/\(ASCE\)0733-9410\(1995\)121:12\(870](https://doi.org/10.1061/(ASCE)0733-9410(1995)121:12(870)
23. Hosono Y, Yoshimine M. Effects of anisotropic consolidation and initial shear load on liquefaction resistance of sand in simple shear condition. *Geotechnical engineering for disaster mitigation and rehabilitation*. 2008:352-8. https://doi.org/10.1007/978-3-540-79846-0_37
24. Wei X, Yang J. Cyclic behavior and liquefaction resistance of silty sands with presence of initial static shear stress. *Soil Dynamics and Earthquake Engineering*. 2019;122:274-89. <https://doi.org/10.1016/j.soildyn.2018.11.029>
25. Pan K, Yang Z. Effects of initial static shear on cyclic resistance and pore pressure generation of saturated sand. *Acta Geotechnica*. 2018;13(2):473-87. <https://doi.org/10.1007/s11440-017-0614-5>
26. Marandi SM, Rasti AR. Parametric Study of the Covering Soil of Tunnels Constructed in Liquefiable Soil. *International Journal of Engineering*. 2012;25(4):333-46. <https://doi.org/10.5829/idosi.ije.2012.25.04a.05>
27. Iraj A. Evaluating Finn-Byrne Model in Liquefaction Analysis of Quay Wall and Cantilevered Retaining Wall Models. *International Journal of Engineering*. 2023;36(6):1075-91. <https://doi.org/10.5829/ije.2023.36.06c.06>
28. Fakharian K, Shabani F. Monotonic and cyclic experimental results of Chamkhaleh SAND in southern Caspian Sea. The Twenty-first International Offshore and Polar Engineering Conference. 2011. https://www.researchgate.net/publication/370124695_Monotonic_and_Cyclic_Experimental_Results_of_Chamkhaleh_Sand_in_Southern_Caspian_Sea
29. Hoseini MH, Noorzad A, Zamanian M. Physical Modelling of a Strip Footing on a Geosynthetic Reinforced Soil Wall Containing Tire Shred Subjected to Monotonic and Cyclic Loading. *International Journal of Engineering*. 2021;34(10):2266-79. <https://doi.org/10.5829/ije.2021.34.10a.08>
30. Lee KL, Seed HB. Dynamic strength of anisotropically consolidated sand. *Journal of the Soil Mechanics and Foundations Division*. 1967;93(5):169-90. <https://doi.org/10.1061/JSFEAQ.0001019>
31. Seed HB. Earthquake-resistant design of earth dams. 1981.
32. Hosono Y, Yoshimine M, editors. Liquefaction of sand in simple shear condition. Proceedings of the international conference on cyclic behaviour of soils and liquefaction phenomena, Bochum, Germany; 2004. <https://doi.org/10.1201/9781439833452.ch16>
33. Hezarkhani A. Calculation of Mass Transfer and Element Mobility During the Hydrothermal Alteration in the Sungun PORPHYRY Copper Deposit Iran. *International Journal of Engineering*. 2002;15(4):391-408. https://www.ije.ir/article_71405_886c695fec0df2515fb2215538e9fa66.pdf
34. Ahmadi A, Bazaz JB. A new analytical model to predict the effect of suction removal on vacuum preloading of fine copper tailings. *Engineering Geology*. 2023;322:107176. <https://doi.org/10.1016/j.enggeo.2023.107176>
35. Ladd R. Preparing test specimens using undercompaction. *Geotechnical testing journal*. 1978;1(1):16-23. <https://doi.org/10.1520/GTJ10364J>
36. Karim ME, Alam M. Effect of nonplastic silt content on undrained shear strength of sand-silt mixtures. *International Journal of Geo-Engineering*. 2017;8(1):1-26. <https://doi.org/10.1186/s40703-017-0051-1>
37. Ishihara K, Tatsuoka F, Yasuda S. Undrained deformation and liquefaction of sand under cyclic stresses. *Soils and foundations*. 1975;15(1):29-44. <https://doi.org/10.3208/sandf1972.15.29>
38. Zhao J, Guo N. Unique critical state characteristics in granular media considering fabric anisotropy. *Géotechnique*. 2013;63(8):695-704. <https://doi.org/10.1680/geot.12.P.040>
39. Vaid YP, Chern J-C. Effect of static shear on resistance to liquefaction. *Soils and foundations*. 1983;23(1):47-60. <https://doi.org/10.3208/sandf1972.23.47>
40. Rasouli M, Moradi M, Ghalandarzadeh A. Effects of initial static shear stress orientation on cyclic behavior of calcareous sand. *Marine Georesources & Geotechnology*. 2021;39(5):554-68. <https://doi.org/10.1080/1064119X.2020.1726535>
41. Nadjafi M, Gholami P. Reliability Analysis of Notched Plates under Anisotropic Damage Based on Uniaxial Loading Using Continuum Damage Mechanics Approach. *International Journal of Engineering*. 2021;34(1):253-62. <https://doi.org/10.5829/ije.2021.34.01a.28>
42. Labibi H, Gerami M, Hosseini M. Sensitivity Analysis of Behavior of Simple Trapezoidal Steel Plates to Introduce a New Yielding Damper. *International Journal of Engineering*. 2021;34(10):2302-12. <https://doi.org/10.5829/ije.2021.34.10a.11>

- https://www.ije.ir/article_135667_63950229f30671722991ba6c2fc875a5.pdf
43. Ravikumar S, Kothandaraman S. Experimental Study on Performance of Ductile and Non-ductile Reinforced Concrete Exterior Beam-column Joint. *International Journal of Engineering*. 2022;35(7):1237-45. 10.5829/ije.2022.35.07a.03 https://www.ije.ir/article_147153_bc7874f6272869eca36d21efa0ff30c3.pdf
44. Danesh N, Mahmoodabadi MJ, Fathi AR. Investigation of the Damping Performance of a Shape Memory Alloy Beam. *International Journal of Engineering*. 2023;36(7):1369-82. 10.5829/ije.2023.36.07a.17 https://www.ije.ir/article_168122_470fa321ebd4ef0928a196fe888c0238.pdf
45. Javdanian H. Evaluation of soil liquefaction potential using energy approach: experimental and statistical investigation. *Bulletin of Engineering Geology and the Environment*. 2019;78(3):1697-708. <https://doi.org/10.1007/s10064-017-1201-6>

COPYRIGHTS

©2024 The author(s). This is an open access article distributed under the terms of the Creative Commons Attribution (CC BY 4.0), which permits unrestricted use, distribution, and reproduction in any medium, as long as the original authors and source are cited. No permission is required from the authors or the publishers.

**Persian Abstract****چکیده**

فعالیت های معدنی، از جمله اکتشاف، حفاری، و ساخت و ساز، اخیراً رشد چشمگیری داشته است. از این رو؛ استفاده از ضایعات معدنی با کمترین آسیب زیست محیطی یک نگرانی قابل توجه بوده است. سدهای باطله یکی از راه حل های رایجی است که زباله های حفاری را به منظور حفاظت از محیط زیست و حفظ منابع آب به صورت ایمن ذخیره می کند. این مقاله به عنوان مطالعه موردی به بررسی اثر بارهای یکنواخت و لرزه ای بر سیلت خالص مورد استفاده در یک سد باطله در شمال غرب ایران می پردازد. مقادیر مختلف تنش برشی استاتیک اولیه با استفاده از یک سیستم سه محوری سیکلی خودکار انجام می شود. آزمایش های فشاری زهکشی نشده مونوتونیک با تراکم نسبتاً ثابت و با در نظر گرفتن سه مقدار ۵۰، ۱۰۰ و ۱۵۰ کیلو پاسکال برای تنش مؤثر میانگین انجام شد. بسته به تراکم اولیه نمونه ها، با اعمال فشار محصور کننده موثر ۱۰۰ کیلو پاسکال، دانسیته های اولیه را بین ۲۵ تا ۳۰ درصد نسبت به شرایط اولیه افزایش داد. همچنین اثر نسبت تنش برشی استاتیکی اولیه با سه مقدار صفر، ۰/۲ و ۰/۴ نیز مورد ارزیابی قرار گرفت. هیچ نقطه ای اوجی برای نمونه های تحت شرایط $\alpha = 0$ مشاهده نشد، در حالی که، نمونه هایی با شرایط $\alpha = 0.4$ قبل از رسیدن به نقطه تبدیل فاز با یک نقطه اوج مواجه شدند. نتایج آزمایش های سیکلی به منظور ارزیابی انرژی ظرفیت و فشار منفذ باقی مانده بر اساس رویکرد انرژی کرنش استفاده شدند. آزمایش های سیکلی بر روی نمونه ها با در نظر گرفتن دامنه برشی ۰/۷۵ درصد و فرکانس ۰/۳ هرتز انجام گردید. نشان داده شده است که بیشترین اتلاف انرژی در اولین سیکل با بالاترین سختی رخ می دهد. برای $\alpha = 0$ ، چگالی انرژی از $474(J/m^3)$ به $1147/4(J/m^3)$ افزایش یافت، با این حال، افزایش شدیدتر در چگالی انرژی در شرایط $\alpha = 0.4$ از $682(J/m^3)$ به $5839(J/m^3)$ اندازه گیری گردید. همچنین مشخص شده است که اعمال تنش برشی اولیه تأثیر قابل توجهی بر مقاومت مونوتونیک و نیز مقاومت روانگرایی سیلت ها دارد. افزایش α از صفر به ۰/۴ باعث افزایش خطی مقاومت برشی نمونه ها در محدوده ۲۰ کیلو پاسکال تا ۷۰ کیلو پاسکال شد. سپس نتایج این مقاله از طریق برخی مطالعات قبلی به طور دقیق تأیید شدند.

AIMS AND SCOPE

The objective of the International Journal of Engineering is to provide a forum for communication of information among the world's scientific and technological community and Iranian scientists and engineers. This journal intends to be of interest and utility to researchers and practitioners in the academic, industrial and governmental sectors. All original research contributions of significant value focused on basics, applications and aspects areas of engineering discipline are welcome.

This journal is published in three quarterly transactions: Transactions A (Basics) deal with the engineering fundamentals, Transactions B (Applications) are concerned with the application of the engineering knowledge in the daily life of the human being and Transactions C (Aspects) - starting from January 2012 - emphasize on the main engineering aspects whose elaboration can yield knowledge and expertise that can equally serve all branches of engineering discipline.

This journal will publish authoritative papers on theoretical and experimental researches and advanced applications embodying the results of extensive field, plant, laboratory or theoretical investigation or new interpretations of existing problems. It may also feature - when appropriate - research notes, technical notes, state-of-the-art survey type papers, short communications, letters to the editor, meeting schedules and conference announcements. The language of publication is English. Each paper should contain an abstract both in English and in Persian. However, for the authors who are not familiar with Persian, the publisher will prepare the latter. The abstracts should not exceed 250 words.

All manuscripts will be peer-reviewed by qualified reviewers. The material should be presented clearly and concisely:

- *Full papers* must be based on completed original works of significant novelty. The papers are not strictly limited in length. However, lengthy contributions may be delayed due to limited space. It is advised to keep papers limited to 7500 words.
- *Research notes* are considered as short items that include theoretical or experimental results of immediate current interest.
- *Technical notes* are also considered as short items of enough technical acceptability with more rapid publication appeal. The length of a research or technical note is recommended not to exceed 2500 words or 4 journal pages (including figures and tables).

Review papers are only considered from highly qualified well-known authors generally assigned by the editorial board or editor in chief. Short communications and letters to the editor should contain a text of about 1000 words and whatever figures and tables that may be required to support the text. They include discussion of full papers and short items and should contribute to the original article by providing confirmation or additional interpretation. Discussion of papers will be referred to author(s) for reply and will concurrently be published with reply of author(s).

INSTRUCTIONS FOR AUTHORS

Submission of a manuscript represents that it has neither been published nor submitted for publication elsewhere and is result of research carried out by author(s). Presentation in a conference and appearance in a symposium proceeding is not considered prior publication.

Authors are required to include a list describing all the symbols and abbreviations in the paper. Use of the international system of measurement units is mandatory.

- On-line submission of manuscripts results in faster publication process and is recommended. Instructions are given in the IJE web sites: www.ije.ir-www.ijeir.info
- Hardcopy submissions must include MS Word and jpg files.
- Manuscripts should be typewritten on one side of A4 paper, double-spaced, with adequate margins.
- References should be numbered in brackets and appear in sequence through the text. List of references should be given at the end of the paper.
- Figure captions are to be indicated under the illustrations. They should sufficiently explain the figures.
- Illustrations should appear in their appropriate places in the text.
- Tables and diagrams should be submitted in a form suitable for reproduction.
- Photographs should be of high quality saved as jpg files.
- Tables, Illustrations, Figures and Diagrams will be normally printed in single column width (8cm). Exceptionally large ones may be printed across two columns (17cm).

PAGE CHARGES AND REPRINTS

The papers are strictly limited in length, maximum 8 journal pages (including figures and tables). For the additional to 8 journal pages, there will be page charges. It is advised to keep papers limited to 3500 words.

Page Charges for Papers More Than 8 Pages (Including Abstract)

For International Author ***	\$55 / per page
For Local Author	100,000 Toman / per page

AUTHOR CHECKLIST

- Author(s), bio-data including affiliation(s) and mail and e-mail addresses).
- Manuscript including abstracts, key words, illustrations, tables, figures with figure captions and list of references.
- MS Word files of the paper.



THOMSON REUTERS

WEB OF SCIENCE



Scopus®



CAS®

A DIVISION OF THE
AMERICAN CHEMICAL SOCIETY



 Crossref



Scientific Indexing Services

Google
Scholar